UNIVERSITÄT BAYREUTH

Präklinische Studien neuer multimodaler, antitumoraler Hybridwirkstoffe mittels klassischer 2D- und realitätsnäherer 3D-Tumorzellkulturassays

DISSERTATION

vorgelegt von

Sofia Isolde Bär

geboren in Bayreuth

Bayreuth, 2023

UNIVERSITÄT BAYREUTH

Präklinische Studien neuer multimodaler, antitumoraler Hybridwirkstoffe mittels klassischer 2D- und realitätsnäherer 3D-Tumorzellkulturassays

DISSERTATION

zur Erlangung des akademischen Grades einer
Doktorin der Naturwissenschaften (Dr. rer. nat.)
an der Fakultät für Biologie, Chemie und Geowissenschaften
der Universität Bayreuth

vorgelegt von
Sofia Isolde Bär
geboren in Bayreuth

Bayreuth, 2023

Die vorliegende Arbeit wurde in der Zeit von März 2020 bis September 2022 in Bayreuth am Lehrstuhl für Organische Chemie I der Universität Bayreuth unter der Betreuung von Herrn Prof. Dr. Rainer Schobert angefertigt.

Vollständiger Abdruck der von der Fakultät für Biologie, Chemie und Geowissenschaften der Universität Bayreuth genehmigten Dissertation zur Erlangung des akademischen Grades einer Doktorin der Naturwissenschaften (Dr. rer. nat.).

Dissertation eingereicht am:	14.09.2022
Zulassung durch die Promotionskommission:	21.09.2022
Wissenschaftliches Kolloquium:	08.05.2023

Amtierender Dekan: Prof. Dr. Benedikt Westermann

Prüfungsausschuss:

Prof. Dr. Rainer Schobert	(Gutachter)
Prof. Dr. Stephan Schwarzinger	(Gutachter)
Prof. Dr. Matthias Ullmann	(Vorsitz)

Prof. Dr. Klaus Ersfeld

(Weitere Gutachter: Prof. Dr. Olaf Stemmann)

„Ich habe gelernt, dass der Weg des Fortschritts weder kurz noch unbeschwerlich ist.“

- Marie Skłodowska Curie

Inhaltsverzeichnis

Abkürzungsverzeichnis

ADME	Absorption, Distribution, Metabolismus und Elimination
CA-4	Combretastatin A-4
CCC	cholangiozellularem Karzinom
CDDP	*cis*-Diammindichloroplatin(II)
DLC	*delocalized lipophilic cation*
DMSO	Dimethylsulfoxid
DNA	Desoxyribonukleinsäure
EGFR	*epidermal growth factor receptor*
EMSA	*electrophoretic mobility shift assay*
EtdBr	Ethidiumbromid
EZM	Extrazelluläre Matrix
HCC	hepatozellulärem Karzinom
HER2	*human epidermal growth factor receptor 2*
HAT	Histon-Acetyltransferasen
HDAC	Histondeacetylase
HDACi	HDAC Inhibitor
HSP	*heat shock protein*
IAP	*inhibitor of apoptosis protein*
IC_{50}	halbmaximale, inhibitorische Konzentration
IgG	Immunglobulin-G
LDH	Lactat Dehydrogenase
LMP	lysosomale Membran Permeabilisierung
mAbs	monoklonale Antikörper
MCTS	*multicellular tumour spheroids*
MMP	Matrixmetalloprotease
$\Delta\Psi m$	mitochondriales Membranpotenzial
MTIC	Methyltriazenoimidazol-carboxamid
MTT	3-(4,5-Dimethylthiazol-2-yl)-2,5-diphenyltetrazoliumbromid
NCI	*national cancer institute*
NF-κB	Nuklearfaktor kappa-B
NHC	N-heterozyklisches Carben
p27	Cyclin-abhängiger Kinase-Inhibitor 1B
PI	Propidiumiodid
ROS	reaktive Sauerstoffspezies
RTK	Rezeptor Threonin-Kinase
SAHA	Suberoylanilid Hydroxamsäure

SI	Selektivitätsindex
STK	Serin/Threonin-Kinase
TKI	Tyrosinkinase Inhibitor
TrxR	Thioredoxin Reduktase
TSA	Trichostatin A
UPP	*ubiquitin proteasome pathway*
VEGF	*vascular endothelial growth factor*
VEGFR	VEGF Rezeptor

Bei allen weiteren Abkürzungen handelt es sich um gängige Abkürzungen und SI-Einheiten, welche laut ihrer Definition verwendet wurden.

Summary

Cancer continues to be at the center of the health problems of our century. In addition to the health burden for those affected, the burden on the health care system and the social system also represents an enormous societal problem. In the field of anti-tumour agents, enormous progress has been made in the last decade, made possible by intensive medical and molecular biology research. In the context of the rising world population, the demand for cancer drugs is increasing and the number of treatment-resistant cases is also rising. In addition, the late detected cancer cases, related to the Covid-19 pandemic, bring the current cancer related medical situation to a sharp climax. These factors highlight the relevance of research into new therapeutic options, with cost and resource savings also becoming increasingly central.

In this thesis, new potential chemotherapeutic agents combining structural properties of different established anticancer drug groups were preclinically evaluated to circumvent existing resistances and to establish new mechanisms of action. Their pleiotropic mechanism of action was investigated. In parallel, three-dimensional cell models were used to increase the relevance of preclinical findings. They improve the resource efficiency of basic research and help to gain deeper insight in tumour associated effects.

The drug series investigated in this work can be classified broadly into two categories. On the one hand, hybrid metal-based drugs, on the other hand, chimeric histone deacetylase inhibitors (HDACi).

The series of platinum-based compounds are derived from the successful chemotherapeutic agent cisplatin, for which alternatives are urgently needed due to numerous severe side effects and increasing number of detected cancer cases. By combining the platinum complex with an N-heterocyclic carbene (NHC) motif, the stability of the complexes was increased while introducing numerous structural variation possibilities.

A neutral and a cationic *cis*-[bis(1,3-dibenzylimidazol-2-ylidene)Cl(L)]platinum(II) complex showed potent cytotoxic effect on cancer cells, associated with intracellular accumulation in mitochondria. NHC ligands altered the DNA-associated mechanism of action typical of cisplatin. Introduction of a cationic character enhanced cellular uptake and eventually induced mitochondrial induced apoptosis in 518A2 melanoma cells.

The comparison of a *cis*-series with the corresponding *trans*-series of bis(benzimidazol-2-ylidene)dichlorido]platinum(II) complexes reverses the paradigm of only *cis*-platinum complexes being suitable cancer therapeutics. *Trans*-Pt complexes of this series showed strong cancer-specific cytotoxicity even in the cisplatin-resistant HT-29 colon carcinoma cell line. In addition, fluorescence microscopy demonstrated enrichment of the *trans*-configured complexes outside the nucleus, excluding a cisplatin-typical mechanism of action.

The other group of metal-based hybrid agents is based on Au as the central atom. A series of 1,3-diethyl-4-(p-methoxyphenyl)-5-(3,4,5-trimethoxyphenyl)imidazol-2-ylidene(L)gold(I) complexes induced

apoptosis in cancer cells, independent of their p53 functionality. A dependence of intracellular accumulation in different organelles on charge, size and lipophilicity of the ligands could be demonstrated by confocal microscopy. This concept allows organelle-specific intracellular accumulation of certain bioactive agents through specific ligands, thus enabling a reduction in side effects.

A series of phosphane(9-ribosylpurine-6-thiolato)gold(I) complexes combines metal complexes with heterocyclic antimetabolites. Here, the hybrid structure improved cytotoxicity and selectivity towards cancer cells. In addition, the complexes showed high efficacy against multidrug-resistant as well as p53 mutant tumour cells.

The second class of compounds investigated in this work are chimeric HDACi, which combine the structural motifs of the vascular disruptive compound CA-4 with that of the FDA-approved HDAC inhibitor SAHA. A promising compound with the trivial name broxbam has been investigated for its potential suitability in the treatment of liver carcinomas using corresponding cell lines. Its inhibitory effect on HDAC 6 is significantly stronger than that of the established drug SAHA. This is accompanied by reduced migration, anti-angiogenic effects, and apoptosis induction. Broxbam also induces significant growth inhibition of hepatoblastoma microtumours in a 3D tumour model.

Further representatives of this substance class were investigated with regard to their effect on colon carcinoma cell lines. The chimeric structure significantly improved cancer-selective cytotoxicity. In connection with this, a reduction in expression of the cancer-specific apoptosis inhibitor survivin was demonstrated.

Finally, the therapeutic potential of this class of compounds was investigated using 3D cell culture assays to obtain a better assessment of the effect of the compounds in multicellular tumour assemblies and thus to make a more precise statement regarding their suitability as anticancer drugs. First, the effect of the two chimeric HDACi compounds troxbam and troxham on multicellular tumour spheroids (MCTS) was investigated. In contrast to 2D cell cultures, 3D models consider the influence of tumour microenvironment, gradients of nutrients, oxygen, and drug concentration. Also, in the 3D model, the chimeric compounds convinced by significant growth inhibition and caspase 9 mediated apoptosis induction. Using a bioreactor system, an animal model was mimicked to study the tumour growth inhibitory effect in larger tumours, and an impressive effect was also documented. A derivative of the chimeric structure series also showed great potential in 3D tumour systems, far surpassing its structural relatives in terms of selectivity.

Zusammenfassung

Krebs steht nach wie vor im Zentrum der gesundheitlichen Probleme unseres Jahrhunderts. Neben der gesundheitlichen Belastung für Betroffene, stellt die Belastung des Gesundheits- als auch des Sozialsystems auch ein enormes gesellschaftliches Problem dar. Im Bereich der antitumoralen Wirkstoffe konnte in der letzten Dekade ein enormer Fortschritt verzeichnet werden, welcher durch intensive medizinische und molekularbiologische Forschung ermöglicht wurde. Im Zusammenhang mit der wachsenden Weltbevölkerung, steigt die Nachfrage nach Krebsmedikamenten und die Anzahl an Therapie-resistenten Fällen nimmt zu. Zusätzlich steigt die Zahl an spät erkannten Krebserkrankungen in Zusammenhang mit der Covid-19 Pandemie. Diese Faktoren spitzen die aktuelle Lage zu. Das verdeutlicht die Relevanz der Forschung an neuen Therapiemöglichkeiten, wobei auch die Kosten- und Ressourceneinsparung immer zentraler wird.

Im Rahmen dieser Arbeit wurden neue potenzielle Chemotherapeutika, welche strukturelle Eigenschaften verschiedener etablierter krebshemmender Wirkstoffgruppen vereinen, präklinisch evaluiert, um bestehende Resistenzen zu umgehen und neue Wirkmechanismen zu etablieren. Deren hybrider Wirkmechanismus wurde untersucht, wobei parallel unter Einbezug dreidimensionaler Zellmodelle die Relevanz der gewonnenen präklinischen Erkenntnisse erhöht werden sollte, um die Grundlagenforschung ressourcenschonender zu gestalten und um tiefere Einblicke in tumorassoziierte Effekte zu ermöglichen.

Die Wirkstoffserien, welche im Rahmen dieser Arbeit untersucht wurden, lassen sich grob in zwei Klassen einteilen. Zum einen hybride Metall-basierte Wirkstoffe, zum anderen chimäre Histondeacetylaseinhibitoren (HDACi).

Die Serien Platin-basierter Substanzen, sind abgeleitet vom erfolgreichen Chemotherapeutikum Cisplatin, für welches durch zahlreiche schwere Nebenwirkungen und zunehmende Anzahl neu diagnostizierter Krebserkrankungen dringend Alternativen benötigt werden. Durch die Kombination des Platin-Komplexes mit einem N-heterocyclischen Carben (NHC) Motiv wurde die Stabilität der Komplexe erhöht und gleichzeitig zahlreiche strukturelle Variationsmöglichkeiten eingebracht.

Ein neutraler und ein kationischer *cis*-[Bis(1,3-dibenzylimidazol-2-yliden)Cl(L)]platin(II)-Komplex, zeigten starke zytotoxische Wirkung auf Krebszellen, assoziiert mit intrazellulärer Anreicherung in den Mitochondrien. Durch die NHC-Liganden wurde der für Cisplatin typische DNA assoziiert Wirkmechanismus verändert. Durch Einführung eines kationischen Charakters wurde die zelluläre Aufnahme verbessert und schließlich mitochondrial induzierte Apoptose in 518A2 Melanomzellen ausgelöst.

Der Vergleich einer *cis*-Serie mit der entsprechenden *trans*-Serie von Bis(benzimidazol-2-yliden)dichlorido]platin(II)-Komplexen, bricht mit dem Paradigma dass nur *cis*-Platin-Komplexe geeignete Krebstherapeutika seien. *Trans*-Pt-Komplexe dieser Serie zeigten starke krebsspezifische Zytotoxizität auch bei der Cisplatin resistenten HT-29 Kolonkarzinom Zelllinie. Zudem konnte mittels

Fluoreszenzmikroskopie eine Anreicherung der *trans*-konfigurierten Komplexe außerhalb des Zellkerns nachgewiesen werden, was einen Cisplatin-typischen Wirkmechanismus ausschließt.

Die andere Gruppe Metall-basierter hybrider Wirkstoffe basiert auf Au als Zentralatom. Eine Serie von 1,3-Diethyl-4-(*p*-methoxyphenyl)-5-(3,4,5-trimethoxyphenyl)imidazol-2-yliden(L)gold(I)-Komplexen induzierte zum einen Apoptose in Krebszellen, unabhängig von deren p53 Funktionalität. Zum anderen konnte mittels konfokalmikroskopischer Untersuchungen eine Abhängigkeit der intrazellulären Anreicherung in verschiedene Organelle von Ladung, Größe und Lipophilie der Liganden nachgewiesen werden. Dieses Konzept ermöglicht durch bestimmte Liganden die organellspezifische intrazelluläre Anreicherung bestimmter bioaktiver Wirkstoffe und somit eine Verringerung der Nebenwirkungen.

Eine Serie von Phosphan(9-ribosylpurin-6-thiolato)gold(I)-Komplexen vereint Metall-Komplexe mit heterocyclischen Antimetaboliten. Hier konnten durch die hybride Struktur Zytotoxizität und Selektivität gegenüber Krebszellen verbessert werden. Zudem zeigten die Komplexe hohe Wirksamkeit sowohl gegen multiresistente als auch p53 mutante Tumorzellen.

Die zweite Klasse, der im Rahmen dieser Arbeit untersuchten Substanzen, bilden chimäre HDACi, welche die Strukturmotive der vaskular disruptiven Verbindung CA-4 mit dem des FDA zugelassenen HDACi SAHA verbinden. Eine vielversprechende Substanz mit dem Trivialnamen Broxbam wurde hinsichtlich ihrer potenziellen Eignung zur Behandlung von Leberkarzinomen an entsprechenden Zelllinien untersucht. Ihre inhibierende Wirkung auf HDAC 6 ist dabei signifikant stärker als die des etablierten Wirkstoffs SAHA. Damit einher gehen verringerte Migration, anti-angiogene Effekte und Induktion von Apoptose. Auch im 3D Modell induziert Broxbam eine signifikante Wachstumsinhibition von Hepatoblastom-Mikrotumoren.

Weitere Vertreter dieser Substanzklasse wurden hinsichtlich ihrer Wirkung auf Kolonkarzinom Zelllinien untersucht. Durch die chimäre Struktur konnte die krebsselektive Zytotoxizität deutlich verbessert werden. Im Zusammenhang damit konnte eine Verringerung der Expression des Krebs-spezifischen Apoptose-Inhibitors Survivin nachgewiesen werden.

Das therapeutische Potenzial dieser Verbindungsklasse wurde schließlich mittels 3D Zellkulturassays untersucht, um die Wirkung der Substanzen im 3D Zellverbund besser abschätzen, und somit eine präzisere Aussage bezüglich ihrer Eignung als Krebsmedikamente treffen zu können. Zunächst wurde die Wirkung der chimären HDACi Substanzen Troxbam und Troxham auf *multicellular tumour spheroids* (MCTS) untersucht. Im Gegensatz zu 2D Zellkulturen, berücksichtigen 3D Modelle den Einfluss der Tumormikroumgebung, Gradienten von Nährstoffen, Sauerstoff und Wirkstoff. Auch im 3D Modell überzeugten die hybriden Substanzen durch signifikante Wachstumsinhibition und Caspase 9 vermittelte Apoptoseinduktion. Mittels Bioreaktorsystem wurde ein Tiermodell nach-empfunden, um die wachstumsinhibierende Wirkung in größeren Tumoren untersuchen zu können, wobei ebenfalls ein eindrücklicher Effekt dokumentiert werden konnte. Ein Derivat zeigte auch im 3D Tumor-Systemen großes Potenzial, welches die Selektivität seiner Strukturverwandten bei weitem übertrifft.

1 Einleitung

1.1 Krebs als gesundheitliches und gesellschaftliches Problem

Im Jahr 2022 zählen Krebserkrankungen zu den führenden Todesursachen weltweit.[1] Neben jährlich etwa 10 Millionen registrierten Todesfällen in Folge einer Krebserkrankung, werden weltweit auch etwa 20 Millionen Neuerkrankungen gemeldet.[1, 2] Statistisch erkranken jeder zweite Mann und jede dritte Frau im Laufe ihres Lebens mindestens einmal an Krebs. Die häufigsten Formen von Neuerkrankungen sind dabei Krebserkrankungen der weiblichen Brust, der Lunge, des Darms und der männlichen Prostata.[1, 2] Aufgrund der global steigenden Bevölkerungszahlen, aber auch der verbesserten Früherkennungsmethoden, wird eine Erhöhung der Neuerkrankungen auf 28.4 Millionen neue Fälle bis 2040 prognostiziert.[1, 2]

Krebserkrankungen stellen neben ihrer gesundheitlichen Belastung für Betroffene auch durch die Belastung des Gesundheits- und des Sozialsystems, ein enormes gesellschaftliches Problem dar. Die finanzielle Belastung stellt ein weiteres Problem im Zusammenhang mit Krebserkrankungen dar.[3] Neben den reinen materiellen Behandlungskosten, stehen unter anderem Kosten für psychologische Therapien, Arbeitsunfähigkeit, Kinderbetreuung und Rehamaßnahmen in direktem Zusammenhang mit einer Krebsdiagnose.[3]

Zu den Problemen der steigenden Zahlen und der steigenden finanziellen Last kommen noch krebsspezifische Resistenzprobleme, welche die Lage weiter zuspitzen. Ein weiterer Faktor, welcher die medizinische Lage der letzten Jahre maßgeblich beeinflusst hat, ist die Covid-19 Pandemie.[4] Zum einen führte die parallele Erkrankung von Krebspatienten mit Covid in einem Drittel der Fälle zu einer drastischen Verschlechterung der Überlebensprognose. Zum anderen kam ein Faktor zum Tragen, dessen Auswirkungen bis heute signifikant sind.[4] Infolge der zahlreichen Einschränkungen im Zuge der Pandemie, versagte das Krebsfrüherkennungssystem in zahlreichen Fällen und verzögerte Therapien, was zu einem weiteren Anstieg an spät erkannten Krebserkrankungen und geringeren Überlebensraten führte.[5]

Diese Faktoren verdeutlichen die Relevanz der Forschung an neuen Therapiemöglichkeiten, wobei auch die Kosten- und Ressourceneinsparung immer zentraler wird.

1.2 Rolle der Krebsmedikamente im Wandel der Zeit

Nach wie vor stellt der Einsatz von Medikamenten neben operativen Eingriffen und der Strahlentherapie einen Pfeiler der Krebsbehandlung dar. Während im frühen 20. Jahrhundert noch das Paradigma galt, je mehr Masse entfernt wird, desto höher stehen die Heilungschancen, sind inzwischen minimalinvasive Eingriffe und Kombinationstherapien medizinisch aktuell.[6] Im Zuge der Kombinationstherapie lässt sich zwischen neoadjuvanter und adjuvanter Therapie unterscheiden. Die neoadjuvanten Therapie bezeichnet eine nicht-operative Behandlung zur Reduktion der Tumormasse im Vorfeld eines operativen Eingriffs zur Entfernung des Tumors.[7]

Meist findet diese Methode Anwendung, wenn ein Tumor nicht oder schwierig operabel ist.[7] Bei der adjuvanten Therapie folgt auf die operative Tumorentfernung eine Therapie, welche die im Körper verbleibenden Krebszellen eliminieren soll.[8]

Krebsmedikamente werden häufig unter dem Begriff Chemotherapeutika zusammengefasst. Aus einer chemischen bzw. biochemischen Perspektive, können nahezu alle Medikamente, welche bei der Behandlung von Krebs eingesetzt werden, als Chemotherapeutika klassifiziert werden, einschließlich Immuntherapien und Hormontherapien.[9] Im Folgenden sollen jedoch vornehmlich niedermolekulare Medikamente, auch umgangssprachlich als Chemotherapeutika bezeichnet, näher behandelt werden.

Die chemotherapeutische Behandlung von Krebserkrankungen wie wir sie heute kennen, hat ihren Ursprung in der Mitte des 20. Jahrhunderts.[9] Seitdem sind einige Fortschritte (vgl. Abb. 1) gelungen. Aber auch die Grenzen der klassischen Chemotherapie werden zunehmend verstanden und es wird an neuen Ansätzen gearbeitet, um diese zu umgehen.

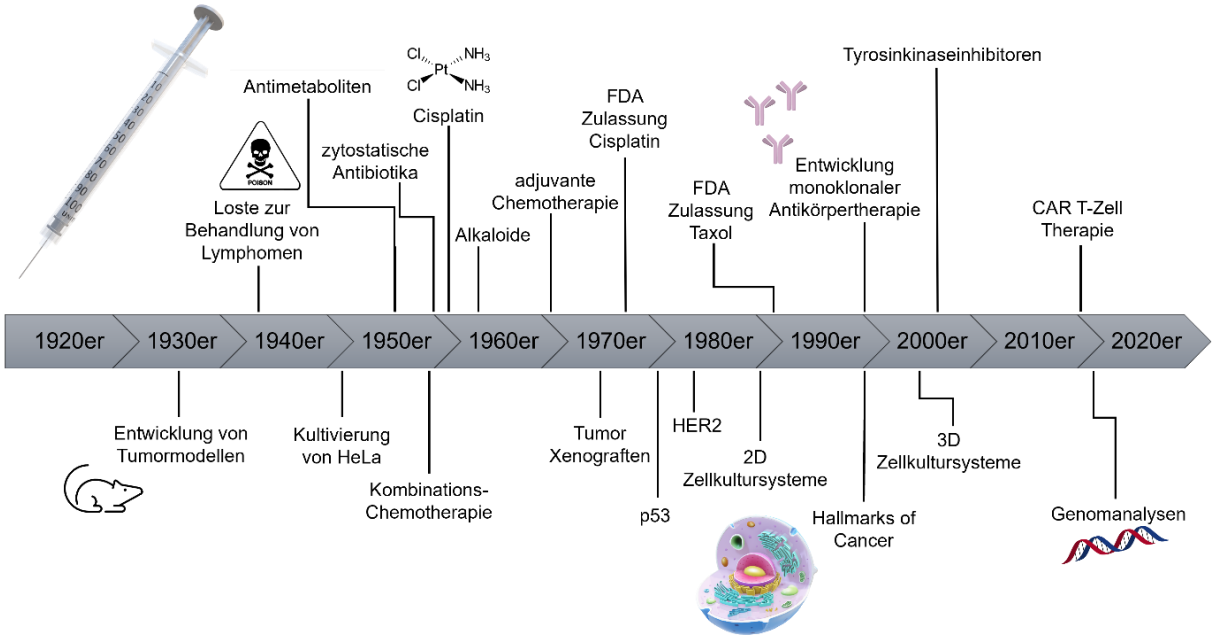

Abbildung 1. Meilensteine der letzten 100 Jahre in der Entwicklung von Krebsmedikamenten. Eigene Abbildung, modifiziert nach [10, 11].

1.2.1 Empirische Ansätze und ihre Substanzklassen

Der Begriff Chemotherapie wie er heute im Sprachgebrauch verwendet wird, wurde zu Beginn des 20. Jahrhunderts geprägt und bezeichnet die Verwendung von Chemikalien zur Behandlung von Krankheiten.[10] Mitte des 20. Jahrhunderts begann die klinische Anwendung von Chemotherapien bei der Behandlung von Krebserkrankungen. Die ersten Chemotherapeutika aus dieser Zeit basierten auf empirischen Entdeckungen und deren rationaler, klinisch orientierter Weiterentwicklung zu Krebsmedikamenten. Zwei der populärsten Beispiele dieser Ära sind Folsäureantagonisten und Loste.[9] Zudem wurde im gleichen Zeitraum die antitumorale Wirkung einiger Antibiotika entdeckt.[10]

1.2.1.1 Alkylanzien

Alkylanzien sind eine der ältesten und die meistangewandte Gruppe der Krebsmedikamente.[12] Die Gruppe der alkylierenden Krebsmedikamente geht auf Beobachtungen aus den beiden Weltkriegen zurück. Es wurde festgestellt, dass sowohl das Knochenmark, als auch die Lymphknoten von Soldaten welche Senfgasangriffen ausgesetzt waren deutlich verringert bzw. verkleinert waren.[10] Senfgas ist der Trivialname für Bis(2-chlorethyl)sulfid aus der Gruppe der Loste. Diese hochreaktiven Verbindungen führen zu starken Gewebeschäden durch Hemmung der Zellteilung. Basierend auf diesen Beobachtungen entwickelte sich in den 1940er Jahren der Ansatz Loste zur Behandlung von Lymphomen zu verwenden.

In der Onkologie bezeichnen Alkylanzien antineoplastische Substanzen, welche verschiedene Biomoleküle wie Nukleinsäuren, Nukleotide, Proteine und Aminosäuren irreversibel alkylieren.[13] Der Wirkmechanismus basiert hauptsächlich auf der Alkylierung der DNA und kann entweder an einem Einzelstrang oder durch Quervernetzung beider DNA Stränge ablaufen.[12] Dies führt zu starken Schäden der DNA, wodurch Replikation oder Transkription und schließlich die Zellteilung inhibiert werden.[12] Inzwischen gibt es mehrere Gruppen von Alkylanzien (vgl. Abb. 2), welche Anwendung in der Chemotherapie von Krebserkrankungen finden. Diese lassen sich grob zwei Arten von Wirkmechanismen zuordnen.

Die erste Art beruht auf der Alkylierung von DNA durch kovalente Bindung nukleophiler Positionen, dies führt zu Strangbrüchen und Vernetzungen und schließlich wird die DNA-Replikation gestört. Dieser Art lässt sich die traditionelle Alkylanzien Gruppe der Stickstoff-Lost-Derivate zuordnen.[13, 14] Diese reagieren aufgrund ihres Elektronenmangels mit den Nukleophilen der DNA, meist an der N7 Position der Guanin-Basen.[13, 14] Weitere Vertreter dieses Wirkmechanismus sind Alkylsulfonate, Nitrosoharnstoffe, Aziridine und Methyltriazenoimidazol-carboxamid (MTIC) basierte Substanzen.[13, 15]

Die zweite Art der „Alkylanzien“ ist die Gruppe der Platinverbindungen. Deren Wirkmechanismus unterscheidet sich insofern von den Lost-Derivaten, dass sie aufgrund ihrer Elektrophilie an die N7 Position der Guanin- bzw. Adenin-Basen koordinieren.[13] Sie führen hauptsächlich zu Quervernetzungen zwischen den beiden DNA Einzelsträngen und stören somit die DNA Replikation.

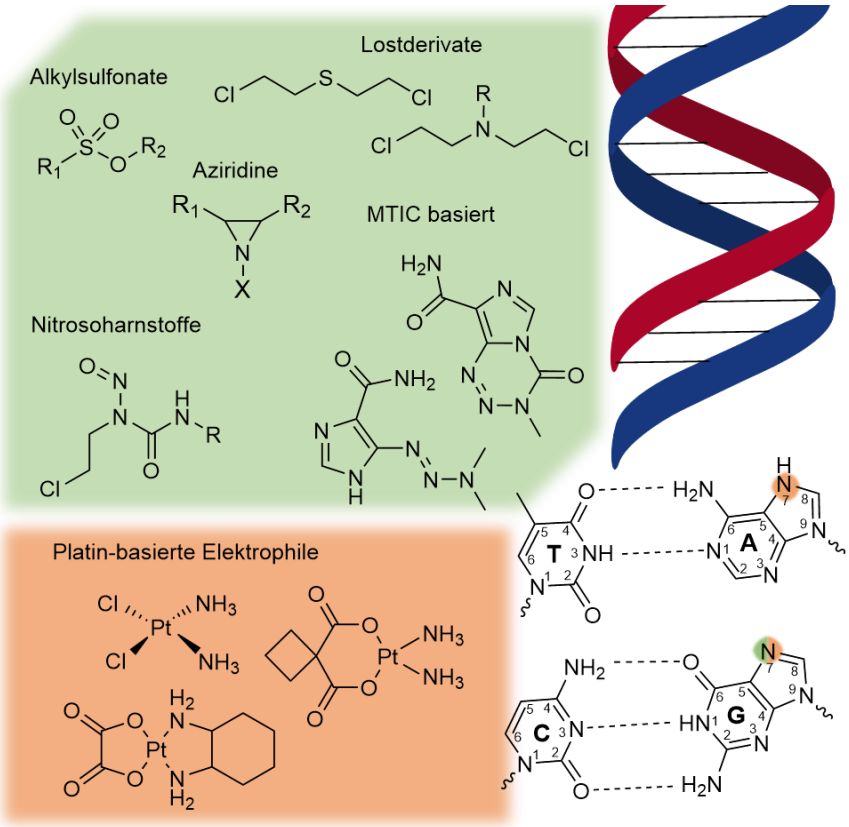

Abbildung 2. Übersicht über die Hauptgruppen der Alkylanzien und ihrer Hauptangriffspunkte an der DNA. Eigene Abbildung, modifiziert nach [14, 16].

1.2.1.2 Antimetaboliten

Die zuerst entdeckte Klasse an Antimetaboliten bildeten die Antifolate. Diese wurden in den 1950er Jahren entwickelt.[17] Basierend auf der klinischen Beobachtung eines scheinbar beschleunigten Krankheitsverlaufs akuter Leukämiepatienten nach der Gabe von Folsäurekonjugaten, entwickelte sich der Ansatz der Verwendung von Antagonisten der Folsäure zur Behandlung von Leukämie.[18] Nachdem anfangs verwendete Folsäureantagonisten deutlich zu toxisch wirkten, wurden bald wirksame Chemotherapeutika und basierend auf diesem Ansatz zahlreiche weitere Antimetaboliten entwickelt.[17, 18] Heute bilden Antimetaboliten eine eigene Gruppe der Krebsmedikamente, und umfassen neben Folsäureanaloga auch Pyrimidin- und Purinanaloga.[19] Antimetaboliten welche als Krebsmedikamente eingesetzt werden greifen, wie in Abbildung 3 dargestellt, auf verschiedenen Ebenen in den DNA und RNA Metabolismus ein.

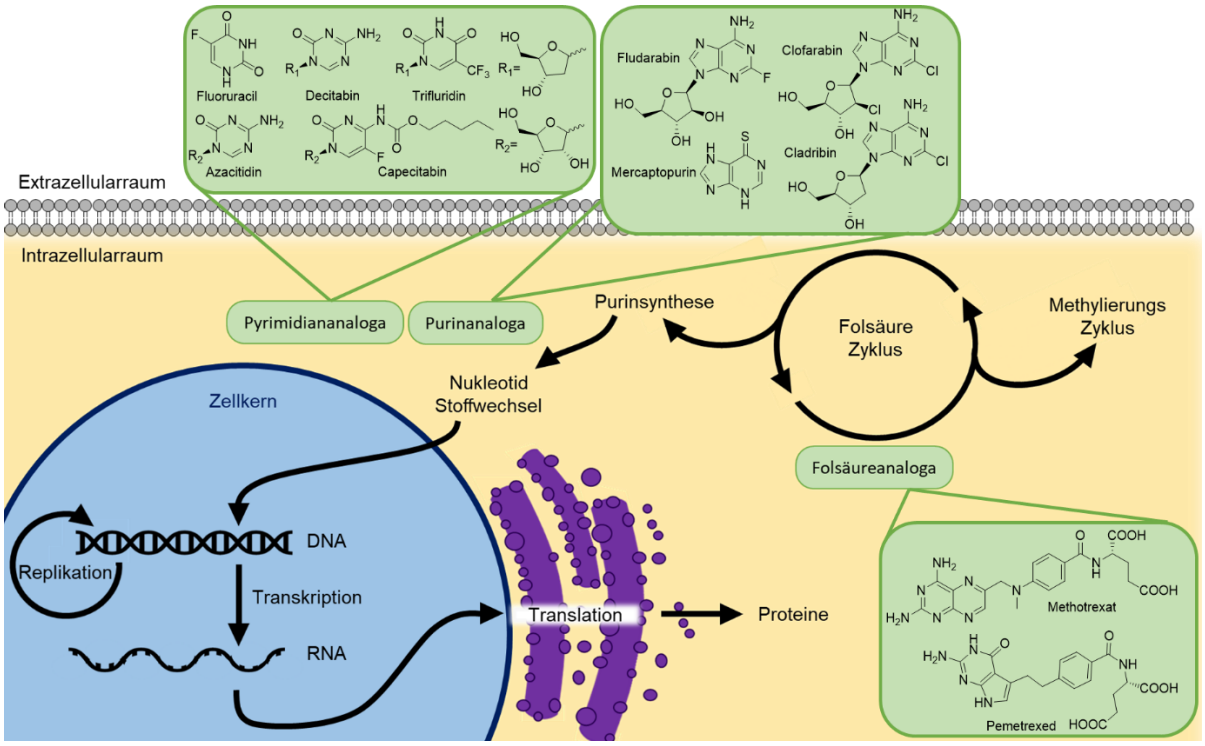

Abbildung 3. Übersicht über in Deutschland zugelassene Antimetaboliten und ihre Rolle im DNA/RNA Metabolismus. Eigene Abbildung, modifiziert nach [16].

Folsäureanaloga, auch Antifolate genannt stören den Folsäurezyklus.[17] Durch ihre strukturelle Ähnlichkeit zur Folsäure inhibieren sie zentrale Enzyme des Folsäurezyklus, insbesondere die Dihydrofolatreduktase, wodurch weitere *downstream* Mechanismen wie die Purinsynthese und der Nukleotidstoffwechsel gestört werden.[17, 20] Derzeit in Deutschland als Zytostatika zugelassene Antimetaboliten aus der Gruppe der Folsäureanaloga sind Methotrexat zur Behandlung verschiedener Krebserkrankungen und Pemetrexed, welches zur Behandlung von Lungenkarzinomen verwendet wird.[16]

Pyrimidin- und Purinanaloga greifen etwas weiter *downstream* in den Nukleotidmetabolismus ein.[21] Sie werden im Zuge des Nukleotidstoffwechsels als Bausteine für die Synthese von DNA oder RNA verwendet.[21, 22] Diese falschen Basen stören im weiteren Verlauf verschiedene Enzyme im Zuge der DNA Replikation und Transkription, beziehungsweise bei der RNA Translation, was zu verschiedenen Zellschäden führt.[22] Bereits geringe strukturelle Änderungen der Antimetaboliten haben einen großen Effekt auf ihre Wirkung, was das Potenzial dieser Substanzklasse hervorhebt.[22] Die in Deutschland aktuell zugelassenen Pyrimidinanaloga sind Fluoruracil, Decitabin, Trifluridin, Azacitidin und Capecitabin.[16] Zu den zugelassenen Purinanaloga zählen Fludarabin, Clofarabin, Mercaptopurin und Cladribin.[16]

1.2.1.3 Zytotoxische Antibiotika

Die Entdeckung der zytotoxischen Wirkung von Antibiotika geht ebenfalls auf die Zeit des zweiten Weltkriegs zurück. Im Rahmen eines groß angelegten Antibiotika Screenings zur Bekämpfung von Wundinfektionen wurden erste antitumorale Wirkungen bestimmter Verbindungen beobachtet.[10] Das Antibiotikum Actinomycin D stammt aus dieser Zeit und wird bis heute vorrangig zur Behandlung von Tumoren bei Kindern angewandt.[10, 23]

Der Wirkmechanismus der zytotoxischen Antibiotika setzt ebenfalls auf Ebene der DNA an. Durch Interkalieren und Alkylieren der DNA, wird der Transkriptionsprozess behindert, was in der Störung der RNA Synthese resultiert.[10, 23]

1.2.1.4 Spindelgifte

Der Ansatz der Anwendung von Spindelgiften als Zytostatika ist etwas jünger und datiert in den 1960er und 1970er Jahren mit der Entdeckung von Taxol und der Vinca-Alkaloide Vincristin und Vinblastin.[24] Taxol wurde im Rahmen eines groß angelegten Pflanzenscreenings des National Cancer Institute (NCI) aus der Rinde der pazifischen Eibe *axus brevifolia* extrahiert, und aufgrund seiner cytotoxischen Wirkung für die Entwicklung neuer Medikamente verwendet.[24] Der ebenfalls bekannte Name Paclitaxel bezeichnet ein Taxol Generikum, welches um die Jahrtausendwende auf den Markt kam.[24] Vincristin und Vinblastin sind ebenfalls pflanzlichen Ursprungs. Diese stammen aus dem rosafarbenen Immergrün *catharanthus roseus*.[25] Sie finden Anwendung in der chemotherapeutischen Behandlung zahlreicher Krebsarten. Dazu zählen unter anderem Lymphome und Brustkrebs.[25] Ein weiteres bekanntes Spindelgift pflanzlicher Herkunft welches Anwendung in der Krebstherapie findet ist Combretastatin A-4, ein *cis*-Stilben welches seinen Ursprung aus der südafrikanischen Langfadenart *combretum caffrum* hat.[26]

Die Spindelgifte lassen sich auf Basis ihres Wirkmechanismus in zwei Klassen einteilen (vgl. Abb. 4). Zum einen in die Klasse der Mikrotubuli-destabilisierenden Agenzien, zu der Vincristin, Vinblastin und Combretastatin A-4 zählen.[27, 28] Vinflunin und Vinorelbin sind strukturelle Verwandte der Vinca Alkaloide Vinblastin und Vincrisitn, welche für die Behandlung von Urothelzellkarzinomen, Bronchialkarzinomen und Mammakarzinomen, in Deutschland zugelassen sind.[16] Zum Anderen in die Klasse der Mikrotubuli-stabilisierenden Agenzien zu denen Taxol zählt.[27] Daraus abgeleitet sind die zugelassenen Krebsmedikamente Paclitaxel (Taxol) und Docetaxel.[16] Eine ähnliche Wirkung wie Taxol induziert das Makrolid Epothilon, welches bakteriellen Ursprungs ist (*Sorangium cellulosum*).[29, 30]

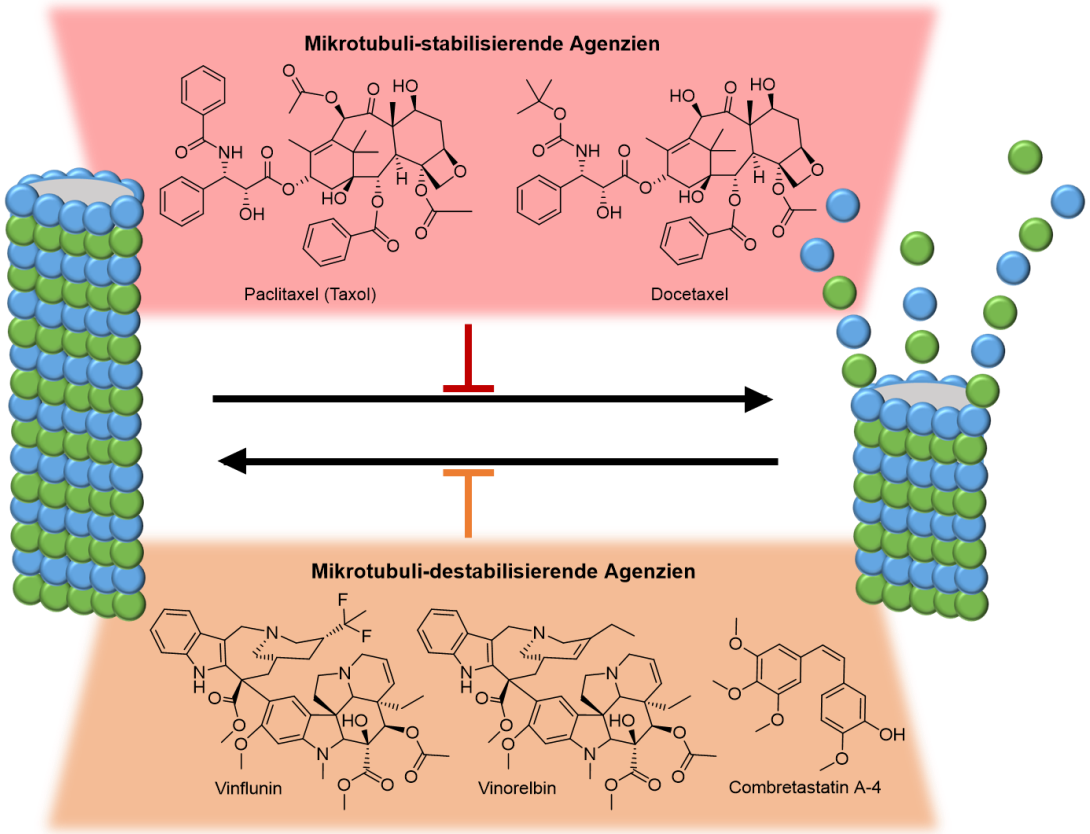

Abbildung 4. Übersicht über den Einfluss Mikrotubuli-stabilisierender und -destabilisierender Agenzien auf das Gleichgewicht zwischen polymerisierten Tubulin und depolymerisierten Tubulin Monomeren. Eigene Abbildung, modifiziert nach [30].

Durch die Störung der Polymerisation bzw. Depolymerisation der Mikrotubuli, verschiebt sich das Gleichgewicht, welches normalerweise zwischen polymerisierten Tubulin- und depolymerisierten Tubulin-Monomeren besteht.[31, 32] Eine direkte Folge dessen ist die Störung des Zellzyklus, welcher in Krebszellen besonders aktiviert ist.[33] Zudem sind die Migrationsfähigkeit der Zellen und die Bildung von Blutgefäßen betroffen.[33] Direkt assoziiert mit dem Wachstum von Tumoren ist die Anregung des Wachstums neuer Blutgefäße, um die entstehende Tumormasse mit Nährstoffen und Sauerstoff zu versorgen.[33] Es ist bekannt, dass Mikrotubuli eine zentrale Rolle bei der Angiogenese spielen.[33] Mikrotubuli destabilisierende Agenzien wirken in der Regel vaskular disruptiv und anti-angiogen zugleich, während Mikrotubuli stabilisierende Agenzien zumeist anti-angiogen wirken.[34]

1.2.2 Zielgerichetete Therapie und ihre Substanzklassen

Die Chemotherapie, welche auf der Vernichtung von Krebszellen mittels toxischer Substanzen beruht, war lange Zeit der einzige Weg zur Behandlung von Krebserkrankungen. Der größte Nachteil dieser Chemotherapie ist, dass die verwendeten toxischen Substanzen nicht zwischen Krebszellen und gesunden Zellen unterscheiden, was zu starken Nebenwirkungen führt.[35] Hier setzt die Idee der zielgerichteten (*targeted*) Krebstherapie an. Um eine zielgerichtete, sogenannte *targeted* Krebstherapie

zu ermöglichen, ist es zunächst von grundlegender Bedeutung die Charakteristika von Krebszellen zu kennen, welche diese von gesunden Zellen unterscheiden; die sogenannten *Hallmarks of cancer*.

1.2.2.1 Hallmarks of cancer

Um Diagnose und Therapiemöglichkeiten zu optimieren ist es essenziell die Charakteristika, welche eine Krebserkrankung ausmachen, zu kennen und für deren Bekämpfung auszunutzen. In diesem Zusammenhang bahnbrechend war die Veröffentlichung HANAHANs und WEINBERGs *Hallmarks of Cancer* im Jahr 2000.[36] Diese fassen Krebs als eine Krankheit zusammen, welche auf komplexer, dynamischer Transformation des Genoms ursprünglich gesunder Zellen basiert. Diese Veränderungen lassen sich sechs übergreifenden Merkmalen zuordnen; Signal-unabhängige Wachstumsstimulation, Resistenz gegenüber wachstumsinhibierenden Signalen, Umgehung von Apoptose, unbegrenzte Teilungsfähigkeit, Stimulation von Angiogenese, Invasion in umliegendes Gewebe mit der Fähigkeit zu Metastasieren. 2011 erweiterten HANAHAN und WEINBERG die *Hallmarks of Cancer* mit ihrer Veröffentlichung *Hallmarks of Cancer: The Next Generation*.[37] Diese erweitern die bisherigen sechs Merkmale um vier weitere biologische Charakteristika; Reprogrammierung des Metabolismus, Umgehung der Immunantwort, genetische Instabilität und tumorfördernde Entzündung.[37] 2021 wurden die *Hallmarks* schließlich um einige Dimensionen erweitert, womit sich die Veröffentlichung *Hallmarks of Cancer: New Dimensions* befasst.[38]

Das Konzept der *Hallmarks of cancer* ist ein zentraler Leitfaden, an welchem sich die Forschung und Entwicklung von Diagnose- und Behandlungsmöglichkeiten orientieren. Um einen bösartigen, invasiven Status zu entwickeln, müssen potenzielle Krebszellen zahlreiche Modifikationen durchlaufen, um die sogenannten *Hallmarks* zu erreichen (vgl. Abb. 5).[36-38] Dies verdeutlichen die komplexen molekularen Mechanismen, die einer Krebserkrankung zugrunde liegen. Zudem können nur Zellen mit einer erhöhten Entwicklungsrate, wie beispielsweise Stammzellen, die komplexen molekularbiologischen Veränderungen aufrechterhalten und zu Fortschritt und Metastasierung der Krankheit beitragen. Dazu zählen auch Zell-Zell Interaktionen und Interaktionen mit der Mikroumgebung der Krebszellen, welche eingebettet sind in Entzündungs-, Immunreaktions- und Stoffwechselwege.[39] Die vielseitigen charakteristischen Veränderungen der Krebszellen, welche sie von gesunden Zellen unterscheiden, bieten zahlreiche selektive Angriffspunkte für die Krebstherapie.

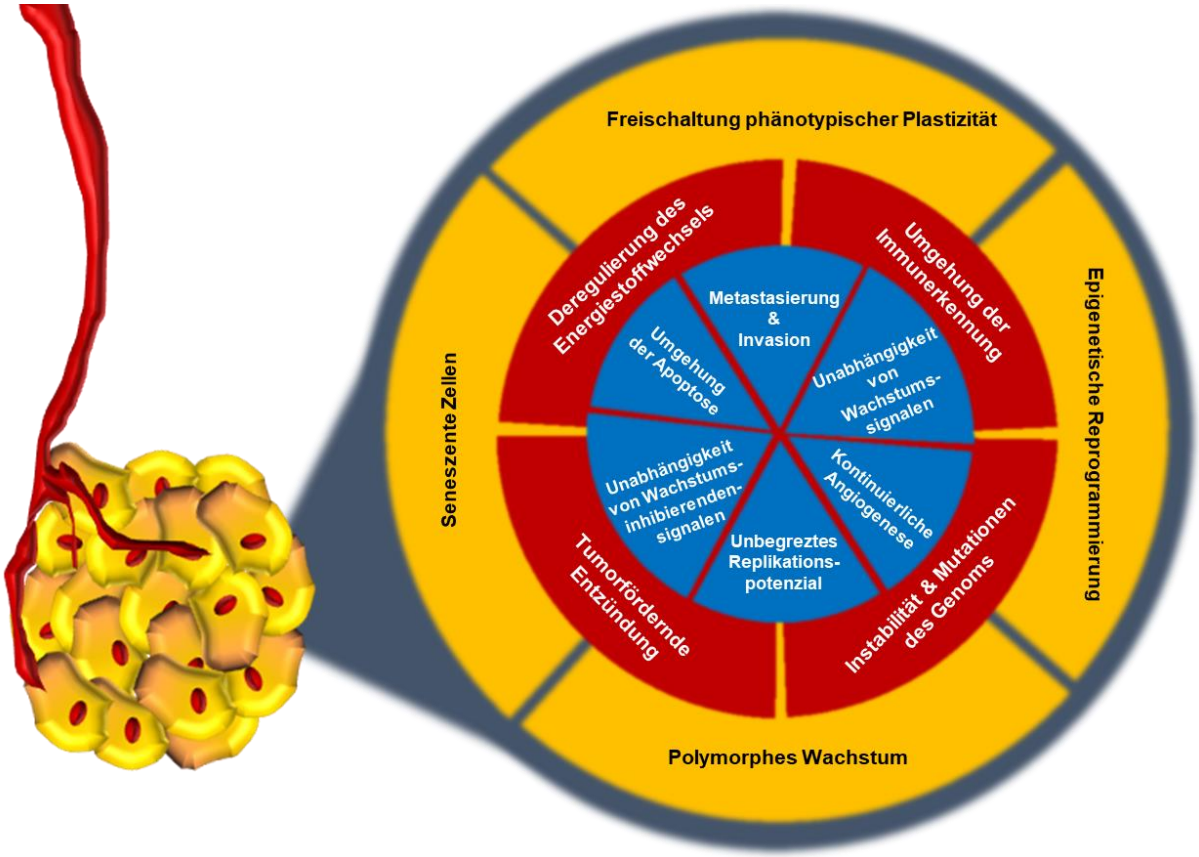

Abbildung 5. Übersichtsdarstellung der *Hallmarks of Cancer* (blau) sowie deren *Next Generation* (rot) und *New Dimensions* (gelb), eigene Abbildung, modifiziert nach [36–38].

Aus den Charakteristika nach denen sich Zellen als Krebszellen klassifizieren lassen, ist es auch möglich Angriffspunkte für die gezielte Bekämpfung dieser entarteten Zellen abzuleiten. Die sogenannte zielgerichtete (*targeted*) Krebstherapie befasst sich spezifisch mit biologischen Makromolekülen, welche in Wachstum, Zellteilung und Metastasierung von Krebszellen involviert sind. Grundsätzlich lässt sich die zielgerichtete Therapie nach zwei Ansätzen einteilen; die Therapie mit monoklonalen Antikörpern und die Therapie mit niedermolekularen Inhibitoren.

1.2.2.2 Monoklonale Antikörper und Antikörperkonstrukte

Während das Prinzip der Antikörper schon seit Ende des 19. Jahrhunderts bekannt ist, hat schließlich erst der wissenschaftliche Fortschritt des neuen Jahrtausends Antikörper als Therapiewerkzeuge zugänglich gemacht.[40, 41] Bei therapeutischen Antikörpern handelt es sich typischerweise um monoklonale Antikörper (mAbs) des γ-Immunoglobulin (IgG) Isotyps.[41] Erste Methoden zur Produktion von mAbs für die therapeutische Anwendung wurden Mitte der 1970er Jahre entwickelt.[42, 43] Ein zentrales Problem der frühen mAbs Entwicklung war die starke Immunabwehr der Patienten, da die ersten therapeutischen mAbs murinen Ursprungs waren. Als schließlich in den späten 1980er Jahren eine Methode zur Humanisierung der mAbs entwickelt wurde und schließlich im Laufe der 1990er Jahre der Zugang zu humanen mAbs gelang, wurde die Anwendung humaner mAbs ein zentraler Bestandteil der Medizin.[44]

Ein Prinzip der Anwendung von mAbs bei der Krebstherapie beruht auf Antikörpern, welche sich spezifisch gegen ein bestimmtes Protein oder Polyglycan richten, welches charakteristisch auf der Oberfläche von Krebszellen exprimiert wird. Dies führt dazu, dass die betreffenden Antikörper selektiv an Krebszellen binden. Dieser therapeutische Ansatz ist besonders attraktiv, wenn es gelingt, dass im Zuge der Bindung eine *downstream* Signalkaskade der Krebszelle gestört wird oder der mAb an eine toxisch wirkende Substanz gebunden ist.[45]

Ein weiterer, jüngerer Ansatz der Krebstherapie mittels mAbs ist die sogenannte Immunotherapie, bei welcher nicht die Krebszellen direkt angegriffen werden, sondern das Immunsystem stimuliert wird diese zu erkennen und zu bekämpfen.[46] Krebszellen sind in der Lage die natürliche Immunabwehr des Körpers mittels verschiedener Resistenzmechanismen zu umgehen.[47] Durch den Einsatz spezieller mAbs ist es möglich das Immunsystem zu stimulieren, sodass es die Krebszellen erkennt und gezielt angreift.[47]

MAbs werden erfolgreich in der Therapie zahlreicher Krebsarten eingesetzt, unter anderem für die Behandlung des Hodgkin Lymphoms sowie von Kolorektalkarzinomen, Mammakarzinomen, fortgeschrittenem Melanom, Leukämie und einigen mehr.[41] Die Zahl der für die Krebstherapie zugelassenen mAbs steigt seit der Jahrtausendwende kontinuierlich an.[44] Die mAbs-basierte Therapie ist neben Operationen, Bestrahlung und Chemotherapie mit Zytostatika, inzwischen eine der zentralen Komponenten der Krebstherapie.[44]

1.2.2.3 Niedermolekulare Inhibitoren

Neben Makromolekülen wie den mAbs spielt die Verwendung niedermolekularer Inhibitoren eine zentrale Rolle in der *targeted* Krebstherapie.[35] Diese decken eine große Bandbreite an *targets* ab, nach denen sie sich klassifizieren lassen.[35]

1.2.2.3.1 Tyrosin- und Serin/Threonin-Kinaseinhibitoren

Als Kinasen, auch Proteinkinasen, wird eine Klasse von Enzymen bezeichnet, welche die reversible Phosphorylierung von Proteinen katalysieren. Sie sind somit in zahlreichen zellulären Signaltransduktionswegen als Schlüsselenzyme involviert.[48] Sie spielen in zahlreichen Signalkaskaden eine Schlüsselrolle für die Weiterleitung und Verarbeitung von Signalen. Die Kinase-vermittelte Phosphorylierung von Zielproteinen ist ein streng regulierter Prozess, bei dem jegliche Störung zu einer Erkrankung des gesamten Organismus führen kann. Fehlregulationen von Kinasen sind an zahlreichen Prozessen der Karzinogenese beteiligt.[48] Diese Erkenntnis hat zum einen zum besseren Verständnis der Karzinogenese beigetragen und zum anderen die Entwicklung der *targeted cancer therapy* auf diesem Feld ermöglicht.[48] Aufgrund der Vielzahl an beteiligten Kinasen, ist die Varianz an mittlerweile entwickelten Inhibitorklassen groß. Die größte Gruppe der niedermolekularen Kinaseinhibitoren bilden Tyrosin- (TKIs) und Serin/Threonin-Kinaseinhibitoren (STKis). Diese Bezeichnung der Kinasen geht auf die Aminosäuren der Proteine zurück, welche von den jeweiligen Kinasen phosphoryliert werden.

Da die Mehrzahl der Serinkinasen auch Threonin phosphorylieren und umgekehrt, werden beide als Serin/Threonin-Kinasen und die entsprechenden Inhibitoren als Serin/Threonin-Kinaseinhibitoren zusammengefasst.[48, 49]

Viele Krebsmedikamente zielen auf extrazelluläre Rezeptor Tyrosinkinasen (RTKs) ab, weil durch ihre aberrante Aktivierung nachgeschaltete Signalwege, welche mit zentralen zytoplasmatischen Serin/Threonin-Kinasen (STKs) assoziiert sind, gestört werden.[49] Bei zahlreichen Krebsarten liegt eine Überexpression und somit Überaktivierung von RTKs vor, da sie die Progression von Krebs begünstigen. RTKs übermitteln extrazelluläre Signale ins Zytoplasma und schließlich zum Nukleus, was die Aktivierung weiterer Signalwege induziert. Neben RTKs gibt es auch zytosolische Tyrosinkinasen, welche durch intrazelluläre Signale aktiviert werden.[49] Wenn es gelingt zentrale Tyrosinkinasen die in Krebszellen aktiv sind zu inhibieren, ist es möglich Apoptose auszulösen. Zwei bedeutende Beispiele für krebsassoziierte RTK Familien sind die Familien der *epidermal growth factor receptors* (EGFRs) und *vascular endothelial growth factor receptors* (VEGFRs).[49] Bei 20-25% aller Brustkrebserkrankungen liegt eine Mutation des *human epidermal growth factor receptor 2* (HER2) vor. Basierend auf dieser Tatsche wurden in den letzten Jahren einige TKIs entwickelt, welche HER2 und andere Rezeptoren der EGFR Familie als *target* haben.[50] Dieser Ansatz gilt als vielversprechender Durchbruch in der Therapie von Brustkrebs.[50] VEGFR Überexpression und Überaktivierung ist eine Schlüsselmutation von Tumorzellen, da sie Angiogenese und somit die Sicherstellung der Nährstoffversorgung des wachsenden Tumors induziert.[49] Angiogeneseinhibitoren zeigen großes Potenzial in der Krebstherapie, da sie das Nährstoffversorgungsnetzwerk der Tumore angreifen.[49]

Wie bereits erwähnt, sind STKs weiter *downstream* angesiedelt und vermitteln zytoplasmatische und nukleäre Effektoren, insbesondere Regulatoren des Zellzyklus und der Apoptose.[49] Zentrale Regulatoren des Zellzyklus, welche mit der Progression von Krebs assoziiert werden sind die STKs Aurora 2 und Cyclin dependend Kinasen (CDKs). Weitere STK assoziierte Signalwege sind der Akt-Signalweg, der mTOR-Signalweg und der Ras-Raf-MAPK Signalweg, welche essentiell zur Proliferation von Krebszellen beitragen.[49]

1.2.2.3.2 Proteasominhibitoren

Proteasominhibitoren zielen auf den Proteinase-Komplex ab, welcher hauptverantwortlich für den intrazellulären Proteinabbau ist.[51] Dieser Abbauprozess wird als *ubiquitin proteasome pathway* (UPP) bezeichnet und ist in ein weites Spektrum an zellulären Prozessen, wie Zellzyklusregulation, Apoptose, Transkription, DNA Reparatur, Proteinqualitätskontrolle und Antigenpräsentation, involviert.[52] Der UPP ist essentieller zentraler Bestandteil krebsassoziierter Mechanismen wie Karzinogenese und Metastasierung, da Zellzyklus, Apoptoseregulation und Angiogenese in Krebszellen verstärkt ablaufen.[53] Der UPP prozessiert mehr als 80% aller zellulären Proteine. Durch die Störung dessen und der damit verbundenen zellulären Prozesse, kommt es vorranging zum Absterben der Krebszellen. Wichtige UPP assoziierte onkogene Prozesse sind die Herunterregulierung von Zellzyklus- und

Tumorsuppressorproteinen wie p53 und Cyclin-abhängiger Kinase-Inhibitor 1B (p27) oder die Hochregulierung von onkogenen Proteinen, einschließlich der Aktivierung des Nuklearfaktors kappa-B (NF-κB).[54]

1.2.2.3.3 Histondeacetylaseinhibitoren

Die reversible Acetylierung von Histonen und anderen Proteinen ist eine der häufigsten posttranslationalen Modifikationen und wird von den antagonistisch agierenden Histon-Acetyltransferasen (HAT) und Histondeacetylasen (HDAC) gesteuert (vgl. Abb. 6).[55] Sie spielen eine zentrale Rolle bei der Regulation des Zugriffs von Transkriptionsfaktoren auf die DNA und beeinflussen somit die Genexpression.[56] Durch Acetylierung mit HAT wird die positive Ladung der Histon-Lysinreste neutralisiert, was in einer entspannten Chromatinkonformation und damit besserer Zugänglichkeit für die Transkriptionsmaschinerie resultiert.[55] Im Gegensatz dazu resultiert die Entfernung der Acetylgruppen durch HDAC zu Chromatinkondensation und zur somit unterdrückter Gentranskription.[55] Typisch für Krebszellen ist eine Überexpression von HDAC und damit verbunden die Hypoacetylierung der Histone im Vergleich zu gesundem Gewebe.[56] Die erhöhte HDAC Aktivität und daraus resultierende transkriptionelle Unterdrückung von Genen ist essentiell für die Progression bestimmter Krebsarten und daher ein geeigneter Angriffspunkt für die Krebstherapie mittels niedermolekularer Inhibitoren.[56] Durch sogenannte HDAC Inhibitoren (HDACi) ist es möglich HDAC zu inhibieren und somit die krebsassoziierte transkriptionelle Unterdrückung von Genen aufzuheben. Eine Behandlung mit HDACi führt zu weitreichenden Effekten in Krebszellen, diese reichen von Zellzyklusarrest über Apoptose Induktion bis hin zu anti-angiogenen Effekten.[57]

Mittlerweile sind mehrere Klassen an HDACi bekannt, dazu zählen Carboxylate mit geringem Molekulargewicht, Hydroxamsäuren, Benzamide, Epoxyketone, cyclische Peptide und Hybridmoleküle.[58] Der Wirkmechanismus der meisten von ihnen basiert auf der Bindung des Zn^{2+}, welches essentieller Bestandteil der katalytischen Domäne der HDAC ist.[58] Einer der bekanntesten HDACi mit FDA Zulassung in den USA ist Suberoylanilid Hydroxamsäure (SAHA, auch Vorinostat) welche dort unter dem Handelsnamen Zolinza vertrieben wird.[58, 59] SAHA ist ein Abkömmling des Antibiotikums Trichostatin A (TSA), welches natürlichen Ursprungs ist.[58, 59]

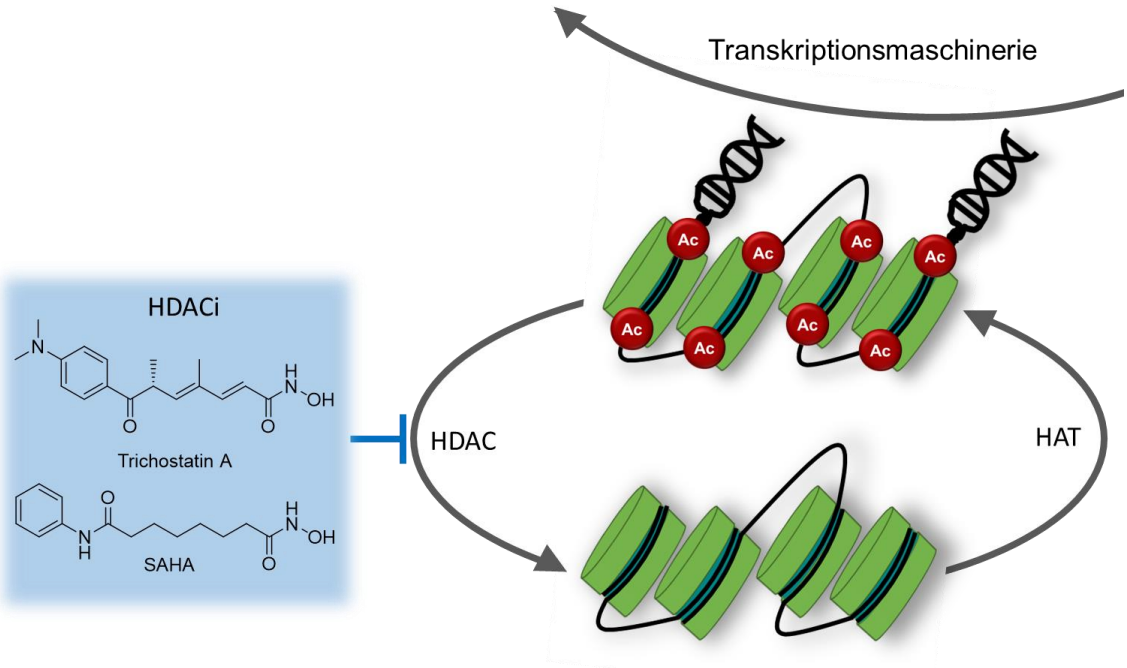

Abbildung 6. Schematische Darstellung der antagonistischen Wirkung von HAT und HDAC in Zellen, mit Angriffsort von HDACi. Eigene Abbildung, modifiziert nach [58].

1.2.2.3.4 Weitere Inhibitoren

Matrixmetalloproteasen (MMP) sind Endopeptidasen, welche in den Prozess der Metastasierung involviert sind, indem sie die extrazelluläre Matrix (EZM) abbauen. Insbesondere die Gelatinasen MMP-2 und -9 sind involviert in Migration und Invasion von Krebszellen. Durch ihre Inhibition ist es möglich den Prozess der Metastasierung zu unterbinden.[49]

Ein weiterer potenzieller Angriffspunkt von niedermolekularen Inhibitoren sind *heat shock proteins* (HSP), dabei handelt es sich um Chaperone welche zu korrekter Faltung und Transport von Proteinen beitragen. Von zentralem Interesse ist dabei das HSP90, da es in zahlreiche onkologische Signalwege involviert ist.[49] Beispielsweise ist ein enger Zusammenhang mit HER2 bekannt.

Schließlich kann auch direkt das Auslösen von Apoptose in Krebszellen ein angestrebter Mechanismus sein, welcher durch niedermolekulare Inhibitoren ausgelöst wird. Zentrale Angriffspunkte sind hierbei unter anderem die Wiederherstellung des wildtypischen Zustands des Tumorsupressorproteins p53.[49] Der Verlust der wildtypischen Funktion des p53 Proteins, welches eine Vielzahl an Transkriptionsfaktoren koordiniert, welche Tumorentstehung und Progression unterdrücken, ist ein gemeinsames Merkmal vieler Krebsarten.[60]

Es gibt auch Ansätze, bei denen eine direkte Aktivierung der Effektor-Caspase 3 erfolgt, welche Teil der katalytischen Caspase-Kaskade ist, wodurch Apoptose induziert wird.[49, 61]

Die zahlreichen potenziellen Angriffspunkte von niedermolekularen Inhibitoren verdeutlichen die große Bandbreite an Ansätzen zur Entwicklung neuer Medikamente, wobei gleichzeitig die enge Vernetzung

der Signalwege deutlich wird, was die erfolgreiche Einführung neuer zielgerichteter Wirkstoffe vor große Herausforderungen stellt.

Ein weiterer vielversprechender Ansatz ist die Hemmung der Thioredoxin Reduktase (TrxR) durch TrxR Hemmer wie beispielsweise Auranofin.[62] Bisher als Medikament zur Behandlung rheumatoider Arthritis, wird seine Wirkung gegen Krebs aktuell in klinischen Studien näher untersucht. TrxR wird in den meisten Krebsarten überexprimiert und eignet sich daher als Therapie *target*. Durch sein Gold-Triethylphosphin-Motiv weist der Gold(I)-Komplex Auranofin eine hohe Selektivität gegenüber Schwefel- und Selen-bindenden Proteinen auf. Da es sich bei TrxR um Seleonoenzyme handelt (TrxR1 cytoplasmatisch und TrxR2 mitochondrial) werden diese durch Auranofin inhibiert, was in einer Störung des zellulären Reduktions- und Oxidations-Systems und damit verbundenen zytotoxischen Erhöhung intrazellulärer reaktiver Sauerstoffspezies (ROS) resultiert. Durch Auranofin werden zudem der Akt-Signalweg, der mTOR-Signalweg und einige weitere zelluläre Prozesse, welche für Proliferation, Apoptose und Angiogenese wichtig sind, inhibiert.[62]

1.2.3 Multimodale Hybridwirkstoffe

Ein Ansatz des Wirkstoffdesigns zur Umgehung entstehender Resistenzen unter Ausnutzung der therapeutischen Erfolge etablierter Wirkstoffgruppen ist die Entwicklung von Hybridwirkstoffen. Der Bereich hybrider antitumoraler Wirkstoffe gewinnt zunehmend an Relevanz, da es mittels dieser Wirkstoffe häufig möglich ist pharmakologische Hürden und Resistenzen gegenüber konventionellen Krebsmedikamenten zu überwinden.[63] Ein weiterer Vorteil gegenüber der Vielzahl an konventionellen Krebsmedikamenten ist das Ansprechen mehrerer *targets* durch ein Molekül.[64] Verbesserung der Selektivität und gleichzeitig Umgehung von Resistenzen führen im Bereich der Entwicklung neuer hybrider Wirkstoffe zu stetiger Evolution und machen ihn zu einem essenziellen Bestandteil der Forschung an neuen Krebsmedikamenten.[63, 64] Hybridsubstanzen bezeichnen Verbindungen, welche durch Kombination bekannter Strukturmotive bzw. Pharmakophore entstehen.[63] Es wird auch häufig die alternative Bezeichnung chimäre Substanzen verwendet.

Ziel ist es, die strukturellen Motive von etablierten Wirkstoffen in einem neuen Molekül zu kombinieren, sodass entweder beide Wirkungen erhalten bleiben, verbessert werden, oder ein neuer, hoch potenter Wirkmechanismus entsteht. Dabei sollen, im Optimalfall, Aktivität, Selektivität und biopharmazeutische Eigenschaften (Absorption, Distribution, Metabolismus und Elimination (ADME)) gegenüber beiden Ausgangssubstanzen verbessert werden.[63] Prinzipiell ist es mit diesem Ansatz möglich, alle Substanzklassen zu chimären Wirkstoffen zu hybridisieren. Die vielfältigen Kombinationsmöglichkeiten erschweren eine Klassifizierung der resultierenden Hybridstrukturen. Jedoch erzielt die Verwendung einiger Strukturmotive besonders häufig vielversprechende Ergebnisse und damit assoziiert, tauchen neue hybride Substanzen mit antitumoralen Eigenschaften vermehrt in der Literatur auf. So basiert eine Vielzahl hybrider antitumoraler Substanzen auf dem Cisplatin-Motiv beziehungsweise anderen Metallen.[65] Ein weiteres häufig verwendetes Strukturmotiv ist die

Hydroxamsäureeinheit, welche im Krebsmedikament Vorinostat wiederzufinden ist.[66, 67] Weitere gern verwendete Motive sind unter anderem *cis*-Stilbene wie das im Tubulinpolymerisationshemmer CA-4, Antimetaboliten und Curcumin.[68]

Um das große Potenzial multimodaler hybrider Substanzen ausschöpfen zu können, darf bei deren Design eine zentrale Herausforderung nicht außer Acht gelassen werden. Durch die Kopplung zweier Pharmakophore, besteht die Gefahr, dass das resultierende Molekül gegen die, für Pharmazeutika kritischen, Lipinski Regeln verstößt und somit prinzipiell als Arzneistoff ungeeignet ist.[64] Durch ihre große und komplexe Struktur weisen die chimären Substanzen zumeist ein hohes Molekulargewicht und hohe Lipophilie auf, was in den meisten Fällen in schlechter Bioverfügbarkeit resultiert.[64, 68, 69] Somit stellt die Erhaltung der Wasserlöslichkeit und Bioverfügbarkeit eine der größten Herausforderungen im Design multimodaler hybrider Substanzen dar. Gelingt es diese Herausforderung zu meistern, resultieren vielversprechende Substanzen mit optimierten Eigenschaften, für deren Erfolg es in der Literatur bereits zahlreiche Beispiele gibt.[66-68, 71, 72]

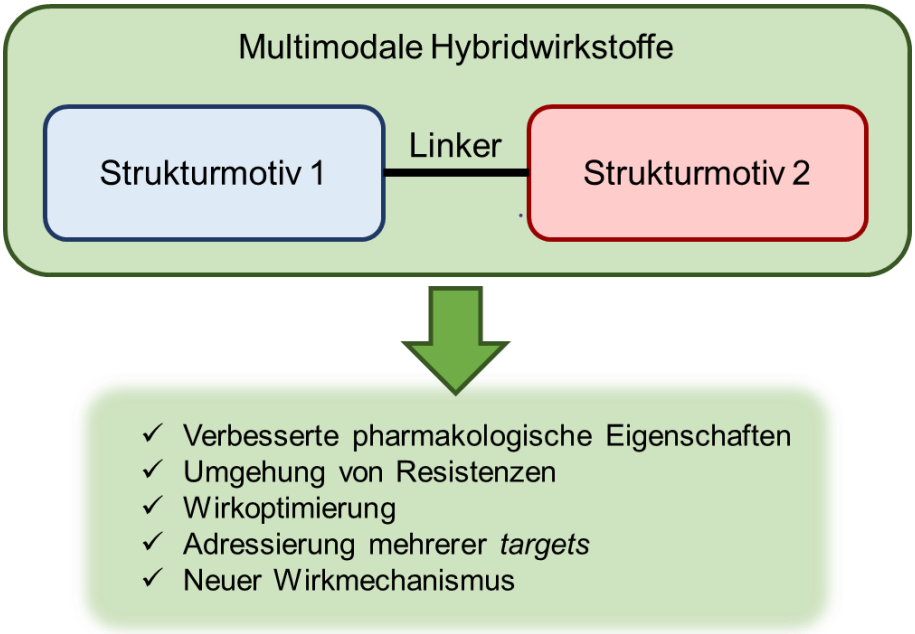

Abbildung 7. Modell der strukturellen Zusammensetzung neuer Hybridsubstanzen, auch als chimäre Substanzen bezeichnet, welche in der Regel strukturell an zwei etablierten Strukturmotiven orientiert sind und über einer sogenannten Linker miteinander verbunden werden. Dadurch sollen multimodale Hybridwirkstoffe mit optimierten Eigenschaften entstehen. Eigene Abbildung, modifiziert nach [69].

1.2.3.1 Hybride Metall-basierte Substanzen

Seit seiner Erfolgsgeschichte als Krebsmedikament ist *cis*-Diammindichloroplatin(II) (CDDP) ein leuchtendes Beispiel für die Eignung Metall-basierter Wirkstoffe zur Behandlung von Krebserkrankungen.[70] Die zunehmende Anzahl neuer Krebsdiagnosen und die starken Nebenwirkungen verfügbarer Chemotherapeutika befeuern die Suche nach Analoga mit verbesserten pharmakologischen Eigenschaften. Nach einigen wenigen erfolgreichen Platin-basierten Verbindungen

wie Carbo- und Oxaliplatin, wurde die Suche auf Komplexe anderer Übergangsmetalle ausgeweitet. Seit der Entdeckung der Eignung von N-heterocyclischen Carbenen (NHCs) als Liganden stabiler Metall-Komplexe Ende der 1970er Jahre, nahm das pharmakologische Interesse an dieser Verbindungsklasse deutlich zu.[70] Es sind einige Beispiele für Pt-NHC-Komplexe bekannt, die gegen CDDP resistente Krebszelllinien aktiv sind. Durch die Strukturkombination aus Platin und NHC ist es somit möglich, Resistenzen zu umgehen und auch andere zelluläre *targets* neben der DNA zu adressieren.[70] Auch wurde inzwischen das Paradigma gebrochen, dass sich nur *cis*-Platin Verbindungen als Krebsmedikamente eignen. Die Anzahl aktiver *trans*-Pt-Komplexe steigt stetig, wobei durch die eingesetzten Liganden verschiedenste *targets* adressierbar sind.[70]

Gleiches gilt für die Verwendung anderer Zentralmetalle, wie beispielsweise Gold. Mittlerweile sind Goldverbindungen eine vielversprechende Strukturklasse für die Behandlung von Krebs und auch anderen Erkrankungen.[70] Dies lässt sich zurückführen auf die Entdeckung der antitumoralen Wirkung des Antirheumatikums Auranofin, bei welchem es sich um einen Gold-Koordinationskomplex handelt. Dessen zentrales Strukturmotiv ist ein Phosphin-Au Motiv, von welchem sich das stabilere NHC-Au Motiv ableiten lässt.[70] Mittlerweile sind zahlreiche antitumoral wirkende NHC-Au-Komplexe bekannt. Es gibt unter anderem einige Beispiele deren intrazelluläre *targets* sich durch Feinjustierung der Liganden ansteuern lassen.[70, 71]

1.2.3.2 Hybride Hydroxamsäure-basierte Substanzen

Die funktionelle Gruppe „Hydroxamsäure“ ist das zentrale Strukturmotiv vieler HDACi und eignet sich besonders gut zur Einführung in hybride bzw. chimäre Wirkstoffe.[64, 72] Durch die Hybridisierung mit anderen Strukturmotiven ließen sich bereits einige vielversprechende Substanzen gewinnen, welche deutlich potentere HDAC Inhibitoren sind, beziehungsweise die Krebs-spezifische Zytotoxizität der etablierten HDACi deutlich überbieten.[64] Durch die Verbindung der Zink-bindenden Einheit von HDACi mit einem weiteren Strukturmotiv über eine Linkergruppe, wird eine Vielzahl an möglichen hybriden Substanzen zugänglich. So ist es möglich, mittels eines hybriden Moleküls, weitere *targets* neben HDAC zu adressieren.[66, 67] Das Feld chimärer HDACi ist vergleichsweise neu und bisher relativ unbekannt. Aufgrund der steigenden Anzahl vielversprechender Substanzen aus dieser Gruppe, welche neben der Behandlung von Krebs auch für die Behandlung anderer Erkrankungen in Betracht gezogen werden, gewinnt es jedoch zunehmend an Interesse.[66] Es sind bereits einige Serien hybrider HDACi bekannt bei denen unter anderem Hybridisierungen mit Kinaseinhibitoren, Platin-Komplexen oder Mikrotubuli-destabilisierenden Agenzien vorgenommen wurden.[67]

1.3 Rolle der präklinischen Forschung

Bei der Entwicklung neuer Wirkstoffe für die Behandlung von Krebserkrankungen stehen zunächst präklinische Studien im Vordergrund. Im Zuge des sogenannten *screenings* werden neue potentielle Chemotherapeutika mittels *in vitro* Versuchen und Tiermodellen hinsichtlich ihrer Wirksamkeit und

Spezifizität untersucht. Die Verwendung von Tiermodellen im größeren Maßstab steht aufgrund ihrer ethischen Problematik seit vielen Jahren in der Kritik und die Gesetzgebungen werden zunehmend restriktiver. Aufgrund dessen basiert die präklinische Evaluation neuer potentieller Chemotherapeutika vornehmlich auf der Verwendung von *in vitro* Methoden.[73]

1.3.1 2D Monolayer Zellkultur

Mit Beginn der Forschung an Krebsmedikamenten im Zuge der modernen Medizin Mitte des 20. Jahrhunderts, entstand auch die Nachfrage nach *screening* Modellen für neue potenzielle antitumorale Substanzen. Präklinische Studien potenzieller Krebsmedikamente wurden zunächst an Tumor-Modellen aus der Maus durchgeführt.[74] Erste erfolgreiche Versuche der Zellkultivierung von Hühnerembryos gelangen bereits in den 1910er Jahren.[75] Es dauerte jedoch noch fast ein halbes Jahrhundert bis zur erfolgreichen Kultur menschlicher Zellen.[75] Dieser Meilenstein gelang in den 1950er Jahren mit der erfolgreichen Kultivierung der HeLa Zellen.[75] Die Etablierung dauerhaft kultivierbarer menschlicher Krebszelllinien ermöglichte große Fortschritte in der Erforschung der zentralen zellbiologischen und pathophysiologischen Prozesse von Krebszellen. Mit steigender Anzahl erfolgreich kultivierbarer Krebszelllinien etablierten sich schnell kommerzielle Wachstumsfaktoren und Kulturmedien, was dazu führte, dass gegen Ende des 20. Jahrhunderts das *screening* potentieller Wirkstoffe an großen Krebszellpanels möglich war.[75] Die stabile Kultivierung von Krebszellen ermöglichte zahlreiche Meilensteine der Medizingeschichte wie die Entwicklung der Polio-Impfung sowie mehrerer Krebsmedikamente.[75]

Auch heute noch spielen Zellkulturen eine zentrale Rolle in der Krebsforschung. Sie dienen dabei als wichtige präklinische Modellsysteme, um sowohl mechanistische und therapeutische Informationen über Krebserkrankungen als auch neue potenzielle Medikamente zu gewinnen.[75] Die am häufigsten verwendete Art der Zellkultur in der Grundlagen- und präklinischen Forschung an Krebszellen und -Medikamenten ist die adhärente zweidimensionale (2D) Zellkultur. Hier wachsen die Zellen als *monolayer* in speziellen Zellkulturgefäßen und sind dabei adhärent an deren Plastikboden.[76] Diese Art der Zellkultur hat zahlreiche Vorteile, wie einfache und gleichzeitig kostengünstige Handhabung, gute Reproduzierbarkeit und Anwendbarkeit in Hochdurchsatzverfahren.[76] Auf Basis dessen wurden vielfältige Assays entwickelt, um die Eignung neuer Substanzen als potenzielle Krebsmedikamente zu untersuchen und deren zellulären Wirkmechanismus aufzudecken. Seit 1990 gibt es vom *National Cancer Insitute* (NCI) ein *screening* Verfahren zur Untersuchung potenzieller antitumoraler Substanzen, bei dem 60 humane Krebszelllinien eingesetzt werden. Die verwendeten Zelllinien sind die am häufigsten verwendeten Zelllinien der Krebsforschung und somit global weit verbreitet in Laboren, welche sich mit Krebs-, beziehungsweise Wirkstoffforschung beschäftigen.[77] Neben Wirkstoff-*screenings*, dienen sie mittlerweile durch die Etablierung moderner Sequenzierungsmethoden und -*omics* Analysen auch zur Verbesserung des Verständnisses der Tumorbiologie.[77]

Mit zunehmendem Verständnis der zellbiologischen Hintergründe von Tumoren werden auch die Nachteile von 2D Zellkulturen immer deutlicher. Die Zellen, welche die Grundlage der Untersuchungen bilden, sind alle uniform und es entstehen somit keine relevanten Zell-Zell oder Zell-Umgebungs Beziehungen, welche die in einem Tumor herrschenden Bedingungen abbilden würden. Durch die Monokultur in der 2D Ebene verändern sich Phänotyp und Differenzierungsgrad der Zellen gegenüber zum Ursprungsgewebe.[76] Damit assoziiert sind Veränderungen in Funktion, Organisationsstruktur, Sekretion und zellulären Signalwegen.[76] Zudem ist es nicht möglich mittels 2D Monolayerkulturen die Gradienten an Nährstoff-, Sauerstoff- und insbesondere Wirkstoffkonzentration abzubilden, wie sie im 3D Tumor vorherrschen (vgl. Abb. 8).[78] Die Rate an Substanzen welche nach ihrer erfolgreichen präklinischen Untersuchung erfolgreich durch Phase I Studien geht, liegt unter 5%.[79] Ein Grund dafür ist die schwierige Übertragbarkeit von Ergebnissen aus 2D *in vitro* Systemen in *in vivo* Systeme.[79] Zusammengefasst bilden 2D Zellkulturen die *in vivo* vorherrschenden Bedingungen von Tumoren unzureichend ab und daher sollten auch in frühen präklinischen Studien und Grundlagenforschung 3D Zellkulturen ergänzend angewendet werden.[78]

1.3.2 3D Zellkultur Systeme

Aufgrund der zahlreichen Vorteile, die 3D Zellkultur Systeme mit sich bringen (vgl. Abb. 8), steigt das Interesse der Forschenden an ihnen zunehmend. Durch die jüngsten Fortschritte der Zellbiologie und des *tissue engineering*, etablieren sich 3D Systeme in den letzten Jahren exponentiell.[78] Dabei haben sich mittlerweile verschiedene Ansätze etabliert *in vivo* ähnliche Bedingungen zu schaffen, welche morphologische, funktionale und Aspekte der Mikroumgebung berücksichtigen.[78] Eine zentrale Grundlage der 3D Zellkultur sind sogenannte Spheroide. Dabei handelt es sich um Zellaggregate welche Mikrotumore imitieren sollen. Spheroide ahmen *in vivo* Tumore effizienter nach als 2D Modelle, da sie verschiedene Zellschichten erzeugen, welche sich in Nährstoff-, Sauerstoff- und Wirkstoffkonzentration unterscheiden.[78] Zudem werden Morphologie, Polarität, Zell-Zell Interaktionen und Genexpression *in vivo* näher abgebildet.[78]

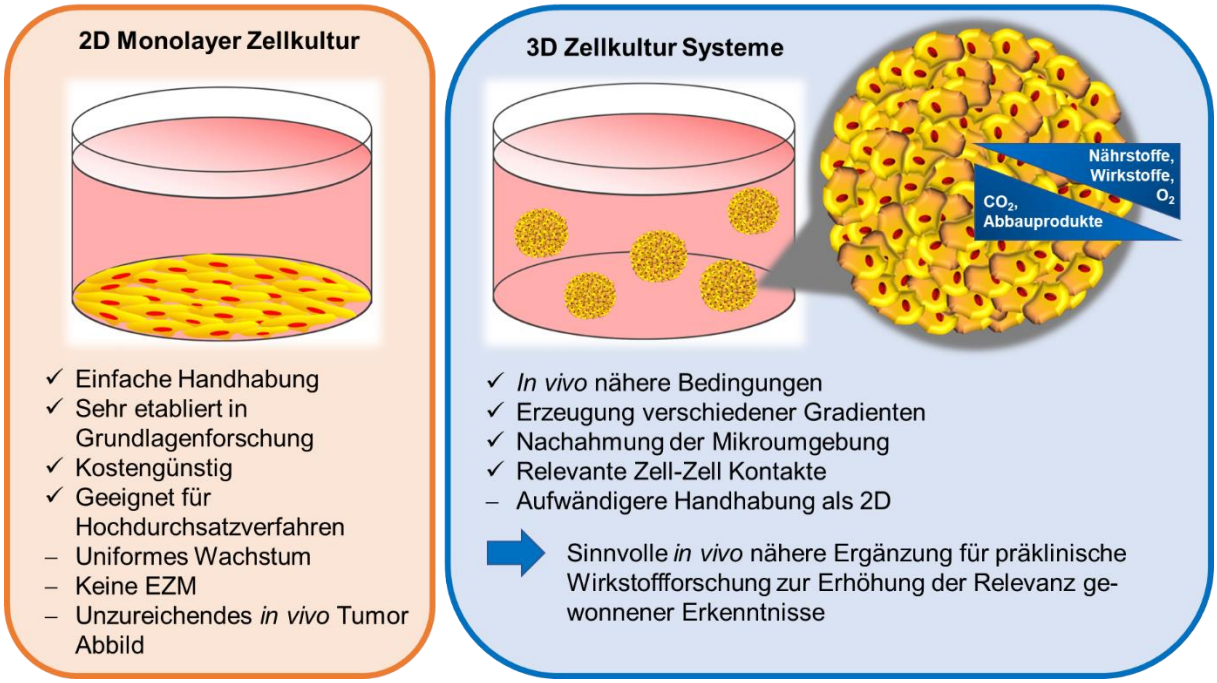

Abbildung 8. Schematische Darstellung der 2D Monolayer Zellkultur und der 3D Zellkultur Systeme und ihrer zentralen Merkmale, eigene Abbildung , modifiziert nach [78].

Zur Stimulation der Spheroidbildung gibt es verschiedene Möglichkeiten. Dazu gehören die sogenannte *liquid overlay* Technik, *hanging drops* und Bioreaktoren.[78] Prinzipiell zielen alle diese Methoden darauf ab, das adhärente Wachstum der Zellen an einer (Plastik-) Oberfläche zu verhindern und die Zellen dadurch zu stimulieren sich miteinander zu Sphäroiden zu verbinden.[78] Weiterentwicklungen auf diesem Feld ermöglichen zudem die Einführung eines weiteren, *in vivo* näheren Faktors; der EZM. Techniken die dies ermöglichen sind die Verwendung von Hydrogelen, Scaffolds oder 3D *bioprinting*.[78] Dabei umgeben verschiedene Biopolymere die Spheroide welche die EZM nachahmen. Die Zusammensetzung der Biopolymere kann dabei entsprechend an das Ursprungsgewebe des verwendeten Zelltyps angepasst werden, dazu gehören Collagen, Hyaluronsäure, Chitosan, Alginat und Gelatine.[78]

Nach wie vor ist ihre Handhabung jedoch deutlich zeit- und kostenintensiver als die der 2D Monolayerkulturen.[79] Trotz dieses Aspekts stellen sie ein wichtiges Modell der Grundlagenforschung dar und ermöglichen die Erhöhung der Relevanz präklinischer Forschung an neuen potenziellen antitumoralen Substanzen.[79] Ziel ist es die Übertragbarkeit präklinischer Wirkstoffuntersuchungen zu erhöhen und schwache präklinische Kandidaten im Vorfeld effizienter aussortieren zu können.[79]

1.3.3 Tiermodelle

Tiermodelle sind die letzte Stufe der präklinischen Wirkstoffforschung und werden eingesetzt, wenn sich die Substanzen in zellbasierten *assays* als besonders vielversprechend erwiesen haben. Die ersten Tiermodelle als Basis für Wirkstoffscreenings wurden in den 1970er Jahren entwickelt, als es gelang humanes Tumorgewebe als Tumorxenograft in immundefizienten Mäusen zu kultivieren.[80] Mittlerweile hat sich eine Vielzahl an murinen Modellen zur Untersuchung potenzieller antitumoraler

Wirkstoffe entwickelt.[81] Aufgrund der zuvor genannten schlechten Übertragbarkeit der 2D Zellmodelle wird der präklinische Wirkstoffentwicklungsprozess in großen Teilen zu Lasten der Versuchstiere ausgetragen.[79] Neben Aspekten des Tierschutzes, spricht auch die schlechte Übertragbarkeit von Tiermodellen auf den Menschen gegen den Routineeinsatz von Tiermodellen in der präklinischen Wirkstoffforschung.[82, 83] Denn trotz der zahlreichen Verwendung von Tiermodellen konnte die Erfolgsrate von Substanzen als potenzielle Wirkstoffe in Phase I Studien nicht signifikant erhöht werden, was die Etablierung eines humanen, *in vivo* nahen Modells nahelegt.[79] 3D Zellmodelle haben das Potenzial einen Teil der Tiermodelle zu ersetzen und damit die große Lücke zwischen 2D Monolayer Kultur und Tiermodell zu schließen, da sie humane Zellen in einer *in vivo* nahen Umgebung abbilden.[76, 79]

2 Zielsetzung

Die moderne Krebstherapie mit niedermolekularen Medikamenten wie wir sie heute kennen, hat ihren Ursprung Mitte des 20. Jahrhunderts.[9] Seitdem sind mit fortschreitendem medizinischen, biochemischen und auch technischen Verständnis zahlreiche Meilensteine auf diesem Feld erreicht worden.[10, 11] Trotz aller Fortschritte, liegt die Rate an präklinisch erfolgreichen Substanzen welche erfolgreich klinische Phase I Studien bestehen bei unter 5%.[79] Dies liegt unter anderem an der schlechten Übertragbarkeit von präklinischen Studien auf die *in vivo* Anwendung potenzieller Chemotherapeutika.[79] Weder 2D Monolayer Zellkulturen noch Tiermodelle sind geeignet, um die humanen *in vivo* Tumorbedingungen adäquat abzubilden.[79] Zudem treten zunehmend Fälle von Resistenzen gegen etablierte Chemotherapeutika auf, und die steigende Weltbevölkerung, sowie die zugespitzte medizinische Lage im Zuge der Covid-Pandemie belasten das Gesundheitssystem enorm.[1, 3–5]

Im Rahmen dieser Arbeit sollen neue multimodale, antitumorale Hybridwirkstoffe mittels präklinischer Studien hinsichtlich ihrer Eignung als potenzielle Chemotherapeutika untersucht werden. Im Fokus steht dabei die Aufklärung der intrazellulären Wirkmechanismen auf molekularer Ebene. Bei den zu evaluierenden Hybridsubstanzen handelt es sich um Vertreter zweier Substanzklassen. Zum einen um hybride Metall-basierte Wirkstoffe und zum anderen um chimäre Histondeacetylaseinhibitoren (HDACi). Das Prinzip multimodaler, chimärer Substanzen basiert auf der strukturellen Kombination zweier etablierter Strukturmotive, wodurch Hybridverbindungen mit optimierten Eigenschaften erzeugt werden sollen. Die präklinische Evaluation und Aufklärung der Wirkmechanismen erfolgt mittels verschiedener 2D Tumorzellkultur-basierter Assays als auch *in vivo* Studien (Zebrafisch und Hühnerei) und schließlich unter Verwendung *in vivo* näherer 3D-Tumorzellkulturassays. Durch die Etablierung von 3D Zellkultur-basierten Assays, soll zum einen die Relevanz der präklinischen Studien erhöht werden und zum anderen ein Beitrag zur Schließung der großen Lücke zwischen präklinischen und klinischen Studien geleistet werden.

Insgesamt soll mittels Erweiterung klassischer 2D- durch realitätsnähere 3D-Tumorzellkulturassays der Erkenntnisgewinn aus präklinischen Studien optimiert werden und durch die Evaluierung von Hybridsubstanzen eine neue Sichtweise auf etablierte Strukturmotive geschaffen werden.

3 Synopsis

3.1 Übersicht der Teilprojekte

Die vorliegende Dissertation enthält 4 Publikationen und 3 Manuskripte (vgl. Abb. 9), welche sich mit der Aufklärung intrazellulärer *targets* und molekularer Wirkmechanismen neuer, potenzieller hybrider Chemotherapeutika, unter Zuhilfenahme von 2D und 3D Tumorzellkulturassays befassen. Die dabei untersuchten Substanzen lassen sich den beiden Klassen hybride Metall-basierte Wirkstoffe und chimäre HDACi zuordnen.

Zur Klasse der Metall-basierten Substanzen zählen *cis*-NHC-Pt(II)-Komplexe, mit Mitochondrien-assoziiertem Wirkmechanismus, welcher sich in hohem Maße von dem für *cis*-Pt(II)-Komplexe postulierten, ausschließlich DNA-assoziierten Wirkmechanismus unterscheidet. Zudem konnte mittels einer weiteren Pt-NHC-basierten Serie, neben der antitumoralen Wirkung von *cis*-Pt-Komplexen, auch eine signifikante antitumorale Wirkung von *trans* konfigurierten Pt-Komplexe demonstriert werden.

Des Weiteren wurde für antitumorale NHC-Au(I)-Komplexe neben verstärkter Wirkung auf resistente Tumorzellen die Abhängigkeit der intrazellulären Anreicherung und damit des Wirkorts von Art und Charakter des sekundären Liganden nachgewiesen. Schließlich wurde eine Serie von Au(I)-Thiopurin-Komplexen untersucht, welche die Effektivität und Selektivität von Purin-Antimetaboliten verbesserten.

Die untersuchten HDACi basierten Verbindungen umfassten verschiedene CA-4-HDACi-Konjugate. Ein Vertreter diese Serie ist der chimäre HDACi und Zytoskelett Inhibitor Broxbam, welcher sich durch seine pleiotrope Wirkung als vielversprechender Kandidat für die Behandlung von Leberkarzinomen erwies. Die Untersuchung einer weiteren Serie von Vertretern dieser Substanzklasse ergab neben einem multimodalen Wirkmechanismus die Herunterregulierung des tumorassoziierten Apoptose-inhibierenden Proteins Survivin. Schließlich wurden die beiden potenten Vertreter dieser Klasse Troxbam und Troxham mittels 3D-Zellkultur Assays und 3D *in vitro* Mikrotumoren hinsichtlich ihrer Wirkung im 3D tumor-ähnlichem System untersucht. Dies ermöglichte die frühe präklinische Untersuchung der Substanzen im Kontext einer Tumormikroumgebung, welche in diesem Ausmaß sonst nur in Tiermodellen möglich ist.

Die im Rahmen dieser Arbeit untersuchten Testsubstanzen wurden am Lehrstuhl für Organische Chemie I der Universität Bayreuth synthetisiert und charakterisiert. Die Untersuchung der intrazellulären Zielstrukturen und molekularer Wirkmechanismen erfolgte hauptsächlich am Lehrstuhl für Organische Chemie I und am Lehrstuhl für Genetik der Universität Bayreuth sowie in Kooperation mit dem Institut für Biophysik der Akademie der Wissenschaften der tschechischen Republik in Brünn (Tschechische Republik), dem Lehrstuhl für Biophysik der Palacky Universität in Olmütz (Tschechische Republik), dem Physiologischen Institut und dem Institut für vegetative Physiologie der Charité Berlin, dem Institut für translationale Immunologie der Universitätsmedizin Mainz und der Care Group Sight Solution in Dabhasa (Vadodara, Indien).

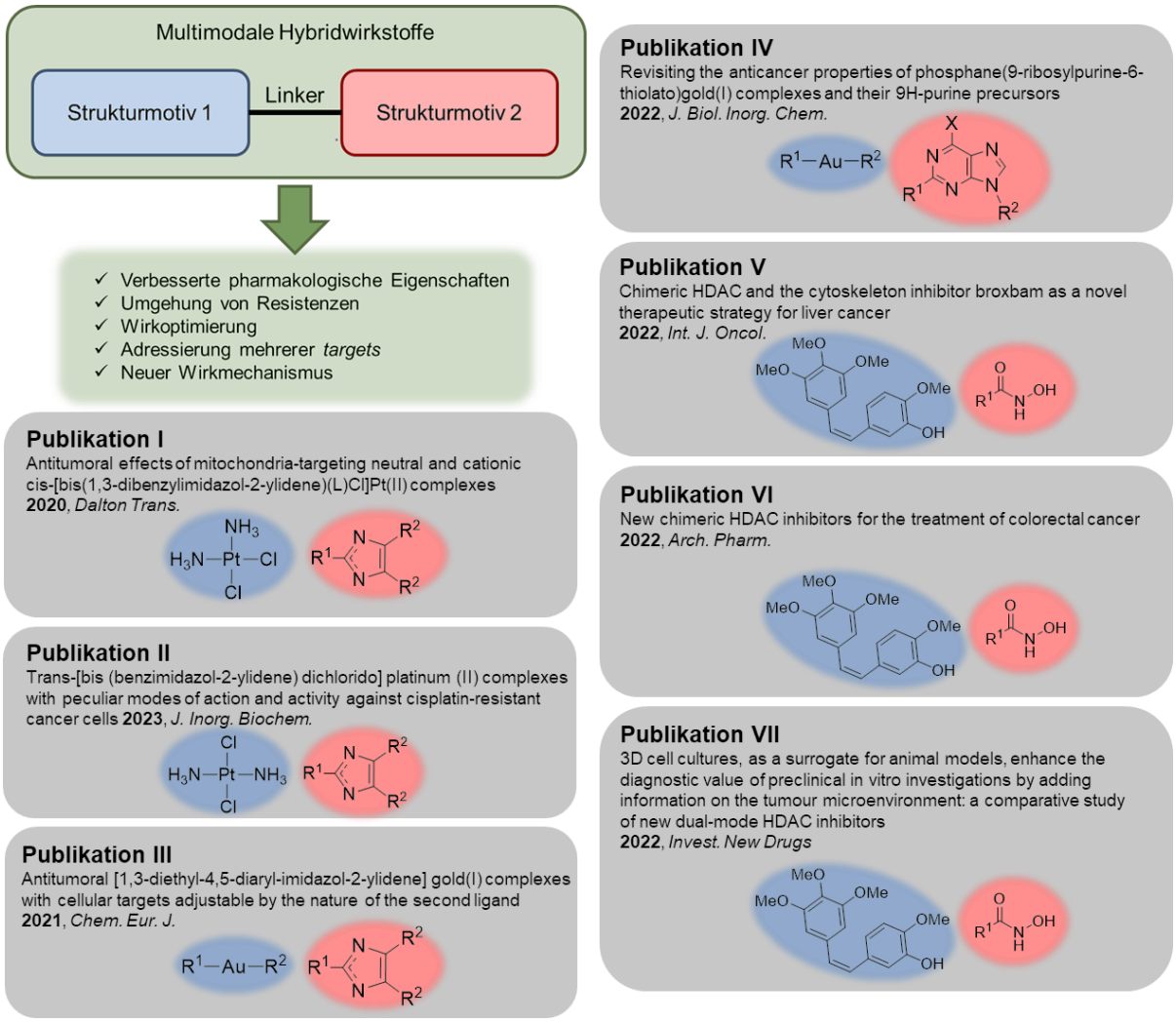

Abbildung 9. Multimodale Hybridwirkstoffe, welche auch als chimäre Substanzen bezeichnet werden, können durch strukturelle Kombinationen verschiedene Eigenschaften aufweisen, welche Vorteile gegenüber etablierten Chemotherapeutika darstellen.[63] Abgebildet sind die einzelnen Studien dieser Arbeit mit ihren jeweils zugrunde liegenden Strukturmotiven. Publikation I beschreibt NHC-Platin-Komplexe mit gegenüber Cisplatin verbesserten pharmakologischen Eigenschaften und einem neuen Wirkmechanismus. Publikation II behandelt hybride Platin-NHC-Komplexe in *trans* Geometrie, welche die Umgehung von Cisplatin-Resistenzen und einen neuen Wirkmechanismus ermöglichen. Publikation III behandelt eine Serie an hybriden NHC-Gold-Komplexen, deren intrazelluläre Anreicherung sich mittels des zweiten Liganden steuern lässt. Diese Serie ermöglicht verbesserte pharmakologische Eigenschaften, die Umgehung von Resistenzen, Wirkoptimierung und neue Wirkmechanismen. In Publikation IV wird eine Serie an Purin-Gold-Antimetaboliten untersucht, welche verbesserte pharmakologische Eigenschaften und somit eine Wirkoptimierung sowie die Adressierung mehrerer *targets* ermöglichen. Publikation V, Publikation VI und Publikation VII behandeln verschiedene Vertreter einer Serie chimärer CA-4-HDACi Derivate, welche verbesserte pharmakologische Eigenschaften, Wirkoptimierung und die Adressierung mehrerer *targets* ermöglichen. Zudem wurden die in Publikation VII beschriebenen Ergebnisse mittels verschiedener 3D Zellkultur-Assays gewonnen, was einen tieferen Einblick in die Wirkung potenzieller Chemotherapeutika im 3D tumor-assoziierten Kontext ermöglicht.

3.2 Antitumorale Wirkung neutraler und kationischer *cis*-NHC-Pt(II)-Komplexe, welche auf das intrazelluläre *target* Mitochondrien abzielen [Publikation I]

Der erste Artikel behandelt weiterentwickelte hybride Cisplatin-Analoga der Art *cis*-[(NHC)^1(NHC)^2(L)Cl]Pt(II). Das NHC Imidazol Motiv dient vornehmlich der Erhöhung der Stabilität der Komplexe unter physiologischen Bedingungen. Bei den im Artikel hinsichtlich ihrer biologischen Wirkmechanismen untersuchten Substanzen handelt es sich um zwei besonders aktive Vertreter einer größeren Serie aus *cis*-NHC-Pt(II)-Komplexen mit Chlorido-, beziehungsweise Triphenylphosphin-Liganden.[84, 85]

Die beiden strukturellen Vertreter stellen die Auswirkung eines neutralen bzw. kationischen NHC Charakters auf die Bioaktivität gegenüber. Aus dem kationischen Charakter resultiert eine deutlich erhöhte *in vitro* Zytotoxizität und Selektivität gegenüber Krebszelllinien, was mit nachweislich erhöhter zellulärer Aufnahme korreliert. Die für Cisplatin charakteristische DNA-Interaktion konnte für beide Komplexe *in vitro* nachgewiesen werden, wobei deren DNA-Interaktion die der Leitstruktur deutlich übersteigt, was somit für den Erfolg des pleiotropen Strukturmotivs spricht. Zudem konnten einige weitere interessante Wirkmechanismen der Komplexe nachgewiesen werden, welche außerhalb des Cisplatin-typischen Wirkspektrums liegen. Dazu zählt insbesondere die mittels Alkinyl-Analoga in Melanomzellen nachgewiesene Akkumulation in den Mitochondrien, welche mit Verringerung des mitochondrialen Membranpotenzials ($\Delta\Psi m$) und Erhöhung des intrazellulären Levels reaktiver Sauerstoffspezies (ROS) einhergeht.

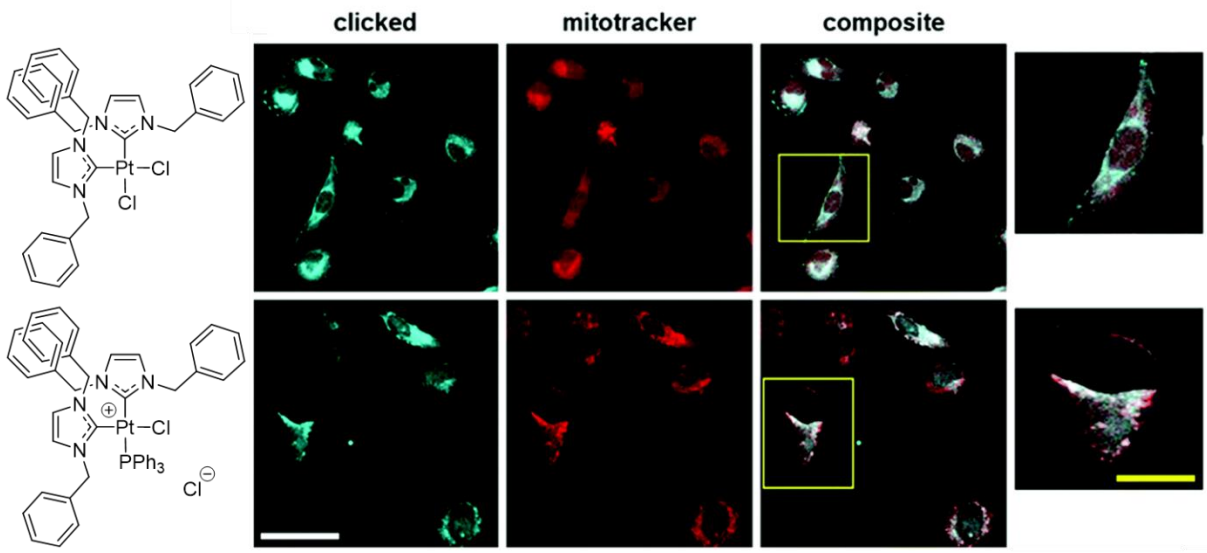

Abbildung 10. Darstellung der untersuchten Strukturen und ihrer Anreicherung in den Mitochondrien von 518A2 Melanomzellen, wo sie neben DNA assoziierten Effekten, mitochondrial assoziierte Effekte wie Verringerung des $\Delta\Psi m$ und Erhöhung des zellulären ROS Levels induzieren.

Des Weiteren induziert der kationische Pt(II)-Komplex in hohem Maße die Bildung von Aktin *stress fibers*. In diesem Zusammenhang konnte ein G1-Zellzyklus-Arrest und die Induktion von Apoptose nachgewiesen werden. Für den korrespondierenden neutralen Komplex waren letztere Beobachtungen nicht oder nur in sehr geringem Maße zutreffend. Die insgesamt bessere Aktivität des kationischen Komplexes lässt sich mit großer Wahrscheinlichkeit auf seinen DLC (*delocalized lipophilic cation*) Charakter zurückführen. DLCs sind für ihre Eigenschaften bekannt, Lipidschichten zu überwinden und sich, aufgrund des negativen inneren Membranpotenzials, selektiv in Mitochondrien anzureichern.[86, 87] Aus dieser Studie kann geschlussfolgert werden, dass hybride NHC-Platin(II)-Komplexe eine Mitochondrien assoziierte Wirkung von Pt-Komplexen ermöglichen und somit den für Cisplatin typischen reinen DNA assoziierten Wirkmechanismus umgehen, was es ermöglicht, Cisplatin-resistente Zellen zu adressieren.

Weitere Details in: ***Antitumoral effects of mitochondria-targeting neutral and cationic cis-[bis(1,3-dibenzylimidazol-2-ylidene)(L)Cl]Pt(II) complexes***

Matthias Rothemund[+], Sofia I. Bär[+], Tobias Rehm, Viktor Brabec und Rainer Schobert

Dalton Trans., **2020**, 49, 8901

[Publikation I]

[+] diese Autoren haben zu gleichen Anteilen zum Manuskript beigetragen

3.3 *Trans*-[Bis(benzimidazol-2-yliden)dichloro]platin(II)-Komplexe mit besonderer Wirkungsweise und Aktivität gegen Cisplatin-resistente Krebszellen

[Publikation II]

Im Rahmen dieses Manuskripts wird jeweils eine Serie von *cis*- und eine Serie von *trans*-[Bis(benzimidazol-2-yliden)dichloro]platin(II)-Komplexen hinsichtlich ihrer Zytotoxizität gegenüber Krebszellen und ihrer zellulären *targets* untersucht. Dabei handelt es sich um hybride Substanzen, welche durch Komplexierung von Platin mit NHCs, genauer Benzimidazolderivaten, in *cis*- und *trans*-Konfiguration aufgebaut wurden. Bioaktive NHC-Komplexe mit Platin als Zentralatom zeigen zunehmend Potential, aufgrund ihrer Verbesserten physiologischen Eigenschaften und ihrer Wirkung gegen CDDP resistente Krebszelllinien.[88, 89]

Im Rahmen dieser Studie wurden 16 Benzimidazol-Platin(II)-Komplexe synthetisiert, diese umfassen *cis*-DMSO- und *cis*-Bis(benzimidazol)-Komplexe und auch *trans*-Bis(benzimidazol)-Komplexe. Die Stabilität der Komplexe unter physiologischen Bedingungen wurde mittels ^{1}H- and ^{195}Pt-NMR nachgewiesen.

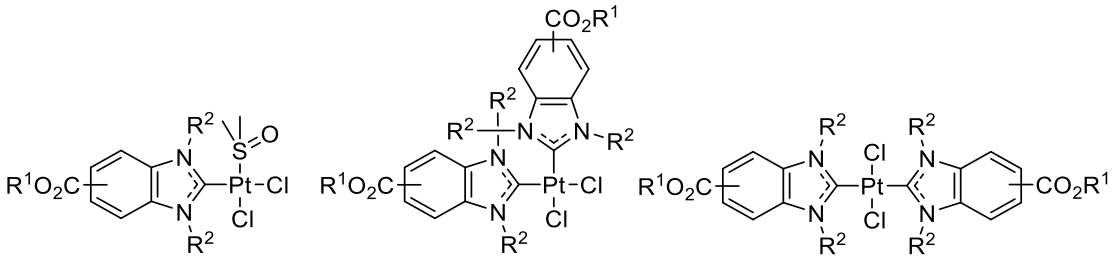

Abbildung 11. Übersicht über die verschiedenen Grundstrukturen der im Rahmen dieses Projekts untersuchten Benzimidazol-Platin-Komplexe, sowie deren aktivste Derivate **12b** und **8c**.

Mittels MTT-Assay basierter Untersuchung der hybriden Benzimidazol-Platin-Komplexe konnten gegen Cisplatin-resistente Krebszelllinien IC_{50} Werte (halbmaximale inhibitorische Konzentration; Maß für antiproliferative bzw. zytotoxische Wirkung von Substanzen) im einstelligen Mikromolaren bis in den zweistelligen Nanomolaren Bereich nachgewiesen werden. Dabei wurde deutlich, dass *cis*-Bis(benzimidazol)-Komplexe generell aktiver sind als deren DMSO Verwandten. Im weiteren Verlauf der Studie wurden die aktivsten Vertreter **12b** der *cis*- und **8c** der *trans*-Serie mittels biochemischer Assays weiter bezüglich ihrer zellulären *targets* und Wirkmechanismen in HCT116 Darmkrebszellen untersucht. Aufnahmestudien mittels ICP-MS zeigten, dass die starke zytotoxische Wirkung der *trans*-Komplexe nicht mit ihrer zellulären Aufnahme assoziiert ist. Das NHC System führt im Fall des *cis*-Komplexes **12b** zu einer deutlich erhöhten Aufnahme im Vergleich zu CDDP, während der *trans*-Komplex **8c** deutlich schlechter aufgenommen wird. Die starke zytotoxische Wirkung von **8c** trotz geringer Aufnahme unterstreicht seine Effektivität. Unselektive Toxizität konnte mittels Lactat

Dehydrogenase (LDH) Assay ausgeschlossen werden, da Freisetzung von LDH in Folge der Permeabilisierung der Plasmamembran als Zeichen von Nekrose gilt.[90] Dahingegen konnte die Induktion des apoptotischen Zelltods durch beide Komplexe nachgewiesen werden. Eng verknüpft mit Apoptose ist der Verlust des $\Delta\Psi m$ und der daraus resultierende Anstieg intrazellulärer ROS Level.[91, 92] Diese Effekte wurden auch von den Komplexen **12b** und **8c** induziert. Im weiteren Verlauf der Studien zeigte der *cis*-Komplex **12b**, Cisplatin-typische Effekte, welche sich in Form eines veränderten Zellzyklus und Induktion von DNA Konformationsänderungen nachweisen ließ. Der *trans*-Komplex **8c** induzierte hingegen keinen dieser Effekte, was einen Cisplatin untypischen Wirkmechanismus voraussetzt. Um die intrazellulare Lokalisation der Komplexe abzubilden, wurden strukturelle Analoga synthetisiert, welche mittels intrazellulärer Click Reaktion mit einem Fluorophor gekoppelt werden konnten. Somit konnte die erwartete Anreicherung des *cis*-Komplexes im Zellkern bestätigt, und der *trans*-Komplex im Bereich der Mitochondrien lokalisiert werden. Bereits in Publikation I wurden Platin-Komplexe vorgestellt, welche sich in Mitochondrien anreichern und die mitochondriale Funktion beeinträchtigen.[89] Die aktuelle Studie unterstreicht die Eignung hybrider *trans*-NHC-Komplexe von Platin(II) als Anti-Krebs Verbindungen, welche auf andere Strukturen als die DNA abzielen und spricht somit gegen das alte Paradigma, dass *trans*-Platin Verbindungen ungeeignet als Krebsmedikamente sind.[93]

Manuskript: ***Trans-[bis(benzimidazol-2-ylidine)dichlorido]platinum(II) complexes with peculiar modes of action and activity against cisplatin resistant cancer cells***

Sofia I. Bär[+], Sebastian W. Schleser[+], Natalie Oberhuber, Alexander Herrmann, Luca Schlotte, Stefanie E. Weber and Rainer Schobert

J. Inorg. Biochem. **2023**, 238, 112028

[Publikation II]

[+] diese Autoren haben zu gleichen Anteilen zum Manuskript beigetragen

3.4 Zielgerichtete antitumorale Wirkstoffe: (Imidazol-2-yliden)(L)gold(I)-Komplexe deren intrazelluläre *targets* mittels des sekundären Liganden feinjustierbar sind

[Publikation III]

Die Eignung hybrider Metall-NHC-Komplexe als potenzielle Chemotherapeutika konnte in den beiden vorhergehenden Artikeln am Beispiel des Platins verdeutlicht werden. Durch Entdeckung der antitumoralen Eigenschaften des Antirheumatikums Auranofin, rückte Gold als Zentralatom in den Fokus des Wirkstoffdesigns. Der Wirkmechanismus von Auranofin basiert auf Inhibition der mitochondrialen TrxR und der Erhöhung der mitochondrialen Permeabilität.[94, 95] Eine direkte Folge dessen ist die Erhöhung des intrazellulären ROS Levels, Freisetzung von Cytochrom C und somit die Induktion von Apoptose.[96]

Diese Eigenschafen in Kombination mit der Stabilität, welche durch Einführung des NHC Motivs gewonnen werden kann[97], sollten mit einer Serie aus Au(I)-NHC-Komplexen, welche auf dem CA-4 Strukturmotiv in Verbindung mit NHCs aufbauen, realisiert werden. Strukturelle Anthracen-Analoga der untersuchten Testverbindungen, wurden im Rahmen dieser Arbeit zur intrazellulären Lokalisation der Verbindungen verwendet. Dabei wurde der Zusammenhang zwischen Art des sekundären Liganden am Gold-Zentrum und der Ladung des Komplexes mit intrazellulärer Lokalisation und Wirkung auf die Krebszelllinien aufgeklärt. Die ermittelten IC_{50} Werte der Verbindungen weisen auf einen Zusammenhang des DLC Charakters und der zytotoxischen Wirkung hin. Mit zunehmender Delokalisation der positiven Ladung der Gold-Komplexe steigt deren zytotoxische Wirkung auf die untersuchten Zelllinien. Die unterschiedliche intrazelluläre Lokalisation der Komplexe, welche mittels fluoreszenter Anthracen Analoga in Melanomzellen dokumentiert wurde, weist auf unterschiedliche Wirkmechanismen in Abhängigkeit von der Art des sekundären Liganden L hin. Basierend darauf wurde die Wirkung der Verbindungen auf typische zelluläre *targets* unter Berücksichtigung der Bereiche der Akkumulation untersucht. Unabhängig von Lokalisation, wurde für alle Testsubstanzen die Induktion des apoptotischen Zelltods nachgewiesen.

Aufgrund der Lokalisation des neutralen Komplexes **4b** (L = Cl) im Bereich des Zellkerns wurde eine potentielle DNA Interaktion der Verbindung **4b** und des strukturellen Analogons **4a** (L = Cl) mittels Ethidiumbromid (EtdBr) Sättigungsassay und *electrophoretic mobility shift assay* (EMSA) untersucht und nachgewiesen. Der EtdBr Sättigungsassay weist auf eine starke DNA-Interaktion der Substanzen **4** hin, welche die Wirkung von CDDP deutlich übersteigt. Die Ergebnisse des EMSA bestätigen die Interaktion der Substanzen **4** mit DNA. Substanz **4a** zeigt hier einen deutlich verringerten Effekt im Vergleich zu CDDP, was im Einklang mit der bekannten nicht-kovalenten Interaktion von NHC-Gold-Komplexen mit DNA steht.[98]

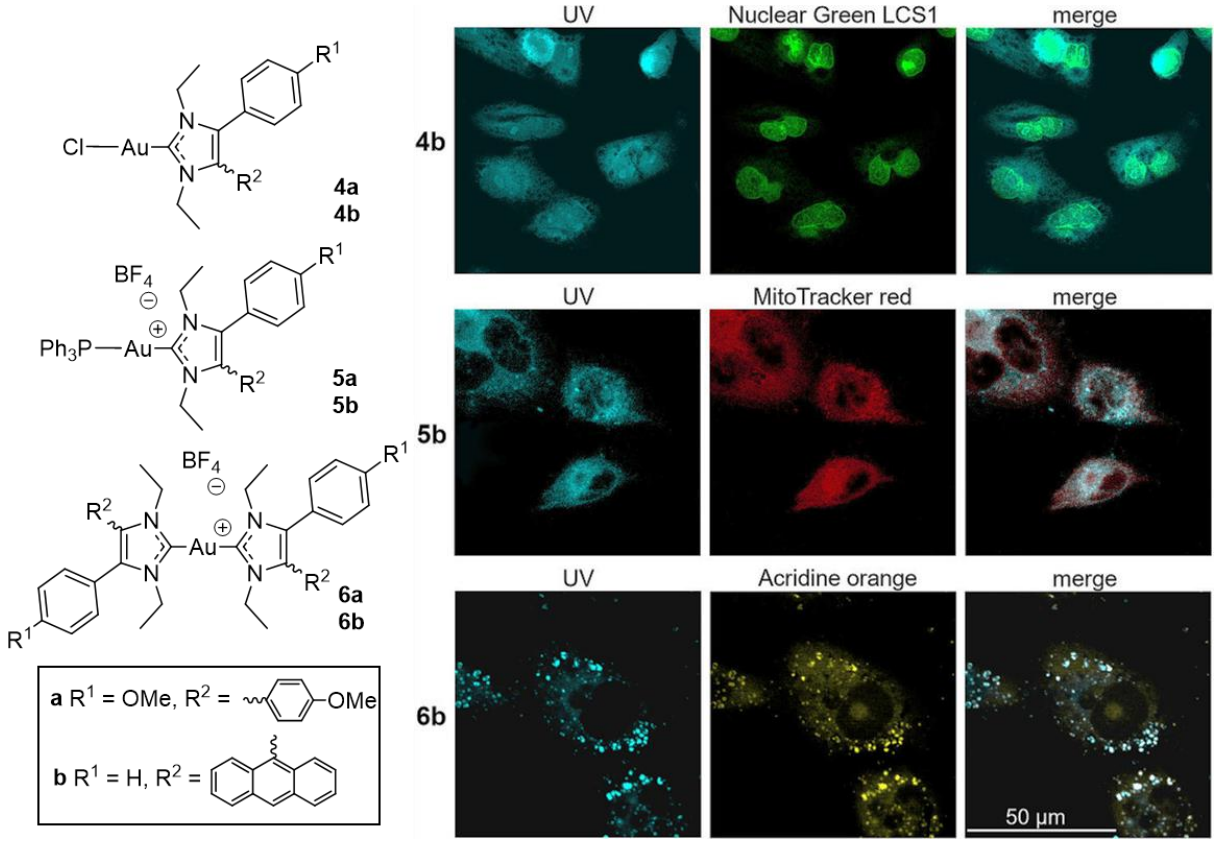

Abbildung 12. Strukturen der (Imidazol-2-yliden)(L)gold(I)-Komplex Serie und ihrer intrazellulären Anreicherung, welche mittels der Anthracen Reihe **b** dokumentiert wurde. Konfokal-Fluoreszenzmikroskopische Aufnahmen in 518A2 Melanomzellen. Emission der Komplexe (UV), Cofärbung der jeweiligen Zellkompartimente (mittlere Spalte) und deren *merge* (rechte Spalte). Aufnahmen erfolgten bei 2000 x Vergrößerung.

Der kationische Komplex **5b** (L = PPh_3) wurde im Bereich der Mitochondrien lokalisiert. Basierend darauf wurde die Wirkung des Komplexes **5b** sowie seines strukturellen Analogons **5a** auf Mitochondrien-assoziierte zelluläre Mechanismen untersucht. Die antitumorale Wirkung einiger anderer Gold(I)-Komplexe basiert hauptsächlich auf der Inhibition der TrxR, einem Schlüsselenzym des zellulären Schutzmechanismus vor oxidativem Stress. Für die kationischen Komplexe **5** wurde im dreistelligen nanomolaren Konzentrationsbereich eine inhibierende Wirkung auf TrxR nachgewiesen, welche die Wirkung des bekannten TrxR-Inhibitors Auranofin übersteigt. Infolgedessen konnten sowohl die Erhöhung der intrazellulären ROS Level als auch die Verringerung des $\Delta\Psi m$ durch die Komplexe **5** nachgewiesen werden.

Eine Anreicherung des Bis-NHC-Komplex **6b** in den Lysosomen konnte nachgewiesen werden. Passend dazu konnte eine durch die Komplexe **6** induzierte zeitabhängige Abnahme des Lysosomenmembranpotenzials dokumentiert werden. Dies deutet auf lysosomale Membran Permeabilisierung (LMP) hin, welche zum Austritt des Lysosomeninhalts in das Cytoplasma führt, was den p53-unabhängigen lysosomalen Zelltod induzieren kann [99].

Zusammenfassend konnte nachgewiesen werden, dass sich die jeweiligen Strukturverwandten **a** und **b** der Serie in ihrem intrazellulären Wirkmechanismus ähneln, was die Vergleichbarkeit der gewonnenen Ergebnisse der **a** und **b** Reihe bestätigt. Die Ergebnisse dieser Studie zeigen, dass es möglich ist durch den sekundären Liganden L die Ladung, Größe und Lipophilie der hybriden Komplexe und somit die intrazelluläre Anreicherung derer zu steuern. Dieses Konzept der Lenkung eines bioaktiven chimären Metall-Komplexes an ein spezifisches intrazelluläres *target* kann dazu beitragen unerwünschte Nebeneffekte zu reduzieren und die Effektivität der Substanzen zu verbessern.

Weitere Details in: ***Guided Antitumoural Drugs: (Imidazol-2-ylidene)(L)gold(I) Complexes Seeking Cellular Targets Controlled by the Nature of Ligand L***

Sofia I. Bär[+], Madeleine Gold[+], Sebastian W. Schleser, Tobias Rehm, Alexander Bär, Leonhard Köhler, Lucas R. Carnell, Bernhard Biersack, and Rainer Schobert

Chem. Eur. J. **2021**, 27, 5003

[Publikation III]

[+] diese Autoren haben zu gleichen Anteilen zum Manuskript beigetragen

3.5 Wiederbetrachtung der antitumoralen Eigenschaften von Phosphan(9-ribosylpurin-6-thiolat)-gold(I)-Komplexen und ihrer 9*H*-Purin Vorläufer [Publikation IV]

Der vierte Artikel dieser Arbeit behandelt die Übertragung des hybriden Metall-NHC Motivs auf die Substanzgruppe der Antimetaboliten. Das für seine TrxR inhibierenden Eigenschaften bekannte Gold-Motiv des Auranofins wurde mit dem Strukturmotiv der etablierten antitumoralen Antimetaboliten 6-Mercaptopurin (6-MP) und 6-Thioguanin (6-TG) verknüpft. Diese werden zur Entfaltung ihrer Wirkung *in vivo* zunächst in die entsprechenden Nukleotidanaloga umgewandelt, was zur Folge hat, dass ihre entsprechenden Nukeloside auch als wirksame Substanzen zur Behandlung von Krebs gelten.[100, 101] Es ist bereits bekannt dass eine Verknüpfung dieser Thiopurine mit verschiedenen Triorganylphosphan-Gold(I) Fragmenten zu einer Verbesserung ihrer Effektivität führt.[102–104]

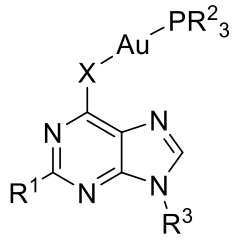

5 R^1 = H, R^2 = Ph, R^3 = D-Rib, X = S
6 R^1 = NH_2, R^2 = Ph, R^3 = D-Rib, X = S

Abbildung 13. Grundstruktur der untersuchten hybriden Antimetaboliten-Gold-Komplexe und der aktivsten Verbindung **5,** sowie der Verbindung **6** mit der stärksten zellulären Aufnahme.

Die im Rahmen dieser Studien untersuchte Wirkstoffserie umfasste vier literaturbekannte Triorganylphosphan(9*H*-Purin-6-thiolat)-Gold(I)-Komplexe mit bzw. ohne 2-NH_2-Substituenden[102] sowie vier neue strukturelle Analoga mit Thioguanosin- und Thioinosin-Liganden, einen dimeren Komplex dieser Art und einen analogen Purin-6-Selenat-Gold(I)-Komplex. Zunächst wurde die Stabilität der Komplexe unter physiologischen Bedingungen über 72 h mittels NMR bestätigt. Mittels MTT basierter Bestimmung der Zytotoxizität gegen ein Panel aus sieben humanen Krebszelllinien konnten IC_{50} Werte bis in den dreistelligen nanomolaren Bereich ermittelt werden. Es zeigte sich eine strukturabhängige Verbesserung der Zytotoxizität durch die Einführung eines 9-D-Ribosyls, zudem zeigten die Triphenylphosphan Komplexe eine generell bessere Wirkung als ihre Triethylphosphan Analoga. Interessanterweise zeigten diese Effekte keine Auswirkungen auf die zelluläre Aufnahme, wobei Komplex **6** durch seine besonders starke Aufnahme hervorstach. Im weiteren Verlauf wurde der potenteste Komplex **5** weiter bezüglich seines intrazellulären Wirkmechanismus untersucht. Dieser zeigte einen bipolaren Effekt auf den Zellzyklus von 518A2 Melanomzellen; bei niedrigen Konzentrationen wurde ein G1-Arrest induziert, wie es für andere bekannte Thiopurine typisch ist, während in hohen Konzentrationen ein S-Arrest induziert wurde, wie er für Auranofin typisch ist. Die letztere Wirkung ist höchstwahrscheinlich auf seine ausgeprägte Hemmung von TrxR zurückzuführen. Komplex **5** löste zudem auch schwere DNA-Läsionen und Fragmentierung aus, was letztlich zur Apoptose der Krebszellen führte.

Somit ist diese Serie ein weiteres Beispiel für das hohe Potenzial chimärer Strukturen hinsichtlich ihrer Eignung als Krebsmedikamente, da durch Kombination verschiedener Strukturen verschiedene Effekte miteinander verbunden werden können, welche durch ein Molekül induzierbar sind.

Manuskript: ***Revisiting the anticancer properties of phosphane(9-ribosylpurine-6-thiolato)gold(I) complexes and their 9H-purine precursors***

Luisa Kober[+], Sebastian W. Schleser[+], Sofia I. Bär and Rainer Schobert

J. Biol. Chem. **2022**, 27, 731

[Publikation IV]

[+] diese Autoren haben zu gleichen Anteilen zum Manuskript beigetragen

3.6 Der chimäre HDAC- und Zytoskelett-Inhibitor Broxbam als neue therapeutische Strategie für die Behandlung von Leberkarzinomen [Publikation V]

Patienten welche an hepatozellulärem Karzinom (HCC) oder cholangiozellularem Karzinom (CCC) erkranken haben eine durchschnittliche 5-Jahres Überlebensrate von nur 20%, damit zählen HCC und CCC zu den tödlichsten Krebsarten.[2] Aufgrund der sehr begrenzten Behandlungsmöglichkeiten ist hier die Nachfrage nach neuen klinisch relevanten Therapeutika besonders präsent. Die dritte Publikation behandelt den multimodalen HDAC und Zytokelett Inhibitor Broxbam, welcher durch strukturelle Kombination der etablierten Pharmakophore CA-4[28] und SAHA[58, 59] synthetisiert wurde. CA-4 ist ein Vertreter der Mikrotubuli-destabilisierenden Agenzien und SAHA ein Vertreter der HDACi.[28, 58, 59] Broxbam ist Derivat einer Serie chimärer HDACi, welche bereits publiziert wurden, wobei die molekularen Wirkmechanismen von Broxbam jedoch nicht weiter charakterisiert wurden.[105]

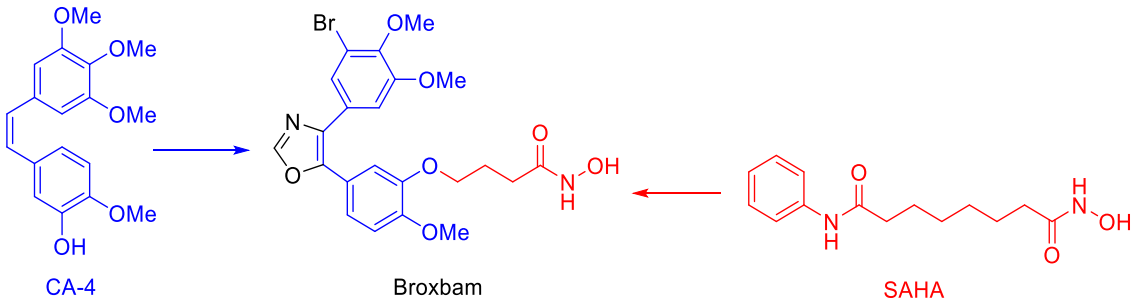

Abbildung 14. Strukturen des Mikrotubuli-destablisierenden Agens CA-4, sowie des HDACi SAHA, welche als strukturelle Grundlage für die chimäre Substanz Broxbam dienen.

Die potenzielle Eignung von Broxbam als Krebstherapeutikum wurde an den vier primären Leberkrebszelllinien Huh7, HepG2, TFK1 und EGI1 untersucht. Dabei reduzierte die Hybridsubstanz die Proliferation der Krebszellen sowohl Zeit- als auch Dosis-abhängig im sub-mikromolaren Konzentrationsbereich (IC_{50} ~0.6 µM). Bereits an diese Stelle zeigt sich, dass die Wirkung von Broxbam die Effektivität der etablierten Substanz SAHA übertrifft (IC_{50} 1.4-3.2 µM), was für den Erfolg der chimären Kombination spricht. Die Wirkung von Broxbam basiert zum einen molekular auf HDAC Inhibition, insbesondere der HDAC 6, wodurch mitochondrial vermittelte Apoptose induziert wird. Zum anderen konnte eine Tubulinpolymerisations-hemmende Wirkung nachgewiesen werden, welche sich durch verringerte Migrationsfähigkeit als auch anti-angiogene Effekte äußerte, was sich sowohl auf das CA-4 Motiv als auch die HDAC 6 Inhibition zurückführen lässt. Denn es ist bekannt, dass HDAC 6 auch als Tubulin Deacetylase fungiert und somit zelluläre Tubulin-assoziierte Mechanismen, wie das

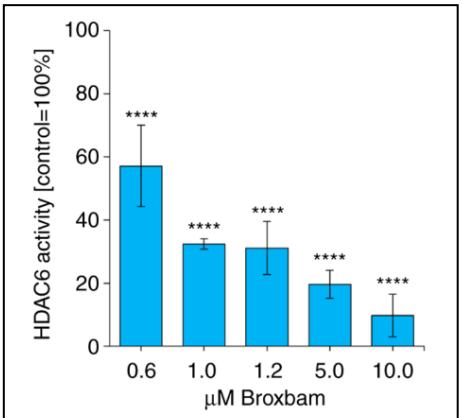

Abbildung 15. HDAC 6 Aktivität nach Behandlung mit der Hybrid-substanz Broxbam.

Zytoskelett und die Migrationsfähigkeit beeinflusst.[106] Auch *in vivo* zeigt die Verbindung potente antitumorale als auch antiangiogene Eigenschaften, ohne dabei signifikant toxisch zu wirken. Im Rahmen dieser Studie wurden zudem 3D Tumormodelle aus Leberkrebszellen verwendet, welche auf der Chorioallantoismembran von Hühnereiern kultiviert wurden. Die 3D Modelle dienen einer Erhöhung der Relevanz der präklinisch gewonnen Daten, da sie eine *in vivo* nähere Abbildung der Tumorbedingungen ermöglichen.[78]

Abschließend ist festzuhalten, dass die kürzlich vorgestellte chimäre Substanz Broxbam[105], ein vielversprechender, pleiotrop wirkender HDACi ist, welcher als potenzieller Wirkstoff für die Behandlung von Leberkrebs für weitere Studien in Betracht gezogen werden sollte.

Weitere Details in: ***Chimeric HDAC and the cytoskeleton inhibitor broxbam as a novel therapeutic strategy for liver cancer***

Sofia I. Bär, Alexandra Dittmer, Bianca Nitzsche, Gohar Ter-Avetisyan, Michael Fähling Adrian Klefenz, Leonhard Kaps, Bernhard Biersack, Rainer Schobert und Michael Höpfner

Int. J. Oncol., **2022**, 60, 73

[Publikation V]

3.7 Neue chimäre HDAC Inhibitoren für die Behandlung von Kolonkarzinomen [Publikation VI]

Darmkrebs liegt auf Platz drei der Todesursachen, welche mit einer Krebserkrankung assoziiert sind [107]. Dies ist unter anderem begründet durch die hohe Rückfallrate, welche sich in hohem Maße auf aggressive Behandlungsmethoden und zunehmende Resistenzentwicklung zurückführen lässt.[108, 109] Um diese Problematik beheben zu können, wird an neuen Behandlungsmöglichkeiten geforscht. Ein vielversprechender chemotherapeutischer Ansatz sind chimäre, niedermolekulare Wirkstoffe, welche die Wirkmechanismen verschiedener etablierter Chemotherapeutika vereinen und somit eine neue, verbesserte Substanz resultiert.[63, 64]

Im Rahmen dieser Studie wurden vier chimäre Substanzen, welche sie Strukturmotive HDACi und CA-4 vereinen, hinsichtlich ihrer biologischen Aktivität gegenüber Tumorzelllinien untersucht. Diese umfassen bei beiden literaturbekannten Substanzen Troxbam und Troxham[105] sowie die Synthese der beiden neuen Strukturen Animthioxam und Brimbam. Die selektive Zytotoxizität gegenüber Krebszellen wurde mittels MTT-Assay ermittelt, wobei sich die Substanz Troxbam mit einem Selektivitätsindex (SI) von ≥ 68.1 als außergewöhnlich selektiv gegenüber Krebszellen zeigte (CA-4 SI 19.5, SAHA SI ≥ 32.5). Der duale Wirkmechanismus äußerte sich in der Adressierung HDACi- als auch CA-4-spezifischer *targets*. Der aktivste Vertreter induzierte einen G2-M Arrest des Zellzyklus von HCT116 Darmkrebszellen, welcher assoziiert ist mit HDAC Inhibition und der Induktion von Apoptose.[110, 111] Zudem konnte eine effektive Reduktion des Metastasierungspotenzials und der zellulären Dynamik durch die Testverbindungen induziert werden, was sich darauf zurückführen lässt, dass die Aktivität des CA-4 Motivs in den chimären Substanzen weitestgehend erhalten bleibt. Neben der generellen HDAC inhibierenden Aktivität wurden mittels Western Blot die Expressionslevels des Apoptose inhibierenden Proteins Survivin überprüft, welches assoziiert ist mit HDAC Aktivität und unter anderem Einfluss hat auf Voranschreiten des Zellzyklus und die Chemoresistenz von Krebszellen.[112] Es konnte eine signifikante Verringerung der Survivin Expression durch Troxbam und Troxham nachgewiesen werden, welche vergleichbar mit der Wirkung des monomodalen HDACi SAHA ist. Die Adressierung dieses *targets* ist von besonderer Bedeutung, da Survivin in der Regel ausschließlich von Krebszellen exprimiert wird und somit ein Alleinstellungsmerkmal maligner Zellen ist.[112]

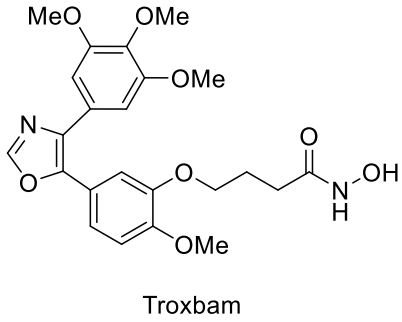

Troxbam

Abbildung 16. Struktur des aktivsten Vertreters Troxbam, der vorgestellten Reihe an chimären HDACi.

Die Ergebnisse dieser Studie belegen die multimodale Wirkung der Hybridsubstanzen und damit den Erfolg der Kombination des HDACi Motivs mit dem Mikrotubuli-polymerisations Hemmer CA-4. Es

konnten zum einen die Leistruktur typischen Wirkungen erhalten bleiben und zum andern die Aktivität und Selektivität verbesserte werden.

Manuskript: ***New chimeric HDAC inhibitors for the treatment of colorectal cancer***

Sofia I. Bär, Rohan Pradhan, Bernhard Biersack, Bianca Nitzsche, Michael Höpfner und Rainer Schobert

Arch. Pharm. **2022**, 356, 2200422

[Publikation VI]

3.8 3D Zellkultur Systeme als Alternative zu Tierversuchen verbessern den diagnostischen Wert präklinischer *in vitro* Untersuchungen durch zusätzliche Informationen über das Tumormikroenvironment: eine Vergleichsstudie neuer bimodaler HDAC-Inhibitoren [Publikation VII]

Nach wie vor ist die Etablierung neuer Wirkstoffe eine Ressourcen-aufwändiger Prozess bei dem weniger als 5% der präklinisch erfolgreichen Substanzen über Phase I in klinischen Studien hinauskommen.[79] Neben dem Ansatz chimärer Substanzen, welche durch strukturelle Kombination etablierter Pharmakophore, neue potente Wirkstoffe hervorbringen sollen, spielt auch die Verbesserung der präklinischen Methoden eine zentrale Rolle.[70, 78] Konventionell verwendete 2D Monolayer Zellkultursysteme haben zahlreiche Fortschritte der Forschung an neuen Krebstherapien ermöglicht, bilden jedoch zentrale *in vivo* Bedingungen nicht oder nur unzureichend ab.[78]

In dieser Publikation wird die Untersuchung potenzieller antitumoraler Substanzen mit Hilfe 3D Zellkulturmethoden zur Erhöhung der Relevanz präklinischen Studien beschrieben. Im Gegensatz zu konventionellen 2D basierten Zellkulturassays, beziehen 3D Zellkulturassays zentrale Effekte wie Wirkstoffaufnahme und Verteilung, als auch den Einfluss der Tumormikroumgebung im tumorähnlichen Modell mit ein.[78] Für die Untersuchung der chimären Testverbindungen wurden *multicellular tumour spheroids* (MCTS) aus Kolonkarzinomzellen und Mikrotumore, welche mittels Bioreaktorsystem generiert wurden, verwendet. Charakteristische Messgrößen, welche sich in 2D Assays etabliert haben, sollten auf 3D MCTS übertragen werden. Bei den untersuchten Testsubstanzen handelt es sich um kürzlich publizierte, jedoch nicht näher hinsichtlich biologischer Aktivität charakterisierte chimäre Verbindungen Troxbam und Troxham.[105] Diese vereinen die Struktur des etablierten HDACi SAHA mit der des Mikrotubuli-destabilisierenden Agens CA-4 und unterscheiden sich in der Kettenlänge des Linkers. Bereits bei Untersuchung der wachstumsinhibierenden Eigenschaften der Esterbindungen, wurde ein Unterschied zum etablierten 2D System erkenntlich, da die angewandten IC_{50} Konzentration, welche mittels 2D Assay ermittelt wurde, im Falle der Leisubstanz CA-4 zu keiner Verringerung des MCTS Wachstums führte. Im weiteren Verlauf der Studie wurde die Verteilung toter Zellen im Inneren der MCTS im Zusammenhang mit der Substanzbehandlung mittels Propidiumiodid (PI) Färbung fluoreszenzmikroskopisch analysiert. PI kann lediglich die permeabilisierte Zellmembran toter Zellen

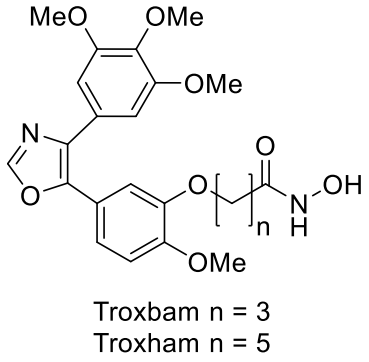

Abbildung 17. Übersichtsstruktur der HDACi und CA-4 abgeleiteten Hybrid-substanzen Troxbam und Troxham.

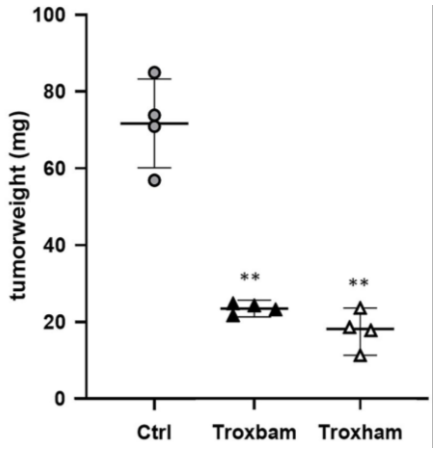

Abbildung 18. Finale Tumormassen von in vitro Mikrotumoren, nach einer Wachstumsperiode von 28 Tagen. Substanzbehandlung erfolgte an Tag 21, DMSO diente als Kontrolle (Ctrl).

passieren und färbt somit selektiv die DNA abgestorbener Zellen an.[113] Des Weiteren konnten mittels (immuno)fluoreszenz Mikroskopie die Erhöhung der ROS Level in den MCTS in Folge der Substanzbehandlung nachgewiesen werden sowie die Caspase 9 vermittelte Aktivierung des apoptotischen Zelltods. Schließlich wurde die wachstumsinhibierende Wirkung der hybriden Substanzen auf *in vitro*, mittels eines Bioreaktorsystems, generierte Mikrotumore untersucht, dabei konnte für beide Testverbindungen eine signifikante Reduktion des Tumorwachstums verzeichnet werden.

Diese Studie bezieht 3D tumor-assoziierte Aspekte in die Evaluation potenzieller multimodaler, anti-tumoraler Wirkstoffe ein. 3D basierte Zellkultursysteme können zum einen Tiermodelle in gewissen Punkten ersetzen und zum anderen stellen sie eine wertvolle Ergänzung zum präklinischen Medikamentenscreening dar.

Weitere Details in: ***3D cell cultures, as a surrogate for animal models, enhance the diagnostic value of preclinical in vitro investigations by adding information on the tumour microenvironment: a comparative study of new dual-mode HDAC inhibitors***

Sofia I. Bär, Bernhard Biersack und Rainer Schobert

Invest. New Drugs, **2022**, 40, 953

[Publikation VII]

4 Literaturverzeichnis

[1] H. Sung, J. Ferlay, R. L. Siegel, M. Laversanne, I. Soerjomataram, A. Jemal, F. Bray, Global Cancer Statistics 2020: GLOBOCAN Estimates of Incidence and Mortality Worldwide for 36 Cancers in 185 Countries (**2021**), *CA Cancer J Clin*, *71*, 209. DOI: 10.3322/caac.21660.

[2] R. L. Siegel, K. D. Miller, H. E. Fuchs, A. Jemal, Cancer Statistics, 2021 (**2021**), *CA Cancer J Clin*, *71*, 7. DOI: 10.3322/caac.21654.

[3] S. M. Jones, N. B. Henrikson, L. Panattoni, K. L. Syrjala, V. Shankaran, A theoretical model of financial burden after cancer diagnosis (**2020**), *Future Oncol*, *16*, 3095. DOI: 10.2217/fon-2020-0547.

[4] O. M. Al-Quteimat, A. M. Amer, The Impact of the COVID-19 Pandemic on Cancer Patients (**2020**), *Am J Clin Oncol*, *43*, 452. DOI: 10.1097/COC.0000000000000712.

[5] J. Wise, Covid-19: Cancer mortality could rise at least 20% because of pandemic, study finds (**2020**), *Brit Med J*, *369*, 1735. DOI: 10.1136/bmj.m1735.

[6] L. Wyld, R. A. Audisio, G. J. Poston, The evolution of cancer surgery and future perspectives (**2015**), *Nat Rev Clin Oncol*, *12*, 115. DOI: 10.1038/nrclinonc.2014.191.

[7] J. S. D. Mieog, J. A. van der Hage, C. J. H. van de Velde, Neoadjuvant chemotherapy for operable breast cancer (**2007**), *Br J Surg*, *94*, 1189. DOI: 10.1002/bjs.5894.

[8] H. E. Skipper, Adjuvant chemotherapy (**1978**), *Cancer*, *41*, 936. DOI: 10.1002/1097-0142(197803)41:3%3C936:AID-CNCR2820410322%3E3.0.CO;2-B.

[9] D. Galmarini, C. M. Galmarini, F. C. Galmarini, Cancer chemotherapy: a critical analysis of its 60 years of history (**2012**), *Crit Rev Oncol Hematol*, *84*, 181. DOI: 10.1016/j.critrevonc.2012.03.002.

[10] V. T. DeVita, E. Chu, A history of cancer chemotherapy (**2008**), *Cancer Res*, *68*, 8643. DOI: 10.1158/0008-5472.CAN-07-6611.

[11] B. A. Chabner, T. G. Roberts, Timeline: Chemotherapy and the war on cancer (**2005**), *Nat Rev Cancer*, *5*, 65. DOI: 10.1038/nrc1529.

[12] R. Ralhan, J. Kaur, Alkylating agents and cancer therapy (**2007**), *Expert Opinion on Therapeutic Patents*, *17*, 1061. DOI: 10.1517/13543776.17.9.1061.

[13] B. T. Oronsky, T. Reid, S. J. Knox, J. J. Scicinski, The scarlet letter of alkylation: a mini review of selective alkylating agents (**2012**), *Transl Oncol*, *5*, 226. DOI: 10.1593/tlo.12187.

[14] D. Fu, J. A. Calvo, L. D. Samson, Balancing repair and tolerance of DNA damage caused by alkylating agents (**2012**), *Nat Rev Cancer*, *12*, 104. DOI: 10.1038/nrc3185.

[15] J. M. Reid, D. C. Stevens, J. Rubin, M. M. Ames, Pharmacokinetics of 3-methyl-(triazen-1-yl)imidazole-4-carboximide following administration of temozolomide to patients with advanced cancer (**1997**), *Clin Cancer Res*, *3*, 2393. PMID: 9815639

[16] ROTE LISTE 2022 Buchausgabe Einzelausgabe: Arzneimittelverzeichnis für Deutschland (einschließlich EU-Zulassungen und bestimmter Medizinprodukte), 1st ed. Rote Liste Service GmbH, Frankfurt am Main (**2022**) ISBN: 978-3-946057-74-1

[17] M. Visentin, R. Zhao, I. D. Goldman, The antifolates (**2012**), *Hematol Oncol Clin North Am*, *26*, 629. DOI: 10.1016/j.hoc.2012.02.002.

[18] S. Farber, L. K. Diamond, Temporary remissions in acute leukemia in children produced by folic acid antagonist, 4-aminopteroyl-glutamic acid (**1948**), *N Engl J Med*, *238*, 787. DOI: 10.1056/nejm194806032382301.

[19] M. Tiwari, Antimetabolites: established cancer therapy (**2012**), *J Cancer Res Ther*, *8*, 510. DOI: 10.4103/0973-1482.106526.

[20] I. M. Kompis, K. Islam, R. L. Then, DNA and RNA synthesis: antifolates (**2005**), *Chem Rev*, *105*, 593. DOI: 10.1021/cr0301144.

[21] S. Hatse, E. de Clercq, J. Balzarini, Role of antimetabolites of purine and pyrimidine nucleotide metabolism in tumor cell differentiation (**1999**), *Biochem Pharmacol*, *58*, 539. DOI: 10.1016/S0006-2952(99)00035-0.

[22] W. B. Parker, Enzymology of purine and pyrimidine antimetabolites used in the treatment of cancer (**2009**), *Chem Rev*, *109*, 2880. DOI: 10.1021/cr900028p.

[23] C. R. Hill, M. Cole, J. Errington, G. Malik, A. V. Boddy, G. J. Veal, Characterisation of the clinical pharmacokinetics of actinomycin D and the influence of ABCB1 pharmacogenetic variation on actinomycin D disposition in children with cancer (**2014**), *Clin Pharmacokinet*, *53*, 741. DOI: 10.1007/s40262-014-0153-2.

[24] B. A. Weaver, How Taxol/paclitaxel kills cancer cells (**2014**), *Mol Biol Cell*, *25*, 2677. DOI: 10.1091/mbc.E14-04-0916.

[25] M. Moudi, R. Go, C. Y. S. Yien, M. Nazre, Vinca alkaloids (**2013**), *Int J Prev Med*, *4*, 1231. PMID: 24404355

[26] J. Griggs, J. C. Metcalfe, R. Hesketh, Targeting tumour vasculature: the development of combretastatin A4 (**2001**), *Lancet Oncol*, *2*, 82. DOI: 10.1016/S1470-2045(00)00224-2.

[27] J. Tischer, F. Gergely, Anti-mitotic therapies in cancer (**2019**), *J Cell Biol*, *218*, 10. DOI: 10.1083/jcb.201808077.

[28] E. Abma, S. Daminet, P. Smets, Y. Ni, H. de Rooster, Combretastatin A4-phosphate and its potential in veterinary oncology: a review (**2017**), *Vet Comp Oncol*, *15*, 184. DOI: 10.1111/vco.12150.

[29] H. Reichenbach, Myxobacteria, producers of novel bioactive substances (**2001**), *J Ind Microbiol Biotechnol*, *27*, 149. DOI: 10.1038/sj.jim.7000025.

[30] S. Banerjee, D.-J. Hwang, W. Li, D. D. Miller, Current Advances of Tubulin Inhibitors in Nanoparticle Drug Delivery and Vascular Disruption/Angiogenesis (**2016**), *Molecules*, *21*. DOI: 10.3390/molecules21111468.

[31] R. C. Weisenberg, W. J. Deery, P. J. Dickinson, Tubulin-nucleotide interactions during the polymerization and depolymerization of microtubules (**1976**), *Biochemistry*, *15*, 4248. DOI: 10.1021/bi00664a018.

[32] H. Y. Kueh, T. J. Mitchison, Structural plasticity in actin and tubulin polymer dynamics (**2009**), *Science*, *325*, 960. DOI: 10.1126/science.1168823.

[33] E. Pasquier, S. Honoré, D. Braguer, Microtubule-targeting agents in angiogenesis: where do we stand? (**2006**), *Drug Resist Updat*, *9*, 74. DOI: 10.1016/j.drup.2006.04.003.

[34] E. L. Schwartz, Antivascular actions of microtubule-binding drugs (**2009**), *Clin Cancer Res*, *15*, 2594. DOI: 10.1158/1078-0432.CCR-08-2710.

[35] L. Zhong, Y. Li, L. Xiong, W. Wang, M. Wu, T. Yuan, W. Yang, C. Tian, Z. Miao, T. Wang, S. Yang, Small molecules in targeted cancer therapy: advances, challenges, and future perspectives (**2021**), *Signal Transduct Target Ther*, *6*, 201. DOI: 10.1038/s41392-021-00572-w.

[36] D. Hanahan, R. A. Weinberg, The Hallmarks of Cancer (**2000**), *Cell*, *100*, 57. DOI: 10.1016/S0092-8674(00)81683-9.

[37] D. Hanahan, R. A. Weinberg, Hallmarks of cancer: the next generation (**2011**), *Cell*, *144*, 646. DOI: 10.1016/j.cell.2011.02.013.

[38] D. Hanahan, Hallmarks of Cancer: New Dimensions (**2022**), *Cancer Discov*, *12*, 31. DOI: 10.1158/2159-8290.CD-21-1059.

[39] P. Hainaut, A. Plymoth, Targeting the hallmarks of cancer: towards a rational approach to next-generation cancer therapy (**2013**), *Curr Opin Oncol*, *25*, 50. DOI: 10.1097/CCO.0b013e32835b651e.

[40] E. von Behring, Ueber das Zustandekommen der Diphtherie-Immunität und der Tetanus-Immunität bei Thieren (**1890**), *Phillips-Universität Marburg*. DOI: 10.17192/eb2013.0164.

[41] N. A. P. S. Buss, S. J. Henderson, M. McFarlane, J. M. Shenton, L. de Haan, Monoclonal antibody therapeutics: history and future (**2012**), *Curr Opin Pharmacol*, *12*, 615. DOI: 10.1016/j.coph.2012.08.001.

[42] J. Schwaber, E. P. Cohen, Human x mouse somatic cell hybrid clone secreting immunoglobulins of both parental types (**1973**), *Nature*, *244*, 444. DOI: 10.1038/244444a0.

[43] G. Köhler, C. Milstein, Continuous cultures of fused cells secreting antibody of predefined specificity (**1975**), *Nature*, *256*, 495. DOI: 10.1038/256495a0.

[44] D. Zahavi, L. Weiner, Monoclonal Antibodies in Cancer Therapy (**2020**), *Antibodies (Basel)*, *9*. DOI: 10.3390/antib9030034.

[45] M. von Mehren, G. P. Adams, L. M. Weiner, Monoclonal antibody therapy for cancer (**2003**), *Annu Rev Med*, *54*, 343. DOI: 10.1146/annurev.med.54.101601.152442.

[46] J. Couzin-Frankel, Breakthrough of the year 2013. Cancer immunotherapy (**2013**), *Science*, *342*, 1432. DOI: 10.1126/science.342.6165.1432.

[47] S. Farkona, E. P. Diamandis, I. M. Blasutig, Cancer immunotherapy: the beginning of the end of cancer? (**2016**), *BMC Med*, *14*, 73. DOI: 10.1186/s12916-016-0623-5.

[48] R. Kannaiyan, D. Mahadevan, A comprehend e review of protein kinase inhibitors for cancer therapy (**2018**), *Expert Rev Anticancer Ther*, *18*, 1249. DOI: 10.1080/14737140.2018.1527688.

[49] Lavanya V, Mohamed Adil A, Neesar Ahmed, Arun K. Rishi and Shazia Jamal, Small molecule inhibitors as emerging cancer therapeutics (**2014**), *Integr Cancer Sci Therap*, *1*. DOI: 10.15761/ICST.1000109.

[50] I. Schlam, S. M. Swain, HER2-positive breast cancer and tyrosine kinase inhibitors: the time is now (**2021**), *NPJ Breast Cancer*, *7*, 56. DOI: 10.1038/s41523-021-00265-1.

[51] P. M. Voorhees, R. Z. Orlowski, The proteasome and proteasome inhibitors in cancer therapy (**2006**), *Annu Rev Pharmacol Toxicol*, *46*, 189. DOI: 10.1146/annurev.pharmtox.46.120604.141300.

[52] L. J. Crawford, B. Walker, A. E. Irvine, Proteasome inhibitors in cancer therapy (**2011**), *J Cell Commun Signal*, *5*, 101. DOI: 10.1007/s12079-011-0121-7.

[53] J. Adams, The development of proteasome inhibitors as anticancer drugs (**2004**), *Cancer Cell*, *5*, 417. DOI: 10.1016/s1535-6108(04)00120-5.

[54] E. E. Manasanch, R. Z. Orlowski, Proteasome inhibitors in cancer therapy (**2017**), *Nat Rev Clin Oncol*, *14*, 417. DOI: 10.1038/nrclinonc.2016.206.

[55] B. Barneda-Zahonero, M. Parra, Histone deacetylases and cancer (**2012**), *Mol Oncol*, *6*, 579. DOI: 10.1016/j.molonc.2012.07.003.

[56] A. A. Lane, B. A. Chabner, Histone deacetylase inhibitors in cancer therapy (**2009**), *J Clin Oncol*, *27*, 5459. DOI: 10.1200/JCO.2009.22.1291.

[57] T. Eckschlager, J. Plch, M. Stiborova, J. Hrabeta, Histone Deacetylase Inhibitors as Anticancer Drugs (**2017**), *Int J Mol Sci*, *18*. DOI: 10.3390/ijms18071414.

[58] L. A. M. Kulka, P.-V. Fangmann, D. Panfilova, H. Olzscha, Impact of HDAC Inhibitors on Protein Quality Control Systems: Consequences for Precision Medicine in Malignant Disease (**2020**), *Front Cell Dev Biol*, *8*, 425. DOI: 10.3389/fcell.2020.00425.

[59] P. A. Marks, R. Breslow, Dimethyl sulfoxide to vorinostat: development of this histone deacetylase inhibitor as an anticancer drug (**2007**), *Nat Biotechnol*, *25*, 84. DOI: 10.1038/nbt1272.

[60] P. A. J. Muller, K. H. Vousden, p53 mutations in cancer (**2013**), *Nat Cell Biol*, *15*, 2. DOI: 10.1038/ncb2641.

[61] A. G. Porter, R. U. Jänicke, Emerging roles of caspase-3 in apoptosis (**1999**), *Cell Death Differ*, *6*, 99. DOI: 10.1038/sj.cdd.4400476.

[62] F. H. Abdalbari, C. M. Telleria, The gold complex auranofin: new perspectives for cancer therapy (**2021**), *Discov Oncol*, *12*, 42. DOI: 10.1007/s12672-021-00439-0.

[63] S. Fortin, G. Bérubé, Advances in the development of hybrid anticancer drugs (**2013**), *Expert Opin Drug Discov*, *8*, 1029. DOI: 10.1517/17460441.2013.798296.

[64] Shalini, V. Kumar, Have molecular hybrids delivered effective anti-cancer treatments and what should future drug discovery focus on? (**2021**), *Expert Opin Drug Discov*, *16*, 335. DOI: 10.1080/17460441.2021.1850686.

[65] N. Muhammad, Z. Guo, Metal-based anticancer chemotherapeutic agents (**2014**), *Curr Opin Chem Biol*, *19*, 144. DOI: 10.1016/j.cbpa.2014.02.003.

[66] G. N. Vaidya, P. Rana, A. Venkatesh, D. R. Chatterjee, D. Contractor, D. P. Satpute, M. Nagpure, A. Jain, D. Kumar, Paradigm shift of "classical" HDAC inhibitors to "hybrid" HDAC inhibitors in therapeutic interventions (**2021**), *Eur J Med Chem*, *209*, 112844. DOI: 10.1016/j.ejmech.2020.112844.

[67] A. K. A. Bass, M. S. El-Zoghbi, E.-S. M. Nageeb, M. F. A. Mohamed, M. Badr, G. E.-D. A. Abuo-Rahma, Comprehensive review for anticancer hybridized multitargeting HDAC inhibitors (**2021**), *Eur J Med Chem*, *209*, 112904. DOI: 10.1016/j.ejmech.2020.112904.

[68] M. Szumilak, A. Wiktorowska-Owczarek, A. Stanczak, Hybrid Drugs-A Strategy for Overcoming Anticancer Drug Resistance? (**2021**), *Molecules*, *26*. DOI: 10.3390/molecules26092601.

[69] B. Meunier, Hybrid molecules with a dual mode of action: dream or reality? (**2008**), *Acc Chem Res*, *41*, 69. DOI: 10.1021/ar7000843.

[70] A. Gautier, F. Cisnetti, Advances in metal-carbene complexes as potent anti-cancer agents (**2012**), *Metallomics*, *4*, 23. DOI: 10.1039/c1mt00123j.

[71] S. I. Bär, M. Gold, S. W. Schleser, T. Rehm, A. Bär, L. Köhler, L. R. Carnell, B. Biersack, R. Schobert, Guided Antitumoural Drugs: (Imidazol-2-ylidene)(L)gold(I) Complexes Seeking Cellular Targets Controlled by the Nature of Ligand L (**2021**), *Chemistry*, *27*, 5003. DOI: 10.1002/chem.202005451.

[72] B. Biersack, S. Polat, M. Höpfner, Anticancer properties of chimeric HDAC and kinase inhibitors (**2022**), *Semin Cancer Biol*, *83*, 472. DOI: 10.1016/j.semcancer.2020.11.005.

[73] S. Kumar, S. Bajaj, R. B. Bodla, Preclinical screening methods in cancer (**2016**), *Indian J Pharmacol*, *48*, 481. DOI: 10.4103/0253-7613.190716.

[74] M. Suggitt, M. C. Bibby, 50 years of preclinical anticancer drug screening: empirical to target-driven approaches (**2005**), *Clin Cancer Res*, *11*, 971. DOI: Review.

[75] P. Mirabelli, L. Coppola, M. Salvatore, Cancer Cell Lines Are Useful Model Systems for Medical Research (**2019**), *Cancers (Basel)*, *11*. DOI: 10.3390/cancers11081098.

[76] M. Kapałczyńska, T. Kolenda, W. Przybyła, M. Zajączkowska, A. Teresiak, V. Filas, M. Ibbs, R. Bliźniak, Ł. Łuczewski, K. Lamperska, 2D and 3D cell cultures - a comparison of different types of cancer cell cultures (**2018**), *Arch Med Sci*, *14*, 910. DOI: 10.5114/aoms.2016.63743.

[77] O. D. Abaan, E. C. Polley, S. R. Davis, Y. J. Zhu, S. Bilke, R. L. Walker, M. Pineda, Y. Gindin, Y. Jiang, W. C. Reinhold, S. L. Holbeck, R. M. Simon, J. H. Doroshow, Y. Pommier, P. S. Meltzer, The exomes of the NCI-60 panel: a genomic resource for cancer biology and systems pharmacology (**2013**), *Cancer Res*, *73*, 4372. DOI: 10.1158/0008-5472.CAN-12-3342.

[78] N. Chaicharoenaudomrung, P. Kunhorm, P. Noisa, Three-dimensional cell culture systems as an in vitro platform for cancer and stem cell modeling (**2019**), *World J Stem Cells*, *11*, 1065. DOI: 10.4252/wjsc.v11.i12.1065.

[79] L. Belfiore, B. Aghaei, A. M. K. Law, J. C. Dobrowolski, L. J. Raftery, A. D. Tjandra, C. Yee, A. Piloni, A. Volkerling, C. J. Ferris, M. Engel, Generation and analysis of 3D cell culture models for drug discovery (**2021**), *Eur J Pharm Sci*, *163*, 105876. DOI: 10.1016/j.ejps.2021.105876.

[80] B. A. Ruggeri, F. Camp, S. Miknyoczki, Animal models of disease: pre-clinical animal models of cancer and their applications and utility in drug discovery (**2014**), *Biochem Pharmacol*, *87*, 150. DOI: 10.1016/j.bcp.2013.06.020.

[81] D.-J. Cheon, S. Orsulic, Mouse models of cancer (**2011**), *Annu Rev Pathol*, *6*, 95. DOI: 10.1146/annurev.pathol.3.121806.154244.

[82] J. Bailey, M. Thew, M. Balls, An analysis of the use of animal models in predicting human toxicology and drug safety (**2014**), *Altern Lab Anim*, *42*, 181. DOI: 10.1177/026119291404200306.

[83] G. A. van Norman, Limitations of Animal Studies for Predicting Toxicity in Clinical Trials: Is it Time to Rethink Our Current Approach? (**2019**), *JACC Basic Transl Sci*, *4*, 845. DOI: 10.1016/j.jacbts.2019.10.008.

[84] J. K. Muenzner, T. Rehm, B. Biersack, A. Casini, I. A. M. de Graaf, P. Worawutputtapong, A. Noor, R. Kempe, V. Brabec, J. Kasparkova, R. Schobert, Adjusting the DNA Interaction and Anticancer Activity of Pt(II) N-Heterocyclic Carbene Complexes by Steric Shielding of the Trans Leaving Group (**2015**), *J Med Chem*, *58*, 6283. DOI: 10.1021/acs.jmedchem.5b00896.

[85] T. Rehm, M. Rothemund, J. K. Muenzner, A. Noor, R. Kempe, R. Schobert, Novel cis-(NHC)1(NHC)2(L)Clplatinum(ii) complexes - synthesis, structures, and anticancer activities (**2016**), *Dalton Trans.*, *45*, 15390. DOI: 10.1039/C6DT02350A.

[86] S. B. Aher, P. N. Muskawar, K. Thenmozhi, P. R. Bhagat, Recent developments of metal N-heterocyclic carbenes as anticancer agents (**2014**), *Eur J Med Chem*, *81*, 408. DOI: 10.1016/j.ejmech.2014.05.036.

[87] J. S. Modica-Napolitano, J. R. Aprille, Delocalized lipophilic cations selectively target the mitochondria of carcinoma cells (**2001**), *Adv Drug Deliv Rev*, *49*, 63. DOI: 10.1016/S0169-409X(01)00125-9.

[88] S. Bellemin-Laponnaz, N-Heterocyclic Carbene Platinum Complexes: A Big Step Forward for Effective Antitumor Compounds (**2020**), *Eur J Inorg Chem*, 10. DOI: 10.1002/ejic.201900960.

[89] M. Rothemund, S. I. Bär, T. Rehm, H. Kostrhunova, V. Brabec, R. Schobert, Antitumoral effects of mitochondria-targeting neutral and cationic cis-bis(1,3-dibenzylimidazol-2-ylidene)Cl(L)Pt(ii) complexes (**2020**), *Dalton Trans.*, *49*, 8901. DOI: 10.1039/D0DT01664K.

[90] F. K.-M. Chan, K. Moriwaki, M. J. de Rosa, Detection of necrosis by release of lactate dehydrogenase activity (**2013**), *Methods Mol Biol*, *979*, 65. DOI: 10.1007/978-1-62703-290-2_7.

[91] M. P. Murphy, How mitochondria produce reactive oxygen species (**2009**), *Biochem J*, *417*, 1. DOI: 10.1042/bj20081386.

[92] J. D. Ly, D. R. Grubb, A. Lawen, The mitochondrial membrane potential (deltapsi(m)) in apoptosis; an update (**2003**), *Apoptosis*, *8*, 115. DOI: 10.1023/A:1022945107762.

[93] S. P. Fricker, L. R. Kelland, in *Metal Compounds in Cancer Therapy* (Eds: S. P. Fricker)32–45. Springer Netherlands. Dordrecht (**1994**) ISBN: 78-94-011-1252-9

[94] S. Gromer, L. D. Arscott, C. H. Williams, R. H. Schirmer, K. Becker, Human placenta thioredoxin reductase. Isolation of the selenoenzyme, steady state kinetics, and inhibition by therapeutic gold compounds (**1998**), *J Biol Chem*, *273*, 20096. DOI: 10.1074/jbc.273.32.20096.

[95] M. P. Rigobello, G. Scutari, R. Boscolo, A. Bindoli, Induction of mitochondrial permeability transition by auranofin, a gold(I)-phosphine derivative (**2002**), *Br J Pharmacol*, *136*, 1162. DOI: 10.1038/sj.bjp.0704823.

[96] M. J. McKeage, Gold opens mitochondrial pathways to apoptosis (**2002**), *Br J Pharmacol*, *136*, 1081. DOI: 10.1038/sj.bjp.0704822.

[97] T. Zou, C.-N. Lok, P.-K. Wan, Z.-F. Zhang, S.-K. Fung, C.-M. Che, Anticancer metal-N-heterocyclic carbene complexes of gold, platinum and palladium (**2018**), *Curr Opin Chem Biol*, *43*, 30. DOI: 10.1016/j.cbpa.2017.10.014.

[98] Ö. Karaca, S. M. Meier-Menches, A. Casini, F. E. Kühn, On the binding modes of metal NHC complexes with DNA secondary structures: implications for therapy and imaging (**2017**), *Chem Commun (Camb)*, *53*, 8249. DOI: 10.1039/c7cc03074f.

[99] F. Wang, R. Gómez-Sintes, P. Boya, Lysosomal membrane permeabilization and cell death (**2018**), *Traffic*, *19*, 918. DOI: 10.1111/tra.12613.

[100] S. Coulthard, L. Hogarth, The thiopurines: an update (**2005**), *Invest New Drugs*, *23*, 523. DOI: 10.1007/s10637-005-4020-8.

[101] M. Presta, M. Rusnati, M. Belleri, L. Morbidelli, M. Ziche, D. Ribatti, Purine analogue 6-methylmercaptopurine riboside inhibits early and late phases of the angiogenesis process (**1999**), *Cancer Res*, *59*, 2417. PMID: 10344752

[102] E. R. Tiekink, P. D. Cookson, B. M. Linahan, L. K. Webster, In vitro antitumour activity of some triorganophosphinegold(i) thionucleobases (**1994**), *Met Based Drugs*, *1*, 299. DOI: 10.1155/mbd.1994.299.

[103] L. K. Webster, S. Rainone, E. Horn, E. R. Tiekink, Anti-tumor activity, in vitro and in vivo, of some triphenylphosphinegold(i) thionucleobases (**1996**), *Met Based Drugs*, *3*, 63. DOI: 10.1155/MBD.1996.63.

[104] M. W. Whitehouse, P. D. Cookson, G. Siasios, E. R. Tiekink, Anti-arthritic activity in rats of some phosphinegold(i) thionucleobases and related thiolates (**1998**), *Met Based Drugs*, *5*, 245. DOI: 10.1155/mbd.1998.245.

[105] F. Schmitt, L. C. Gosch, A. Dittmer, M. Rothemund, T. Mueller, R. Schobert, B. Biersack, A. Volkamer, M. Höpfner, Oxazole-Bridged Combretastatin A-4 Derivatives with Tethered Hydroxamic Acids: Structure–Activity Relations of New Inhibitors of HDAC and/or Tubulin Function (**2019**), *Int J Mol Sci*, *20*. DOI: 10.3390/ijms20020383.

[106] C. Hubbert, A. Guardiola, R. Shao, Y. Kawaguchi, A. Ito, A. Nixon, M. Yoshida, X.-F. Wang, T.-P. Yao, HDAC6 is a microtubule-associated deacetylase (**2002**), *Nature*, *417*, 455. DOI: 10.1038/417455a.

[107] R. L. Siegel, K. D. Miller, H. E. Fuchs, A. Jemal, Cancer statistics, 2022 (**2022**), *CA Cancer J Clin*, *72*, 7. DOI: 10.3322/caac.21708.

[108] Z. Liu, T. Lu, J. Li, L. Wang, K. Xu, Q. Dang, C. Guo, L. Liu, D. Jiao, Z. Sun, X. Han, Development and clinical validation of a novel six-gene signature for accurately predicting the recurrence risk of patients with stage II/III colorectal cancer (**2021**), *Cancer Cell Int*, *21*, 359. DOI: 10.1186/s12935-021-02070-z.

[109] W. A. Hammond, A. Swaika, K. Mody, Pharmacologic resistance in colorectal cancer: a review (**2016**), *Ther Adv Med Oncol*, *8*, 57. DOI: 10.1177/1758834015614530.

[110] S. Zhu, Y. Li, L. Zhao, P. Hou, C. Shangguan, R. Yao, W. Zhang, Y. Zhang, J. Tan, B. Huang, J. Lu, TSA-induced JMJD2B downregulation is associated with cyclin B1-dependent survivin degradation and apoptosis in LNCap cells (**2012**), *J Cell Biochem*, *113*, 2375. DOI: 10.1002/jcb.24109.

[111] W. Feng, D. Cai, B. Zhang, G. Lou, X. Zou, Combination of HDAC inhibitor TSA and silibinin induces cell cycle arrest and apoptosis by targeting survivin and cyclinB1/Cdk1 in pancreatic cancer cells (**2015**), *Biomed Pharmacother*, *74*, 257. DOI: 10.1016/j.biopha.2015.08.017.

[112] A. C. Mita, M. M. Mita, S. T. Nawrocki, F. J. Giles, Survivin: key regulator of mitosis and apoptosis and novel target for cancer therapeutics (**2008**), *Clin Cancer Res*, *14*, 5000. DOI: 10.1158/1078-0432.CCR-08-0746.

[113] L. C. Crowley, A. P. Scott, B. J. Marfell, J. A. Boughaba, G. Chojnowski, N. J. Waterhouse, Measuring Cell Death by Propidium Iodide Uptake and Flow Cytometry (**2016**), *Cold Spring Harb Protoc*, *2016*. DOI: 10.1101/pdb.prot087163

5 Publikationen mit Darstellung des Eigenanteils

Die im Rahmen dieser Dissertation vorgestellten Publikationen und Manuskripte wurden in Kooperation mit weiteren Mitarbeitern der Universität Bayreuth und anderen externen Arbeitsgruppen angefertigt. Im Folgenden werden die Kooperationspartner jeder Publikation aufgeführt und die Anteile aller Autoren jeder Publikation detailliert dargestellt.

5.1 Publikation I mit Darstellung des Eigenanteils

Publikation I entstand unter Zusammenarbeit mit Dr. M. Rothemund und unter Mitarbeit von Dr. T. Rehm, Mitarbeiter des Arbeitskreises Organische Chemie I der Universität Bayreuth unter der Leitung von Prof. Dr. R. Schobert sowie durch Kooperation mit den Mitarbeitern H. Kostrhunova und Prof. Dr. V. Brabec des Instituts für Biophysik der Akademie der Wissenschaften in Brünn (Tschechien).

5.1.1 Eigenanteil an Publikation I

Die Publikation wurde in ***Dalton Transactions*** veröffentlicht, unter dem Titel

„Antitumoral effects of mitochondria-targeting neutral and cationic cis-[bis(1,3-dibenzylimidazol-2-ylidene)(L)Cl]Pt(II) complexes“

von den Autoren

Matthias Rothemund[+], Sofia I. Bär[+], Tobias Rehm, Viktor Brabec und Rainer Schobert

[+] diese Autoren haben zu gleichen Anteilen zum Manuskript beigetragen

Eigenanteil:	Konzeption, Durchführung, Auswertung und graphischer Darstellung folgender biochemischer Assays: Zytotoxizitätstests via MTT-Assay, Messung des mitochondrialen Membranpotenzials, Messung reaktiver Sauerstoffspezies und Zytoskelettfärbung. Zudem; Verfassen des Manuskripts gemeinsam mit Matthias Rothemund, einschließlich der Diskussion und Interpretation der Ergebnisse und Revision des Manuskripts.
Matthias Rothemund:	Konzeption, Durchführung, Auswertung und graphischer Darstellung folgender biochemischer Assays: Zytotoxizitätstests via MTT-Assay, DNA-Interaktionsstudien mittels EtBr-Assay, Zellzyklusanalysen Colokalisation und Apoptosenachweis mittels Caspase-3/7 Assay. Verfassung entsprechender Manuskriptpassagen mit Beteiligung an Diskussion und Korrektur.

Tobias Rehm:	Synthese, Reinigung und Analytik der Testverbindungen, Verfassung entsprechender Manuskriptpassagen.
Hana Kostrhunova und Victor Brabec:	Messung der zellulären Aufnahme der Testverbindungen.
Rainer Schobert:	Überarbeitung, Diskussion und Korrektur des Manuskripts.

5.1.2 Publikation I

Antitumoral effects of mitochondria-targeting neutral and cationic cis-[bis(1,3-dibenzylimidazol-2-ylidene)Cl(L)]Pt(II) complexes

Matthias Rothemund,[+a] Sofia I. Bär,[+a] Tobias Rehm,[a] Hana Kostrhunova,[b] Viktor Brabec,[b] and Rainer Schobert*[a]

[a]Organic Chemistry Laboratory, University of Bayreuth, Universitaetsstrasse 30, 95440 Bayreuth, Germany

[b]Czech Academy of Sciences, Institute of Biophysics, Kralovopolska 135, CZ-61265, Czech Republic

[+]These authors contributed equally to this work.

*E-mail: rainer.schobert@uni-bayreuth.de

Dalton Trans., **2020**, 49, 8901

https://doi.org/10.1039/D0DT01664K

Dalton Transactions

ROYAL SOCIETY OF CHEMISTRY

PAPER

View Article Online
View Journal | View Issue

Check for updates

Cite this: *Dalton Trans.*, 2020, **49**, 8901

Antitumoral effects of mitochondria-targeting neutral and cationic *cis*-[bis(1,3-dibenzylimidazol-2-ylidene)Cl(L)]Pt(II) complexes†

Matthias Rothemund,‡[a] Sofia I. Bär,‡[a] Tobias Rehm,[a] Hana Kostrhunova,[b] Viktor Brabec[b] and Rainer Schobert*[a]

Recently, we opened a synthetic access to antitumoral platinum complexes of the type *cis*-[(NHC)^1(NHC)^{2}Pt^{II}Cl(L)] which interact with DNA in a way correlated to the complex charge and to the sterical accessibility of the leaving chlorido ligand. We now identified mitochondria rather than nuclei as the cellular target of the neutral dichlorido complex **1** (L = Cl) and the delocalized lipophilic cationic phosphine complex **2** (L = PPh_3), both carrying the same *cis*-bis(1,3-dibenzylimidazol-2-ylidene) ligands. Their uptake into 518A2 melanoma cells was concentration-dependent and distinctly greater for complex **2** which was also more cytotoxic against sensitive cancer cell lines with submicromolar IC_{50} values. Both complexes interfered strongly with various forms of DNA *in vitro*, but only complex **2** caused a melanoma cell cycle arrest in G1-phase, setting both apart from the S-phase arresting drug cisplatin. Studies of the intracellular localisation of **1** and **2** were carried out with their alkyne-tagged analogues **6** and **7**, which showed identical patterns of cancer cell cytotoxicity, cell cycle interference and effects on mitochondria. Click reactions with 7-hydroxycoumarin azide, colocalisation with Mitotracker™ and confocal microscopy, proved complexes **6** and **7** to accumulate mainly in the mitochondria rather than the nuclei of melanoma cells. Complex **1** and even more so complex **2** reduced the mitochondrial membrane potential and also increased the cellular ROS levels. As a consequence, both complexes caused stress fibre formation in the F-actin cytoskeleton of melanoma cells, most distinctly so complex **2** which also activated the apoptotic cascade mediated by capases-3 and -7.

Received 7th May 2020,
Accepted 15th June 2020

DOI: 10.1039/d0dt01664k

rsc.li/dalton

Introduction

The serendipitous discovery of the biological effects of *cis*-diamminodichloridoplatinum(II) (cisplatin; CDDP) by Rosenberg *et al.* almost five decades ago led to an intensive worldwide study and screening of congeneric platinum coordination complexes, culminating in the FDA approval of the mainstay tumor therapeutics carboplatin and oxaliplatin.[1] In recent years, the interest of medicinal chemists in antitumoral metallodrugs was rekindled by the growing evidence that organoplatinum complexes carrying *N*-heterocyclic carbene (NHC) ligands offer more means of fine-tuning and optimising their pharmacological properties due to the variability of both the *N*-heterocycle and its substituents.[2] Recently, we reported on the synthesis of platinum(II) complexes of type *cis*-[(NHC)^1(NHC)^{2}Pt^{II}Cl(L)] bearing two – optionally different – *cis*-oriented (benz)imidazol-2-ylidene ligands. Preliminary tests showed their modes of antitumoral action to be dependent not only on these NHC ligands but also decisively on their secondary ligands L and their overall charge. Fig. 1 depicts two typical complexes.[3,4] The neutral complex **1**, like derivatives with further residues on the phenyl rings not shown here, was

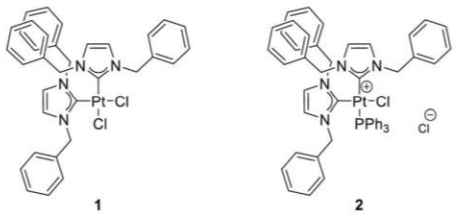

Fig. 1 Structures of complexes **1** (L = Cl) and **2** (L = PPh_3) of the type *cis*-[bis(1,3-dibenzylimidazol-2-ylidene)Pt^{II}Cl(L)].[4]

[a]*Organic Chemistry Laboratory, University of Bayreuth, Universitaetsstrasse 30, 95440 Bayreuth, Germany. E-mail: Rainer.Schobert@uni-bayreuth.de*
[b]*Czech Academy of Sciences, Institute of Biophysics, Kralovopolska 135, CZ-61265, Czech Republic*

†Electronic supplementary information (ESI) available: NMR spectra of **6** and **7**, uptake of complexes **1** and **2** by 518A2 melanoma cells, electrophoretic mobility shift assays of **1**, **2**, **6**, and **7**, *etc*. See DOI: 10.1039/d0dt01664k

‡These authors contributed equally to this work.

cytotoxic with IC_{50} values generally in the low micromolar range, and gave rise to a band shift of plasmid DNA in electrophoretic mobility shift assays (EMSA) comparable to cisplatin. Exchange of a chlorido ligand for triphenylphosphine afforded cationic complexes like **2**, which were more cytotoxic against cancer cells with IC_{50} values in the nanomolar range, and which caused an aggregation rather than coordination of DNA *in vitro*.[4]

Investigations of related neutral mono-NHC complexes of type *cis*-[(benzimidazol-2-ylidene)$Pt^{II}Cl_2(L)$] and cationic complexes *trans*-[(benzimidazol-2-ylidene)$Pt^{II}Cl(L)_2]^+Cl^-$ gave a more nuanced picture.[5] While the cationic complexes were also more cytotoxic against cancer cells than the neutral ones, DNA interaction of the latter *in vitro* depended decisively on the ligands L.[5] In order to find out whether cellular DNA is an actual target of *cis*-[(1,3-dibenzylimidazol-2-ylidene)$_2Pt^{II}Cl(L)$] complexes **1** and **2** and to further elucidate their modes of action, we synthesized their 4-ethynylbenzyl derivatives **6** and **7** for intracellular localisation *via* alkyne–azide click reactions.[6]

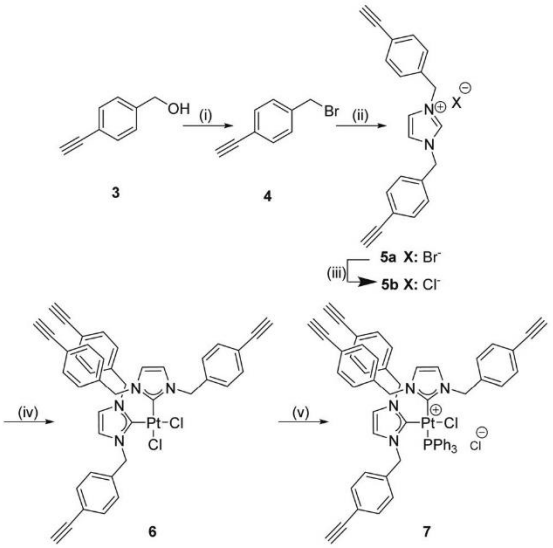

Scheme 1 Syntheses of bis[1,3-(4-ethynylbenzyl)imidazol-2-ylidene] Pt^{II} complexes **6** and **7**. Reagents and conditions: (i) NBS, PPh_3, CH_2Cl_2, 40 °C, 3 h, 96% (ii) imidazole, K_2CO_3, MeCN, 80 °C, 16 h, 100%; (iii) Ag_2CO_3, HNO_3, EtOH, rt, 2 h, then HCl, 68%; (iv) *cis*-[$Pt^{II}Cl_2(DMSO)_2$], KO^tBu, CH_2Cl_2, rt, 24 h, 40%; (v) PPh_3, CH_2Cl_2, rt, 2 h, 82%.

Results and discussion

Synthesis and characterization

4-Ethynylbenzyl bromide **4** was synthesized from the corresponding benzyl alcohol **3**, NBS and PPh_3. It was reacted with imidazole under basic conditions to give the imidazolium bromide **5a**. To prevent anionic exchange during the next steps, bromide **5a** was converted to the imidazolium chloride **5b**. The latter was deprotonated with KO^tBu to generate the free carbene, which was trapped with half an equivalent of *cis*-[$Pt^{II}Cl_2(DMSO)_2$] to afford the desired *cis*-(bis-NHC)Cl_2Pt^{II} complex **6**. *cis*-[$Pt^{II}Cl_2(DMSO)_2$] can be prepared by adding a three-fold excess of DMSO to K_2PtCl_4 in water and allowing the solution to stand at room temperature until yellow crystals precipitate.[7] Cationic complex **7** was obtained from reaction of complex **6** with an excess of PPh_3 (Scheme 1).

As for complexes **1** and **2**, the NMR spectra of the new alkyne derivatives confirmed their *cis* configuration and the perpendicular orientation of their imidazole rings with respect to the PtCl(L) plane. The ^1H NMR spectra reflected the inequivalency of the geminal protons of each benzylic CH_2 group giving rise to two (for **6**) or four (for **7**) doublets which were 0.73 ppm apart in the case of **6** and 0.71/0.74 ppm for complex **7**. In the ^{13}C NMR spectra the carbene carbons of complex **6** peaked at 146.7 ppm and those of complex **7** appeared as doublets at 145.8 ppm with $^2J_{CP}$ = 10 Hz (*cis* to PPh_3) and at 163.2 ppm with $^2J_{CP}$ = 151 Hz (*trans* to PPh_3).

Biological evaluation

Inhibition of cancer cell proliferation. Complexes **1** and **2** had previously been tested for antiproliferative effects on various cancer cell lines as members of a larger series of similar NHC platinum(II) complexes with distinct antitumoral activity. We now tested them, using the same MTT-assay, against further cell lines such as the colon cancer cell line $HCT116^{wt}$, its p53-deficient mutant $HCT116^{-/-}$, the non-malignant human fibroblasts HDFa, and the multi-drug resistant cervix carcinoma cell line $KB\text{-}V1^{Vbl}$, pre-incubated with verapamil, a competitive inhibitor of the P-gp1 efflux transporter overexpressed in this cell line. In parallel, we also tested the ethynyl-tagged complexes **6** and **7**, to find out whether their cytotoxic pattern across this cell line panel is comparable to that of their analogues **1** and **2** and so ensure their suitability as surrogates for complexes **1** and **2** in intracellular localisation studies *via* alkyne–azide click reactions. As previously reported for other cancer cell lines,[4,5] complex **2** bearing a sterically demanding triphenylphosphine residue and a positive charge, was more cytotoxic than neutral dichlorido complex **1**, with IC_{50} values in the nanomolar or lower micromolar range also against the cell lines listed in Table 1. This pattern was also observed for the alkynyl-tagged complexes **6** and **7**, which showed IC_{50} values similar to those of their congeners **1** and **2**, albeit with a few conspicuous exceptions. All four complexes showed a reduced cytotoxicity against $HCT116^{-/-}$ cells lacking functional tumor suppressor protein p53, which plays an important role in cell cycle progression and in apoptosis activation.[8] Unlike its non-ethynylated parent complex **1**, the neutral complex **6** was virtually inactive against $HCT116^{-/-}$ cells. These results suggest a similarity in the mode of action with cisplatin, which is known to activate p53 upon extensive DNA damage.[9] Inhibition of the P-gp1 efflux pump of multi-drug resistant $Kb\text{-}V1^{Vbl}$ cervix carcinoma cells by pre-incubation with verapamil, which is used clinically as a re-sensi-

Table 1 Means ± SD of IC_{50} values [μM] of cisplatin and compounds **1**, **2**, **6**, **7** in MTT assays against human cell lines[a] after 72 h of incubation as calculated from four independent measurements. * Data taken from ref. 4. ** Data taken from ref. 10

IC_{50} (72 h) [μM]									
	518A2	HT-29	$HCT116^{wt}$	$HCT116^{-/-}$	EaHy926	$Kb\text{-}V1^{Vbl}$	$Kb\text{-}V1^{Vbl+vpm}$[b]	HDFa	SI[b]
Cisplatin	2.6 ± 0.7*	8.3 ± 0.5*	5.7 ± 0.3*	9.2 ± 0.5*	21.1 ± 2.5	2.2 ± 0.3**	0.23 ± 0.08*	>50	>9.0
1	6.2 ± 0.4*	14.6 ± 1.4*	2.3 ± 0.8	14.1 ± 0.9	6.8 ± 1.6*	11.7 ± 0.8*	6.3 ± 0.6	4.5 ± 0.5	0.6
2	0.86 ± 0.05*	0.82 ± 0.06*	0.51 ± 0.04	1.6 ± 0.1	0.48 ± 0.01*	7.3 ± 1.2*	0.99 ± 0.16	3.1 ± 0.4	4.2
6	5.6 ± 0.2	13.12 ± 1.0	1.1 ± 0.1	>50	12.5 ± 2.2	25.9 ± 3.4	>50	>50	>7.5
7	1.2 ± 0.2	0.66 ± 0.26	0.14 ± 0.03	2.0 ± 0.3	0.63 ± 0.10	34.1 ± 3.8	34.5 ± 4.2	3.4 ± 1.9	5.1

[a] 518A2 – melanoma, HT-29 – colon adenocarcinoma, $HCT116^{wt}$ – colon carcinoma (wildtype), $HCT116^{-/-}$ – colon carcinoma (p53 knock-out mutant), EaHy926 – endothelial hybrid, $Kb\text{-}V1^{Vbl}$ – cervix carcinoma, HDFa – human dermal fibroblasts. [b] Vbl – vinblastine, vpm – verapamil, SI – selectivity index.

tizer of refractory tumours, led to an enhanced activity of complexes **1** and **2** but not of the alkynyl-tagged complexes **6** and **7**, indicating that the latter are no substrates of P-gp1.

To determine the selectivity of the complexes for tumour cells, we tested them for their toxicity against the non-malignant fibroblast cells HDFa and calculated a selectivity index (SI) by dividing their IC_{50} against the fibroblasts by the average IC_{50} values against the unadulterated cancer cell lines 518A2, HT-29, and $HCT116^{wt}$. Like cisplatin, complex **6** was inactive against the HDFa cells and thus can be regarded highly cancer cell selective. Complexes **2** and **7** also showed a marked selectivity for cancer cells, whereas complex **1** was somewhat selective only towards $HCT116^{wt}$ colon cancer cells.

Cellular uptake. To find out whether the greater cytotoxicity of the cationic complex **2** stems from an actual increase in toxicity due to the positive charge and the bulkier phosphine ligand or from an enhanced uptake into the cells, we measured the platinum content of 518A2 cells after 8 h of incubation with complexes **1** and **2** (1 μM and 5 μM) by ICP-MS (Fig. 2; *cf.* SI for exact values). The observed divergence in uptake rates of complexes **1** and **2** by a concentration-dependent factor of 2.5 (for 5 μM) to 7 (for 1 μM) reflects the previously measured[4] difference in their IC_{50} values against this cell line fairly well, *i.e.* 6.2 μM for **1** and 0.86 μM for **2**. This suggests that they do not differ much in their intrinsic antiproliferative activities. Such ostensible hikes in cytotoxicity upon increasing the charge and bulkiness, and hence the uptake rates, were previously reported by us[5] for related benzimidazol-2-ylidene complexes of platinum and more systematically by Osella *et al.*[11] for cisplatin, carboplatin, oxaliplatin and close congeners.

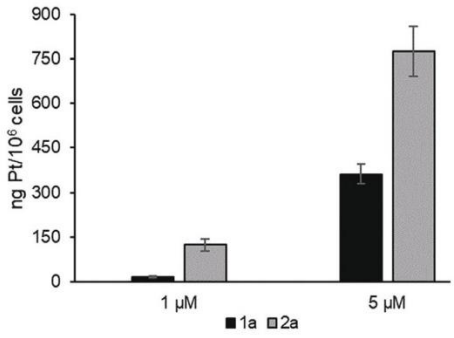

Fig. 2 Platinum content of 518A2 melanoma cells after 8 h incubation with 1 μM or 5 μM of complexes **1** and **2**, measured *via* ICP-MS.

DNA-interaction. While the canonical mechanism of action of cisplatin and related coordination complexes of platinum(II) rests upon coordinative bonds to DNA bases, cross-link formation and eventually cell cycle arrest and apoptosis,[12] evidence has accumulated that NHC-complexes of platinum may interact with DNA in a different way, implying DNA aggregation rather than coordination and electrostatic rather than covalent bonding.[3–5] Therefore the DNA interaction of complexes **1**, **2**, **6** and **7** was investigated *in vitro* by electrophoretic mobility shift assays (EMSA) with circular plasmid DNA. All complexes showed similar band shift patterns in EMSA experiments (Fig. S8†) as previously tested neutral and cationic imidazol-2-ylidene[3,4] and some benzimidazol-2-ylidene complexes.[5] The neutral complexes **1** and **6** gave rise to band shifts of the compact covalently closed circular (ccc) form reminiscent of those caused by cisplatin, while the cationic complexes **2** and **7** did not shift the bands of the ccc form at concentrations up to 10 μM, yet at higher concentrations led to precipitation of DNA aggregates in the agarose gel pockets. In other words, the neutral complexes **1** and **6** appear to interact with DNA like cisplatin by forming coordination complexes with DNA bases, while the cationic complexes **2** and **7** are likely to aggregate DNA *via* electrostatic attraction. In ethidium bromide saturation assays complexes **1** and **2** caused a distinct concentration-dependent reduction of the fluorescence of ethidium bromide intercalated in linear salmon sperm DNA, exceeding that by cisplatin markedly (Fig. 3). It is reasonable to assume that the complexes **1** and **2** interact with DNA like some of the structurally related benzimidazol-2-ylidene platinum(II) complexes investigated by us earlier.[5] These bound to DNA quickly *via* electrostatic attraction to its negatively charged backbone which over time was replaced by tighter coordinative bonding.

Cell cycle analysis. Previously, we found that certain imidazol-2-ylidene and benzimidazol-2-ylidene complexes of platinum(II) interfered with the cell cycle of cancer cells differently

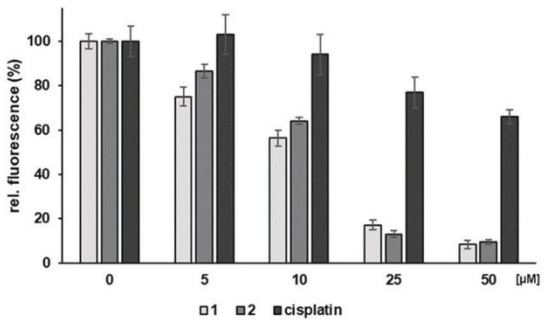

Fig. 3 Relative fluorescence intensities of ethidium bromide, intercalated in linear salmon sperm DNA after 2 h treatment with **1**, **2** or cisplatin in different concentrations. Experiments were conducted in triplicate for each substance and concentration.

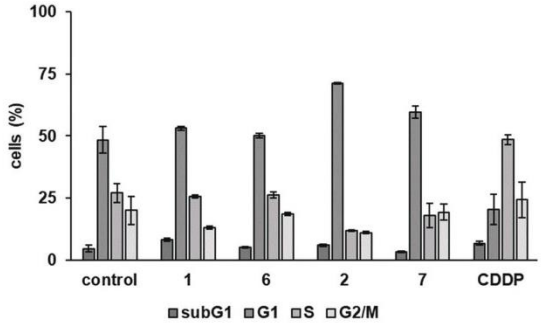

Fig. 4 Cell cycle analysis of 518A2 melanoma cells after 24 h incubation at 37 °C with 5 μM of **1** or **6**, 500 nM of **2** or **7**, and 2 μM of CDDP as a positive control. DMF was used as a negative control. Data shown are based on three independent experiments per substance and concentration.

from cisplatin which typically induces an S-phase or a twofold S-phase *cum* G2/M-phase arrest.[3,5] We now studied the effects of complexes **1**, **2**, **6**, **7**, and cisplatin on the cell cycle of 518A2 melanoma cells (Fig. 4). While CDDP stops the cell cycle of 518A2 melanoma cells during the S-phase, the neutral complexes **1** and **6** had virtually no effect on the distribution of cells in the individual phases of the cell cycle, apart from a marginal rise in the G1-phase population. In contrast, the cationic complex **2** and its ethynyl-substituted derivative **7** initiated a pronounced G1-phase arrest of the melanoma cell cycle, fully in line with earlier results for other cationic imidazol-2-ylidene platinum(II) complexes.[3] Two conclusions can be drawn: first, both types of complexes **1**/**6** and **2**/**7** had effects different from that of cisplatin, and second, the similarity of the effects of complexes **1** and **2** and their respective ethynyl-tagged derivatives **6** and **7** justifies the use of the latter as surrogates in localisation studies.

Colocalisation. To test if the compounds accumulate in the nucleus or if the differences in their modes of action from that of cisplatin originate from a different target location, we treated 518A2 melanoma cells with the ethynyl-substituted complexes **6** and **7** (30 min, 30 μM). The intracellular distribution was visualized *via* Cu(I)-catalysed click reaction with 3-azido-7-hydroxycoumarin in a mixture of $CuSO_4$ and ascorbic acid in BSA buffer. This gave a turquoise fluorescent triazole. Confocal microscopy of the treated cells, co-stained with Mitotracker™ (Thermofisher) found both complexes mainly to be located at the mitochondria (Fig. 5). Using the framed cells in Fig. 5, the Pearson correlation coefficient (PC) and Li's colocalisation quotient (LICQ) were calculated as a measure of colocalisation accuracy, using imageJ and the colocalisation plugin JaCoP.[13,14] Both complexes showed high PC values (a value of 1 corresponds to complete colocalisation) and LICQ values (a value of 0.5 corresponds to complete colocalisation) for the localisation of complexes **6** (PC: 0.89, LICQ: 0.46) and **7** (PC: 0.90, LICQ: 0.47) at the mitochondria of the selected cells. This stands in stark contrast to the tendency of most known platinum complexes to accumulate in the nucleus, but falls in line with reports on charged and lipophilic complexes addressing other cellular targets than nuclear DNA.[15–17] There are also many reports on complexes, predominantly of gold, of the type "delocalized lipophilic cations" (DLC) accumulating in mitochondria.[18–22] DLCs are able to pass lipid layers and selectively accumulate in mitochondria which feature a negative inner transmembrane potential.[23–25]

Changes of the mitochondrial membrane potential Ψ and of ROS levels. The accumulation of complexes **6** and **7** in mitochondria suggests that their closely related congeners **1** and **2** might also operate by a mitochondria-associated mechanism of action. The integrity of the mitochondrial membrane potential ΔΨ (MMP ΔΨ) is a prerequisite for cellular functionality. ΔΨ is built up by a H^+-gradient across the inner mitochondrial membrane and drives the ATP synthesis by oxidative phosphorylation.[26] The impact of complexes **1**, **2**, **6**, and **7** on the MMP was evaluated using the cationic dye tetramethyl rhodamine methyl ester (TMRM), which accumulates proportionally to ΔΨ in the mitochondria. All complexes led to a significant decrease of ΔΨ with the parent complexes **1** and **2** slightly more so than their alkyne-tagged derivatives **6** and **7** (Fig. 6). A reduced ΔΨ lowers the amount of TMRM accumulating inside the mitochondria and consequently leads to a reduced fluorescence signal. Disruptions of the mitochondrial functionality often lead to an increase of cellular ROS levels, which play a pivotal role in cellular signaling, up to the point where they can activate p21, causing a G1-arrest and an upstream activation of p53.[27,28] Typical intracellular sources of ROS are peroxisomes, which are relevant to the oxidative metabolism of long-chained fatty acids. During this metabolic pathway H_2O_2 is formed as a side product. Furthermore, mitochondria are a main source of intracellular ROS due to the mitochondrial respiratory chain.[28,29] Cancer cells in general show elevated levels of ROS due to their increased proliferation rate and thus are prone to ROS-induced cell death.[30] Therefore, effects of all four complexes on the intracellular ROS level of 518A2 melanoma cells were determined, using the fluorescent

View Article Online
Dalton Transactions Paper

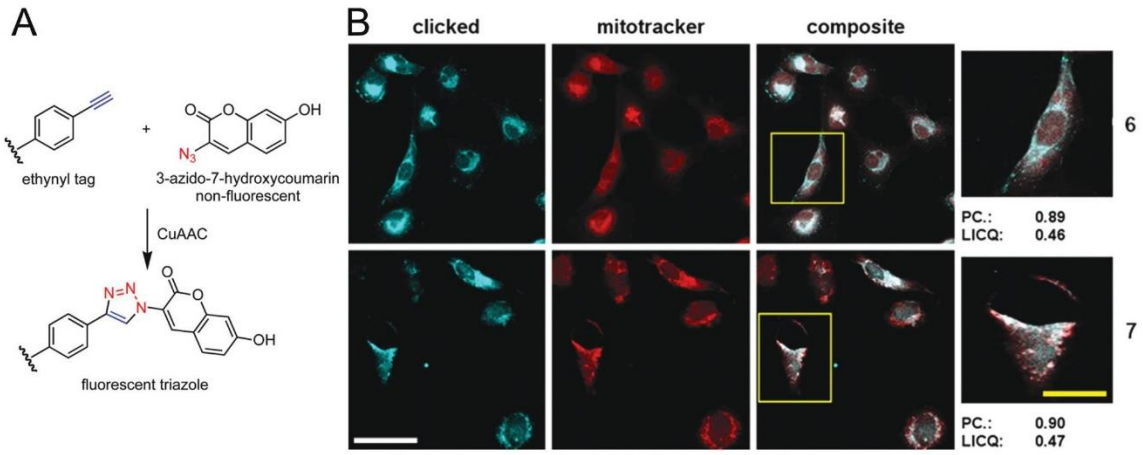

Fig. 5 A: Schematic copper(I)-catalysed 1,3-dipolar azide–alkyne cycloaddition (CuAAC; click reaction) of ethynyl-substituted complexes **6** or **7** with 3-azido-7-hydroxycoumarin in a mixture of $CuSO_4$ and ascorbic acid in BSA buffer to give turquoise fluorescent triazoles. B: Localisation of complexes **6** and **7** in 518A2 melanoma cells visualized *via* click reaction (turquoise) and documented by confocal fluorescence microscopy and co-staining of the mitochondria with Mitotracker™ (red) 30 min after incubation with 30 μM of the complexes. Pearson's coefficient (PC) and Li's colocalisation quotient (LICQ) were calculated for the marked cells (yellow box), using imageJ and JaCoP.[13,14] Scale: white: 50 μm, yellow 25 μm.

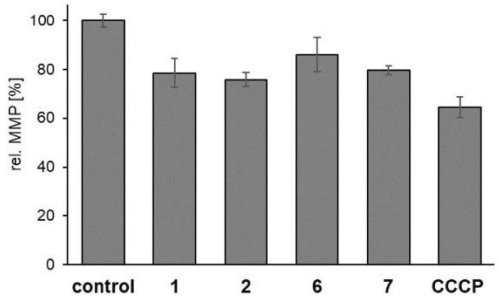

Fig. 6 Relative MMP ΔΨ of 518A2 melanoma cells, determined by fluorescence of the cationic lipophilic dye TMRM, after treatment with complexes **1**, **2**, **6**, and **7** (each 10 μM, 1 h). Carbonyl cyanide *m*-chlorophenylhydrazone (CCCP, 10 μM) was used as a positive control and DMF treated negative controls were set to 100%. Means ± SDs were calculated from three independent experiments.

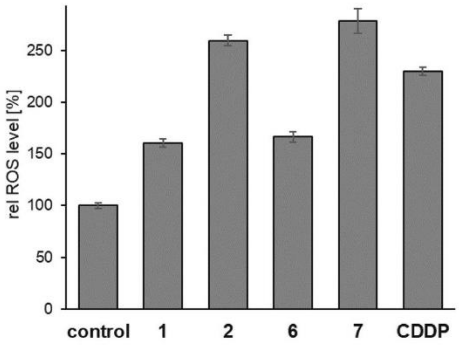

Fig. 7 Increase of the intracellular ROS levels of 518A2 melanoma cells, measured with DCFH-DA assays, after 1 h incubation at 37 °C with 10 μM of **1**, **2**, **6**, **7** or CDDP as a positive control. DMF was used as a negative control. Means ± SD were calculated from three independent experiments.

dye DCFH-DA, which is converted inside the cells to a non-fluorescent dye, while in the presence of ROS it is oxidized to highly fluorescent dicholorofluorescin. Treatment with each of the complexes **1**, **2**, **6** or **7** led to an increase in the ROS level which was most pronounced for the cationic complexes **2** and **7** (Fig. 7), in keeping with the greater cellular uptake of complex **2** when compared with that of neutral complex **1**. Within the two pairs of corresponding un-tagged and alkyne-tagged complexes **1**/**6** and **2**/**7**, the ROS promoting effect of the respective alkyne derivative, *i.e.* **6** or **7**, was slightly greater than that of the corresponding unt-tagged complex, *i.e.* **1** or **2**. The ROS level elevation by the neutral complexes **1** and **6** was obviously insufficient to cause a G1 arrest, typical of ROS induced cellular death,[22,23] as shown in Fig. 4.

Effects on the cytoskeleton. Changes in cell cycle progression, mitochondrial function, and ROS levels are often associated with changes in the structure of different components of the cytoskeleton. *Via* immunofluorescence staining of the microtubules and actin filaments of 518A2 melanoma cells the effects of the complexes **1**, **2**, **6**, and **7** on these cytoskeletal components were investigated. All complexes induced visible changes in the cytoskeleton of 518A2 melanoma cells (Fig. 8). In comparison to cells treated with DMF only, cells treated with 3 μM or 6 μM of complex **1** showed stress fibre formation throughout the cells and beginning decomposition of the actin filaments. The microtubules appeared slightly more diffuse than in the negative control and protruding more from

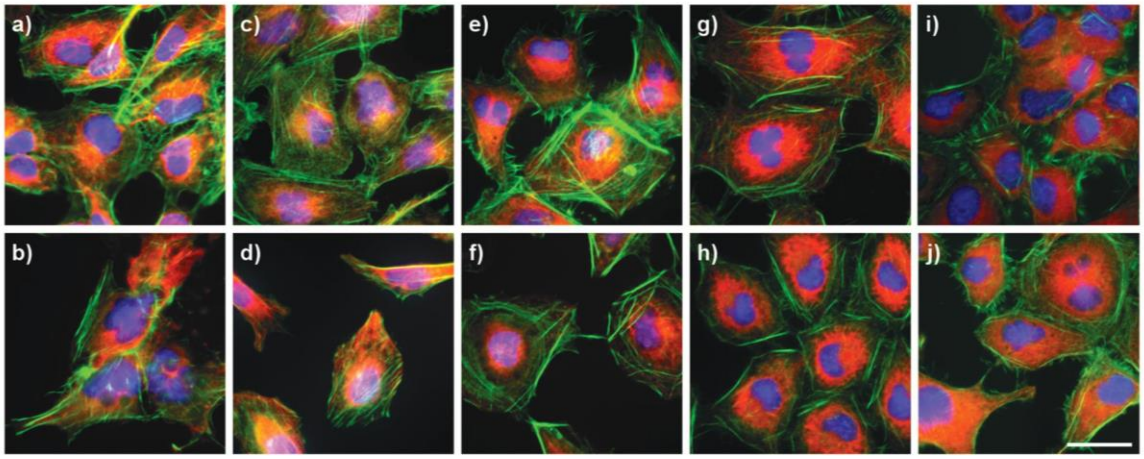

Fig. 8 Fluorescence staining of the nuclei (DAPI, blue), F-actin (Acti-stain™, green) and microtubules (Alexa Fluor 546, red) of 518A2 melanoma cells after 24 h of incubation with (a) DMF as control, (b) combretastatin-A4 as a positive control (25 nM), (c) **1** (3 μM), (d) **1** (6 μM), (e) **2** (400 nM), (f) **2** (800 nM), (g) **6** (3 μM), (h) **6** (6 μM), (i) **7** (500 nM), (j) **7** (1 μM). Scalebar: 30 μm. Images shown are representative of at least four independent experiments.

a point near the nucleus (Fig. 8c and d). Complex **2** led to similar changes in the cytoskeleton already at nanomolar concentrations. The tubulin network appeared to be even more concentrated around the nucleus and the actin stress fibre filaments formed thick bundles beneath the cell walls, almost tracing the cell membrane (Fig. 8e and f). The effects of complexes **6** and **7** largely resembled those of their analogues **1** and **2** (Fig. 8g–j), although they showed no interaction with purified tubulin (Fig. S9†). Stress fibre formation is often linked to a ROS-induced G1-phase arrest of the cell cycle,[28] as observed for complexes **2** and **7** (Fig. 4). The less distinct stress fibre formation induced by complexes **1** and **6** is in line with their missing cell cycle arrest. Further downstream in the mechanism of action, a strong cytoskeletal disruption is likely to accelerate the activation of caspase-3, resulting in cell apoptosis.[31]

Caspase-3/-7 mediated apoptosis induction. Since any deregulation of the mitochondrial function, as that ascertained for complexes **1**, **2**, **6** and **7** may trigger cytochrome c release and thus eventually apoptosis,[32] these complexes were also investigated for their ability to activate the effector caspases-3 and -7 (Fig. 9) by means of a fluorescence based caspase-3/-7 assay. While the neutral complexes **1** and **6** did not induce the activation of caspases-3/-7, complex **2** almost quadrupled and complex **7** more than doubled the amount of active caspases, surpassing the positive control staurosporine, albeit only in a concentration nearly ten times its IC_{50}(72 h). The lack of caspase-3/-7 induction by complexes **1** and **6** fits in well with the lower uptake of **1** and the lower ROS production rates by complexes **1** and **6** in 518A2 melanoma cells and with their missing interference with their cell cycle. Maybe, complexes **1** and **6** induce cell death *via* a caspase-independent mitochondria-associated pathway.[33]

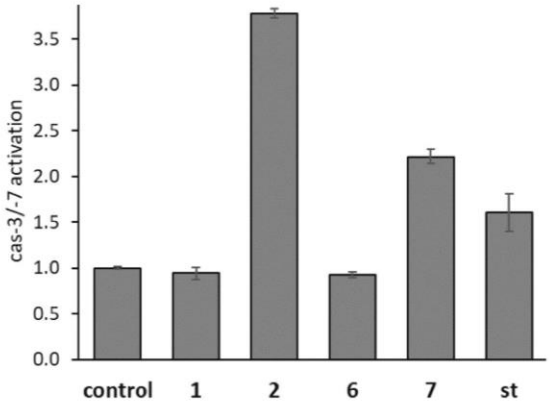

Fig. 9 Activation of caspases-3/-7 in 518A2 melanoma cells after 4 h of incubation with 10 μM of **1**, **2**, **6** and **7** or 2 μM staurosporine (st) as a positive control in comparison DMF as a negative control, measured using the Apo-ONE® homogenous caspase-3/7 assay kit (Promega). Values were corrected for the cell viability as obtained from MTT assays (>80% for all experiments). Means ± SD were calculated from three independent experiments.

Materials and methods

Chemical synthesis

General. All chemicals and reagents were purchased from Sigma Aldrich, Fluka, Merck, Acros Alfa Aesar, or ABCR and were used without further purification. Melting points are uncorrected; NMR spectra were run on a 500 MHz spectrometer; chemical shifts are given in ppm (δ) and referenced relative to the internal solvent signal; ^{195}Pt NMR shifts are quoted relative to $\Xi(^{195}\text{Pt}) = 21.496784$ MHz, K_2PtCl_4 was used

as external standard (δ = −1612.81); for ^{31}P NMR spectra H_3PO_4 was used as an external standard; mass spectra: direct inlet, EI, 70 eV; absorbance and fluorescence measurements: Tecan F200; flow cytometry: Beckman Coulter Cytomics FC 500, fluorescence microscopy: Zeiss Axioplan 2 and Leica Confocal TCS SP5.

1-(Bromomethyl)-4-ethynylbenzene (4). Under dry conditions and an argon atmosphere, 4-ethynylbenzylic alcohol **3** (400 mg, 3.03 mmol) in dry CH_2Cl_2 (30 mL) was treated with *N*-bromosuccinimide (1.078 g, 6.05 mmol, 2 eq.) and PPh_3 (1.588 g, 6.05 mmol, 2 equiv.) After stirring for 3 h at 40 °C the mixture was poured on water (100 mL) and the aqueous phase was extracted with CH_2Cl_2. The combined organic layers were washed with brine, dried with Na_2SO_4 and evaporated. The product was purified by column chromatography (SiO_2, hexame/ethyl acetate 2 : 1). Yield: 564 mg (2.89 mmol, 96%), yellow oil. ^{1}H NMR (500 MHz, $CDCl_3$): δ 3.11 (s, 1 H, C≡CH), 4.48 (s, 2 H, CH_2), 7.36 (d, J = 8.2 Hz, 2 H, *m*-Ph), 7.47 (d, J = 7.9 Hz, 2 H, *o*-Ph); ^{13}C NMR (125 MHz, $CDCl_3$): δ 32.7 (CH_2), 78.0 (C_q), 83.1 (C_q), 122.2 (C_q), 129.0 (Ar), 132.5 (Ar), 138.4 (C_q).

1,3-Di(4-ethynylbenzyl)imidazolium bromide (5a). A mixture of **4** (564 mg, 2.89 mmol, 2.3 equiv.), imidazole (85.6 mg, 1.26 mmol), K_2CO_3 (174 mg, 1.26 mmol, 1 equiv.), and acetonitrile (25 mL) was stirred for 17 h at 80 °C. After evaporation of the solvent the residue was taken up in CH_2Cl_2, washed with water and dried over Na_2SO_4. The product was precipitated by adding hexane. Yield: 477 mg (1.26 mmol, 100%), amber solid of m.p. 232 °C. ^{1}H NMR (500 MHz, DMSO-d_6): δ 4.28 (s, 2 H, C≡CH), 5.46 (s, 4 H, CH_2), 7.43 (d, J = 8.2 Hz, 4 H, *m*-Ph), 7.54 (d, J = 8.2 Hz, 4 H, *o*-Ph), 7.84 (d, J = 1.5 Hz, 2 H, Imi-4,5), 9.39 (s, 1 H, 2-H); ^{13}C NMR (125 MHz, $CDCl_3$): δ 51.7 (CH_2), 81.8 (C_q), 82.9 (C_q), 122.2 (C_q), 123.0 (Imi-4,5), 128.7 (Ar), 132.3 (Ar), 135.4 (Imi-2), 136.6 (C_q); *m*/*z* (EI): 297, 182, 115.

1,3-Di(4-ethynylbenzyl)imidazolium chloride (5b). To **5a** (115 mg, 305 µmol) in ethanol (6 mL) were added Ag_2CO_3 (96 mg, 348 µmol, 1.14 equiv.) and three drops HNO_3 (65%). After stirring for 3.5 h at room temperature the silver halides were filtered off and the filtrate was treated with HCl (75 µl, 2.3 equiv.), neutralized with $NaHCO_3$ and filtered again. After removal of the solvent, desolving of the residue in CH_2Cl_2 and another filtration step, the product was precipitated with hexane. Yield: 69 mg (207 µmol, 68%); colorless solid. ^{1}H NMR (500 MHz, DMSO-d_6): δ 4.28 (2 H, s, C≡CH), 5.44 (4 H, s, N-CH_2), 7.42 (4 H, d, J = 8 Hz, *m*-Ph), 7.54 (4 H, d, J = 8 Hz, *o*-Ph), 7.83 (2 H, d, J = 2 Hz, 4,5-H), 9.36 (1 H, s, 2-H).

***cis*-[Dichlorido-bis(1,3-di(4-ethynylbenzyl)imidazol-2-ylidene)] platinum(II) (6).** A solution of *cis*-[$Pt^{II}Cl_2(DMSO)_2$] (39 mg, 90 µmol) and 1,3-di(4-ethynylbenzyl)imidazolium chloride (69 mg, 207 µmol, 2.3 equiv.) in dry CH_2Cl_2 (10 mL) under argon atmosphere was treated with KO^{t}Bu (30 mg, 270 µmol, 3 equiv.). After stirring for 24 h at room temperature, the solution was filtered to remove solid by-products, the filtrate was concentrated *in vacuo*, and the remaining solid was first crystalized from CH_2Cl_2/Et_2O and then purified by column chromatography (silica gel, CH_2Cl_2 + 1% → 2.5% methanol). Yield: 31 mg (36 µmol, 40%); colorless solid of m.p. >360 °C (dec.). Elemental analysis (%): calc. for $C_{42}H_{34}N_4Cl_2Pt$ (860.75): C, 58.61; H, 3.98; N, 6.51. Found: C, 58.47; H, 4.19; N, 5.94. ^{1}H NMR (500 MHz, DMSO-d_6): δ 4.20 (4 H, s, C≡CH), 5.22 (4 H, d, J = 15.3 Hz, CH_2), 5.85 (4 H, d, J = 15.3 Hz, CH_2), 6.95 (4 H, s, Imi), 7.24 (8 H, d, J = 8.2 Hz, Ar), 7.43 (8 H, d, J = 8.2 Hz, Ar); ^{13}C NMR (125 MHz, DMSO-d_6): δ 52.5 (CH_2), 81.2 (C≡*C*H), 83.2 (C_q), 121.2 (C_q), 121.7 (Imi), 127.9 (Ar), 131.9 (Ar), 136.8 (C_q), 146.7 (NCN); ^{195}Pt NMR (DMSO-d_6): δ −3583 ppm; *m*/*z* (EI): 662, 648, 453, 312, 277, 115, 36.

***cis*-[Chlorido-bis(1,3-di(4-ethynylbenzyl)imidazol-2-ylidene) (triphenylphosphine)]platinum(II) chloride (7).** A solution of complex **6** (15 mg, 17.5 µmol) and triphenylphosphine (24 mg, 92 µmol, 5 equiv.) in CH_2Cl_2/methanol (9 mL/1 mL) was stirred at room temperature for 72 h. The crude product was crystalized from CH_2Cl_2/Et_2O. Yield: 16 mg (14.3 µmol, 82%); colorless solid of m.p. 237 °C (dec.). ^{1}H NMR (500 MHz, DMSO-d_6): δ 4.25 (4 H, d, J = 7.9 Hz, C≡CH), 4.79 (2 H, d, J = 15.7 Hz, CH_2), 4.97 (2 H, d, J = 15.1 Hz, CH_2), 5.50 (2 H, d, J = 15.7 Hz, CH_2), 5.71 (2 H, d, J = 15.1 Hz, CH_2), 6.81 (4 H, d, J = 7.9 Hz, Imi), 7.08 (4 H, d, J = 5.0 Hz, Ar), 7.14 (4 H, d, J = 7.9 Hz, Ar), 7.30 (4 H, d, J = 7.9 Hz, Ar), 7.41–7.46 (16 H, m, Ar), 7.57 (3 H, t, J = 6.6 Hz, *p*-PPh_3); ^{13}C NMR (125 MHz, DMSO-d_6): δ 53.3 (CH_2), 53.6 (CH_2), 81.9 (C_q), 82.1 (C_q), 83.3 (C_q), 83.5 (C_q), 122.0 (C_q), 123.2 (Imi), 123.6 (Imi), 127.9 (Ar), 128.5 (Ar), 129.3 (d, J = 55.4 Hz, P–C), 129.4 (d, J = 12 Hz, PPh_3), 131.9 (Ar), 132.5 (d, J = 12 Hz, PPh_3), 134.3 (PPh_3), 135.3 (Ar–C_q), 136.6 (Ar–C_q), 145.8 (d, J = 10 Hz, $NC^{cis^P}N$), 163.2 (d, J = 151 Hz, $NC^{trans^P}N$); ^{31}P NMR (DMSO-d_6): δ 12.9 (s, J = 2356 Hz); ^{195}Pt NMR (DMSO-d_6): δ −4112 (d, J = 2401 Hz).

Biological evaluation

Cell culture conditions and stock solutions. The 518A2 melanoma cells (Department of Radiotherapy & Radiobiology, University Hospital Vienna, Austria), the HT-29 (DSMZ ACC-299), HCT116 (DSMZ ACC-581) colon carcinoma cells, the EaHy926 (ATCC CRL-2922) endothelial cells, the HDFa (ATCC® PCS-201-012™) human dermal fibroblasts, the Kb-V1 (DSMZ ACC-149) cervix carcinoma cells were cultivated in Dulbeccos Modified Eagle Medium (Gibco, ThermoFisher), supplemented with 10% fetal bovine serum (Biochrom) and 1% Antibiotic-Antimycotic (Gibco, ThermoFisher) at 37 °C, 95% humidity and 5% CO_2. For a stable multi-drug resistance the Kb-V1 cells were treated regularly with 340 nM vinblastine. The platinum complexes used in the biological assays were dissolved in DMF (10 mM) and freshly diluted appropriately with sterile water. If not indicated otherwise all incubation steps of the bioassays were conducted under cell culture conditions.

Inhibition of cell growth (MTT assay).[34] *Via* the MTT (3-(4,5-dimethylthiazol-2-yl)-2,5-diphenyltetrazolium bromide, Glentham life sciences) based proliferation assay, the complexes **1**, **2**, **6** and **7** were investigated for their anti-proliferative effect on the aforementioned cell lines. Cells were seeded at 0.05 × 10^6 cells per mL (cpm) or at 0.1 × 10^6 cpm (HDFa) into the wells of 96-well microtiter plates (100 µL per well) and

incubated for 24 h. Appropriate dilutions in H_2O of the complexes or equal amounts of the solvent were added into the wells (final concentrations 100 μM–5 nM) and the cells were further incubated for 72 h. Before staining of the viable cells the plates were centrifuged (300*g*, 5 min, 4 °C) and the old medium was discarded. 50 μL of a 0.05% MTT solution (PBS) were added to each well. Subsequent to another 2 h of incubation the plates were centrifuged as before and the MTT solution was discarded again. To dissolve the cells and the formed violet water-insoluble formazan, 25 μL of an SDS/DMSO solution (10%, 0.6% AcOH) were added to each well and the plates were further incubated for at least 1 h. The absorbances at 570 nm (formazan) and at 630 nm (background) were measured. The absorbance of formazan is directly linked to the amount of metabolically active (viable) cells in the wells. The absorbance of the wells treated with the solvent was set to 100% viable cells, and the percentage of viable cells in the wells treated with the platinum complexes was calculated accordingly. IC_{50} values were determined using Graphpad Prism, means and SD were calculated from four independent experiments.

Uptake into 518A2 melanoma cells *via* ICP-MS. 518A2 melanoma cells were seeded at a density of 2×10^6 cells per dish and grown overnight. The cells were treated with **1** or **2** at final concentrations of 1 μM and 5 μM for 8 hours. The cells were harvested, washed twice with PBS, counted and pelleted. Cell pellets were lyzed using the microwave digestion system (MARS5, CEM) with HCl. The platinum content was determined with ICP-MS.

Ethidium bromide saturation assay (EtdBr assay). The DNA interaction of **1** and **2** with linear salmon sperm DNA (ThermoFisher) was investigated utilizing the increase of fluorescence upon intercalation of ethidium bromide between the bases of DNA.[35] Alterations of the DNA structure by, *e.g.* small molecules change the ethidium bromide fluorescence. 1 μg of salmon sperm DNA in TE-buffer (Tris/HCl 10 mM, EDTA 1 mM, pH 8.0) was treated with 5 μM, 10 μM, 25 μM, 50 μM or the solvent (equal to 50 μM) for 2 h at 37 °C inside the wells of a 96-well black well plate. EtdBr-DNA adduct fluorescence was measured at λ_{ex} = 535 nm and λ_{em} = 595 nm. The background fluorescence was measured from samples prepared analogously but without the DNA and was subtracted from the sample values. Changes in the fluorescence intensity of the wells containing the DNA treated with the compounds were calculated in relation to the fluorescence of the wells treated with the solvent (set to 100%). Means and SD were calculated from triplicates.

Cell cycle analysis. The effects of **1**, **2**, **6** and **7** on the cell cycle progression of 518A2 melanoma cells were investigated *via* flow cytometry. 518A2 cells were seeded into the wells of 6-well microtiter plates (0.05×10^6 cpm, 3 mL per well). After an incubation period of 24 h appropriate dilutions of the test complexes or the solvent were added into the wells to give final concentrations of 5 μM (**1**, **6**), 500 nM (**2**, **7**) or 2 μM (CDDP). After 24 h of incubation the medium of each well was transferred into precooled centrifugation tubes (on ice) and the cells were washed with 1 mL PBS. After trypsination (500 μL per well) the cells were transferred into the respective tube and the wells were washed multiple times with PBS to transfer the remaining cells as well. The cells were pelletized by centrifugation (300*g*, 5 min, 4 °C). The pellet was resuspended with 1 mL ice-cold EtOH (70%) and the cells were fixed for at least 1 h on ice. The cellular DNA was stained with propidium iodide (PI) buffer (50 μg mL^{-1} PI, 0.1% sodium citrate, 50 μg mL^{-1} RNase A, freshly added) for 30 min at 37 °C before, depending on pellet size, 300–500 μL PBS were added. The PI fluorescence, *i.e.* the amount of DNA inside the cells, was measured *via* flow cytometry. Using the CXP analysis software, provided by Beckman Coulter, the distribution of the cell population of each well between the phases of the cell cycle (G1, S, G2/M, sub-G1) was determined. Means and SD were calculated from triplicates.

Colocalisation. 518A2 cells (0.05×10^6 cpm) were seeded onto cover slips (borosilicate glass, Carl Roth) inside the wells of 24-well microtiter plates (0.5 mL per well) and incubated for 24 h. The medium was removed and the cells were washed once with 1 mL PBS before 500 μL (250 nM in FBS-free DMEM) of Mitotracker™ Red CM-H_2Xros (ThermoFisher Scientific) were added into each well and the cells were incubated for 30 min at 37 °C. The staining solution was discarded and the cells were washed twice with 1 mL PBS before they were overlaid with complete DMEM medium (500 μL per well). The cells were treated with **6** or **7** at a final concentration of 30 μM for 30 min at 37 °C before fixation, blocking and permeabilization was done analogously to the fluorescence staining of the cytoskeleton. 200 μL of click working solution (2 mM $CuSO_4$, 5 mM sodium ascorbate, 0.1 mM 3-azido-7-hydroxycoumarin, 1% BSA in PBS) were added into each well. The cells were incubated for 30 min at RT in the dark before the click solution was discarded and the cells were washed three times with 1% BSA in PBS for 5 min. The coverslips were embedded in mowiol mounting medium. Confocal fluorescence images were taken at 1 Airy and colocalisation parameters were calculated for one cell using the ImageJ Plugin JaCOP.[13,14]

Mitochondrial membrane potential assay. For the examination of the effect on the mitochondrial membrane potential (MMP) of complexes **1** and **2** the cationic dye tetramethylrhodamine methyl ester (TMRM) was used. TMRM accumulates in mitochondria in quantities proportional to the MMP. For the assay melanoma cells 518A2 (0.25×10^6 cpm) were seeded in a black 96-well plate (Brand pureGrade™) and a transparent 96-well plate, for corresponding MTT-assay (100 μL per well), and incubated for 24 h. The medium was then replaced by standard assay buffer (80 mM NaCl, 75 mM KCl, 25 mM D-glucose, 25 mM HEPES, pH 7.4) (90 μL per well). Test compounds in standard assay buffer were added (10 μL per well) to obtain the desired final concentration. Carbonylcyanide *m*-chlorophenylhydrazone (CCCP), a known decoupling agent of oxidative phosphorylation, was used as a positive control, followed by an incubation period of 1 h. Then, a TMRM solution (2 μM in standard assay buffer) was added (10 μL per well) and cells were further incubated for

10 min at rt. Cells were washed three times with PBS (160 μL per well), PBS was added (100 μL per well) and the fluorescence of the TMRM remaining inside the cells was measured after 15 min (ex/em 535/590 nm). The fluorescence signal was standardized relative to the cell viability as determined by a concomitant MTT-assay.

Reactive oxygen species (ROS) assay. ROS were detected using the 2,7-dichlorofluorescin diacetate (DCFH-DA) assay which is based on the oxidation of the dye by ROS inside the cells to give the highly fluorescent 2,7-dichlorodihydrofluorescin. In case of oxidative stress, cellular levels of ROS rise and cause oxidative damages. Melanoma cells (518A2) were seeded in a black 96-well plate (0.1×10^6 cpm, 100 μL per well) and incubated for 24 h under standard cell culture conditions. The medium was replaced by serum-free medium, containing DCFH-DA (20 μM), followed by an incubation for 30 min. The cells were washed twice with PBS and fresh serum-free medium was added, before the cells were treated with test compounds **1** or **2** for 1 h. Solvent served as a negative, and hydrogen peroxide as a positive control. Next, the cells were washed twice with PBS, fresh PBS was added (100 μL per well) and the fluorescence was measured (ex/em 485/535 nm). The fluorescence intensity values were corrected for the amount of viable cells as determined *via* MTT assays, and were calculated in relation to the control which was set as 100%.

Fluorescence staining. 518A2 (0.05×10^6 cpm) or EaHy926 (0.1×10^6 cpm) cells were seeded onto cover slips (borosilicate glass, Carl Roth) inside the wells of 24-well microtiter plates (0.5 mL per well) and incubated for 24 h. Dilutions of **1**, **2**, **6**, **7** or combretastatin-A4 in H_2O were added into each well and the cells were incubated for another 24 h. For fixation of the cells the medium was discarded and the cells were washed with 1 mL PBS (37 °C) for 30 s, the cells were incubated with 3.7% formaldehyde (PBS) for 20 min at rt. The formaldehyde solution was removed, and the cells were washed three times with PBS (1 mL) to completely remove the formaldehyde as it could interfere with the fluorescence staining. Blocking and permeabilization of the cells was done with 500 μL of 1% BSA in PBS (0.5% Triton X-100) for 30 min at rt. For staining of the microtubules, the cells inside each well were incubated with 200 μL of 1% BSA in PBS containing the primary antibody mouse anti-α-tubulin (Invitrogen, 1 : 300) for 1 h at 37 °C. The solution was discarded, and the wells were washed three times with 1 mL PBS before the secondary antibody goat anti-mouse Alexa Fluor 546 (Invitrogen, 1 : 300) was added (200 μL per well, 1% BSA in PBS). After another incubation step (1 h) in the dark at rt the solution was discarded again, and the wells were washed three times with PBS (1 mL). For staining of the actin components of the cytoskeleton, cells were incubated with 200 μL of 100 nM (PBS) of Acti-stain™ (Cytoskeleton) for 1 h in the dark at rt. The staining solution was discarded and the cells in each well were washed twice with 1 ml PBS and overlaid with 500 μL sterile water before the coverslips were embedded in mowiol mounting medium (+1 μg mL^{-1} DAPI). The condition of the cytoskeleton was documented by fluorescence microscopy.

Caspases-3/-7 activation. Using the Apo-One® homogeneous caspase-3/-7 assay kit (Promega), complexes **1**, **2**, **6** and **7** were tested for their ability to activate the apoptosis-associated caspases-3 and -7. 518A2 melanoma cells were seeded at 0.1×10^6 cpm into the wells of a 96-black well plate (67.5 μL per well) and the plate was incubated for 24 h under standard cell culture conditions. The cells were treated with 10 μM of **1**, **2**, **6** and **7**, 2 μM of the positive control staurosporine (st) or equivalent amounts of the solvent as negative control for 4 h at 37 °C. The substrate (100×) was diluted in assay buffer, provided in the kit. The substrate dilution was added to the wells (75 μL per well). After 2 h of incubation at rt in the dark the fluorescence of the processed substrate was measured at λ_{ex} = 499 nm and λ_{em} = 527 nm. A second microtiter plate was treated analogously for MTT assays.

Conclusions

The aim of this in-depth study was to identify the structural factors that govern the uptake rates and sites of accumulation in cancer cells, the molecular targets, and the modes of antitumoral action of two closely related *cis*-[bis(1,3-dibenzylimidazol-2-ylidene)$Pt^{II}Cl(L)$] complexes sharing the same lipophilic NHC ligands while differing in their overall charge (neutral *vs.* cationic) and the bulkiness of their secondary ligands (Cl_2 *vs.* Cl,PPh_3). Both complexes **1** (L = Cl) and **2** (L = PPh_3) interacted strongly with purified DNA *in vitro*, modifying its morphology in EMSA and ethidium bromide assays to a greater extent than cisplatin. The uptake into melanoma cells was significantly greater for complex **2** than for complex **1**, possibly because of its DLC character, or by being a substrate of the organic cation transporters (OCT). Surprisingly, their ethynyl-tagged analogues **6** and **7**, regardless of their initial charge, accumulated at the mitochondria rather than the nuclei of the melanoma cells, which might be due to their DLC character overriding the tendency of Pt(II) to form coordination complexes with DNA bases. All complexes **1**, **2**, **6** and **7** impaired the functionality of the mitochondria by decreasing their membrane potential and thus elevating the levels of reactive oxygen species. In the case of complexes **2** and **7**, but not **1** and **6**, with the lipophilicity and bulkiness of the PPh_3 residue being the discriminating factor, these effects are great enough to induce a G1-phase arrest of the melanoma cell cycle and a remodeling of the actin filaments to stress fibres. The elevated ROS levels are presumably also causative for the activation of caspase-3/-7 mediated apoptosis in the case of complexes **2** and **7**. Their consistently lower IC_{50} values in MTT-assays against various cancer cell lines are in keeping with this mechanistic rationale.

The upshot of this study is that NHC-platinum(II) complexes may be used to selectively target mitochondria rather than nuclei and DNA, thus bypassing the notorious DNA-repair associated resistance against platinum tumour therapy.

Conflicts of interest

There are no conflicts of interest.

Acknowledgements

R. S. thanks the Deutsche Forschungsgemeinschaft (DFG) for a grant (Scho 402/12-2), V. B. was supported by the Czech Science Foundation (grant 18-09502S). We thank Franziska Gillsch (University Bayreuth) for providing a new batch of complex **7**.

Notes and references

1 (*a*) B. Rosenberg, L. Van Camp, J. E. Trosko, *et al.*, *Nature*, 1969, **222**, 385; (*b*) B. Rosenberg and L. Van Camp, *Cancer Res.*, 1970, **30**, 1799; (*c*) S. Dilruba and G. V. Kalayda, *Cancer Chemother. Pharmacol.*, 2016, **77**, 1103.
2 (*a*) S. Bellemin-Laponnaz, *Eur. J. Inorg. Chem.*, 2020, **2020**, 10; (*b*) T. Zou, C.-N. Lok, P.-K. Wan, *et al.*, *Curr. Opin. Chem. Biol.*, 2018, **43**, 30.
3 J. K. Muenzner, T. Rehm, B. Biersack, *et al.*, *J. Med. Chem.*, 2015, **58**, 6283.
4 T. Rehm, M. Rothemund, J. K. Muenzner, *et al.*, *Dalton Trans.*, 2016, **45**, 15390.
5 T. Rehm, M. Rothemund, A. Bär, *et al.*, *Dalton Trans.*, 2018, **47**, 17367.
6 L. Yang, C. Chumsae, J. B. Kaplan, *et al.*, *Bioconjugate Chem.*, 2017, **28**, 2302.
7 (*a*) J. H. Price, A. N. Williamson, R. F. Schramm, *et al.*, *Inorg. Chem.*, 1972, **11**, 1280; (*b*) N. I. Dodoff, D. Kovala-Demertzi, M. Kubiak, *et al.*, *Z. Naturforsch., B: J. Chem. Sci.*, 2006, **61**, 1110.
8 J. Chen, *Cold Spring Harbor Perspect. Med.*, 2016, **6**, a026104.
9 B. S. Cummings and R. G. Schnellmann, *J. Pharmacol. Exp. Ther.*, 2002, **302**, 8.
10 M. Gold, Y. Mujahid, K. Ahmed, *et al.*, *J. Biol. Inorg. Chem.*, 2019, **24**, 647.
11 A. Ghezzi, M. Aceto, C. Cassino, E. Gabano and D. Osella, *J. Inorg. Biochem.*, 2004, **98**, 73.
12 (*a*) J. Reedijk and P. H. Lohman, *Pharm. Weekbl., Sci.*, 1985, **7**, 173; (*b*) M. H. Hanigan and P. Devarajan, *Cancer Ther.*, 2003, **1**, 47.
13 M. D. Abramoff, P. J. Magalhães and S. J. Ram, *Biophotonics Int.*, 2004, **11**, 36.
14 S. Bolte and F. P. Cordelières, *J. Microsc.*, 2006, **224**, 213.
15 Z. Zhu, Z. Wang, C. Zhang, *et al.*, *Chem. Sci.*, 2019, **10**, 3089.
16 G. M. Tozer, C. Kanthou, C. S. Parkins, *et al.*, *Int. J. Exp. Pathol.*, 2002, **83**, 21.
17 L. Vincent, P. Kermani, L. M. Young, *et al.*, *J. Clin. Invest.*, 2005, **115**, 2992.
18 S. Trapp and R. Horobin, *Eur. Biophys. J.*, 2005, **34**, 959.
19 B. Bertrand and A. Casini, *Dalton Trans.*, 2014, **43**, 4209.
20 A. Casini and L. Messori, *Curr. Top. Med. Chem.*, 2011, **11**, 2647.
21 L. Oehninger, R. Rubbiani and I. Ott, *Dalton Trans.*, 2013, **42**, 3269.
22 S. J. Berners-Price and A. Filipovska, *Aust. J. Chem.*, 2008, **61**, 661.
23 C. I. Yeo, K. K. Ooi and E. R. T. Tiekink, *Molecules*, 2018, **23**, 1410.
24 S. B. Aher, P. N. Muskawar, K. Thenmozhi, *et al.*, *Eur. J. Med. Chem.*, 2014, **81**, 408.
25 J. S. Modica-Napolitano and J. R. Aprille, *Adv. Drug Delivery Rev.*, 2001, **49**, 63.
26 P. D. Boyer, B. Chance, L. Ernster, *et al.*, *Annu. Rev. Biochem.*, 1977, **46**, 955.
27 B. Liu, Y. Chen and D. K. St Clair, *Free Radicals Biol. Med.*, 2008, **44**, 1529.
28 J. Boonstra and J. A. Post, *Gene*, 2004, **337**, 1.
29 V. Adam-Vizi and C. Chinopoulos, *Trends Pharmacol. Sci.*, 2006, **27**, 639.
30 G.-Y. Liou and P. Storz, *Free Radical Res.*, 2010, **44**, 479.
31 Y. Yamazaki, M. Tsuruga, D. Zhou, *et al.*, *Exp. Cell Res.*, 2000, **259**, 64.
32 S. A. Lakhani, A. Masud, K. Kuida, *et al.*, *Science*, 2006, **311**, 847.
33 M. Donovan and T. G. Cotter, *Biochim. Biophys. Acta*, 2004, **1644**, 133.
34 T. Mosmann, *J. Immunol. Methods*, 1983, **65**, 55.
35 J.-B. Lepecq and C. Paoletti, *J. Mol. Biol.*, 1967, **27**, 87.

Supporting Information

Antitumoral effects of mitochondria-targeting neutral and cationic *cis*-[bis(1,3-dibenzylimidazol-2-ylidene)Cl(L)]Pt(II) complexes

Matthias Rothemund,[1] Sofia I. Bär,[1] Tobias Rehm,[1] Hana Kostrhunova,[2] Victor Brabec,[2] Rainer Schobert[1,*]

[1] Organic Chemistry Laboratory, University of Bayreuth, Universitätsstr. 30, 95447 Bayreuth, Germany

[2] Czech Academy of Sciences, Institute of Biophysics, Kraloyopolka 135, CZ-61264, Czech Republic.

Table of content:

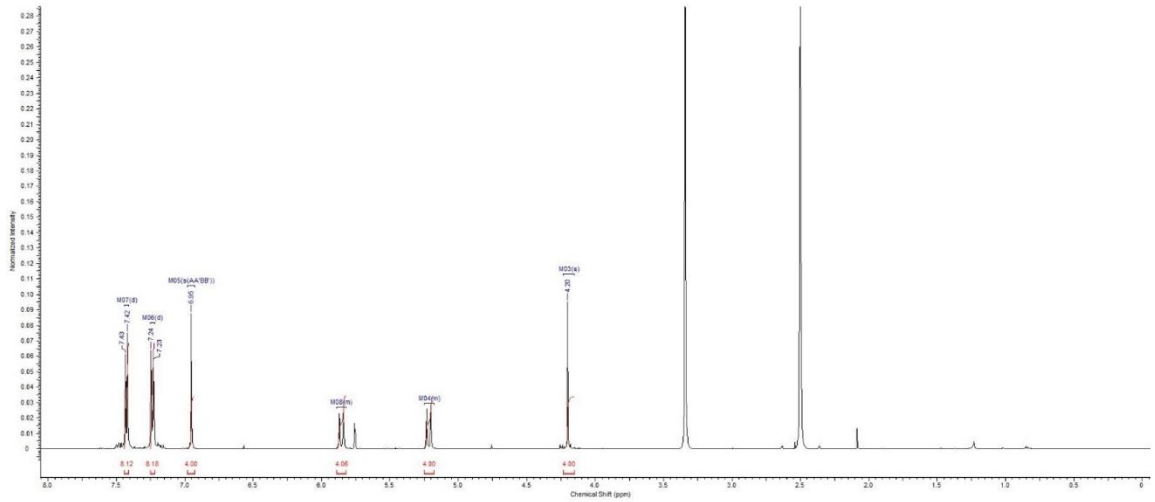

Figure S1. ^{1}H-NMR spectrum (500 MHz, DMSO-d_6) of complex **6**.

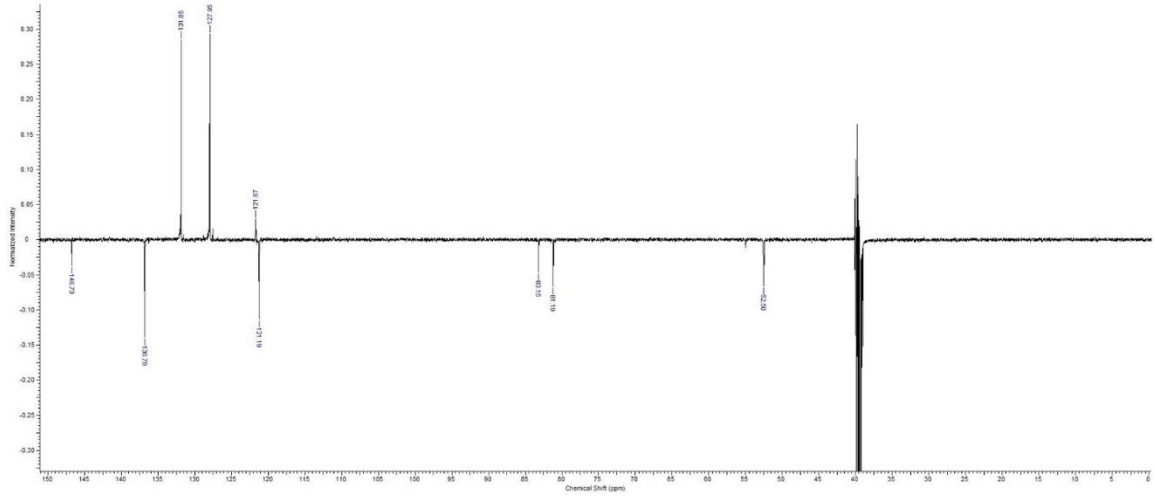

Figure S2. ^{13}C-NMR spectrum (125 MHz, DMSO-d_6) of complex **6**.

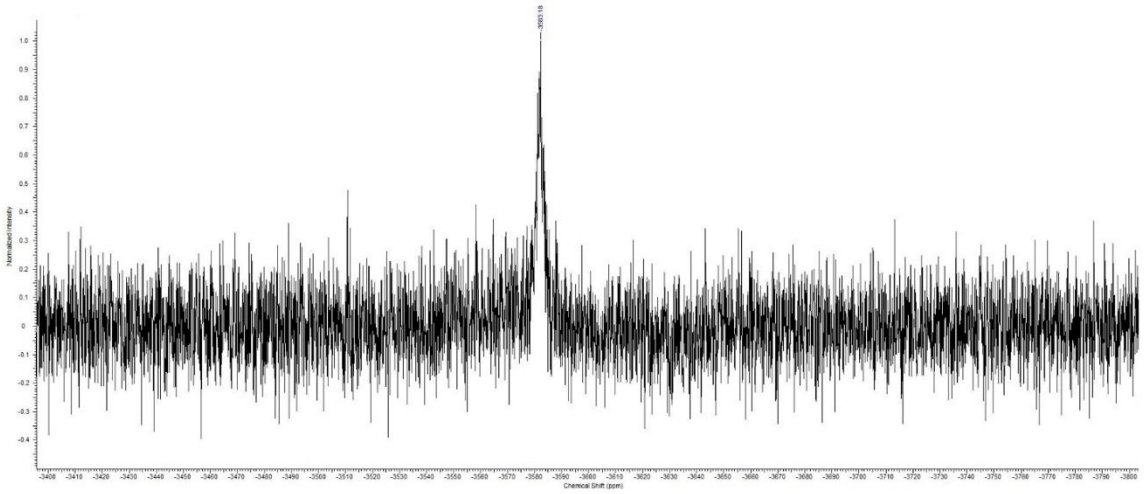

Figure S3. ^{195}Pt-NMR spectrum (DMSO-d_6) of complex **6**.

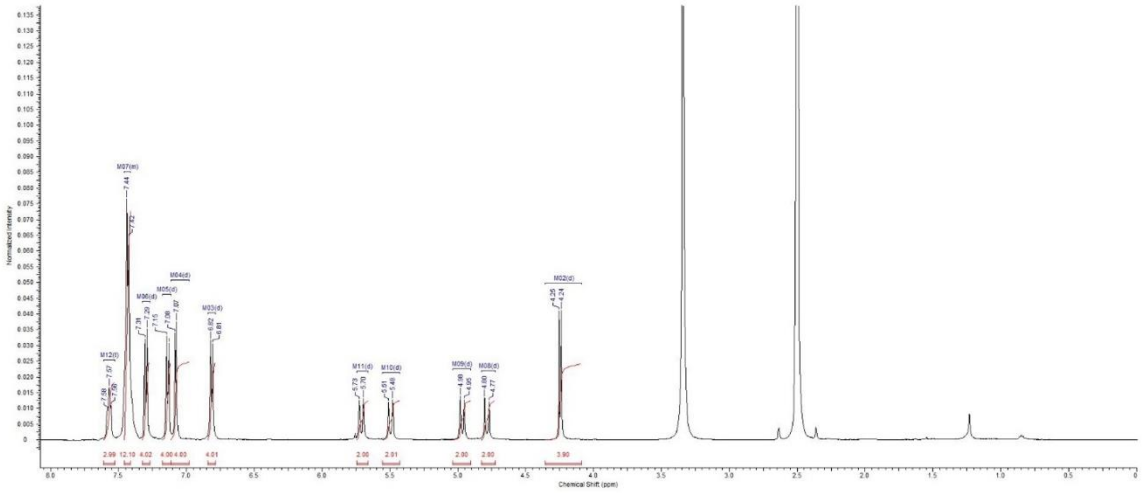

Figure S4. ^{1}H-NMR spectrum (500 MHz, DMSO-d_6) of complex **7**.

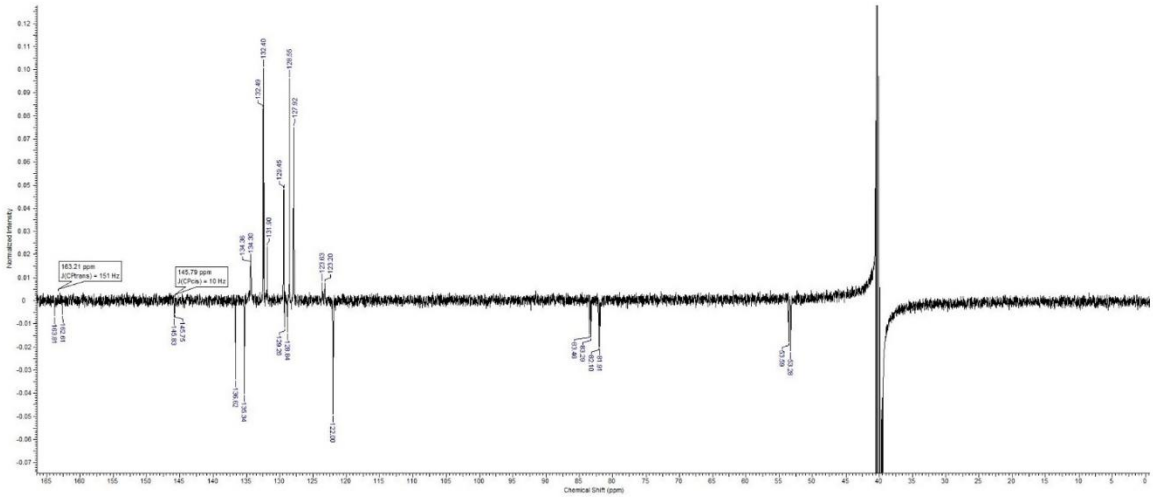

Figure S5. ^{13}C-NMR spectrum (125 MHz, DMSO-d_6) of complex **7**.

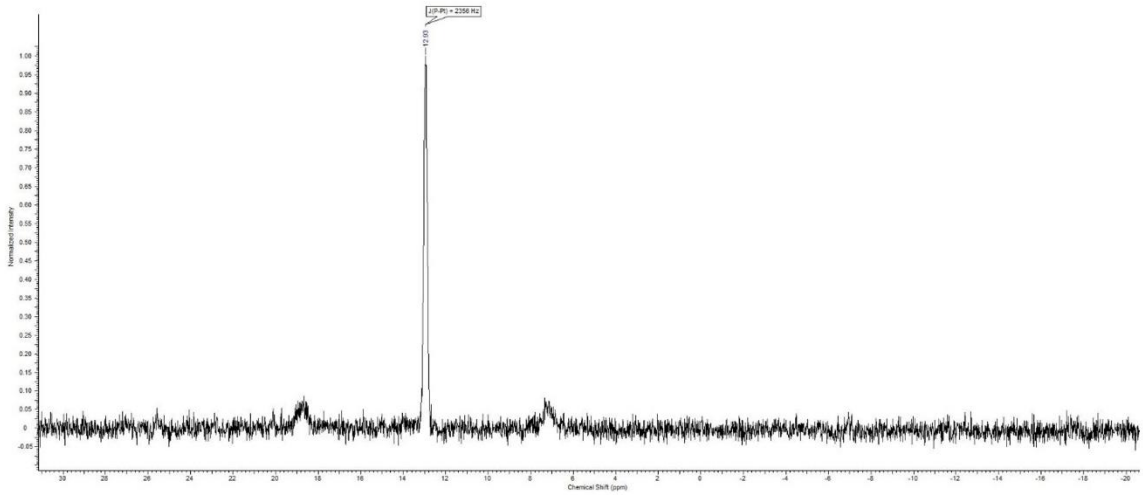

Figure S6. ^{31}P-NMR spectrum (DMSO-d_6) of complex **7**.

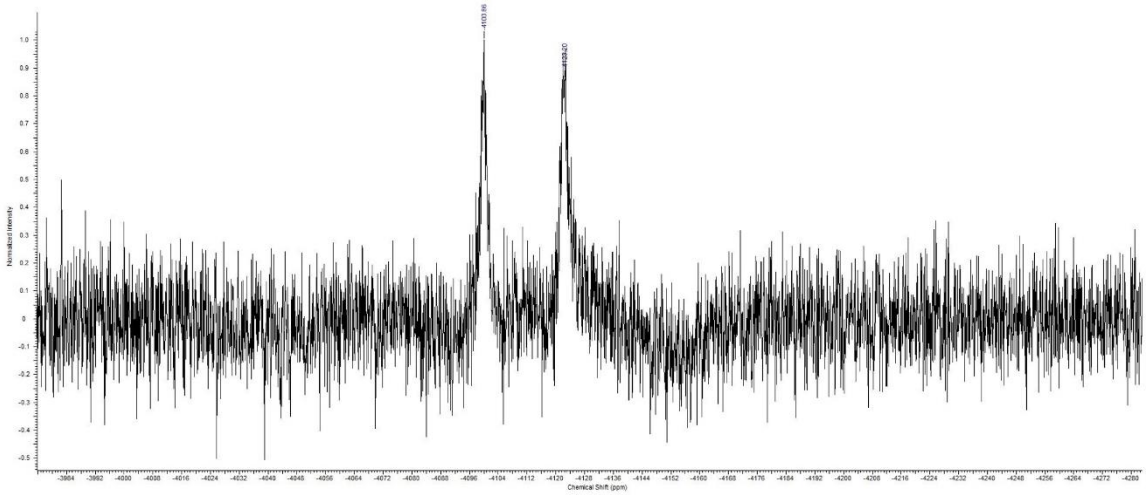

Figure S7. ^{195}Pt-NMR spectrum (DMSO-d_6) of complex **7**.

Uptake of 1 and 2 into 518A2 cells via ICP-MS

Table S1. Uptake of **1** or **2** in 518A2 melanoma cells, after 8 h of incubation with 1 or 5 μM of the complexes.

	ng Pt/10^6 cells	
	1 μM	**5 μM**
1	17.4 ± 3.9	362 ± 33
2	124 ± 21	774 ± 83

Experimental procedure of electrophoretic mobility shift assays (EMSA) with complexes 1, 2, 6, 7 and cisplatin

The effects of **1**, **2**, **6**, and **7** on the topology of circular pBR322 plasmid DNA were investigated via EMSA. Changes in the running behaviour of the DNA bands during agarose gel electrophoresis indicate an interaction between the platinum complexes and the plasmid DNA, forcing it from the compact covalently closed circular (ccc) form into the bulkier open circular form. 1.5 µg of pBR322 plasmid DNA (> 90% in the ccc form, ThermoFisher) in TE-buffer *(cf.* EtdBr Assay) were treated with 0, 5, 10, 25 or 50 µM of the platinum complexes (final sampe volume 20 µL) for 24 h at 37 °C. After addition of 5×DNA sample buffer (Tris/HCl 10 mM, 25% glycerine, bromphenol blue, pH 8.0, sterile filtered) agarose gelelectrophoresis (1% in Tris/HCl 4.5 mM, boracic acid 4.5 mM, EDTA 1.25 mM, pH 8.3) was run at 66 V for 4 h. DNA bands were stained for 30 min with EtdBr and documented with a UV transilluminator.

Agarose gels of EMSA with 1, 2, 6, 7 or cisplatin

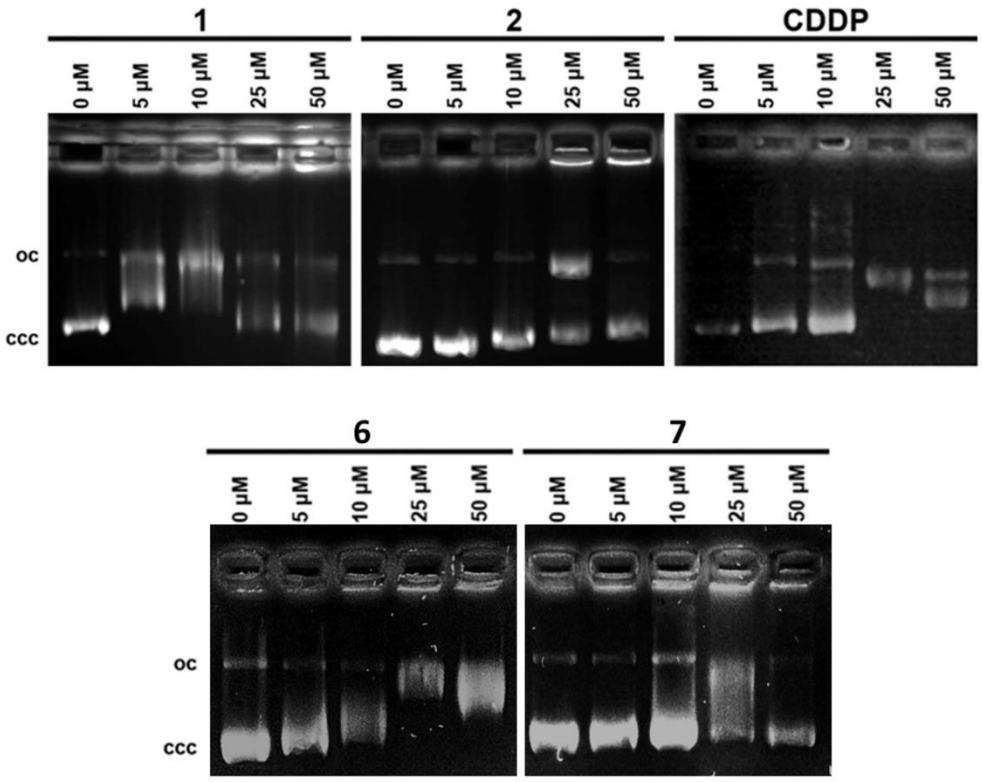

Figure S8. Agarose gel of EMSA with pBR322 plasmid DNA after 24 h of incubation with **1**, **2, 6, 7** or cisplatin at 0, 5, 10, 25 or 50 µM.

Experimental procedure for tubulin polymerisation assays of 6, 7 and CA-4

The tubulin binding capacity of complexes **6**, **7** as well as of the known tubulin polymerisation inhibitor CA-4, which served as a control, was investigated using the tubulin polymerisation assay which was conducted in clear black 96-well plates (Brand). A 2-fold polymerisation buffer was freshly prepared by adding 20% glycerol and GTP (end concentration 3 mM) to BRB80-Buffer. To 50 µL/well 2-fold polymerisation buffer were added 11.1 µL of 10-fold substance solution and gently mixed. The corresponding solvent and combretastatin A4 served as controls. The microplate reader was pre-heated to 37 °C and 50 µL/well of purified pig brain solution was added. The progression of the optical density at 340 nm was observed in 20 sec intervals for at least 120 min, using a Tecan Microplate reader. The assay was conducted twice per compound and concentration, and mean values of each double determination were calculated. The values of the optical density were plotted against time in 5 min intervals.

Tubulin polymerisation assays with 6, 7 and CA-4

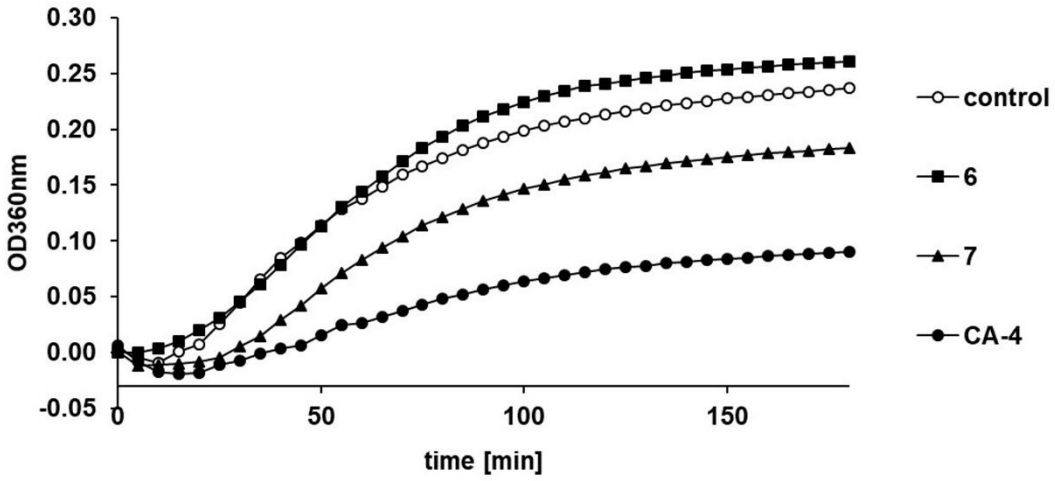

Figure S9. Progression of polymerisation of purified tubulin monomers in response to treatment with 10 µM each of complexes **6** and **7** and combretastatin A4 for 3 h; mean values of double determinations .

5.2 Publikation II mit Darstellung des Eigenanteils

Publikation II entstand unter Zusammenarbeit mit S. W. Schleser und unter Mitarbeit von N. Oberhuber, A. Herrmann und S. E. Weber, Mitarbeiter der Arbeitskreises Organische Chemie I der Universität Bayreuth unter der Leitung von Prof. Dr. R. Schobert.

5.2.1 Eigenanteil an Publikation II

Die Publikation wurde in ***Journal of Inorganic Biochemistry*** veröffentlicht, unter dem Titel

„ Trans-[bis(benzimidazol-2-ylidine)dichlorido]platinum(II) complexes with peculiar modes of action and activity against cisplatin-resistant cancer cells “

von den Autoren

Sofia I. Bär[+], Sebastian W. Schleser[+], Natalie Oberhuber, Alexander Herrmann, Luca Schlotte, Stefanie E. Weber and Rainer Schobert

[+] diese Autoren haben zu gleichen Anteilen zum Manuskript beigetragen

Eigenanteil:	Konzeption, Durchführung, Auswertung und graphischer Darstellung folgender biochemischer Assays: Zytotoxizitätstests via MTT-Assay, Messung der Apoptose Aktivität, Messung des mitochondrialen Membranpotenzials, Messung reaktiver Sauerstoffspezies, Zellzyklusmessungen und intrazellulare Lokalisation mittels Click Chemie. Zudem; Verfassen des biochemischen Teils des Manuskripts sowie der Einleitung.
Sebastian W. Schleser:	Synthese, Reinigung, Analytik und Stabilitätsmessung der Testverbindungen, Verfassung entsprechender Manuskriptpassagen.
Natalie Oberhuber:	Durchführung additiver MTTs, LDH Messungen.
Alexander Herrmann:	Messung der zellulären Aufnahme der Testverbindungen und Durchführung der DNA Interaktions-Assays.
Luca Schlotte und Stefanie E. Weber:	Synthese und Analytik der „clickbaren“ Verbindungen.
Rainer Schobert:	Überarbeitung, Diskussion und Korrektur des Manuskripts.

5.2.2 Publikation II

Trans-[bis(benzimidazol-2-ylidine)dichlorido]platinum(II) complexes with peculiar modes of action and activity against cisplatin-resistant cancer cells

Sofia I. Bär[+], Sebastian W. Schleser[+], Natalie Oberhuber, Alexander Herrmann, Luca Schlotte, Stefanie E. Weber and Rainer Schobert*

Organic Chemistry Laboratory, University of Bayreuth, Universitaetsstrasse 30, 95440 Bayreuth, Germany

[+]These authors contributed equally to this work.

*E-mail: rainer.schobert@uni-bayreuth.de

J. Inorg. Biochem., **2023**, 238, 112028

https://doi.org/10.1016/j.jinorgbio.2022.112028

Journal of Inorganic Biochemistry 238 (2023) 112028

Contents lists available at ScienceDirect

Journal of Inorganic Biochemistry

journal homepage: www.elsevier.com/locate/jinorgbio

Trans-[bis(benzimidazol-2-ylidene)dichlorido]platinum(II) complexes with peculiar modes of action and activity against cisplatin-resistant cancer cells

Sofia I. Bär [1], Sebastian W. Schleser [1], Natalie Oberhuber, Alexander Herrmann, Luca Schlotte, Stefanie E. Weber, Rainer Schobert [*]

Organic Chemistry Laboratory, University of Bayreuth, Universitaetsstrasse 30, 95447 Bayreuth, Germany

ARTICLE INFO

Keywords:
Trans-NHC platinum complexes
Anticancer drugs
DNA binding
Cisplatin resistance
Click chemistry
Subcellular localisation

ABSTRACT

Three series of *cis*- and *trans*-[bis(benzimidazol-2-ylidene)dichlorido]platinum(II) and *cis*-[(benzimidazol-2-ylidene)(DMSO)dichlorido]platinum(II) complexes were synthesised and screened for cytotoxicity against six human cancer cell lines. Depending on their N-alkyl and 5-alkoxycarbonyl substituents, two-digit nanomolar to single-digit micromolar IC_{50} values against cancer cell lines intrinsically resistant to or ill-responding to cisplatin were reached by both *cis*- and *trans*-configured complexes. The stability of the complexes under aqueous biotest conditions was shown via ^{1}H and ^{195}Pt NMR monitoring to be dependent on their configuration and their N-substituents. Localisation studies employing click reactions with 1-alkyne- or cyclopropene-tagged derivatives revealed that the *cis*-complexes accumulated in the cell nuclei and the *trans*-complexes in the mitochondria. While the most active *cis*-complexes showed modes of action akin to those of cisplatin, the most active *trans*-complexes differed from cisplatin by much lower rates of cellular uptake and ROS production, and by their non-interaction with the cell cycle and the DNA of cancer cells. Thus, we identified structural key elements for the synthesis of optimised *trans*-configured NHC platinum(II) complexes with high activity also against cisplatin-refractory cancer cells.

1. Introduction

N-heterocyclic carbene (NHC) complexes of platinum are of interest both as potential catalysts and anticancer agents, depending on their particular structures and ligands [1–3] Bioactive NHC complexes of platinum have received increasing attention in recent years, due to their advantages over the clinical mainstay anticancer drug cisplatin (CDDP) [4], whose applicability is limited by side effects and by triggering tumour resistance. They are an ideal playground for drug developers because of their structural simplicity and variability, and their ease of synthesis and purification when compared e.g. with monoclonal antibodies. Readily adjustable structural parameters such as the bulkiness and electronic effects of the N-substituents, as well as the choice, positioning and substitutability of further ligands allow a finetuning of their lipophilicity, membrane pervasiveness and interference with DNA and proteins. Libraries of structural derivatives are easily accessible for rational structure-activity studies [5]. Accordingly, a large number of new platinum complexes have been synthesised and screened in recent years, with only a few being active against CDDP-resistant cancers. Concluding from the inactivity of the *trans*-isomer of cisplatin (*trans*-(diammine-dichlorido)platinum(II); a.k.a. transplatin), it was assumed that *trans*-configured complexes of platinum(II) are generally unsuitable as chemotherapeutics [6,7]. Over the years, however, numerous exceptions to this rule have accumulated, necessitating a reevaluation of *trans* platinum complexes [8]. Early on, it was observed that substitution of ammine ligands with bulkier ligands in transplatin may result in a high anticancer activity [8,9]. By now, there are a large number of *trans* platinum complexes with a broad spectrum of properties and modes of action [10]. A comparatively new development of the last decade are platinum NHC complexes, which combine the strong cytotoxic effect of DNA-binding complex fragments with the chemical stability and structural variability of NHC ligands [5]. Some of them, and *trans*-configured complexes in particular, are active even against CDDP resistant cancer cells and tumours [5].

* Corresponding author.
E-mail address: rainer.schobert@uni-bayreuth.de (R. Schobert).
[1] These authors contributed equally to this work.

https://doi.org/10.1016/j.jinorgbio.2022.112028
Received 15 August 2022; Received in revised form 27 September 2022; Accepted 11 October 2022
Available online 14 October 2022

2. Experimental

2.1. General

Starting compounds were purchased from *Sigma-Aldrich* (St. Louis, United States), *TCI* (Tokio, Japan), *Merck* (Darmstadt, Germany), *abcr* (Karlsruhe, Germany), *Acros Organics* (Fair Lawn, United States), *VWR* (Radnor, United States) and used without further purification. All reactions with moisture-sensitive reagents were carried out under an argon atmosphere in water-free solvents. Unless stated otherwise, the solvents were purified and dried using standard methods. Synthetic protocols for precursors **2**–**7**, **14**–**15** and **17**–**21** can be found in the supporting information.

Elemental analyses were carried out with a *Perkin-Elmer* (Waltham, United States) 2400 CHN elemental analyzer. Nuclear magnetic resonance (NMR) spectra were measured using a *Bruker* (Bellerica, USA) DRX spectrometer at ambient temperature. Chemical shifts are given in parts per million (δ) downfield from tetramethylsilane as internal standard. As internal standard for ^{1}H NMR spectra the resonance signal of the residual proton of $CDCl_3$ ($\delta = 7.26$ ppm), DMSO-d_6 ($\delta = 2.50$ ppm) or MeOD-d_4 ($\delta = 3.31$ ppm) was used. For ^{13}C NMR spectra the resonance signal of the carbon atom of $CDCl_3$ ($\delta = 77.1$ ppm), DMSO-d_6 ($\delta = 39.5$ ppm) or MeOD-d_4 ($\delta = 49.0$ ppm) was used. The ^{1}H NMR spectra were measured at 500 MHz, ^{13}C NMR spectra at 125 MHz and ^{195}Pt NMR spectra at 107 MHz. For signal multiplicities the following abbreviations were used: s = singlet, d = doublet, t = triplet, m = multiplet, dd = doublet of doublets, dt = doublet of triplets, dq = doublet of quartets with the prefix v meaning virtual. Coupling constants are given in Hz. Melting points were taken with an Electrothermal 9100 apparatus and are uncorrected. Mass spectra were recorded either on a Varian (Palo Alto, USA) MAT 311A (EI) or a ThermoFisher Scientific (Waltham, United States) UPLC/Orbitrap MS system (HRMS-ESI).

2.2. Chemistry

2.2.1. General synthesis of trans-[Pt^{II}Cl$_2$(NHC)$_2$] complexes 8 and 9

The silver complexes **6a-c** or **7a-c** (1.00 eq.) and K_2PtCl_4 (0.50 eq.) were dissolved in CH_2Cl_2 (1 mL/10 μmol) and stirred at rt. for 4 d. The solution was filtered over celite and the solvent was evaporated. The crude products were purified by column chromatography (silica gel 60, EtOAc/MeOH 98:2) and subsequently precipitated from *n*-pentane at 4 °C affording the products as white powders after drying in vacuo.

2.2.1.1. trans-[Dichlorido-bis(5-(methoxycarbonyl)-1,3-dimethylbenzimidazol-2-ylidene)]platinum(II) ***(8a)***. 51.0 mg (75.6 μmol, 67%) from **6a** (78.0 mg, 224 μmol, 1.00 eq.), K_2PtCl_4 (46.6 mg, 112 μmol, 0.50 eq.), CH_2Cl_2 (20.0 mL); $R_f = 0.78$ (EtOAc/MeOH 98:2); m.p. 320 °C; ^{1}H NMR (500 MHz, $CDCl_3$) $\delta = 8.15$ (s, 2H, H^{ar}), 8.08 (d, $J = 8.4$ Hz, 2H, H^{ar}), 7.45 (vdd, $J = 8.5$ Hz, 2H, H^{ar}), 4.42 (vdd, $J = 9.9$ Hz, 2.1 Hz, 4H, NCH_2), 3.98 (s, 6H, OCH_3); ^{13}C NMR (125 MHz, $CDCl_3$) $\delta = 181.0$ (s, NCN), 166.7 (s, COOMe), 137.8 (s, C^{ar}), 134.8 (s, C^{ar}), 125.5 (s, C^{ar}), 125.1 (s, C^{ar}), 112.3 (s, C^{ar}), 110.1 (s, C^{ar}), 52.6 (s, OCH_3), 34.3 (s, NCH_3), 34.2 (s, NCH_3); ^{195}Pt NMR (107 MHz, $CDCl_3$) $\delta = -3247.8$; *m/z* (EI, pos): 674 [M]$^+$, 638 [M-Cl]$^+$, 601 [M-2Cl]$^+$; Anal. Calcd. for $C_{22}H_{24}Cl_2N_4O_4Pt$ (674.4): C, 39.18; H, 3.59; N, 8.31. Found: C, 38.10; H, 3.69; N, 7.67.

2.2.1.2. trans-[Dichlorido-bis(5-(methoxycarbonyl)-1,3-diethylbenzimidazol-2-ylidene)]platinum(II) ***(8b)***. 93.0 mg (127 μmol, 93%) from **6b** (103 mg, 274 μmol, 1.00 eq.), K_2PtCl_4 (56.9 mg, 137 μmol, 0.50 eq.) in CH_2Cl_2 (30.0 mL). Rf = 0.78 (EtOAc/MeOH 98:2); m.p. 250 °C; ^{1}H NMR (500 MHz, $CDCl_3$) $\delta_H = 8.15$ (s, 2H, H^{ar}), 8.04 (vdd, $J = 8.5$ Hz, 1.4 Hz, 2H, H^{ar}), 7.46 (vdd, $J = 8.5$ Hz, 1.4 Hz, 2H, H^{ar}), 5.05–4.92 (m, 8H, NCH_2), 3.98 (s, 6H, OCH_3), 1.78 (t, $J = 7.3$ Hz, 12H, CH_3); ^{13}C NMR (125 MHz, $CDCl_3$) $\delta_C = 181.4$ (s, NCN), 166.8 (s, COOMe), 137.0 (s, Car), 133.9 (s, C^{ar}), 125.3 (s, C^{ar}), 124.9 (s, C^{ar}), 112.4 (s, C^{ar}), 110.1 (s, C^{ar}), 52.5 (s, OCH_3), 42.9 (s, NCH_2), 15.3 (s, CH_3); ^{195}Pt NMR (107 MHz, $CDCl_3$) $\delta_{Pt} = -3267.0$; *m/z* (EI, pos): 730 [M]$^+$, 693 [M-Cl]$^+$, 657 [M-2Cl]$^+$; Anal. Calcd. for $C_{26}H_{32}Cl_2N_4O_4Pt$ (730.6): C, 42.75; H, 4.42; N, 7.67. Found: C, 43.52; H, 4.55; N, 7.42.

2.2.1.3. trans-[Dichlorido-bis(5-(methoxycarbonyl)-1,3-dibenzylbenzimidazol-2-ylidene)] platinum(II) ***(8c)***. 106 mg (108 μmol, 90%) from **6c** (120 mg, 240 μmol, 1.00 eq.), K_2PtCl_4 (49.8 mg, 120 μmol, 0.50 eq.) in CH_2Cl_2 (20.0 mL). Rf = 0.88 (EtOAc/MeOH 98:2); m.p. 290 °C; ^{1}H NMR (500 MHz, $CDCl_3$) $\delta_H = 7.92$ (s, 2H, H^{ar}), 7.83 (vdd, $J = 8.6$ Hz, 1.5 Hz, 2H, H^{ar}), 7.55–7.43 (m, 8H, H^{ar}), 7.28–7.12 (m, 14H, H^{ar}), 6.10 (vd, $J = 4.3$ Hz, 8H, NCH_2), 3.86 (s, 6H, OCH_3); ^{13}C NMR (125 MHz, $CDCl_3$) $\delta_C = 182.0$ (s, NCN), 166.5 (s, COOMe), 137.8 (s, C^{ar}), 135.4 (s, C^{ar}), 134.4 (s, C^{ar}), 128.9 (s, C^{ar}), 128.1 (s, C^{ar}), 127.7 (s, C^{ar}), 127.6 (s, C^{ar}), 125.6 (s, C^{ar}), 125.1 (s, C^{ar}) 113.2 (s, C^{ar}), 111.2 (s, C^{ar}), 52.5 (s, OCH_3), 52.0 (s, NCH_2), 51.7 (s, NCH_2); ^{195}Pt NMR (107 MHz, $CDCl_3$) $\delta_{Pt} = -3285.7$; *m/z* (EI, pos): 978 [M]$^+$, 942 [M-Cl]$^-$, 905 [M-2Cl]$^+$; Anal. Calcd. for $C_{46}H_{40}Cl_2N_4O_4Pt$ (978.8): C, 56.45; H, 4.12; N, 5.72. Found: C, 55.61; H, 4.06; N, 5.61.

2.2.1.4. trans-[Dichlorido-bis(5-(ethoxycarbonyl)-1,3-dimethylbenzimidazol-2-ylidene)]platinum(II) ***(9a)***. 115 mg (164 μmol, 79%) from **7a** (150 mg, 415 μmol, 1.00 eq.), K_2PtCl_4 (86.1 mg, 207 μmol, 0.50 eq.) in CH_2Cl_2 (40.0 mL). Rf = 0.76 (EtOAc/MeOH 98:2); m.p. 340 °C; ^{1}H NMR (500 MHz, $CDCl_3$) $\delta_H = 8.14$ (s, 2H, H^{ar}), 8.07 (vdd, $J = 8.4$ Hz, 1.4 Hz, 2H, H^{ar}), 7.44 (vdd, $J = 8.5$ Hz, 1.3 Hz, 2H, H^{ar}), 4.51–4.37 (m, 16H, OCH_2, NCH_3), 1.45 (t, $J = 7.1$ Hz, CH_3). ^{13}C NMR (125 MHz, $CDCl_3$) $\delta_C = 180.9$ (s, NCN), 166.3 (s, $COOCH_2$), 137.8 (s, C^{ar}), 134.8 (s, C^{ar}), 125.9 (s, C^{ar}), 125.1 (s, C^{ar}), 112.2 (s, C^{ar}), 110.0 (s, C^{ar}), 61.6 (s, OCH_2), 34.3 (s, NCH_3), 14.5 (s, CH_3). ^{195}Pt NMR (107 MHz, $CDCl_3$) $\delta_{Pt} = -3246.9$. *m/z* (EI, pos): 702 [M]$^+$, 666 [M-Cl]$^+$, 630 [M-2Cl]$^+$. Anal. Calcd. for $C_{24}H_{28}Cl_2N_4O_4Pt$ (702.5): C, 41.03; H, 4.02; N, 7.98. Found: C, 40.26; H, 4.42; N, 7.75.

2.2.1.5. trans-[Dichlorido-bis(5-(ethoxycarbonyl)-1,3-diethylbenzimidazol-2-ylidene)]platinum(II) ***(9b)***. 24.0 mg (31.6 μmol, 20%) from **7b** (156 mg, 324 μmol, 1.00 eq.), K_2PtCl_4 (67.3 mg, 162 μmol, 0.50 eq.) in CH_2Cl_2 (30.0 mL). Rf = 0.84 (EtOAc/MeOH 98:2); m.p. 260 °C; ^{1}H NMR (500 MHz, $CDCl_3$) $\delta_H = 8.08$ (s, 2H, H^{ar}), 7.98 (vdd, $J = 8.5$ Hz, 1.4 Hz, 2H, H^{ar}), 7.39 (vdd, $J = 8.5$ Hz, 1.3 Hz, 2H, H^{ar}), 4.98–4.80 (m, 8H, NCH_2), 4.37 (q, $J = 7.1$ Hz, 4H, OCH_2), 1.38 (t, $J = 7.1$ Hz, 6H, CH_3; ^{13}C NMR (125 MHz, $CDCl_3$) $\delta_C = 181.1$ (s, NCN), 166.2 (s, $COOCH_2$), 136.7 (s, C^{ar}), 133.8 (s, C^{ar}), 125.5 (s, C^{ar}), 124.7 (s, C^{ar}), 112.2 (s, C^{ar}), 110.0 (s, C^{ar}), 61.4 (s, OCH_2), 42.8 (d, $J = 6.5$ Hz, NCH_2), 15.2 (s, CH_3), 15.0 (s, CH_3), 14.4 (s, CH_3); ^{195}Pt NMR (107 MHz, $CDCl_3$) $\delta_{Pt} = -3271.4$; *m/z* (EI, pos): 758 [M]$^+$, 685 [M-Cl]$^+$, 657 [M-2Cl]$^+$; Anal. Calcd. For $C_{28}H_{36}Cl_2N_4O_4Pt$ (758.6): C, 44.33; H, 4.78; N, 7.39. Found: C, 43.96; H, 4.67; N, 7.40.

2.2.1.6. trans-[Dichlorido-bis(5-(ethoxycarbonyl)-1,3-dibenzylbenzimidazol-2-ylidene)]platinum(II) ***(9c)***. 82.0 mg (81.4 μmol, 42%) from **7c** (200 mg, 389 μmol, 1.00 eq.), K_2PtCl_4 (80.8 mg, 195 μmol, 0.50 eq.) in CH_2Cl_2 (39.0 mL). Rf = 0.87 (EtOAc/MeOH 98:2); m.p. 190 °C; ^{1}H NMR (500 MHz, $CDCl_3$) $\delta_H = 7.91$ (s, 2H, H^{ar}), 7.83 (d, $J = 8.5$ Hz, 2H, H^{ar}), 7.54–7.42 (m, 8H, H^{ar}), 7.25–7.21 (m, 12H, H^{ar}), 7.18 (d, $J = 8.7$ Hz, 2H, H^{ar}), 6.12–6.06 (m, 8H, NCH_2), 4.31 (q, $J = 7.1$ Hz 4H, OCH_2), 1.33 (t, $J = 7.1$ Hz, 6H, CH_3); ^{13}C NMR (125 MHz, $CDCl_3$) $\delta_C = 181.7$ (s, NCN), 165.9 (s, $COOCH_2$), 137.1 (s, C^{ar}), 135.4 (s, C^{ar}), 134.3 (s, C^{ar}), 128.8 (s, C^{ar}), 128.0 (s, C^{ar}), 127.6 (s, C^{ar}), 125.8 (s, C^{ar}), 124.9 (s, C^{ar}), 113.1 (s, C^{ar}), 111.1 (s, C^{ar}), 61.3 (s, OCH_2), 51.5 (d, $J = 6.5$ Hz, NCH_2), 14.3 (s, CH_3); ^{195}Pt NMR (107 MHz, $CDCl_3$) $\delta_{Pt} = -3284.8$; *m/z* (EI, pos): 1006 [M]$^+$, 969 [M-Cl]$^+$, 933 [M-2Cl]$^+$. Anal. Calcd. for $C_{46}H_{40}Cl_2N_4O_4Pt$ (1006.9): C, 57.26; H, 4.40; N, 5.56. Found: C, 57.05; H, 4.24; N, 5.50.

2.2.2. General synthesis of cis-[Pt^{II}Cl$_2$(DMSO)(NHC)] complexes 10 and 11

The silver complexes **6a**–**c** or **7a**–**c** (1.00 eq.) and K_2PtCl_4 (1.00 eq.) were dissolved in DMSO (1 mL/10 μmol). The mixture was stirred at 60 °C for 24 h. The silver halides were precipitated by adding CH_2Cl_2 and the resulting solution was filtered over celite. DMSO was removed via extraction with water followed by drying of the organic layer over Na_2SO_4 and removal of the solvent. The crude product was purified by column chromatography (silica gel 60, EtOAc/MeOH 98:2) and precipitated from *n*-pentane at 4 °C affording the product as white powder after drying in vacuo.

*2.2.2.1. cis-[Dichlorido-(5-methoxycarbonyl-1,3-dimethylbenzimidazol-2-ylidene)(dimethylsulfoxide)] platinum(II) **(10a)**.* 47.0 mg (85.7 μmol, 80%) from **6a** (37.0 mg, 107 μmol, 1.00 eq.), K_2PtCl_4 (44.2 mg, 106 μmol, 1.00 eq.) in DMSO (10.0 mL). Rf = 0.50 (EtOAc/MeOH 98:2); m.p. 195 °C; ^{1}H NMR (500 MHz, $CDCl_3$) δ_H = 8.17 (s, 1H, H^{ar}), 8.10 (vdd, *J* = 8.5 Hz, 1.4 Hz, 1H, H^{ar}), 7.48 (d, *J* = 8.6 Hz, 1H, H^{ar}), 4.27 (vd, *J* = 8.7 Hz, 6H, NCH_3), 3.98 (s, 3H, OCH_3), 3.58 (d, *J* = 2.0 Hz, 6H, SCH_3); ^{13}C NMR (125 MHz, $CDCl_3$) δ_C = 166.1 (s, COOMe), 158.4 (s, NCN), 136.9 (s, C^{ar}), 133.9 (s, C^{ar}), 126.4 (s, C^{ar}), 125.8 (s, C^{ar}), 112.8 (s, C^{ar}), 110.6 (s, C^{ar}), 52.8 (s, OCH_3), 46.2 (s, SCH_3), 34.9 (s, NCH_3); ^{195}Pt NMR (107 MHz, $CDCl_3$) δ_{Pt} = −3560.7; *m/z* (EI, pos): 548 [M]$^-$, 469 [M-DMSO]$^+$, 433 [M-DMSO-Cl]$^+$. Anal. Calcd. for $C_{13}H_{18}Cl_2N_2O_3PtS$ (548.3): C, 28.48; H, 3.31; N, 5.11; S, 5.85. Found: C, 28.19; H, 3.25; N, 4.97; S, 5.69.

*2.2.2.2. cis-[Dichlorido-(5-methoxycarbonyl-1,3-diethylbenzimidazol-2-ylidene)(dimethylsulfoxide)] platinum(II) **(10b)**.* 190 mg (330 μmol, 84%) from **6b** (150 mg, 399 μmol, 1.00 eq.), K_2PtCl_4 (165 mg, 399 μmol, 1.00 eq.) in DMSO (40.0 mL). m.p. 180 °C; ^{1}H NMR (500 MHz, $CDCl_3$) δ_H = 8.18 (s, 1H, H^{ar}), 8.08 (vdd, *J* = 8.6 Hz, 1.4 Hz, 1H, H^{ar}), 7.50 (d, *J* = 8.6 Hz, 1H, H^{ar}), 4.87 (q, *J* = 7.4 Hz, 4H, NCH_2), 3.98 (s, 3H, OCH_3), 3.57 (s, 6H, SCH_3), 1.66 (t, *J* = 7.3 Hz, 6H, CH_3); ^{13}C NMR (125 MHz, $CDCl_3$) δ_C = 166.3 (s, COOMe), 157.2 (s, NCN), 136.2 (s, C^{ar}), 133.2 (s, C^{ar}), 126.3 (s, C^{ar}), 125.6 (s, C^{ar}), 113.2 (s, C^{ar}), 111.1 (s, C^{ar}), 52.7 (s, OCH_3), 44.1 (s, SCH_3), 41.2 (s, NCH_2), 14.7 (s, CH_3); ^{195}Pt NMR (107 MHz, $CDCl_3$) δ_{Pt} = −3556.2; *m/z* (EI, pos): 576 [M]$^+$, 498 [M-DMSO]$^+$, 426 [M-DMSO-Cl]$^+$. Anal. Calcd. for $C_{15}H_{22}Cl_2N_2O_3PtS$ (576.4): C, 31.26; H, 3.85; N, 4.86; S, 5.56. Found: C, 30.51; H, 3.81; N, 5.00; S, 5.79.

*2.2.2.3. cis-[Dichlorido-(5-methoxycarbonyl-1,3-dibenzylbenzimidazol-2-ylidene)(dimethylsulfoxide)] platinum(II) **(10c)**.* 145 mg (207 μmol, 86%) from **6c** (120 mg, 240 μmol, 1.00 eq.), K_2PtCl_4 (99.7 mg, 240 μmol, 1.00 eq.) in DMSO (25.0 mL). m.p. 250 °C; ^{1}H NMR (500 MHz, $CDCl_3$) δ_H = 7.99 (s, 1H, H^{ar}), 7.94 (d, *J* = 8.6 Hz, 1H, H^{ar}), 7.45–7.39 (m, 11H, H^{ar}), 6.18 (vdd, *J* = 30.8 Hz, 16.0 Hz, 2H, NCH_2), 6.00 (vdd, *J* = 31.8 Hz, 16.0 Hz, 2H, NCH_2), 3.89 (s, 3H, OCH_3), 3.11 (s, 3H, SCH_3), 3.02 (s, 3H, SCH_3); ^{13}C NMR (125 MHz, $CDCl_3$) δ_C = 165.6 (s, COOMe), 160.1 (s, NCN), 136.4 (s, C^{ar}), 134.1 (s, C^{ar}), 133.9 (s, C^{ar}), 133.7 (s, C^{ar}), 128.9 (s, C^{ar}), 128.3 (s, C^{ar}), 127.2 (s, C^{ar}), 126.3 (s, C^{ar}), 125.5 (s, C^{ar}), 113.3 (s, C^{ar}), 111.5 (s, C^{ar}), 52.4 (s, CH_3), 52.2 (s, CH_3), 52.1 (s, CH_3) 45.2 (s, NCH_2), 45.0 (s, NCH_2); ^{195}Pt NMR (107 MHz, $CDCl_3$) δ_{Pt} = −3545.6; *m/z* (EI, pos): 550 [M-DMSO-2Cl]$^+$. Anal. Calcd. for $C_{25}H_{26}Cl_2N_2O_3PtS$ (700.5): C, 42.86; H, 3.74; N, 4.00; S, 4.58. Found: C, 42.91; H, 3.79; N, 4.32; S, 4.40.

*2.2.2.4. cis-[Dichlorido-(5-ethoxycarbonyl-1,3-dimethylbenzimidazol-2-ylidene)(dimethylsulfoxide)] platinum(II) **(11a)**.* 221 mg (393 μmol, 75%) from **7a** (190 mg, 526 μmol, 1.00 eq.), K_2PtCl_4 (218 mg, 526 μmol, 1.00 eq.) in DMSO (50.0 mL). m.p. 260 °C; ^{1}H NMR (500 MHz, $CDCl_3$) δ_H = 8.15 (s, 1H, H^{ar}), 8.09 (d, *J* = 8.5 Hz, 1H, H^{ar}), 7.47 (d, *J* = 8.5 Hz, 1H, H^{ar}), 4.43 (q, *J* = 6.8 Hz, 2H, OCH_2), 4.28 (s, 3H, NCH_3), 4.26 (s, 3H, NCH_3), 3.57 (s, 6H, SCH_3), 1.43 (t, 3H, *J* = 7.1 Hz, CH_3); ^{13}C NMR (125 MHz, $CDCl_3$) δ_C = 165.6 (s, $COOCH_2$), 158.2 (s, NCN), 136.8 (s, C^{ar}), 133.9 (s, C^{ar}), 126.7 (s, C^{ar}), 125.7 (s, C^{ar}), 112.7 (s, C^{ar}), 110.6 (s, C^{ar}), 61.6 (s, OCH_2), 46.3 (s, SCH_3), 41.1 (s, SCH_3) 34.9 (d, *J* = 5.0 Hz, NCH_3), 14.4 (s, CH_3); ^{195}Pt NMR (107 MHz, $CDCl_3$) δ_{Pt} = −3560.0; *m/z* (EI, pos): 562 [M]$^+$, 484 [M-DMSO]$^+$, 447 [M-DMSO-Cl]$^+$, 412 [M-DMSO-2Cl]$^+$. Anal. Calcd. for $C_{14}H_{20}Cl_2N_2O_3PtS$ (562.4): C, 29.90; H, 3.58; N, 4.98; S, 5.70. Found: C, 30.22; H, 3.68; N, 4.80; S, 5.72.

*2.2.2.5. cis-[Dichlorido-(5-ethoxycarbonyl-1,3-diethylbenzimidazol-2-ylidene)(dimethylsulfoxide)] platinum(II) **(11b)**.* 120 mg (251 μmol, 88%) from **7b** (111 mg, 285 μmol, 1.00 eq.), K_2PtCl_4 (118 mg, 285 μmol, 1.00 eq.) in DMSO (29.0 mL); m.p. 190 °C; ^{1}H NMR (500 MHz, $CDCl_3$) δ_H = 8.17 (s, 1H, H^{ar}), 8.08 (vdd, *J* = 8.5 Hz, 1.6 Hz, 1H, H^{ar}), 7.49 (d, *J* = 8.5 Hz, 1H, H^{ar}), 4.91–4.83 (m, 4H, NCH_2), 4.44 (q, *J* = 7.1 Hz, 2H, OCH_2), 3.57 (s, 6H, SCH_3), 1.66 (vdt, *J* = 11.3 Hz, 7.3 Hz, 6H, CH_3), 1.44 (t, *J* = 7.1 Hz, 3H, CH_3); ^{13}C NMR (125 MHz, $CDCl_3$) δ_C = 165.5 (s, $COOCH_2$), 157.0 (s, NCN), 135.9 (s, C^{ar}), 133.0 (s, C^{ar}), 126.4 (s, C^{ar}), 125.3 (s, C^{ar}), 112.9 (s, C^{ar}), 110.7 (s, C^{ar}), 61.5 (s, OCH_2), 46.1 (s, SCH_3), 43.8 (d, *J* = 5.0 Hz, NCH_2) 14.5 (s, CH_3), 14.3 (s, CH_3); ^{195}Pt NMR (107 MHz, $CDCl_3$) δ_{Pt} = −3557.1; *m/z* (EI, pos): 590 [M]$^+$, 512 [M-DMSO]$^+$, 476 [M-DMSO-Cl]$^+$, 439 [M-DMSO-2Cl]$^+$; Anal. Calcd. for $C_{16}H_{24}Cl_2N_2O_3PtS$ (590.4): C, 32.55; H, 4.10; N, 4.74; S, 5.43. Found: C, 33.34; H, 3.78; N, 4.81; S, 5.27.

*2.2.2.6. cis-[Dichlorido-(5-ethoxycarbonyl-1,3-dibenzylbenzimidazol-2-ylidene)(dimethylsulfoxide)] platinum(II) **(11c)**.* 52.0 mg (79.8 μmol, 83%) from **7c** (49.0 mg, 95.4 μmol, 1.00 eq.), K_2PtCl_4 (39.6 mg, 95.4 μmol, 1.00 eq.) in DMSO (10.0 mL). m.p. 210 °C; ^{1}H NMR (500 MHz, $CDCl_3$) δ_H = 7.98 (s, 1H, H^{ar}), 7.93 (d, *J* = 8.6 Hz, 1H, H^{ar}), 7.46–7.31 (m, 11H, H^{ar}), 6.16 (vdd, *J* = 20.2 Hz, 15.9 Hz, 2H, NCH_2), 6.01 (vdd, *J* = 23.2 Hz, 16.9 Hz, 2H, NCH_2), 4.33 (q, *J* = 7.1 Hz, 2H, OCH_2), 3.11 (s, 3H, SCH_3), 3.03 (s, 3H, SCH_3), 1.43 (t, *J* = 7.1 Hz, 3H, CH_3); ^{13}C NMR (125 MHz, $CDCl_3$) δ_C = 165.5 (s, $COOCH_2$), 160.2 (s, NCN), 136.7 (s, C^{ar}), 134.5 (s, C^{ar}), 134.3 (s, C^{ar}), 134.1 (s, C^{ar}), 129.3 (s, C^{ar}), 128.7 (s, C^{ar}), 127.6 (s, C^{ar}), 127.0 (s, C^{ar}), 125.9 (s, C^{ar}), 113.7 (s, C^{ar}), 111.8 (s, C^{ar}), 61.4 (s, OCH_2), 52.8 (s, SCH_3), 52.5 (s, SCH_3) 45.5 (s, NCH_2), 45.4 (s, NCH_2), 14.4 (s, CH_3); ^{195}Pt NMR (107 MHz, $CDCl_3$) δ_{Pt} = −3545.5; *m/z* (EI, pos): 561 [M-DMSO-2Cl]$^+$. Anal. Calcd. for $C_{26}H_{28}Cl_2N_2O_3PtS$ (714.6): C, 43.70; H, 3.95; N, 3.92; S, 4.49. Found: C, 43.24; H, 3.48; N, 3.87; S, 4.84.

2.2.3. General synthesis of cis-[Pt^{II}Cl$_2$(NHC)$_2$] complexes 12 and 13

The *cis*-[Pt^{II}Cl$_2$(DMSO)(NHC)] complexes **10a**–**b** or **11a**–**b** (1.00 eq.), KO^{t}Bu (1.50 eq.) and the respective benzimidazolium chloride **4** or **5** (1.20 eq.) were dissolved in dry CH_2Cl_2 (1 mL/10 μmol). The mixture was stirred at rt. for 3 d under inert gas atmosphere. The solution was filtered over Celite and the solvent was evaporated. The crude product was purified by column chromatography (silica gel 60, EtOAc/MeOH 98:2) and precipitated from *n*-pentane at 4 °C affording the product as white powder after drying in vacuo.

*2.2.3.1. cis-[Dichlorido-bis(5-methoxycarbonyl-1,3-dimethylbenzimidazol-2-ylidene)platinum(II) **(12a)**.* 28.0 mg (41.5 μmol, 46%) from **10a** (50.0 mg, 91.2 μmol, 1.00 eq.), KO^{t}Bu (15.5 mg, 137 μmol, 1.50 eq.) and benzimidazolium chloride **4a** (26.0 mg, 109 μmol, 1.20 eq.) in dry CH_2Cl_2 (10.0 mL); R_f = 0.50 (EtOAc/MeOH 98:2); m.p. 240 °C; ^{1}H NMR (500 MHz, $CDCl_3$) δ_H = 8.06 (s, 2H, H^{ar}), 8.02 (d, *J* = 8.6 Hz, 2H, H^{ar}), 7.40 (vdd, *J* = 8.5 Hz, 3.5 Hz, 2H, H^{ar}), 4.23 (vt, *J* = 6.4 Hz, 12H, NCH_3), 3.94 (s, 6H, OCH_3); ^{13}C NMR (125 MHz, $CDCl_3$) δ_C = 166.2 (s, COOMe), 162.7 (s, NCN), 137.2 (s, C^{ar}) 134.2 (s, C^{ar}), 126.2 (s, C^{ar}), 125.7 (s, C^{ar}), 112.4 (s, C^{ar}), 110.4 (s, C^{ar}), 52.7 (s, OMe), 35.3 (NCH_3), 35.2 (NCH_3); ^{195}Pt NMR (107 MHz, $CDCl_3$) δ_{Pt} = −3656.8; HRMS (ESI): *m/z* calculated for $C_{22}H_{24}Cl_2N_4O_4Pt$ [M]: 673.08223. Found: 679.13933 [M-Cl + MeCN]$^+$. Anal. Calcd.: C, 39.18; H, 3.59; N, 8.31. Found: C, 38.08; H, 3.68; N, 7.88.

2.2.3.2. cis-[Dichlorido-bis(5-methoxycarbonyl-1,3-diethylbenzimidazol-2-ylidene)]platinum(II) ***(12b)***. 25.0 mg (34.2 µmol, 26%) from **10b** (75.0 mg, 130 µmol, 1.00 eq.), KO^{t}Bu (21.9 mg, 195 µmol, 1.50 eq.) and benzimidazolium chloride **4b** (42.0 mg, 156 µmol, 1.20 eq.) in dry CH_2Cl_2 (15.0 mL); R_f = 0.51 (EtOAc/MeOH 98:2); m.p. 250 °C; ^{1}H NMR (500 MHz, $CDCl_3$) δ_H = 8.09 (s, 2H, H^{ar}), 8.01 (d, J = 8.5 Hz, 2H, H^{ar}), 7.43 (vdd, J = 8.5 Hz, 3.5 Hz, 2H, H^{ar}), 5.09 (vdq, J = 9.7 Hz, 7.1 Hz, 4H, NCH_2), 4.68 (vdq, J = 9.7 Hz, 7.1 Hz, 4H, NCH_2), 3.95 (s, 6H, OCH_3), 1.50–1.46 (m, 12H, CH_3); ^{13}C NMR (125 MHz, $CDCl_3$) δ_C = 166.2 (s, COOMe), 162.0 (s, NCN), 136.4 (s, C^{ar}) 133.3 (s, C^{ar}), 125.8 (s, C^{ar}), 125.3 (s, C^{ar}), 112.7 (s, C^{ar}), 110.7 (s, C^{ar}), 52.6 (s, OMe), 44.0 (s, NCH_2), 43.9 (s, NCH_2), 14.1 (s, CH_3); ^{195}Pt NMR (107 MHz, $CDCl_3$) δ_{Pt} = −3627.6; HRMS (ESI): *m/z* calculated for $C_{26}H_{32}Cl_2N_4O_4Pt$ [M]: 729.14483. Found: 735.20132 $[M\text{-}Cl + MeCN]^+$, 695.17263 $[M\text{-}Cl]^+$, 658.19338 $[M\text{-}2Cl]^+$; Anal. Calcd.: C, 42.75; H, 4.42; N, 7.67. Found: C, 42.66; H, 4.37; N, 7.50.

2.2.3.3. cis-[Dichlorido-bis(5-ethoxycarbonyl-1,3-dimethylbenzimidazol-2-ylidene)]platinum(II) ***(13a)***. 30.0 mg (42.7 µmol, 26%) from **11a** (93.0 mg, 165 µmol, 1.00 eq.), KO^{t}Bu (27.8 mg, 248 µmol, 1.50 eq.) and benzimidazolium chloride **5a** (50.6 mg, 198 µmol, 1.20 eq.) in dry CH_2Cl_2 (15.0 mL). R_f = 0.20 (EtOAc/MeOH 98:2); m.p. 320 °C; ^{1}H NMR (500 MHz, $CDCl_3$) δ_H = 8.09–8.00 (m, 4H, H^{ar}), 7.39 (vdd, J = 8.5 Hz, 4.3 Hz, 2H, H^{ar}), 4,41 (vdq, J = 8.7 Hz, 7.2 Hz, 6H, OCH_2), 4.23 (vdd, J = 10.3 Hz, 5.8 Hz, 12H, NCH_3), 1.44 (t, J = 7.1 Hz, 6H, CH_3); ^{13}C NMR (125 MHz, $CDCl_3$) δ_C = 166.7 (s, COOEt), 162.6 (s, NCN), 137.0 (s, C^{ar}) 134.1 (s, C^{ar}), 126.5 (s, C^{ar}), 125.6 (s, C^{ar}), 112.2 (s, C^{ar}), 110.1 (s, C^{ar}), 61.6 (s, OCH_2), 35.2 (NCH_3), 35.1 (NCH_3), 14.4 (s, CH_3); ^{195}Pt NMR (107 MHz, $CDCl_3$) δ_{Pt} = −3654.3; *m/z* (EI, pos): 702 [M], 666 [M-Cl], 630 [M-2Cl]; Anal. Calcd. for $C_{24}H_{28}Cl_2N_4O_4Pt$ (702.5): C, 41.03; H, 4.02; N, 7.98. Found: C, 41.88; H, 3.03; N, 7.75.

2.2.3.4. cis-[Dichlorido-bis(5-ethoxycarbonyl-1,3-diethylbenzimidazol-2-ylidene)]platinum(II) ***(13b)***. 80.0 mg (105 µmol, 57%) from **11b** (110 mg, 186 µmol, 1.00 eq.), KO^{t}Bu (31.4 mg, 280 µmol, 1.50 eq.) and the respective benzimidazole chloride (**5b**) (63.2 mg, 224 µmol, 1.20 eq.) in dry CH_2Cl_2 (20.0 mL); R_f = 0.50 (EtOAc/MeOH 98:2); m.p. 290 °C; ^{1}H NMR (500 MHz, $CDCl_3$) δ_H = 8.08 (s, 2H, H^{ar}), 8.01 (d, J = 8.6 Hz, 2H, H^{ar}), 7.42 (vdd, J = 8.6 Hz, 4.3 Hz, 2H, H^{ar}), 5.14–5.03 (m, 4H, NCH_2), 4.72–4.63 (m, 4H, NCH_2), 4.41 (q, J = 7.0 Hz, 4H, OCH_2), 1.48 (vdd, J = 7.2 Hz, 3.0 Hz, 12H, CH_3), 1.41 (t, J = 7.1 Hz, 6H, CH_3); ^{13}C NMR (125 MHz, $CDCl_3$) δ_C = 166.7 (s, COOEt), 161.7 (s, NCN), 136.3 (s, C^{ar}) 133.3 (s, C^{ar}), 126.2 (s, C^{ar}), 125.3 (s, C^{ar}), 112.7 (s, C^{ar}), 110.7 (s, C^{ar}), 61.6 (s, OCH_2), 44.0 (s, NCH_2), 43.9 (s, NCH_2), 14.5 (s, CH_3), 14.4 (s, CH_3), 14.3 (s, CH_3); ^{195}Pt NMR (107 MHz, $CDCl_3$) δ_{Pt} = −3627.9; *m/z* (EI, pos): 758 $[M]^+$, 722 $[M\text{-}Cl]^+$, 657 $[M\text{-}2Cl]^+$; Anal. Calcd. for $C_{28}H_{36}Cl_2N_4O_4Pt$ (758.6): C, 44.33; H, 4.78; N, 7.39. Found: C, 43.40; H, 4.56; N, 7.05.

2.2.4. Synthesis of clickable complexes 16 and 22

cis-[Dichlorido-(5-methoxycarbonyl-1,3-dipropargylbenzimidazol-2-ylidene)(dimethylsulfoxid)]platinum(II) **(16).**

Cis-[Cl_2(DMSO)$_2$]Pt(II) (60.0 mg, 142 µmol, 1.00 eq.) and benzimidazolium chloride **15** (94.4 mg, 327 µmol, 2.30 eq.) were dissolved in dry CH_2Cl_2 (15 mL) and treated with KO^{t}Bu (47.8 mg, 426 µmol, 3.00 eq.). The mixture was stirred at rt. for 18 h and filtered over Celite®. The solvent was evaporated and the crude product was purified by column chromatography (silica gel 60, EtOAc/MeOH 98:2) affording **16** as a yellow powder (60.7 mg, 112 µmol, 79%) after drying in vacuo; m.p. 310 °C; R_f = 0.50 (EtOAc/MeOH 98:2); ^{1}H NMR (500 MHz, $CDCl_3$) δ_H = 8.36 (d, J = 1.4 Hz, 2H, H^{ar}), 8.15 (dd, J = 8.6 Hz, 1.4 Hz, 2H, H^{ar}), 7.70 (d, J = 8.6 Hz, 2H, H^{ar}), 6.00 (dt, J = 18.0 Hz, 2.7 Hz, 4H, NCH_2), 5.30 (dt, J = 18.0 Hz, 2.1 Hz, 4H, NCH_2), 3.60 (s, 6H, SCH_3), 3.99 (s, 6H, OMe), 2.56 (dt, J = 5.3 Hz, 2.6 Hz, 4H, CH); ^{13}C NMR (125 MHz, $CDCl_3$) δ_C = 165.9 (s, COOMe), 159.5 (s, NCN), 135.8 (s, C^{ar}), 132.9 (s, C^{ar}), 127.1 (s, C^{ar}), 126.4 (s, C^{ar}), 113.5 (s, C^{ar}), 111.6 (s, C^{ar}), 76.2 (s), 76.1 (s), 75.5 (s), 75.4 (s), 52.7 (s, OCH_2), 46.0 (s, SCH_3), 38.6 (s, NCH_2), 38.5 (s, NCH_2); ^{195}Pt NMR (107 MHz, $CDCl_3$) δ_{Pt} = −3550.2; HRMS (ESI): *m/z* calculated for $C_{17}H_{18}Cl_2N_2O_3PtS$ [M]: 595.00629. Found: 638.04989 $[M\text{-}Cl + DMSO]^+$, 601.06189 $[M\text{-}Cl + MeCN]^+$, 560.03634 $[M\text{-}Cl]^+$ 482.02161 $[M\text{-}Cl\text{-}DMSO]^+$; Anal. Calcd.: C, 34.24; H, 3.04; N, 4.70; S, 5.38. Found: C, 31.04; H, 3.94; N, 4.49; S, 5.97.

2.2.4.1. trans-[Dichlorido-bis(5-(dimethylcyclopropenyl)methyl-carbonyl-1,3-diethylbenzimidazol-2-ylidene)]platinum(II) ***(22)***. Silver complex **21** (46.0 mg, 86.3 µmol 1.00 eq.) and K_2PtCl_4 (18.0 mg, 43.0 µmol, 0.50 eq.) were dissolved in CH_2Cl_2 (5 mL) and stirred at rt. for 4 d. The solution was filtered over celite® and the solvent was evaporated. The crude products were purified by column chromatography (silica gel 60, EtOAc/MeOH 98:2) and subsequently precipitated from *n*-pentane at 4 °C affording the product as white solid (12.0 mg, 13.9 µmol, 32%) after drying in vacuo; m.p. 230 °C; R_f = 0.90 (EtOAc/MeOH 98:2) ^{1}H NMR (500 MHz, $CDCl_3$) δ_H = 8.17 (s, 2H, H^{ar}), 8.06 (dd, J = 8.4, 1.4 Hz, 2H, H^{ar}), 7.46 (dd, J = 8.6, 1.3 Hz, 2H, H^{ar}), 5.00 (dq, J = 14.1 Hz, 7.0, Hz, 8H, NCH_2), 4.28 (d, J = 5.1 Hz, 2H, OCH_2), 2.04 (s, 12H, CH_3), 1.78 (dt, J = 8.9, 5.4, 12H, CH_3), 1.70 (t, J = 5.1 Hz, 2H, CH); ^{13}C NMR (125 MHz, $CDCl_3$) δ_C = 179.9 (s, NCN), 165.3 (s, $COOCH_2$), 135.6 (s, C^{ar}), 132.7 (s, C^{ar}), 124.9 (s, C^{ar}), 123.6 (s, C^{ar}), 111.1 (s, C^{ar}), 108.9 (s), 108.7 (s), 71.8 (OCH_2), 41.7 (d, J = 5.0 Hz, CH_2), 18.3 (CH), 14.1 (d, J = 15.4 Hz, CH3), 9.4 (s, CH_3); ^{195}Pt NMR (107 MHz, $CDCl_3$) δ_{Pt} = −3265.5; HRMS (ESI): *m/z* calculated for $C_{36}H_{44}Cl_2N_4O_4Pt$ [M]: 861.23874. Found: 861.23819; Anal. Calcd.: C, 50.12; H, 5.14; N, 6.49. Found: C, 49.39; H, 3.82; N, 5.77.

2.3. Biochemical evaluation

2.3.1. Stock solutions and dilution series

Stock solutions of test compounds were dissolved in DMSO (10 mM) if not noted otherwise and stored at −23 °C. When applying them to biotests, the desired predilution series was freshly diluted with water or PBS and then added to the cell culture media.

2.3.2. MTT cell viability assay [11]

All complexes stable in solution were investigated for their antiproliferative effect on nine human cell lines, using the 3-(4,5-dimethylthiazol-2-yl)-2,5-diphenyltetrazolium bromide (MTT) based cell viability assay. Cells were seeded in 96 well microtiter plates (Sarstedt) with a cell density of 0.05×10^6 cells per mL and 100 µL per well and incubated for 24 h. A dilution series of test compounds was added to the wells, ranging in twelve steps from 100 µM – 5 nM, equal amounts of DMSO were added as controls. Treated cells were incubated for a further 72 h. Then, 12.5 µL per well of MTT solution (0.05% in PBS) were added, followed by another 2 h of incubation. The plates were centrifuged, the medium was discarded and 25 µL per well of SDS solution in DMSO (10% SDS, 0.6% AcOH in DMSO) were added to dissolve formazan and the plates were incubated for a further hour. Absorbances at 570 nm and 630 nm were measured using a plate reader (Tecan). The background absorbance (630 nm) was subtracted from the formazan signal (570 nm). The resulting absorbance is directly proportional to the amount of viable cells, the control was normalised to 100% viable cells and, accordingly, the viability of cells treated with the test compounds was calculated. IC_{50} values were calculated based on a sigmoidal fit model using GraphPad Prism. Means and SD were calculated from at least four independent experiments. To calculate the selectivity index (SI), the mean value of all IC_{50} values across the cancer cell lines was first calculated for each test substance. The IC_{50} value for the non-malignant cells (HDFa) was then divided by the mean value over all cancer cell lines. The higher the resulting ratio, the more selective the compound is for cancer over HDFa cells.

2.3.3. Cellular uptake measurement via ICP-MS

Cells were seeded at a density of 2×10^6 cells per dish in cell culture dishes (Sarstedt) and grown overnight, then treated with test compounds at a final concentration of 5 μM for 5 h. The cell monolayer was washed twice with PBS, the cells were harvested by trypsination, counted and pelleted (4 °C, 150 g, 5 min). The cell pellets were solubilised with aqua regia (reflux, 20 min), the platinum content was determined by ICP-MS. Means and SD were calculated from at least two independent experiments.

2.3.4. LDH cytotoxicity assay[12]

Cells were seeded in 96 well flat bottom microtiter plates (Sarstedt) with 100 μL per well and a cell density of 0.05×10^6 cells per mL. Wells containing medium alone were additionally set for background measurement. The cells were allowed to grow overnight, then treated with 11.1 μL of 10-fold concentrated test compound dilutions and further incubated for 24 h. As positive control 10 μL per well of lysis solution (9% Triton-X100 in Millipore H_2O) were added and incubated for 45 min to maintain maximum LDH release. The same amount was added to maximum release background correction wells, containing medium only. After centrifugation (4 °C, 150 *g*, 5 min) 50 μL of the supernatant of each well were transferred on a fresh microtiter plate followed by addition of 50 μL LDH assay buffer (223 mg 2-*p*-iodophenyl-3-*p*-nitrophenyl-5-phenyltetrazolium chloride, 57 mg *N*-methylphenazonium methyl sulfate, 575 mg *N*-adenine dinucleotide, 3.2 g lactic acid in 480 mL 200 mM Tris-Cl, pH 8.0) per well. The plate was incubated in the dark for 10–30 min at rt. 50 μL stop solution (1 M acetic acid) were added per well and the absorbance was measured at 490 nm. The mean value of the background wells was subtracted from the negative control and the test wells as well as the mean value of the maximum release wells was subtracted from the value of the maximum LDH release wells. The percentage of LDH release was calculated, the maximum LDH release was set to 100% and the negative control at 0% release. Means and SD were calculated from at least three independent experiments.

2.3.5. Apoptotic events

2.3.5.1. Caspase 3/7 activation. The assay was conducted, following the manufacturer's instructions, using the Cell Meter Caspase 3/7 activity apoptosis assay kit (AAT Bioquest). Briefly, the cells were seeded in 96 well flat black microtiter plates at a density of 0.22×10^6 cells per mL and 90 μL per well. After 24 h of incubation, 10 μL per well of prediluted test compounds were added to obtain a final concentration of 10 μM, and the cells were incubated for a further 6 h. 100 μL per well of Caspase 3/7 substrate working solution were added and the plates were incubated for another hour in the dark at rt. The fluorescence was measured using a microplate reader (Tecan) at ex/em = 490/525 nm.

2.3.5.2. Mitochondrial membrane potential assay. To assess the effect of the test compounds on the mitochondrial membrane potential (MMP) the cationic dye tetramethylrhodamine methyl ester (TMRM) was used. Due to its delocalised lipophilic cation (DLC) character, TMRM accumulates in mitochondria quantitatively, proportional to the MMP. The cells were seeded in 96 well flat black microtiter plates (Brand) with a cell density of 0.2×10^6 cells per mL and 100 μL per well. A corresponding MTT was conducted identically in transparent 96 well microtiter plates (Sarstedt). The plates were incubated for 24 h under standard cell culture conditions. The medium was replaced by 90 μL per well standard assay buffer (80 mM NaCl, 75 mM KCl, 25 mM D-Glucose, 25 mM HEPES, pH 7.4 in H_2O) and 10 μL per well of tenfold dilutions of test compounds were added. Carbonylcyanide *m*-chlorophenylhydrazone (CCCP), a known decoupling agent, served as a positive control [13] and a corresponding dilution of DMSO served as a negative control. Substance-treated cells were further incubated for 1 h. 10 μL per well of a TMRM solution (2 μM in standard assay buffer) were added and the cells were incubated for a further 10 min at rt. Each well was rinsed three times with PBS, 100 μL per well of PBS were added and the fluorescence of remaining TMRM was measured (ex/em 535/590 nm). The results were standardised by correlation with those of the corresponding MTT assays and normalised with respect to the negative control.

2.3.5.3. Reactive oxygen species (ROS) assay [14]. The cellular levels of ROS were determined by means of 2,7-dichlorofluorescin diacetate (DCFH-DA). The assay is based on the oxidation of DCFH-DA by intracellular ROS to give strongly fluorescent 2,7-dichlorodihydrofluorescin. The cells were seeded in 96 flat black well plates (Brand) with 100 μL per well and a density of 0.2×10^6 cells per mL. A corresponding MTT was conducted identically in transparent 96 well microtiter plate (Sarstedt). The cells were allowed to grow for 24 h. The medium was replaced by serum-free medium containing DCFH-DA (20 μM) followed by 30 min of incubation to enable cells to take up the dye. To eliminate remaining dye, the cells were rinsed twice with PBS, and fresh medium was added. 11.1 μL of tenfold predilutions of the test compounds were added per well. Corresponding dilutions of DMSO served as negative and of CDDP served as positive control. The treated cells were incubated for 1 h, before being rinsed twice again with PBS. After addition of 100 μL of fresh PBS per well the fluorescence was measured (ex/em 485/535 nm). The results were standardised by correlation with those of the corresponding MTT assays and normalised with respect to the negative control.

2.3.6. Influence on the cell cycle

$HCT116^{wt}$ cells were seeded in 6 well plates (Sarstedt) with 3 mL per well and a cell density of 0.05×10^6 cells per mL, incubated for 24 h, treated with concentrations of the test compounds corresponding to their IC_{50} values, and incubated for a further 24 h. The supernatant of each sample was transferred into a separate tube on ice, the cell monolayer was rinsed once with PBS, and the cells were harvested using trypsin and also transferred into the tube. The cells were pelleted (4 °C, 150 g, 5 min), resuspended in 1 mL of ice-cold EtOH (70%) and stored for at least 1 h at 4 °C. *prior* to propidium iodide (PI) staining, the cells were centrifuged (150 *g*, 5 min), the supernatant was discarded, and the cells were layered with 1 mL PBS for 5 min. The cells were centrifuged again and the resulting pellet was resuspended in 200 μL of PI staining solution (50 μg/mL PI, 1% sodium citrate in PBS) containing 1 μL RNase (10 mg/mL stock solution) and incubated in the dark for 30 min at 37 °C. The cell cycle phase distribution was assessed by flow cytometry (Beckmann Coulter). Means and SD were calculated from at least three independent experiments.

2.3.7. DNA interaction

2.3.7.1. Ethidium bromide saturation assay (EtdBr assay). The interaction of the test complexes with linear DNA was assessed using the EtdBr assay, which is based on the fact that ethidium bromide intercalates into DNA enhancing its fluorescence while intercalation is hindered by alterations of the DNA structure, e.g. by small molecules interfering with DNA [15]. In wells of a 96 well black flat bottom microtiter plates a solution of 1 μg of linear salmon sperm DNA (ThermoFisher) in TE buffer (10 mM Tris-Cl, 1 mM EDTA, pH 8.0) was treated with concentration series (final concentrations: 25 μM, 50 μM, 75 μM and 100 μM) of compounds. A corresponding amount of DMSO was used as a control (0 μM). After an incubation period of 2 h at 37 °C, 100 μL per well of ethidium bromide solution (10 μg/mL in TE buffer) was added and the plate was incubated for 5 min in the dark. Background samples were prepared analogously but without DNA addition. The fluorescence of any EtdBr-DNA adducts was monitored at an excitation wavelength of 535 nm and an emission wavelength of 595 nm. After background subtraction, changes in fluorescence intensity were calculated in relation to the control (set to 100%). Means and SD were calculated from at

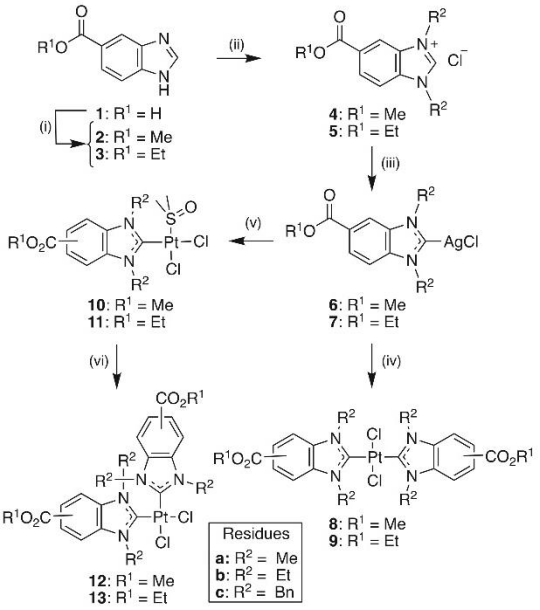

Scheme 1. General synthetic route to *trans*-bis(NHC)-, *cis*-NHC(DMSO)- and *cis*-bis(*NHC*)platinum(II) complexes. Reagents and conditions: (i) MeOH or EtOH, H_2SO_4, reflux, 24 h; (ii) 1. MeI or EtI or BnBr, K_2CO_3, MeCN, reflux, 24 h; 2. Ag_2CO_3, HNO_3, then HCl, EtOH, r.t., light exclusion, 3.5 h; (iii) Ag_2O, CH_2Cl_2, light exclusion, r.t., 24 h; (iv) 0.5 eq. K_2PtCl_4, CH_2Cl_2, r.t., 4 d; (v) 1.0 eq. K_2PtCl_4, DMSO, 60 °C, 24 h; (vi) benzimidazolium salt **4** or **5**, KOtBu, CH_2Cl_2, r.t., 3d.

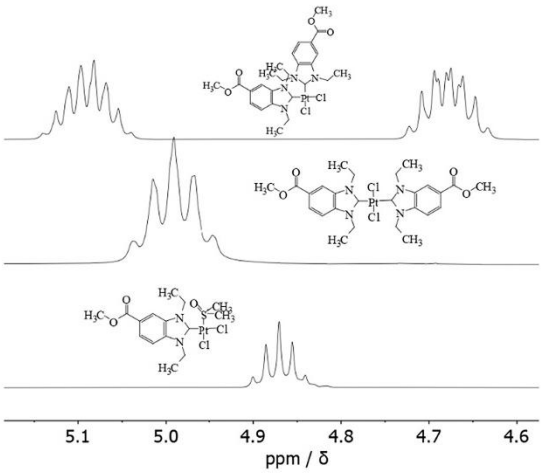

Fig. 1. NCH_2 signals in ^1H NMR spectra of *cis*-DMSO(NHC) complex **10b** (bottom), *trans*-bis(NHC) complex **8b** (middle), and *cis*-bis(NHC) complex **12b** (top), recorded in $CDCl_3$.

least three independent experiments.

2.3.7.2. Electrophoretic mobility shift assay (EMSA). To distinguish whether the DNA interaction is of an electrostatic or covalent nature, a

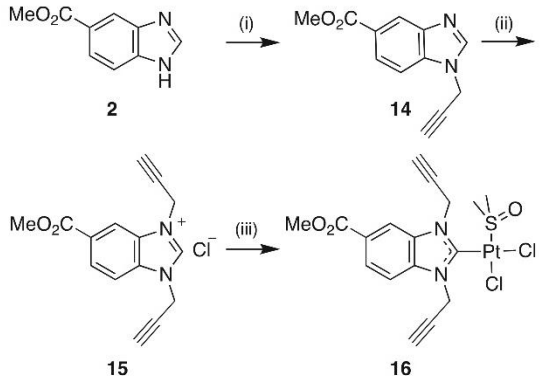

Scheme 2. Synthesis of propargyl-bearing *cis*-(DMSO)(NHC) platinum(II) complex **16**. Reagents and conditions: (i) Propargyl bromide, K_2CO_3, MeCN, 60 °C, 24 h, 81%; (ii) 1. Propargyl bromide, 1,4-dioxane, 130 °C, 24 h; 2. Ag_2CO_3, HNO_3, then HCl, EtOH, r.t., light exclusion, 3.5 h, 52% over two steps; (iii) *cis*-$(DMSO)_2PtCl_2$, CH_2Cl_2, r.t., 24 h, 79%.

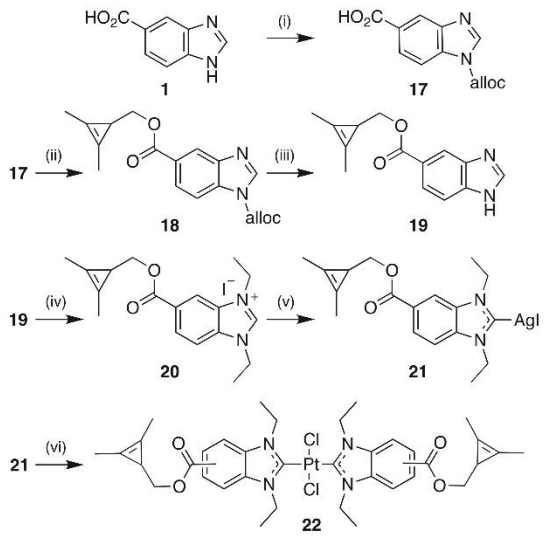

Scheme 3. Synthesis of cyclopropene-bearing *trans*-bis(NHC) platinum(II) complex **22**. Reagents and conditions: (i) Alloc-Cl, 10% $Na_2CO_{3(aq.)}$, 1,4-dioxane, r.t., 16 h, 97%; (ii) EDC·HCl, DMAP, CH_2Cl_2, r.t., 24 h, 58%; (iii) Pd $(dpa)_2$, dppb, Et_2NH, r.t., THF, 4 h, 75%; (iv) EtI, K_2CO_3, MeCN, reflux, 48 h, 72%; (v) Ag_2O, CH_2Cl_2, light exclusion, r.t., 24 h, 58%; (vi) 0.5 eq. K_2PtCl_4, CH_2Cl_2, r.t., 4 d, 32%.

second DNA interaction assay was conducted. 1.5 μg of circular plasmid pBR322 DNA were incubated in TE buffer (10 mM Tris-Cl, 1 mM EDTA, pH 8.0) with different concentrations of test compounds (final concentrations: 5 μM, 10 μM, 25 μM and 50 μM). A corresponding volume of DMSO was added to the control (0 μM) with a final volume of 20 μL of each sample. The samples ware incubated for 16 h at 37 °C and subjected to 1% agarose gel electrophoresis in 0.5×TBE buffer (45 mM Tris-Cl, 45 mM boric acid, 1.25 mM EDTA, pH 8.0) for 4 h at 66 V. The agarose gel was stained for 20 min with EtdBr (10 μg/mL in 0.5 TBE buffer) solution and the results documented using UV excitation.

Table 1
Means ± SD ($n = 4$) of IC_{50} values [μM] of complexes **8–13** and CDDP against nine human cell lines and their respective selectivity indices (SI). Determined by MTT assays over 72 h, calculated of four independent measurements. * data from [19], n.d. = not determined.

IC_{50} 72 h (μM)										
	518A2	$HCT116^{wt}$	$HCT116^{p53-}$	U87	EaHy926	HeLa	MCF7	HT29	HDFa	SI
8a	13.8 ± 0.7	22.6 ± 0.4	25.3 ± 3.9	1.1 ± 0.5	>50	>50	25.4 ± 2.7	31.0 ± 3.7	n.d.	n.d.
8b	>50	>50	3.8 ± 0.5	>50	>50	3.3 ± 0.8	0.56 ± 0.05	>50	n.d.	n.d.
8c	>50	0.16 ± 0.02	0.49 ± 0.04	>50	0.12 ± 0.03	0.05 ± 0.02	0.26 ± 0.06	3.7 ± 0.4	>50	> 3.8
9a	15.3 ± 1	3.3 ± 0.7	0.7 ± 0.08	14 ± 1.2	6.1 ± 0.2	12.6 ± 1.4	4.0 ± 0.8	7.9 + 0.9	n.d.	n.d.
9b	>50	>50	31.9 ± 4	>50	>50	>50	4.3 ± 0.2	34.8 ± 4.4	n.d.	n.d.
9c	>50	>50	>50	>50	>50	>50	>50	>50	n.d.	n.d.
10a	>50	>50	>50	>50	>50	>50	>50	>50	n.d.	n.d.
10b	> 50	45.7 ± 2.9	17.7 ± 0.4	16.3 ± 2.9	> 50	33.9 ± 4.0	>50	>50	n.d.	n.d.
10c	19.2 ± 1.5	16.3 ± 1.6	1.6 ± 0.1	1.07 ± 0.04	9.4 ± 0.3	1.3 ± 0.3	24.0 ± 3.5	>50	n.d.	n.d.
11a	>50	>50	>50	>50	>50	>50	>50	>50	n.d.	n.d.
11b	>50	>50	>50	>50	>50	>50	>50	>50	n.d.	n.d.
11c	14.6 ± 1.3	16.4 ± 1.3	9.5 ± 1.5	>50	45.6 ± 5.9	>50	48.2 ± 1.9	>50	n.d.	n.d.
12a	> 50	35.6 ± 3.4	>50	>50	48.7 ± 1.4	>50	>50	>50	n.d.	n.d.
12b	31.2 ± 2.2	2.3 ± 0.2	1.7 ± 0.2	1.3 ± 0.1	4.8 ± 0.5	2.9 ± 2	>50	>50	>50	> 2.8
13a	>50	>50	>50	>50	>50	>50	>50	>50	n.d.	n.d.
13b	14.2 ± 2.3	6.9 ± 0.5	16.2 ± 2.6	32.5 ± 1.0	3.5 ± 2	18.4 ± 2.2	>50	>50	n.d.	n.d.
CDDP	2.6 ± 0.7*	0.14 ± 0.03*	2.0 ± 0.3*	3.8 ± 0.3	0.63 ± 0.1*	8.6 ± 0.6	5.4 ± 0.7	>50	>50*	> 5.5

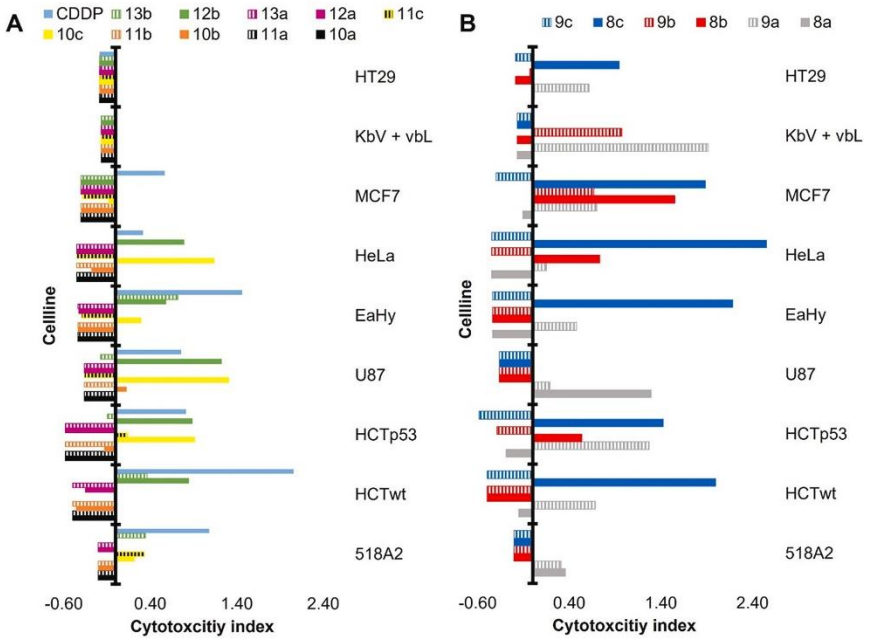

Fig. 2. Cytotoxicity indices (CI) of the complexes **8a–13b** across all tested cancer cell lines. To determine the CI, the IC_{50} values were logarithmised with log base of 10 and then the mean value of the logarithmised IC_{50} values over all tested compounds were determined for each cell line. The difference between the individual values and this mean value gave the individual CI for each substance and cell line. The different colours indicate the methyl and ethyl esters that belong together structurally. **A)** CIs of all *cis*-configured complexes. **B)** CIs of all *trans*-configured complexes.

2.3.8. Intracellular localisation using click chemistry

To assess the localisation of active complexes of the *cis* (e.g. **10**) and *trans* (e.g. **8**) series in HCT116 colon carcinoma cells, we used the 'clickable' congeners **16** and **22**. HCT116 cells (0.1×10^6 cells per mL, 0.5 mL per well) were seeded onto cover slips (borosilicate glass, Carl Roth) inside the wells of 24-well microtiter plates and were allowed to grow overnight. The medium was removed and the cells were washed with 1 mL PBS and treated with complexes **16** or **22** at a final concentration of 25 μM for 30 min at 37 °C. Fixation, blocking and permeabilisation was done analogously to the fluorescence staining of the cytoskeleton. 200 μL of click working solution [for **16**: 2 mM $CuSO_4$, 5 mM sodium ascorbate, 0.1 mM 3-azido-7-hydroxycoumarin, in PBS. For **22**: BDP-FL-tetrazin (Lumiprobe Catalog Number: 114E0) in PBS 1:1000] were added to each well. The cells were incubated for 30 min at rt. in the dark before the click solution was discarded and the cells were washed three times with PBS for 5 min. For co-staining, the cells were either treated with propidium iodide (50 μg/mL, after fixation and permeabilisation) or Mitotracker™ Red CM-H2Xros (before substance addition, ThermoFisher Scientific, 250 nM in FBS-free DMEM). Coverslips were mounted (VECTASHIELD® PLUS Antifade Mounting

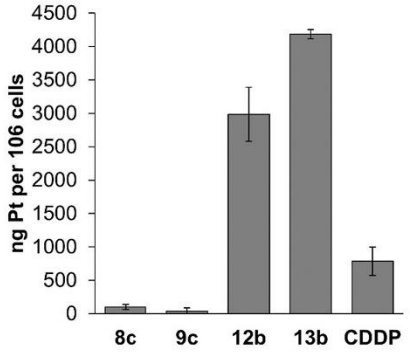

Fig. 3. Cellular uptake of *trans*-bis(*NHC*)Cl_2Pt complexes **8c** and **9c** as well as *cis*-bis(*NHC*)Cl_2Pt complexes **12b** and **13b**, and of CDDP into HCT116^{wt} cells after 5 h treatment with 5 μM. Measured via ICP-MS.

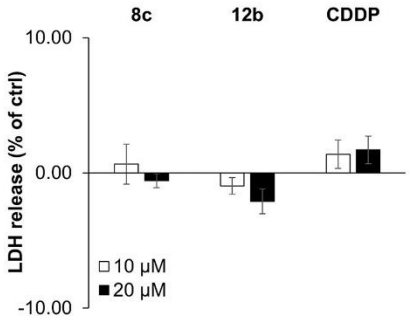

Fig. 4. LDH release, measured as formazan absorbance of HCT116^{wt} cells after 24 h treatment with complexes **8c**, **12b** or CDDP in different concentrations, relative to a negative control which was set as 0%. Mean ± SD; $n = 3$.

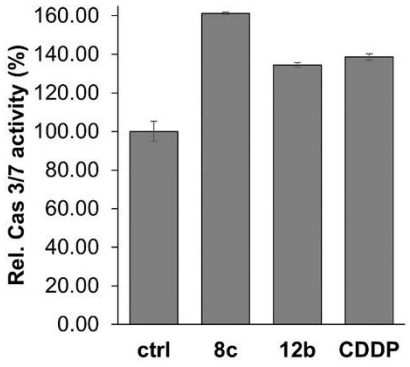

Fig. 5. Relative levels of caspase-3/7 activity in HCT116^{wt} cells after 6 h incubation with 10 μM of complexes **8c** and **12b**. An equal concentration of CDDP served as a positive control and corresponding amounts of DMSO as a negative control (ctrl). Fluorescence values were corrected for the cell viability obtained from corresponding MTT assays and normalised relative to the negative control set at 100%. Means ± SD, n = 3.

Medium) and fluorescence images were acquired using fluorescence microscopy. Images were processed using Image J.

3. Results and discussion

3.1. Complex syntheses

The synthetic route (Scheme 1) leading to *cis*- and *trans*-[bis(5-alkoxycarbonyl-1,3-dialkyl-benzimidazol-2-ylidene)dichlorido]platinum(II), and *cis*-[(DMSO)(5-alkoxycarbonyl-1,3-dialkyl-benzimidazol-2-ylidene)dichlorido]platinum(II) complexes, respectively, follows protocols previously published by *Rehm* et al. [16] All in vitro evaluated complexes were characterised by ^{1}H, ^{13}C and ^{195}Pt NMR spectra, EI or ESI mass spectrometry and elemental analysis.

Benzimidazole-5-carboxylic acid (**1**) was converted to either methyl ester **2** or ethyl ester **3** via *Fischer* esterification [17]. These esters were N,N′-dialkylated with MeI, EtI or BnBr in one step following a protocol by *Schmidt* et al., leading to the benzimidazolium halides in nearly quantitative yields with high purity [18]. As the required excess of benzyl bromide could not be removed by rotary evaporation, the 1,3-dibenzylbenzimidazolium bromides needed several precipitation cycles for sufficient purity. Anion metathesis was necessary for the iodides in order to prevent a halide exchange in the final *cis*-bis(NHC) complexes [19]. Treatment of the iodides and bromides with $AgNO_3$ and then HCl afforded the corresponding benzimidazolium chlorides **4** and **5**. However, a similar procedure was not necessary for the synthesis of the *trans*-bis(NHC) complexes **8** and **9** since there is no excess of free anions, and because the silver halides precipitate from CH_2Cl_2 as easy to remove by-products.

The NHC-silver(I) complexes **6a–c** and **7a–c** were obtained by treating the benzimidazolium halides with half an equivalent of Ag_2O in the dark for 24 h. Consumption of the starting material was monitored by the vanishing of the 2-H signal in the ^{1}H NMR spectra. Filtration over Celite® and precipitation from pentane led to white or beige powders, which were used without further purification. Transmetalation with 0.5 equivalents of K_2PtCl_4 for four days in CH_2Cl_2 led to the *trans*-[bis(*NHC*)dichlorido]platinum(II) complexes **8a–c** and **9a–c**. The *cis*-[(DMSO)(NHC)Cl_2]Pt^{II} complexes **10** and **11**, which were used as precursors for the *cis*-[bis(*NHC*)dichlorido]platinum(II) complexes **12** and **13**, were obtained by stirring the respective silver complex with an equimolar amount of K_2PtCl_4 in excess DMSO as described previously [20]. This route is also applicable to the synthesis of complexes bearing two different *cis*-positioned NHC ligands which are not accessible from the more common $(DMSO)_2PtCl_2$ [21] or $(COD)PtCl_2$ [22] precursors. The monocarbene complexes **10** and **11** were treated with an excess of the respective benzimidazolium chloride **4** or **5** and KOtBu in CH_2Cl_2 to liberate the corresponding NHC ligand. While **10a**, **10b** as well as **11a** and **11b** were readily converted into their respective *cis*-bis(NHC) complexes, the N,N′-dibenzyl substituted complexes **10c** and **11c** did not react under identical or modified conditions, possibly due to the steric demand of the benzyl residues.

The configuration of the complexes was confirmed by ^{1}H NMR spectra. While the *trans*-bis(NHC) complexes **8** and **9** displayed a single signal group for all identical NCH_n protons, the corresponding protons of the *cis*-bis(NHC) complexes **12** and **13** resonated as two separate signal groups. The perpendicular orientation of the NHC ligands relative to the plane spanned by $PtCl_2$ leads to one proton facing a chlorido ligand while the other is facing the second carbene ligand. Due to the square planar nature of such complexes [16,20,23,24] the *cis*-configuration leads to higher steric hinderance and thus to an upfield shift. This effect increases with the size of the N-substituent. Fig. 1 depicts the NCH_2 range of the ^{1}H NMR spectra of complexes **12b** and **8b**. It shows a virtual doublet of quartets (vdq) for the *trans*-bis(NHC) complex **8b** at 4.99 ppm and two dq at 5.09 ppm and 4.68 ppm for the *cis*-bis(NHC) complex **12b**. A smaller DMSO ligand, *cis*-positioned to the NHC ligand as in complex **10b**, obviously does not lead to a split of the NCH_2 proton signals

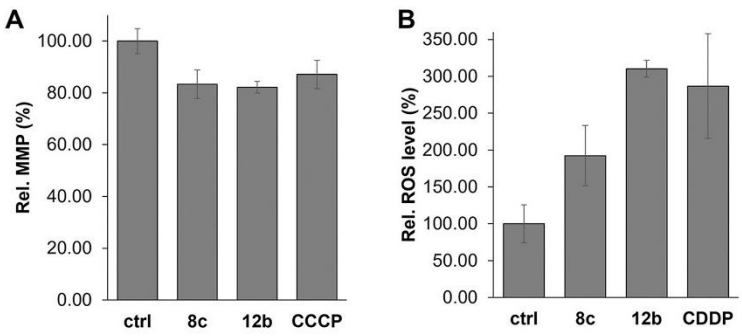

Fig. 6. A) Relative mitochondrial membrane potential/integrity (MMP) of HCT116^{wt} cells treated with complexes **8c** and **12b** (10 μM) for 1 h. Carbocyanide-*m*-chlorophenylhydrazone (CCCP) served as a positive control, corresponding amounts of DMSO as a negative control (ctrl). **B)** Relative intracellular reactive oxygen species levels of HCT116^{wt} cells treated with complexes **8c** and **12b** (10 μM) for 1 h. CDDP served as a positive control, corresponding amounts of DMSO as a negative control (ctrl). Mean ± SD, $n = 3$.

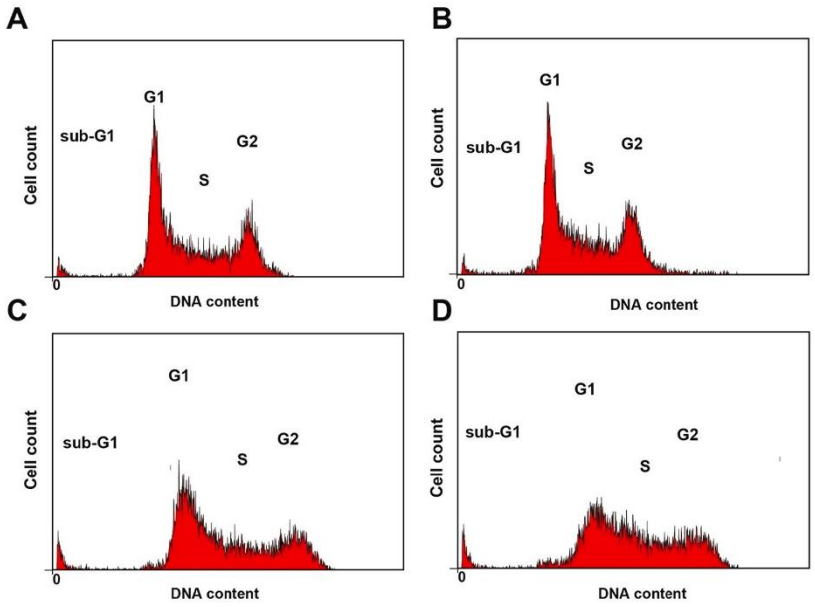

ig. 7. Cell cycle profiles of HCT116^{wt} cells treated for 24 h with IC_{50} concentrations of **8c** (B), **12b** (C) and CDDP (D), the corresponding amount of DMSO was used is a control (A). Images are representative of at least three experiments.

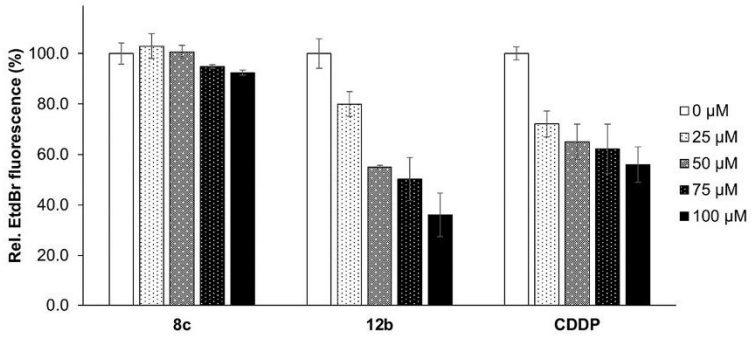

Fig. 8. Relative EtBr fluorescence intensities of intercalated EtdBr in linear salmon sperm DNA after 2 h incubation with CDDP, **12b** or **8c**. Mean ± SD, $n = 3$.

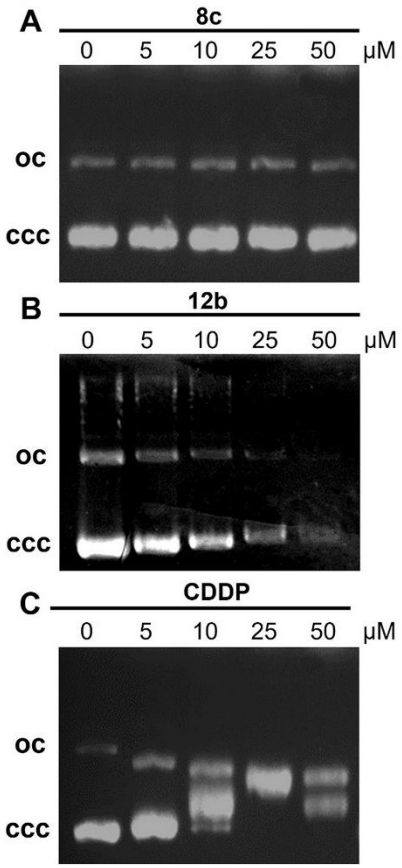

Fig. 9. EMSAs with circular plasmid DNA after 16 h treatment with complexes **8c** (A) and **12b** (B). CDDP was used as a positive control (C). Images were documented under UV excitation and they are representative of at least two independent experiments.

(Fig. 1).

In line with this reasoning, the *N*-benzyl substituted *cis*-(DMSO)(NHC) complex **10c** showed a similar if smaller split of its NCH_2 signal with two virtual doublets of doublets (vdd) at 6.18 ppm and 6.00 ppm. These vdd are 45 Hz apart, consistent with the doublet caused by the methyl groups of DMSO, thereby confirming the *cis* and perpendicular orientation relative to the $PtCl_2$ square. The first splitting to give a doublet consequently originates from the spatial arrangement of protons. The further doublet overlapping on this apparently comes from the ester group, which is either above or below the plane spanned by the ligands. This holds for all complexes and, due to the restricted rotatability of the NHC ligands [25], leads to two constitutional isomers and consequently to two possible arrangements of the *cis*-(DMSO)(NHC) complexes and four of the bis(NHC) complexes.

Differences can also be seen in the ppm range of the chemical shift of the NCN carbon in ^{13}C NMR spectra and of the shift of platinum in ^{195}Pt spectra (cf. Supporting Information). The chemical shifts of the C-2 in ^{13}C NMR spectra of *trans*-bis(NHC) complexes lie around 181 ppm, those of *cis*-bis(NHC) complexes around 162 ppm and those of *cis*-(DMSO)(NHC) complexes around 158 ppm. The same holds for the shifts of Pt in ^{195}Pt spectra. *Trans*-Bis(NHC) complexes lie around −3270 ppm, *cis*-bis(NHC) complexes at −3640 ppm and *cis*-(DMSO)(NHC) complexes at −3550 ppm.

Neither the *cis*-(DMSO)(NHC) complexes **10** and **11** nor the *cis*-bis(NHC)-complexes **12** and **13** showed a change of their signals in ^1H NMR spectra over a period of at least three days when dissolved in DMSO +5% D_2O, i.e. under test conditions. They can thus be considered stable. Exemplary ^{195}Pt NMR stability studies in DMSO-d_6 without the addition of D_2O were conducted with one complex of each series, i. e. **10c** and **13b**. They revealed that neither a change of the shift of the platinum signal nor any new peak appeared over the course of three days (cf. Supporting Information).

Some *trans*-bis(NHC) complexes, and **9a** in particular, however, showed intriguing stability pattern. Its ^1H NMR spectrum in DMSO-d_6 right after the addition of water showed twice as many signals in the aromatic region compared to its spectrum recorded in $CDCl_3$ (cf. Supporting Information). In addition, the clear splits visible in the latter blur into undefined multiplets for the NMe and the OCH_2 group, respectively, and into a virtual doublet of triplets of the aliphatic CH_3. These in turn converge over the time period of three days to form a new species whose shifts are slightly elevated but match the expected range and multiplicity of such complexes. Additionally, a ^{195}Pt NMR stability study with **9a** in DMSO-d_6 was carried out. The results are consistent with the findings of the ^1H measurements. In the spectra measured after 0 h a shift of −600 ppm was observed, probably due to an exchange of a chlorido for a DMSO ligand leading to a cationic complex. This is in keeping with reports that *trans*-platinum complexes are more reactive than their *cis*-analogues [26–28]. However, the spectrum did not keep changing over time. Addition of $AgBF_4$ after 72 h then caused the residual platinum signal of the starting material at −3255 ppm to completely disappear. A mass spectrum of this solution taken after 96 h showed only the mass of $Pt(NHC)_2(DMSO)Cl$. The same complex dissolved in $CDCl_3$ + 5% D_2O with intense and hourlong vortexing before each measurement showed no change in its ^{195}Pt or ^1H NMR spectra. Consequently, it can be assumed that no ligand exchange with water took place. A comparison of the *trans*-bis(NHC) complexes **8a**–**c** and **9a**–**c** with each other revealed that the ^1H NMR spectra of the benzyl substituted complexes did not change much over time. The number of signals of the *N*-ethyl substituted complexes **8b** and **9b** increased with time, indicating a slow ligand exchange. In contrast, the number of peaks of the *N*-methyl substituted complexes **8a** and **9a** decreased with time, converging to the spectrum obtained in $CDCl_3$, and so indicating a faster ligand exchange. The rate of the ligand exchange seems to depend on the size of the N-substituent.

Another point worth mentioning is that the ester functionality does not undergo saponification neither under mildly basic and aqueous conditions caused by the intermediate AgOH and the leaving group H_2O during the formation of (NHC)Ag(I) salts [29], nor under strongly basic conditions which prevail during the synthesis of the *cis*-bis(NHC) complexes. Furthermore, the respective *trans*-bis(NHC) complexes are way less polar than their *cis*-(DMSO)(NHC) or *cis*-bis(NHC) analogues as indicated by TLC and their solubilities.

Our group has recently shown that *cis*-bis(NHC) complexes behave akin to cisplatin and accumulate in the cell nuclei [19]. The aim of this work was therefore to investigate the subcellular accumulation of cis-(DMSO)(NHC) complexes **10** and **11** and especially that of the promising *trans*-bis(NHC) complexes **8** and **9**. Hence, clickable analogues were synthesised. The propargyl group was chosen as N-substituent with the smallest possible structural alteration (Scheme 2). The *N*,*N*′-dipropargyl benzimidazolium salt **15** could not be prepared like the salts **4** and **5** via one-pot N,N′-dialkylation. As a workaround, salt **15** was prepared in three steps with a purification via column chromatography of the *mono*-propargylated intermediate **14**. The former could neither be converted to the *cis*-(NHC)(DMSO) platinum complex **16** in several steps via an intermediate silver complex, in analogy to the conversion of the salts **4**, **5** to the complexes **10**, **11** in scheme 1. We assume that the formation of silver alkyne π-complexes is favoured over that of the desired carbene complex. Complex **16** was eventually obtained by deprotonating salt **15** and reacting the resulting carbene right away with *cis*-$(DMSO)_2PtCl_2$.

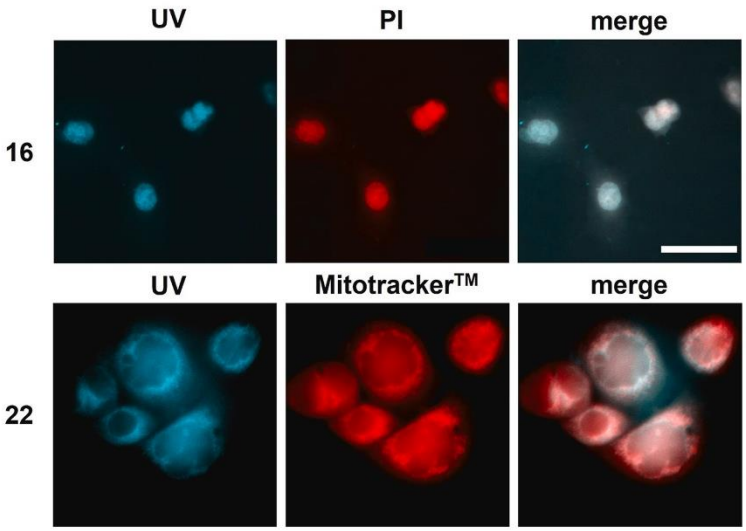

Fig. 10. Fluorescence microscopy images of HCT116 colon cancer cells treated 30 min with 25 μM of complexes **16** or **22** followed by click chemistry with fluorophore bearing reagents (ex/em 350/420–480 nm). Nuclei were counterstained with PI (ex/em 490/640), mitochondria were counterstained using Mitotracker™ (ex/em 580/610). The images shown are representative of at least four independent experiments. Scale bar corresponds to 30 μM.

The circumstance that complexation with silver led to decomposition also made transmetalation with K_2PtCl_4 to give the corresponding *trans* complexes impossible. Neither are there any platinum dichlorido precursors with good leaving groups in *trans* position. Treating the carbene obtained in situ by deprotonation of salt **15** with K_2PtCl_4 also failed to afford the corresponding *trans* complex. This is consistent with literature describing problems of Cu-catalysed click chemistry of azides with alkynes, especially in the presence of d^{10} metals [5]. Accordingly, a different click chemistry methodology was chosen for the visualisation of *trans* complexes differing structurewise only marginally from the complexes **8** and **9**. The methyl or ethyl ester groups of the latter were replaced by (2,3-dimethylcycloprop-2-en-1-yl)methoxycarbonyl residues, capable of undergoing metal-free, ring-strain promoted *Diels-Alder*-type click reactions with tetrazines (Scheme 3). This is the first time this methodology was applied to the visualisation of an organometallic compound. The required (2,3-dimethylcycloprop-2-en-1-yl) methanol was synthesised as described in literature [30]. The amine of benzimidazole **1** had to be protected with an alloc group prior to a *Steglich-Hassner* esterification which afforded ester **18**. Its deprotection gave ester **19** which was N,'N-diethylated furnishing benzimidazolium iodide **20**. The latter was converted with Ag_2O to silver NHC complex **21** which was transmetalated with K_2PtCl_4 to give the desired *trans*-bis (NHC) platinum complex **22**.

3.2. Anticancer activity

3.2.1. Cytotoxicity and cellular uptake

The complexes were investigated for their cytotoxicity over 72 h against various human cancer cell lines including 518A2 melanoma, $HCT116^{wt}$ and its $HCT116^{p53\ /\ }$ knockout mutant colon carcinoma, U87 glioblastoma, EaHy926 somatic cell hybrid, HeLa cervix carcinoma, MCF7 breast cancer, and HT-29 colon cancer cells, as well as human non-malignant dermal fibroblasts HDFa using the MTT cell viability assay. Their IC_{50} values are shown in Table 1.

To better identify the most active compounds across all cell lines, the cytotoxicity indices of the substances were determined with respect to the cell lines used (Fig. 2)

The complexes **9c**, **10a**, **11a**, **11b**, **12a** and **13a** showed no significant cytotoxic effect on the cancer cell lines studied. The complexes **8a**, **8b**, **9b**, **10b**, **11c** and **13b** were moderately active with IC_{50} values in the one- to two-digit micromolar range. Conspicuous cytotoxicities were observed for the complexes **8c**, **9a**, **10c** and **12b**, with *trans*-bis(NHC) complex **8c** and *cis*-bis(NHC) complex **12b** in particular standing out with two-digit nanomolar IC_{50} values.

Complexes of the methyl ester series tend to be more cytotoxic than their ethyl analogues, and the *cis*-bis(NHC) complexes were more cytotoxic than the corresponding *cis*-(DMSO)(NHC) complexes. Furthermore, the *trans*-bis(NHC) complexes tended to be more cytotoxic than the *cis* complexes, and cytoxicity generally increased with the size of the substituents at the N-atoms of the benzimidazole. The finding that platinum(II) complexes with *trans*-positioned leaving groups may also be cytotoxic against cancer cells, like the more common *cis*-configured platinum(II) complexes, is not new. It has even been reported that *trans* complexes of platinum(II) may show activity against CDDP resistant tumour cell lines [9]. This fits with our findings for *trans*-bis(NHC) complexes **8c** and **9a** which showed antiproliferative activity against CDDP-resistant HT-29 colon carcinoma cells.

3.2.2. Uptake in cancer cells measured with ICP-MS

In order to clarify whether the high cytotoxicity of complexes **8c** and **12b** is intrinsic and structure-dependent, or a consequence of a particularly high cellular concentration, we assessed their cellular uptake by $HCT116^{wt}$ colon carcinoma cells via ICP-MS in comparison to CDDP and ethyl esters **9c** and **13b**, which are structurewise closely related to **8c** and **12b** (Fig. 3).

The uptake of the *trans*-bis(NHC) complexes **8c** and **9c** is apparently more limited than that of the *cis*-complexes **12b**, **13b** and CDDP. The divergence in cellular uptake is not related to the respective IC_{50} values. The impressive cytotoxicity of complex **8c** against $HCT116^{wt}$ cells exceeded that of **12b**, **13b** and CDDP by far, despite its comparatively low uptake, whereas **9c** is completely inactive. Therefore, the strong cytotoxicity of **8c** is intrinsic, structure-dependent and based on mechanistic reasons. As recently shown by Rehm et al., the uptake of platinum compounds may also be directly linked to structural features [23]. A generally weak uptake of *trans*-platinum complexes is assumed.

3.2.3. Unselective toxicity

In order to assess the degree of toxicity leading to necrosis caused by complexes **8c** and **12b**, a lactate dehydrogenase (LDH) release assay was conducted. LDH release is considered as a benchmark for necrotic cells, as it is a consequence of plasma membrane permeabilisation [12]. LDH release assays were conducted with HCT116^{wt} cells. LDH release is measured as absorbance by a coloured formazan which is the product of an LDH-associated NADH reduction of a colourless tetrazolium salt [12]. No significant increase in LDH levels was detected after an incubation period of 24 h (Fig. 4). This indicates that the complexes have no unselective cytotoxic effects and that the membrane integrity of HCT116^{wt} cells was maintained over 24 h of exposure to concentrations clearly exceeding the IC_{50} of the complexes. Thus, a key precondition for suitability as potential drugs was fulfilled, and their mode of action was further investigated.

3.2.4. Induction of apoptosis, mediated by caspase-3/-7 activation

The absence of an LDH increase upon cell treatment with compounds **8c** and **12b** hints at a medicinally favourable apoptotic rather than necrotic type of cancer cell death. Mechanistically, this would imply that the complexes trigger an apoptosis cascade via activation of caspases [31]. To confirm this for the complexes **8c** and **12b**, a caspase-3/7 activation assay was performed [32]. Both complexes activated caspases-3/7 in HCT116^{wt} colon carcinoma cells at least as strongly as CDDP did (Fig. 5).

3.2.5. Mitochondrial membrane potential and ROS levels

Closely linked to apoptotic events is the loss of the mitochondrial membrane potential (MMP) and the resulting increase in intracellular ROS levels [32,33]. The MMP can be assessed by means of the fluorescent, cationic dye tetramethylrhodamin methyl ester ($TMRM^+$) which accumulates in the negatively charged intact mitochondrial membranes [5]. The integrity of MMP in HCT116^{wt} cells was distinctly diminished upon treatment with complexes **8c** and **12b** (Fig. 6A). The disturbance of the MMP often leads to a rise in intracellular ROS levels, due to the permeability of the mitochondrial membranes allowing intramitochondrial ROS to enter the cytosol [6]. The ROS levels in HCT116^{wt} cells treated with complexes **8c** and **12b** were assessed with dichlorodihydrofluorescein diacetate (DCFH-DA), a fluorogenic dye which measures hydroxyl, peroxyl and other reactive oxygen species in live cells (Fig. 6B). Treatment of the cells with complexes **8c** or **12b** led to an increase of ROS levels, most distinctly so for the *cis*-complex **12b**, probably because of the lower uptake of *trans*-complex **8c** into these cells. Together with the results of the caspase-3/7 activation assays, these studies suggest a mitochondria-associated induction of apoptosis by both complexes **8c** and **12b**.

3.2.6. Influence on the cell cycle

The clinically established *cis*-configured platinum(II) complexes structurally modify cellular DNA and so interfere with its normal function. As a consequence, alterations of the cell cycle occur due to an inhibition of the cellular replication and transcription machinery, eventually leading to cell apoptosis [34]. Cisplatin typically induces an S-Phase or a dual S−/G_2M-Phase arrest in cancer cells [20,23]. We now monitored the interference of the platinum(II) complexes **8c** and **12b** at their respective IC_{50} concentrations with the cell cycle of HCT116^{wt} cells using propidium iodide staining and flow cytometry. No significant changes in the typical cell cycle progression of these colon cancer cells, compared to the control (Fig. 7A), was observed upon treatment with *trans*-complex **8c** (Fig. 7B). In contrast, treatment with *cis*-complex **12b** (Fig. 7C) led to a distinct change in cell cycle phase distribution similar to CDDP (Fig. 7D). Therefore, a mode of action similar to that of cisplatin may be assumed for *cis*-complex **12b**, whereas *trans*-complex **8c** seems to act in a different way.

3.2.7. DNA interaction

The mechanism of action of CDDP and most other effective *cis*-configured Pt(II) complexes is based on the formation of strong coordinative bonds between the metal centre and DNA bases [35]. Due to the *cis* configuration of complex **12b** and the CDDP-like type of cell cycle arrest it elicits in treated cancer cells, a DNA-associated mechanism of action is standing to reason. To verify this and to further elucidate the mechanism of action of the *trans*-complexes, DNA-based ethidium bromide (EtdBr) saturation assays and electrophoretic mobility shift assays (EMSA) were performed. Incubation of linear salmon sperm DNA with complex **12b** led to a strong concentration-dependent reduction of the fluorescence of intercalated EtdBr as the metalated DNA offers fewer accessible sites for intercalation. This effect was even more pronounced for complex **12b** when compared to that by CDDP (Fig. 8). The *trans*-bis(NHC) complex **8c** did not give rise to such an effect, indicating a mode of action not associated with DNA metalation.

In order to identify the nature of the DNA interaction of complex **12b** an EMSA was conducted. The comparison of EtdBr and EMSA results allows to distinguish between strong covalent/coordinative and merely electrostatic interactions of metalating agents and DNA. Treatment of circular plasmid DNA with *cis*-complex **12b** (Fig. 9B) revealed a concentration-dependent relaxation of the ccc (covalently closed circular) form to the oc (open circular) form akin to, yet less pronounced than, that caused by CDDP (Fig. 9C). In line with its lack of interaction with linear DNA in the EtdBr assay, the *trans*-complex **8c** had no effect on circular plasmid DNA either (Fig. 9A), also indicating a DNA-independent mode of action.

These findings support a DNA-associated mode of action for *cis*-complex **12b**. Together with its CDDP-like cell cycle arrest, the results of our study suggest a mode of action of **12b** quite reminiscent of that of CDDP. The mechanisms of action leading to the extraordinary cytotoxic effect of the *trans* platinum(II) complex **8c** remains to be elucidated in more detail.

3.2.8. Intracellular localisation

Complexes **16** and **22** were synthesised as representatives of the groups of *cis*- and *trans*-complexes that can be converted to fluorescent products using click chemistry after they have reached their respective cellular targets. Using this method, the distribution of the complexes inside the treated cells can be traced. An enrichment of *cis*-complex **16** in the area of the nuclei of treated colon cancer cells was observed, matching the DNA-binding properties of *cis*-Pt complexes in general and those of the *cis*-complexes studied here. In contrast, *trans*-complex **22** accumulated in regions outside the nuclei, mainly in the area of the cytoplasm including mitochondria (Fig. 10). This suggests that the *trans*-complexes **8** and **9** very likely do not interfer with DNA, as already suspected. In the past, we had already reported on NHC-platinum complexes which accumulate in mitochondria and interfere with mitochondrial function [19]. The current findings underline the suitability of *trans*-complexes of platinum(II) as anti-cancer compounds targeting structures other than DNA.

4. Conclusion

The current work studied the influence of the N-alkyl and 5-alkoxycarbonyl substituents of *cis*- and *trans*-[bis(benzimidazol-2-ylidene) dichlorido]platinum(II) complexes **12**/**13** and **8**/**9** on their stability in aqueous media, their cytotoxicity against cancer cells, and their underlying properties and modes of action.

The intrinsic cytotoxicity and the cell line specificity of both series of complexes depended to a large extent on their ester and their N-alkyl residues whereas their uptake into cancer cells did not. However, the most active *trans*-complexes and the most active *cis*-complexes carried different such residues. Far less was taken up of *trans*-complexes **8**/**9** by HCT116 colon carcinoma cells when compared to *cis*-complexes **12**/**13**.

While the *cis*-complexes appeared to operate by mechanisms of

action akin to those of cisplatin, the *trans*-complexes addressed different targets, e.g. such associated with mitochondria rather than DNA, although having a lesser effect on the mitochondrial membrane potential and the release of ROS. The subcellular localisation of *trans* complex **22** in mitochondrial organelles by the first-time bioorthogonal clicking of a cyclopropene-bearing complex with a fluorogenic tetrazine supports this finding. The *trans*-complexes had also no effect on the cell cycle of cancer cells. Most intriguing, however, is their high activity against cisplatin-refractory cancer cells.

Combination therapies of inactive transplatin with drugs affecting the DNA and its function such as the antimetabolite 5-fluorouracil had been reported to enhance the anticancer effect of the latter [36]. It would be interesting to test whether combinations of our active *trans*-complexes with 5-FU lead to an even greater overall anticancer effect.

Further work is necessary to fully elucidate the mode of action of *trans*-[bis(benzimidazol-2-ylidene)dichlorido]platinum(II) complexes and to pinpoint the optimum set of N- and aryl-substituents.

Source of funding

Deutsche Forschungsgemeinschaft grant Scho 402/12-2

Declaration of Competing Interest

The authors declare that they have no known competing financial interests or personal relationships that could have appeared to influence the work reported in this paper.

Data availability

Data will be made available on request.

Acknowledgements

R.S. thanks the Deutsche Forschungsgemeinschaft for financial support (grant Scho 402/12-2). We thank Dr. Ulrike Lacher (University of Bayreuth) for mass spectra. We thank Kim Wagner for supporting work on MTTs and buffer preparation, as well as Manuel Wayand and Moritz Röder for precursor synthesis.

Appendix A. Supplementary data

Supplementary data to this article can be found online at https://doi.org/10.1016/j.jinorgbio.2022.112028.

References

[1] S. Zhao, Z. Yang, G. Jiang, S. Huang, M. Bian, Y. Lu, W. Liu, An overview of anticancer platinum N-heterocyclic carbene complexes, Coord. Chem. Rev. 449 (2021), 214217, https://doi.org/10.1016/j.ccr.2021.214217.
[2] S.B. Aher, P.N. Muskawar, K. Thenmozhi, P.R. Bhagat, Recent developments of metal N-heterocyclic carbenes as anticancer agents, Eur. J. Med. Chem. 81 (2014) 408–419, https://doi.org/10.1016/j.ejmech.2014.05.036.
[3] A.V. Astakhov, S.B. Soliev, E.G. Gordeev, V.M. Chernyshev, V.P. Ananikov, Relative stabilities of M/NHC complexes (M – Ni, Pd, Pt) against R–NHC, X–NHC and X–X couplings in M(0)/M(ii) and M(ii)/M(iv) catalytic cycles: a theoretical study, Dalton Trans. 4845 (2019) 17052–17062, https://doi.org/10.1039/C9DT03266E.
[4] B. Rosenberg, L. VanCamp, The successful regression of large solid sarcoma 180 tumors by platinum compounds, Cancer Res. 306 (1970) 1799–1802.
[5] S. Bellemin-Laponnaz, N-heterocyclic carbene platinum complexes: a big step forward for effective antitumor compounds, Chem. Eur. J. 20201 (2020) 10–20, https://doi.org/10.1002/ejic.201900960.
[6] M.J. Cleare, J.D. Hoeschele, Studies on the antitumor activity of group VIII transition metal complexes. *Part I. Platinum (II) complexes*, Bioinorg. 23 (1973) 187–210, https://doi.org/10.1016/S0006-3061(00)80249-5.
[7] S.E. Sherman, S.J. Lippard, Structural aspects of platinum anticancer drug interactions with DNA, Chem. Rev. 875 (1987) 1153–1181, https://doi.org/10.1021/cr00081a013.
[8] M. Coluccia, G. Natile, Trans-platinum complexes in cancer therapy, Anti Cancer Agents Med. Chem. 71 (2007) 111–123, https://doi.org/10.2174/187152007779314080.
[9] G. Natile, M. Coluccia, Current status of trans-platinum compounds in cancer therapy, Coord. Chem. Rev. 216 (2001) 383–410, https://doi.org/10.1016/S0010-8545(01)00315-0.
[10] U. Kalinowska-Lis, J. Ochocki, K. Matlawska-Wasowska, Trans geometry in platinum antitumor complexes, Coord. Chem. Rev. 252 (2008) 1328–1345, https://doi.org/10.1016/j.ccr.2007.07.015.
[11] D.M.L. Morgan, Tetrazolium (MTT) assay for cellular viability and activity, in: D. M.L. Morgan (Ed.), Polyamine Protocols, Humana Press, Totowa, NJ, 1998, pp. 179–184.
[12] F.K. Chan, K. Moriwaki, M.J. De Rosa, Detection of necrosis by release of lactate dehydrogenase activity, Methods Mol. Biol. 979 (2013) 65–70, https://doi.org/10.1007/978-1-62703-290-2_7.
[13] C.E. Ganote, S.C. Armstrong, Effects of CCCP-induced mitochondrial uncoupling and cyclosporin A on cell volume, cell injury and preconditioning protection of isolated rabbit cardiomyocytes, J. Mol. Cell. Cardiol. 357 (2003) 749–759, https://doi.org/10.1016/S0022-2828(03)00114-7.
[14] E. Eruslanov, S. Kusmartsev, Identification of ROS using oxidized DCFDA and flow-cytometry, in: D. Armstrong (Ed.), Advanced Protocols in Oxidative Stress II, Humana Press, Totowa, NJ, 2010, pp. 57–72.
[15] C. Qiao, S. Bi, Y. Sun, D. Song, H. Zhang, W. Zhou, Study of interactions of anthraquinones with DNA using ethidium bromide as a fluorescence probe, Spectrochim. Acta A Mol. Biomol. Spectrosc. 701 (2008) 136–143, https://doi.org/10.1016/j.saa.2007.07.038.
[16] T. Rehm, M. Rothemund, T. Dietel, R. Kempe, R. Schobert, Synthesis, structures and cytotoxic effects in vitro of cis- and trans-[PtIVCl4(NHC)2] complexes and their PtII precursors, Dalton Trans. 4843 (2019) 16358–16365, https://doi.org/10.1039/C9DT02438G.
[17] K. Salorinne, R.W.Y. Man, C.-H. Li, M. Taki, M. Nambo, C.M. Crudden, Water-soluble N-heterocyclic carbene-protected gold nanoparticles: size-controlled synthesis, stability, and optical properties, Angew. Chem. Int. Ed. 5622 (2017) 6198–6202, https://doi.org/10.1002/anie.201701605.
[18] C. Schmidt, B. Karge, R. Misgeld, A. Prokop, R. Franke, M. Brönstrup, I. Ott, Gold(I) NHC complexes: antiproliferative activity, cellular uptake, inhibition of mammalian and bacterial thioredoxin reductases, and gram-positive directed antibacterial effects, Chem. Eur. J. 238 (2017) 1869–1880, https://doi.org/10.1002/chem.201604512.
[19] M. Rothemund, S.I. Bär, T. Rehm, H. Kostrhunova, V. Brabec, R. Schobert, Antitumoral effects of mitochondria-targeting neutral and cationic cis-[bis(1,3-dibenzylimidazol-2-ylidene)Cl(L)]Pt(ii) complexes, Dalton Trans. 4926 (2020) 8901–8910, https://doi.org/10.1039/D0DT01664K.
[20] J.K. Muenzner, T. Rehm, B. Biersack, A. Casini, I.A. de Graaf, P. Worawutputtapong, A. Noor, R. Kempe, V. Brabec, J. Kasparkova, R. Schobert, Adjusting the DNA interaction and anticancer activity of Pt(II) N-heterocyclic carbene complexes by steric shielding of the trans leaving group, J. Med. Chem. 5815 (2015) 6283–6292, https://doi.org/10.1021/acs.jmedchem.5b00896.
[21] S. Fantasia, A. Pasini, S.P. Nolan, Platinum(II) mediated C(sp3)-H activation of tetramethylthiourea, Dalton Trans. 38 (2009) 8107–8110, https://doi.org/10.1039/b911164f.
[22] L.C. Lewis-Alleyne, B.S. Bassil, T. Böttcher, G.-V. Röschenthaler, Selective synthesis of cis- and trans-[(NHCMe)2PtCl2] and [NHCMePt(cod)Cl][NHCMePtCl3] using NHCMeSiCl4, Dalton Trans. 4342 (2014) 15700–15703, https://doi.org/10.1039/C4DT02214A.
[23] T. Rehm, M. Rothemund, A. Bär, T. Dietel, R. Kempe, H. Kostrhunova, V. Brabec, J. Kasparkova, R. Schobert, N,N-Dialkylbenzimidazol-2-ylidene platinum complexes – effects of alkyl residues and ancillary cis-ligands on anticancer activity, Dalton Trans. 4748 (2018) 17367–17381, https://doi.org/10.1039/C8DT03360A.
[24] T. Rehm, M. Rothemund, J.K. Muenzner, A. Noor, R. Kempe, R. Schobert, Novel cis-[(NHC)1(NHC)2(L)Cl]platinum(ii) complexes – synthesis, structures, and anticancer activities, Dalton Trans. 4539 (2016) 15390–15398, https://doi.org/10.1039/C6DT02350A.
[25] C.P. Newman, R.J. Deeth, G.J. Clarkson, J.P. Rourke, Synthesis of mixed NHC/L platinum(II) complexes: restricted rotation of the NHC Group, Organometallics 2625 (2007) 6225–6233, https://doi.org/10.1021/om700671y.
[26] T. Peleg-Shulman, Y. Najajreh, D. Gibson, Interactions of cisplatin and transplatin with proteins. Comparison of binding kinetics, binding sites and reactivity of the Pt-protein adducts of cisplatin and transplatin towards biological nucleophiles, J. Inorg. Biochem. 91 (2002) 306–311, https://doi.org/10.1016/S0162-0134(02)00362-8.
[27] T. Kishimoto, Y. Yoshikawa, K. Yoshikawa, S. Komeda, Different effects of cisplatin and Transplatin on the higher-order structure of DNA and gene expression, Int. J. Mol. Sci. 211 (2019), https://doi.org/10.3390/ijms21010034.
[28] V. Marchán, E. Pedroso, A. Grandas, Insights into the reaction of transplatin with DNA and proteins: methionine-mediated formation of histidine-guanine trans-Pt(NH3)2 cross-links, Chemistry 10 (2004) 5369–5375, https://doi.org/10.1002/chem.200400470.
[29] J.M. Hayes, M. Viciano, E. Peris, G. Ujaque, A. Lledós, Mechanism of formation of silver N-heterocyclic carbenes using silver oxide: a theoretical study, Organometallics 2625 (2007) 6170–6183, https://doi.org/10.1021/om700898d.
[30] J.M.J.M. Ravasco, C.M. Monteiro, A.F. Trindade, Cyclopropenes: a new tool for the study of biological systems, Org. Chem.Front. 46 (2017) 1167–1198, https://doi.org/10.1039/C7QO00054E.
[31] S. Fulda, K.M. Debatin, Caspase activation in cancer therapy, in: Madame Curie Bioscience Database [Internet], Landes Bioscience, Austin (TX), 2022.
[32] M.P. Murphy, How mitochondria produce reactive oxygen species, Biochem. J. 4171 (2009) 1–13, https://doi.org/10.1042/bj20081386.

[33] J.D. Ly, D.R. Grubb, A. Lawen, The mitochondrial membrane potential (deltapsi (m)) in apoptosis; an update, Apoptosis 82 (2003) 115–128, https://doi.org/10.1023/a:1022945107762.
[34] S. Ahmad, Platinum-DNA interactions and subsequent cellular processes controlling sensitivity to anticancer platinum complexes, Chem. Biodivers. 73 (2010) 543–566, https://doi.org/10.1002/cbdv.200800340.
[35] J. Reedijk, P.H. Lohman, Cisplatin: synthesis, antitumour activity and mechanism of action, Pharm. Weekbl. Sci. 75 (1985) 173–180, https://doi.org/10.1007/bf02307573.
[36] B. Nakata, S. Yamagata, I. Kanehara, T. Shirasaka, K. Hirakawa, Transplatin, a cisplatin trans-isomer, may enhance the anticancer effect of 5-fluorouracil, J. Exp. Clin. Cancer Res. 252 (2006) 195–200.

SUPPORTING INFORMATION

Trans-[bis(benzimidazol-2-ylidene)dichlorido]platinum(II) complexes with peculiar modes of action and activity against cisplatin-resistant cancer cells

Sofia I. Bär[+], Sebastian W. Schleser[+], Natalie Oberhuber, Alexander Herrmann, Luca Schlotte, Stefanie E. Weber and Rainer Schobert[*]

Organic Chemistry Laboratory, University of Bayreuth, Universitaetsstrasse 30, 95447 Bayreuth, Germany

[+]These authors contributed equally to this work

[*]Corresponding author

E-mail address: rainer.schobert@uni-bayreuth.de

Fax: 0049-921-552671

Phone: 0049-921-552679

Conflicts of interest: There are no conflicts of interest

Source of funding: Deutsche Forschungsgemeinschaft grant Scho 402/12-2

Table of content

1 Synthesis and characterization of used precursors

1.1 General procedure for the esterification of 1H-Benzimidazole-5-carboxylic acid

1H-benzimidazol-5-carboxylic acid (1.00 eq.) was suspended in ROH (3 mL/mmol) and concentrated H_2SO_4 (2.40 eq.) was added to the solution. Subsequently the mixture was stirred at 100 °C for 24 h. Afterwards, the solvent was removed under reduced pressure and the residue was dissolved in EtOAc (50 mL/mmol). The organic phase was then washed with saturated $Na_2CO_{3(aq.)}$ (50 mL/mmol). The aqueous phase was extracted with EtOAc (3 · 50 mL/mmol) and the combined organic phases were washed with brine (50 mL/mmol), dried over Na_2SO_4 and filtrated. The solvent was evaporated and the product could be afforded as brown powder after drying in vacuum.

Methyl 1H-benzimidazol-5-carboxylate **(2)**

872 mg (4.96 mmol, 80%) from **1** (1.00 g, 6.70 mmol, 1.00 eq.), H_2SO_4 (783 µL, 14.8 mmol, 2.40 eq.) in MeOH (15.0 mL). ^{1}H NMR (500 MHz, $CDCl_3$) δ_H = 11.2 (s, 1H, NH), 8.43 (s, 1H, H^{ar}), 8.25 (s, 1H, H^{ar}), 8.03 (vdd, J = 8.5 Hz, 1.5 Hz, 1H, H^{ar}), 7.69 (d, J = 8.5 Hz 1H, H^{ar}), 3.95 (s, 3H, OCH_3); ^{13}C NMR (125 MHz, $CDCl_3$) δ_C = 167.7 (s, $COOCH_3$), 142.8 (s, C^{ar}), 125.1 (s, C^{ar}), 124.5 (s, C^{ar}), 52.3 (s, OCH_3).

The NMR spectra match previously reported data.[1]

Ethyl 1H-benzimidazol-5-carboxylate **(3)**

2.01 g (10.6 mmol, 86%) from **1** (2.00 g, 12.3 mmol, 1.00 eq.), H_2SO_4 (1.59 mL, 29.6 mmol, 2.40 eq.) in EtOH (30.0 mL). ^{1}H NMR (500 MHz, DMSO-d_6) δ_H = 13.0 (s, 1H, NH), 8.45 (s, 1H, H^{ar}), 8.34 (s, 1H, H^{ar}), 8.02 (vdd, J = 8.5 Hz, 1.6 Hz, 1H, H^{ar}), 7.69 (d, J = 8.7 Hz, 1H, H^{ar}), 4.39 (q, J = 7.1 Hz 2H, OCH_2), 1.38 (t, J = 7.1 Hz, 3H, CH_3); ^{13}C NMR (125 MHz, $CDCl_3$) δ_C

= 167.4 (s, $COOCH_2$), 143.3 (s, C^{ar}), 140.9 (s, C^{ar}), 137.9 (s, C^{ar}), 125.2 (s, C^{ar}), 124.4 (s, C^{ar}), 118.3 (s, C^{ar}), 114.9 (s, C^{ar}), 61.2 (s, OCH_2), 14.4 (s, CH_3).

The NMR spectra match previously reported data.[2]

1.2 General procedure for N-alkylation and halide exchange

1H-benzimidazol-5-carboxylate (1.00 eq.) and K_2CO_3 (1.70 eq.) were suspended in MeCN (20 mL/mmol). The mixture was treated with RX (6.00 eq.) and stirred at reflux for 24 h. Subsequently the solvent was removed under reduced pressure and the residue was dissolved in CH_2Cl_2. After filtration, the solvent was concentrated in vacuum and the residue was precipitated in ether. Drying the precipitate *in vacuo* afforded the product as pale yellow to brown powder. The respective halide (1.00 eq.) and Ag_2CO_3 (1.14 eq.) were suspended in EtOH (20 mL/mmol). Concentrated HNO_3 (10 drops/mmol) was added and the suspension was stirred for 3.5 h while being shielded from light. After the silver halides were filtered off, concentrated HCl (2.30 eq.) was added dropwise and the solution stirred for 10 min. Afterwards the solution was neutralized by adding saturated $NaHCO_{3(aq)}$ and filtered once more. Subsequently the solvent was evaporated and the residue was dissolved in CH_2Cl_2. After another filtration step, the solution was concentrated and precipitated in *n*-pentane. After drying *in vacuo*, the product could be isolated as white to yellow powder.

1,3-dimethyl-5-(methoxycarbonyl)-1H-benzimidazol-3-ium chloride **(4a)**

850 mg (2.56 mmol, 90%) from **2** (500 mg, 2.84 mmol, 1.00 eq.), K_2CO_3 (667 mg, 4.82 mmol, 1.70 eq.) and MeI (1.06 mL, 17.0 mmol, 6.00 eq.) in MeCN (50.0 mL). ^{1}H NMR (500 MHz, $CDCl_3$) δ_H = 11.3 (s, 1H, CH), 8.42 (s, 1H, H^{ar}), 8.37 (d, J = 1.5 Hz, 1H, H^{ar}), 7.78 (d, J = 1.5 Hz, 1H, H^{ar}), 4.31 (s, 6H, CH_3), 4.02 (s, 3H, OCH_3); ^{13}C NMR (125 MHz, $CDCl_3$) δ_C = 165.2

(s, $COOCH_3$), 134.5 (s, C^{ar}), 131.8 (s, C^{ar}), 129.6 (s, C^{ar}), 128.5 (s, C^{ar}), 114.8 (s, C^{ar}), 112.9 (s, C^{ar}), 52.9 (s, OCH_3), 34.4 (NCH_3), 33.8 (s, NCH_3).

170 mg (706 µmol, 59%) from 1,3-dimethyl-5-(methoxycarbonyl)-1H-benzimidazol-3-ium iodide (400 mg, 1.20 mmol, 1.00 eq.), Ag_2CO_3 (379 mg, 1.37 mmol, 1.14 eq.), HNO_3 (12 drops) and HCl (229 µL, 2.77 mmol, 2.30 eq.) in EtOH (25.0 mL). ^{1}H NMR (500 MHz, $CDCl_3$) δ_H = 11.0 (s, 1H, CH), 8.41 (s, 1H, H^{ar}), 8.34 (vdd, J = 8.7 Hz, 1.5 Hz, 1H, H^{ar}), 7.78 (d, J = 8.7 Hz, 1H, H^{ar}), 4.26 (d, J = 4.3 Hz, 6H, CH_3), 4.01 (s, 3H, OCH_3); ^{13}C NMR (125 MHz, $CDCl_3$) δ_C = 165.3 (s, $COOCH_3$), 147.0 (s, NCN), 134.7 (s, C^{ar}), 131.8 (s, C^{ar}), 129.3 (s, C^{ar}), 128.2 (s, C^{ar}), 114.7 (s, C^{ar}), 112.9 (s, C^{ar}), 53.0 (s, OCH_3), 33.9 (NCH_3), 33.8 (s, NCH_3).

1,3-dimethyl-5-(methoxycarbonyl)-1H-benzimidazol-3-ium chloride **(4b)**

1.20 g (3.33 mmol, 98%) from Methyl 1H-benzimidazol-5-carboxylate (**2**) (600 mg, 3.41 mmol, 1.00 eq.), K_2CO_3 (800 mg, 5.79 mmol, 1.70 eq.) and EtI (1.64 mL, 20.4 mmol, 6.00 eq.) in MeCN (50.0 mL). ^{1}H NMR (500 MHz, $CDCl_3$) δ_H = 11.5 (s, 1H, CH), 8.44 (s, 1H, H^{ar}), 8.36 (d, J = 1.5 Hz, 1H, H^{ar}), 7.79 (d, J = 1.5 Hz, 1H, H^{ar}), 4.73 (vdq, J = 7.4 Hz, 4.0 Hz, 4H, CH_2), 4.03 (s, 3H, OCH_3), 1.83 (vdt, J = 10.0 Hz, 7.5 Hz, 6H, CH_3); ^{13}C NMR (125 MHz, $CDCl_3$) δ_C = 165.3 (s, $COOCH_2$), 143.6 (NCN), 131.1 (s, C^{ar}), 129.3 (s, C^{ar}), 128.2 (s, C^{ar}), 115.0 (s, C^{ar}), 113.5 (s, C^{ar}), 53.0 (s, OCH_3), 43.7 (NCH_2), 43.5 (NCH_2), 14.9 (s, CH_3).

330 mg (1.23 mmol, 88%) from 1,3-diethyl-5-(methoxycarbonyl)-1H-benzimidazol-3-ium iodide (500 mg, 1.39 mmol, 1.00 eq.), Ag_2CO_3 (436 mg, 1.58 mmol, 1.14 eq.), HNO_3 (14 drops) and HCl (264 µL, 3.19 mmol, 2.30 eq.) in EtOH (25.0 mL). ^{1}H NMR (500 MHz, $CDCl_3$) δ_H = 11.0 (s, 1H, CH), 8.42 (s, 1H, H^{ar}), 8.32 (d, J = 8.7 Hz, 1H, H^{ar}), 7.82 (vdd, J = 8.8 Hz, 2.9 Hz, 1H, H^{ar}), 4.69 (vdq, J = 7.4 Hz, 2.0 Hz, 4H, CH_2), 4.00 (s, 3H, OCH_3), 1.77 – 1.65 (m, 6H, CH_3). ^{13}C NMR (125 MHz, $CDCl_3$) δ_C = 165.3 (s, $COOCH_3$), 134.1 (s, C^{ar}), 131.7 (s, C^{ar}), 129.2

(s, C^{ar}), 128.1 (s, C^{ar}), 115.0 (s, C^{ar}), 113.2 (s, C^{ar}), 53.0 (s, OCH_3), 43.3 (NCH_2), 14.8 (s, CH_3), 14.7 (s, CH_3).

1,3-dimethyl-5-(methoxycarbonyl)-1H-benzimidazol-3-ium chloride **(4c)**

937 mg (2.14 mmol, 76%) from **2** (500 mg, 2.84 mmol, 1.00 eq.), K_2CO_3 (667 mg, 4.82 mmol, 1.70 eq.) and BnBr (2.02 mL, 17.0 mmol, 6.00 eq.) in MeCN (50.0 mL). ^{1}H NMR (500 MHz, $CDCl_3$) δ_H = 12.0 (s, 1H, CH), 8.28 (s, 1H, H^{ar}), 8.18 (vdd, *J* = 8.8 Hz, 1.5 Hz, 1H, H^{ar}), 7.62 (m, 3H, H^{ar}), 7.53 (m, 2H, H^{ar}), 7.46 (m, 6H, H^{ar}), 5.89 (s, 4H, CH_2), 3.95 (s, 3H, OCH_3). ^{13}C NMR (125 MHz, $CDCl_3$) δ_C = 165.1 (s, COOMe), 145.3 (NCN), 134.1 (s, C^{ar}), 132.4 (s, C^{ar}), 132.2 (s, C^{ar}), 131.3 (s, C^{ar}), 129.5 (s, C^{ar}), 129.4 (s, C^{ar}), 129.3 (s, C^{ar}), 128.5 (s, C^{ar}), 128.1 (s, C^{ar}) 115.6 (s, C^{ar}), 114.2 (s, C^{ar}), 53.0 (s, OCH_3), 52.2 (s, NCH_2), 52.0 (s, NCH_2).

208 mg (513 µmol, 58%) from 1,3-dibenzyl-5-(methoxycarbonyl)-1H-benzimidazol-3-ium bromide (400 mg, 914 µmol, 1.00 eq.), Ag_2CO_3 (288 mg, 1.04 mmol, 1.14 eq.), HNO_3 (11 drops) and HCl (174 µL, 2.10 mmol, 2.30 eq.) in EtOH (25.0 mL). ^{1}H NMR (500 MHz, $CDCl_3$) δ_H = 11.4 (s, 1H, CH), 8.24 (vd, 1H, *J* = 1.4 Hz, H^{ar}), 8.12 (vdd, *J* = 8.7 Hz, 1.4 Hz, 1H, H^{ar}), 7.69 (d, *J* = 8.8 Hz, 1H, H^{ar}), 7.48 – 7.43 (m, 4H, H^{ar}), 7.37 – 7.27 (m, 6H, H^{ar}), 5.78 (vd, *J* = 8.8 Hz, 4H, CH_2), 3.90 (s, 3H, OCH_3); ^{13}C NMR (125 MHz, $CDCl_3$) δ_C = 165.2 (s, $COOCH_3$), 146.5 (s, NCN), 134.2 (s, C^{ar}), 132.5 (s, C^{ar}), 132.4 (s, C^{ar}), 131.4 (s, C^{ar}), 129.5 (s, C^{ar}), 129.4 (s, C^{ar}), 129.3 (s, C^{ar}), 129.2 (s, C^{ar}), 129.1 (s, C^{ar}), 128.4 (s, C^{ar}), 128.2 (s, C^{ar}), 128.0 (s, C^{ar}), 115.5 (s, C^{ar}), 114.0 (s, C^{ar}) 52.9 (s, OCH_3), 51.8 (NCH_2), 51.7 (s, NCH_2).

1,3-dimethyl-5-(ethoxycarbonyl)-1H-benzimidazol-3-ium chloride **(5a)**

400 mg (1.07 mmol, 68%) from **3** (300 mg, 1.58 mmol, 1.00 eq.), K_2CO_3 (371 mg, 2.68 mmol, 1.70 eq.) and MeI (761 µL, 9.46 mmol, 6.00 eq.) in MeCN (30.0 mL). ^{1}H NMR (500 MHz, $CDCl_3$) δ_H = 11.3 (s, 1H, CH), 8.34 (s, 1H, H^{ar}), 8.31 (dd, *J* = 8.7 Hz, 1.3 Hz, 1H, H^{ar}), 7.76 (dd, *J* = 8.7 Hz, 1.5 Hz, 1H, H^{ar}), 4.46 (q, *J* = 7.1 Hz, 2H, OCH_2), 4.16 (s, 6H, NCH_3), 1.45 (t, *J* =

7.1 Hz, 3H, CH_3); ^{13}C NMR (125 MHz, $CDCl_3$) δ_C = 164.8 (s, $COOCH_2$), 144.9 (s, NCN), 134.5 (s, C^{ar}), 131.7 (s, C^{ar}), 129.7 (s, C^{ar}), 128.2 (s, C^{ar}), 114.7 (s, C^{ar}), 113.3 (s, C^{ar}), 62.1 (s, OCH_3), 34.8 (NCH_3), 34.5 (s, NCH_3), 14.3 (s, CH_3).

530 mg (2.08 mmol, 80%) from 1,3-dimethyl-5-(ethoxycarbonyl)-1H-benzimidazol-3-ium iodide (900 mg, 2.60 mmol, 1.00 eq.), Ag_2CO_3 (817 mg, 2.96 mmol, 1.14 eq.), HNO_3 (25 drops) and HCl (495 µL, 5.98 mmol, 2.30 eq.) in EtOH (50.0 mL). ^1H NMR (500 MHz, $CDCl_3$) δ_H = 10.9 (s, 1H, CH), 8.35 (s, 1H, H^{ar}), 8.30 (d, J = 8.7 Hz, 1H, H^{ar}), 7.71 (d, J = 8.7 Hz, 1H, H^{ar}), 4.41 (q, J = 7.1 Hz, 2H, OCH_2), 4.19 (d, J = 6.8 Hz, 6H, NCH_3), 1.40 (t, J = 7.1 Hz, 3H, CH_3); ^{13}C NMR (125 MHz, $CDCl_3$) δ_C = 164.9 (s, $COOCH_2$), 146.1 (s, NCN), 134.5 (s, C^{ar}), 131.8 (s, C^{ar}), 129.6 (s, C^{ar}), 128.1 (s, C^{ar}), 114.6 (s, C^{ar}), 113.0 (s, C^{ar}), 62.1 (s, OCH_2), 33.8 (NCH_3), 33.7 (s, NCH_3), 14.3 (s, CH_3).

1,3-diethyl-5-(ethoxycarbonyl)-1H-benzimidazol-3-ium chloride **(5b)**

883 mg (2.55 mmol, 97%) from **3** (500 mg, 2.63 mmol, 1.00 eq.), K_2CO_3 (618 mg, 4.47 mmol, 1.70 eq.) and EtI (982 µL, 15.8 mmol, 6.00 eq.) in MeCN (50.0 mL). ^1H NMR (500 MHz, $CDCl_3$) δ_H = 11.1 (s, 1H, CH), 8.44 (s, 1H, H^{ar}), 8.36 (vdd, J = 8.8 Hz, 1.4 Hz, 1H, H^{ar}), 7.83 (vdd, J = 8.7 Hz, 1.54 Hz, 1H, H^{ar}), 4.68 (vdq, J = 7.4 Hz, 3.6 Hz, 4H, CH_2), 4.50 (q, J = 7.1 Hz 2H, OCH_2), 1.74 (vdt, J = 9.7 Hz, 7.3 Hz, 6H, CH_3), 1.48 (t, J = 7.1 Hz, 3H, CH_3); ^{13}C NMR (125 MHz, $CDCl_3$) δ_C = 164.8 (s, $COOCH_2$), 146.7 (s, NCN), 134.0 (s, C^{ar}), 131.2 (s, C^{ar}), 129.7 (s, C^{ar}), 128.1 (s, C^{ar}), 114.9 (s, C^{ar}), 112.9 (s, C^{ar}), 62.2 (s, OCH_2), 43.3 (vd, J = 3.2 Hz, NCH_2), 14.9 (s, CH_3), 14.7 (s, CH_3), 14.3 (s, CH_3).

422 mg (1.66 mmol, 80%) from 1,3-diethyl-5-(ethoxycarbonyl)-1H-benzimidazol-3-ium iodide (717 mg, 1.92 mmol, 1.00 eq.), Ag_2CO_3 (602 mg, 2.18 mmol, 1.14 eq.), HNO_3 (20 drops) and HCl (365 µL, 4.41 mmol, 2.30 eq.) in EtOH (50.0 mL). ^1H NMR (500 MHz, $CDCl_3$)

δ_H = 11.4 (s, 1H, CH), 8.42 (s, 1H, H^{ar}), 8.36 (dd, *J* = 8.7 Hz, 1.4 Hz, 1H, H^{ar}), 7.79 (dd, *J* = 8.7 Hz, 1.54 Hz, 1H, H^{ar}), 4.73 (dq, *J* = 7.4 Hz, 1.3 Hz, 4H, CH_2), 4.48 (q, *J* = 7.2 Hz 2H, OCH_2), 1.81 (dt, *J* = 10.0 Hz, 7.4 Hz, 6H, CH_3), 1.46 (t, *J* = 7.2 Hz, 3H, CH_3); ^{13}C NMR (125 MHz, $CDCl_3$) δ_C = 164.8 (s, $COOCH_2$), 143.3 (NCN), 133.9 (s, C^{ar}), 131.1 (s, C^{ar}), 129.6 (s, C^{ar}), 128.2 (s, C^{ar}), 114.9 (s, C^{ar}), 113.6 (s, C^{ar}), 62.1 (s, OCH_3), 43.7 (NCH_2), 43.5 (NCH_2), 14.9 (s, CH_3), 14.8 (s, CH_3), 14.3 (s, CH_3) .

1,3-dibenzyl-5-(ethoxycarbonyl)-1H-benzimidazol-3-ium chloride **(5c)**

933 mg (2.07 mmol, 98%) from **3** (400 mg, 2.10 mmol, 1.00 eq.), K_2CO_3 (494 mg, 3.58 mmol, 1.70 eq.) and BnBr (1.50 mL, 12.6 mmol, 6.00 eq.) in MeCN (40.0 mL). ^{1}H NMR (500 MHz, $CDCl_3$) δ_H = 12.1 (s, 1H, CH), 8.30 (s, 1H, H^{ar}), 8.21 (d, *J* = 8.5 Hz, 1H, H^{ar}), 7.72-7.36 (m, 11H, H^{ar}), 5.93 (s, 4H, CH_2), 4.43 (q, *J* = 7.1 Hz, 2H, OCH_2), 1.42 (t, *J* = 7.1 Hz, 3H, CH_3); ^{13}C NMR (125 MHz, $CDCl_3$) δ_C = 164.6 (s, $COOCH_2$), 134.0 (s, C^{ar}), 132.5 (s, C^{ar}), 132.3 (s, C^{ar}), 131.2 (s, C^{ar}), 129.5 (s, C^{ar}), 129.4 (s, C^{ar}), 129.3 (s, C^{ar}), 129.2 (s, C^{ar}), 128.5 (s, C^{ar}), 128.4 (s, C^{ar}), 128.0 (s, C^{ar}), 115.5 (s, C^{ar}), 114.3 (s, C^{ar}), 61.9 (s, OCH_2), 52.0 (NCH_2), 51.9 (s, NCH_2), 14.2 (s, CH_3).

72.0 mg (177 µmol, 67%) from 1,3-diethyl-5-(ethoxycarbonyl)-1H-benzimidazol-3-ium bromide (120 mg, 266 µmol, 1.00 eq.), Ag_2CO_3 (83.6 mg, 303 µmol, 1.14 eq.), HNO_3 (3 drops) and HCl (50.6 µL, 612 µmol, 2.30 eq.) in EtOH (5.00 mL). ^{1}H NMR (500 MHz, $CDCl_3$) δ_H = 11.3 (s, 1H, CH), 8.21 (s, 1H, H^{ar}), 8.12 (dd, *J* = 8.7 Hz, 1.4 Hz, 1H, H^{ar}), 7.64 (d, *J* = 8.7 Hz, 1H, H^{ar}), 7.46-7.42 (m, 4H, H^{ar}), 7.35-7.25 (m, 6H, H^{ar}), 5.77 (s, 2H, NCH_2), 5.76 (s, 2H, NCH_2), 4.34 (q, *J* = 7.1 Hz, 2H, OCH_2), 1.35 (t, *J* = 7.1 Hz, 3H, CH_3); ^{13}C NMR (125 MHz, $CDCl_3$) δ_C = 164.7 (s, $COOCH_2$), 146.5 (NCN), 134.1 (s, C^{ar}), 132.5 (s, C^{ar}), 132.4 (s, C^{ar}), 131.4 (s, C^{ar}), 129.5 (s, C^{ar}), 129.4 (s, C^{ar}), 129.3 (s, C^{ar}), 128.4 (s, C^{ar}), 128.0 (s, C^{ar}), 115.5 (s, C^{ar}), 114.0 (s, C^{ar}), 62.0 (s, OCH_2), 51.9 (NCH_2), 51.8 (s, NCH_2), 14.2 (s, CH_3).

1.3 General procedure for silver complexation

Benzimidazoleium-5-carboxylate chloride (1.00 eq.) and Ag_2O (0.50 eq.) were dissolved in CH_2Cl_2 (25 mL/mmol) and stirred for 24 h while being shielded from light. Subsequently the solution was filtered over Celite, concentrated and the residue precipitated in *n*-pentane. After drying *in vacuo*, the product could be isolated as white powder.

[5-methoxycarbonyl-1,3-dimethylbenzimidazol-2-ylidene] silver(I) chlorido **(6a)**

385 mg (1.11 mmol, 89%) from **04a** (300 mg, 1.25 mmol, 1.00 eq.), Ag_2O (144 mg, 623 µmol, 0.50 eq.) in CH_2Cl_2 (30.0 mL). ^{1}H NMR (500 MHz, DMSO-d_6) δ_H = 8.19 (s, 1H, H^{ar}), 8.14 (vdd, J = 8.5 Hz, 1.5 Hz, 1H, H^{ar}), 7.50 (vdd, J = 8.6 Hz, 0.6 Hz, 1H, H^{ar}), 4.11 (d, J = 6.7 Hz, 6H, NCH_3), 3.99 (s, 3H, OCH_3); ^{13}C NMR (125 MHz, $CDCl_3$) δ_C = 166.3 (s, $COOCH_3$), 137.1 (s, C^{ar}), 134.2 (s, C^{ar}), 126.5 (s, C^{ar}), 125.8 (s, C^{ar}), 113.2 (s, C^{ar}), 111.0 (s, C^{ar}), 52.7 (s, OCH_3), 36.0 (s, NCH_3).

[5-methoxycarbonyl-1,3-diethylbenzimidazol-2-ylidene] silver(I) chlorido **(6b)**

34.0 mg (90.5 µmol, 35%) from **04b** (70.0 mg, 261 µmol, 1.00 eq.), Ag_2O (36.2 mg, 133 µmol, 0.50 eq.) in CH_2Cl_2 (50.0 mL). ^{1}H NMR (500 MHz, DMSO-d_6) δ_H = 8.43 (s, 1H, H^{ar}), 8.07 (d, J = 8.5 Hz, 1H, H^{ar}), 7.99 (d, J = 8.6 Hz, 1H, H^{ar}), 4.63 (q, J = 7.3 Hz, 4H, CH_2), 3.93 (s, 3H, OCH_3), 1.49 (t, J = 7.5 Hz, 6H, CH_3); ^{13}C NMR (125 MHz, $CDCl_3$) δ_C = 198.1 (s, NCN), 166.7 (s, $COOCH_3$), 136.6 (s, C^{ar}), 133.6 (s, C^{ar}), 125.4 (s, C^{ar}), 124.9 (s, C^{ar}), 112.9 (s, C^{ar}), 110.6 (s, C^{ar}), 52.5 (s, OCH_3), 44.3 (d, J = 4.1 Hz, NCH_2), 16.1 (s, CH_3), 16.0 (s, CH_3).

[5-methoxycarbonyl-1,3-dibenzylbenzimidazol-2-ylidene] silver(I) chlorido **(6c)**

Yield: 452 mg (904 µmol, 89%) from **04c** (400 mg, 1.02 mmol, 1.00 eq.), Ag_2O (142 mg, 611 µmol, 0.50 eq.) in CH_2Cl_2 (25.0 mL). ^{1}H NMR (500 MHz, $CDCl_3$) δ_H = 8.29 (s, 1H, H^{ar}), 7.99 (vdd, J = 8.7 Hz, 1.5 Hz, 1H, H^{ar}), 7.87 (d, J = 8.7 Hz, 1H, H^{ar}), 7.38-7.27 (m, 10H, H^{ar}),

5.86 (s, 2H, CH_2), 5.80 (s, 2H, CH_2) 3.86 (s, 3H, OCH_3); ^{13}C NMR (125 MHz, $CDCl_3$) δ_C = 196.2 (s, NCN), 166.2 (s, $COOCH_3$), 136.9 (s, C^{ar}), 135.2 (s, C^{ar}), 135.1 (s, C^{ar}), 134.0 (s, C^{ar}), 129.1 (s, C^{ar}), 129.0 (s, C^{ar}), 128.4 (s, C^{ar}), 127.3 (s, C^{ar}), 126.2 (s, C^{ar}), 125.6 (s, C^{ar}), 113.6 (s, C^{ar}), 111.8 (s, C^{ar}), 53.5 (s, OCH_3), 53.2 (NCH_2), 52.5 (s, NCH_2).

[5-ethoxycarbonyl-1,3-dimethylbenzimidazol-2-ylidene] silver(I) chlorido **(7a)**

434 mg (1.20 mmol, 92%) from **05a** (380 mg, 1.49 mmol, 1.00 eq.), Ag_2O (173 mg, 746 µmol, 0.50 eq.) in CH_2Cl_2 (40.0 mL). ^1H NMR (500 MHz, $CDCl_3$) δ_H = 8.21 (s, 1H, H^{ar}), 8.17 (vdd, J = 8.5 Hz, 1.5 Hz, 1H, H^{ar}), 7.53 (d, J = 8.5 Hz 1H, H^{ar}), 4.45 (q, J = 7.0 Hz, 2H, OCH_2), 4.12 (s, 6H, NCH_3), 1.45 (t, J = 7.0 Hz, 3H, CH_3); ^{13}C NMR (125 MHz, $CDCl_3$) δ_C = 191.8 (s, NCN), 165.8 (s, $COOCH_2$), 137.1 (s, C^{ar}), 134.2 (s, C^{ar}), 126.9 (s, C^{ar}), 125.9 (s, C^{ar}), 113.2 (s, C^{ar}), 111.0 (s, C^{ar}), 61.7 (s, OCH_2), 36.1 (d, J = 3.6 Hz, NCH_3), 14.4 (s, CH_3).

[5-ethoxycarbonyl-1,3-diethylbenzimidazol-2-ylidene] silver(I) chlorido **(7b)**

507 mg (1.30 mmol, 74%) from (**5b**) (450 mg, 1.59 mmol, 1.00 eq.), Ag_2O (205 mg, 883 µmol, 0.50 eq.) in CH_2Cl_2 (45.0 mL). ^1H NMR (500 MHz, $CDCl_3$) δ_H = 8.22 (s, 1H, H^{ar}), 8.14 (vdd, J = 8.6 Hz, 1.4 Hz, 1H, H^{ar}), 7.55 (d, J = 8.6 Hz 1H, H^{ar}), 4.52 (vdq, J = 9.0 Hz, 7.3 Hz, 4H, NCH_2), 4.45 (q, J = 7.1 Hz, 2H, OCH_2), 1.57 (vdt, J = 9.0 Hz, 7.3 Hz, 6H, CH_3), 1.44 (t, J = 7.1 Hz, 3H, CH_3); ^{13}C NMR (125 MHz, $CDCl_3$) δ_C = 189.3 (s, NCN), 165.8 (s, $COOCH_2$), 136.2 (s, C^{ar}), 133.3 (s, C^{ar}), 126.8 (s, C^{ar}), 125.7 (s, C^{ar}), 113.3 (s, C^{ar}), 111.2 (s, C^{ar}), 61.7 (s, OCH_2), 45.0 (d, J = 2.7 Hz, NCH_2), 16.1 (s, CH_3), 16.0 (s, CH_3), 14.4 (s, CH_3).

Chlorido [5-ethoxycarbonyl-1,3-dibenzylbenzimidazol-2-ylidene] silver(I) chlorido **(7c)**

313 mg (609 µmol, 83%) from **5c** (300 mg, 737 µmol, 1.00 eq.), Ag_2O (85.4 mg, 369 µmol, 0.50 eq.) in CH_2Cl_2 (15.0 mL). ^1H NMR (500 MHz, $CDCl_3$) δ_H = 8.10 (s, 1H, H^{ar}), 8.01 (d, J = 8.6 Hz, 1H, H^{ar}), 7.40 – 7.30 (m, 11H, H^{ar}), 5.68 (s, 4H, NCH_2), 4.37 (q, J = 7.1 Hz, 2H, OCH_2), 1.37 (t, J = 7.1 Hz, 3H, CH_3); ^{13}C NMR (125 MHz, $CDCl_3$) δ_C = 196.0 (s, NCN), 165.7 (s,

$COOCH_2$), 136.8 (s, C^{ar}), 135.0 (s, C^{ar}), 134.0 (s, C^{ar}), 129.1 (s, C^{ar}), 128.5 (s, C^{ar}), 127.4 (s, C^{ar}), 127.3 (s, C^{ar}), 126.7 (s, C^{ar}), 113.7 (s, C^{ar}), 111.7 (s, C^{ar}), 61.5 (s, OCH_2), 53.5 (NCH_2), 53.3 (s, NCH_2), 14.3 (s, CH_3).

1.4 Procedures for the synthesis of the precursors of clickable complexes **16** and **22**

Methyl 1-(prop-2-yn-1-yl)-1H-benzimidazol-5-carboxylate **(14)**

2 (600 mg, 3.41 mmol, 1.00 eq.) and K_2CO_3 (471 mg, 3.41 mmol, 1.00 eq.) were suspended in DMF (50 mL). The mixture was treated with bromopropyne (760 µL, 6.82 mmol, 80% in toluene, 2.00 eq.) and stirred at 60 °C for 24 h. Subsequently the solvent was removed under reduced pressure and the residue was dissolved in chloroform (150 mL). Water (2 · 150 mL) was added to remove K_2CO_3 and the combined aqueous phases were extracted with chloroform (150 mL). The combined organic phases were dried over Na_2SO_4, filtered and the solvent was concentrated in vacuum. The crude product was purified by column chromatography (Silica gel 60, EtOAc/MeOH 95:5) affording it as brown powder (594 mg, 2.76 mmol, 81%) after drying *in vacuo*. Rf = 0.52 (EtOAc/MeOH 95:5); ^{1}H NMR (500 MHz, $CDCl_3$) δ_H = 8.54 (dd, *J* = 1.5 Hz, 0.7 Hz, 1H, H^{ar}), 8.24 (dd, *J* = 1.5 Hz, 0.7 Hz, 1H, H^{ar}), 8.16 (s, 1H, H^{ar}), 8.11 (s, 1H, H^{ar}), 8.08 (dd, *J* = 8.5 Hz, 1.5 Hz, 1H, H^{ar}), 8.03 (dd, *J* = 8.5 Hz, 1.6 Hz, 1H, H^{ar}), 7.83 (dd, *J* = 8.5 Hz, 0.7 Hz, 1H, H^{ar}), 7.51 (dd, *J* = 8.6 Hz, 0.6 Hz, 1H, H^{ar}), 4.99 (d, *J* = 2.6 Hz, 4H, NCH_2), 3.97 (s, 6H, OMe), 2.54 (dt, *J* = 6.1 Hz, 2.6 Hz, 2H, CH). ^{13}C NMR (125 MHz, $CDCl_3$) δ_C = 167.4 (s, COOMe), 167.3 (s, COOMe), 147.4 (s, C^{ar}), 144.8 (s, C^{ar}), 143.9 (s, C^{ar}), 143.6 (s, C^{ar}), 136.5 (s, C^{ar}), 133.1 (s, C^{ar}), 125.3 (s, C^{ar}), 125.0 (s, C^{ar}), 124.9 (s, C^{ar}), 124.0 (s, C^{ar}), 123.0 (s, C^{ar}), 120.3 (s, C^{ar}), 112.0 (s, C^{ar}), 109.5 (s, C^{ar}), 75.6 (s, CH), 75.4 (s, CH), 52.3 (OMe), 52.2 (OMe), 34.9 (NCH_2).

5-(methoxycarbonyl)-1,3-di(prop-2-yn-1-yl)-1H-benzimidazol-3-ium chloride **(15)**

14 (561 mg, 2.62 mmol, 1.00 eq.) and bromopropyne (1.16 mL, 10.5 mmol, 80% in toluene, 4.00 eq.) were dissolved in 1,4-dioxane (20 mL). The mixture was stirred at 130 °C for 24 h. Subsequently the solution was cooled to rt and filtered. The filter cake was rinsed with cold 1,4-dioxane and dried in vacuum affording the product as brown powder (784 mg, 2.35 mmol, 90%) after drying *in vacuo*. ^{1}H NMR (500 MHz, $CDCl_3$) δ_H = 11.8 (s, 1H, NCHN), 8.61 (s, 1H, H^{ar}), 8.39 (dd, *J* = 8.8 Hz, 1.4 Hz, 1H, H^{ar}), 8.00 (d, *J* = 8.8 Hz, 1H, H^{ar}), 5.68 (d, *J* = 2.6 Hz, 4H, NCH_2), 4.03 (s, 3H, OMe), 2.71 (dt, *J* = 10.9 Hz, 2.6 Hz, 2H, CH). ^{13}C NMR (125 MHz, $CDCl_3$) δ_C = 166.1 (s, COOMe), 144.9 (s, C^{ar}), 133.6 (s, C^{ar}), 130.9 (s, C^{ar}), 129.9 (s, C^{ar}), 128.7 (s, C^{ar}), 115.7 (s, C^{ar}), 114.0 (s, C^{ar}), 78.4 (s, CH), 78.2 (s, CH), 53.1 (OMe), 38.4 (NCH_2).

5-(methoxycarbonyl)-1,3-di(prop-2-yn-1-yl)-1H-benzimidazol-3-ium bromide (400 mg, 1.20 mmol, 1.00 eq.) and Ag_2CO_3 (377 mg, 1.37 mmol, 1.14 eq.) were suspended in EtOH (25 mL). Concentrated HNO_3 (12 drops) was added and the suspension was stirred for 3.5 h while being shielded from light. After the silver halides were filtered off, concentrated HCl (300 µL, 2.76 mmol, 2.30 eq.) was added dropwise and the solution stirred for 10 min. Afterwards the solution was neutralized by adding saturated $NaHCO_{3(aq)}$ and filtered once more. Subsequently the solvent was evaporated and the residue was dissolved in CH_2Cl_2. After another filtration step, the solution was concentrated and precipitated in *n*-pentane. After drying *in vacuo*, the product could be isolated as yellow powder (202 mg, 700 µmol, 58%). ^{1}H NMR (500 MHz, $CDCl_3$) δ_H = 11.2 (s, 1H, NCHN), 8.55 (s, 1H, H^{ar}), 8.33 (dd, *J* = 8.7 Hz, 1.5 Hz, 1H, H^{ar}), 8.00 (d, *J* = 8.8 Hz, 1H, H^{ar}), 5.52 (t, *J* = 3.2 Hz, 4H, NCH_2), 4.03 (s, 3H, OMe), 2.69 (dt, *J* = 10.2 Hz, 2.6 Hz, 2H, CH).

1-((allyloxy)carbonyl)-1H-benzimidazol-5-carboxylic acid **(17)**

1 (1.30 g, 8.02 mmol, 1.00 eq.) was dissolved in 10% $Na_2CO_{3(aq.)}$ (22.5 mL) and 1,4-dioxane (13.5 mL) and cooled to 0 °C. Allyl chloroformate (1.71 mL, 16.0 mmol, 2.00 eq.) was added dropwise and the mixture was left stirring at et for 16 h. Afterwards the solution was washed with Et_2O (3 · 50 mL) and the aqueous phase was acidified with 2 n HCl. After extraction with EtOAc (5 · 60 mL), the combined organic phases were dried over $MgSO_4$, filtrated and the solvent was evaporated. The residue was dried in vacuo affording **17** (1.91 g, 7.78 mmol, 97%) as beige powder. ^{1}H NMR (500 MHz, MeOD) δ_H = 8.56 (s, 1H, H^{ar}), 8.46 (s, 1H, H^{ar}), 7.90 – 7.85 (m, 1H, H^{ar}), 7.56 (d, *J* = 8.4 Hz, 1H, H^{ar}), 6.04 – 5.96 (m, 1H, H^{alloc}), 5.41 – 5.36 (m, 1H, H^{alloc}), 5.25 (d, *J* = 10.5 Hz, 1H, H^{alloc}), 4.86 (d, *J* = 6.9 Hz, 2H, H^{alloc}); ^{13}C NMR (125 MHz, MeOD) δ_C = 168.3 (s, COOH), 148.7 (s), 146.2 (s), 130.9 (s), 126.7 (s), 125.8 (s), 124.0 (s), 121.5 (s), 119.3 (s), 119.2 (s), 116.1 (s), 113.8 (s), 68.6 (s).

Only one regioisomer shown.

1-allyl 5-((2,3-dimethylcycloprop-2-en-1-yl)methyl) 1H-benzimidazol-1,5-dicarboxylate **(18)**

17 (1.86 g, 7.55 mmol, 1.30 eq.) was suspended in dry CH_2Cl_2 (100 mL) and cooled to 0 °C. DMAP (922 mg, 7.55 mmol, 1.30 eq.) and EDC·HCl (1.45 g, 7.55 mmol, 1.30 eq.) were added portionwise and the solution was left stirring at 0 °C for 1h after which 2,3-Dimethyl-2-cyclopropene-1-methanol (570 mg, 5.81 mmol, 1.00 eq.) in dry CH_2Cl_2 (30 mL) was added dropwise over a period of 30 min. After complete addition, stirring was continued for 24 h at rt. Consequently the solution was diluted with EtOAc and washed with 0.5 m H_2SO_4. The aqueous phase was extracted with EtOAc (3 · 100 mL) and the combined organic phases were dried over Na_2SO_4. The solvent was evaporated after filtration and the residue was purified via column chromatography (Cyclohexane/EtOAc 3:1) affording the ester as yellowish oil (1.10 g, 3.37 mmol, 58%). Rf (Cyclohexane/EtOAc 3:1): 0.20; 0.16; ^{1}H NMR (500 MHz, $CDCl_3$) δ_H = 8.48 (s, 1H, H^{ar}), 8.45 (d, *J* = 1.5 Hz, 1H, H^{ar}), 8.09 (dd, *J* = 8.5 Hz, 1.5 Hz, H^{ar}), 8.00 (d, *J* =

8.6 Hz, 1H, H^{ar}), 6.08 – 6.00 (m, 1H, H^{Alloc}), 5.47 (dd, *J* = 17.2 Hz, 1.4 Hz, 1H, H^{Alloc}), 5.38 (dd, *J* = 10.4 Hz, 1.2 Hz, 1H, H^{Alloc}), 4.94 (d, *J* = 8.6 Hz, 2H, CH_2^{Alloc}), 4.20 (d, *J* = 5.2 Hz, OCH_2), 2.00 (s, 6H, CH_3), 1.63 (t, *J* = 5.2 Hz, 1H, CH); ^{13}C NMR (125 MHz, $CDCl_3$) δ_C = 166.5 (s, $COOCH_2$), 148.9 (s, $NCOOCH_2$), 143.8 (s, NCN), 134.2 (s, C^{ar}), 130.4 (s, C^{ar}), 127.7 (s, C^{ar}), 126.9 (s, C^{ar}), 122.5 (s, C^{ar}), 120.8 (s, C^{ar}), 114.0 (s, C^{ar}), 109.7 (s, C=C), 72.7 (s, OCH_2), 68.7 (s, OCH_2), 26.9 (s), 19.2 (s), 10.4 (s, CH_3).

Only one regioisomer shown.

(2,3-dimethylcycloprop-2-en-1-yl)methyl 1H-benzimidazol-5-carboxylate **(19)**

18 (450 mg, 1.38 mmol, 1.00 eq.) was dissolved in dry THF (10 mL) and Et_2NH (428 µL, 4.14 mmol, 3.00 eq.), dppb (29.4 mg, 68.9 µmol, 0.05 eq.) and $Pd(dba)_2$ (39.6 mg, 68.9 µmol, 0.05 eq.) were added. The solution was left stirring at rt for 1h after which it was filtrated over a bed of Celite® and silica. The solvent was evaporated and the residue was purified via column chromatography (EtOAc/MeOH 98:2) affording the ester as yellow oil (250 mg, 1.03 mmol, 75%). Rf (Cyclohexane/EtOAc 3:1): 0.24; ^1H NMR (500 MHz, MeOD) δ_H = 8.33 (s, 2H, H^{ar}), 7.98 (dd, *J* = 8.5 Hz, 1.5 Hz, 1H, H^{ar}), 7.67 (d, *J* = 8.6 Hz, H^{ar}), 4.24 (d, *J* = 5.0 Hz, 1H, H^{ar}), 2.04 (s, 6H, CH_3), 1.67 (t, *J* = 5.0 Hz, 1H, CH); ^{13}C NMR (125 MHz, MeOD) δ_C = 167.3 (s, $COOCH_2$), 143.7 (s, NCN), 123.6 (s, C^{ar}), 109.7 (s, C=C), 71.9 (s, OCH_2), 38.6 (s, OCH_2), 19.2 (s, CH), 8.8 (s, CH_3).

5-(((2,3-dimethylcycloprop-2-en-1-yl)methoxy)carbonyl)-1,3-diethyl-1H-benzimidazol-3-ium iodide **(20)**

19 (275 mg, 1.14 mmol, 1.00 eq.) and K_2CO_3 (314 mg, 2.27 mmol, 2.00 eq.) were suspended in MeCN (20 mL). The mixture was treated with EtI (1.64 mL, 20.5 mmol, 18.0 eq.) and stirred

at 70 °C for 24 h. Subsequently the solvent was removed under reduced pressure and the residue was dissolved in CH_2Cl_2. After filtration, the solvent was evaporated affording the ylidine iodide as yellow powder (246 mg, 825 µmol, 72%). ^{1}H NMR (500 MHz, $CDCl_3$) δ_H = 11.25 (s, NC*H*N), 8.41 (d, *J* = 1.4 Hz, 1H, H^{ar}), 8.34 (dd, *J* = 8.7 Hz, 1.5 Hz, 1H, H^{ar}), 7.81 (d, *J* = 8.8 Hz, H^{ar}), 4.74 (vp, *J* = 7.3 Hz, 4H, NCH_2), 4.29 (d, *J* = 5.2 Hz, 2H, CH_2), 2.02 (s, 6H, CH_3), 1.80 (dt, *J* = 9.2 Hz, 7.3 Hz, 6H, CH_3), 1.67 (t, *J* = 5.2 Hz, 1H, CH); ^{13}C NMR (125 MHz, $CDCl_3$) δ_C = 164.9 (s, $COOCH_2$), 143.5 (s, NCN), 133.8 (s, C^{ar}), 131.1 (s, C^{ar}), 130.3 (s, C^{ar}), 128.2 (s, C^{ar}), 114.9 (s, C^{ar}), 113.1 (s, C^{ar}), 109.6 (s, C=C), 73.9 (s, OCH_2), 43.5 (d, *J* = 18.2 Hz, CH_3), 19.3 (s, CH), 14.9 (d, *J* = 3.5 Hz, CH_3), 10.5 (s, CH_3).

(5-(((2,3-dimethylcycloprop-2-en-1-yl)methoxy)carbonyl)-1,3-diethylbenzimidazol-2-ylidene silver(I) iodide **(21)**

20 (88.0 mg, 206 µmol, 1.00 eq.) was dissolved in dry DCM (10 mL). The solution was shielded from light before Ag_2O (28.7 mg, 124 µmol, 0.60 eq.) was added. The mixture was stirred at rt for 18 hours after which the mixture was filtered over Celite® and the solvent was evaporated. Redissolving the residue in DCM and precipitating the complex in *n*-pentane afforded **21** as white powder (64.0 mg, 63.8 µmol, 58%). ^{1}H NMR (500 MHz, $CDCl_3$) δ_H = 8.16 (d, *J* = 1.4 Hz, 1H, H^{ar}), 8.07 (dd, *J* = 8.5 Hz, 1.4 Hz, 1H, H^{ar}), 7.45 (d, *J* = 8.5 Hz, H^{ar}), 4.61 (vp, *J* = 7.1 Hz 4H, NCH_2), 4.26 (d, *J* = 5.1 Hz, 2H, CH_2), 2.03 (s, 6H, CH_3), 1.68 (t, *J* = 5.1 Hz, 1H, CH), 1.54 (dt, *J* = 7.2 Hz, 5.7 Hz, 6H, CH_3); ^{13}C NMR (125 MHz, $CDCl_3$) δ_C = 197.0 (s, N*C*N), 166.3 (s, $COOCH_2$), 136.4 (s, C^{ar}), 133.5 (s, C^{ar}), 126.3 (s, C^{ar}), 124.8 (s, C^{ar}), 112.8 (s, C^{ar}), 110.5 (s, C^{ar}), 109.7 (s, C=C), 72.9 (s, OCH_2), 44.2 (s, CH_3), 19.3 (s, CH), 16.0 (d, *J* = 9.0 Hz, CH_3), 10.4 (s, CH_3).

2. Biological evaluation

2.1 Stock solutions

The test compounds were dissolved in DMSO with a concentration of 10 mM and stored at -23 °C. Prior to biological experiments they were diluted to desired concentration with sterile Millipore water.

2.2 Cell culture conditions

518A2 human melanoma cells (Department of Radiotherapy & Radiobiology, University Hospital Vienna, Austria), HCT116^{wt} (DSMZ ACC-581) and its HCT116$^{p53-/-}$ knockout mutant colon carcinoma cells, U87 glioblastoma cells (ATCC HTB-14), EA.hy926 somatic cell hybrid cells (ATCC CRL-2922), HeLa cervix carcinoma cells (DSMZ ACC-57), MCF-7 breast cancer cells (DSMZ ACC-115), HT-29 cisplatin resistant colon cancer cells (DSMZ ACC-299) and non-malignant human dermal fibroblasts HDFa (ATCC PCS-201-012) were cultured in Dulbeccos Modified Eagle medium (PAN biotech), supplemented with 10% (v/v) fetale bovine serum (Sigma Aldrich) and 1% (v/v) ZellShield (Minerva Biolabs) at 37 °C under 95% humidity and 5% CO_2. If not noted otherwise, all bioassay steps including cells were conducted under these standard cell culture conditions.

Appendix

NMR spectra of Pt(II) complexes

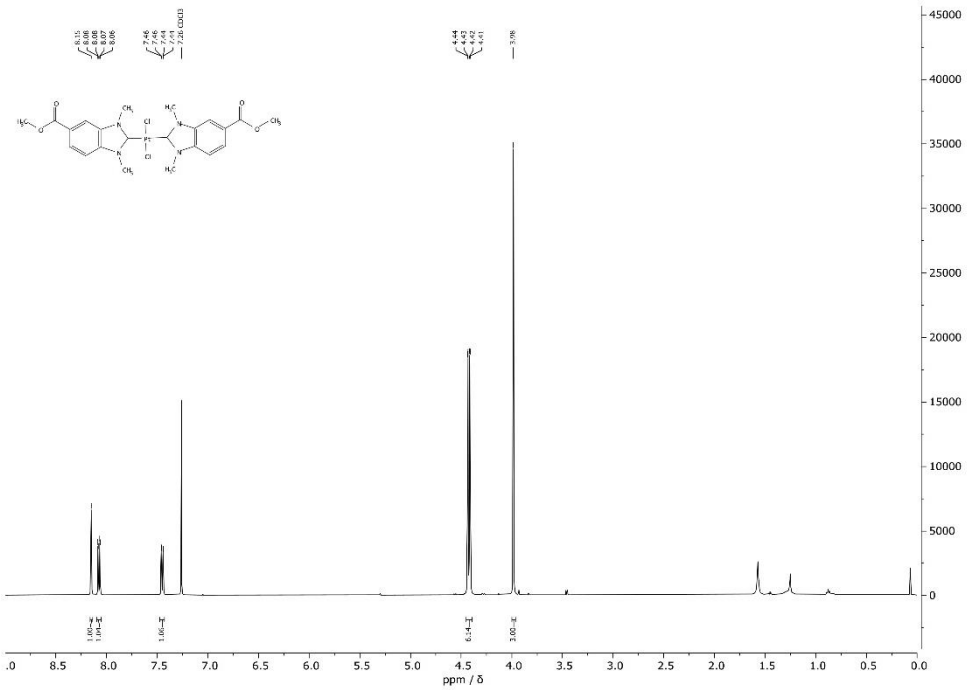

Fig. 1. ^{1}H-NMR spectrum of **8a** in $CDCl_3$.

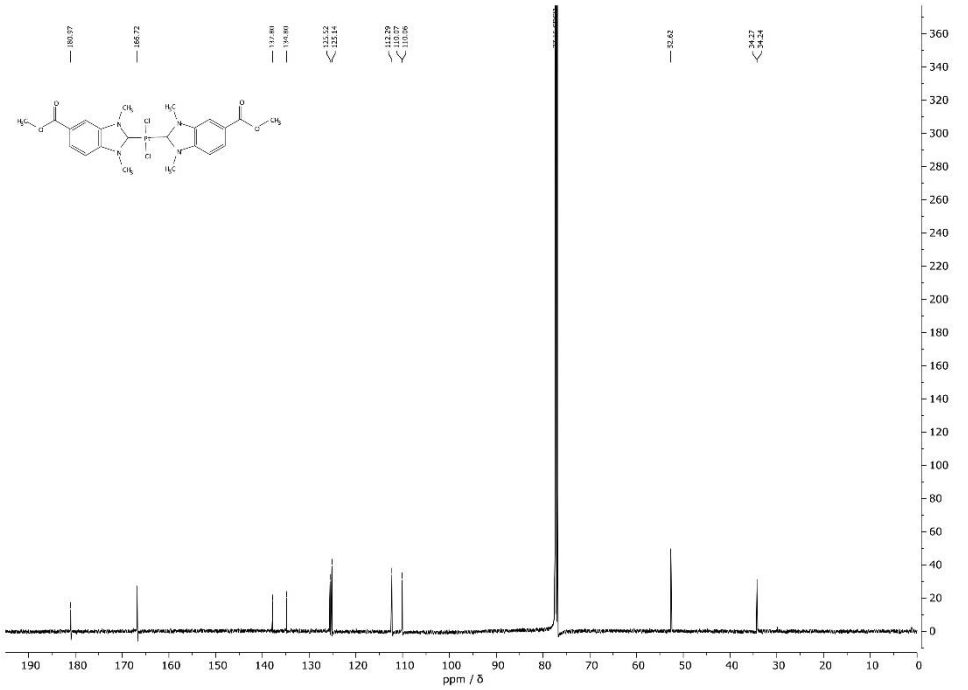

Fig. 2. ^{13}C-NMR spectrum of **8a** in $CDCl_3$.

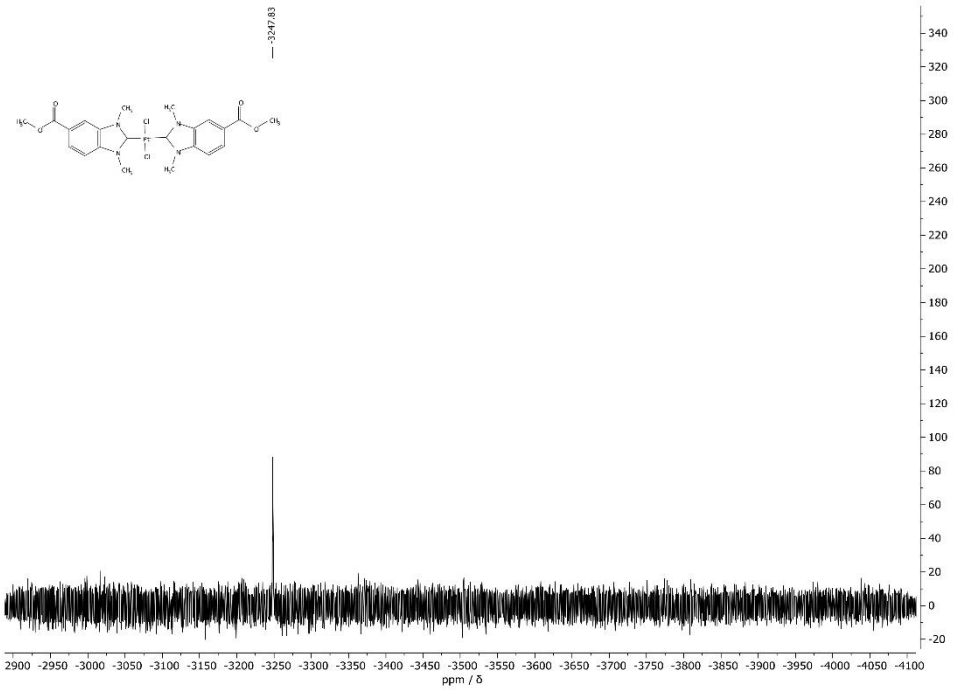

Fig. 3. ^{195}Pt-NMR spectrum of **8a** in $CDCl_3$.

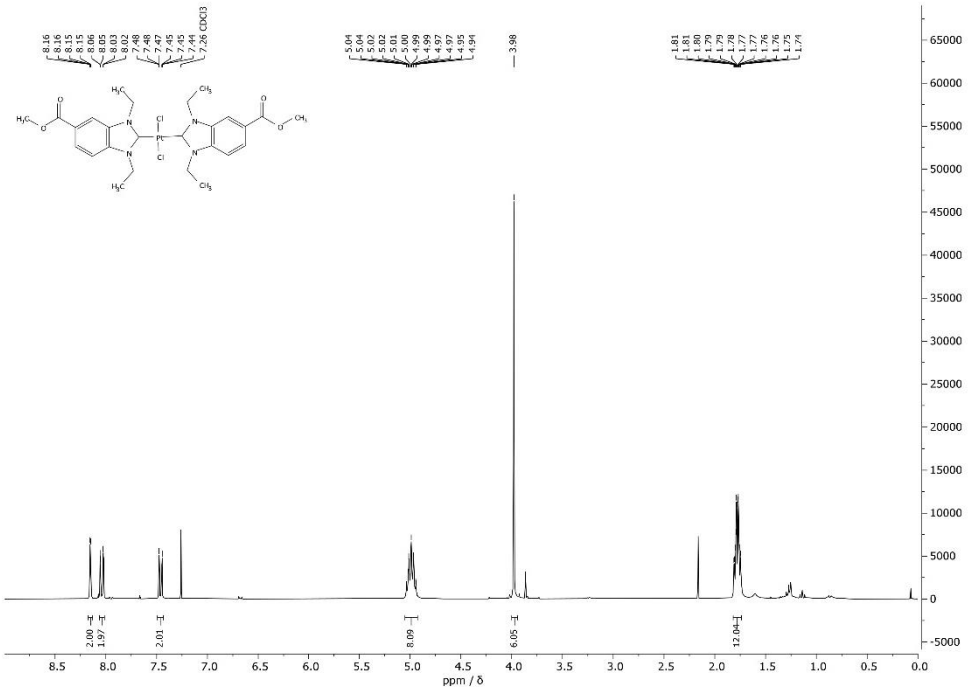

Fig. 4. ^{1}H-NMR spectrum of **8b** in $CDCl_3$.

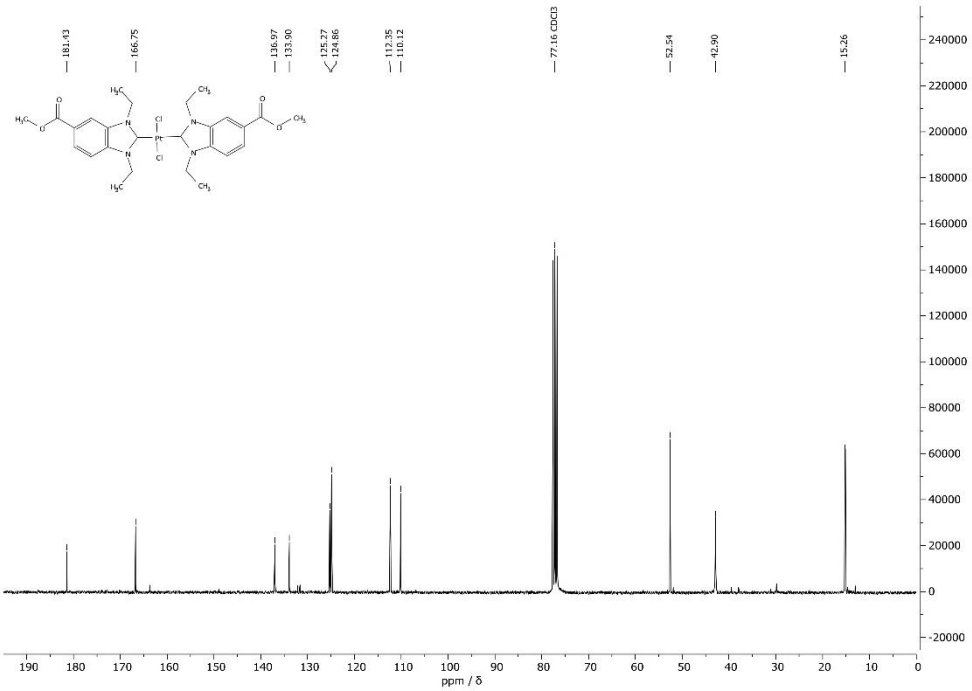

Fig. 5. ^{13}C-NMR spectrum of **8b** in $CDCl_3$.

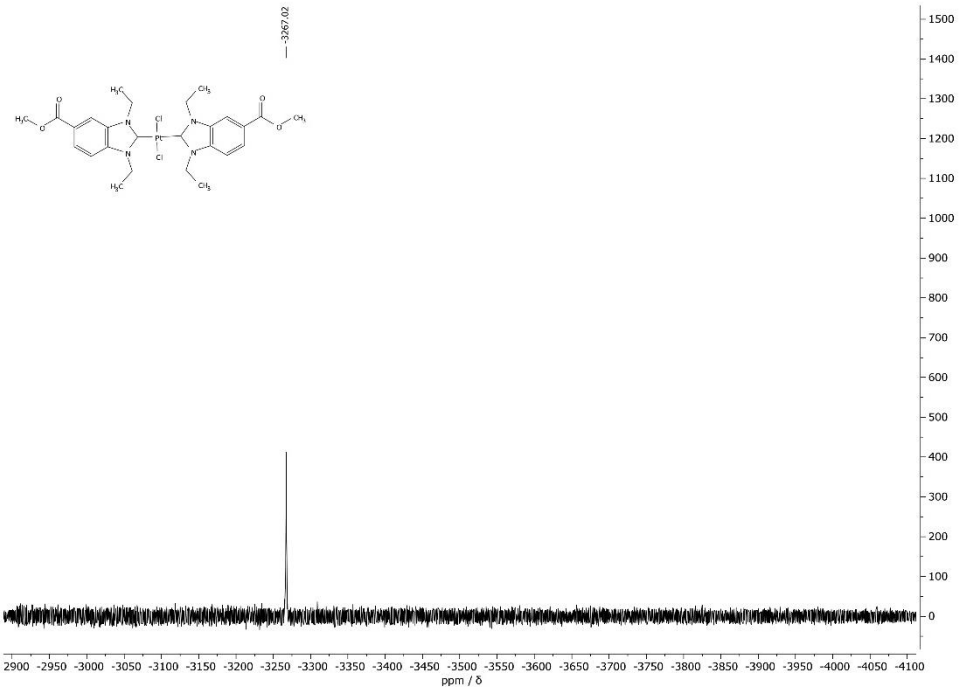

Fig. 6. ^{195}Pt-NMR spectrum of **8b** in $CDCl_3$.

XIX

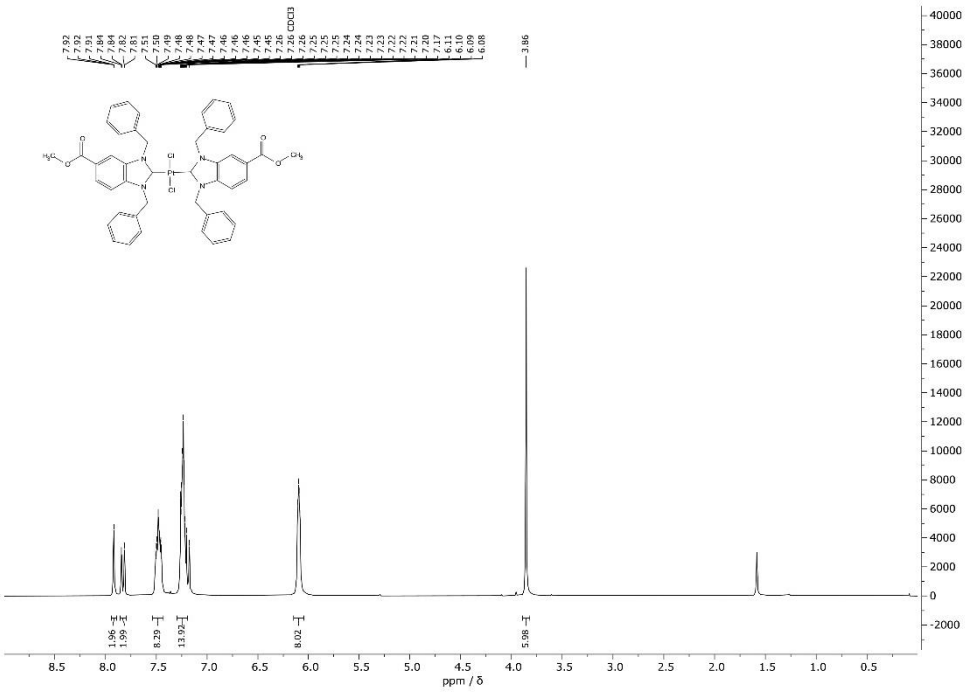

Fig. 7. ^{1}H-NMR spectrum of **8c** in $CDCl_3$.

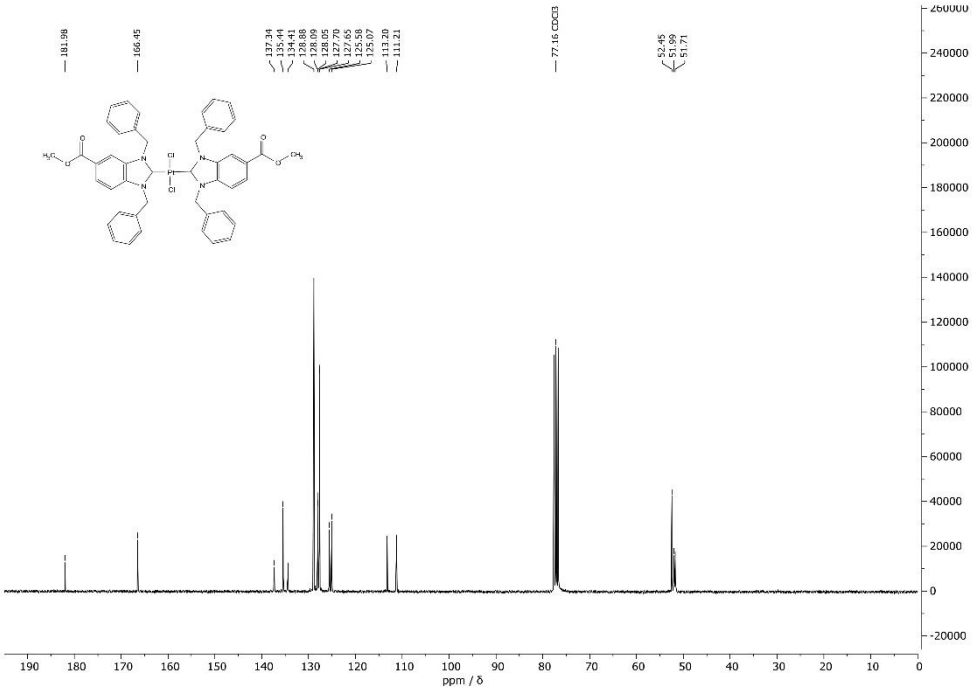

Fig. 8. ^{13}C-NMR spectrum of **8c** in $CDCl_3$.

XX

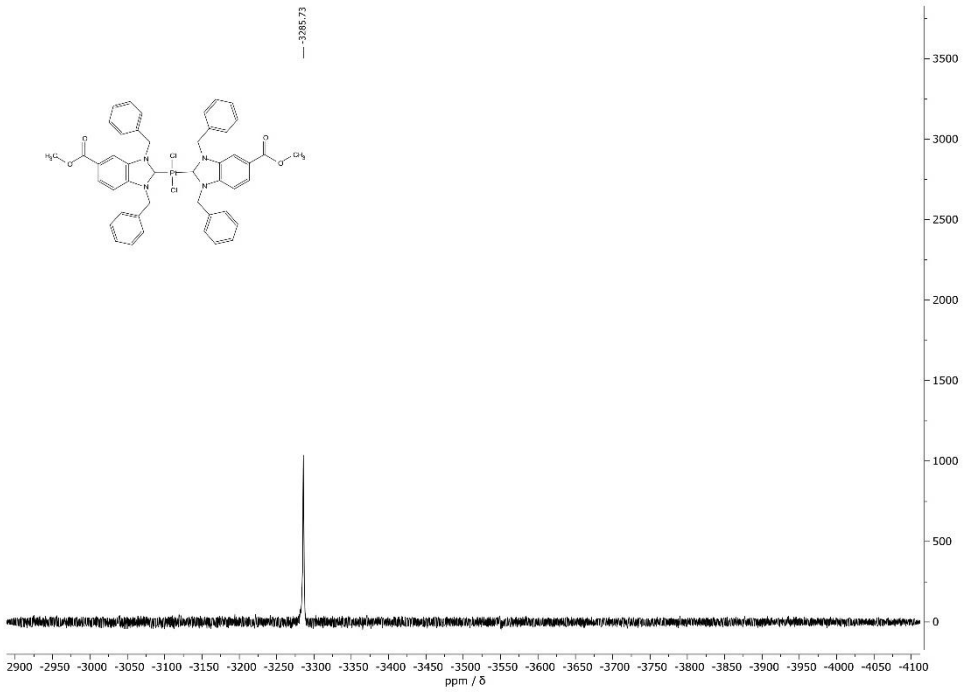

Fig. 9. ^{195}Pt-NMR spectrum of **8c** in $CDCl_3$.

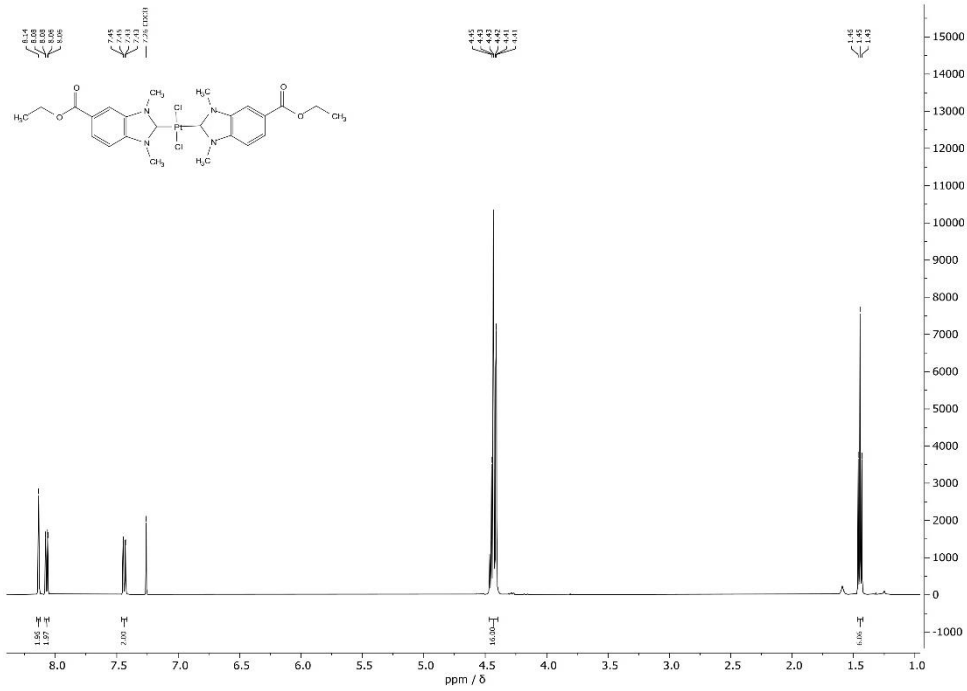

Fig. 10. ^{1}H-NMR spectrum of **9a** in $CDCl_3$.

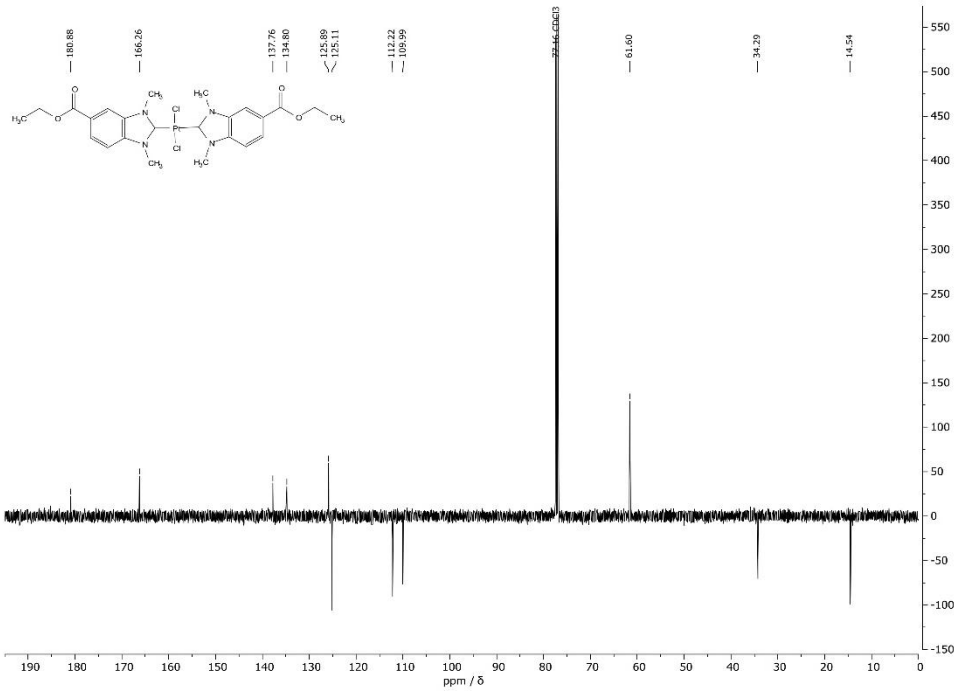

Fig. 11. ^{13}C-NMR spectrum of **9a** in $CDCl_3$.

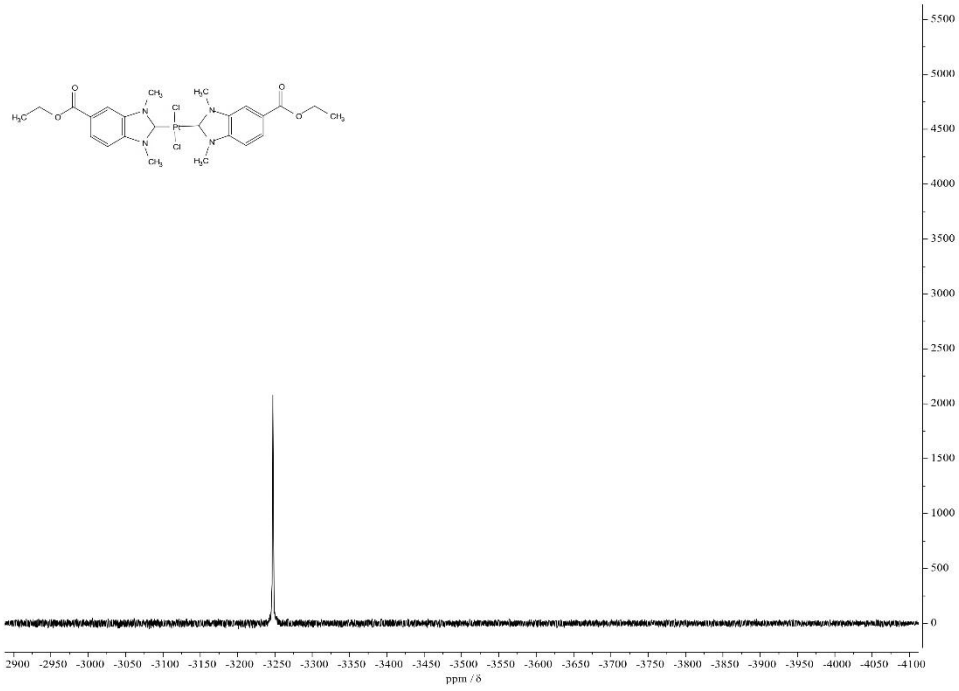

Fig. 12. ^{195}Pt-NMR spectrum of **9a** in $CDCl_3$.

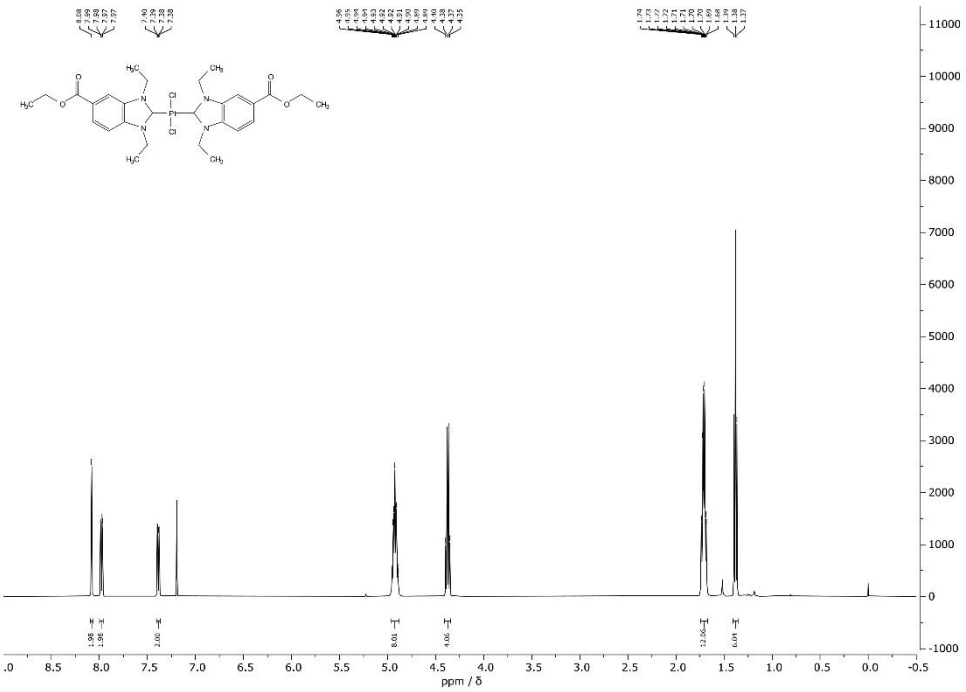

Fig. 13. ^{1}H-NMR spectrum of **9b** in $CDCl_3$.

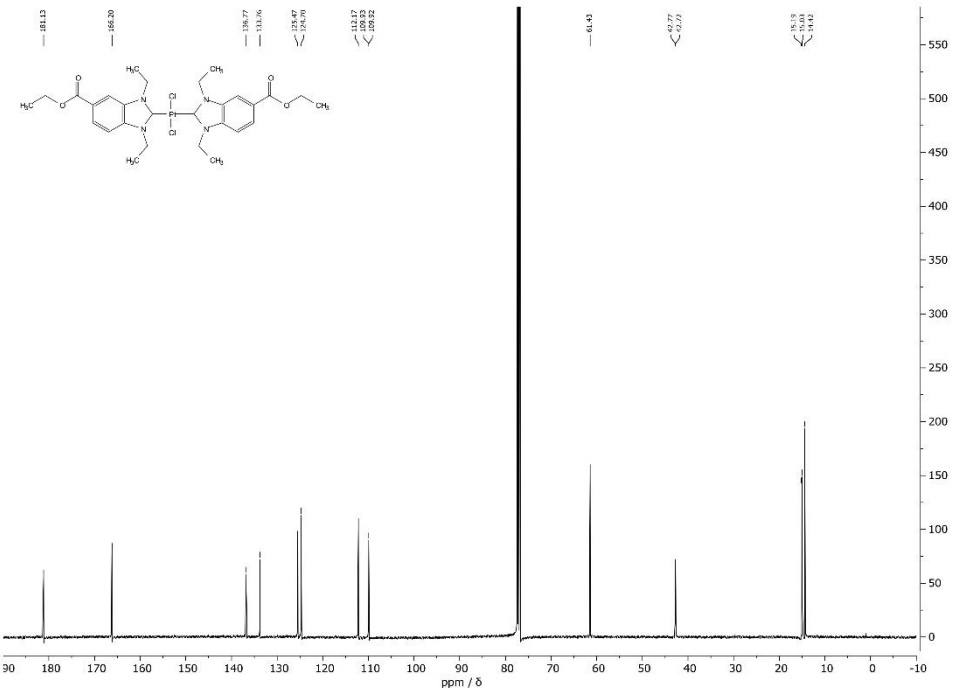

Fig. 14. ^{13}C-NMR spectrum of **9b** in $CDCl_3$.

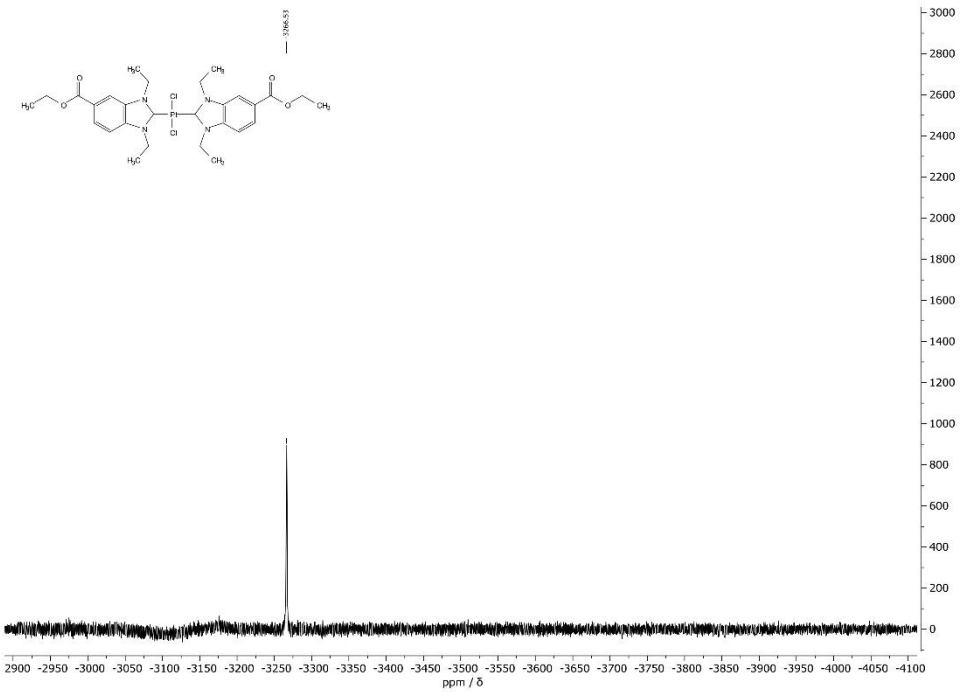

Fig. 15. ^{195}Pt-NMR spectrum of **9b** in $CDCl_3$.

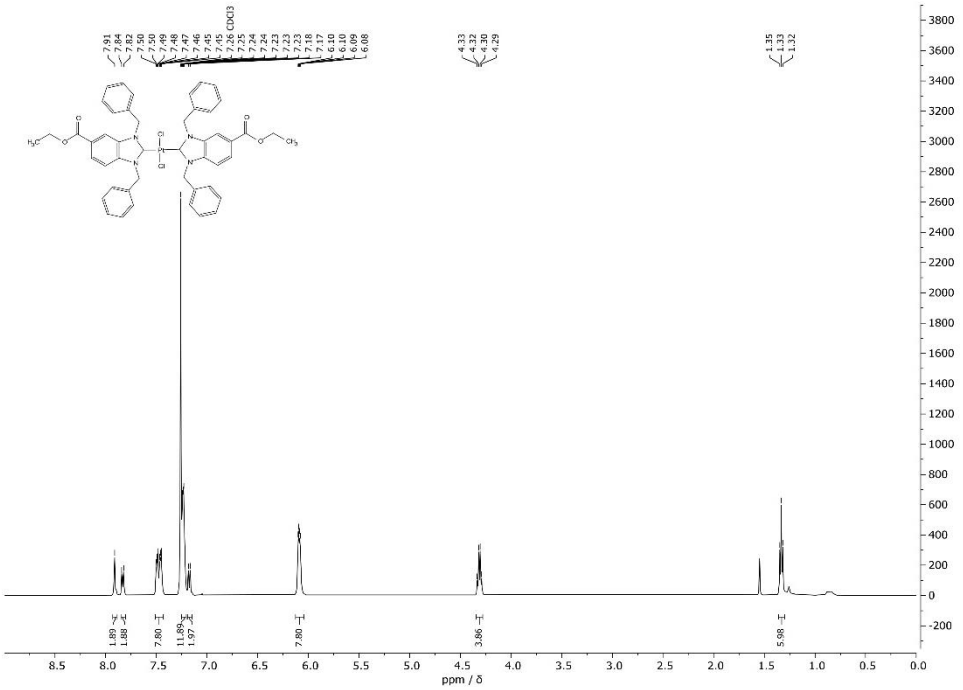

Fig. 16. ^{1}H-NMR spectrum of **9c** in $CDCl_3$.

XXIV

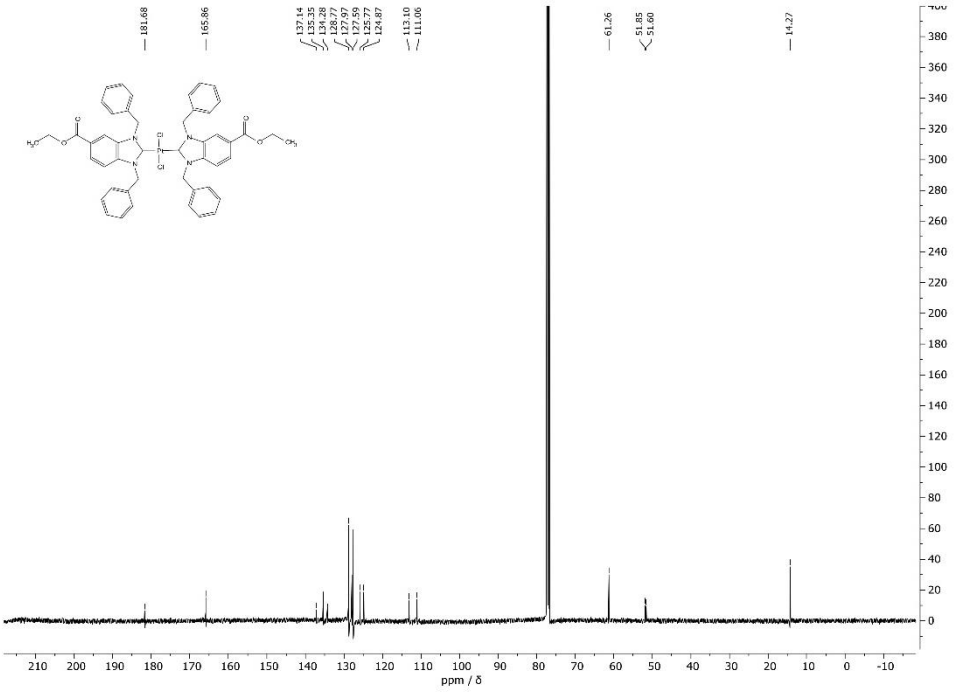

Fig. 17. ^{13}C-NMR spectrum of **9c** in $CDCl_3$.

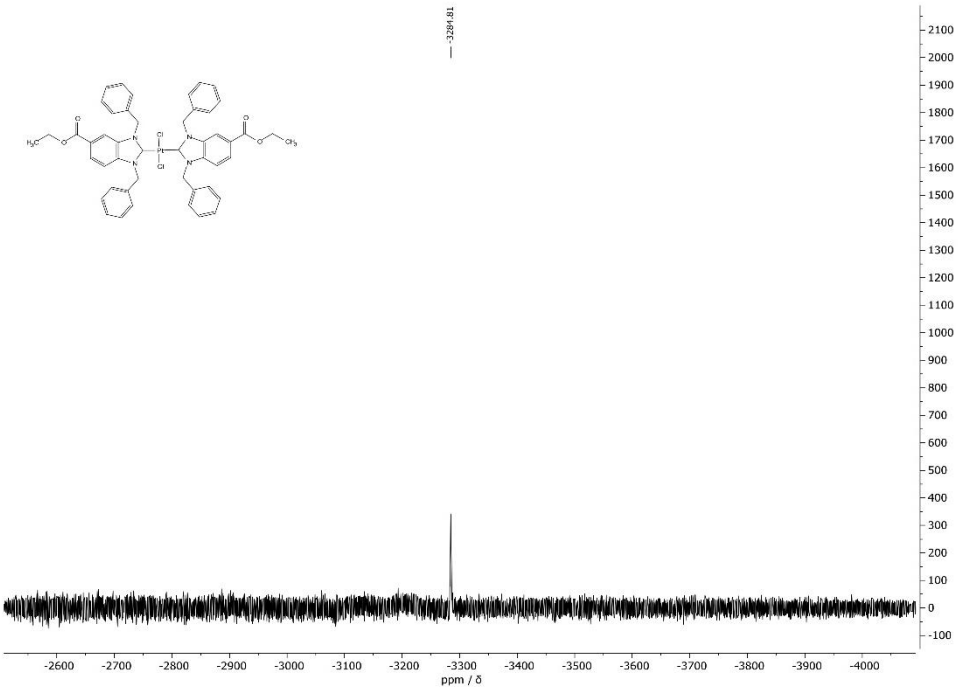

Fig. 18. ^{195}Pt-NMR spectrum of **9c** in $CDCl_3$.

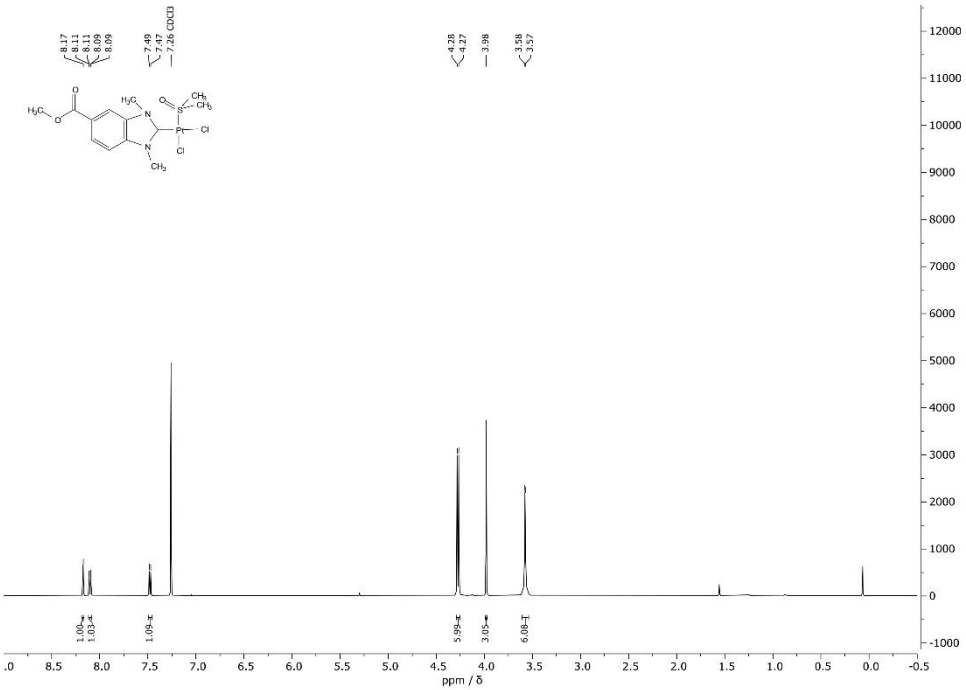

Fig. 19. ^{1}H-NMR spectrum of **10a** in $CDCl_3$.

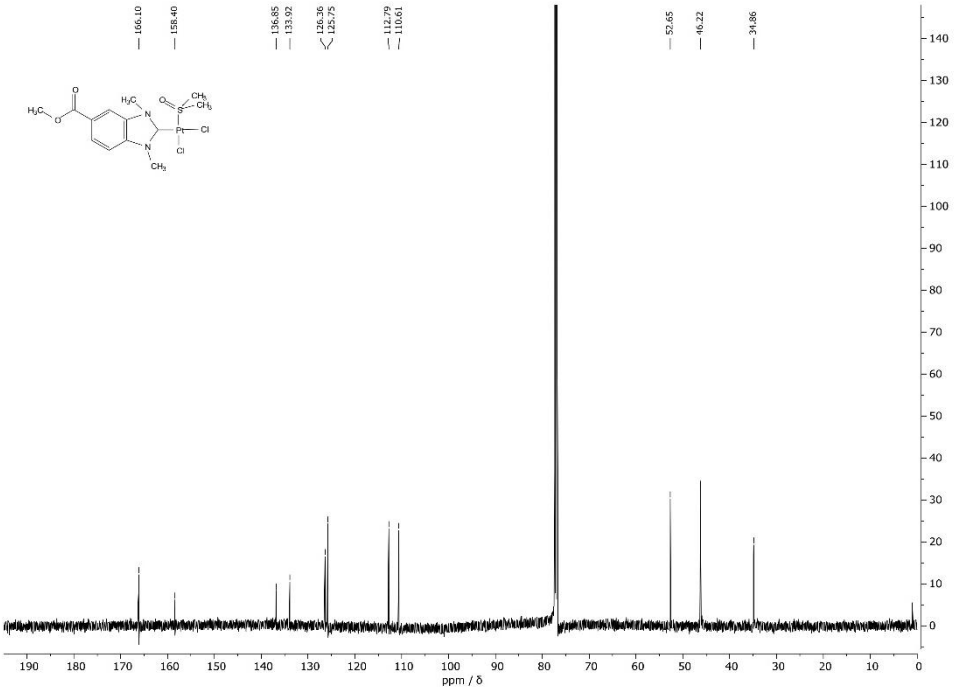

Fig. 20. ^{13}C-NMR spectrum of **10a** in $CDCl_3$.

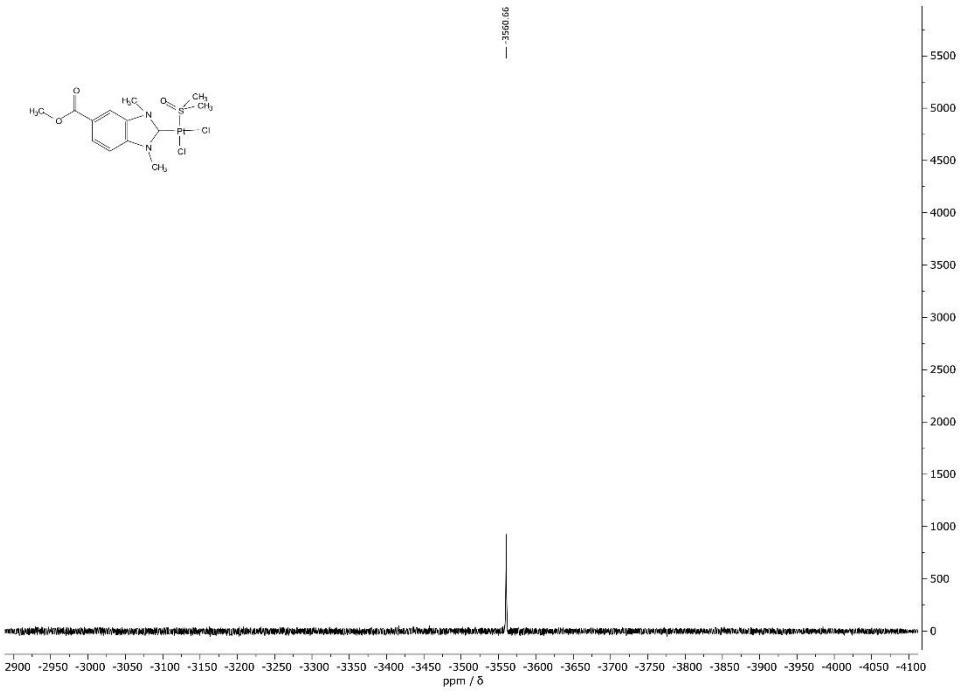

Fig. 21. ^{195}Pt-NMR spectrum of **10a** in $CDCl_3$.

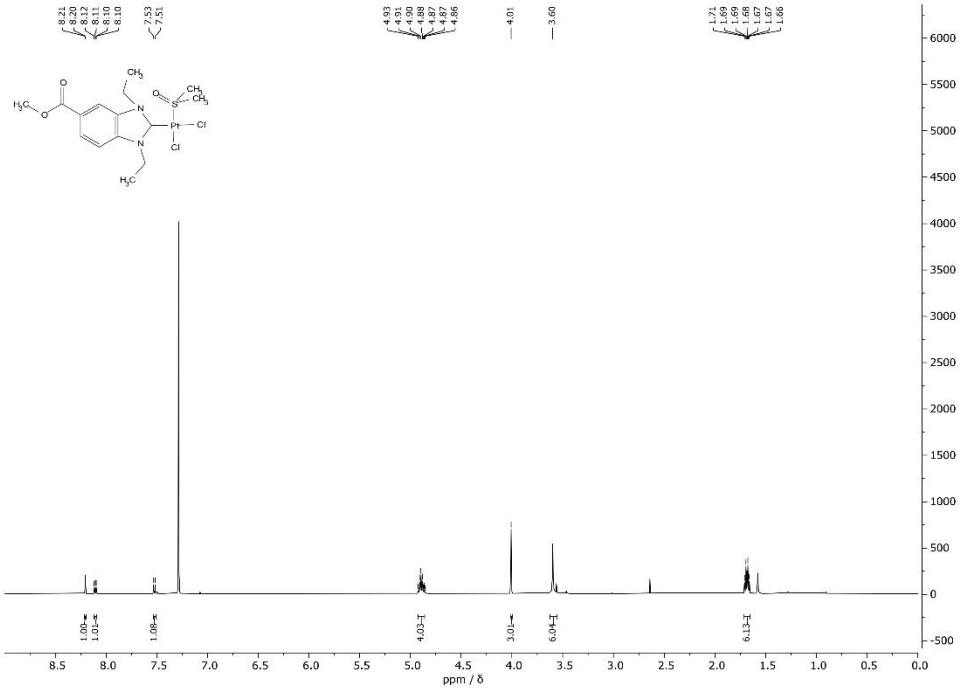

Fig. 22. ^{1}H-NMR spectrum of **10b** in $CDCl_3$.

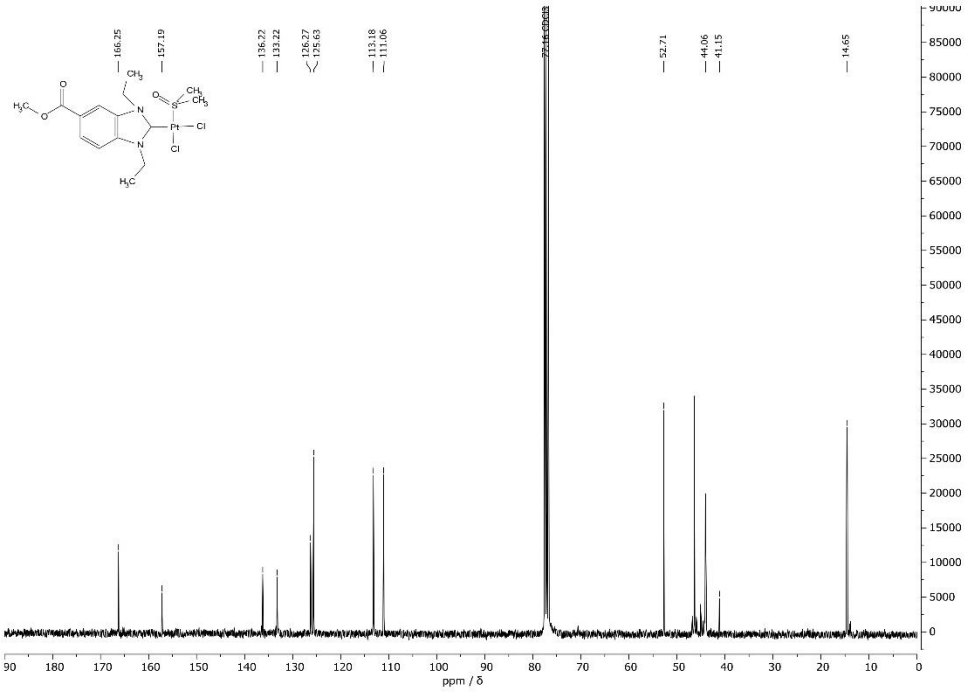

Fig. 23. ^{13}C-NMR spectrum of **10b** in $CDCl_3$.

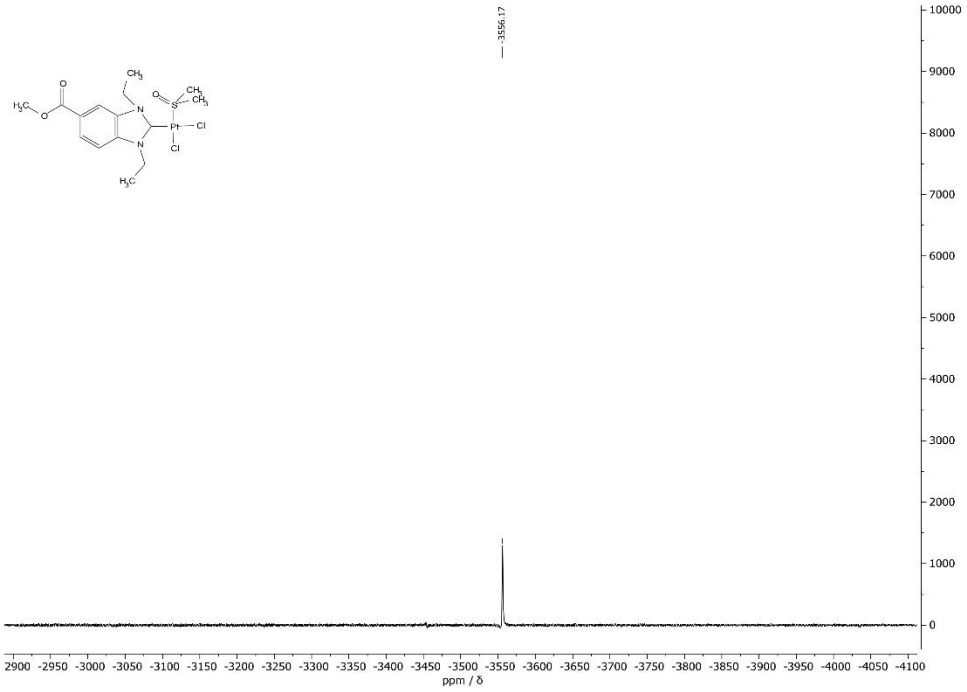

Fig. 24. ^{195}Pt-NMR spectrum of **10b** in $CDCl_3$.

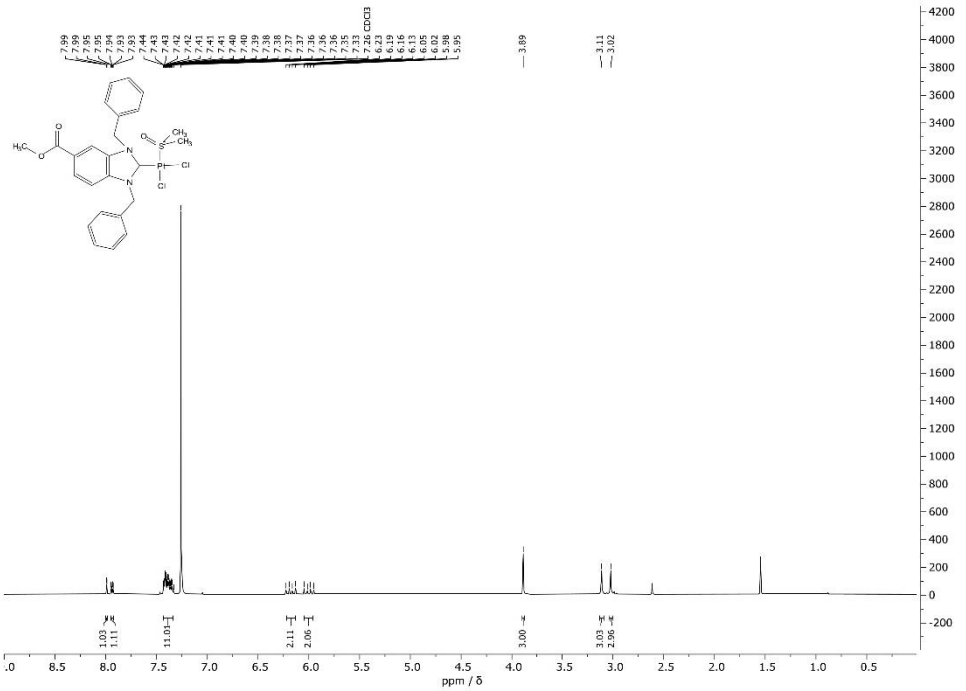

Fig. 25. ^{1}H-NMR spectrum of **10c** in $CDCl_3$.

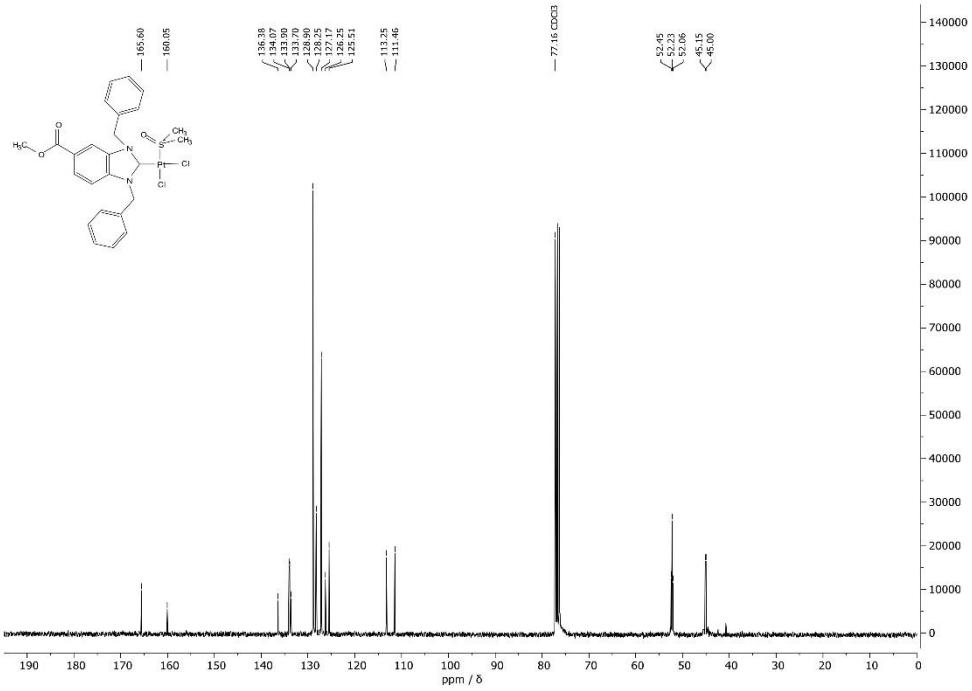

Fig. 26. ^{13}C-NMR spectrum of **10c** in $CDCl_3$.

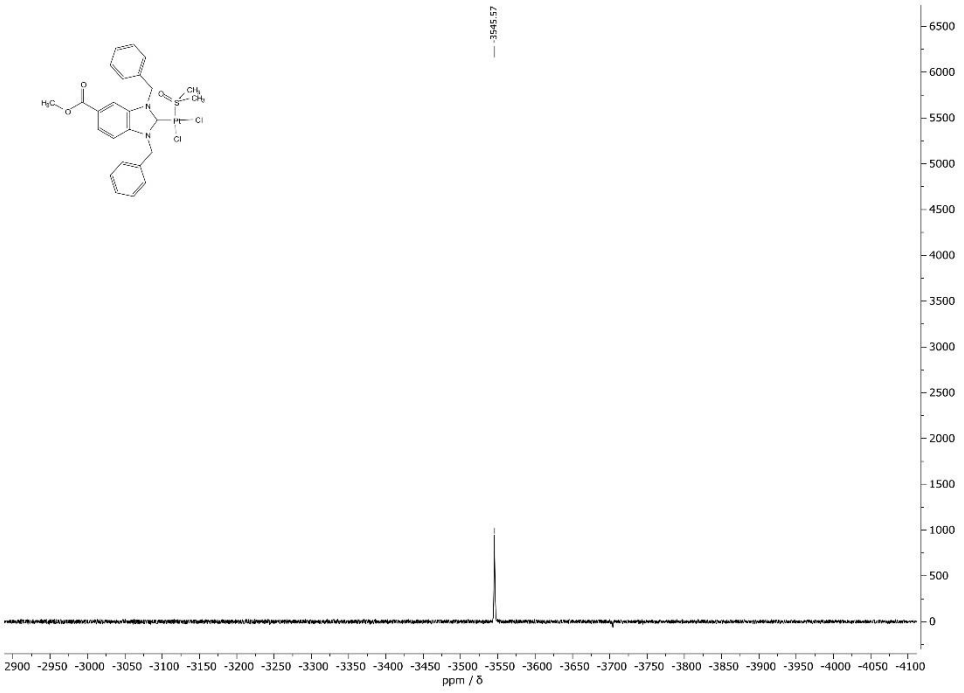

Fig. 27. ^{195}Pt-NMR spectrum of **10c** in $CDCl_3$.

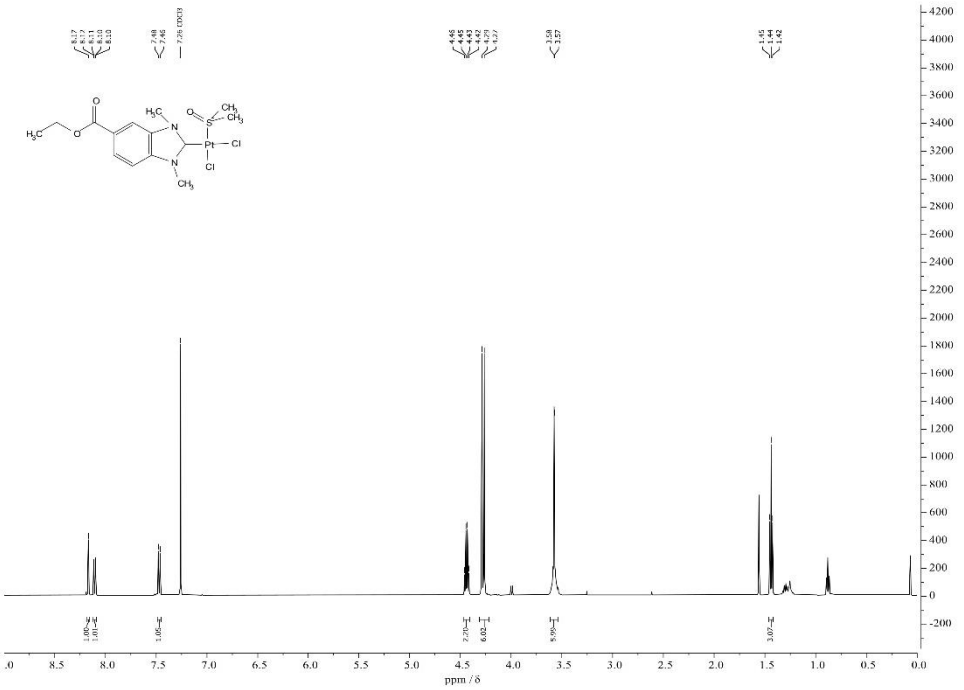

Fig. 28. ^{1}H-NMR spectrum of **11a** in $CDCl_3$.

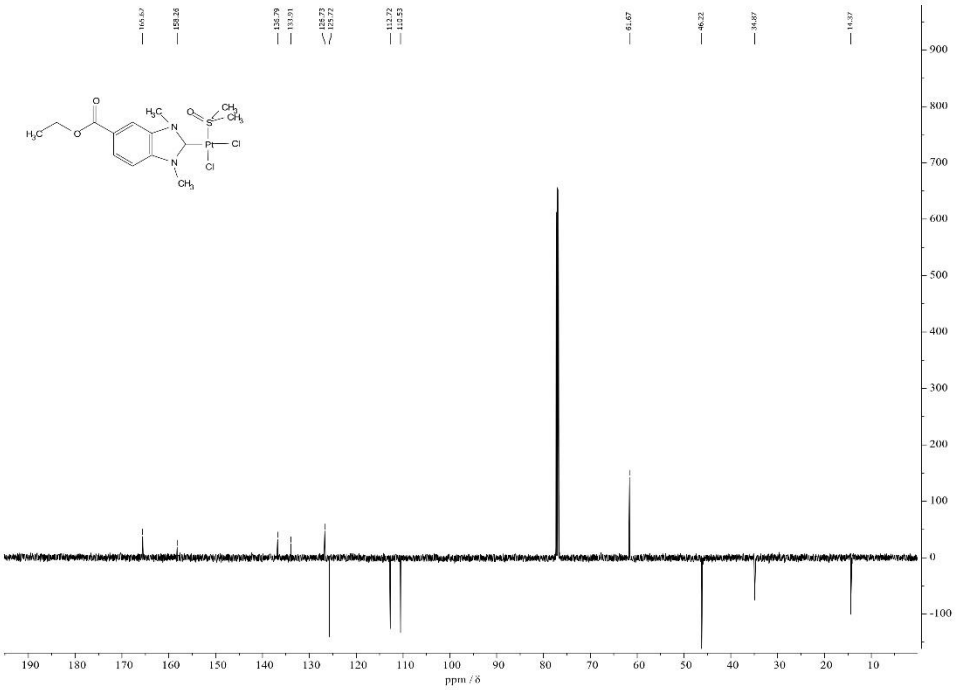

Fig. 29. ^{13}C-NMR spectrum of **11a** in $CDCl_3$.

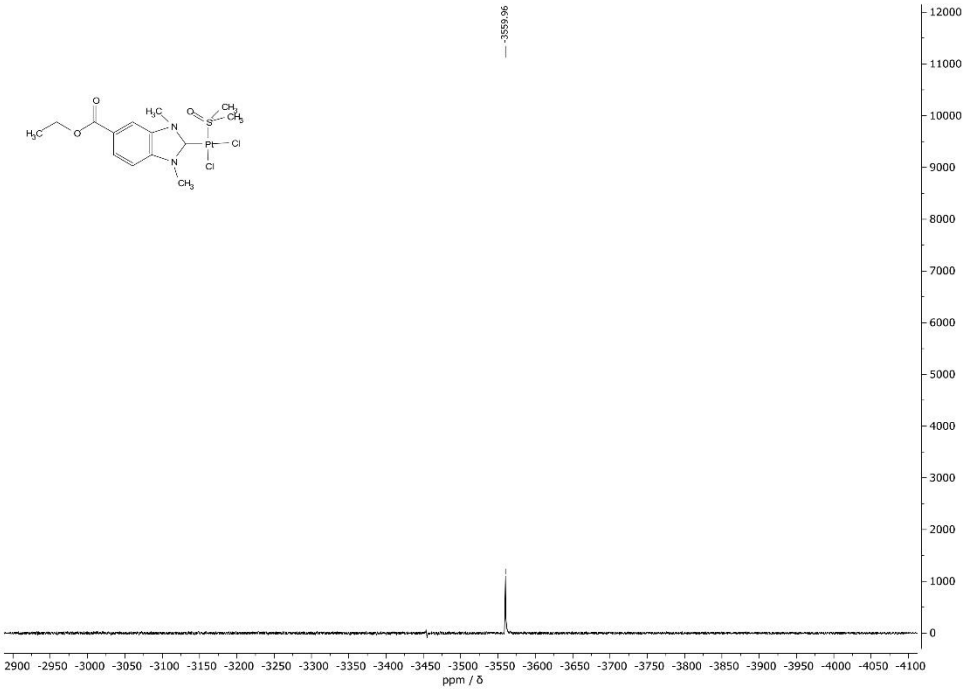

Fig. 30. ^{195}Pt-NMR spectrum of **11a** in $CDCl_3$.

XXXI

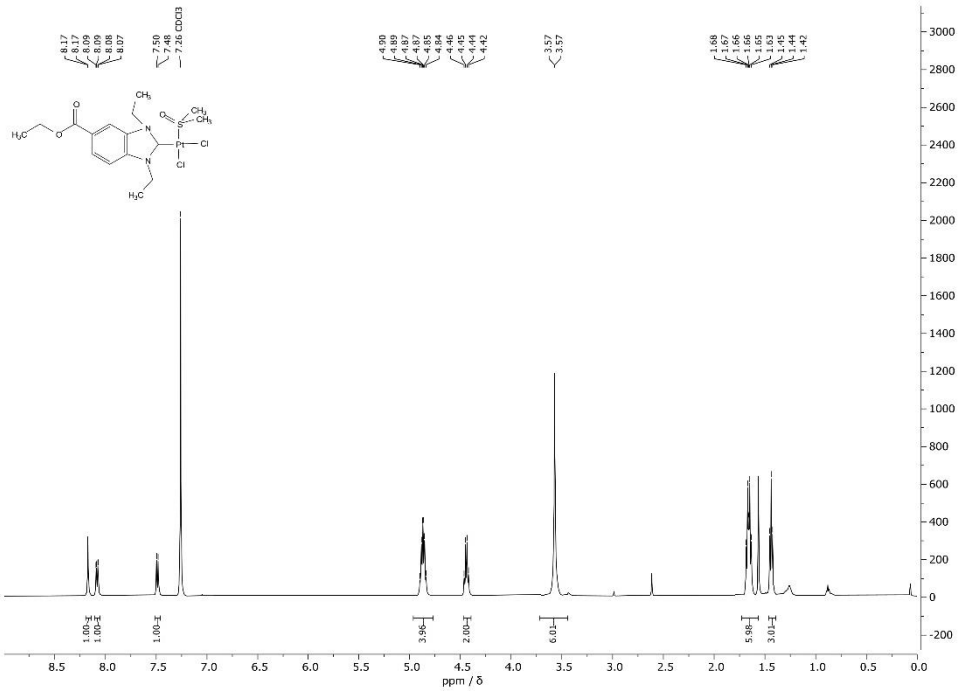

Fig. 31. ^{1}H-NMR spectrum of **11b** in $CDCl_3$.

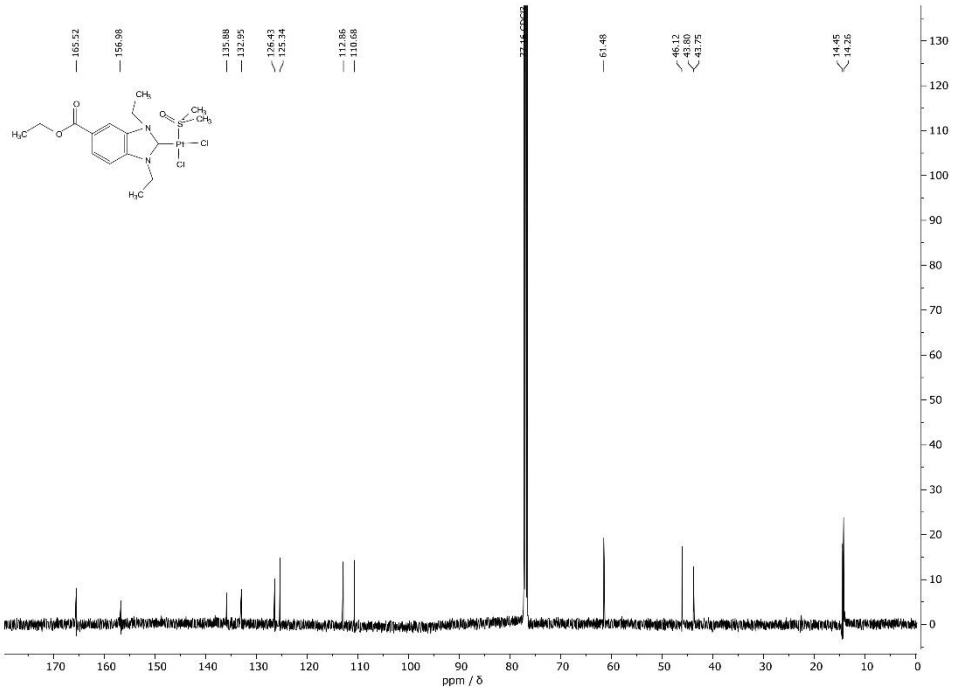

Fig. 32. ^{13}C-NMR spectrum of **11b** in $CDCl_3$.

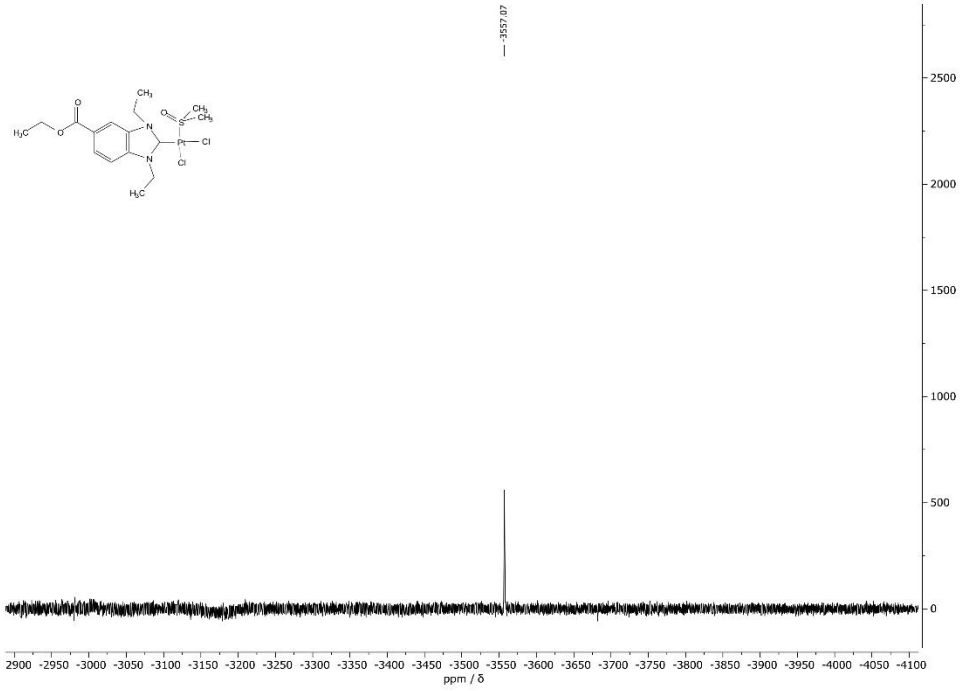

Fig. 33. ^{195}Pt-NMR spectrum of **11b** in $CDCl_3$.

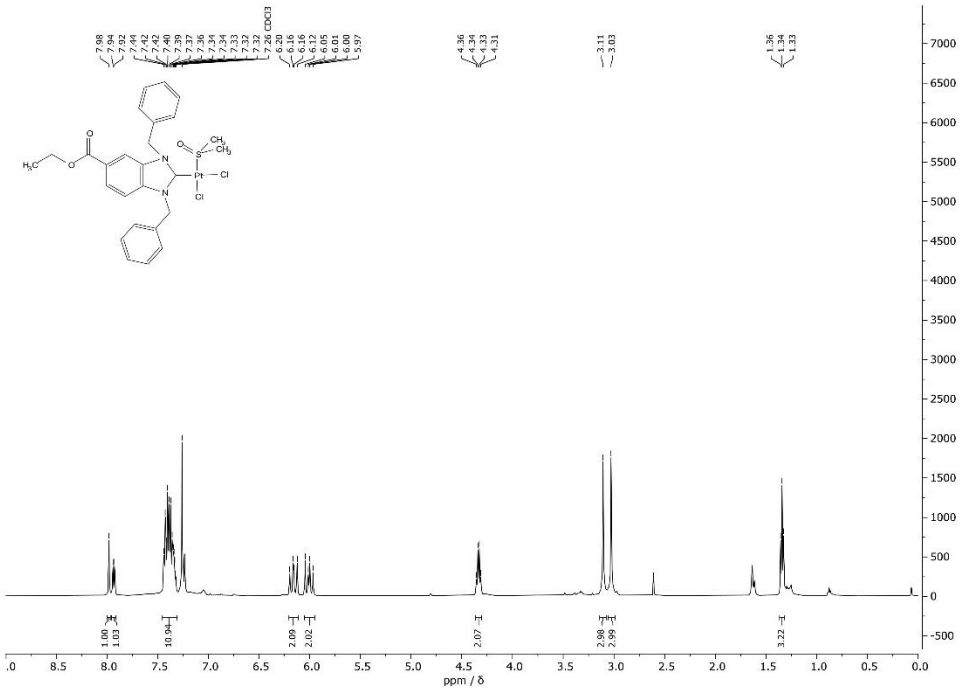

Fig. 34. ^{1}H-NMR spectrum of **11c** in $CDCl_3$.

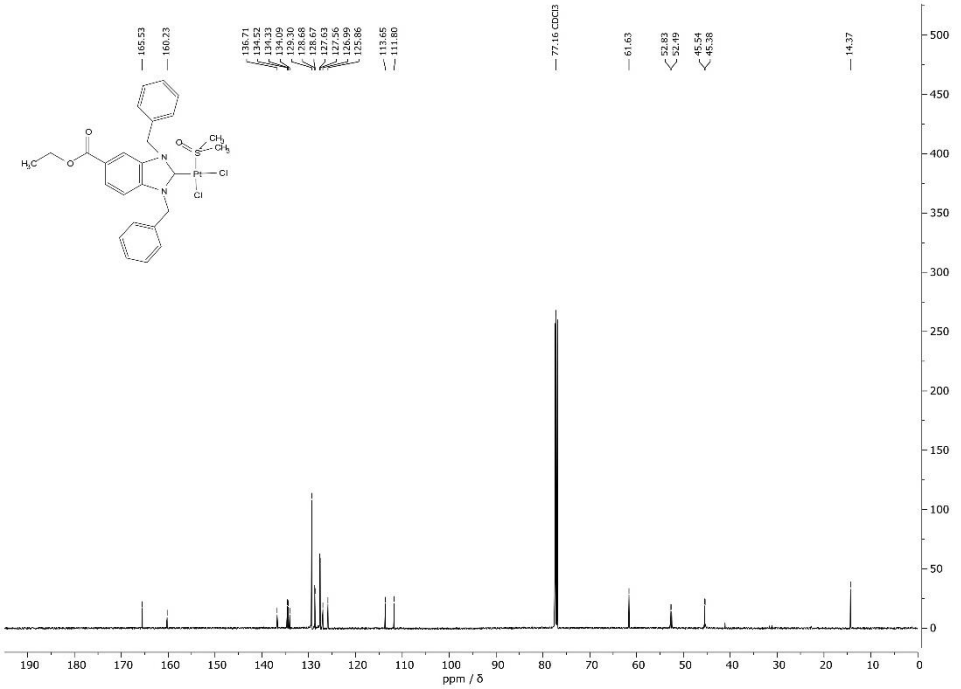

Fig. 35. ^{13}C-NMR spectrum of **11c** in $CDCl_3$.

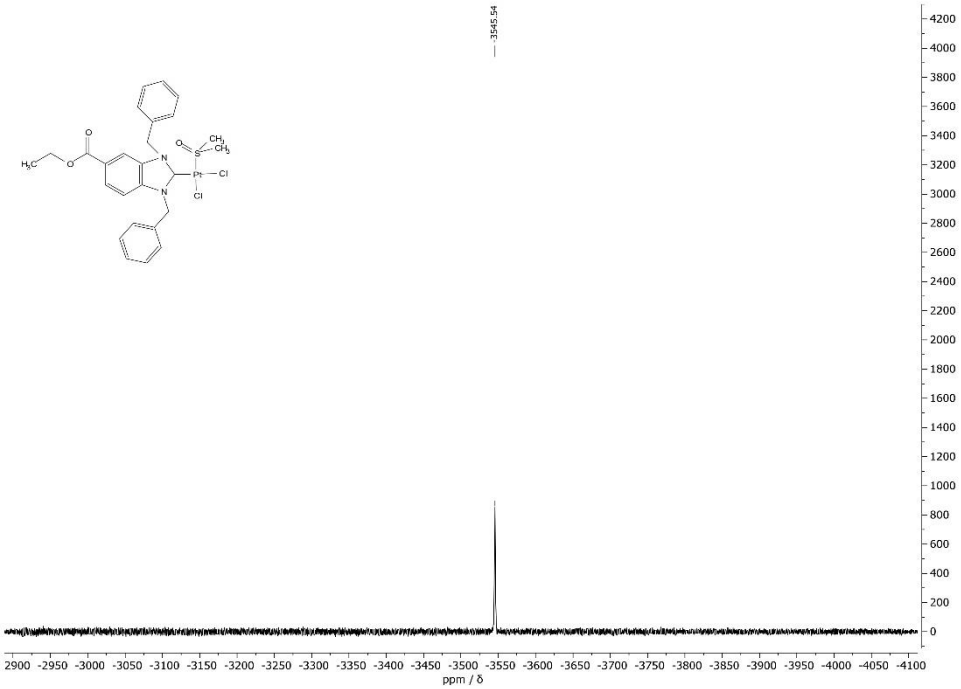

Fig. 36. ^{195}Pt-NMR spectrum of **11c** in $CDCl_3$.

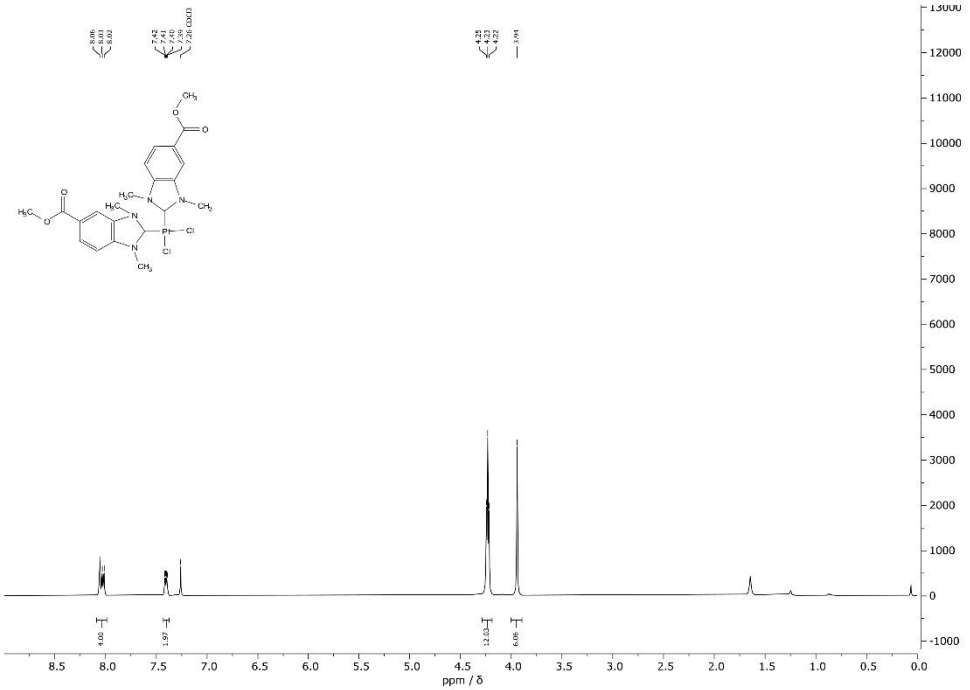

Fig. 37. ^{1}H-NMR spectrum of **12a** in $CDCl_3$.

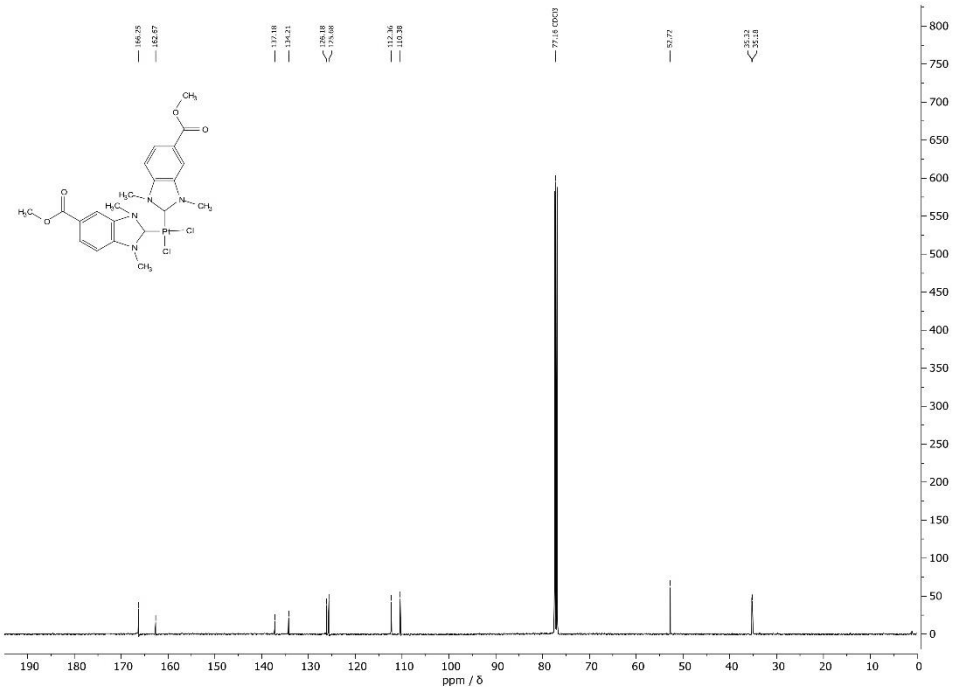

Fig. 38. ^{13}C-NMR spectrum of **12a** in $CDCl_3$.

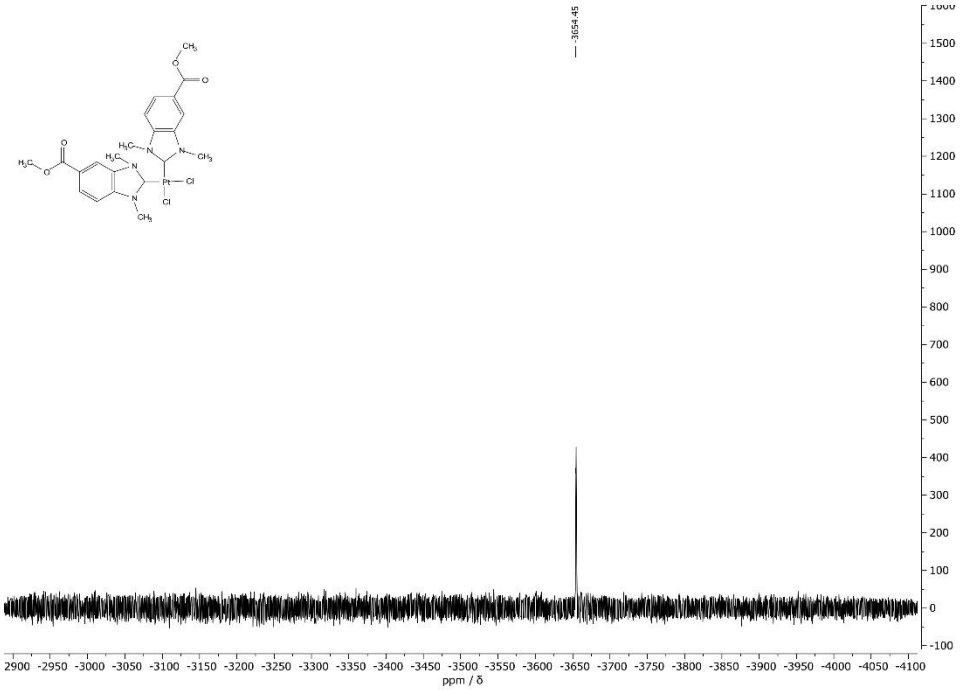

Fig. 39. ^{195}Pt-NMR spectrum of **12a** in $CDCl_3$.

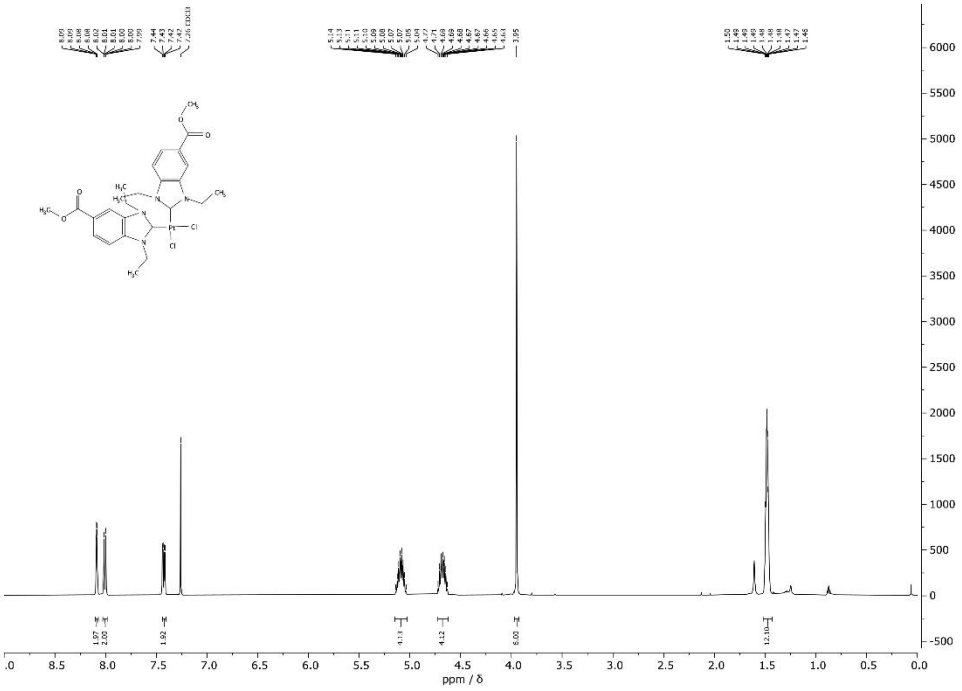

Fig. 40. ^{1}H-NMR spectrum of **12b** in $CDCl_3$.

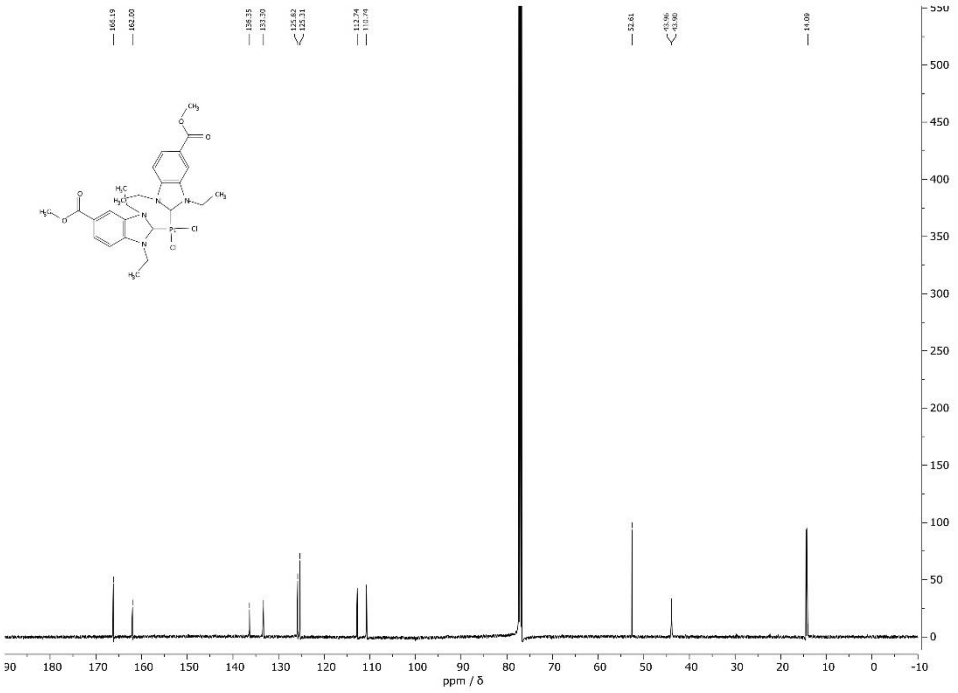

Fig. 41. ^{13}C-NMR spectrum of **12b** in $CDCl_3$.

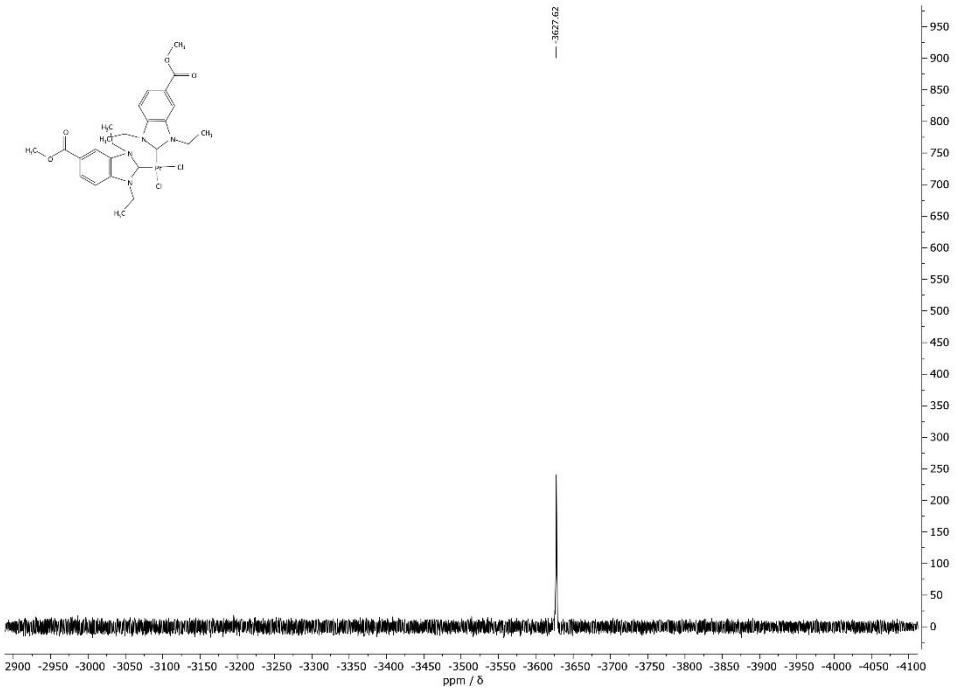

Fig. 42. ^{195}Pt-NMR spectrum of **12b** in $CDCl_3$.

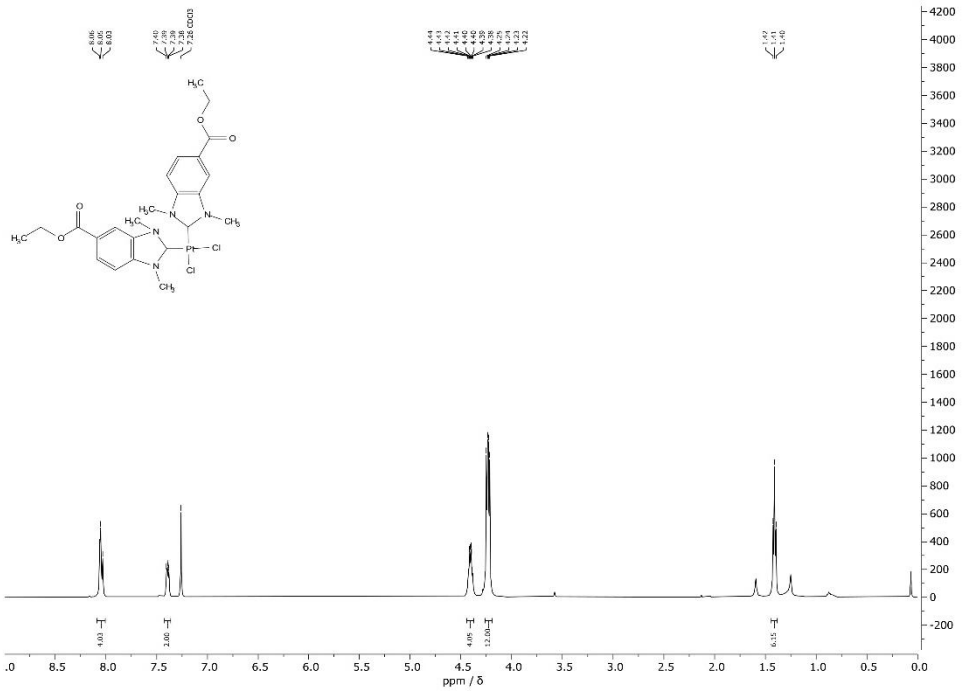

Fig. 43. ^{1}H-NMR spectrum of **13a** in $CDCl_3$.

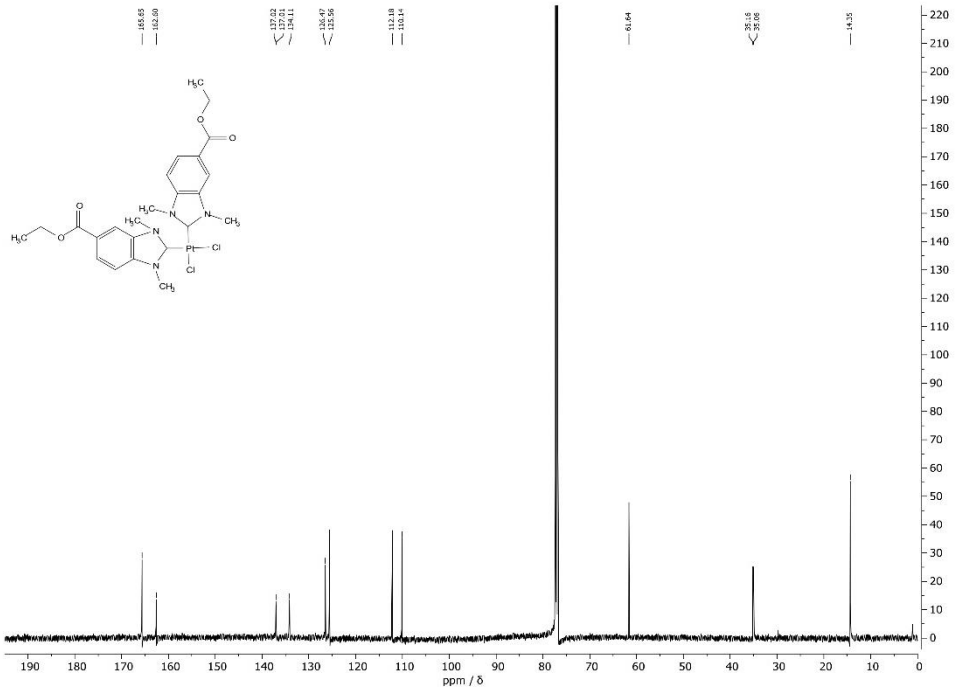

Fig. 44. ^{13}C-NMR spectrum of **13a** in $CDCl_3$.

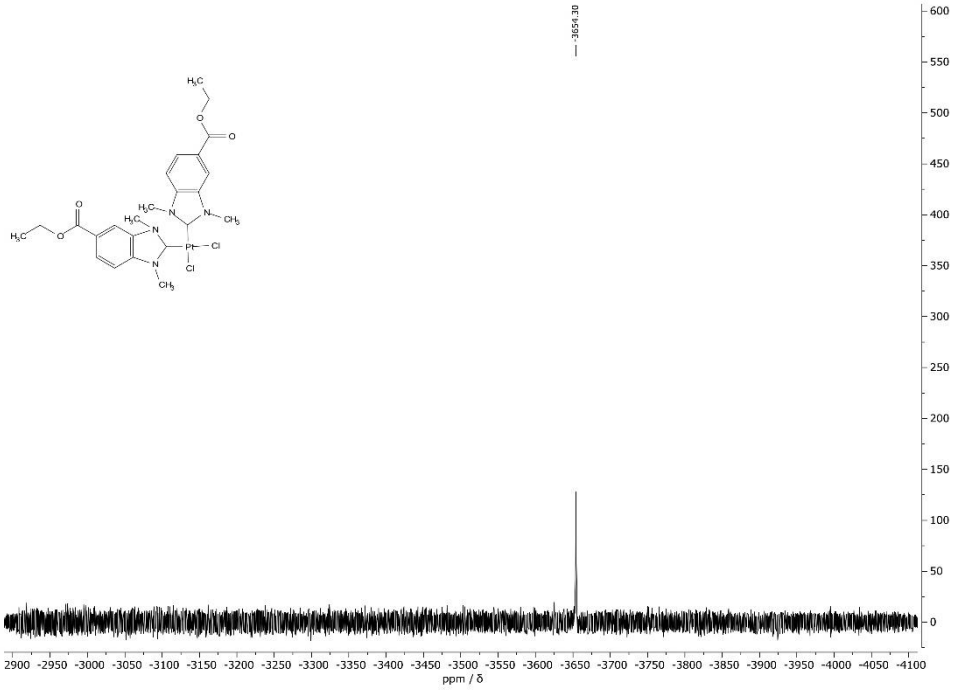

Fig. 45. ^{195}Pt-NMR spectrum of **13a** in $CDCl_3$.

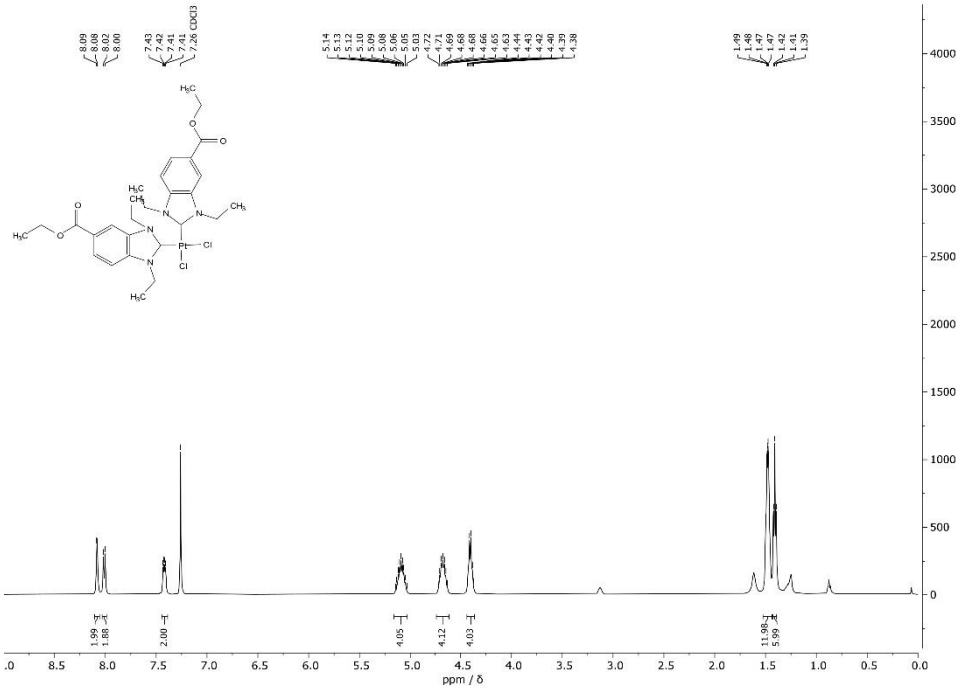

Fig. 46. ^{1}H-NMR spectrum of **13b** in $CDCl_3$.

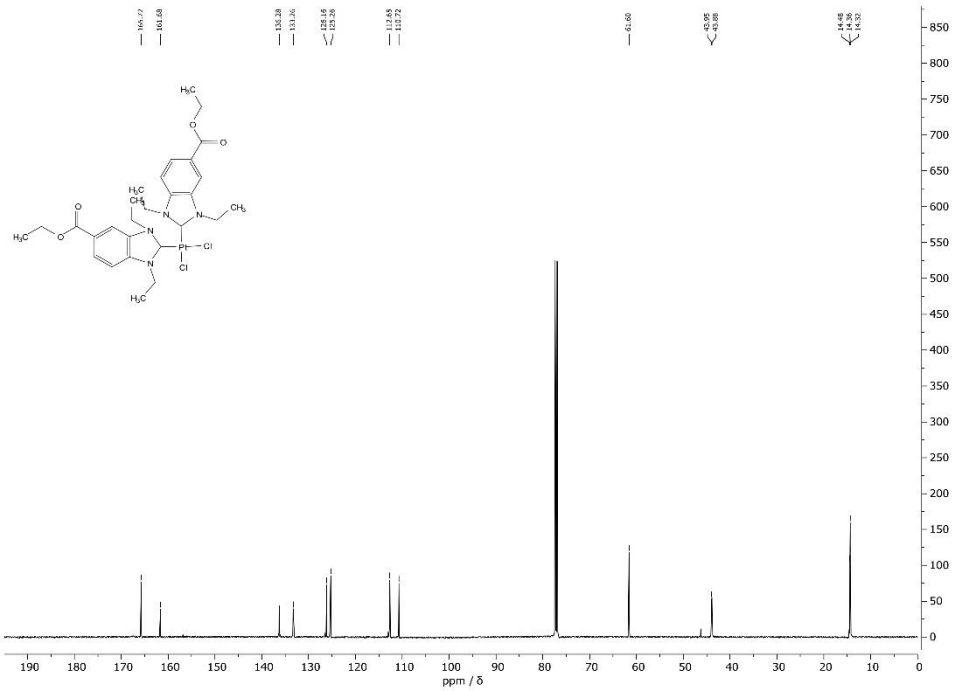

Fig. 47. ^{13}C-NMR spectrum of **13b** in $CDCl_3$.

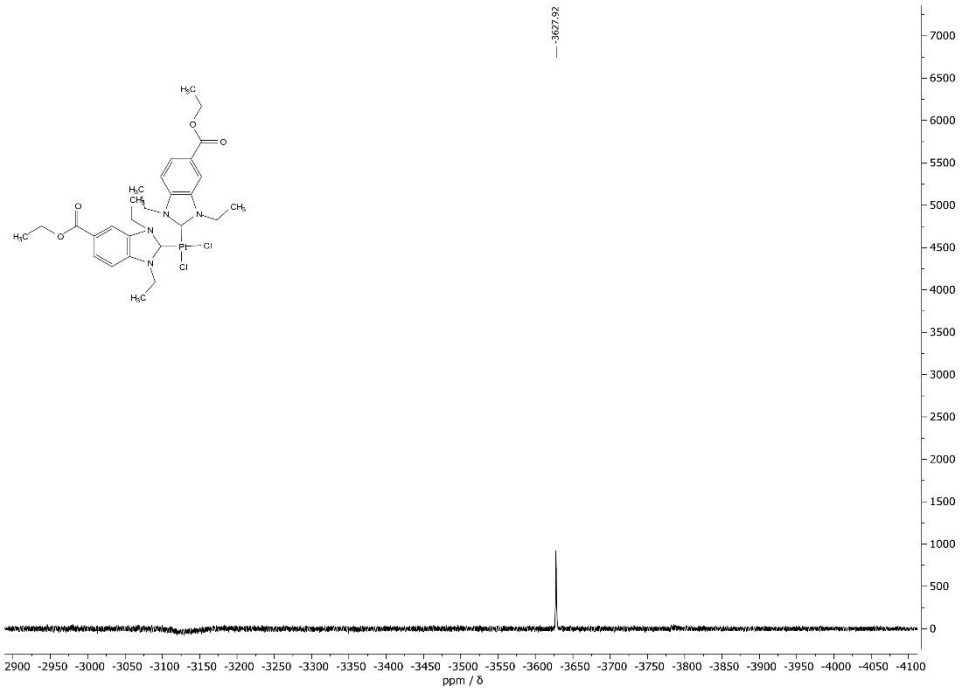

Fig. 48. ^{195}Pt-NMR spectrum of **13b** in $CDCl_3$.

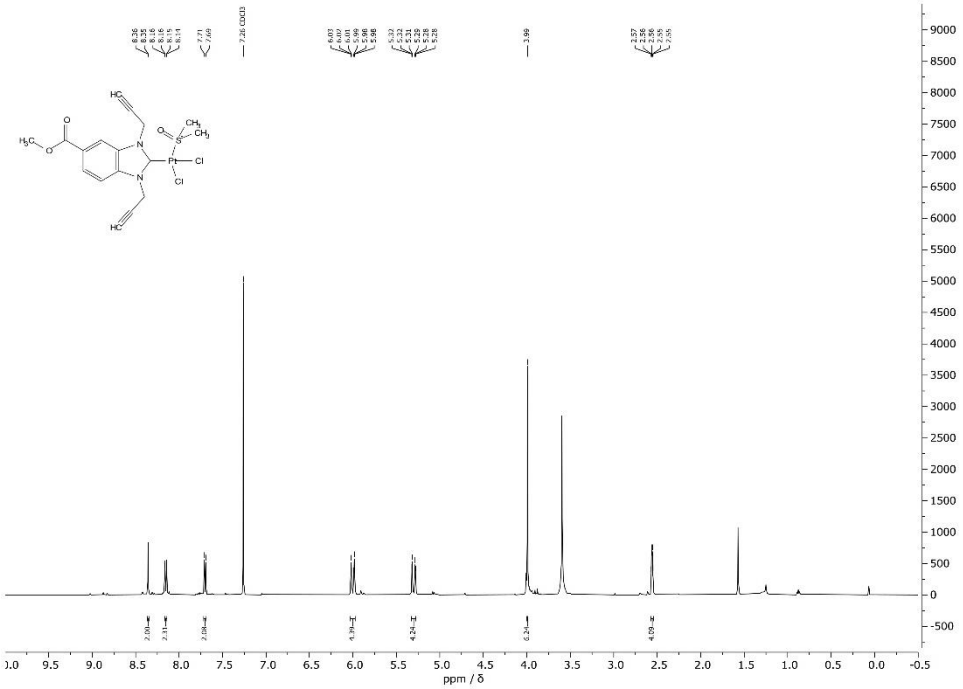

Fig. 49. ^{1}H-NMR spectrum of **16** in $CDCl_3$.

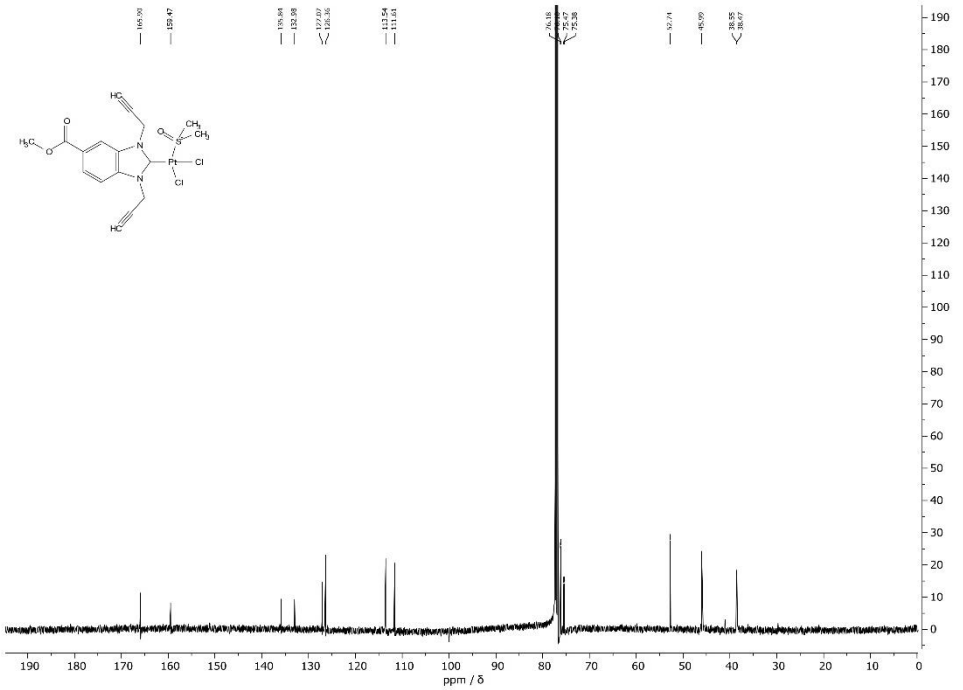

Fig. 50. ^{13}C-NMR spectrum of **16** in $CDCl_3$.

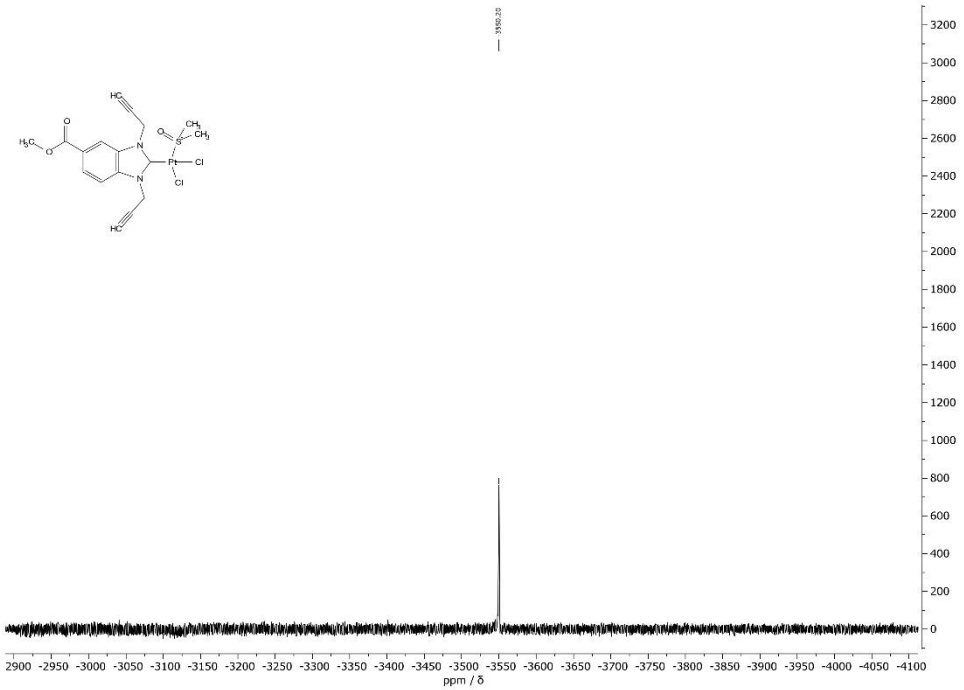

Fig. 51. ^{195}Pt-NMR spectrum of **16** in $CDCl_3$.

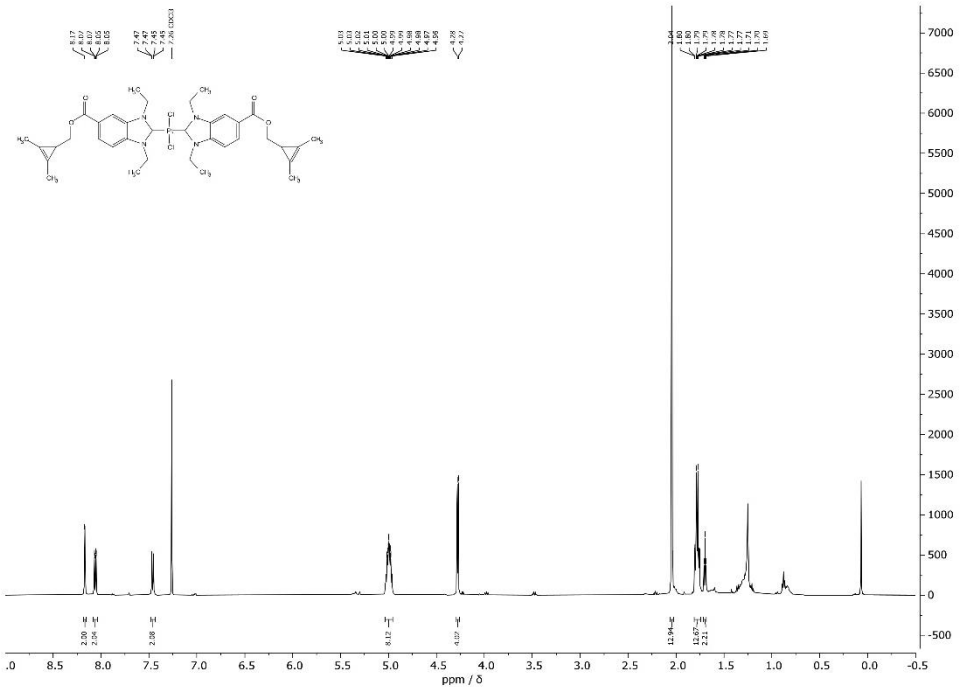

Fig. 52. ^{1}H-NMR spectrum of **22** in $CDCl_3$.

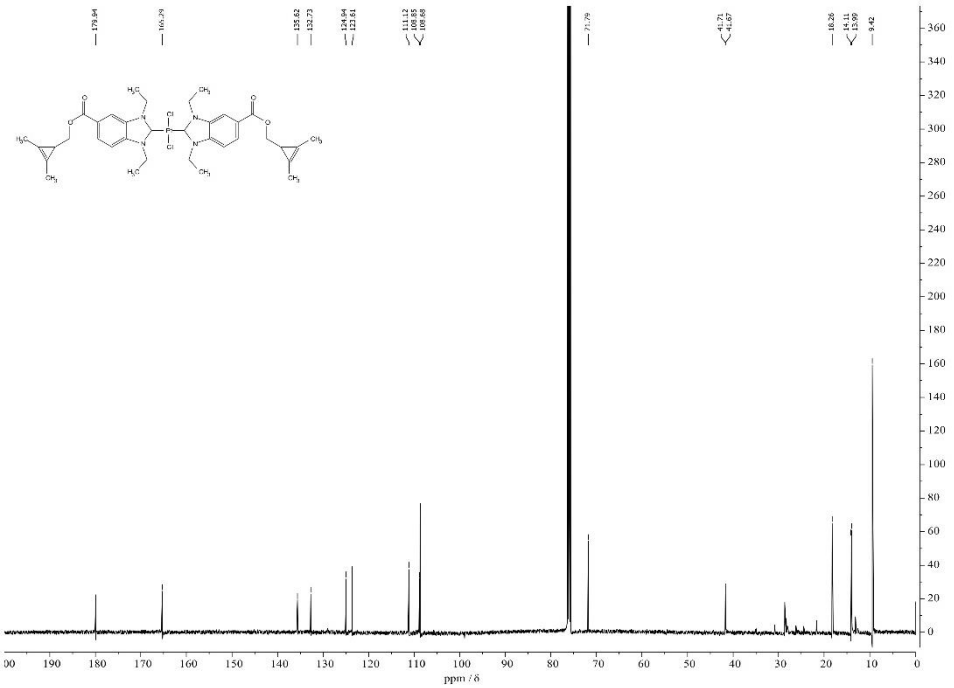

Fig. 53. ^{13}C-NMR spectrum of **22** in $CDCl_3$.

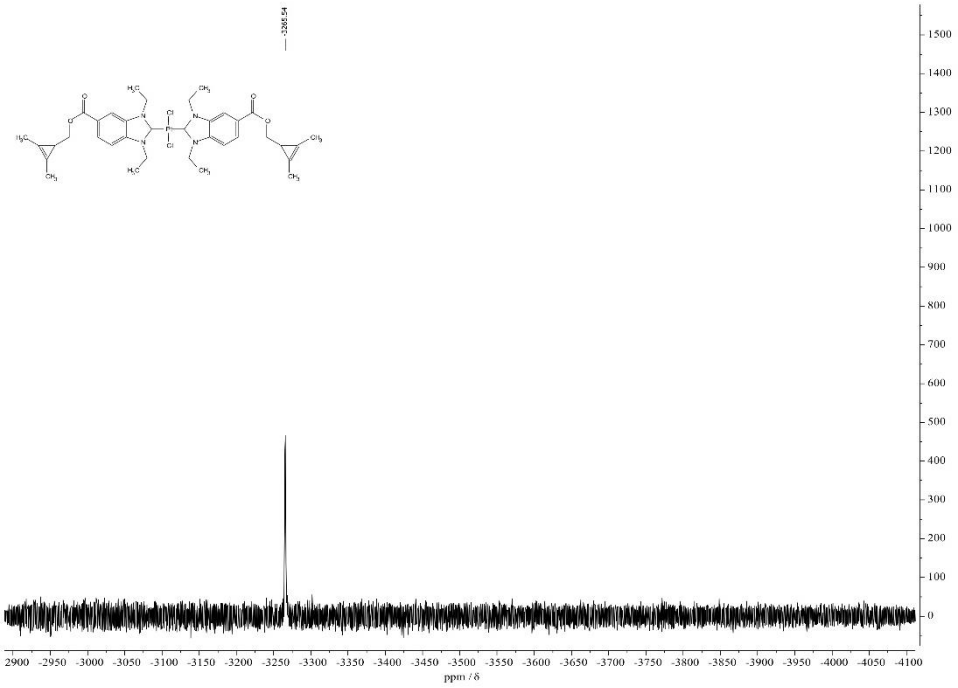

Fig. 54. ^{195}Pt-NMR spectrum of **22** in $CDCl_3$

XLIII

Stability studies of Pt(II) complexes

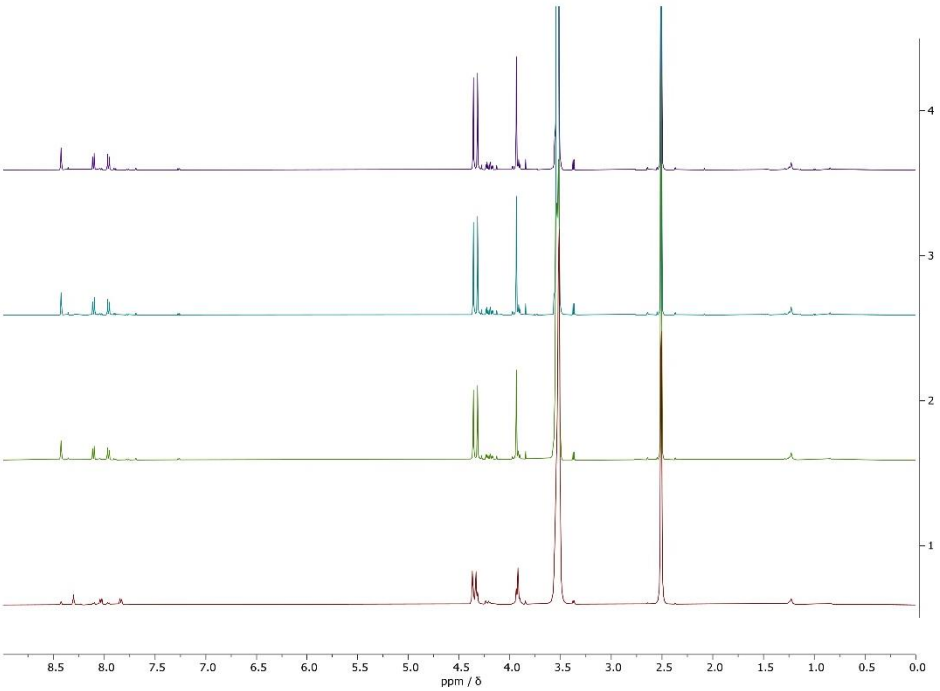

Fig. 55. ^{1}H-NMR spectrum of **8a** in DMSO-d_6 + 5% D_2O after 0h (red), 24h (green), 48h (cyan) and 72h (purple).

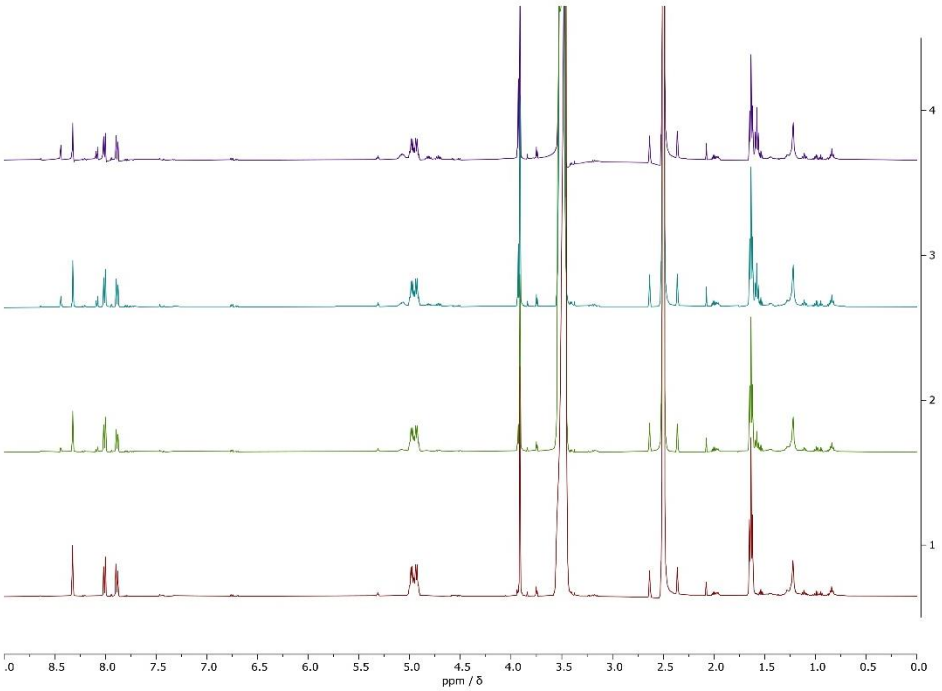

Fig. 56. ^{1}H-NMR spectrum of **8b** in DMSO-d_6 + 5% D_2O after 0h (red), 24h (green), 48h (cyan) and 72h (purple).

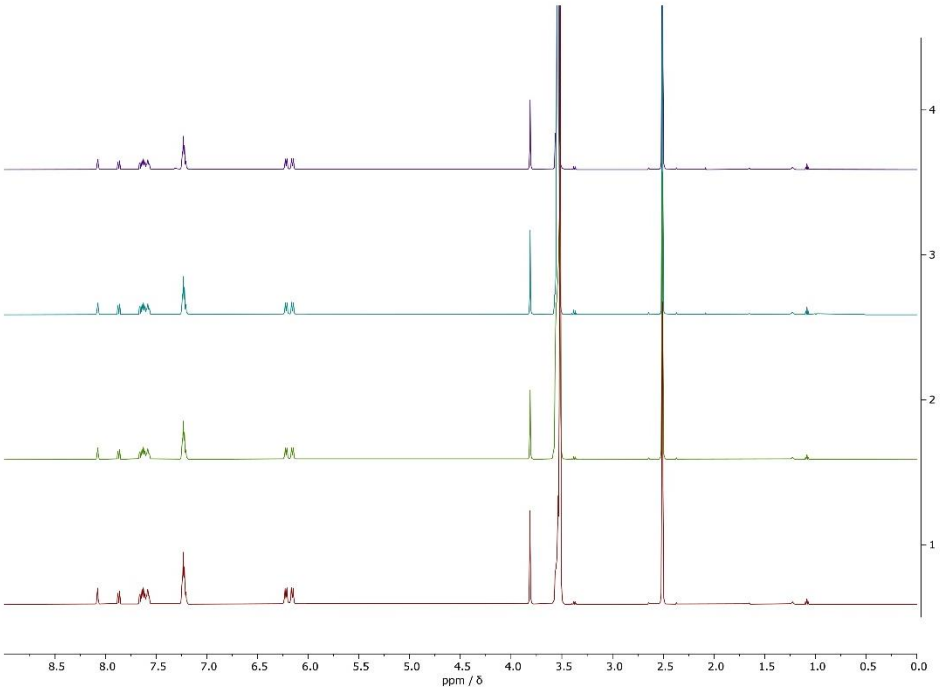

Fig. 57. ^{1}H-NMR spectrum of **8c** in DMSO-d_6 + 5% D_2O after 0h (red), 24h (green), 48h (cyan) and 72h (purple).

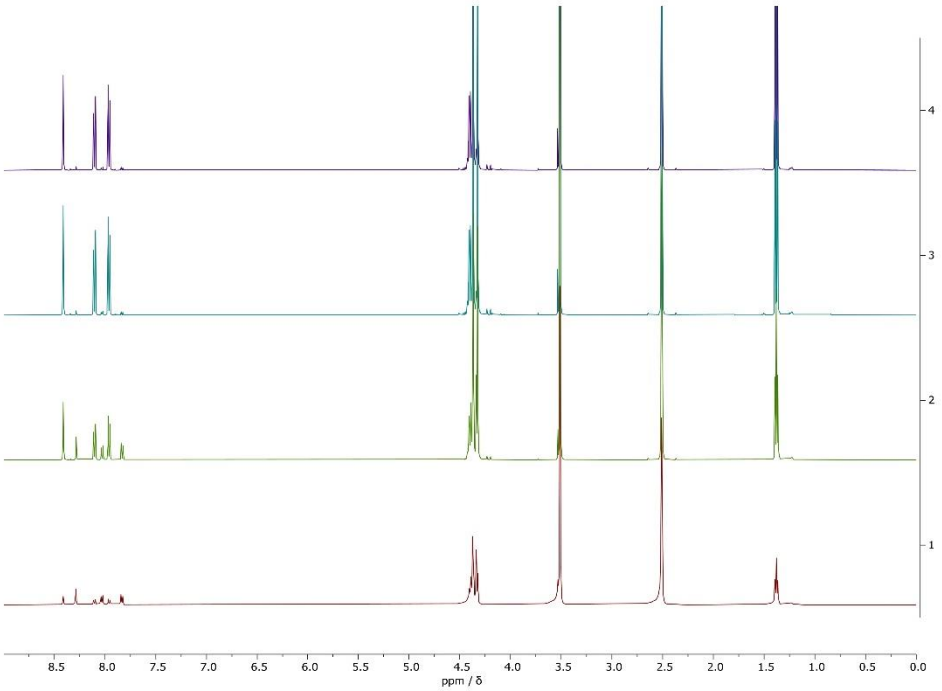

Fig. 58. ^{1}H-NMR spectrum of **9a** in DMSO-d_6 + 5% D_2O after 0h (red), 24h (green), 48h (cyan) and 72h (purple).

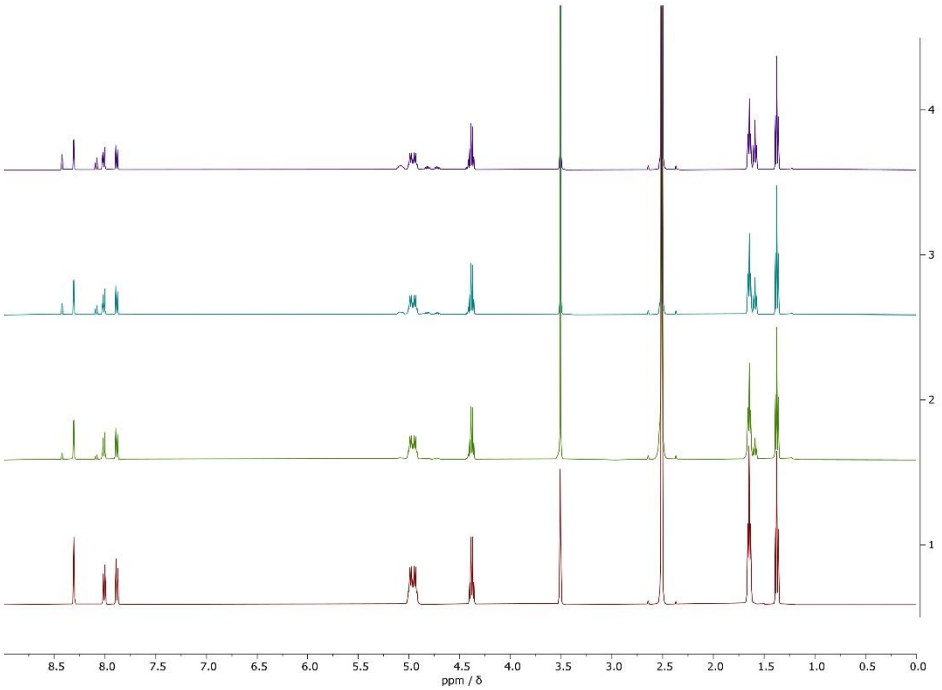

Fig. 59. ^{1}H-NMR spectrum of **9b** in DMSO-d_6 + 5% D_2O after 0h (red), 24h (green), 48h (cyan) and 72h (purple).

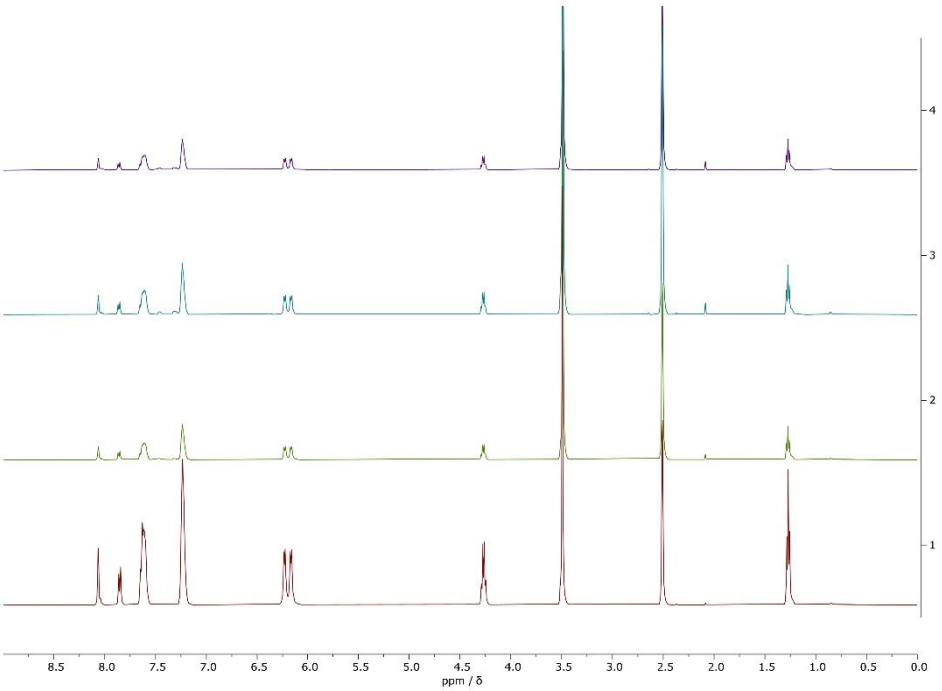

Fig. 60. ^{1}H-NMR spectrum of **9c** in DMSO-d_6 + 5% D_2O after 0h (red), 24h (green), 48h (cyan) and 72h (purple).

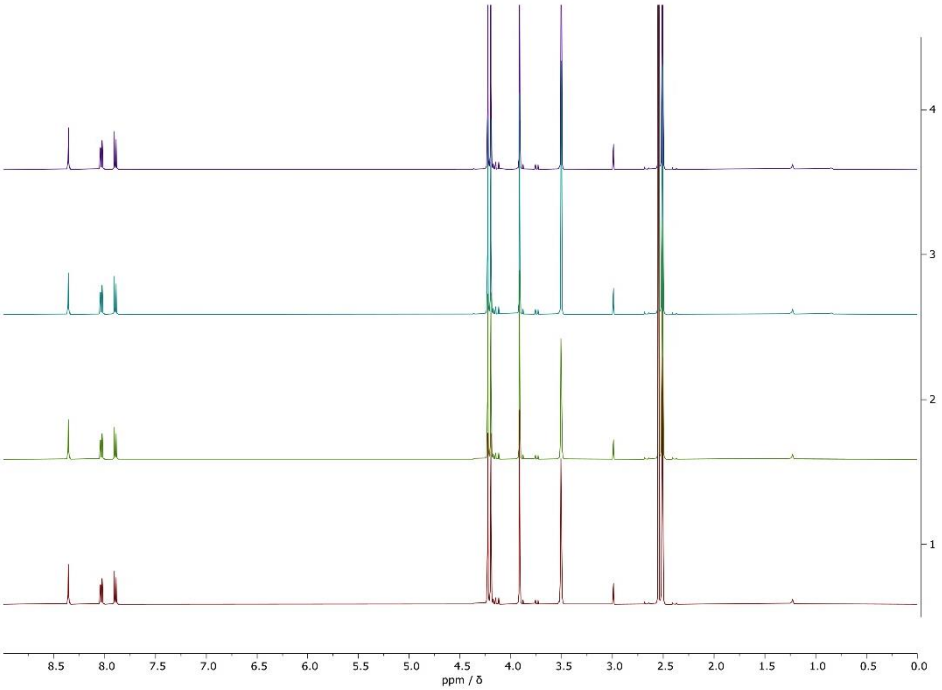

Fig. 61. ^{1}H-NMR spectrum of **10a** in DMSO-d_6 + 5% D_2O after 0h (red), 24h (green), 48h (cyan) and 72h (purple).

XLVII

#

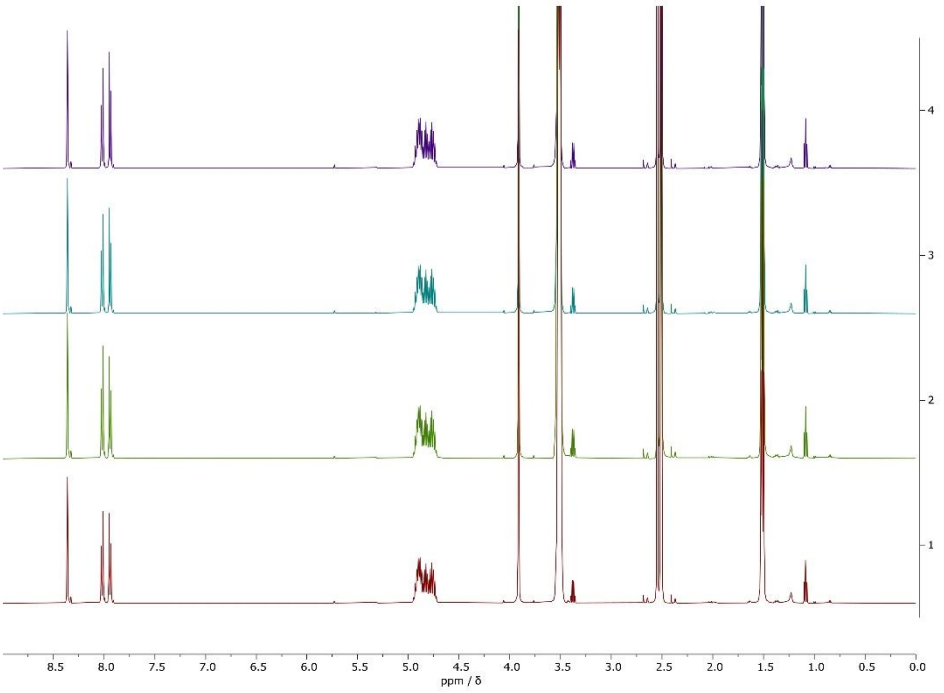

Fig. 62. ^{1}H-NMR spectrum of **10b** in DMSO-d_6 + 5% D_2O after 0h (red), 24h (green), 48h (cyan) and 72h (purple).

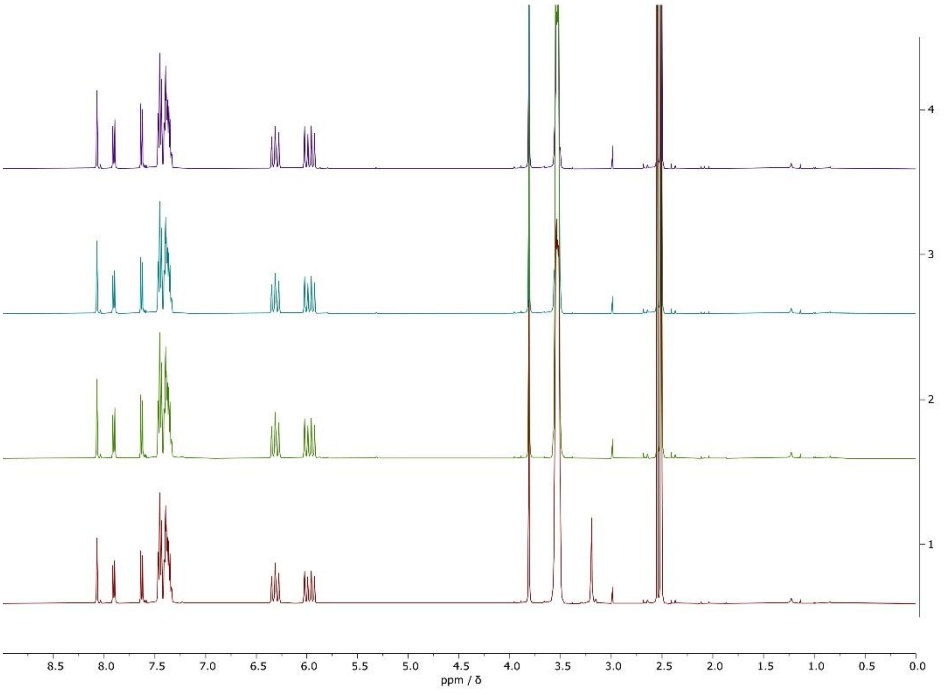

Fig. 63. ^{1}H-NMR spectrum of **10c** in DMSO-d_6 + 5% D_2O after 0h (red), 24h (green), 48h (cyan) and 72h (purple).

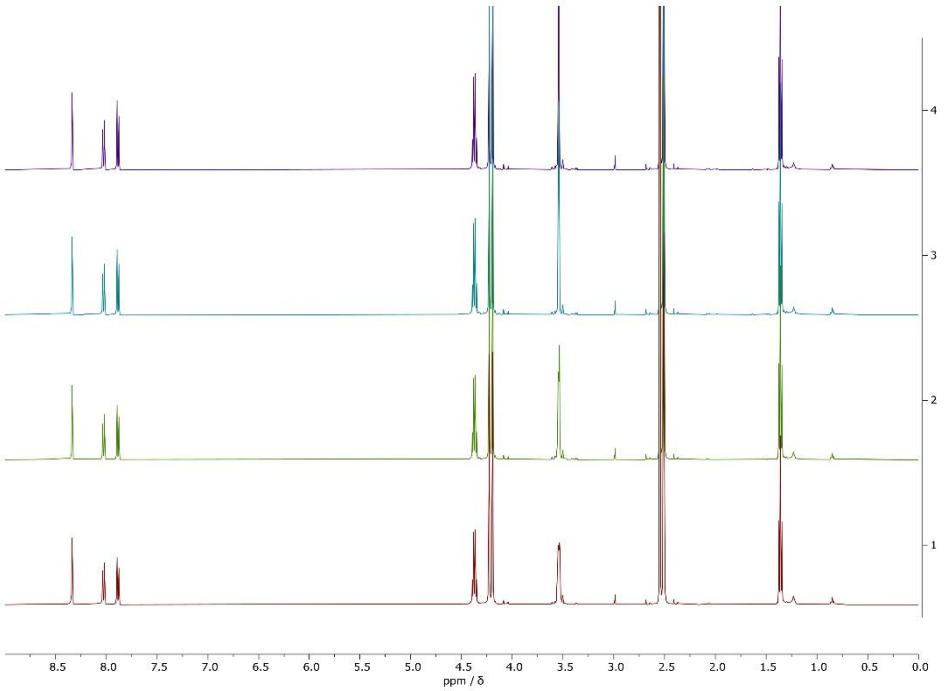

Fig. 64. ^{1}H-NMR spectrum of **11a** in DMSO-d_6 + 5% D_2O after 0h (red), 24h (green), 48h (cyan) and 72h (purple).

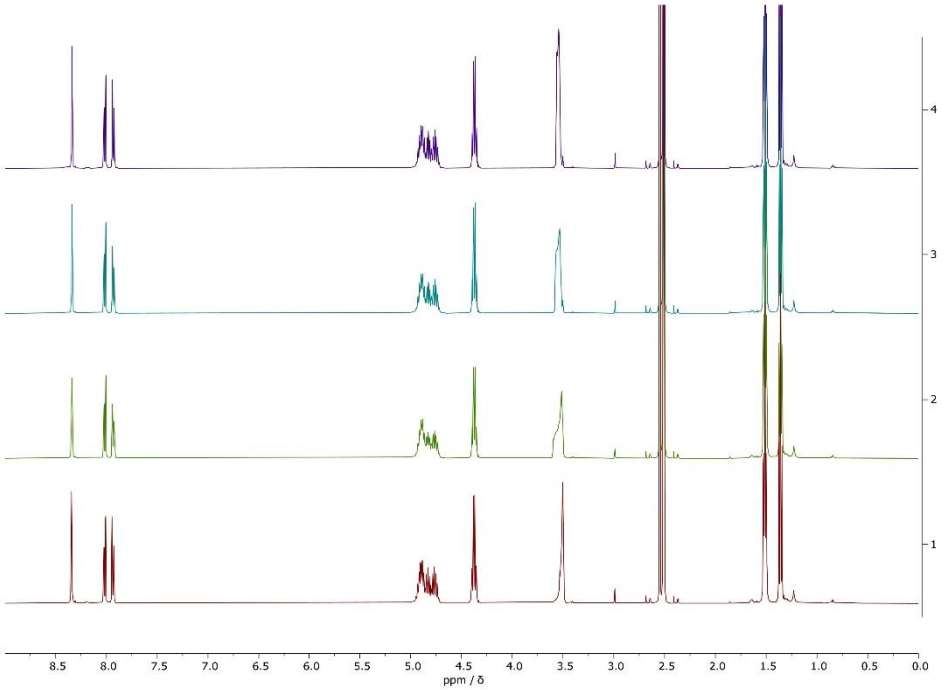

Fig. 65. ^{1}H-NMR spectrum of **11b** in DMSO-d_6 + 5% D_2O after 0h (red), 24h (green), 48h (cyan) and 72h (purple).

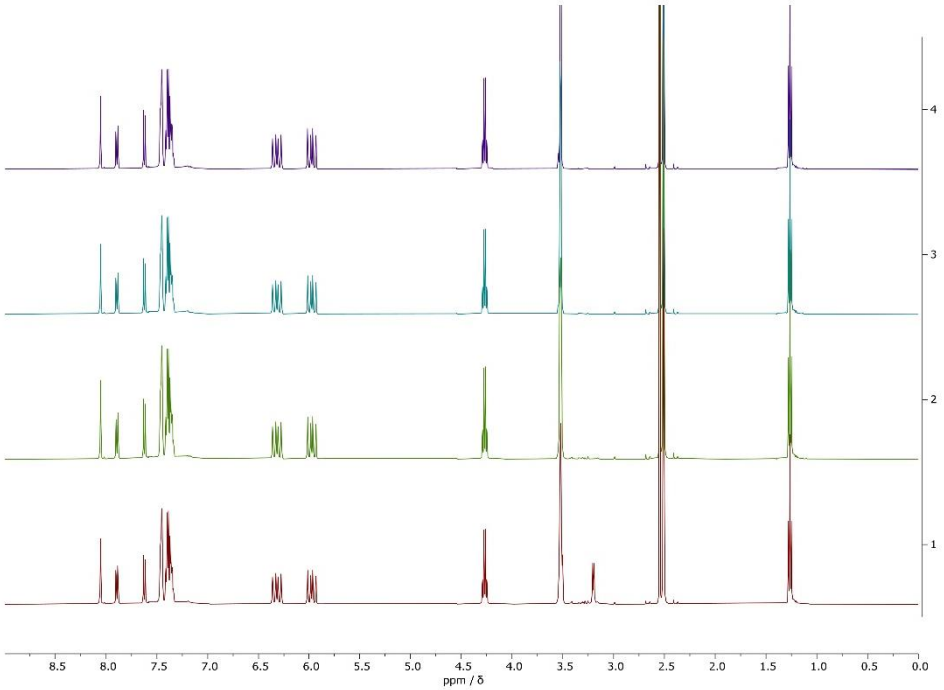

Fig. 66. ^{1}H-NMR spectrum of **11c** in DMSO-d_6 + 5% D_2O after 0h (red), 24h (green), 48h (cyan) and 72h (purple).

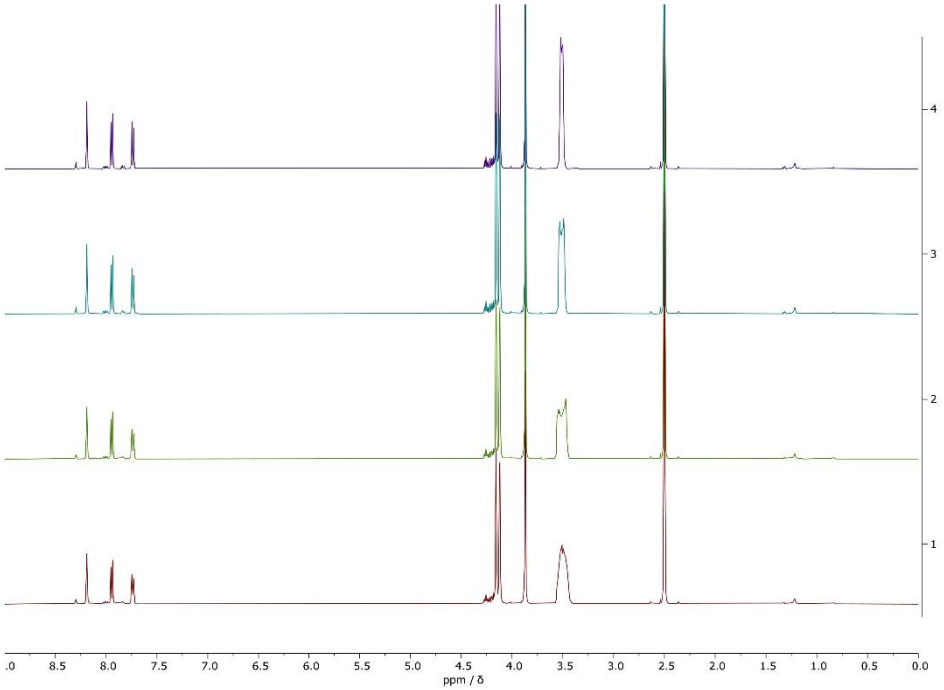

Fig. 67. ^{1}H-NMR spectrum of **12a** in DMSO-d_6 + 5% D_2O after 0h (red), 24h (green), 48h (cyan) and 72h (purple).

L

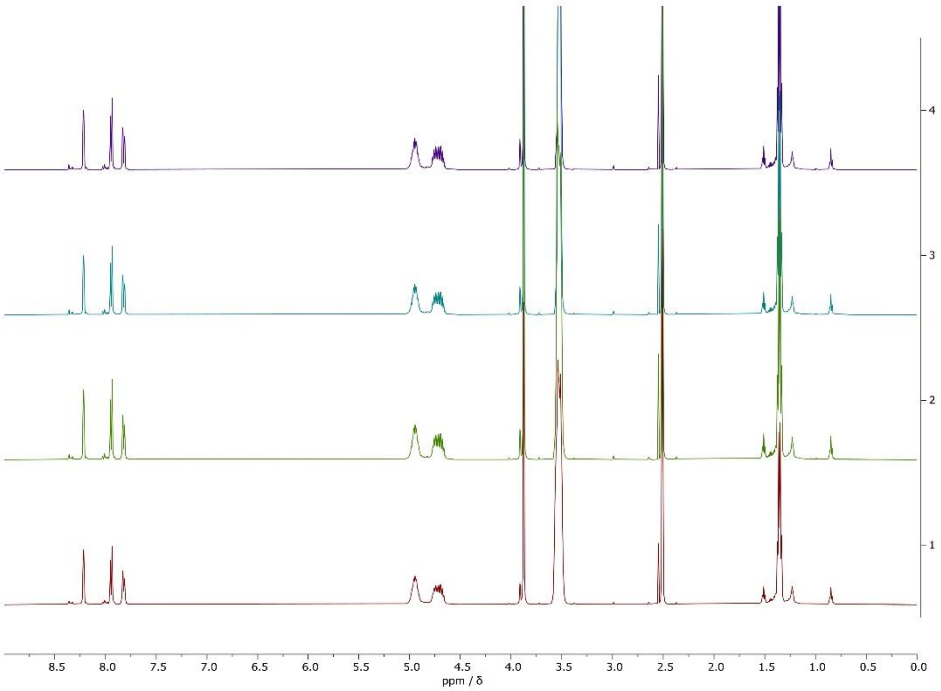

Fig. 68. ^{1}H-NMR spectrum of **12b** in DMSO-d_6 + 5% D_2O after 0h (red), 24h (green), 48h (cyan) and 72h (purple).

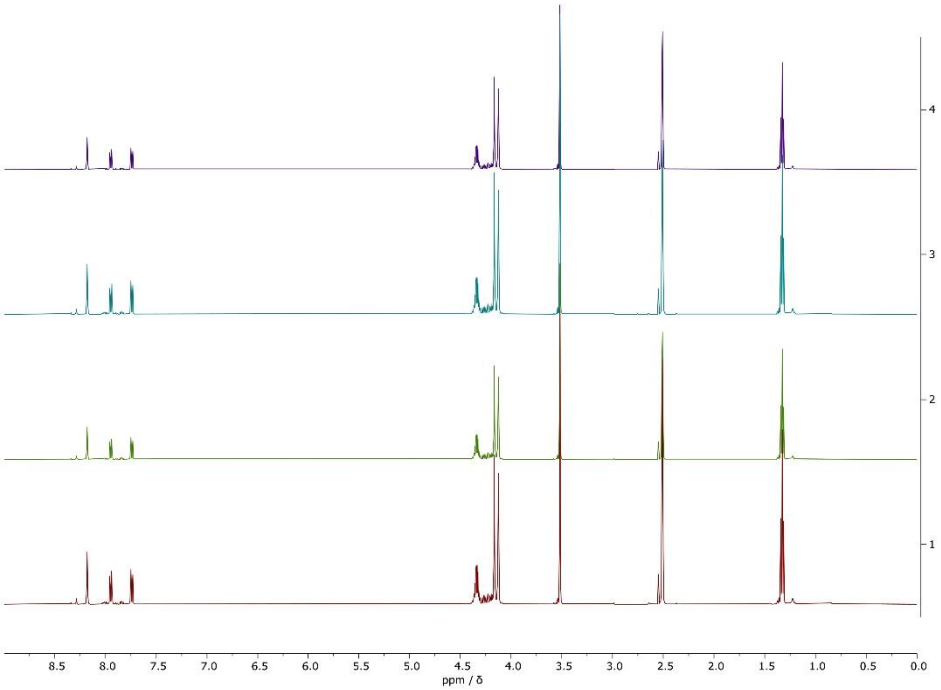

Fig. 69. ^{1}H-NMR spectrum of **13a** in DMSO-d_6 + 5% D_2O after 0h (red), 24h (green), 48h (cyan) and 72h (purple).

LI

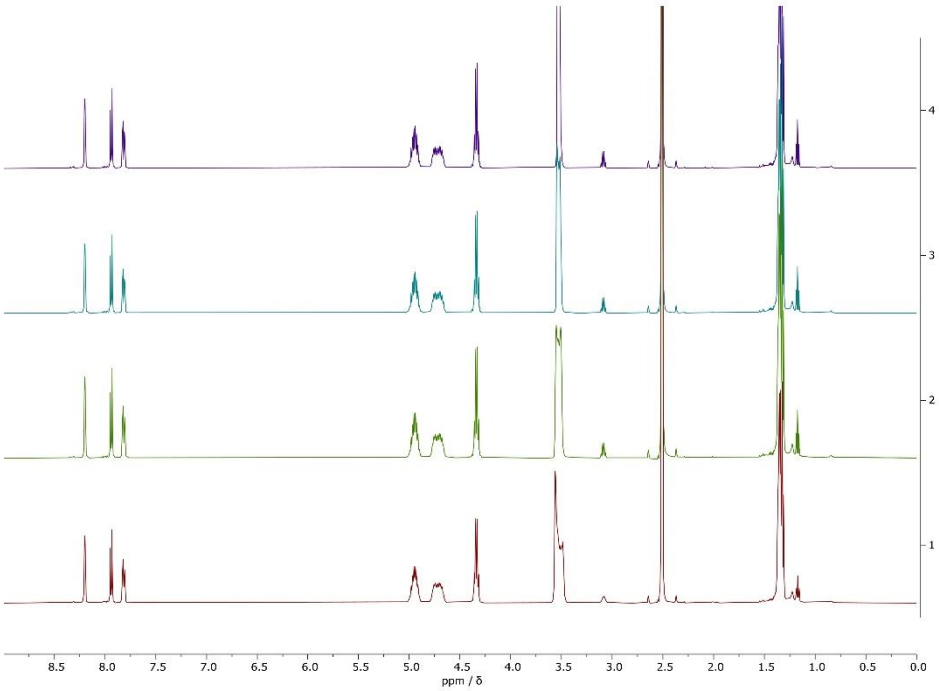

Fig. 70. ^{1}H-NMR spectrum of **13b** in DMSO-d_6 + 5% D_2O after 0h (red), 24h (green), 48h (cyan) and 72h (purple).

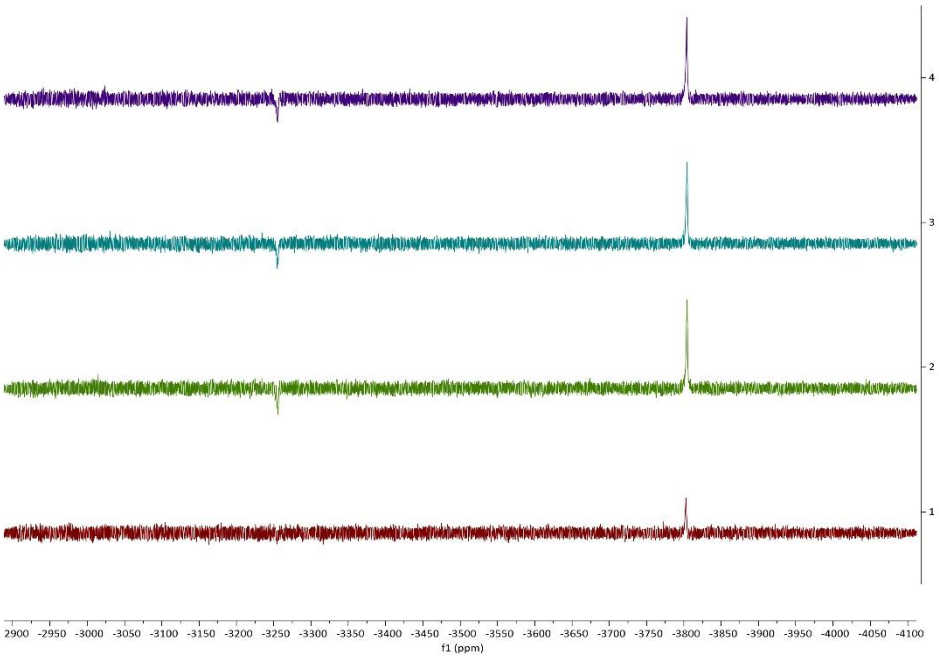

Fig. 71. ^{195}Pt-NMR spectrum of **9a** in DMSO-d_6 after 0h (red), 24h (green), 48h (cyan) and 72h (purple).

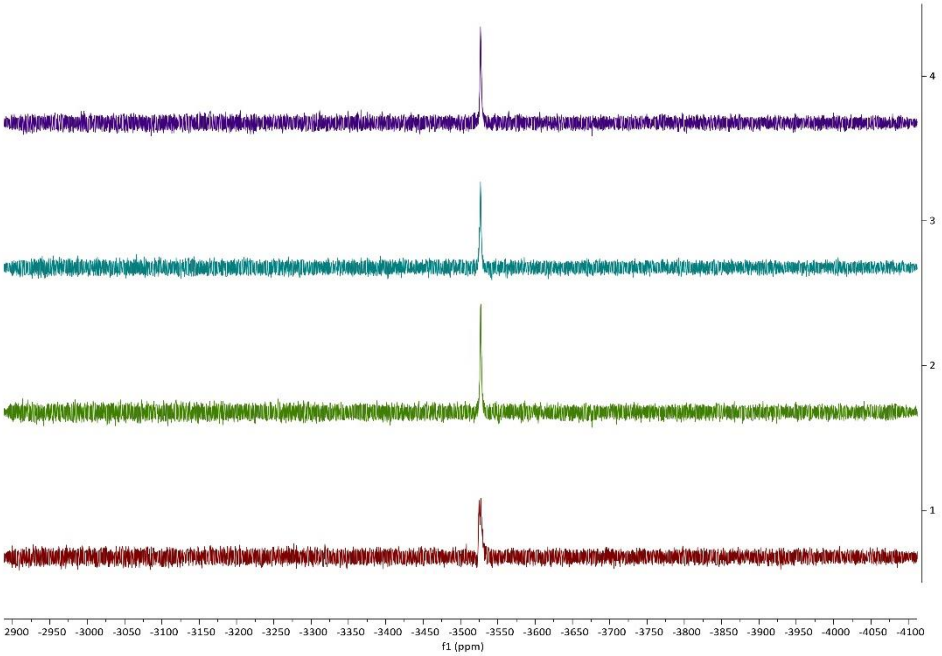

Fig. 72. ^{195}Pt-NMR spectrum of **10c** in DMSO-d_6 after 0h (red), 24h (green), 48h (cyan) and 72h (purple).

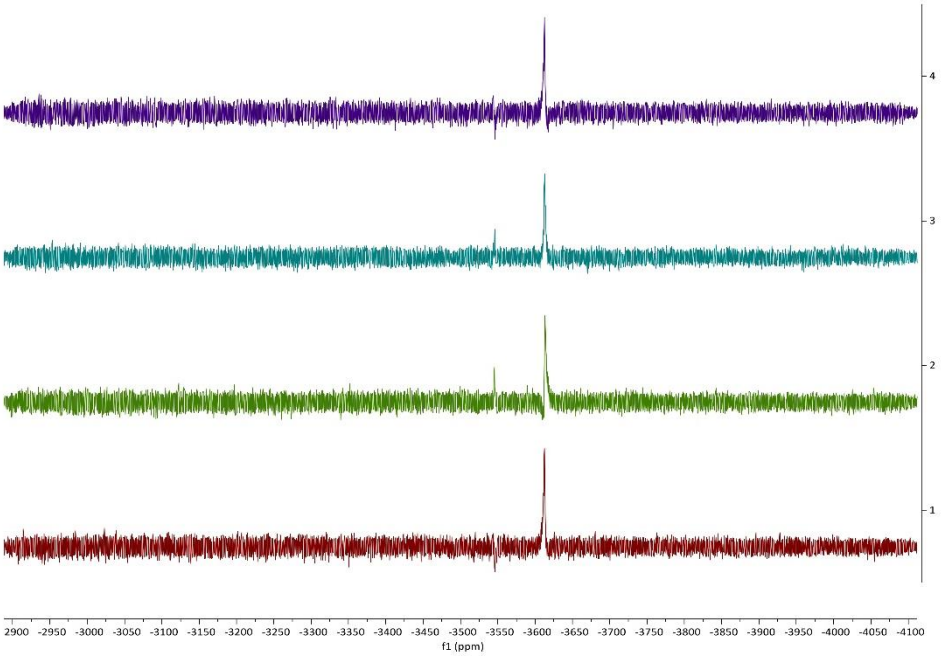

Fig. 73. ^{195}Pt-NMR spectrum of **13b** in DMSO-d_6 after 0h (red), 24h (green), 48h (cyan) and 72h (purple).

LIII

References

1. Senadi, G.C., Kudale, V.S., and Wang, J.-J., *Sustainable methine sources for the synthesis of heterocycles under metal- and peroxide-free conditions*, Green Chem., 21 (2019), 979-985, https://doi.org/10.1039/C8GC03839B
2. Gao, X., et al., *Atmospheric CO2 promoted synthesis of N-containing heterocycles over $B(C_6F_5)_3$ catalyst*, New Journal of Chemistry, 40 (2016), 8282-8287, https://doi.org/10.1039/C6NJ01721E

5.3 Publikation III mit Darstellung des Eigenanteils

Publikation III entstand unter Zusammenarbeit mit Dr. M. Gold und unter Mitarbeit von S. W. Schleser, Dr. T. Rehm, Dr. A. Bär, L. Köhler. L. Carnell und Dr. B. Biersack Mitarbeiter des Arbeitskreises Organische Chemie I der Universität Bayreuth unter der Leitung von Prof. Dr. R. Schobert

5.3.1 Eigenanteil an Publikation III

Die Publikation wurde in ***Chemistry – A European Journal*** veröffentlicht, unter dem Titel

„Antitumoral [1,3-diethyl-4,5-diaryl-imidazol-2-ylidene]gold(I) complexes with cellular targets adjustable by the nature of the second ligand“

von den Autoren

Sofia I. Bär[+], Madeleine Gold[+], Sebastian W. Schleser, Alexander Bär, Bernhard Biersack, Tobias Rehm, Leonhard Köhler, Luisa Kober und Rainer Schobert

[+] diese Autoren haben zu gleichen Anteilen zum Manuskript beigetragen

Eigenanteil:	Konzeption, Durchführung, Auswertung und graphischer Darstellung folgender biochemischer Assays: Zytotoxizitätstests via MTT-Assay, Lokalisation der Substanzen mittels Cofärbung, Zellzyklusanalyse, Messung des mitochondrialen Membranpotenzials, Messung reaktiver Sauerstoffspezies, Messung der lysosomalen Integrität und Zytoskelettfärbung mittels Immunofluoreszenz. Zudem; Verfassen des Manuskripts gemeinsam mit Madeleine Gold, einschließlich der Diskussion und Interpretation der Ergebnisse und Revision des Manuskripts.
Madeleine Gold:	Konzeption, Durchführung, Auswertung und graphischer Darstellung folgender biochemischer Assays: Zytotoxizitätstests via MTT-Assay, Apoptosenachweis mittels Caspase-3/7 Assay, DNA-Interaktionsstudien mittels EtBr-Assay, Thioredoxin-Reduktase Assay, Verfassung entsprechender Manuskriptpassagen mit Beteiligung an Diskussion und Korrektur.
Sebastian W. Schleser:	Synthese, Reinigung und Analytik der Testverbindungen, Verfassung entsprechender Manuskriptpassagen.
Tobias Rehm:	Synthese, Reinigung und Analytik der Testverbindungen.

Alexander Bär:	Synthese, Reinigung und Analytik der Testverbindungen, Verfassung entsprechender Manuskriptpassagen mit grafischen Darstellungen.
Leonhard Köhler:	DNA-Interaktionsstudien mittels EMSA-Assay
Lucas R. Carnell:	Unterstützende Arbeiten bei Zytotoxizitätstests via MTT-Assay, Tubulinpolymerisationsassay und Zytoskelettfärbung mittels Immunofluoreszenz.
Bernhard Biersack:	Synthese, Reinigung und Analytik der Testverbindungen Verfassung entsprechender Manuskriptpassagen.
Rainer Schobert:	Überarbeitung, Diskussion und Korrektur des Manuskripts.

5.3.2 Publikation III

Guided Antitumoural Drugs: (Imidazol-2-ylidene)(L)gold(I) Complexes Seeking Cellular Targets Controlled by the Nature of Ligand L

Sofia I. Bär[+], Madeleine Gold[+], Sebastian W. Schleser, Tobias Rehm, Alexander Bär, Leonhard Köhler, Lucas R. Carnell, Bernhard Biersack, and Rainer Schobert*

Organic Chemistry Laboratory, University of Bayreuth, Universitaetsstrasse 30, 95440 Bayreuth, Germany

[+]These authors contributed equally to this work.

*E-mail: rainer.schobert@uni-bayreuth.de

Chem. Eur. J. **2021**, 27, 5003

https://doi.org/10.1002/chem.202005451

Chemistry–A European Journal | Full Paper doi.org/10.1002/chem.202005451 | Chemistry Europe European Chemical Societies Publishing

Ligand Effects

Guided Antitumoural Drugs: (Imidazol-2-ylidene)(L)gold(I) Complexes Seeking Cellular Targets Controlled by the Nature of Ligand L

Sofia I. Bär[+], Madeleine Gold[+], Sebastian W. Schleser, Tobias Rehm, Alexander Bär, Leonhard Köhler, Lucas R. Carnell, Bernhard Biersack, and Rainer Schobert*[a]

Abstract: Three [1,3-diethyl-4-(*p*-methoxyphenyl)-5-(3,4,5-trimethoxyphenyl)imidazol-2-ylidene](L)gold(I) complexes, **4a** (L = Cl), **5a** (L = PPh_3), and **6a** (L = same N-heterocyclic carbene (NHC)), and their fluorescent [4-(anthracen-9-yl)-1,3-diethyl-5-phenylimidazol-2-ylidene](L)gold(I) analogues, **4b**, **5b**, and **6b**, respectively, were studied for their localisation and effects in cancer cells. Despite their identical NHC ligands, the last three accumulated in different compartments of melanoma cells, namely, the nucleus (**4b**), mitochondria (**5b**), or lysosomes (**6b**). Ligand L was also more decisive for the site of accumulation than the NHC ligand because the couples **4a**/**4b**, **5a**/**5b**, and **6a**/**6b**, carrying different NHC ligands, afforded similar results in cytotoxicity tests, and tests on targets typically found at their sites of accumulation, such as DNA in nuclei, reactive oxygen species and thioredoxin reductase in mitochondria, and lysosomal membranes. Regardless of the site of accumulation, cancer cell apoptosis was eventually induced. The concept of guiding a bioactive complex fragment to a particular subcellular target by secondary ligand L could reduce unwanted side effects.

Introduction

Although N-heterocyclic carbene (NHC) complexes have been much used as catalysts, their medicinal relevance was recognised surprisingly late, given their chemical stability under physiological conditions and their structural flexibility.[1,2] Unlike cisplatin (CDDP) and related platinum coordination complexes, which all lead to DNA adducts, resulting in an inhibition of the cancer cell cycle and eventually in apoptotic cancer cell death,[3] NHC complexes of various metals may address a broader array of molecular targets. Complexes with the character of delocalised lipophilic cations (DLCs) were found to selectively accumulate in mitochondria, which can be explained by their negative inner transmembrane potential.[4,5] Because cancer cells have a more hyperpolarised mitochondrial membrane potential (MMP) than normal cells, the selective accumulation of metal–carbene complexes with DLC character in cancer cells can be expected.[5,6] With the detection of antitumour activity of the antirheumatic gold(I) compound auranofin, (2,3,4,6-tetra-*O*-acetyl-1-thio-β-D-glucopyranosato)(triethylphosphane)gold, gold complexes came to the fore as potential anticancer drug candidates.[7] Auranofin mainly acts through the inhibition of mitochondrial thioredoxin reductase (TrxR) and by enhancing the mitochondrial permeability.[8,9] Through the inhibition of TrxR activity, the intracellular levels of reactive oxygen species (ROS) rise, which damages predominantly cancer cells because of their elevated ROS levels compared with healthy cells.[10] As a result, cytochrome c is released into the cytosol, triggering apoptotic cell death.[11] Due to their stability, NHC ligands can also be annulated and substituted in multifarious ways, allowing the mimicking or combinatorial attachment of pharmacophores to afford pleiotropic drugs.[12] Herein, we report on NHC gold(I) complexes **4a**–**6a**, carrying a 1,3-diethyl-4-(4-methoxyphenyl)-5-(3,4,5-trimethoxyphenyl)imidazol-2-ylidene ligand, akin to the natural antimitotic combretastatin A4 (CA-4), and differing only in the second ligand on the gold atom (Scheme 1). Preliminary studies had shown strong cytotoxicity against cancer cells with IC_{50} values in the low triple- to double-digit nanomolar range for complex **6a**, but its actual mechanism of action remained unclear.[13] A second series of complexes **4b**–**6b**, bearing the same "second ligands L", yet a better detectable fluorescent 1,3-diethyl-4-(anthracen-9-yl)-5-phenylimidazol-2-ylidene ligand, were synthesised and studied for their intracellular accumulation and their modes of anticancer action. The aim of this study was to find out whether ligand L could be used to set the site of accumulation, and thus, the targets and nature of antitumour effects of gold complexes with identical or closely related NHC li-

[a] S. I. Bär,[+] M. Gold,[+] S. W. Schleser, Dr. T. Rehm, A. Bär, L. Köhler, L. R. Carnell, Dr. B. Biersack, Prof. Dr. R. Schobert
Organic Chemistry Laboratory, University Bayreuth
Universitaetsstr. 30, 95447 Bayreuth (Germany)
E-mail: Rainer.Schobert@uni-bayreuth.de

[+] These authors contributed equally to this work.

Supporting information and the ORCID identification numbers for the authors of this article can be found under: https://doi.org/10.1002/chem.202005451.

Chemistry–A European Journal | Full Paper doi.org/10.1002/chem.202005451 | Chemistry Europe European Chemical Societies Publishing

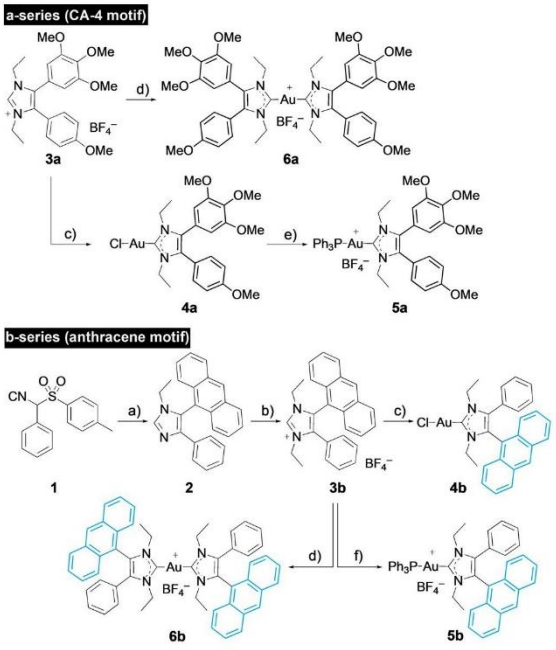

Scheme 1. Syntheses of complexes **4**–**6**: a) 9-formylanthracene, $EtNH_2$/THF, AcOH, EtOH, reflux, 2 h, then **1**, K_2CO_3, reflux 6 h, 61%; b) 1) EtI, MeCN, reflux, 48 h; 2) $NaBF_4$, acetone, RT, 1 h, 95%; c) Ag_2O (0.5 equiv), CH_2Cl_2, RT, 5 h, then $[AuCl(SMe_2)]$ (1 equiv), LiCl, RT, 24 h, 92%; d) Ag_2O (0.5 equiv), CH_2Cl_2, RT, 5 h, then $[AuCl(SMe_2)]$ (0.5 equiv), RT, 24 h, 88%; e) PPh_3, $NaBF_4$, CH_2Cl_2, RT, 24 h, 79%; f) $[AuCl(PPh_3)]$, KO*t*Bu, CH_2Cl_2, RT, 24 h, 70%.

gands. This was particularly tempting because similar *cis*-[{bis(1,3-dibenzylimidazol-2-ylidene)Cl(L)}Pt^{II}] complexes were previously shown by us to always accumulate in mitochondria, regardless of the charge of the complex and nature of ligands L.[14] Likewise, Ott et al. reported a triad of (1,3-diethylbenzimidazol-2-ylidene)(L)gold(I) complexes with the same ligands (L = Cl, PPh_3, NHC), which all localised in the mitochondria, albeit to different degrees.[15]

Results and Discussion

Synthesis

The new gold(I) NHC complexes were prepared from imidazolium salts **3a** and **3b** (Scheme 1). Compound **3b** was synthesised analogously to known compound **3a** by the van Leusen reaction of toluenesulfonylmethyl isocyanide (TosMIC) reagent **1** with 9-formylanthracene, followed by N-alkylation and anion exchange of the resulting imidazole **2**. Reactions of **3a** and **3b** with Ag_2O and transmetalation of the corresponding silver carbene complexes with different amounts of $[AuCl(SMe_2)]$ afforded mono- and bis-carbene gold(I) complexes **4a/b** and **6a/b** analogously to literature procedures.[12,13] New cationic complex **5a** was prepared by the reaction of complex **4a** with triphenylphosphane. Complex **5b** was obtained by diprotonation of **3b** and reaction of the free carbene with $[AuCl(PPh_3)]$. The stability of all complexes **4**–**6** in aqueous solution was ascertained by ^1H NMR spectroscopic monitoring over a period of 72 h (see the Supporting Information).

Cytotoxicity against cancer cells

All complexes **4**–**6** had an antiproliferative effect, with IC_{50} values in the three-digit nanomolar to low double-digit micromolar range, on cells of the human cancer cell lines HCT-116^{wt}, its p53 knockout mutant HCT-116$^{p53-/-}$ (both colon cancer), 518A2 (melanoma), HeLa, and multi-drug-resistant KB-V1^{Vbl} (both cervical carcinoma; Table 1). For complexes **4a**, **5a** and **6a** bearing a CA-4 analogous NHC ligand, we found that the cytotoxicity increased with their DLC character, that is, in the order **4a** < **5a** < **6a**, except for the KB-V1^{Vbl} cells. A similar trend was observed for the anthracenyl complexes (**4b** < **5b** < **6b**), with the exception of bis-NHC complex **6b**, which is less active than phosphane complex **5b** in 518A2 melanoma and HeLa cervical carcinoma cells. This conformity of cytotoxicities of the **a** and **b** series of complexes suggests similar mechanisms of action. Interestingly, all tested gold complexes, including auranofin, were more active against the p53-knockout mutant HCT-116$^{p53-/-}$, if compared with its wild-type analogue HCT-116^{wt} expressing functional p53 protein. We assume that complexes **4**–**6** induce cancer cell death in a way that is inde-

Table 1. Inhibitory concentrations, IC_{50}[a] [μM], of complexes **4**–**6** upon application to cells of HCT-116^{wt} and HCT-116$^{p53-/-}$ knockout mutant colon carcinomas, 518A2 melanoma, HeLa and mdr KB-V1^{Vbl} cervical carcinomas, and human adult dermal fibroblast cells HDFa.

	IC_{50} [μM][a]					
	HCT-116^{wt}	HCT-116 p$^{53-/-}$	518A2	HeLa	KB-V1^{Vbl}	HDFa
4a	6.6 ± 0.8	2.2 ± 0.4	19.8 ± 2.0	12.4 ± 0.5	> 50	24.6 ± 3.4
4b	16.4 ± 0.2	8.4 ± 0.3	7.9 ± 0.8	23.7 ± 1.1	5.9 ± 1.3	9.0 ± 1.3
5a	1.1 ± 0.3	0.6 ± 0.1	5.0 ± 0.3	3.6 ± 0.7	0.6 ± 0.2	5.8 ± 0.9
5b	1.3 ± 0.6	0.4 ± 0.1	2.9 ± 0.5	1.8 ± 0.4	2.2 ± 0.2	5.9 ± 0.2
6a	0.2 ± 0.02	0.05 ± 0.001	0.4 ± 0.1	0.3 ± 0.02	4.6 ± 0.2	1.4 ± 0.2
6b	0.3 ± 0.03	0.2 ± 0.05	5.5 ± 0.4	3.6 ± 0.4	0.7 ± 0.2	3.2 ± 0.4
auranofin	11.9 ± 0.4	5.0 ± 0.2	1.8 ± 0.03	2.6 ± 0.4	n.d.[b]	13.7 ± 1.0

[a] Values are the means ± standard deviation (SD) determined in four independent experiments and derived from dose–response curves after 72 h incubation by using the 3-(4,5-dimethylthiazol-2-yl)-2,5-diphenyltetrazolium bromide (MTT) assay. [b] Not determined.

Chemistry–A European Journal | Full Paper doi.org/10.1002/chem.202005451 | Chemistry Europe European Chemical Societies Publishing

pendent of p53, as already shown for auranofin[16,17] and for related (1,3-diethylbenzimidazol-2-ylidene)gold(I) complexes.[18] Complexes **4b**, **5** and **6** were also quite active against the multi-drug-resistant cell line KB-V1^{Vbl}, which expresses high levels of Pg-p, an ATP-dependent efflux pump, capable of expelling a variety of xenobiotics. Complexes **5a** and **6b** appear to have a particularly low affinity for Pg-p. Cationic complexes **5b** and **6a** showed some selectivity for cancer over non-malignant cells and are particularly interesting candidates for further studies.

Intracellular localisation

The fluorescent complexes **4b**, **5b** and **6b** were synthesised as easy-to-track analogues of complexes **4a**, **5a** and **6a**, respectively. Well-observable, flat 518A2 melanoma cells were treated with the **b** complexes, then counterstained with dyes specifically accumulating in particular cancer-relevant cellular organelles, and eventually fixed and examined through confocal microscopy (Figure 1). By counterstaining with Nuclear Green, neutral chloride complex **4b** could be localised in the area of the nucleus and to a minor degree in the cytoplasm. This is in line with reports on the nuclear accumulation of neutral gold(I) complexes bearing an aryl-substituted NHC ligand.[19,20] Many established first-line anticancer drugs target cancer cell nuclei,[21] yet suffer from therapeutic shortcomings, including off-target side effects and an early onset of resistance, owing to insufficient nuclear accumulation.[22] Against this background, the enrichment of new (NHC)Au^{I}Cl complex **4b** predominantly in cancer cell nuclei is remarkable. Cationic phosphane complex **5b** accumulated in the mitochondria, as demonstrated by counterstaining of treated 518A2 cells with red mitochondria-selective MitoTracker (Figure 1). Apparently, the DLC character of this complex favours accumulation in the negatively charged mitochondrial compartments over any potential DNA intercalation of the planar anthracene residue. Mitochondria are considered to be promising targets for cancer therapy. A distinct disruption of the MMP typically results in the induction of apoptosis. One of the pro-apoptotic stimuli is an increased mitochondrial ROS production, which, in turn, causes disruption of the MMP.[23] Cationic bis-NHC complex **6b** accumulated mainly in lysosomes within the cytoplasm. It

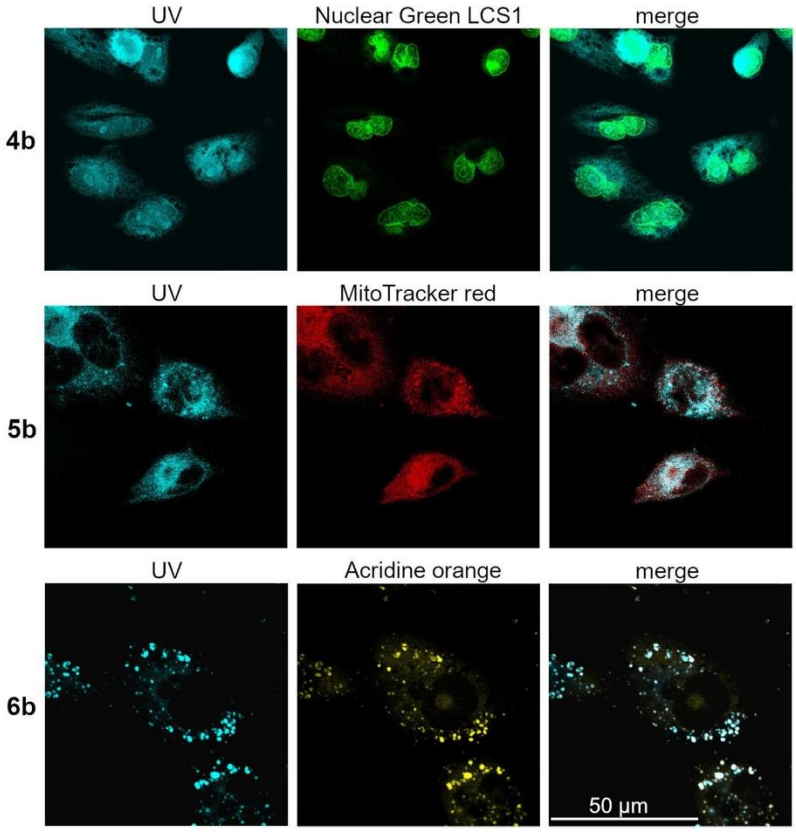

Figure 1. Confocal fluorescence microscopy images of 518A2 melanoma cells incubated for 30 min with 30 µM of complexes **4b**–**6b** (λ_{ex} = 350 nm and λ_{em} = 420–480 nm). The nuclei were counterstained with Nuclear Green LCS1 (abcam; λ_{ex} = 514 nm and λ_{em} = 520–535 nm), the mitochondria with MitoTracker^{TM} (Thermo Fisher; λ_{ex} = 580 nm and λ_{em} = 595–610 nm) and the lysosomes with acridine orange solution (5 µg mL^{-1}, ABCR GmbH; λ_{ex} = 350 nm and λ_{em} = 600–660 nm). Images are representative of at least four independent experiments; 2000-fold magnification.

Chemistry–A European Journal | Full Paper doi.org/10.1002/chem.202005451 | Chemistry Europe European Chemical Societies Publishing

should be noted that Gust et al. found an accumulation of all three [1,3-diethyl-4,5-di(*p*-fluorophenyl)imidazol-2-ylidene](L)-gold(I) analogues of complexes **4a**, **5a** and **6a** in the nuclei of MCF-7 and HT-29 cells upon a 24 h long exposure.[24] So, the organelle-selective accumulation of our **a** complexes after only 30 min might be a kinetic effect. The bottom row of Figure 1 shows confocal fluorescence microscopy images of 518A2 melanoma cells treated with complex **6b** and lysotropic acridine orange, as well as the good match of the blue fluorescence of **6b** (UV) with the orange fluorescence of the counterstained lysosomes. Lysosomes are the recycling centres of the cell and are involved in cellular digestion processes, such as autophagy, endocytosis and phagocytosis. Moreover, the release of lysosomal hydrolases, so called cathepsins, is involved in the induction of cell death.[25,26] Cathepsins mediate caspase- and mitochondrion-independent cell death, especially in cancer cells with mutations in genes involved in the classic apoptotic pathway, for example, the TP53 tumour suppressor gene.[27]

Induction of cancer cell apoptosis

The majority of p53 mutations are missense mutations, as in the case of 518A2 melanoma cells,[28] leading to the expression of dysfunctional p53 proteins with oncogenic activities intensifying malignant properties of cancer cells, such as clinical drug resistance.[29] Because the p53-independent induction of cancer cell apoptosis had been reported for auranofin[17,30] and for (1,3-diethylbenzimidazol-2-ylidene)gold(I) complexes,[18] we investigated if complexes **4**–**6** also lead to an activation of apoptosis (Figure 2). Upon treatment of 518A2 melanoma cells with these complexes, the activation of effector caspases-3 and -7 was observed, which we assumed to be p53 independent, given the results from our cytotoxicity studies. The treated cells showed the typical morphological signs of apoptosis, as well as translocalisation of phosphatidylserines to the outer leaflet of the plasma membrane, which indicated early rather than late apoptosis or necrosis (see the Supporting Information).

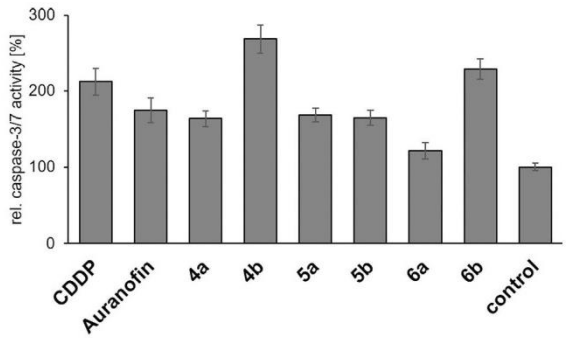

Figure 2. Induction of effector caspase-3/-7 activity in 518A2 melanoma cells after treatment with 5 μM **4**–**6** for 6 h, measured by means of the Apo-ONE® Homogenous Caspase-3/7 Assay Kit (Promega). CDDP was used as a positive control. The vitality of cells was simultaneously tested by MTT assays and was >80% for all experiments, except for complex **6a** (70%). All experiments were performed in triplicate and results quoted as means ± SD. The solvent-treated negative control was set to 100%.

tion). Because about 50% of all human tumours bear p53 mutations, drugs that induce p53-independent programmed cell death are of particular interest.[31,32]

Mechanism of action of complexes 4a and 4b in the nucleus

The antiproliferative effect of CDDP and other platinum complexes is based mainly on their interaction with cellular DNA.[3b,33] Because of the localisation of neutral complex **4b** in the nuclear area, a potential DNA interaction of **4b** and its close structural analogue **4a** was examined by ethidium bromide (EtdBr) saturation assays (Figure 3) and electrophoretic mobility shift assays (EMSAs; Figure 4).

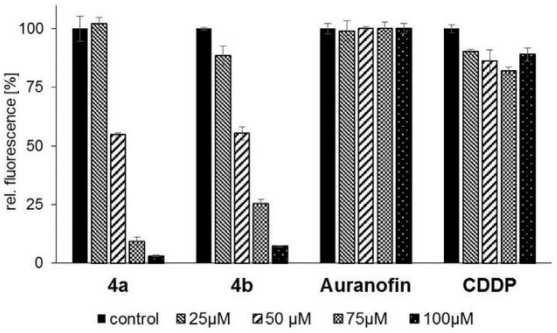

Figure 3. EtdBr saturation assays with 25, 50, 75 and 100 μM **4a**, **4b** and auranofin. CDDP was used as a positive control. Negative controls were treated with an equivalent amount of solvent (DMF or H_2O). All experiments were carried out in triplicate with negative controls set to 100%.

Addition of complexes **4a** or **4b** to linear, double-stranded salmon sperm DNA led to a distinct concentration-dependent displacement, and thus, to a reduction of the fluorescence of intercalated EtdBr, exceeding that caused by CDDP by far. This suggests a strong interaction of both complexes **4** with this DNA form, possibly associated with an alteration of the DNA morphology. Auranofin showed no such effect (Figure 3). In the EMSA with circular plasmid DNA, a slight relaxation, that is, despiralisation, of the covalently closed circular (ccc) DNA form for the benefit of the open circular (oc) form was observed after incubation with complex **4a**, and a stronger relaxation after treatment with complex **4b** (Figure 4). In contrast to CDDP, gold NHC complexes are known to bind non-covalently to DNA, which may be the reason for their weaker effects in the EMSA.[34]

Although auranofin had previously been reported to interact neither with linear DNA nor with circular plasmid DNA,[35] various other gold(I) complexes with readily displaceable ligands (e.g., Cl^-) had shown affinity to different types of DNA.[35,36] Irreparable DNA damage induces apoptosis, normally triggered by the tumour suppressor protein p53. However, apoptosis as a consequence of DNA damage caused by metal complexes had also been reported to proceed independently of p53,[37,38] through the mitogen-activated protein kinase (MAPK) signal-

Chemistry–A European Journal | Full Paper doi.org/10.1002/chem.202005451 | Chemistry Europe European Chemical Societies Publishing

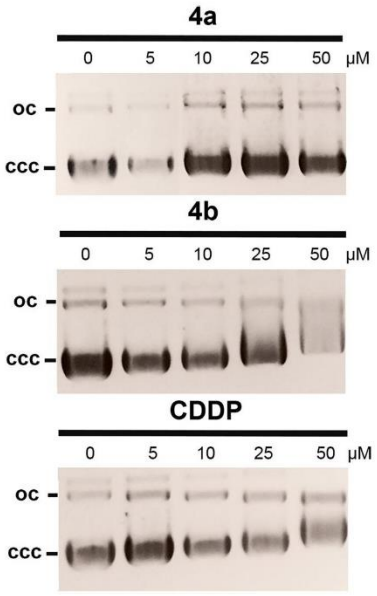

Figure 4. EMSAs with circular pBR322 plasmid DNA after 24 h treatment with complexes **4a** or **4b**, as visualised by UV radiation. CDDP was used as a positive control. Images are representative of at least two independent experiments.

ling pathway involving JNK, p38 and ERK1/2.[37,18] Whether complexes **4**, which we have found to induce cancer cell apoptosis and to be cytotoxic independently of functional p53, operate by a similar mechanism remains to be shown. At present, we cannot exclude that their reactions with further biologically relevant macromolecules might also play a role.[39]

Mechanism of action of complexes 5a and 5b in mitochondria

Because cationic triphenylphosphane complex **5b** was localised in the mitochondria of 518A2 melanoma cells, we anticipated a mitochondria-associated mode of action for **5b** and closely related complex **5a**. The anticancer effect of auranofin, and several other gold(I) complexes, mainly relies on the inhibition of TrxR.[40,41] TrxRs, which catalyse the reduced nicotinamide adenine dinucleotide phosphate (NADPH)-dependent reduction of the redox protein thioredoxin (Trx) and other compounds, are key enzymes for cellular protection against oxidative stress.[42] To date, three different isoforms of TrxR are known: cytosolic TrxR1, mitochondrial TrxR2 and testis-specific TrxR3.[43] Gold complexes, such as auranofin, are thought to inhibit TrxRs by releasing monovalent Au^{I} species, which bind to selenocysteine residues in the active site of the enzyme.[44] This is in line with reports that mono-NHC gold(I) complexes with good leaving groups, such as halides or phosphanes, are better TrxR inhibitors than bis-NHC complexes.[45] For instance, sub-micromolar IC_{50} values were reported by Gust et al. for donor-substituted (1,3-diethyl-4,5-diarylimidazol-2-ylidene)(PPh_3)gold(I) complexes,[24] and by Ott et al. for benzimidazol-2-ylidene analogues,[15,46] whereas few inhibitory bis(1,3-diarylimidazol-2-ylidene) complexes have been reported, to date.[45,47]

If applied in low sub-micromolar concentrations, complexes **5a** and **5b** strongly inhibited the panTrxR activity in colorimetric TrxR microplate assays with 5,5′-dithiobis(2-dinitrobenzoic acid (DTNB; Ellman's reagent) as a substrate (Figure 5). Because many tumours have elevated TrxR levels,[43] and tumour cells are more sensitive to oxidative stress, due to their a priori high intracellular ROS levels relative to non-malignant cells, TrxR are interesting targets for selective antitumour therapy.

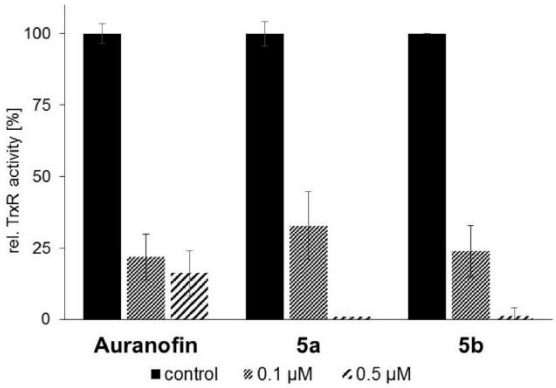

Figure 5. Concentration-dependent inhibition of TrxR activity in cell lysates of 518A2 melanoma cells by gold(I) complexes **5a** and **5b**, and auranofin as a positive control. TrxR-independent substrate reduction was accounted for by experiments in the presence and absence of the specific TrxR inhibitor aurothiomalate. All values are means ± SD of at least three independent experiments with negative controls set to 100%.

TrxR inhibition generally leads to an accumulation of oxidised Trx and ROS in mitochondria, resulting in an increase of mitochondrial permeability.[40] Upon treatment of 518A2 melanoma cells with complexes **5a** and **5b**, we observed a distinct reduction of the MMP through a fluorescence-based microplate assay (Figure 6), exceeding that induced by auranofin, which is in keeping with their stronger TrxR inhibition.

We confirmed these results by an assessment of the intracellular ROS concentrations after treatment of 518A2 melanoma cells with auranofin, CCCP and complexes **5a** and **5b** using the cell permeant, fluorogenic dye 2′,7′-dichlorofluorescein diacetate (DCFH-DA). After diffusion into the cells, DCFH-DA is deacetylated by cellular esterases to a non-fluorescent compound, which is later oxidised by hydroxyl, peroxyl or other ROS to the intensely fluorescent 2′,7′-dichlorofluorescein (DCF), detectable by fluorescence spectroscopy (Figure 7).

We conclude that the cytotoxicity of complexes **5** originates mainly from their inhibition of TrxR in the mitochondria of cancer cells and the subsequent alteration of the intracellular ROS equilibrium.[40] Elevated concentrations of hydrogen peroxide and oxidised Trx2 affect further intra-mitochondrial targets, leading to the opening of the mitochondrial permeability

Chemistry–A European Journal | Full Paper doi.org/10.1002/chem.202005451 | Chemistry Europe European Chemical Societies Publishing

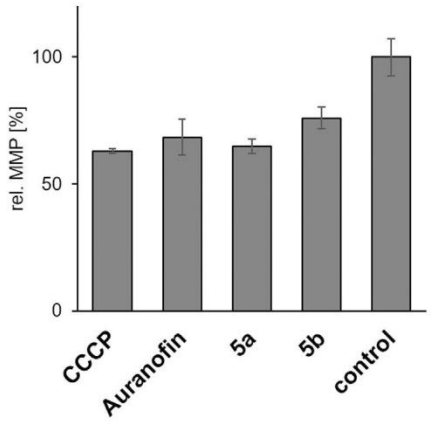

Figure 6. Relative MMP in 518A2 melanoma cells after treatment (45 min) with complexes **5a** and **5b** (10 μM each). Carbonylcyanide-*m*-chlorophenylhydrazone (CCCP) and auranofin (10 μM, each) were used as positive controls and solvent-treated negative controls were set to 100%. Assays were carried out in triplicate.

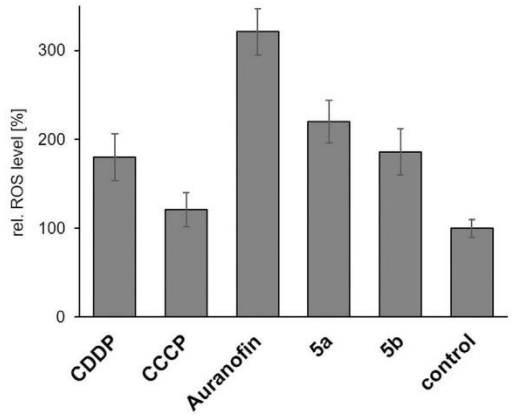

Figure 7. Influence of gold(I) complexes **5a** and **5b**, and auranofin (10 μM each), as well as CCCP (10 μM) as a positive control, on the levels of ROS in 518A2 melanoma cells, as determined by fluorescence-based DCFH-DA assays after an incubation time of 1 h. Negative controls were treated identically with solvent. All values are mean values ± SD from at least four independent experiments with negative controls set to 100%.

transition pore and/or to an increase of the permeability of the outer membrane.[9,48] As a result, hydrogen peroxide is released into the cytosol where it oxidises cytosolic Trx1 irreversibly, due to the inhibition of TrxRs. The elevated levels of hydrogen peroxide and oxidised Trx in the cytosol then activate various signalling pathways, eventually leading to apoptosis, which is likely to be dependent on p38/ERK1/2, rather than p53, as shown for auranofin.[40,49] Because cancer cells, unlike non-malignant cells, are not normally susceptible to mitochondrial membrane permeability transition, the induction of this condition by mitochondria-targeting complexes, such as **5**, could be exploited in a therapeutic context.[50]

Mechanism of action of complexes 6a and 6b in lysosomes

The cationic bis-NHC complex **6b** was localised in the lysosomes of 518A2 melanoma cells. Lysosomes mediate the degradation of macromolecules of intracellular origin or those that are internalised by endocytosis or phagocytosis.[51] These single-membrane acidic organelles (pH 4.5–4.8) are involved in various cellular pathways and different types of cell death, and their functionality is thus inevitable for cellular homeostasis.[51] Various forms of cellular stress lead to lysosomal swelling and lysosomal membrane permeabilisation (LMP), resulting in the release of intralysosomal cargo into the cytoplasm.[51] Amongst others, cathepsins B and D are released into the cytoplasm under stress, where they induce different forms of cell death, including the p53-independent, lysosome-dependent apoptotic cell death.[26,31,51,52] To detect a potential induction of LMP by complexes **6**, we performed a time-dependent staining of lysosomes in solvent- and complex-treated 518A2 melanoma cells (Figure 8). Because the cytotoxicity of both complexes against 518A2 cells in MTT assays was quite different (IC_{50}(**6a**) = 0.4 μM, IC_{50}(**6b**) = 5.5 μM), we adjusted their concentrations accordingly to ensure a sufficient cell viability. The incubation with either complex **6a** or **6b** led to an induction of LMP. The lysotropic orange dye used in this assay selectively accumulates in intact acidic lysosomes. If LMP occurs, the dye is released into the cytosol and the fluorescence of defined lysosomal compartments disappears. As expected, complex **6a**, which had proved to be more active in MTT assays, also led to faster lysosomal disruption after only 2 h of incubation. Cells treated with **6b** showed first signs of LMP only after 4 h of treatment.

Conclusion

The [4-(anthracen-9-yl)-1,3-diethyl-5-phenylimidazol-2-ylidene](L)gold(I) complexes **4b**, **5b**, and **6b** accumulated quickly in different compartments of 518A2 melanoma cells, that is, neutral chlorido complex **4b** in the nuclei, cationic phosphane complex **5b** in mitochondria and large delocalised cationic bis-NHC complex **6b** in the lysosomes. The analogous **a** series of complexes carried a slightly different 4,5-diarylimidazol-2-ylidene ligand. The fact that all couples **4a**/**4b**, **5a**/**5b** and **6a**/**6b** afforded similar results in cytotoxicity tests with cancer cells, and in tests on targets typically found at the identified sites of accumulation, supports the assumption that **a** complexes localise similarly to the **b** complexes, and that the nature of ligand L, which is responsible for the charge, size and lipophilicity of the complex, is decisive for the site of accumulation. However, this phenomenon might be limited to divalent gold(I)–NHC or even to (imidazol-2-ylidene)gold(I) complexes because a comparable series of *cis*-[bis(1,3-dibenzylimidazol-2-ylidene)]Cl(L)Pt^{II}[14] and (1,3-diethylbenzimidazol-2-ylidene)(L)gold(I) complexes,[15] carrying the same ligands L (Cl, PPh_3 or the same NHC ligand), were previously shown to accumulate in mitochondria, regardless of the charge of the complex and the nature of ligand L. The different distributions of DLC complexes **5** (in mitochondria) and **6** (in lysosomes) is explicable by the higher molecular weight and steric demand of

Chemistry–A European Journal | Full Paper doi.org/10.1002/chem.202005451 | Chemistry Europe European Chemical Societies Publishing

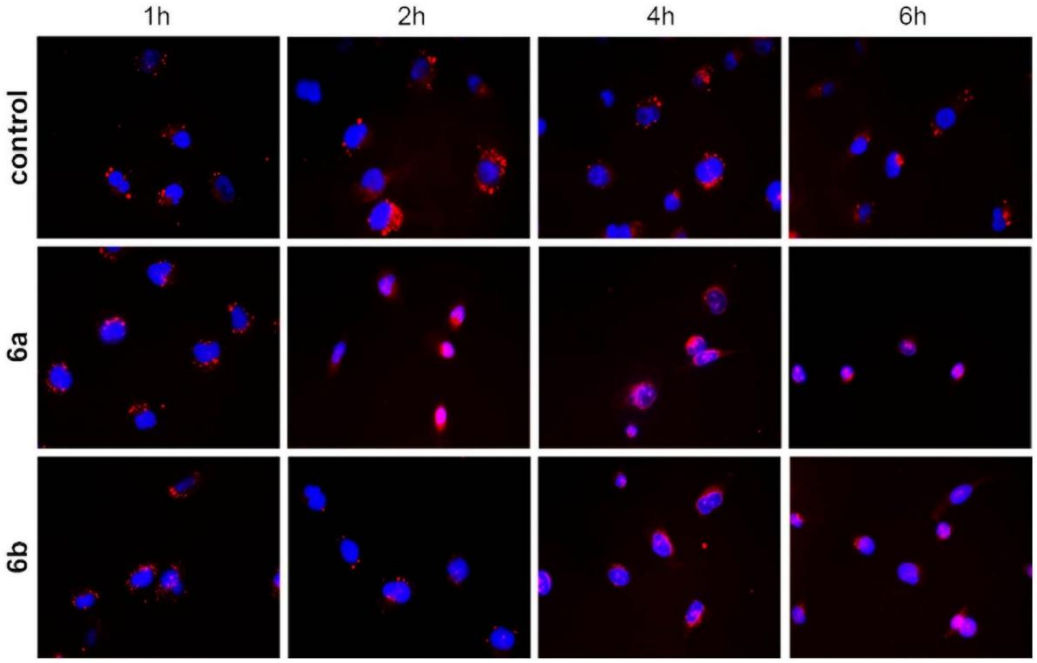

Figure 8. Fluorescence microscopy images of 518A2 melanoma cells treated with solvent (DMF), or complexes **6a** (0.4 μM) or **6b** (5.5 μM), for 1, 2, 4 or 6 h under standard cell-culture conditions; 30 min before each time interval ended, cells were stained with Lysosomal Staining Reagent Orange (Abcam). Nuclear counterstaining was performed by using blue 4′,6-diamidino-2-phenylindole (DAPI). Images are representative of at least ten independent measurements at 400-fold magnification.

the latter, which are too large for embedding in the mitochondrial membrane, and thus, are dealt with by the cellular "waste-to-energy plants", the lysosomes. Once fully understood, the concept of controlling the intracellular distribution of metallodrugs by the choice of secondary ligands and charge of the complex could be exploited in rational drug design.

For the mode of action of new complexes **4**–**6**, we found an eventual induction of p53-independent apoptotic cell death, which was initiated by different effects of the three complex types at their respective sites of accumulation.

Acknowledgements

We thank the Deutsche Forschungsgemeinschaft (DFG) for a grant (Scho 402/12-2). Furthermore, we would like to thank Luisa Kober for her support in identifying the target structures of the compounds, and Dr. Julienne K. Münzner and Dr. Matthias Rothemund for preliminary tests. Open access funding enabled and organized by Projekt DEAL.

Conflict of interest

The authors declare no conflict of interest.

Keywords: cancer · drug discovery · gold · metallodrugs · subcellular localisation

[1] L.-A. Schaper, S. J. Hock, W. A. Herrmann, F. E. Kühn, *Angew. Chem. Int. Ed.* **2013**, *52*, 270–289; *Angew. Chem.* **2013**, *125*, 284–304.
[2] M.-L. Teyssot, A.-S. Jarrousse, M. Manin, A. Chevry, S. Roche, F. Norre, C. Beaudoin, L. Morel, D. Boyer, R. Mahiou, A. Gautier, *Dalton Trans.* **2009**, 6894–6902.
[3] a) B. Rosenberg, L. VanCamp, *Cancer Res.* **1970**, *30*, 1799–1802; b) J. Reedijk, P. H. Lohman, *Pharm. Weekbl. Sci.* **1985**, *7*, 173–180; c) M. H. Hanigan, P. Devarajan, *Cancer Ther.* **2003**, *1*, 47–61; d) C. M. Sorenson, M. A. Barry, A. Eastman, *J. Natl. Cancer Inst.* **1990**, *82*, 749–755.
[4] a) J. S. Modica-Napolitano, J. R. Aprille, *Adv. Drug Delivery Rev.* **2001**, *49*, 63–70; b) C. I. Yeo, K. K. Ooi, E. R. T. Tiekink, *Molecules* **2018**, *23*, 1410.
[5] S. B. Aher, P. N. Muskawar, K. Thenmozhi, P. R. Bhagat, *Eur. J. Med. Chem.* **2014**, *81*, 408–419.
[6] a) L. Oehninger, R. Rubbiani, I. Ott, *Dalton Trans.* **2013**, *42*, 3269–3284; b) C. Hu, X. Li, W. Wang, R. Zhang, L. Deng, *Curr. Med. Chem.* **2014**, *21*, 1220–1230; c) A. Gautier, F. Cisnetti, *Metallomics* **2012**, *4*, 23–32.
[7] a) M. Chaffman, R. N. Brogden, R. C. Heel, T. M. Speight, G. S. Avery, *Drugs* **1984**, *27*, 378–424; b) V. Gandin, A. P. Fernandes, M. P. Rigobello, B. Dani, F. Sorrentino, F. Tisato, M. Björnstedt, A. Bindoli, A. Sturaro, R. Rella, C. Marzano, *Biochem. Pharmacol.* **2010**, *79*, 90–101.
[8] S. Gromer, L. D. Arscott, C. H. Williams, R. H. Schirmer, K. Becker, *J. Biol. Chem.* **1998**, *273*, 20096–20101.
[9] M. P. Rigobello, G. Scutari, R. Boscolo, A. Bindoli, *Br. J. Pharmacol.* **2002**, *136*, 1162–1168.
[10] G.-Y. Liou, P. Storz, *Free Radical Res.* **2010**, *44*, 479–496.
[11] X. Jiang, X. Wang, *Annu. Rev. Biochem.* **2004**, *73*, 87–106.
[12] L. Kaps, B. Biersack, H. Müller-Bunz, K. Mahal, J. Münzner, M. Tacke, T. Mueller, R. Schobert, *J. Inorg. Biochem.* **2012**, *106*, 52–58.

Chemistry–A European Journal | Full Paper doi.org/10.1002/chem.202005451 | Chemistry Europe European Chemical Societies Publishing

[13] J. K. Muenzner, B. Biersack, H. Kalie, I. C. Andronache, L. Kaps, D. Schuppan, F. Sasse, R. Schobert, *ChemMedChem* **2014**, *9*, 1195 – 1204.
[14] M. Rothemund, S. I. Bär, T. Rehm, H. Kostrhunova, V. Brabec, R. Schobert, *Dalton Trans.* **2020**, *49*, 8901 – 8910.
[15] R. Rubbiani, S. Can, I. Kitanovic, H. Alborzinia, M. Stefanopoulou, M. Kokoschka, S. Mönchgesang, W. S. Sheldrick, S. Wölfl, I. Ott, *J. Med. Chem.* **2011**, *54*, 8646 – 8657.
[16] E. Hedström, S. Eriksson, J. Zawacka-Pankau, E. S. J. Arnér, G. Selivanova, *Cell Cycle* **2009**, *8*, 3584 – 3591.
[17] S.-H. Park, J. H. Lee, J. S. Berek, M. C.-T. Hu, *Int. J. Oncol.* **2014**, *45*, 1691 – 1698.
[18] X. Cheng, P. Holenya, S. Can, H. Alborzinia, R. Rubbiani, I. Ott, S. Wölfl, *Molecular Cancer* **2014**, *13*, 221.
[19] B. Bertrand, A. de Almeida, E. P. M. van der Burgt, M. Picquet, A. Citta, A. Folda, M. P. Rigobello, P. Le Gendre, E. Bodio, A. Casini, *Eur. J. Inorg. Chem.* **2014**, 4532 – 4536.
[20] A. Citta, E. Schuh, F. Mohr, A. Folda, M. L. Massimino, A. Casini, M. P. Rigobello, *Metallomics* **2013**, *5*, 1006 – 1015.
[21] a) D. Ingato, J. A. Edson, M. Zakharian, Y. J. Kwon, *ACS Nano* **2018**, *12*, 9568 – 9577; b) L. H. Hurley, *Nat. Rev. Cancer* **2002**, *2*, 188 – 200.
[22] a) A. L. B. Seynhaeve, B. M. Dicheva, S. Hoving, G. A. Koning, T. L. M. ten Hagen, *J. Controlled Release* **2013**, *172*, 330 – 340; b) M. A. Fuertes, C. Alonso, J. M. Pérez, *Chem. Rev.* **2003**, *103*, 645 – 662.
[23] S. Fulda, L. Galluzzi, G. Kroemer, *Nat. Rev. Drug Discovery* **2010**, *9*, 447 – 464.
[24] W. Liu, K. Bensdorf, M. Proetto, A. Hagenbach, U. Abram, R. Gust, *J. Med. Chem.* **2012**, *55*, 3713 – 3724.
[25] a) U. T. Brunk, J. Neuzil, J. W. Eaton, *Redox Rep.* **2001**, *6*, 91 – 97; b) T. Cirman, K. Oresić, G. D. Mazovec, V. Turk, J. C. Reed, R. M. Myers, G. S. Salvesen, B. Turk, *J. Biol. Chem.* **2004**, *279*, 3578 – 3587.
[26] P. Boya, K. Andreau, D. Poncet, N. Zamzami, J.-L. Perfettini, D. Metivier, D. M. Ojcius, M. Jäättelä, G. Kroemer, *J. Exp. Med.* **2003**, *197*, 1323 – 1334.
[27] M. Jäättelä, *Oncogene* **2004**, *23*, 2746 – 2756.
[28] S. F. Zerp, A. van Elsas, L. T. Peltenburg, P. I. Schrier, *Br. J. Cancer* **1999**, *79*, 921 – 926.
[29] A. Parrales, T. Iwakuma, *Front. Oncol.* **2015**, *5*, 288.
[30] B. Tessoulin, G. Descamps, C. Dousset, M. Amiot, C. Pellat-Deceunynck, *Front. Oncol.* **2019**, *9*, 128.
[31] H. Erdal, M. Berndtsson, J. Castro, U. Brunk, M. C. Shoshan, S. Linder, *Proc. Natl. Acad. Sci. USA* **2005**, *102*, 192 – 197.
[32] a) C. Béroud, T. Soussi, *Nucleic Acids Res.* **1998**, *26*, 200 – 204; b) L. Bouaoun, D. Sonkin, M. Ardin, M. Hollstein, G. Byrnes, J. Zavadil, M. Olivier, *Hum. Mutat.* **2016**, *37*, 865 – 876.
[33] D. P. Bancroft, C. A. Lepre, S. J. Lippard, *J. Am. Chem. Soc.* **1990**, *112*, 6860 – 6871.
[34] Ö. Karaca, S. M. Meier-Menches, A. Casini, F. E. Kühn, *Chem. Commun.* **2017**, *53*, 8249 – 8260.
[35] C. K. Mirabelli, C.-M. Sung, J. P. Zimmerman, D. T. Hill, S. Mong, S. T. Crooke, *Biochem. Pharmacol.* **1986**, *35*, 1427 – 1433.
[36] a) C. E. Blank, J. C. Dabrowiak, *J. Inorg. Biochem.* **1984**, *21*, 21 – 29; b) S. Urig, K. Fritz-Wolf, R. Réau, C. Herold-Mende, K. Tóth, E. Davioud-Charvet, K. Becker, *Angew. Chem. Int. Ed.* **2006**, *45*, 1881 – 1886; *Angew. Chem.* **2006**, *118*, 1915 – 1920.
[37] S. L. R. Silva, I. R. S. Baliza, R. B. Dias, C. B. S. Sales, C. A. G. Rocha, M. B. P. Soares, R. S. Correa, A. A. Batista, D. P. Bezerra, *Sci. Rep.* **2019**, *9*, 11094.
[38] a) N. C. de Carvalho, S. P. Neves, R. B. Dias, L. de F. Valverde, C. B. S. Sales, C. A. G. Rocha, M. B. P. Soares, E. R. dos Santos, R. M. M. Oliveira, R. M. Carlos, P. C. L. Nogueira, D. P. Bezerra, *Cell Death Dis.* **2018**, *9*, 79; b) M. Altaf, M. Monim-Ul-Mehboob, A.-N. Kawde, G. Corona, R. Larcher, M. Ogasawara, N. Casagrande, M. Celegato, C. Borghese, Z. H. Siddik, D. Aldinucci, A. A. Isab, *Oncotarget* **2017**, *8*, 490 – 505.
[39] L. Ronconi, D. Fregona, *Dalton Trans.* **2009**, 10670 – 10680.
[40] A. Bindoli, M. P. Rigobello, G. Scutari, C. Gabbiani, A. Casini, L. Messori, *Coord. Chem. Rev.* **2009**, *253*, 1692 – 1707.
[41] a) C. Marzano, V. Gandin, A. Folda, G. Scutari, A. Bindoli, M. P. Rigobello, *Free Radical Biol. Med.* **2007**, *42*, 872 – 881; b) A. Meyer, C. P. Bagowski, M. Kokoschka, M. Stefanopoulou, H. Alborzinia, S. Can, D. H. Vlecken, W. S. Sheldrick, S. Wölfl, I. Ott, *Angew. Chem. Int. Ed.* **2012**, *51*, 8895 – 8899; *Angew. Chem.* **2012**, *124*, 9025 – 9030; c) M. G. Fabbrini, D. Cirri, A. Pratesi, L. Ciofi, T. Marzo, A. Guerri, S. Nistri, A. Dell'Accio, T. Gamberi, M. Severi, A. Bencini, L. Messori, *ChemMedChem* **2019**, *14*, 182 – 188.
[42] D. Mustacich, G. Powis, *Biochem. J.* **2000**, *346*, 1 – 8.
[43] S. Urig, K. Becker, *Semin. Cancer Biol.* **2006**, *16*, 452 – 465.
[44] D. Parsonage, F. Sheng, K. Hirata, A. Debnath, J. H. McKerrow, S. L. Reed, R. Abagyan, L. B. Poole, L. M. Podust, *J. Struct. Biol.* **2016**, *194*, 180 – 190.
[45] C. Zhang, C. Hemmert, H. Gornitzka, O. Cuvillier, M. Zhang, R. W.-Y. Sun, *ChemMedChem* **2018**, *13*, 1218 – 1229.
[46] R. Rubbiani, L. Salassa, A. de Almeida, A. Casini, I. Ott, *ChemMedChem* **2014**, *9*, 1205 – 1210.
[47] J. F. Arambula, R. McCall, K. J. Sidoran, D. Magda, N. A. Mitchell, C. W. Bielawski, V. M. Lynch, J. L. Sessler, K. Arumugam, *Chem. Sci.* **2016**, *7*, 1245 – 1256.
[48] A. G. Cox, K. K. Brown, E. S. J. Arner, M. B. Hampton, *Biochem. Pharmacol.* **2008**, *76*, 1097 – 1109.
[49] S.-J. Park, I.-S. Kim, *Br. J. Pharmacol.* **2005**, *146*, 506 – 513.
[50] G. Kroemer, L. Galluzzi, C. Brenner, *Physiol. Rev.* **2007**, *87*, 99.
[51] F. Wang, R. Gómez-Sintes, P. Boya, *Traffic* **2018**, *19*, 918 – 931.
[52] a) F. Wang, A. Salvati, P. Boya, *Open Biol.* **2018**, *8*, 170271; b) S. Aits, M. Jäättelä, *J. Cell Sci.* **2013**, *126*, 1905 – 1912.

Manuscript received: December 23, 2020
Accepted manuscript online: December 28, 2020
Version of record online: February 8, 2021

Chemistry–A European Journal

Supporting Information

Guided Antitumoural Drugs: (Imidazol-2-ylidene)(L)gold(I) Complexes Seeking Cellular Targets Controlled by the Nature of Ligand L

Sofia I. Bär[+], Madeleine Gold[+], Sebastian W. Schleser, Tobias Rehm, Alexander Bär, Leonhard Köhler, Lucas R. Carnell, Bernhard Biersack, and Rainer Schobert*[a]

Author Contributions

S.B. Formal analysis: Lead; Investigation: Lead; Methodology: Lead; Project administration: Lead; Writing – original draft: Lead
M.G. Formal analysis: Equal; Investigation: Equal; Methodology: Equal; Project administration: Equal; Writing – original draft: Equal
S.S. Formal analysis: Supporting; Investigation: Supporting; Methodology: Supporting
T.R. Formal analysis: Supporting; Investigation: Supporting; Methodology: Supporting
A.B. Formal analysis: Supporting; Investigation: Supporting; Methodology: Supporting
L.K. Formal analysis: Supporting; Investigation: Supporting; Methodology: Supporting
L.C. Formal analysis: Supporting; Methodology: Supporting
B.B. Formal analysis: Supporting; Investigation: Supporting; Methodology: Supporting; Project administration: Supporting.

Table of Contents

Experimental Procedures

Chemical Synthesis and Analytics

General.

Melting points (uncorrected): GALLENKAMP; IR spectra: PERKIN-ELMER Spectrum One FT-IR spectrophotometer with ATR sampling unit; Nuclear magnetic resonance (NMR) spectra: BRUKER DRX 500 Hz spectrometer, chemical shifts are given in parts per million (δ) downfield from tetramethylsilane as internal standard for ^{1}H and ^{13}C; Mass spectra: VARIAN MAT 311A (EI), WATERS UPLC-Q-TOF (ESI), ThermoFisher UPLC/Orbitrap MS system (HRMS-ESI); All starting compounds were purchased from ALDRICH and used without further purification. The known compounds **3a**[1], **4a**[1] and **6a**[1] were prepared according to literature procedures.

5-(Anthracen-9-yl)-1-ethyl-4-phenylimidazole (2). A solution of 9-formylanthracene (700 mg, 3.39 mmol) in ethanol (50 mL) was treated with 2M $EtNH_2$/THF (8.49 mL, 17.0 mmol). Acetic acid (970 μL) was added and the reaction mixture was refluxed for 2 h. After cooling to room temperature, phenyl-TosMIC **1** (1.39 g, 5.09 mmol) and K_2CO_3 (1.88 g, 13.6 mmol) were added and refluxed again for 6 h. The solvent was evaporated, the residue was dissolved in ethyl acetate (100 mL) and washed with water (100 mL) and brine (100 mL), dried over Na_2SO_4, filtered and the filtrate was concentrated in vacuum. The residue was purified by column chromatography (silica gel 60; EtOAc/MeOH: 97/3). Yield: 726 mg (2.08 mmol, 61%); yellow solid; R_f = 0.64; ν_{max}/cm^{-1}: 3053, 2977, 2931, 1623, 1599, 1517, 1501, 1458, 1442, 1398, 1373, 1352, 1343, 1314, 1244, 1224, 1175, 1163, 1135, 1117, 1056, 1067, 1011, 983, 951, 917, 899, 852, 813, 799, 771, 744, 715, 728, 692; ^{1}H NMR (500 MHz, $CDCl_3$): δ 1.01 (3 H, t, J = 7.3 Hz), 3.45 (2 H, q, J = 7.3 Hz), 6.96-6.98 (3 H, m), 7.29-7.31 (2 H, m), 7.38-7.41 (2 H, m), 7.48-7.51 (2 H, m) 7.64 (2 H, d, J = 8.7 Hz), 7.91 (1 H, s), 8.10 (2 H, d, J = 8.7 Hz), 8.64 (1 H, s); ^{13}C NMR (126 MHz, $CDCl_3$): δ 16.4, 40.1, 123.9, 124.5, 125.4, 125.6, 125.7, 126.1, 126.9, 128.1, 128.8, 128.9, 131.5, 134.0, 134.5, 136.8, 140.0.

4-(Anthracen-9-yl)-1,3-diethyl-5-phenylimidazolium tetrafluoroborate (3b).

Compound **2** (500 mg, 1.43 mmol) was dissolved in acetonitrile (100 mL) and iodoethane (6.34 mL) was added. The reaction mixture was stirred at 85 °C for 48 h. The solvent was evaporated and the remainder was crystallised from CH_2Cl_2/*n*-hexane at 4 °C. Yield: 689 mg (1.37 mmol, 95%); yellow solid; ν_{max}/cm^{-1}: 3420, 3118, 3027, 2979, 1622, 1592, 1556, 1520, 1499, 1443, 1386, 1348, 1263, 1193, 1159, 1091, 1074, 1023, 1012, 962, 932, 897, 854, 794, 774, 740, 700; ^{1}H NMR (500 MHz, $CDCl_3$): ^{1}H NMR (500 MHz, $CDCl_3$): δ 1.28 (3 H, t, J = 7.3 Hz), 1.68 (3 H, t, J = 7.3 Hz), 3.91 (2 H, q, J = 7.3 Hz), 4.52 (2 H, q, J = 7.3 Hz), 7.13-7.23 (5 H, m), 7.50-7.55 (2 H, m), 7.59 (2 H, t, J = 8.1 Hz), 7.65 (2 H, d, J = 8.7 Hz) 8.06 (2 H, d, J = 8.4 Hz), 8.62 (1 H, s), 10.83 (1 H, s);^{13}C NMR (126 MHz, $CDCl_3$): δ 15.8, 15.9, 43.6, 44.1, 117.0, 124.4, 124.9, 126.0, 128.3, 128.4, 129.1, 129.2, 129.4, 130.4, 131.0, 131.2, 132.0, 133.9. The resulting 4-(anthracen-9-yl)-1,3-diethyl-5-phenylimidazolium iodide (41 mg, 0.081 mmol) was dissolved in acetone (10 mL) and $NaBF_4$ (13 mg, 0.122 mmol) was added. The reaction mixture was stirred at room temperature for 24 h. After filtration through Mg_2SO_4 the filtrate was concentrated in vacuum and dried. Yield: 38 mg (0.081 mmol, 100%); yellow solid; ν_{max}/cm^{-1}: 3464, 3039, 2982, 1622, 1557, 1520, 1499, 1444, 1387, 1349, 1333, 1305, 1263, 1193, 1065, 1023, 963, 932, 897, 854, 774, 740, 727, 700; ^{1}H NMR (300 MHz, $CDCl_3$): *δ* 1.24 (3 H, t, J = 7.3 Hz), 1.65 (3 H, t, J = 7.3 Hz), 3.88 (2 H, q, J = 7.3 Hz), 4.49 (2 H, q, J = 7.3 Hz), 7.0-7.2 (5 H, m), 7.4-7.6 (4 H, m), 7.67 (2 H, d, J = 8.6 Hz), 8.01 (2 H, d, J = 8.4 Hz), 8.58 (1 H, s), 10.66 (1 H, s); ^{13}C NMR (75.5 MHz, $CDCl_3$): *δ* 15.7, 15.8, 43.5, 44.0, 117.0, 124.3, 124.9, 125.8, 128.2, 128.3, 129.0, 129.1, 129.4, 130.2, 130.9, 131.0, 131.9, 133.9, 137.2; ^{11}B NMR (96.3 MHz, $CDCl_3$): *δ* -0.76.

Chlorido-[4-(anthracen-9-yl)-1,3-diethyl-5-phenylimidazol-2-ylidene]gold(I) (4b).

Compound **3b** (100 mg, 0.198 mmol) was dissolved in CH_2Cl_2 (5 mL) and treated with Ag_2O (27.6 mg, 0.119 mmol). The mixture was stirred in darkness at room temperature for 5 h. Chloro(dimethylsulfide)gold(I) (64.2 mg, 0.218 mmol) and LiCl (84 mg, 1.98 mmol) were added and the reaction mixture was stirred for additional 24 h. The crude product was crystallised from CH_2Cl_2/*n*-hexane at 4 °C. Yield: 111 mg (0.182 mmol, 92%); yellowish solid of of mp > 250 °C (dec.); ν_{max} (ATR)/cm^{-1}: 3051, 2976, 2933, 1622, 1500, 1461, 1427, 1443, 1414, 1344, 1294, 1213, 1115, 1088, 1025, 1013, 997, 962, 933, 896, 851, 819, 775, 757, 727, 699, 652, 607, 582; ^{1}H NMR(500 MHz, $CDCl_3$): δ 0.98 (3 H, t, J = 7.2 Hz), 1.45 (3 H, t, J = 7.1 Hz), 3.81 (2 H, q, J = 7.2 Hz), 4.37 (2 H, q, *J* = 7.2 Hz), 7.07-7.16 (5 H, m), 7.45-7.55 (4 H, m), 7.60 (2 H, d, J = 8.4 Hz), 8.00-8.05 (2 H, m), 8.55 (1 H, s); ^{13}C NMR (125 MHz, $CDCl_3$): δ 17.0, 17.2, 44.7, 44.8, 120.4, 124.7, 125.7, 127.0, 127.5, 127.6, 128.7, 129.1, 129.2, 129.3, 129.4, 130.2, 131.1, 132.0, 133.0, 170.3; *m/z* (ESI, %) 614.2 [M^++CH_3CN] (100). HRMS (ESI) m/z ((M-Cl+MeCN)$^+$) found 614.18508; calcd. 614.18650.

[1,3-Diethyl-5-(4-methoxyphenyl)-4-(3,4,5-trimethoxyphenyl)imidazol-2-ylidene](triphenylphosphane)gold(I) tetrafluoroborate (5a).

Complex **4a** (112 mg, 0.178 mmol) was dissolved in acetone (10 mL) and $NaBF_4$ (36 mg, 0.33 mmol) and triphenylphosphane (61 mg, 0.23 mmol) were added. The reaction mixture was stirred at room temperature for 24 h. The suspension was filtered, the filtrate concentrated in vacuum, and the residue recrystallized from acetone/*n*-hexane. Yield: 132 mg (0.14 mmol, 79%); colorless solid of mp = 107-110 °C; Elemental analysis ($C_{41}H_{43}AuBF_4N_2O_4P$, %) found C 52.14 H 4.47 N 2.93; calcd. C 52.25, H 4.60, N 2.97. ν_{max} (ATR)/cm^{-1}: 3056, 2936, 2836, 1607, 1581, 1516, 1504, 1463, 1437, 1415, 1331, 1292, 1248, 1179, 1124, 1099, 1050, 1024, 997, 887, 839, 811, 748, 711, 693 ^{1}H NMR (500 MHz, $CDCl_3$): δ 1.42 (3H, t, *J* = 7.3 Hz), 1.49 (3H, *J* = 7.2 Hz), 3.76 (3 H, s), 3.82 (3 H, s), 3.85 (3 H, s), 4.27 (2 H, q, *J* = 7.1 Hz), 4.35 (2 H, q, J = 7.1 Hz), 6.44 (3 H, s), 6.92 (6H, vd); 7.21 (3H, vd) 7.46 (15H, m) ^{13}C NMR

(125 MHz, $CDCl_3$): δ 17.5, 17.8, 44.3, 44.6, 55.3, 56.3, 60.9, 107.7, 114.3, 128.8, 128.9, 130.8, 131.9, 133.9, 134.0; ^{31}P NMR (202 MHz, $CDCl_3$): δ 33.8; *m/z* (ESI, %) 855.0 (100) [M^+], 721.4 (22). HRMS (ESI) m/z (M^+) found 855.2577; calcd. 855.2620.

[4-(Anthracen-9-yl)-1,3-diethyl-5-phenylimidazol-2-ylidene](triphenylphosphane)gold(I) tetrafluoroborate (5b).
Compound **3b** (100 mg, 0.198 mmol) in dry CH_2Cl_2 (5 mL) was treated with KO*t*Bu (27 mg, 0.238 mmol) and (PPh_3)AuCl (98 mg, 0.198 mmol). The mixture was stirred at room temperature for 24. The crude product was filtered and crystallised from CH_2Cl_2/*n*-hexane at 4 °C. Yield: 166 mg (0.191 mmol, 96%); white solid of of mp = 165 °C; ν_{max} (ATR)/cm^{-1}: 3051, 2981, 1977, 1622, 1464, 1432, 1345, 1262, 1095, 1025, 895, 849, 775, 737, 690, 607, 565;^1H NMR (500 MHz, $CDCl_3$): δ 1.14 (3 H, t, J = 7.2 Hz), 1.59 (3 H, t, J = 7.2 Hz), 3.92 (2 H, q, J = 7.2 Hz), 4.55 (2 H, q, *J* = 7.2 Hz), 7.10-7.16 (3 H, m), 7.19-7.21 (2 H, m), 7.35-7.39 (6 H, m), 7.42-7.45 (3 H, m), 7.48-7.52 (8 H, m), 7.56-7.59 (2 H, m), 7.73 (2 H, d, J = 8.4 Hz), 8.03 (2 H, d, J = 8.4 Hz), 8.57 (1H, s); ^{13}C NMR (125 MHz, $CDCl_3$): δ 17.6, 17.8, 44.8, 45.1, 120.2, 125.0, 125.7, 127.4, 127.7, 128.8, 128.9, 129.0, 129.4, 129.6, 130.2, 130.6, 131.1, 132.1, 132.2, 133.4 133.9, 134.0, 134.1, 183.9; ^{31}P NMR (202 MHz, $CDCl_3$): δ 30.3; *m/z* (ESI, %) 949.4 (100), 835.2 (7) [M^+], 721.2 (40). HRMS (ESI) m/z (M^+) found 835.2476; calcd. 835.2511.

Bis[4-(anthracen-9-yl)-1,3-diethyl-5-phenylimidazol-2-ylidene]gold(I) tetrafluoroborate (6b).
Compound **3b** (100 mg, 0.198 mmol) was dissolved in CH_2Cl_2/methanol (1:1, 80 mL) and Ag_2O (50.1 mg, 0.216 mmol) was added. The reaction mixture was stirred in the dark at room temperature for 5 h. Chloro(dimethylsulfide)gold(I) (33.9 mg, 0.115 mmol) was added and the reaction mixture was stirred for additional 24 h. The suspension was filtered, the filtrate was concentrated in vacuum and the residue was redissolved in CH_2Cl_2, filtered over $MgSO_4$/Celite, and the filtrate was concentrated in vacuum and the residue dried in vacuum. Yield: 79 mg (0.080 mmol, 88%); reddish solid of mp > 250 °C (dec.); ν_{max}/cm^{-1}: 3052, 2965, 2924, 1623, 1595, 1520, 1498, 1460, 1443, 1407, 1378, 1345, 1294, 1260, 1218, 1161, 1088, 1050, 1012, 988, 961, 917, 896, 852, 774, 757, 737, 698; ^1H NMR (500 MHz, $CDCl_3$): δ 1.13 (6 H, t, J = 7.2 Hz), 1.59 (6 H, t, J = 7.2 Hz), 3.88 (4 H, q, J = 7.2 Hz), 4.49 (4 H, q, J = 7.2 Hz), 7.08-7.22 (10 H, m), 7.51 (4 H, t, J = 8.7 Hz), 7.58 (4 H, t, J = 8.7 Hz), 7.68 (4 H, d, J = 8.4 Hz), 8.04 (4 H, d, J = 8.4 Hz), 8.58 (2 H, s); ^{13}C NMR (126 MHz, $CDCl_3$): δ 17.6, 17.8, 44.7, 44.8, 119.8, 124.6, 124.7, 125.8, 127.1, 127.8, 127.9, 128.9, 129.1, 129.4, 129.5, 129.6, 130.4, 131.1, 131.2, 132.2, 134.0, 183.6; *m/z* (ESI, %) 949.4 [M^+] (100). HRMS (ESI) m/z (M^+) found 949.35035; calcd. 949.35390.

NMR Spectra

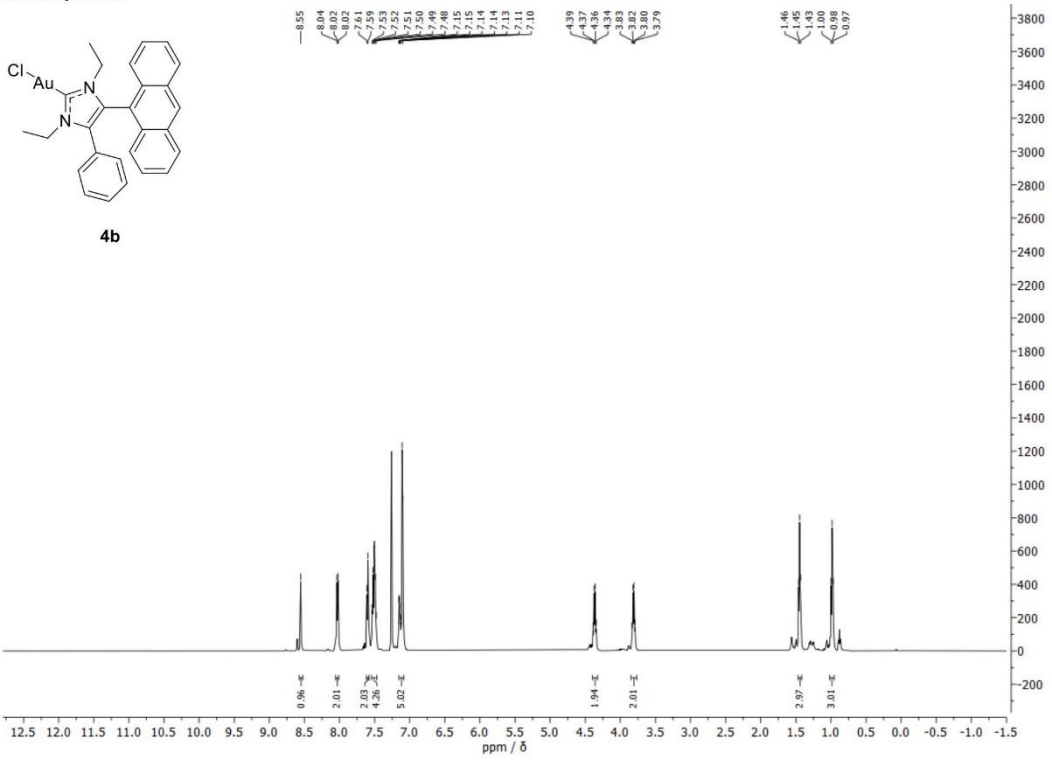

Figure 1:^1H NMR (500 MHz, $CDCl_3$) spectrum of **4b.**

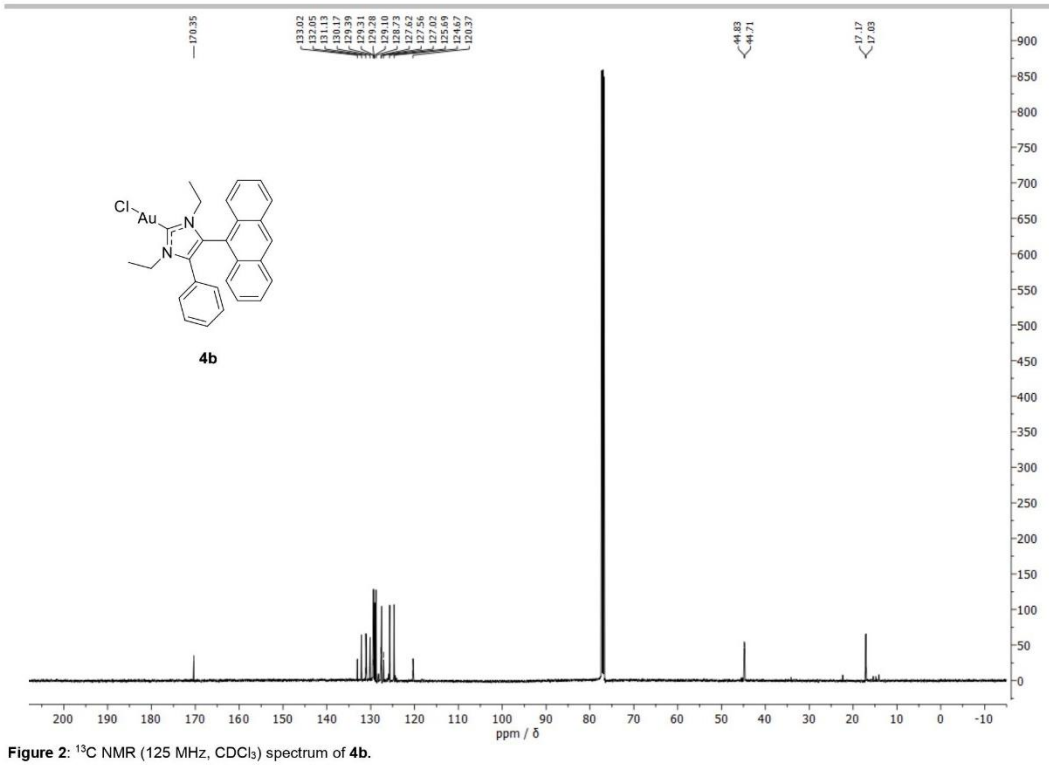

Figure 2: ^{13}C NMR (125 MHz, $CDCl_3$) spectrum of **4b.**

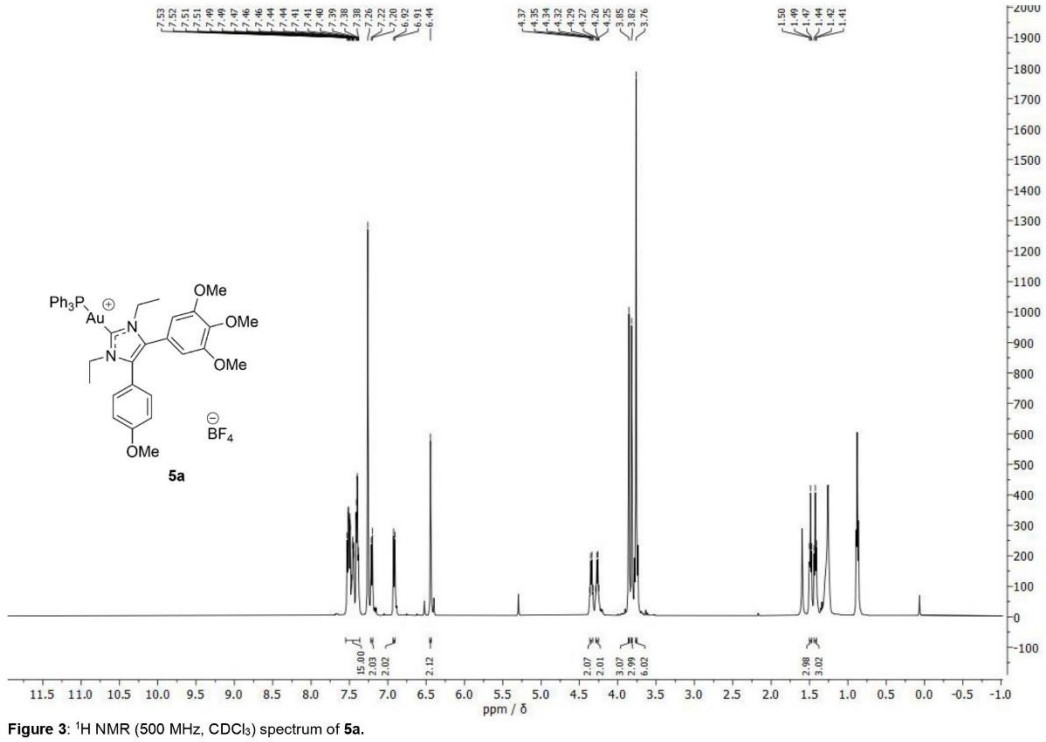

Figure 3: ^{1}H NMR (500 MHz, $CDCl_3$) spectrum of **5a.**

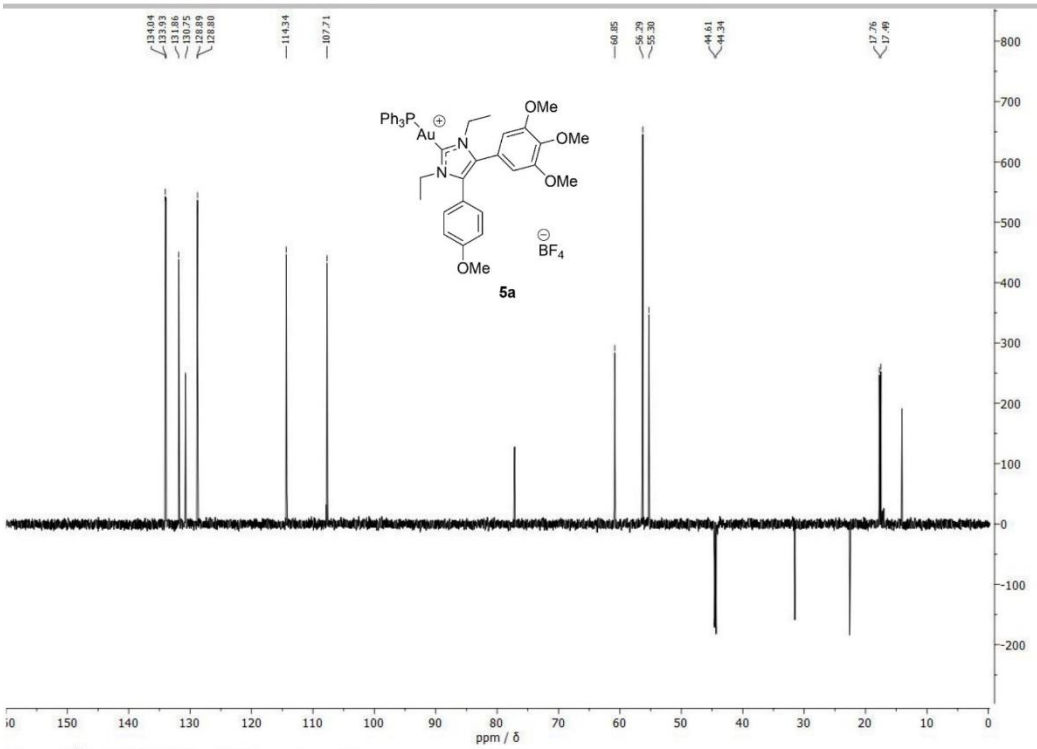

Figure 4: ^{13}C NMR (125 MHz, $CDCl_3$) spectrum of **5a.**

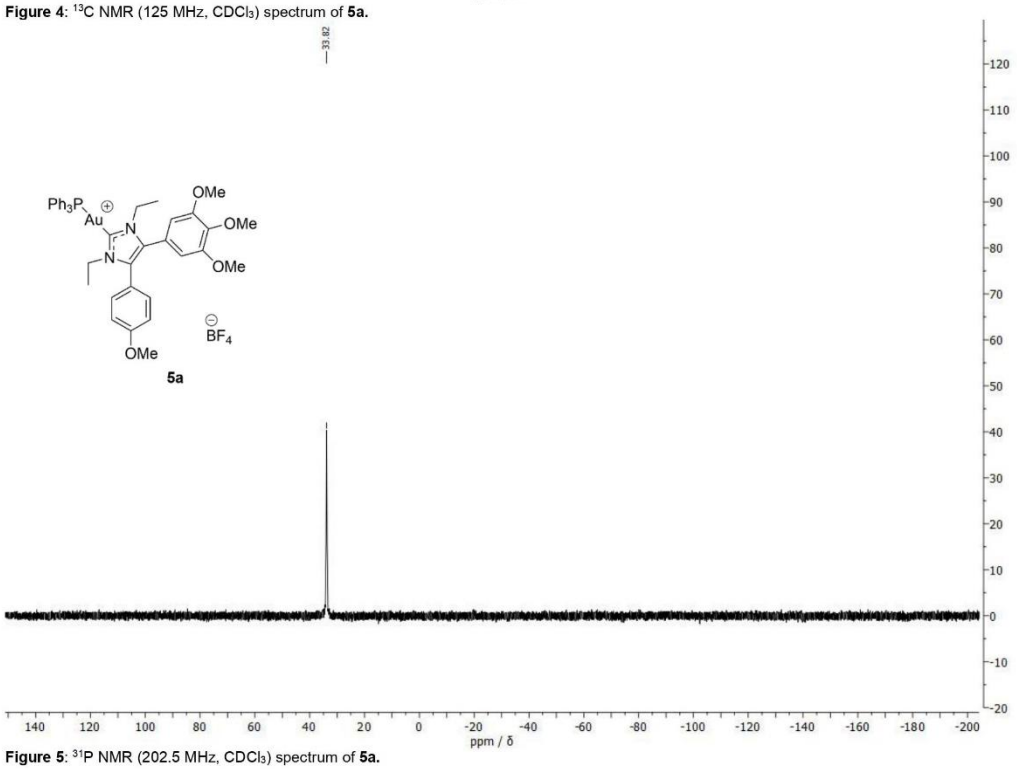

Figure 5: ^{31}P NMR (202.5 MHz, $CDCl_3$) spectrum of **5a.**

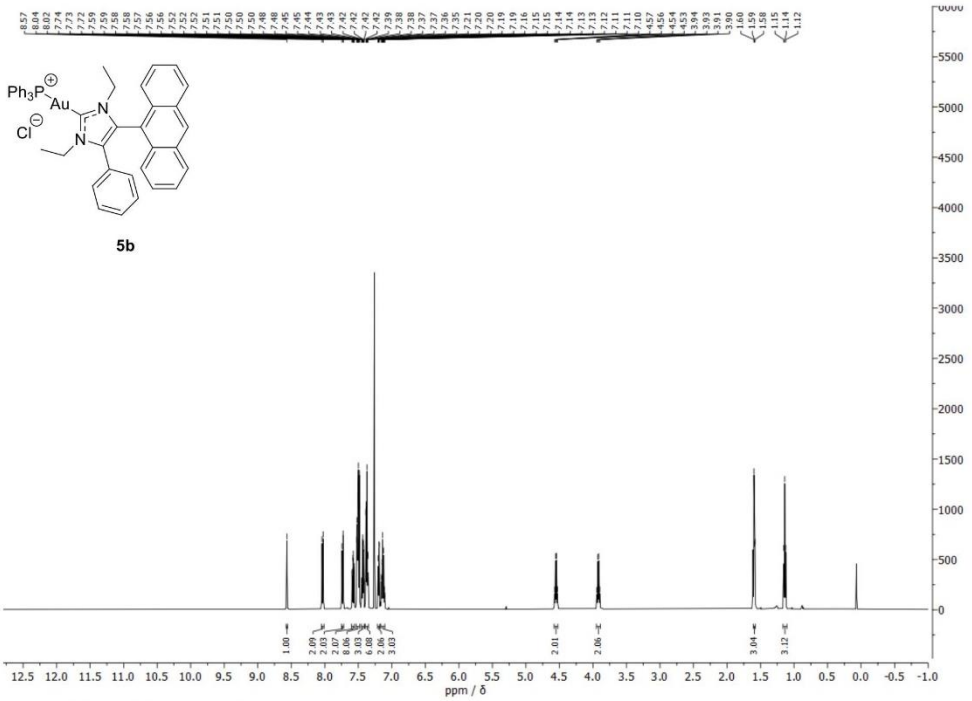

Figure 6: ^{1}H NMR (500 MHz, $CDCl_3$) spectrum of **5b.**

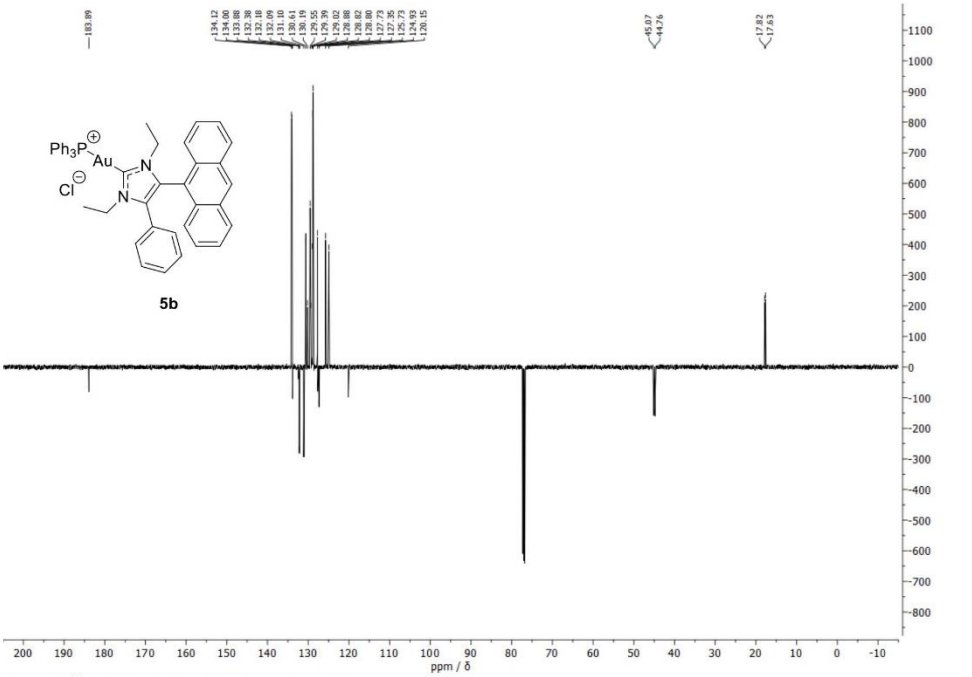

Figure 7: ^{13}C NMR (125 MHz, $CDCl_3$) spectrum of **5b.**

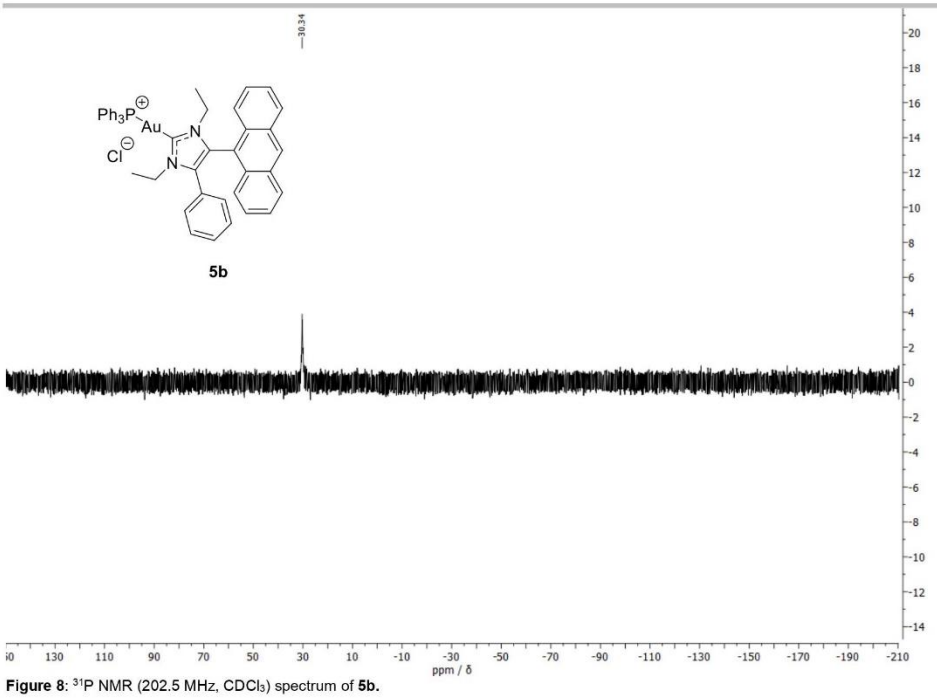

Figure 8: ^{31}P NMR (202.5 MHz, $CDCl_3$) spectrum of **5b.**

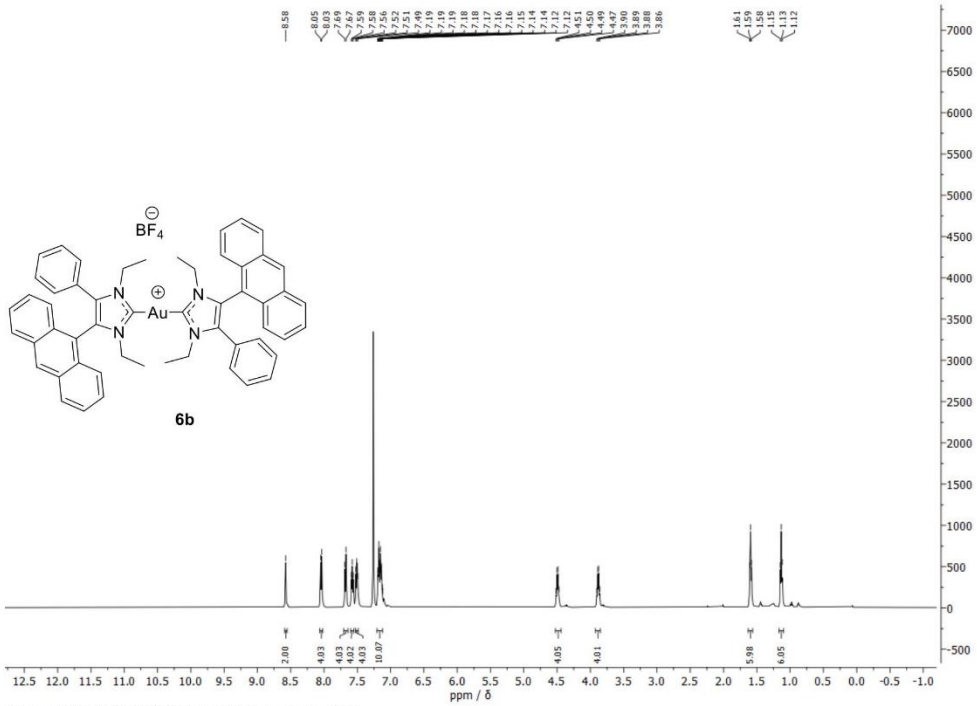

Figure 9: ^{1}H NMR (500 MHz, $CDCl_3$) spectrum of **6b.**

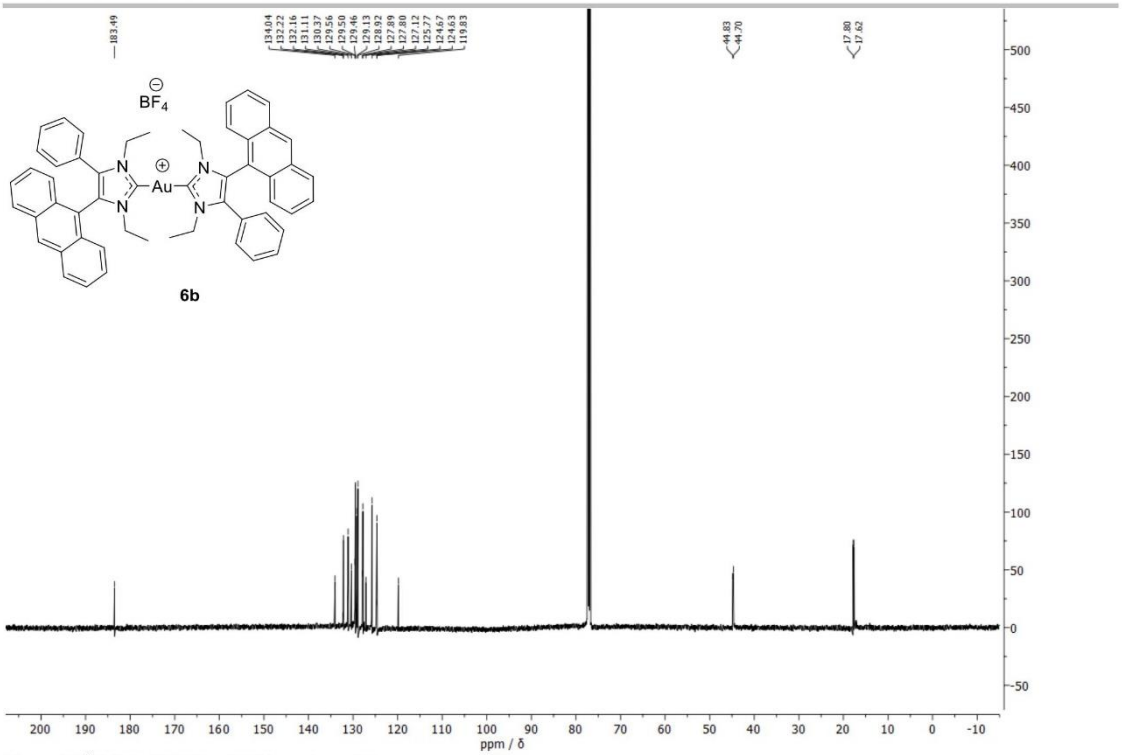

Figure 10: ^{13}C NMR (125 MHz, $CDCl_3$) spectrum of **6b**.

Biochemical Evaluation

Stock solutions of all test compounds were prepared (10 mM in DMF) and stored for at most one week at -20 °C. They were diluted, assay-depending, in ddH_2O, cell culture medium, or buffer.

Cell lines and culture conditions.

518A2 (Department of Radiotherapy and Radiobiology, University Hospital Vienna) human melanoma cells, HCT-116 (ACC-581) human colon carcinoma cells, as well as its p53 knockout mutant cell line HCT-116$^{p53-/-}$, HeLa cervix carcinoma, KB-V1^{Vbl} multi-drug resistant cervix carcinoma cells, and HDFa (ATCC® PCS-201-012™) human dermal fibroblasts were grown in Dulbecco´s Modified Eagle Medium (DMEM; Biochrom) supplemented with 10% (v/v) fetal bovine serum (FBS; Biochrom) and 1% (v/v) Antibiotic-Antimycotic solution (Gibco). The cells were incubated at 37 °C, 5% CO_2, 95% humidified atmosphere and were serially passaged following trypsinisation by using 0.05% trypsin/0.02% EDTA (w/v; Biochrom GmbH, Berlin, Germany). The maximum-tolerated dose of vinblastine was added to the cell culture medium 24 h after every cell passage to keep the KB-V1^{Vbl} cells resistant. The 518A2 melanoma cells are not available from cell banks, yet easily identified by their large size and flattened, spread-out morphology. Mycoplasma contamination was frequently monitored, and only mycoplasma-free cultures were used.

Inhibition of cell growth (MTT assay).[2]

The cytotoxic effect upon treatment with gold complexes **4**–**6** and auranofin for 72 h was determined by standard MTT assays. The tetrazolium salt 3-(4,5-dimethylthiazol-2-yl)-2,5-diphenyltetrazolium bromide (MTT; ABCR) is reduced by viable cells to a violet, water-soluble formazan. 518A2 melanoma cells, colon carcinoma cells HCT-116 and HCT-116$^{p53-/-}$, mdr KB-V1^{Vbl} and HeLa cervix carcinoma cells (5×10^4 cells mL^{-1}, 100 µL/well), as well as HDFa cells (10×10^4 cells mL^{-1}, 100 µL/well) were seeded in 96-well tissue culture plates and cultured for 24 h at 37 °C, 5% CO_2 and 95% humidity. After treatment with the test compounds incubation of cells was continued for 72 h. Blank and solvent controls were treated identically. After addition of a 5 mg mL^{-1} MTT stock solution in phosphate buffered saline (PBS), microplates were incubated for 2 h at 37 °C, centrifuged at 300 g, 4 °C for 5 min and the supernatant was discarded. The precipitate of formazan crystals was then redissolved in a 10% (w/v) solution of sodium dodecylsulfate (SDS; Carl Roth) in DMSO containing 0.6% (v/v) acetic acid. To ensure complete dissolution of the formazan, the microplates were incubated for at least 1 h in the dark. Finally the absorbance at λ = 570 and 630 nm (background) was measured using a microplate reader (Tecan F200). All experiments were carried out in quadruplicate and the percentage of viable cells was calculated as the mean ± SD with controls set to 100%.

Intracellular localisation of gold complexes.
518A2 melanoma cells (500 µL/well, 0.5×10^5 cells/mL) were seeded on glass coverslips in 24-well plates and incubated under cell culture conditions for 24 h. The medium was aspirated and the cells were washed once with PBS. Nuclear counterstaining was performed with Nuclear Green LCS1 (5 µM; abcam) with an incubation time of 15 min under standard cell culture conditions. MitoTracker™ (Thermo Fisher) was used for mitochondrial staining, and the cells were incubated with this dye for 30 min. For lysosomal staining, the cells were incubated 20 min in an acridine orange solution (5 µg/mL, 400 µL/well). The cells were then washed twice with PBS and fresh DMEM was added. Then the cells were treated with the test compounds at a concentration of 30 µM and incubated for 30 min at standard cell culture conditions. The cells were fixed for 20 min at rt after a washing step with PBS in 3.7% formaldehyde solution in PBS, then washed three times and the coverslips were mounted in ProLong™ Gold Antifade Mountant (Invitrogen). The localisation of the test compounds was documented using confocal microscopy (Leica Confocal TCS SP5, 1000× magnification).

Caspase-3/7 activation assay.
For caspase activity measurements the Apo-ONE® Homogenous Caspase-3/7 Assay Kit (Promega Corp., Wisconsin, USA) was used. 518A2 melanoma cells (67.5 µL/well; 2×10^5 cells mL^{-1}) were grown in black 96-well plates for 24 h (37 °C, 5% CO_2 and 95% humidity). After incubation with different concentrations of the test compounds or solvent for 24 h under cell culture conditions, fluorogenic 1× caspase-3/7 substrate solution was added to each well and the substrate transformation by activated caspase-3/7 was performed for 45 min at rt. The fluorescence intensity (λ_{ex}: 485 ± 20 nm, λ_{em}: 530 ± 25 nm) was measured using a microplate reader (Tecan F200). Blank values (caspase-3/7 substrate solution plus test compound/solvent) were subtracted to reduce background signals, and a potential loss of cell viability after the incubation with the test compounds was taken into account by performing an MTT-assay as described above. The caspase-3/7 activity of the remaining vital cells was calculated as means ± SD with solvent controls set to 100%. All experiments were carried out at least in quadruplicate.

Detection of morphological signs of apoptosis.
518A2 melanoma cells (3 mL/well, 5×10^4 cells mL^{-1}) were grown in 6-well plates for 24 h (37 °C, 5% CO_2 and 95% humidity). After incubation with IC_{50} concentrations of the test compounds (staurosporine: 500 nM, **4a**: 19.8 µM, **4b**: 7.9 µM, **5a**: 5.0 µM, **5b**: 2.9 µM, **6a**: 0.4 µM, **6b**: 5.5 µM) or solvent for 2.5 h under cell culture conditions, morphological changes of the cells were documented via brightfield microscopy (ZEISS Axiovert 135 and AxioVert MRc5, 100× magnification).

Annexin-V-FITC/PI staining.
For Annexin-V-FITC staining the TACS® Annexin-V-FITC Apoptosis Detection Kit (Trevigen, Maryland, USA) was used. 518A2 melanoma cells were seeded on glass coverslips (500 µL/well, 5×10^4 cells mL^{-1}) in 24-well plates, incubated under cell culture conditions (37 °C, 5% CO_2 and 95% humidity) for 24 h and treated with IC_{50} concentrations of the test compounds (staurosporine: 500 nM, CDDP: 7.8 µM,[3] **4a**: 19.8 µM, **4b**: 7.9 µM, **5a**: 5.0 µM, **5b**: 2.9 µM, **6a**: 0.4 µM, **6b**: 5.5 µM) or solvent for a further 45 min under cell culture conditions. Afterwards the medium was aspirated and the cells were stained with 150 µL of Annexin-V-FITC/PI staining solution for 15 min according to the manufacturer´s instruction. Apoptosis-induced exposure of phosphatidylserine on the outer leaflet of the cytoplasmic membrane was documented by fluorescence microscopy (ZEISS Imager A1 AX10, 200× magnification). For differentiation between early apoptotic and late apoptotic/necrotic cells (which have lost membrane integrity), cells were counterstained with PI (propidium iodide).

Ethidium bromide saturation assay.
A potential DNA interaction of complexes **4**–**6** was assessed by a fluorescence-based ethidium bromide (EtdBr) staining assay. Salmon sperm DNA (SS-DNA, Sigma-Aldrich) in TE buffer (10 mM Tris-HCl, 1 mM EDTA, pH 8.5) was pipetted into a black 96-well plate to reach a final amount of 1 µg/100 µL assay volume and incubated with varying concentrations of test compounds for 2 h at 37 °C. Afterwards, 100 µL of EtdBr solution (10 µg mL^{-1} in TE buffer) was added to each well. The fluorescence (λ_{ex} = 535 nm, λ_{em} = 595 nm) was measured using a microplate reader (Tecan F200) after 5 min of incubation. Each fluorescence value was corrected for intrinsic compound and EtdBr background fluorescence. A decreased fluorescence indicates an interaction between DNA and test compound which prevents the intercalation of EtdBr molecules into the double-stranded SS-DNA. All experiments were carried out in triplicate and the relative EtdBr fluorescence was quoted as means ± standard deviation with solvent controls set to 100%.

Electrophoretic mobility shift assay (EMSA).
Circular pBR322 plasmid DNA (1.5 µg; Thermoscientific) was incubated with dilution series (0, 25, 50, 75, 100 µM) of the test compounds or CDDP in TE-buffer (10 mM Tris-HCl, 1 mM EDTA, pH 8.5) for 24 h at 37 °C (20 µL total sample volume). Afterwards the DNA samples were subjected to DNA gel electrophoresis using 1% agarose gel in 0.5× TBE-buffer (89 mM Tris, 89 mM boric acid, 25 mM EDTA, pH 8.3). After staining the gels with an EtdBr solution (10 µg mL^{-1} in 0.5× TBE-buffer) for 30 min, DNA bands were visualized using UV excitation. All experiments were performed at least in duplicate.

Inhibition of thioredoxin reductase (TrxR) activity.
For the measurement of thioredoxin reductase (TrxR) activity the TrxR Colorimetric Assay Kit (Cayman Chemical) was used according to manufacturer´s instructions. 1×10^8 518A2 melanoma cells were harvested using a cell scraper, homogenised in 5 mL cold lysis buffer (50 mM K_3PO_4, 1 mM EDTA, pH 7.4) on ice and centrifuged for 15 min (4 °C, 10000×g). The protein concentration of the supernatant was determined via Bradford assays. Then, 10 µL Protease Inhibitor Cocktail Plus (Carl Roth) were added to 1 mL of the cell lysate which was either used for the assay right away or stored at -80 °C. Prior to use, the Assay Buffer was warmed to rt and the cell lysates, NADPH, aurothiomalate (ATM; specific TrxR inhibitor) and rat liver TrxR enzyme were thawed and kept on ice. After determination of the amount of cell lysate to use for optimum TrxR activity, all components were pipetted into the wells of a clear 96 well plate and the enzymatic reactions were initiated by addition of NADPH and 5,5´-dithio-bis(2-dinitrobenzoic acid) (DTNB). Then the absorbance at 405 nm was measured once every minute using a plate reader (Tecan F200) at at least ten time points. The TrxR activity was measured in the presence and absence of ATM. It is established that gold compounds such as ATM are highly specific inhibitors of mitochondrial TrxR.[4] Therefore, in presence of ATM an inhibition of TrxR can be assumed which allows a correction for TrxR-independent DTNB reduction (e.g. via glutathione). The difference between the two results renders the DTNB reduction due to TrxR activity. By plotting the average absorbance values as a function of time the slope of the linear portion of the curve was obtained, and the change of absorbance (ΔA_{405}) per minute could be determined. The values were corrected for unspecific DTNB reduction and the TrxR activity was calculated using the following formula: TrxR activity [µmol/min/mL] = [corrected ΔA/min (sample) / 7.92 mM^{-1}] × [0.2 mL / 0.02 mL] × sample dilution. The assay was conducted at 22 °C. All experiments were performed in triplicate and the solvent-treated negative controls were set to 100%.

Mitochondrial membrane potential.
518A2 melanoma cells (100 µL/well, 0.25×10^6 cells/mL) were seeded in transparent (for viability control via MTT) and black 96-well plates, followed by an incubation period of 24 h under cell culture conditions. The medium was replaced by 90 µL/well standard assay buffer (80 mM NaCl, 75 mM KCl, 25 mM D-Glucose, 25 mM HEPES, pH 7.4 in ddH_2O) and the cells were treated with a volume of 10 µL of various concentrations of test compounds or solvent (DMF). CCCP (10 µM) served as a positive control. The cells were incubated for a further 45 min under standard cell culture conditions. Then 10 µL/well of a TMRM (tetramethylrhodamine methyl ester; Cayman Chemicals) solution were added (2 µM in standard assay buffer), followed by an incubation period of 10 min under exclusion of light. The cells were washed three times (160 µL PBS per well) and the fluorescence signal was measured after adding 100 µL PBS per well (Tecan F200, $\lambda_{ex}/\lambda_{em}$: 535/590 nm). The fluorescence signal was correlated to viability, determined by corresponding MTT assays.

Determination of intracellular concentration of reactive oxygen species (DCFH-DA assay).
518A2 melanoma cells were seeded in black 96 well plates (100 µL/well, 0.1×10^6 cells/mL) and incubated for 24 h under standard cell culture conditions. The medium was replaced by serum-free medium containing 20 µM DCFH-DA, followed by a further incubation periode of 30 min. Cells were washed twice with PBS (100 µL/well) and fresh medium without FBS was added (100 µL/well). After treatment with 10 µM of the test compounds or solvent, the cells were incubated for 1 h under standard cell culture conditions and subsequently washed twice with PBS. The cells were kept in PBS and the fluorescence was measured (Tecan F200, $\lambda_{ex}/\lambda_{em}$: 485/535 nm). Solvent-treated cells were taken as negative controls and their fluorescence was set to 100%.

Lysosomal integrity.
518A2 melanoma cells (500 µL/well, 0.05×10^6 cells/mL) were seeded on glass coverslips in 24 well plates and incubated for 24 h under standard cell culture conditions. Then the cells were treated with the test compounds at IC_{50} concentrations and incubated for 1, 2, 4 or 6 h under standard cell culture conditions. 30 min before each time interval ended, cells were stained with Lysosomal Staining Kit Orange - Cytopainter (Abcam). To this end, medium was aspirated and the cells were washed once with 1 mL HHBS (Hanks Buffer with HEPES; 140 mM NaCl, 5 mM KCl, 1 mM $CaCl_2$, 0.4 mM $MgSO_4 \times 7H_2O$, 0.5 mM $MgCl_2 \times 6H_2O$, 0.3 mM $Na_2HPO_4 \times 2H_2O$, 0.4 mM KH_2PO_4, 6 mM D-glucose, 20 mM HEPES, pH 7.0). The cells were treated with 300 µL staining solution, incubated for 30 min under standard cell culture conditions, washed twice with 1 mL HHBS and fixed for 10 min at rt in 1 mL/well 3.7% formaldehyde in PBS. After three further washing steps, the coverslips were washed with 500 µL ddH_20 and embedded on glass slides with ProLong Gold™ (Invitrogen) containing 1 µg/mL DAPI. Lysosomal and nuclear staining was documented using a fluorescence microscope (Zeiss Imager A1 AX10, 400-fold magnification).

Stability testing via NMR spectroscopy.
Solutions of the test compounds were freshly prepared corresponding to stock solutions in dimethylformamide-d_7, 5 vol-% water-d_2 were added. ^{1}H NMR (500 MHz) spectra (16 scans) were measured at 0 h, 24 h, 48 h and 72 h to demonstrate the stability of the complexes in solution in the presence of water.

Tubulin polymerisation assay.
Purified porcine brain tubulin protein [5 mg/mL in Brinkley´s buffer 80 (BRB80)] containing 10% glycerol and 1.5 mM guanosine 5´-triphosphate (GTP)] was pipetted in a black 96-well half-area plate and mixed with the test compounds or solvent (DMSO) to a final concentration of 10 µM. The microplate was immediately placed in the pre-heated microplate reader (Tecan F200) and polymerisation was measured turbidimetrically at 37 °C by recording the absorption at 340 nm for 2 h in intervals of 20 s. All experiments were at least carried out in duplicate.

Cell cycle analysis.

518A2 melanoma cells (3 mL/well; 5×10^4 cells mL^{-1}) were grown on 6-well tissue culture plates for 24 h (37 °C, 5% CO_2, 95% humidity) and treated with different concentrations of the test compounds or solvent for another 24 h (37 °C, 5% CO_2, 95% humidity). The cells were harvested by trypsinisation and fixed in ice-cold 70% EtOH (1 h, 4 °C). After RNA digestion and propidium iodide (PI; Carl Roth) staining with PI staining solution (50 µg mL^{-1} PI, 0.1% sodium citrate, 50 µg mL^{-1} RNAse A in PBS) for 30 min at 37 °C to quantitatively stain DNA, the fluorescence intensity of 10 000 single cells was measured at λ_{em} = 570 nm (λ_{ex} = 488 nm laser source) with a Beckmann Coulter Cytomics FC500 flow cytometer. The percentage of cells in the different phases of the cell cycle (G1, S and G2/M phase) was determined by CXP software (Beckmann Coulter). The percentage of apoptotic and necrotic cells was derived from sub-G1 peaks.

Results

Influence on cellular morphology

To confirm induction of apoptosis after treatment of 518A2 melanoma cells with complexes **4-6** we additionally documented morphological alterations via brightfield microscopy (Fig. 11).

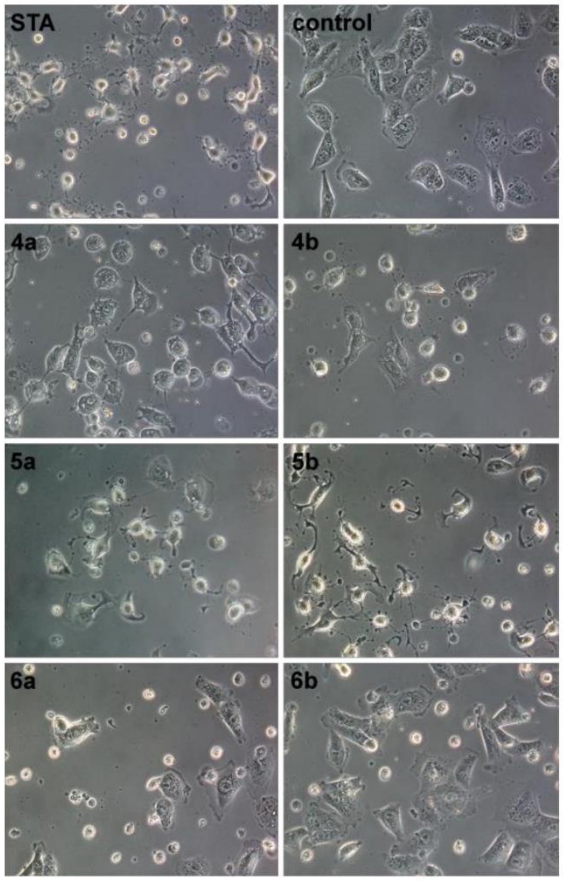

Figure 11: Morphological signs of apoptosis of 518A2 melanoma cells after incubation with staurosporine (STA; 500 nM) as well as IC_{50} concentrations of gold complexes **4-6** for 2.5 h. (**4a**: 19.8 µM, **4b**: 7.9 µM, **5a**: 5.0 µM, **5b**: 2.9 µM, **6a:** 0.4 µM, **6b**: 5.5 µM). Documented using brightfield microscopy, 100× magnification. Images are representative of at least three independent experiments.

Apoptosis detection using Annexin V-FITC and PI

Early apoptotic events upon treatment of 518A2 melanoma cells with gold complexes **4-6** were detected by staining of phosphatitylserines on the outer surface of the cytoplasmic membrane with Annexin-V-FITC. Early apoptotic and late apoptotic/necrotic cells could be differentiated by counterstaining with propidium iodide (PI), which can only enter cells lacking membrane integrity. Results were documented via fluorescence microscopy (Fig. 12).

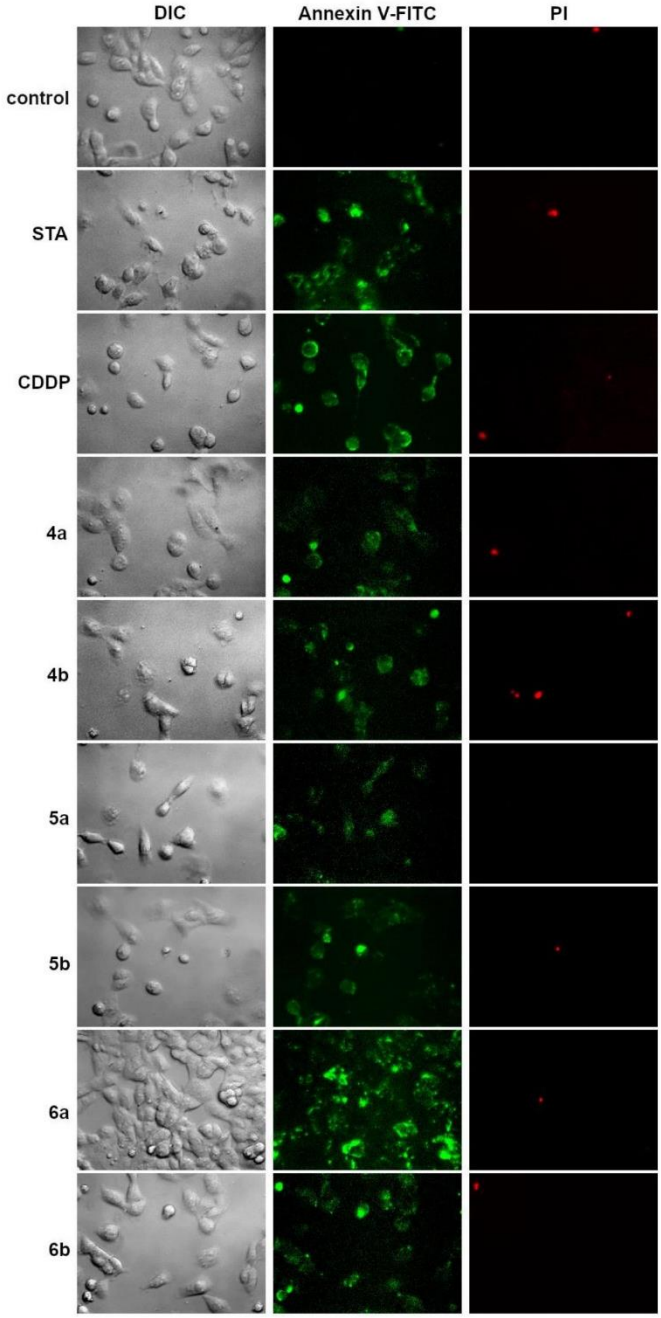

Figure 12: Annexin-V-FITC/PI staining of 518A2 melanoma cells treated with staurosporine (STA; 500 nM), CDDP (7.8 µM) as well as IC_{50} concentrations of gold complexes **4-6** for 45 min. (**4a**: 19.8 µM, **4b**: 7.9 µM, **5a**: 5.0 µM, **5b**: 2.9 µM, **6a**: 0.4 µM, **6b**: 5.5 µM). Documented using fluorescence microscopy, 200× magnification. Images are representative for at least three independent experiments.

Stability testing via NMR spectroscopy

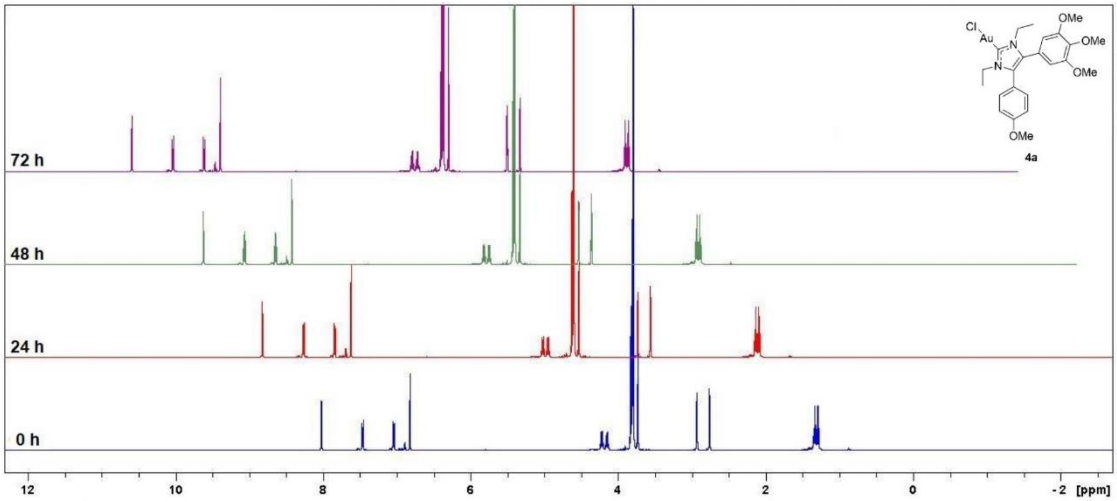

Figure 13: ^{1}H NMR (500 MHz, dimethylformamide-d_7, 5 vol-% water-d_2) spectra of **4a**; 0 h, 24 h, 48 h and 72 h after preparing of stock solution.

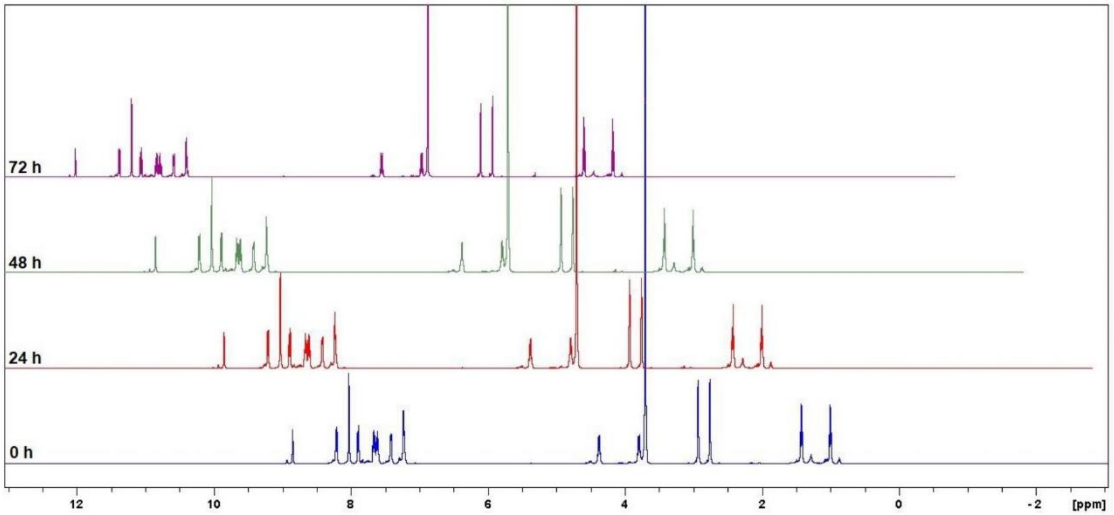

Figure 14: ^{1}H NMR (500 MHz, dimethylformamide-d_7, 5 vol-% water-d_2) spectra of **4b**; 0 h, 24 h, 48 h and 72 h after preparing of stock solution.

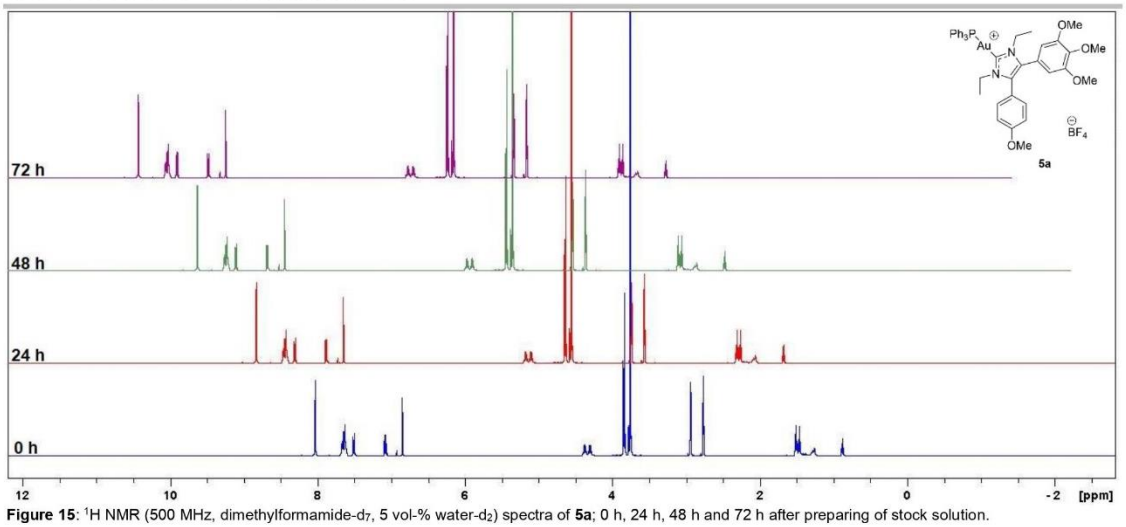

Figure 15: ^{1}H NMR (500 MHz, dimethylformamide-d_7, 5 vol-% water-d_2) spectra of **5a**; 0 h, 24 h, 48 h and 72 h after preparing of stock solution.

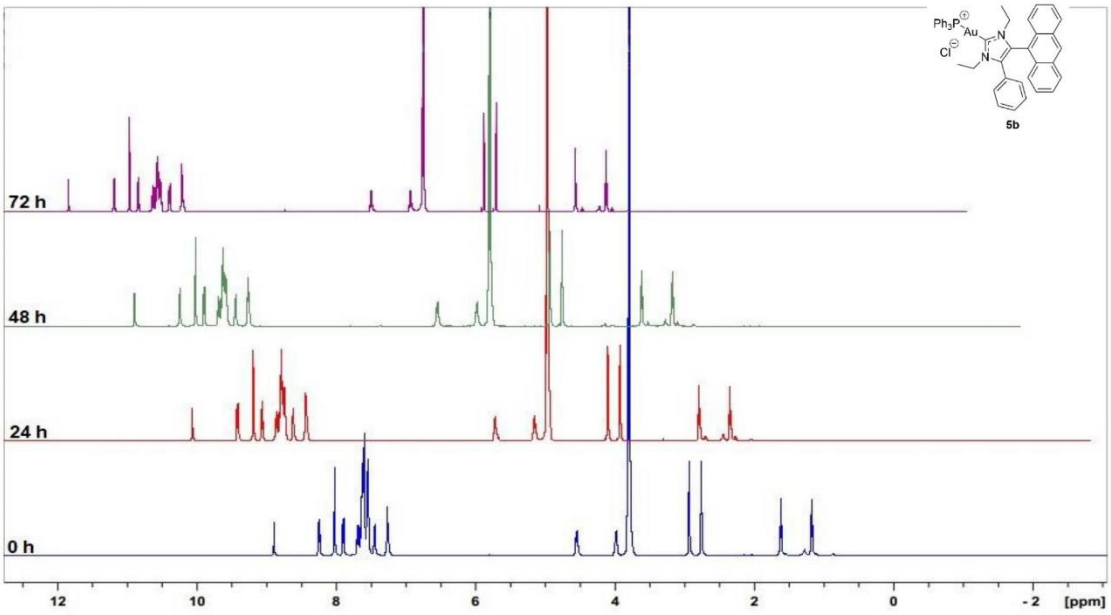

Figure 16: ^{1}H NMR (500 MHz, dimethylformamide-d_7, 5 vol-% water-d_2) spectra of **5b**; 0 h, 24 h, 48 h and 72 h after preparing of stock solution.

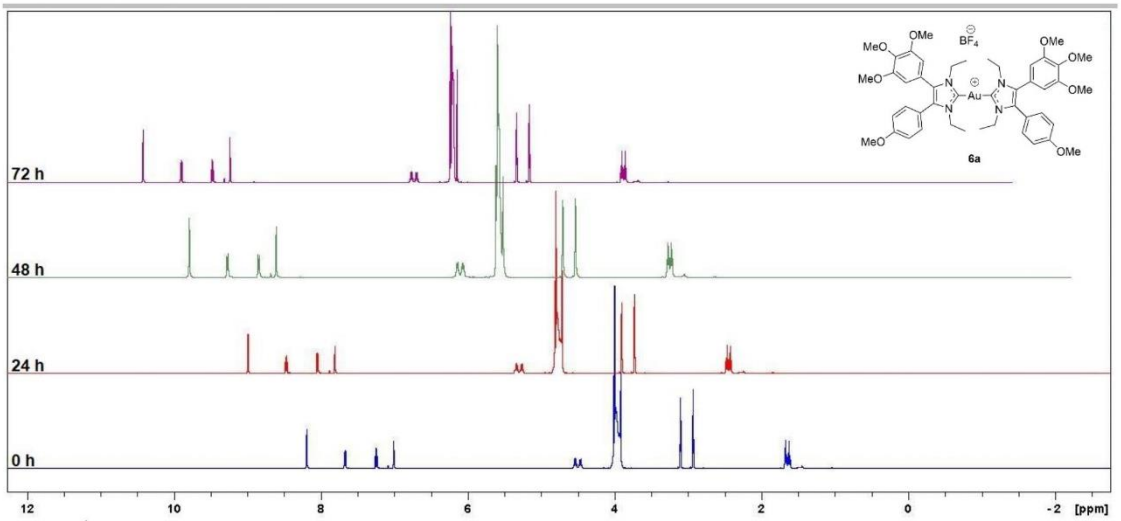

Figure 17: ^{1}H NMR (500 MHz, dimethylformamide-d_7, 5 vol-% water-d_2) spectra of **6a**; 0 h, 24 h, 48 h and 72 h after preparing of stock solution.

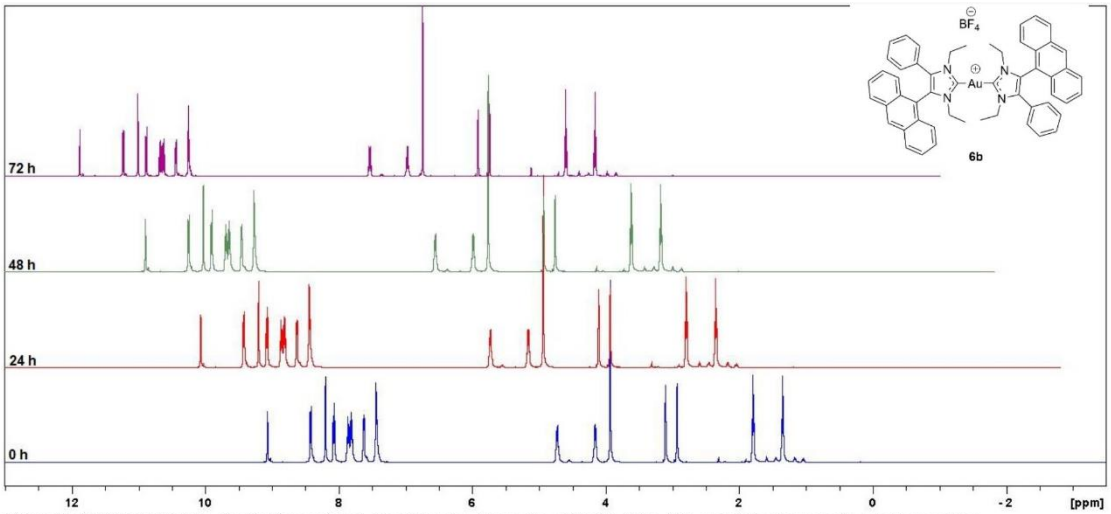

Figure 18: ^{1}H NMR (500 MHz, dimethylformamide-d_7, 5 vol-% water-d_2) spectra of **6b**; 0 h, 24 h, 48 h and 72 h after preparing of stock solution.

Interaction with tubulin

Figure 19 shows the results from tubulin polymerization assays with complexes **4-6**. The known microtubule-destabilizing compound combretastatin A-4 (CA-4) was used as a positive control. With the exception of complexes **5**, which induce a slight inhibition of tubulin polymerization, no effects could be observed for the other test compounds **4** and **6**.

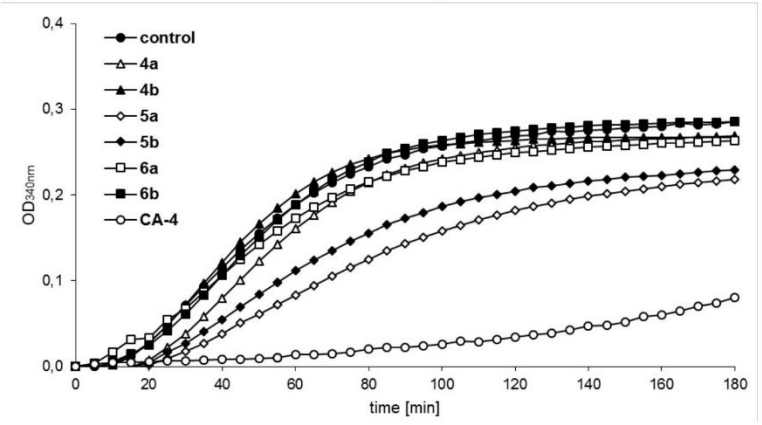

Figure 19: Turbidimetric measurement (OD at 340 ± 20 nm) of the polymerization of monomeric tubulin under the influence of the test compounds **4-6** at a final concentration of 10 µM. DMF was used as negative control, CA-4 at 10 µM was used as positive control. Values are representative of at least two independent measurements.

Influence on the cell cycle of 518A2 melanoma cells

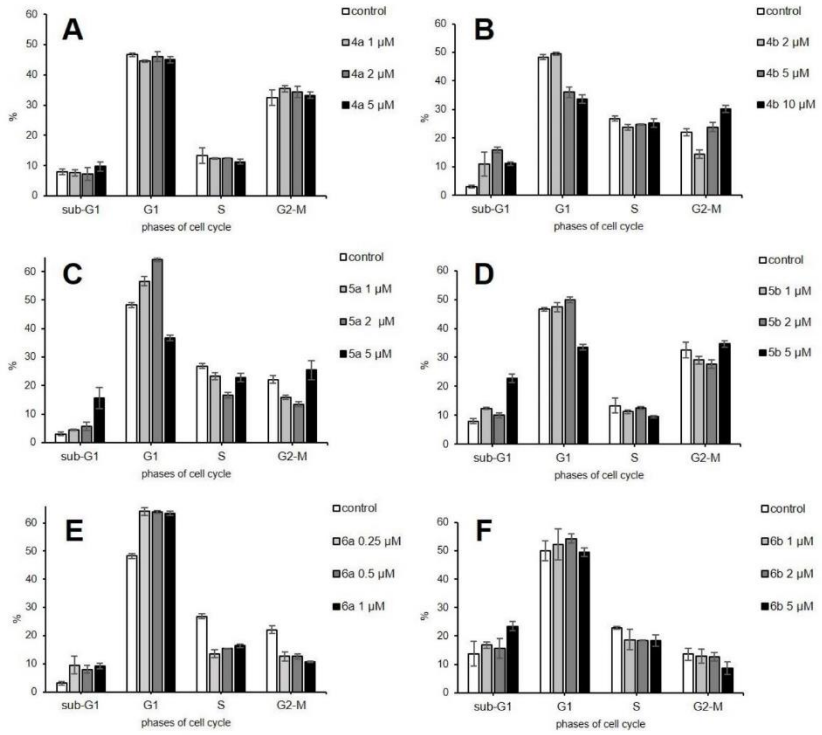

Figure 20. Influence of different concentrations of the test compounds **4a** (A), **4b** (B), **5a** (C), **5b** (D), **6a** (E) and **6b** (F) on the cell cycle of 518A2 melanoma cells measured via flow cytometry and PI staining; as a control the respective volume of solvent was used. Concentrations were adjusted to the IC_{50} values of the compounds for 518A2 melanoma cells in MTT assays. Values are means ± standard deviation derived from three independent assays.

References

[1] J. K. Muenzner, B. Biersack, H. Kalie, I. C. Andronache, L. Kaps, *et al.*, *Chem. Med. Chem.* **2014**, *9*, 1195-1204.
[2] T. Mosmann, *J. Immunol. Methods* **1983**, *65*, 55-63.
[3] M. Gold, Y. Mujahid, K. Ahmed, H. Kostrhunova, J. Kasparkova, *et al., J. Biol. Inorg. Chem.* **2019**, 24, 647-657.
[4] M. P. Rigobello, L. Messori, G. Marcon, M. A. Cinellu, M. Bragadin, *et al*, *J. Inorg. Biochem.* **2004**, 98, 1634-1641

Author Contributions

S. I. Bär: Experimental studies and data acquisition (biochemical assays and stability tests), formal analysis, chemical analysis, project administration, writing of original draft, creation of graphics and art work; degree: lead, equal to M. Gold;
M. Gold: Experimental studies and data acquisition (biochemical assays and elemental analyses), formal analysis, project administration, writing of original draft, creation of graphics and art work; degree: lead, equal to S. I. Bär;
S. W. Schleser: Synthesis of gold(I) complexes, chemical analysis; degree: supporting;
T. Rehm: Synthesis of gold(I) complexes, chemical analyses; degree: supporting;
A. Bär: Synthesis of gold(I) complexes, writing of original draft; degree: supporting;
B. Biersack: Synthesis of gold(I) complexes, writing of original draft; degree: supporting;
L. Köhler: Experimental studies (EMSA); degree: supporting;
L. R. Carnell: Experimental studies (biochemical assays); degree: supporting;
R. Schobert: Project supervision, writing of original draft, funding acquisition, project coordination; degree: corresponding author;

5.4 Publikation IV mit Darstellung des Eigenanteils

Publikation IV entstand unter Mitarbeit von S W. Schleser und L. Kober. Mitarbeiter des Arbeitskreises Organische Chemie I der Universität Bayreuth unter der Leitung von Prof. Dr. R. Schobert.

5.4.1 Eigenanteil an Publikation IV

Die Publikation wurde in ***Journal of Biological Inorganic Chemistry*** veröffentlicht, unter dem Titel

„Revisiting the anticancer properties of phosphane(9-ribosylpurine-6-thiolato)gold(I) complexes and their 9H-purine precursors“

von den Autoren

Luisa Kober[+], Sebastain W. Schleser[+], Sofia I. Bär und Rainer Schobert

[+] diese Autoren haben zu gleichen Anteilen zum Manuskript beigetragen

Eigenanteil:	Konzeption, Durchführung, Auswertung und graphischer Darstellung der Zytotoxizitätstests via MTT-Assay, Durchführung der EMSA Studien und Stabilitätsstudien mittels NMR.
Luisa Kober:	Konzeption, Durchführung, Auswertung und graphischer Darstellung folgender biochemischer Assays: weitere Zytotoxizitätstests via MTT-Assay, zelluläre Aufnahmemessungen, Zellzyklusmessungen, Messung der ROS Level, TrxR Aktivitäts-Assay, Caspase 3/7 Assay. LDH Assay, Tubulinpolymerisationsassay, *Scratch Migration* Assay, Comet Assay und *Tube formation* Assay. Zudem; Verfassen des Manuskripts gemeinsam mit Sebastian W. Schleser, einschließlich der Diskussion und Interpretation der Ergebnisse.
Sebastian W. Schleser:	Synthese, Reinigung und Analytik der Testverbindungen sowie weitere NMR Stabilitätsstudien. Zudem; Verfassen des Manuskripts gemeinsam mit Luisa Kober, einschließlich der Diskussion und Interpretation der Ergebnisse
Rainer Schobert:	Überarbeitung, Diskussion und Korrektur des Manuskripts.

5.4.2 Publikation IV

Revisiting the anticancer properties of phosphane(9-ribosylpurine-6-thiolato)gold(I) complexes and their 9H-purine precursors

Luisa Kober[+], Sebastain W. Schleser[+], Sofia I. Bär and Rainer Schobert*

Organic Chemistry Laboratory, University of Bayreuth, Universitaetsstrasse 30, 95440 Bayreuth, Germany

[+]These authors contributed equally to this work.

*E-mail: rainer.schobert@uni-bayreuth.de

J. Biol. Inorg. Chem., **2022**, 27, 731

https://doi.org/10.1007/s00775-022-01968-x

JBIC Journal of Biological Inorganic Chemistry (2022) 27:731–745
https://doi.org/10.1007/s00775-022-01968-x

ORIGINAL PAPER

Revisiting the anticancer properties of phosphane(9-ribosylpurine-6-thiolato)gold(I) complexes and their 9H-purine precursors

Luisa Kober[1] · Sebastian W. Schleser[1] · Sofia I. Bär[1] · Rainer Schobert[1]

Received: 21 July 2022 / Accepted: 27 September 2022 / Published online: 16 October 2022

Abstract

New mono- and di-nuclear thio-purine and thio-purine nucleoside gold(I) complexes were synthesized, characterized, and evaluated in vitro for biological activities in comparison to related known purine complexes. By combining known anti-tumoral thio-purines with R_3PAu moieties as present in auranofin, complexes with enhanced effects and selectivities were obtained, which not only act as cytostatics, but also disrupt tumor-specific processes. Their IC_{50} values in cytotoxicity test with tumor cell lines ranged from three-digit nanomolar to single-digit micromolar, revealing a tentative structure–activity relationship (SAR). Both the residues R^2 of the phosphane ligand and R^1 at C2 of the pyrimidine ring had a significant impact on the cytotoxicity. In most cases, the introduction of a ribo-furanosyl group at N9 of the purine led to a distinctly more cytotoxic complex. Most complexes were more active against multi-drug-resistant tumor cells or such lacking functional p53 when compared to the respective untreated wild type cell lines. Some nucleoside complexes displayed an interesting dose-dependent dual mode of action regarding cell cycle arrest and DNA repair mechanism. Some phosphane(purine-6-thiolato) gold (I) complexes had a stronger inhibitory effect on the thioredoxin reductase (TrxR) and on the reactive oxygen species (ROS) generation in cancer cells than is typical of other gold complexes. They also led to DNA fragmentation and showed anti-angiogenic effects. Their stability under test conditions was demonstrated by ^{77}Se NMR monitoring of an exemplary selenopurine complex.

Graphical abstract

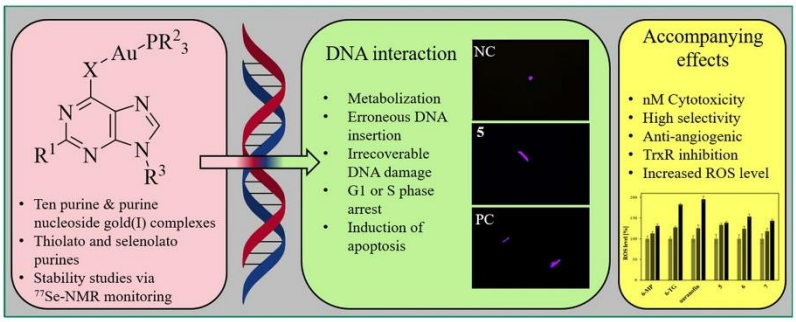

Keywords Anticancer compounds · Gold(I) complexes · Thioredoxin reductase (TrxR) inhibitors · Triorganophosphanes · Nucleosides · Auranofin

Luisa Kober and Sebastian W. Schleser contributed equally to this work.

Extended author information available on the last page of the article

Introduction

Cisplatin has been and still is a mainstay in the chemotherapy of certain cancer entities, despite of its poor cancer selectivity, fast emergence of resistance, and frequent unwanted side effects. Later generation platinum drugs, such as oxaliplatin and carboplatin, while eliciting tumor resistance to a lesser degree than cisplatin, are still associated with severe side effects. For this reason, and in anticipation of a similar, platinum-like efficiency, the search for further metallo-drugs was extended to coordination and organometallic complexes of noble and other late transition metals. Although no such drug has been approved by the FDA for cancer treatment to date [1], auranofin is a successful example of a highly efficacious, multi-modal gold drug with few side effects. Initially designed and approved against rheumatoid arthritis [2], it has shown promising effects against a variety of cancer entities [3–5], in addition to antibacterial and antiviral properties [6]. Extensive SAR studies of structurally related compounds were carried out as early as 1986, in which the phosphane motif was found to be particularly relevant [7]. Recent studies supported these findings, in which the PEt_3Au^+ cation with various halides or thiols also exhibited submicro-molecular cytotoxicities against various human cancer cell lines [8, 9]. Since then, many gold(I) and gold(III) complexes with anti-tumor properties have been evaluated [10]. The choice of ligands and their lipophilicity, size and intrinsic toxicity turned out essential for their bioactivity and bio-distribution as too lipophilic phosphane gold(I) compounds e.g., $[Au(dppe)_2]^+$ tend to display significant hepatotoxicity [11]. One way to compensate for the lipophilicity of phosphanes is to use hydrophilic thiols as second ligands. Needless to say, that these complexes must be stable enough to reach their target, but not too unreactive to interfere with it [9]. The thio analogs of adenine and guanine proved to be particularly potent in this regard. 6-Mercaptopurine (6-MP) and 6-thioguanine (6-TG) are already well studied, clinically established antimetabolites with known modes of action [12]. By coordinating these thiopurines to various triorganylphosphane gold(I) fragments, Tiekink et al. could improve their beneficial effects. In fact, their complexes were cytotoxic even against human cancer cell lines not responsive to the underlying free purines [13–15]. Mechanistically, to exert their effect, they are first converted into their nucleotide analogs in vivo [16]. It is therefore unsurprising that their corresponding nucleosides, such as 6-methylmercaptopurine riboside (6-MMR), are also potent anticancer agents [13–15, 17].

Herein, we further investigate the thio-purine complexes of Tiekink et al. for their cytotoxicity and mechanism of action and we also take a look at the more effective complexes of the thio nucleosides 6-thioguanosine (6-TGS) and 6-thioinosin (6-TNS).

Materials and methods

Chemical synthesis

General

Reactions: all reactions with moisture-sensitive reagents were carried out under argon atmosphere in water-free solvents.

Solvents: unless stated otherwise, the solvents were purified and dried using standard methods.

Purchasable reagents: starting compounds were purchased from Sigma-Aldrich (St. Louis, United States), TCI (Tokyo, Japan), Merck (Darmstadt, Germany), abcr (Karlsruhe, Germany), Acros Organics (Fair Lawn, United States), VWR (Radnor, United States) and used without further purification. Nuclear Magnetic Resonance (NMR) spectra were measured using a Bruker (Bellerica, United States) DRX spectrometer at 500 MHz at ambient temperature. Chemical shifts are given in parts per million (δ). For ^{1}H-NMR spectra the resonance signal of the residual proton of $CDCl_3$ ($\delta = 7.26$ ppm) or DMSO-d_6 ($\delta = 2.50$ ppm) was used as internal standard. For ^{13}C-NMR spectra, the resonance signal of the carbon atom of $CDCl_3$ ($\delta = 77.1$ ppm) or DMSO-d_6 ($\delta = 39.5$ ppm) was used. ^{1}H-NMR spectra were measured at 500 MHz, ^{13}C-NMR spectra at 125 MHz, ^{31}P-NMR spectra at 202 MHz and ^{77}Se-NMR spectra at 95 MHz. For signal multiplicities, the following abbreviations were used: s = singlet, d = doublet, t = triplet, m = multiplet, dd = doublet of doublets, dt = doublet of triplets, dq = doublet of quartets. Coupling constants are given in Hz. Melting points were taken with an Electrothermal 9100 apparatus and are uncorrected. Mass spectra were recorded with a ThermoFisher Scientific (Waltham, United States) UPLC/Orbitrap MS system (HRMS-ESI). High-Performance Liquid Chromatography (HPLC): Analytical HPLC measurements were carried out on a Shimadzu Nexera XR with autosampler SIL-20A and a diode array detector SPD-M20A using the column Eurosphere II 100-3 C18 (150 × 4 mm) from Knauer GmbH (Berlin, Germany). Solvents used for the HPLC system featured the purity level 'HPLC grade'. UV/Vis spectra were obtained using a Varioskan LUX Plate Reader—Multimode Microplate Reader from Thermo Fisher (Waltham, United States).

General protocol for the synthesis of complexes 1–10

The respective thiol (1.00 eq.) and R_3PAuCl (1.00 eq.) were suspended in EtOH (75 mL/mmol) and 200 µm $KOH_{(aq.)}$ (1.00 eq.) was added dropwise. The suspension slowly started to dissolve and was left stirring for 24 h at rt. The solvent was evaporated and the residue was suspended in boiling acetone. After filtration, the solvent was evaporated to leave the complex as a colorless powder.

(1,7-Dihydro-6H-purine-6-thiolato) (triphenylphosphane) gold(I) (1)

84.0 mg (138 µmol, 68%) from 6-MP (34.4 mg, 202 µmol, 1.00 eq.), Ph_3PAuCl (100 mg, 202 µmol, 1.00 eq.) and 200 µm $KOH_{(aq.)}$ (1.01 mL, 202 µmol, 1.00 eq.) in EtOH (15 mL). m.p. 260 °C (decomp.); ^{1}H NMR (500 MHz, DMSO-d_6) δ_H = 13.3 (s, 1H, NH), 8.45 (s, 1H, H^{ar}), 8.26 (s, 1H, H^{ar}), 7.76–7.53 (m, 15H, H^{ar}); ^{13}C NMR (126 MHz, DMSO-d_6) δ_C = 167.7 (s), 149.3 (s), 147.7 (s), 140.2 (s), 132.0 (d, J_{CP} = 14.1 Hz), 130.0 (d, J_{CP} = 2.7 Hz), 127.8 (s), 127.7 (d, J_{CP} = 11.4 Hz), 127.4 (s); ^{31}P NMR (202 MHz, DMSO-d_6) δ_P = 36.38; HRMS (ESI): m/z calculated for $C_{23}H_{18}AuN_4PS + H^+$ [M + H$^+$]: 611.07336. Found: 611.07230.

(2-Amino-1,7-dihydro-6H-purine-6-thiolato) (triphenylphosphane) gold(I) (2)

68.0 mg (109 µmol, 54%) from 6-TG (33.8 mg, 202 µmol, 1.00 eq.), Ph_3PAuCl (100 mg, 202 µmol, 1.00 eq.) and 200 µm $KOH_{(aq.)}$ (1.01 mL, 202 µmol, 1.00 eq.) in EtOH (15 mL). m.p. 260 °C (decomp.); ^{1}H NMR (500 MHz, DMSO-d_6) δ_H = 12.4 (s, 1H, NH), 7.77 (s, 1H, H^{ar}), 7.71–7.58 (m, 15H, H^{ar}), 6.04 (s, NH_2); ^{13}C NMR (126 MHz, DMSO-d_6) δ_C = 170.6 (s), 160.4 (s), 151.7 (s), 138.1 (s), 134.4 (d, J_{CP} = 14.1 Hz), 132.3 (d, J_{CP} = 2.7 Hz), 130.4 (s), 130.0 (d, J_{CP} = 11.4 Hz), 126.3 (s); ^{31}P NMR (202 MHz, DMSO-d_6) δ_P = 36.8; HRMS (ESI): m/z calculated for $C_{23}H_{19}AuN_5PS + H^+$ [M + H$^+$]: 626.08425. Found: 626.08195.

(1,7-Dihydro-6H-purine-6-thiolato) (triethylphosphane) gold(I) (3)

40.0 mg (85.8 µmol, 30%) from 6-MP (48.6 mg, 285 µmol, 1.00 eq.), Et_3PAuCl (100 mg, 285 µmol, 1.00 eq.) and 200 µm $KOH_{(aq.)}$ (1.43 mL, 285 µmol, 1.00 eq.) in EtOH (15 mL). m.p. 240 °C (decomp.); ^{1}H NMR (500 MHz, DMSO-d_6) δ_H = 13.2 (s, 1H, NH), 8.38 (s, 1H, H^{ar}), 8.26 (s, H^{ar}), 1.91 (dt, J = 15.3 Hz, 7.3 Hz, 6H, CH_2), 1.23–1.01 (m, 9H, CH_3); ^{13}C NMR (126 MHz, DMSO-d_6) δ_C = 171.5 (s), 151.5 (s), 149.5 (s), 141.7 (s), 133.1 (s), 17.7 (d, J_{CP} = 34.1 Hz), 9.34 (s); ^{31}P NMR (202 MHz, DMSO-d_6) δ_P = 36.7; HRMS (ESI): m/z calculated for $C_{11}H_{18}AuN_4PS + H^+$ [M + H$^+$]: 467.07336. Found: 467.07161.

(2-Amino-1,7-dihydro-6H-purine-6-thiolato) (triethylphosphane) gold(I) (4)

47.0 mg (97.7 µmol, 34%) from 6-TG (47.7 mg, 285 µmol, 1.00 eq.), Et_3PAuCl (100 mg, 285 µmol, 1.00 eq.) and 200 µm $KOH_{(aq.)}$ (1.43 mL, 285 µmol, 1.00 eq.) in EtOH (15 mL). m.p. 250 °C (decomp.); ^{1}H NMR (500 MHz, DMSO-d_6) δ_H = 12.3 (s, 1H, NH), 7.74 (s, 1H, H^{ar}), 5.91 (s, NH_2), 2.17–1.67 (m, 6H, CH_2), 1.48–0.88 (m, 9H, CH_3); ^{13}C NMR (126 MHz, DMSO-d_6) δ_C = 171.4 (s), 160.1 (s), 151.6 (s), 137.6 (s), 126.6 (s), 17.9 (d, J_{CP} = 33.6 Hz), 9.26 (s); ^{31}P NMR (202 MHz, DMSO-d_6) δ_P = 36.6; HRMS (ESI): m/z calculated for $C_{11}H_{19}AuN_5PS + H^+$ [M + H$^+$]: 482.08425. Found: 482.08282.

(1,7-Dihydro-6H-purine-9-β-D-ribofuranosyl-6-thiolato) (triphenylphosphane) gold(I) (5)

53.0 mg (71.4 µmol, 50%) from 6-TNS (40.2 mg, 141 µmol, 1.00 eq.), Ph_3PAuCl (70.0 mg, 141 µmol, 1.00 eq.) and 200 µm $KOH_{(aq.)}$ (708 µL, 141 µmol, 1.00 eq.) in EtOH (15 mL). The crude product was purified by column chromatography (silica gel 60, CH_2Cl_2/MeOH 95:5). R_f = 0.63 (CH_2Cl_2/MeOH 9:1); m.p. 130 °C (decomp.); ^{1}H NMR (500 MHz, DMSO-d_6) δ_H = 8.56 (s, 1H, H^{ar}), 8.49 (s, 1H, H^{ar}), 7.76–7.58 (m, 15H, H^{ar}), 5.97 (d, J = 5.5 Hz, 1H), 5.51 (d, J = 5.5 Hz, 1H), 5.28–5.17 (m, 2H), 4.59 (d, J = 5.5 Hz, 1H), 4.18 (q, J = 4.5 Hz, 1H), 3.97 (q, J = 3.7 Hz, 1H), 3.71 (dt, J = 12.1, 4.3 Hz, 1H), 3.58 (dd, J = 12.1, 6.4 Hz, 1H); ^{13}C NMR (126 MHz, DMSO-d_6) δ_C = 171.7 (s), 148.5 (s), 134.4 (d, J_{CP} = 14.1 Hz), 133.7 (s), 132.5 (d, J_{CP} = 2.8 Hz), 130.0 (d, J_{CP} = 11.4 Hz), 129.7 (s), 88.4 (s), 86.1 (s), 74.2 (s), 71.4 (s), 61.7 (s); ^{31}P NMR (202 MHz, DMSO-d_6) δ_P = 37.0; HRMS (ESI): m/z calculated for $C_{28}H_{26}AuN_4O_4PS + H^+$ [M + H$^+$]: 743.11561. Found: 743.11528.

(2-Amino-1,7-dihydro-6H-purine-9-β-D-ribofuranosyl-6-thiolato) (triphenylphosphane) gold(I) (6)

56.0 mg (73.9 µmol, 46%) from 6-TGS (48.4 mg, 161 µmol, 1.00 eq.), Ph_3PAuCl (80.0 mg, 162 µmol, 1.00 eq.) and 200 µm $KOH_{(aq.)}$ (809 µL, 162 µmol, 1.00 eq.) in EtOH (15 mL). The crude product was purified by column chromatography (silica gel 60, CH_2Cl_2/MeOH 95:5). R_f = 0.43 (CH_2Cl_2/MeOH 95:5); m.p. 230 °C (decomp.); ^{1}H NMR (500 MHz, DMSO-d_6) δ_H = 8.09 (s, 1H, H^{ar}), 7.82–7.45 (m, 15H, H^{ar}), 6.21 (d, J = 5.5 Hz, 2H, NH_2), 5.80 (d,

J = 5.6 Hz, 1H), 5.42 (d, J = 5.9 Hz, 1H), 5.22 (t, J = 5.6 Hz, 1H), 5.13 (d, J = 4.8 Hz, 1H) 4.48 (q, J = 5.6 Hz, 1H), 4.14 (q, J = 4.5 Hz, 1H), 3.91 (q, J = 3.6 Hz, 1H), 3.67 (dt, J = 12.0, 4.7 Hz, 1H), 3.56 (dd, J = 12.0, 6.2 Hz, 1H); ^{13}C NMR (126 MHz, DMSO-d_6) δ_C = 171.6 (s), 160.1 (s), 150.9 (s), 134.4 (d, J_{CP} = 13.7 Hz), 132.4 (s), 130.0 (d, J_{CP} = 11.4 Hz), 126.6 (s), 87.4 (s), 85.7 (s), 74.0 (s), 70.8 (s), 61.7 (s); ^{31}P NMR (202 MHz, DMSO-d_6) δ_P = 37.1; HRMS (ESI): m/z calculated for $C_{28}H_{27}AuN_5O_4PS + H^+$ [M + H$^+$]: 758.12651. Found: 758.12542.

(1,7-Dihydro-6H-purine-9-β-D-ribofuranosyl-6-thiolato) (triethylphosphane) gold(I) (7)

108 mg (176 µmol, 88%) from 6-TNS (60.0 mg, 200 µmol, 1.00 eq.), Et_3PAuCl (70.0 mg, 200 µmol, 1.00 eq.) and 200 µm $KOH_{(aq.)}$ (1.00 mL, 200 µmol, 1.00 eq.) in EtOH (10 mL). m.p. 200 °C (decomp.); ^{1}H NMR (500 MHz, DMSO-d_6) δ_H = 8.55 (s, 1H, H^{ar}), 8.40 (s, 1H, H^{ar}), 5.93 (d, J = 5.7 Hz, 1H), 5.51 (s, 1H), 5.22 (d, J = 5.9 Hz, 1H), 5.22 (s, 2H), 4.58 (t, J = 5.4 Hz, 1H), 4.16 (dd, J = 4.9 Hz, 3.6 Hz, 1H), 3.95 (q, J = 3.8 Hz, 1H), 3.68 (dd, J = 12.0 Hz, 3.9 Hz, 1H), 3.58–3.49 (m, 1H), 1.96 (dq, J = 10.4, 7.6 Hz, 9H), 1.20 (dt, J = 18.6, 7.6 Hz, 6H). ^{13}C NMR (126 MHz, DMSO-d_6) δ_C = 151.1 (s), 148.0 (s), 141.7 (s), 133.4 (s), 87.8 (s), 85.6 (s), 73.5 (s), 70.3 (s), 17.3 (d, J_{CP} = 33.6 Hz), 8.86 (s). ^{31}P NMR (202 MHz, DMSO-d_6) δ_P = 37.1; HRMS (ESI): m/z calculated for $C_{16}H_{27}AuN_4O_4PS + H^+$ [M + H$^+$]: 599.11561. Found: 599.11330.

(2-Amino-1,7-dihydro-6H-purine-9-β-D-ribofuranosyl-6-thiolato) (triethylphosphane) gold(I) (8)

90.0 mg (150 µmol, 75%) from 6-TGS (56.7 mg, 200 µmol, 1.00 eq.), Et_3PAuCl (70.0 mg, 200 µmol, 1.00 eq.) and 200 µm $KOH_{(aq.)}$ (1.00 mL, 200 µmol, 10.0 eq.) in EtOH (10 mL). m.p. 170 °C (decomp.); ^{1}H NMR (500 MHz, DMSO-d_6) δ_H = 8.07 (s, 1H, H^{ar}), 6.08 (s, 2H, NH_2), 5.76 (d, J = 6.0 Hz, 1H), 5.20 (s, 3H), 5.22 (s, 2H), 4.48 (t, J = 5.5 Hz, 1H), 4.11 (dd, J = 5.0 Hz, 3.4 Hz, 1H), 3.65 (dd, J = 12.0 Hz, 3.9 Hz, 1H), 3.53 (dd, J = 12.0 Hz, 3.9 Hz, 1H), 1.94 (dq, J = 10.2, 7.6 Hz, 6H), 1.19 (dt, J = 18.5, 7.6 Hz, 9H); ^{13}C NMR (126 MHz, DMSO-d_6) δ_C = 171.9 (s), 159.4 (s), 150.4 (s), 137.5 (s), 126.6 (s), 86.7 (s), 85.2 (s), 73.3 (s), 70.4 (s), 61.4 (s), 17.3 (d, J_{CP} = 33.4 Hz), 8.82 (s); ^{31}P NMR (202 MHz, DMSO-d_6) δ_P = 36.8; HRMS (ESI): m/z calculated for $C_{16}H_{27}AuN_5O_4PS + H^+$ [M + H$^+$]: 614.12651. Found: 614.12425.

(1,7-Dihydro-6H-purine-2,6-bisthiolato) (triethylphosphane) gold(I) (9)

66.0 mg (81.3 µmol, 60%) from 2,6-dimercaptopurine (25.0 mg, 136 µmol, 1.00 eq.), Et_3PAuCl (95.1 mg, 271 µmol, 2.00 eq.) and 200 µM $KOH_{(aq.)}$ (1.36 mL, 271 µmol, 1.00 eq.) in EtOH (7 mL). m.p. 200 °C (decomp.); ^{1}H NMR (500 MHz, DMSO-d_6) δ_H = 12.46 (s, 1H, NH), 7.92 (s, 1H, H^{ar}), 1.94 (dq, J = 15.2, 7.7 Hz, 12H), 1.18 (dt, J = 18.6, 7.7 Hz, 18H); ^{13}C NMR (126 MHz, DMSO-d_6) δ_C = 171.7 (s), 169.9 (s), 150.4 (s), 139.3 (s), 129.9 (s), 17.8 (d, J_{CP} = 33.4 Hz), 9.44 (d, J_{CP} = 37.7 Hz); ^{31}P NMR (202 MHz, DMSO-d_6): δ_P = 38.2, 36.6; HRMS (ESI): m/z calculated for $C_{17}H_{32}Au_2N_4P_2S_2 + H^+$ [M + H$^+$]: 813.09259. Found: 813.09361.

6-Selenopurine

6-Chloropurine (250 mg, 1.62 mmol, 1.00 eq.) was dissolved in EtOH (5 mL), treated with selenourea (203 mg, 1.65 mmol, 1.02 eq.) and stirred at 108 °C for 1 h. The suspension was filtered and washed with H_2O. The filter cake was dissolved in 2% $NaHCO_3$(aq.) (25 mL) and the resulting mixture was stirred at 60 °C for 1.5 h. After cooling, the suspension was filtered and the filtrate was treated with acetic acid. Filtration, washing with water and drying in vacuo afforded 6-Selenopurine as orange solid (120 mg, 603 µmol, 37%). ^{1}H NMR (500 MHz, DMSO-d_6) δ_H = 14.26 (s, 1H, SeH), 13.68 (s, 1H, NH), 8.56 (s, 1H, H^{ar}), 8.26 (s, 1H, H^{ar}); ^{13}C NMR (126 MHz, DMSO-d_6) δ_C = 166.1 (s), 151.2 (s), 147.3 (s), 145.6 (s), 131.4 (s); ^{77}Se NMR (95 MHz, DMSO-d_6) δ_{Se} = 370.8. The NMR spectra match previously reported data [18].

(1,7-Dihydro-6H-purine-6-selenolato) (triethylphosphane) gold(I) (10)

72.0 mg (142 µmol, 94%) from 6-selenopurine (30.0 mg, 151 µmol, 1.00 eq.), Et_3PAuCl (52.8 mg, 151 µmol, 1.00 eq.) and 200 µm $KOH_{(aq.)}$ (753 µl, 285 µmol, 1.00 eq.) in EtOH (10 mL). m.p.: 140 °C (decomp.); ^{1}H NMR (500 MHz, DMSO-d_6) δ_H = 13.1 (s, 1H, NH), 8.39 (s, 1H, H^{ar}), 8.33 (s, H^{ar}), 1.94 (dq, J = 10.2 Hz, 7.6 Hz, 6H, CH_2), 1.19 (dt, J = 18.6 Hz, 7.6 Hz, 9H, CH_3); ^{13}C NMR (126 MHz, DMSO-d_6) δ_C = 163.4 (s), 152.1 (s), 151.1 (s), 145.6 (s), 135.5 (s), 17.9 (s), 17.7 (s), 9.28 (s); ^{77}Se NMR (95 MHz, DMSO-d_6) δ_{Se} = 166.6; ^{31}P NMR (202 MHz, DMSO-d_6) δ_P = 38.3; HRMS (ESI): m/z calculated for $C_{11}H_{18}AuN_4PSe + H^+$ [M + H$^+$]: 515.01781. Found: 515.01613.

Biological evaluation

Stock solutions

The test compounds were dissolved in DMSO to a concentration of 10 mM and stored at − 23 °C. Prior to biological experiments, they were diluted to the desired concentration with sterile Millipore water.

Cell culture conditions

518A2 human melanoma cells (Department of Radiotherapy & Radiobiology, University Hospital Vienna, Austria), HCT116^{wt} (DSMZ ACC-581) and its HCT116$^{p53-/-}$ knockout mutant colon carcinoma cells, U87 glioblastoma cells (ATCC HTB-14), EA.hy926 somatic cell hybrid cells (ATCC CRL-2922), HeLa cervix carcinoma cells (DSMZ ACC-57), MCF-7 breast cancer cells (DSMZ ACC-115), HT-29 cisplatin resistant colon cancer cells (DSMZ ACC-299) and non-malignant human dermal fibroblasts HDFa (ATCC PCS-201-012) were cultured in Dulbecco's modified Eagle medium (PAN biotech), supplemented with 10% (v/v) fetal bovine serum (Sigma-Aldrich) and 1% (v/v) ZellShield (Minerva Biolabs) at 37 °C under 95% humidity and 5% CO_2. Unless noted otherwise, all bioassay steps including cells were conducted under these standard cell culture conditions. To maintain stable multidrug resistance in Kb-V1 cells, they were routinely treated with 340 nM vinblastine.

Cytotoxicity and cellular uptake

3-(4,5-dimethylthiazol-2-yl)-2,5-diphenyltetrazolium bromide (MTT) cell viability assay

All complexes stable in solution were investigated for their anti-proliferative effect on nine human cancer cell lines, using the MTT-based cell viability assay [19]. Cells were seeded in 96-well microtiter plates (Sarstedt) with a cell density of 0.05×10^6 cells per ml and 100 µL per well and incubated for 24 h. A dilution series of test compounds was added to the wells, ranging in twelve steps from 100 µM to 5 nM. As a control, equal amounts of DMSO were added. Treated cells were further incubated for 72 h. Then, 12.5 µL per well of MTT solution (0.05% in phosphate-buffered saline (PBS)) was added, followed by another 2 h of incubation. The plates were centrifuged, the medium was discarded and 25 µL per well of SDS solution in DMSO (10% SDS, 0.6% AcOH in DMSO) was added to dissolve the formazan. The plates were incubated for a further hour. Absorbances at 570 nm and 630 nm were measured using a plate reader (Tecan). Background absorbance (630 nm) was subtracted from the formazan signal (570 nm). The resulting absorbance was directly proportional to the amount of viable cells. The control was normalized to 100% viable cells and viability of cells treated with test compounds was calculated accordingly. IC_{50} values were calculated based on a sigmoidal fit model using GraphPad Prism. Means and SD were calculated from at least four independent experiments.

Cellular uptake measurement via ICP-MS

Cells were seeded at a density of 2×10^6 cells per dish in cell culture dishes (Sarstedt) and grown overnight. The cells were then treated with the test compounds at a final concentration of 5 µM for 5 h. The cell monolayer was washed twice with PBS, the cells were harvested by trypsination, counted and pelleted (4 °C, 150×g, 5 min). Cell pellets were solubilized with aqua regia (reflux, 20 min), and the gold content was determined by ICP-MS. Means and SD were calculated from at least two independent experiments.

Lactate dehydrogenase (LDH) cytotoxicity assay

518A2 melanoma cells were seeded in 96-well flat bottom microtiter plates (Sarstedt) with 100 µL per well and a cell density of 0.05×10^6 cells per mL. Wells containing medium alone were additionally set for background measurement. Cells were allowed to grow overnight followed by substance treatment with 11.1 µL of tenfold concentrated test compound dilutions and further incubated for 24 h. As a positive control, 10 µL per well of lysis solution (9% Triton-X 100 in Millipore H_2O) was added and incubated for 45 min to maintain maximum LDH release, the same amount was added to maximum release background correction wells containing only medium. After centrifugation (4 °C, 150×*g*, 5 min), 50 µL of the supernatant of each well was transferred on a fresh microtiter plate followed by addition of 50 µL LDH assay buffer (223 mg of 2-*p*-iodophenyl-3-*p*-nitrophenyl-5-phenyltetrazolium chloride, 57 mg of *N*-methyl-phenazonium methyl sulfate, 575 mg of *N*-adenine dinucleotide, 3.2 g of lactic acid in 480 ml 200 mM Tris–Cl, pH 8.0) per well. The plate was incubated in the dark for 10–30 min at room temperature. Then 50 µL stop solution (1 M acetic acid) was added per well and the absorbance was measured at 490 nm. The mean value of background wells with medium alone was subtracted from the negative control and test wells. Additionally, the mean value of volume correction wells was subtracted from maximum LDH release wells. The percentage of LDH release was calculated, with the maximum LDH release set as 100% and the negative control as 0% release. Means and SD were calculated from at least three independent experiments [20].

Apoptotic events

Caspase 3/7 activation

The assay was conducted, following manufacturer's instructions using the Cell Meter Caspase 3/7 activity apoptosis assay kit (AAT Bioquest) [21]. Briefly, 518A2 melanoma cells were seeded in 96-well flat black microtiter plates with a density of 0.22×10^6 cells per mL and 90 µL per well. After 24 h of incubation, 10 µL per well of tenfold diluted test compounds was added, and the cells were incubated for a further 6 h. Subsequently, 100 µL per well of Caspase 3/7 substrate working solution was added and incubated for 1 h in the dark at room temperature. The fluorescence was measured using a micro-plate reader (Tecan) at ex/em = 490/525 nm.

ROS assay

To determine cellular ROS levels, 2,2′-bis(4-nitrophenyl)-5,5′-diphenyl-3,3′-(3,3′-dimethoxy-4,4′-diphenylene) ditetrazolium chloride (NBT) was used. The assay is based on the reduction of a yellow NBT tetrazolium salt to a blue formazan dye. 518A2 melanoma cells were seeded in 96-well flat bottom microtiter plates (Sarstedt) with 100 µL per well and a cell density of 0.1×10^6 cells per mL. The cells were allowed to grow overnight, followed by substance treatment with 11.1 µL of tenfold concentrated test compound dilutions and further incubated for 24 h. Then plates were centrifuged, the medium was discarded and 50 µL per well of NBT solution (0.1% in PBS) was added. The plates were further incubated for 4 h, centrifuged again and the medium was discarded. After that, 50 µL of 2M KOH solution and 65 µL DMSO had been added per well, incubation was continued for 30 min. The absorbances at 630 nm und 405 nm were measured, using a plate reader (Tecan). The background absorbance (405 nm) was subtracted from the formazan signal (630 nm). The resulting absorbance is directly proportional to the reactive oxygen species level. The control value was normalized to 100% ROS level, and accordingly, the viability of cells treated with test compounds was calculated. Means and SD were calculated from at least four independent experiments [22].

Inhibition of TrxR activity

For the measurement of TrxR activity, the TrxR Colorimetric Assay Kit (Cayman Chemicals) [23] was used according to manufacturer's instructions. 1×10^8 518A2 melanoma cells were harvested using a cell scraper, homogenized in 5 mL of cold lysis buffer (50 mM K_3PO_4, 1 mM EDTA, pH 7.4) on ice and centrifuged for 15 min (4 °C, 10,000×*g*). The protein concentration of the supernatant was determined via Nanodrop. Then, 10 µL Protease Inhibitor Cocktail Plus (Carl Roth) was added to 1 mL of the cell lysate, which was either used for the assay right away or stored at − 80 °C. Prior to use, the assay buffer was warmed to room temperature and the cell lysate, NADPH (Nicotinamide adenine dinucleotide phosphate), ATM (aurothiomalate) and rat liver TrxR enzyme were thawed and kept on ice After determination of the amount of cell lysate for optimum TrxR activity, alle components were pipetted into the wells of a clear 96-well plate and the enzymatic reactions were initiated by addition of NADPH and 5,5′-dithiobis-(2-nitrobenzoic acid (DTNB). Then, the absorbance at 405 nm was measured once every minute using a plate reader (Tecan) at least ten time points. The TrxR activity was measured in the presence and absence of ATM. The difference between the two results renders the DTNB reduction due to TrxR activity. By plotting the average absorbance values as a function of time, the slope of the linear portion of the curve was obtained, and the change of absorbance (ΔA405) per minute could be determined. The values were corrected for unspecific DTNB reduction and the TrxR activity was calculated using the following formula: TrxR activity [µmol/min/mL] = [corrected ΔA/min (sample)/7.92 mM^{-1}] × [0.2 mL/0.02 mL] × sample dilution. The assay was conducted at 22 °C. All experiments were performed in triplicate and the solvent-treated negative controls were set to 100%.

Influence on the cell cycle

The complexes were investigated for their effect on the cell cycle [24]. Cells were seeded in 6-well plates (Sarstedt) with 3 mL per well and a cell density of 0.05×10^6 cells per mL and incubated for 24 h. Cells were treated with concentrations of compounds, corresponding their IC_{50} and further incubated for 24 h. The supernatant of each sample was transferred into a separate tube on ice, the cell monolayer was rinsed once with PBS and the cells were harvested using trypsin, and also transferred into the tube. The cells were pelleted (4 °C, 150 × g, 5 min), re-suspended in 1 mL ice cold EtOH (70%) and stored for at least 1 h at 4 °C. Prior to propidium iodide (PI) staining, the cells were centrifuged (150×*g*, 5 min), the supernatant was discarded and the cells were layered with 1 mL PBS for 5 min. The cells were centrifuged again and the pellet was re-suspended in 200 µL of PI staining solution (50 µg/mL PI, 1% sodium citrate in PBS) containing 1 µL RNase (10 mg/mL stock solution) and incubated in dark for 30 min at 37 °C. The cell cycle distribution was assessed by flow cytometry (Beckmann Coulter). Means and SD were calculated from at least three independent experiments.

Tubulin polymerisation assay

First, 2 × polymerization buffer was prepared, which consisted of 385 µL Brinkley renaturing buffer 80 (BRB 80), 100 µL glycerol, and 15 µL GTP (100 mM). 50 µL of freshly prepared 2 × polymerization buffer was added to µClear black well plates. Subsequently, 11.1 µL each of a tenfold substance pre-dilution in BRB80 was added. In addition, a combretastatin A-4 positive control was prepared analogously. After rapid addition of 50 µL of tubulin per well, the measurement was started on the plate reader at 340 nm. The plate reader measured at 20 s intervals for at least 120 min until the measurement plateau was reached. For evaluation, OD 340 nm was plotted versus time [25].

Inhibition of wound healing (scratch migration assay)

Cells of melanoma cell line 518A2 were seeded in a volume of 500 µL and at a concentration of 0.1×10^6 cells/mL in 24-well plates in triplicate. The plate was incubated (37 °C, 95% humidity, 5% CO_2) for two days until a confluent monolayer was formed. A 10 µL pipette tip was used to create a wound in the cell lawn, the wound was rinsed with PBS and the medium was changed to a FBS-reduced one. Pictures were taken at first time point (0 h) right before the addition of substance at 100-fold pre-dilution. The plate was then incubated again in the incubator and photos were taken at several more time points (6, 12, and 24 h) [262626].

DNA interaction

Ethidium bromide saturation assay (EtdBr assay)

The interaction of the complexes with linear DNA was assessed using the EtdBr assay. Ethidium bromide intercalates into DNA enhancing its fluorescence, while intercalation is hindered by alterations of the DNA structure e.g., by small molecules interfering with DNA [17]. In wells of a 96-well black flat bottom microtiter plates a solution of 1 µg linear salmon sperm DNA (ThermoFisher) in TE buffer (10 mM Tris–Cl, 1 mM EDTA, pH 8.0) was treated with concentration series (final concentrations; 25 µM, 50 µM, 75 µM and 100 µM) of the compounds, a corresponding amount of DMSO was used as a control (0 µM). After an incubation period of 2 h at 37 °C, 100 µL per well of ethidium bromide solution (10 µg/mL in TE buffer) was added and the plate was incubated for 5 min in the dark. Background samples were prepared analogously but without DNA addition. EtdBr–DNA adduct fluorescence was monitored at an excitation wavelength of 535 nm and an emission wavelength of 595 nm. After background subtraction, changes in fluorescence intensity were calculated in relation to control (set to 100%). Means and SD were calculated from at least three independent experiments.

Electrophoretic mobility shift assay (EMSA)

To distinguish whether the DNA interaction is of an electrostatic or covalent nature, a second DNA interaction assay was conducted. 1.5 µg of circular plasmid pBR322 DNA were incubated in TE buffer (10 mM Tris–Cl, 1 mM EDTA, pH 8.0) with different concentrations of test compounds (final concentrations; 5 µM, 10 µM, 25 µM and 50 µM), whereas a corresponding volume of DMSO was added to the control (0 µM) to a final volume of 20 µL of each sample. Samples ware incubated for 16 h at 37 °C and subjected to 1% agarose gel electrophoresis in 0.5 × TBE buffer (45 mM Tris–Cl, 45 mM boric acid, 1.25 mM EDTA, pH 8.0) for 4 h at 66 V. Afterward, the agarose gel was stained for 20 min with EtdBr (10 µg/mL in 0.5 TBE buffer) solution and the result documented using UV excitation.

Comet assay

518A2 melanoma cells were seeded at a concentration of 0.03×10^6 cells/mL and a volume of 2 mL seeded in 6-well plates and incubated overnight (37 °C, 95% humidity, 5% CO_2). In addition, slides were coated with 1.5% agarose and allowed to harden before being stored in a moist place until the next day. On the second day, a 100-fold substance predilution was added to the cells followed by a further incubation of 3–5 h. The selected concentration range was based on Mendonça et al. [27]. Subsequently, the cells were harvested with trypsin and the cell number was adjusted to 0.02×10^6 cells/mL. 0.5% agarose solution was prepared and tempered to a maximum of 50 °C. After mixing 0.4 mL of cell suspension with 1.2 mL of tempered agarose, 200 µL was pipetted onto each of the previously coated slides. After these had hardened, a one-hour incubation followed at 4 °C in lysis buffer. The samples were then electrophoresed at 11 V for 20 min and then incubated for 15 min in neutralization buffer. Finally, the DNA was stained with 30 µL each of 1% ethidium bromide for 30 min, before the slides were washed with PBS for subsequent documentation under a fluorescent microscope with UV excitation (Zeiss Axiovert 135, Ex/Em 300 nm/605 nm).

Tube formation assay

EA.hy926 cells were cultured overnight in endothelial medium (37 °C, 95% humidity, 5% CO_2) instead of DMEM. In addition, Matrigel was thawed on ice in the refrigerator.

Pipette tips and 96-well plates were stored at − 20 °C overnight. The next day, 30 µL of Matrigel was added to each well bubble-free and the well plate was incubated for approximately 45 min (37 °C, 95% humidity, 5% CO_2). Subsequently, 100 µL of cell suspension was added to each well at a concentration of $0.4–0.5 \times 10^6$ cells/mL onto the Matrigel-treated wells and the substances were added in tenfold pre-dilution. This was followed by incubation for approximately 6 h, until tubes formed in the negative control with DMSO. At this point, documentation under the microscope took place [28].

Results

Synthesis and characterization

Chlorotriorganophosphane gold(I) precursors were synthesized according to well established literature protocols [29]. The purine-6-thiolato gold(I) complexes **1**–**9** were synthesized analogously to a procedure by Tiekink et al. (Scheme 1) [30]. No protection of the hydroxy groups of the riboside was necessary due to the higher pKa values of the thiols and their higher aurophilicity, compared to alcohols. The 9*H*-purine-6-thiolato gold(I) complexes **1**–**4** and **9** were obtained with an average yield of 60%, their nucleoside analogs **5**–**8** in yields around 45%. Complexation of 2,6-dimercaptopurine with two equivalents of $(PEt_3)AuCl$ and base afforded the dinuclear complex **9** displaying two peaks in the ^{31}P NMR spectrum. Purine-6-selenolato complex **10** was prepared by reacting 6-chloropurine with selenourea to afford 6-selenopurine which in turn was complexed exactly like the mercaptopurines and nucleosides. All complexes, designated for in vitro bio tests, were characterized by ^{1}H, ^{13}C, ^{31}P and, if applicable, ^{77}Se NMR spectroscopy, as well as ESI mass spectrometry.

None of the complexes showed a change of their signals in ^{1}H NMR spectra (*cf.* Supporting Information) over the period of at least three days when dissolved in DMSO-d_6 + 5% D_2O, i.e., under testing conditions and can thus be considered stable. The disappearance of the amine and hydroxy protons immediately after the addition of water can be explained by the isotope exchange with the D_2O present in large excess. ^{31}P NMR spectra of 9*H*-purine complex **4** and nucleoside complex **7**, measured with additional D_2O, also did not change noticeably in the course of three days, confirming the stability of the coordination of phosphorus to the gold atom. In a further corroboration of the complex stability, the similarity of the chalcogens sulfur and selenium was exploited. The selenolato complex **10** was synthesized and examined for its stability under identical conditions. Since ^{77}Se is a 1/2 spin nucleus with roughly 8% natural abundance, its compounds can be investigated directly. Depending on whether a break in the Se–Au or the Au–PR_3 bond would occur, the shift would change by several hundred ppm and serve as unequivocal evidence. Here, too, no change in the shift of the ^{77}Se NMR signal was observed. In addition, we investigated the stability of complexes **1** and **5** as representatives of the series of purines and purine nucleosides, respectively, in cell culture medium by UV/Vis spectroscopy. Their signals did not change at all in the short period of 0–30 min and also in the longer period of 3 days only slightly by a decrease in their signals intensity. The complexes can thus be considered stable under the test conditions (*cf.* Supporting Information).

Biological evaluation

Cytotoxicity against cancer cells

All complexes **1–9** were evaluated in MTT-assays for their cytotoxicity against cancer cell lines of different tumor entities, as well as a non-malignant fibroblast control cell line (Table 1). In contrast to studies by Tiekink et al., no general improvement in the cytotoxicities of the thio-purines was observed upon complexation with a tri-alkyl-phosphane gold(I) cation. For most cell lines, the IC_{50} values of complexes **1-3** and the corresponding thiopurines were approximately the same. The complexes were sometimes more and sometimes less cytotoxic than the free bases within the range of the standard deviation. Complex **4**, however, was distinctly less active compared to its analogs. The new purine nucleoside complexes, however, showed higher cytotoxicities overall. Complex **5** performed best with IC_{50} values ranging between three-digit nano-molar and single-digit micromolar. Healthy human dermal fibroblasts (HDFa) were far less affected. Complex **5** surpassed the cytotoxic effects of the positive control 6-MP on all listed cancer cell lines. It was also as active on average as the positive controls 6-TG and auranofin. Only 6-MMR displayed a stronger activity than complex **5**, yet was also more cytotoxic against HDFa. Considering all complexes **1–8**, some SAR became apparent. Derivatization of the purine with D-ribose at N9 resulted in stronger cytotoxic effects, at least for the couples **1/5**, **3/7** and **4/8**. The introduction of a $R^1 = NH_2$ group at C2 also had an effect on the cytotoxicity. While complex **1** was less cytotoxic against all tested cell lines than its 2-amino derivative **2**, the 2-H complexes were more active against the tumor cell line panel than their 2-amino congeners in the couples **3/4**, **5/6**, and **7/8**. As to the influence of the phosphane residues R^2, the tri-phenyl-phosphane(9*H*-purine-6-thiolato) complexes **1** and **2** were distinctly more cytotoxic against the tumor cells when compared with their triethylphosphane(9*H*-purine-6-thiolato) analogs **3** and **4**, respectively. No such difference in activities was observed

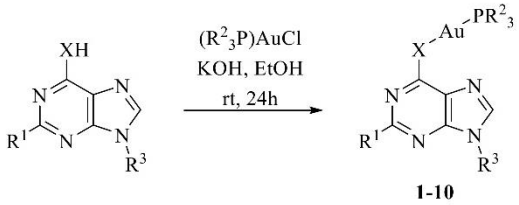

	1	2	3	4	5	6	7	8	9	10
R^1	H	NH_2	H	NH_2	H	NH_2	H	NH_2	$SAuPR^2_3$	H
R^2	Ph	Ph	Et	Et	Ph	Ph	Et	Et	Et	Et
R^3	H	H	H	H	D-Rib	D-Rib	D-Rib	D-Rib	H	H
X	S									Se

Scheme 1 Synthesis of complexes **1–10**

for the corresponding nucleoside complex couples **5/7** and **6/8**.

Tests on tumor cell line mutants in comparison with their wild type also led to telling results. HCT-116 colon carcinoma cells lacking functional p53 protein, which is also frequently mutated in tumors, were more sensitive to all tested complexes than $HCT116^{wt}$ cells. Moreover, complexes **1** and **4–8** showed an increased cytotoxicity against MCF7 breast cancer cells, previously rendered multi-drug resistant by repeated treatment with topotecan, when compared to untreated, sensitive MCF7 cells. In addition, most tested complexes were of similar cytotoxicity against KB-V1 cervix carcinoma cells in the absence and presence of the Pgp-substrate verapamil, clinically used to re-sensitize resistant tumors [31]. This suggests that these complexes are not substrates of ABC-transporter-type efflux pumps [32, 33].

Table 1 Inhibitory concentrations IC_{50} [μM] of 6-MP, 6-TG, 6-MMR, auranofin and complexes **1–9** when applied to EA.hy926 endothelial hybrid cells and cells of human HCT-116, $HCT\text{-}116^{p53-/-}$ (p53 knockout mutant) and HT-29 colon carcinomas, HeLa and mdr $KB\text{-}V1^{Vbl}$ cervix carcinoma (treated with and without 1 μM verapamil), MCF-7 and mdr $MCF\text{-}7^{Topo}$ mamma carcinoma, U-87 glioblastoma, 518A2 melanoma, and human adult dermal fibroblasts HDFa

	EA.hy926	$HCT\text{-}116^{wt}$	$HCT\text{-}116^{p53-/-}$	HeLa	HT-29	$KB\text{-}V1^{Vbl}$
6-MP	0.92 ± 0.04	5.3 ± 0.28	0.58 ± 0.05	1.4 ± 0.10	1.4 ± 0.06	1.6 ± 0.10
6-TG	0.25 ± 0.02	0.97 ± 0.10	1.0 ± 0.02	0.19 ± 0.01	1.2 ± 0.08	0.50 ± 0.05
Auranofin	0.82 ± 0.04	11.9 ± 0.4*	5.0 ± 0.2*	2.6 ± 0.4*	2.0 ± 0.18	1.9 ± 0.07
6-MMR	0.11 ± 0.001	0.10 ± 0.008	0.050 ± 0.001	0.0056 ± 0.0003	–	–
1	2.9 ± 0.70	4.9 ± 1.0	1.7 ± 0.30	2.6 ± 0.04	8.0 ± 0.73	1.9 ± 0.1
2	0.50 ± 0.10	0.80 ± 0.01	0.58 ± 0.01	0.60 ± 0.05	4.4 ± 0.32	0.30 ± 0.07
3	1.5 ± 0.11	6.3 ± 0.30	3.6 ± 0.80	6.8 ± 0.62	6.4 ± 1.4	2.5 ± 0.32
4	1.1 ± 0.08	25 ± 3.1	11 ± 0.50	15 ± 4.1	5.8 ± 1.7	12 ± 1.0
5	0.34 ± 0.03	1.7 ± 0.20	0.30 ± 0.07	0.19 ± 0.01	1.2 ± 0.09	0.50 ± 0.05
6	3.8 ± 0.13	5.5 ± 0.20	1.4 ± 0.30	2.4 ± 0.14	3.1 ± 0.19	0.91 ± 0.09
7	0.43 ± 0.02	1.6 ± 0.20	0.50 ± 0.03	0.51 ± 0.05	2.2 ± 0.17	0.40 ± 0.04
8	1.7 ± 0.14	5.5 ± 0.30	1.8 ± 0.06	2.4 ± 0.21	4.5 ± 0.34	0.70 ± 0.07
9	–	11.2 ± 0.78	3.7 ± 0.35	17.6 ± 0.80	11.1 ± 0.32	–

$KB\text{-}V1^{Vp}$	MCF7	$MCF7^{Topo}$	U-87	518A2	HDFa
1.4 ± 0.14	3.7 ± 0.26	6.4 ± 0.46	1.4 ± 0.13	11 ± 1.1	> 50
0.42 ± 0.04	0.98 ± 0.08	0.90 ± 0.09	1.7 ± 0.08	5.2 ± 0.45	> 50
2.1 ± 0.19	2.2 ± 0.22	4.7 ± 0.43	2.4 ± 0.24	1.8 ± 0.03*	14 ± 1.0*
–	0.090 ± 0.003	–	–	1.4 ± 0.12	5.8 ± 0.46
1.7 ± 0.77	13.0 ± 1.12	6.6 ± 0.65	0.91 ± 0.09	8.0 ± 0.71	–
0.54 ± 0.02	2.2 ± 0.13	3.7 ± 0.37	1.0 ± 0.1	4.4 ± 0.33	–
1.1 ± 0.11	9.4 ± 0.53	10 ± 0.26	6.9 ± 0.47	8.4 ± 0.62	–
10.4 ± 0.95	21 ± 3.40	4.9 ± 0.43	7.0 ± 0.66	16 ± 0.91	–
0.50 ± 0.03	2.4 ± 0.22	1.7 ± 0.14	1.7 ± 0.15	2.6 ± 0.25	36 ± 1.70
1.5 ± 0.11	5.8 ± 0.57	3.2 ± 0.29	1.2 ± 0.12	3.5 ± 0.26	36 ± 3.00
0.62 ± 0.04	2.1 ± 0.20	1.2 ± 0.11	1.1 ± 0.11	3.0 ± 0.21	7.0 ± 0.62
1.8 ± 0.17	10 ± 0.83	3.6 ± 0.34	1.0 ± 0.03	3.4 ± 0.33	7.0 ± 0.70
–	–	–	–	13.4 ± 1.20	–

Values are derived from dose–response curves obtained by measuring the percentage of vital cells of treated wells relative to untreated controls after 72 h of incubation using MTT-assays. Values are means ± SD of at least four independent experiments. Values marked with * were taken from Bär et al. [33]

Cellular uptake

For an assessment of the uptake of the test compounds **1–8** into 518A2 melanoma cells, the gold content of lysed treated cells was measured by ICP-MS (*cf.* Supporting Information). Complex **6**, the only one that features a 2-NH_2 group, a 9-D-ribosyl residue and a tri-phenyl-phosphane ligand, was taken up conspicuously well to a concentration of 164 µg/10^6 cells. Given its moderate IC_{50} value of ca 3.5 µM for this cell line in the MTT-assays, when compared to the other test complexes and auranofin the intrinsic cytotoxicity of complex **6** is rather low. Complex **5** and auranofin were taken up to roughly the same extent which nicely matches their similar cytotoxicities against 518A2 melanoma cells.

Influence on the cell cycle

While 518A2 melanoma cells treated with the solvent DMSO showed the normal distribution over all cell cycle phases, cells treated with the test complexes, 6-MP, or 6-TG accumulated in G1-phase. In contrast, cells treated with IC_{50} concentrations of auranofin were arrested mainly in S-phase (Fig. 1, 2). The incorporation of thiopurines into DNA leads to DNA damage, which the cell tries to repair in G1-phase [34]. Auranofin inhibits TrxR which is important for some cellular processes during S-phase of the cell cycle [35]. Complex **5** displayed both a G_1-phase arrest and an S-phase arrest when applied at approximately twice its IC_{50}. Complex **6** exhibited a similar concentration-dependent bimodal effect. A possible explanation of this effect could be that at lower concentrations the entire compound can be accommodated in the DNA, eliciting a thiopurine-like G_1-phase arrest. With concentration increasing, the cytotoxic effect typical of auranofin comes to the fore, ultimately leading to an S-phase arrest.

Influence on the intracellular ROS concentration

The influence of the complexes **5**–**7**, 6-MP, 6-TG and auranofin on the concentration of ROS in 518A2 melanoma cells was assessed by NBT-assay. All compounds led to a similar increase of ROS levels. TrxR inhibitor auranofin, when applied at a concentration of 5 µM gave rise to the highest ROS levels, presumably due to an accumulation of oxidized thioredoxin [4].(Fig. 2).

Influence on TrxR

Like auranofin, the thiopurines 6-MP and 6-TG also inhibited TrxR. The enzyme is indirectly involved in DNA synthesis, by reducing thioredoxin, which gets oxidized by ribonucleotide reductase [36]. Combining the structural motifs of auranofin and thiopurines led to compounds exhibiting a much stronger inhibition of TrxR. There was no correlation between TrxR activity and ROS levels, which indicates that auranofin is involved in other redox pathways such as the glutathione system [37]. The complexes **5** and **6** inhibited TrxR even more strongly than 6-MP, 6-TG and auranofin (Fig. 3).

Induction of apoptosis and necrosis

Auranofin inhibits the ubiquitin proteasome system, associated with induction of apoptosis [35, 38]. Both thiopurines 6-MP and 6-TG induce programmed cell death via mismatch repair mechanisms [39]. To detect any potential induction of apoptosis by the test complexes, a caspase-based fluorescence assay was used [35, 38]. Both thiopurines 6-MP and 6-TG induce programmed cell death via mismatch repair mechanisms [39]. To detect any potential induction of apoptosis by the test complexes, a caspase-based fluorescence assay was used. Executioner caspases **3** and **7** are activated in the course of the caspase cascade. Their activation can thus be taken as a measure of apoptosis induction. Both thiopurines and auranofin, but also complexes **5–7** led to increased caspase activity levels, most prominently so the complexes **6** and **7** which even exceeded the effects of the three controls.

To prove that apoptotic rather than necrotic cell death was induced, a lactate dehydrogenase (LDH)-based assay was employed. Potential drugs are supposed not to cause necrosis which leads to inflammation of healthy neighboring tissue. The release of the intracellular enzyme LDH upon drug treatment allows to gage the risk of it inducing necrosis. In comparison to a positive control, which shows the maximum LDH release, no enzyme could be detected upon treatment of 518A2 melanoma cells with 6-MP, 6-TG, auranofin or the complexes **5** and **6**. This confirms that the latter induce exclusively apoptosis and no necrosis (*cf.* Supporting Information).

Influence on tubulin polymerization

Since polymerization of tubulin plays an essential role in mitosis, its inhibition is an ideal strategy for cancer therapy. Among the inhibitors of tubulin polymerization there are already many pyrimidine-derived agents [40]. We found that 6-MP and even more so 6-TG inhibited tubulin polymerization in vitro by turbidity measurements at 340 nm using a plate reader. Auranofin also turned out to be a microtubule-destabilizing agent, probably acting by binding to the sulfhydryl groups of tubulin, which were reported to serve as targets of other polymerization inhibitors [41, 42]. Complexes **5** and **6** led to a merely slight inhibition of tubulin polymerization in vitro (*cf.* Supporting Information).

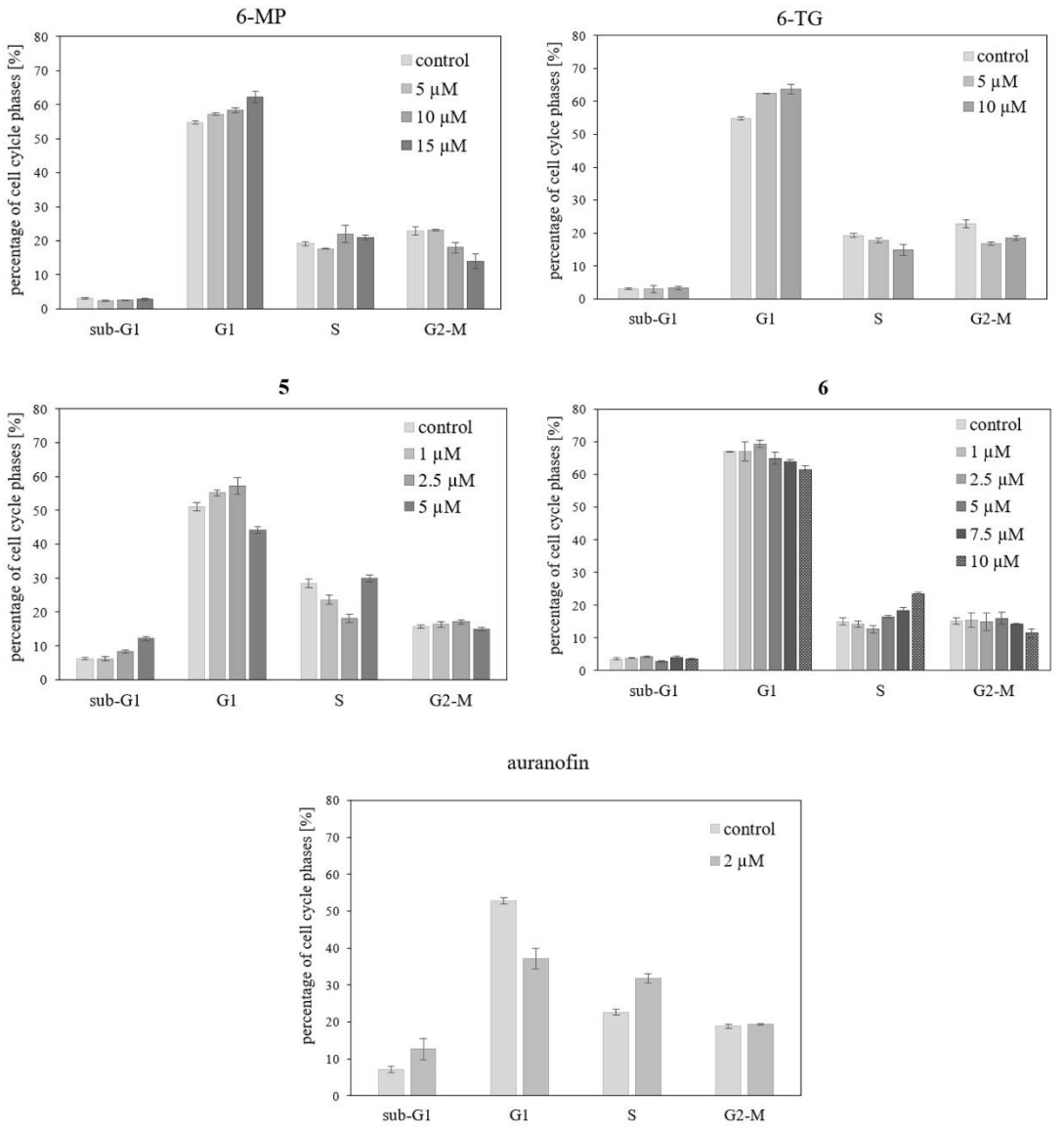

Fig. 1 Effect on the cell cycle of 518A2 melanoma cells after 24 h incubation with different concentrations of 6-MP, 6-TG, and auranofin, as well as complexes **5** and **6**. Percentage of 518A2 melanoma cells in G_1, S and G_2/M cell cycle phases and the proportion of potentially apoptotic cells (sub-G1) as determined by flow cytometry. Values are means ± SD of at least three independent experiments

Inhibition of cancer cell migration

The ability of cancer cells to migrate has been shown to be a prerequisite for the tissue invasion and metastasis. A variety of cell adhesion molecules contribute to tumor suppression and thus reduce cell migration [43]. The scratch migration assay is a simple method for identifying potential inhibitors of cell motility. “Wounds” were created in the lawn of 518A2 melanoma cells and treated with the test compounds. The closure of the scratches was followed photographically and subsequently measured at three different points [44–47]. While complex **5** retarded the closure of the scratch "wound"

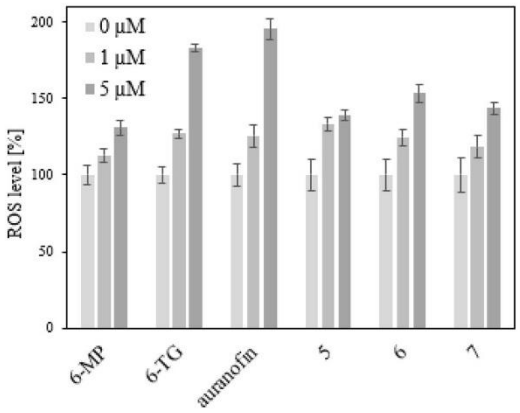

Fig. 2 Relative increase of the intracellular concentration of reactive oxygen species in 518A2 melanoma cells after treatment with solvent (0 µM) or 6-MP, 6-TG, auranofin or complexes **5**–**7** (1 µM and 5 µM) for 24 h. All experiments were performed in sextuplicate. ROS levels were calculated as mean ± SD with respect to untreated control set to 100%

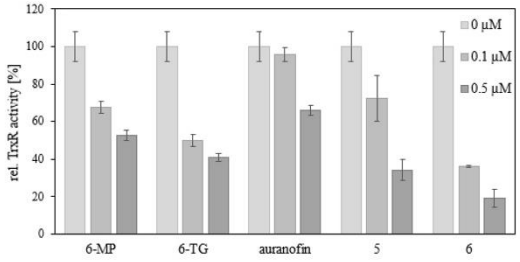

Fig. 3 Concentration-dependent inhibition of TrxR activity in lysates of 518A2 melanoma cells by 6-MP, 6-TG, auranofin and complexes **5** and **6**. TrxR-independent substrate reduction was accounted for by experiments in the presence and absence of the specific TrxR inhibitor aurothiomalate. All values are means ± SD of at least four independent experiments with negative controls (0 µM) set to 100%

relative to an untreated control, complex **6** even accelerated it. The only difference structure-wise between these two is the 2-NH_2 group of **6** (Fig. 4).

Influence on DNA

As the mechanism of action of thiopurines involves interaction with and potential damage of DNA, we carried out electrophoretic mobility shift assays (EMSA) with circular pBR322 plasmid DNA, and ethidium bromide saturation assays with linear salmon sperm DNA, both of which failed to reveal any positive effects for the so far best performing complex **5**. Presumably, it does not interact with DNA

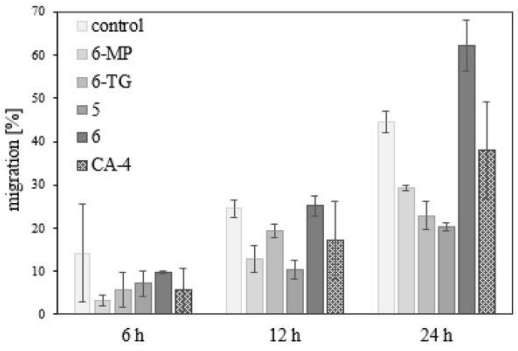

Fig. 4 Effects on cell migration of DMSO (control), 6-MP, 6-TG, complexes **5**–**6** and CA-4 as positive control. 518A2 melanoma cells were treated with the respective IC_{50} concentrations and their measured after 0, 6, 12 and 24 h. All experiments were performed as triplicates. Values are displayed as means ± SD. Migration progress was set to 0% at 0 h

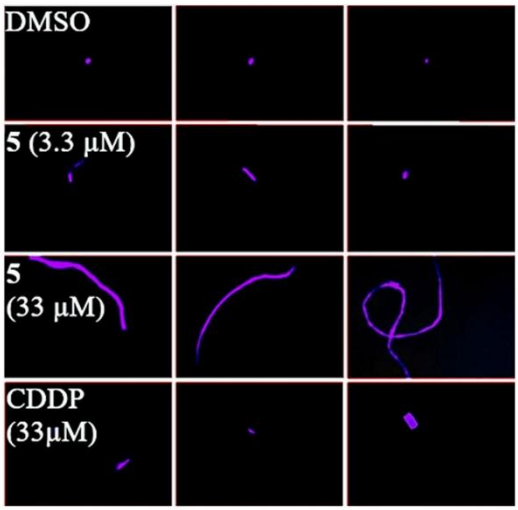

Fig. 5 DNA damage upon treatment with complex **5** (3.3 µM and 33 µM) and CDDP (33 µM) as positive control, documented with comet assays. Treatment with DMSO as a negative control. Photos are representative of the respective compound and concentration. The images were taken at 100-fold magnification and were processed for better recognizability in terms of brightness and contrast. DNA damage is visualized by migration of DNA fragments out of the nucleus, which is reminiscent of a comet tail

directly, but is metabolized in cells similarly to 6-MP and 6-TG, which are erroneously incorporated into DNA eventually leading to apoptosis induction [48]. This assumption was confirmed by comet assays, where treatment of single 518A2 melanoma cells with complex **5** led to DNA damage,

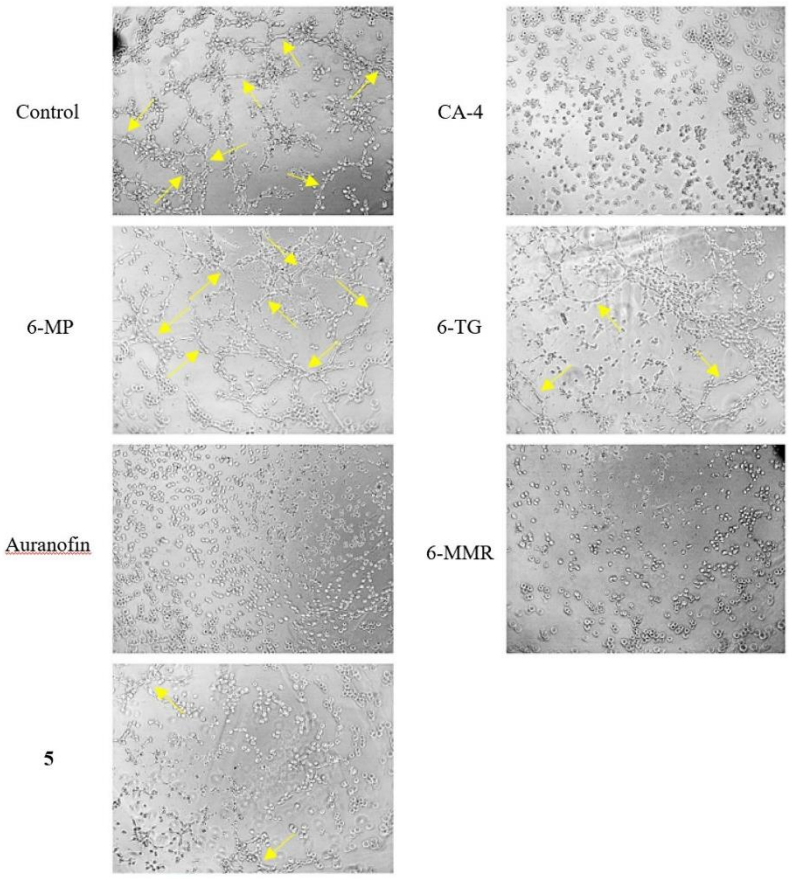

Fig. 6 Tube formation assays: Inhibition of tube formation of Ea.hy926 cells through 6-MP, 6-TG, auranofin, 6-MMR and complex **5**, as well as DMSO (neg. control) and CA-4 (pos. control). The formation of tubes, some of which are indicated by yellow arrows, mimics vessel formation during angiogenesis. The lack of it is an indication for anti-angiogenic effects of test compounds. Final concentrations were 5 µM, except for CA-4 (0.01 µM). Photos are representative of the respective compound. The images were taken at tenfold magnification and were processed for better recognizability in terms of brightness and contrast

which is reflected in the migration of stained DNA fragments during gel electrophoresis (Fig. 5).

Anti-angiogenic effects

Like auranofin, 6-MMR also has an anti-angiogenic effect [17, 35]. Inhibition of angiogenesis is considered a promising strategy in cancer therapy since the growth of tumors requires the development of a vascular network [49]. Auranofin inhibits angiogenesis, at least in zebrafish models, via interference with the VEGF signaling pathway [50]. 6-MMR inhibits the early and late phases of the angiogenesis process. The early phase of angiogenesis is associated with cellular capabilities, such as cell proliferation, cell mobility and sprouting. The late phase comprises the formation of capillary structures, which can be ascertained by the tube formation assay [17]. We could confirm the known inhibitory effects of auranofin and 6-MMR on the formation of blood vessel-like tubes by Ea.hy926 cells. Complete inhibition of tube formation, such as by the positive control CA-4, is evident by the presence exclusively of individual cells, whereas the negative control DMSO allowed the formation of the tube-like structures, mimicking the angiogenesis process. This simple test indicates anti-angiogenic properties of the compounds. 6-TG had a stronger such effect when compared to 6-MP. Interestingly, complex **5** also had such an inhibitory effect, comparable in strength to that of 6-TG (Fig. 6).

Conclusion

Four tri-organyl-phosphane(9*H*-purine-6-thiolato) gold(I) complexes with or without 2-NH_2 residues, as well as four new analogous complexes with 6-TGS and 6-TNS ligands, and a dinuclear 2,6-dimercaptopurine gold(I) complex were synthesized and characterized. The complexation worked for

purines as well as for nucleosides without any change of the reaction conditions. All complexes were stable under test conditions (5% D_2O in DMSO-d_6) over a period of at least three days. This assumption was confirmed by monitoring the stability under these conditions of an analogous purine-6-selenato gold(I) complex via ^{77}Se-NMR spectroscopy.

The gold complexes **1**–**8** showed cytotoxic effects with IC_{50} values in the low micromolar to three-digit nanomolar range against a panel of seven cancer cell lines, with complex **5** performing best on average (0.19–2.5 µM). A few tentative SAR emerged from the MTT assays. In most cases, attachment of a 9-D-ribosyl residue led to an increase in cytotoxicity, whereas NH_2 groups at C2 of the purine had the opposite effect. Complexes with a triphenylphosphane ligand were on average more active than those with triethylphosphane ligands. The cellular uptake of the complexes did not vary much with the residues R^{1-3} with complex **6** sticking out for its conspicuously great uptake. The most cytotoxic complex **5** was investigated in more detail.

Complex **5** exhibited a bipolar effect on the cancer cell cycle, leading to G1-phase arrest, like other known thiopurines, at low concentrations and to S-phase arrest, like auranofin, at higher concentrations. The latter effect is very likely due to its pronounced inhibition of TrxR. Complex **5** also initiated severe DNA lesions and fragmentation, ultimately leading to cancer cell apoptosis.

Supplementary Information The online version contains supplementary material available at https://doi.org/10.1007/s00775-022-01968-x.

Acknowledgements R.S. thanks the Deutsche Forschungsgemeinschaft for financial support (grant Scho 402/12-2). We thank Dr. Ulrike Lacher for high resolution mass spectra and Leonhard H. F. Köhler (both University of Bayreuth) for additional stability studies.

Funding Open Access funding enabled and organized by Projekt DEAL. Deutsche Forschungsgemeinschaft grant Scho 402/12-2

Declarations

Conflict of interest There are no conflicts of interest.

References

1. Ott I, Gust R (2007) Non platinum metal complexes as anti-cancer drugs. Arch Pharm 340:117–126
2. Bernhard GC (1982) Auranofin therapy in rheumatoid arthritis. J Lab Clin Med 100:167–177
3. Fiskus W, Saba N, Shen M, Ghias M, Liu J, Das Gupta S et al (2014) Auranofin induces lethal oxidative and endoplasmic reticulum stress and exerts potent preclinical activity against chronic lymphocytic leukemia. Cancer Res 74:2520–2532
4. Raninga PV, Lee AC, Sinha D, Shik Y-Y, Mittal D, Makhale A et al (2020) Therapeutic cooperation between auranofin, a thioredoxin reductase inhibitor and anti-PD-L1 antibody for treatment of triple-negative breast cancer. Int J Cancer 146:123–136
5. Massai L, Cirri D, Marzo T, Messori L (2022) Auranofin and its analogs as prospective agents for the treatment of colorectal cancer. Cancer Drug Resist 5:1–14
6. AbdelKhalek A, Abutaleb NS, Mohammad H, Seleem MN (2019) Antibacterial and antivirulence activities of auranofin against clostridium difficile. Int J Antimicrob Agents 53:54–62
7. Mirabelli CK, Johnson RK, Hill DT, Faucette LF, Girard GR, Kuo GY et al (1986) Correlation of the in vitro cytotoxic and in vivo antitumor activities of gold (I) coordination complexes. J Med Chem 29:218–223
8. Lima JC, Rodriguez L (2011) Phosphine-gold(I) compounds as anticancer agents: general description and mechanisms of action. Anticancer Agents Med Chem 11:921–928
9. Gandin V, Fernandes AP, Rigobello MP, Dani B, Sorrentino F, Tisato F et al (2010) Cancer cell death induced by phosphine gold(I) compounds targeting thioredoxin reductase. Biochem Pharmacol 79:90–101
10. Lu Y, Ma X, Chang X, Liang Z, Lv L, Shan M et al (2022) Recent development of gold(I) and gold(III) complexes as therapeutic agents for cancer diseases. Chem Soc Rev 51:5518–5556
11. Hoke GD, Rush GF, Bossard GF, McArdle JV, Jensen BD, Mirabelli CK (1988) Mechanism of alterations in isolated rat liver mitochondrial function induced by gold complexes of bidentate phosphines. J Biol Chem 263:11203–11210
12. Munshi PN, Lubin M, Bertino JR (2014) 6-thioguanine: a drug with unrealized potential for cancer therapy. Oncologist 19:760–765
13. Tiekink ERT, Cookson PD, Linahan BM, Webster LK (1994) In vitro antitumour activity of some triorganophosphinegold(I) thionucleobases. MetBased Drugs 1:515303
14. Webster LK, Rainone S, Horn E, Tiekink ERT (1996) Anti-tumor activity, in vitro and in vivo, of some triphenylphosphinegold(i) thionucleobases. MetBased Drugs 3:63–66
15. Whitehouse MW, Cookson PD, Siasios G, Tiekink ERT (1998) Anti-arthritic activity in rats of some phosphinegold(i) thionucleobases and related thiolates. MetBased Drugs 5:245–249
16. Coulthard S, Hogarth L (2005) The thiopurines: an update. Invest New Drugs 23:523–532
17. Presta M, Rusnati M, Belleri M, Morbidelli L, Ziche M, Ribatti D (1999) Purine analogue 6-methylmercaptopurine riboside inhibits early and late phases of the angiogenesis process. Cancer Res 59:2417–2424
18. Mitra R, Pramanik AK, Samuelson AG (2014) Seleno-nucleobases and their water-soluble ruthenium-arene half-sandwich complexes: chemistry and biological activity. Eur J Inorg Chem 2014:5733–5740
19. Morgan DML (1998) Tetrazolium (MTT) assay for cellular viability and activity. In: Morgan DML (ed) Polyamine protocols. Humana Press, Totowa, NJ, pp 179–184

20. Chan FK, Moriwaki K, De Rosa MJ (2013) Detection of necrosis by release of lactate dehydrogenase activity. Methods Mol Biol 979:65–70
21. Cell Meter™ Caspase 3/7 Activity Apoptosis Assay Kit *Green Fluorescence* | AAT Bioquest. https://www.aatbio.com/products/cell-metercaspase-3-7-activity-apoptosis-assay-kit-greenfluorescence?unit=22796
22. Aitken RJ (2018) Nitroblue tetrazolium (NBT) assay. Reprod Biomed Online 36:90–91
23. Montano SJ, Lu J, Gustafsson TN, Holmgren A (2014) Activity assays of mammalian thioredoxin and thioredoxin reductase: fluorescent disulfide substrates, mechanisms, and use with tissue samples. Anal Biochem 449:139–146
24. Jayat C, Ratinaud M-H (1993) Cell cycle analysis by flow cytometry: principles and applications. Biol Cell 78:15–25
25. Zhu T, Wang S-H, Li D, Wang S-Y, Liu X, Song J et al (2021) Progress of tubulin polymerization activity detection methods. Bioorg Med Chem Lett 37:127698
26. Hulkower KI, Herber RL (2011) Cell migration and invasion assays as tools for drug discovery. Pharmaceutics 3:107–124
27. Mendonça LM, Meneghin L, dos Santos GC, dos Santos RA, Takahashi CS, Bianchi M et al (2010) Evaluation of curcumin and cisplatin-induced DNA damage in PC12 cells by the alkaline comet assay. Hum Exp Toxicol 29:635–643
28. DeCicco-Skinner KL, Henry GH, Cataisson C, Tabib T, Gwilliam JC, Watson NJ et al (2014) Endothelial cell tube formation assay for the in vitro study of angiogenesis. J Vis Exp. 91:e51312. https://doi.org/10.3791/51312
29. Zhang C, Hong K, Dong S, Pei C, Zhang X, He C et al (2019) Gold(I)-catalyzed aromatization: expeditious synthesis of polyfunctionalized naphthalenes. iScience 21:499–508
30. Tiekink ERT, Cookson PD, Linahan BM, Webster LK (1994) In vitro antitumour activity of some triorganophosphinegold(I) thionucleobases. Met Based Drugs 1:299–304
31. Williams JB, Buchanan CM, Pitt WG (2018) Codelivery of doxorubicin and verapamil for treating multidrug resistant cancer cells. Pharm Nanotechnol 6:116–123
32. Huber S, Wege AK, Bernhardt G, Buschauer A, Brockhoff G (2015) Topotecan-induced ABCG2 expression in MCF-7 cells is associated with decreased CD24 and EpCAM expression and a loss of tumorigenicity. Cytom A 87:707–716
33. Bär SI, Gold M, Schleser SW, Rehm T, Bär A, Köhler L et al (2021) Guided antitumoural drugs: (imidazol-2-ylidene)(L)gold(I) complexes seeking cellular targets controlled by the nature of Ligand L. Eur J Chem 27:5003–5010
34. Alberts B, Johnson A, Lewis J, Morgan D, Raff M, Roberts K et al (2017) Molekularbiologie Der Zelle, 6th edn. Wiley-VCH, Boschstr, Weinheim, pp 1171–1195
35. Madeira JM, Gibson DL, Kean WF, Klegeris A (2012) The biological activity of auranofin: implications for novel treatment of diseases. Inflammopharmacology 20:297–306
36. Rodwell VW (2018) Metabolism of purine & pyrimidine nucleotides. In: Rodwell VW et al (eds) Harper's illustrated biochemistry, 31st edn. McGraw-Hill Education, New York
37. Onodera T, Momose I, Kawada M (2019) Potential anticancer activity of auranofin. Chem Pharm Bull 67:186–191
38. Ghobrial IM, Witzig TE, Adjei AA (2005) Targeting apoptosis pathways in cancer therapy. CA Cancer J Clin 55:178–194
39. Cara CJ, Pena AS, Sans M, Rodrigo L, Guerrero-Esteo M, Hinojosa J et al (2004) Reviewing the mechanism of action of thiopurine drugs: towards a new paradigm in clinical practice. Med Sci Monit 10:247–254
40. Zhou Z-Z, Shi X-D, Feng H-F, Cheng Y-F, Wang H-T, Xu J-P (2017) Discovery of 9H-purins as potential tubulin polymerization inhibitors: synthesis, biological evaluation and structure-activity relationships. Eur J Med Chem 138:1126–1134
41. Snyder RM, Mirabelli CK, Crooke ST (1987) The cellular pharmacology of auranofin. Semin Arthritis Rheum 17:71–80
42. Luduena RF, Roach MC (1991) Tubulin sulfhydryl groups as probes and targets for antimitotic and antimicrotubule agents. Pharmacol Ther 49:133–152
43. Appert-Collin A, Hubert P, Cremel G, Bennasroune A (2015) Role of ErbB receptors in cancer cell migration and invasion. Front Pharmacol 6:283
44. Eccles S, Box C, Court W (2005) Cell migration assays and their application in cancer drug discovery. Biotech Annu Rev 11:391–421
45. Yang Y, Zhou S, Ouyang R, Yang Y, Tao H, Feng K et al (2016) Improvement in the anticancer activity of 6-mercaptopurine via combination with bismuth(III). Chem Pharm Bull 64:1539–1545
46. Chu M, An X, Zhang D, Li Q, Dai X, Yu H et al (2022) Combination of the 6-thioguanine and disulfiram/Cu synergistically inhibits proliferation of triple-negative breast cancer cells by enhancing DNA damage and disrupting DNA damage checkpoint. Biochim Biophys Acta Mol Cell Res 1869:119169
47. Bhatia M, McGrath KL, DiTrapani G, Charoentong P, Shah F, King MM et al (2016) The thioredoxin system in breast cancer cell invasion and migration. Redox Biol 8:68–78
48. Parker WB (2009) Enzymology of purine and pyrimidine antimetabolites used in the treatment of cancer. Chem Rev 109:2880–2893
49. Carmeliet P, Rakesh K (2000) Angiogenesis in cancer and other diseases. Nature 407:249–257
50. He M-F, Gao X-P, Li S-C, He Z-H, Chen N, Wang Y-B et al (2014) Anti-angiogenic effect of auranofin on HUVECs in vitro and zebrafish in vivo. Eur J Pharmacol 740:240–247

Authors and Affiliations

Luisa Kober[1] · Sebastian W. Schleser[1] · Sofia I. Bär[1] · Rainer Schobert[1]

✉ Rainer Schobert
Rainer.Schobert@uni-bayreuth.de

[1] Organic Chemistry Laboratory, University of Bayreuth, Universitaetsstrasse 30, 95440 Bayreuth, Germany

-Supplementary data-

Revisiting the anticancer properties of phosphane(9-ribosylpurine-6-thiolato)gold(I) complexes and their 9H-purine precursors

Luisa Kober[+] • Sebastian W. Schleser[+] • Sofia I. Bär • Rainer Schobert[*]

Organic Chemistry Laboratory, University of Bayreuth, Universitaetsstrasse 30, 95440 Bayreuth, Germany.

[+]These authors contributed equally to this work

Corresponding Author: Rainer Schobert, Tel.: +49 (0)921-552679,
E-mail: Rainer.Schobert@uni-bayreuth.de, ORCID 0000-0002-8413-4342.

Conflicts of interest: There are no conflicts of interest.

Source of funding: Deutsche Forschungsgemeinschaft grant Scho 402/12-2;

Table of Content

Induction of apoptosis and necrosis

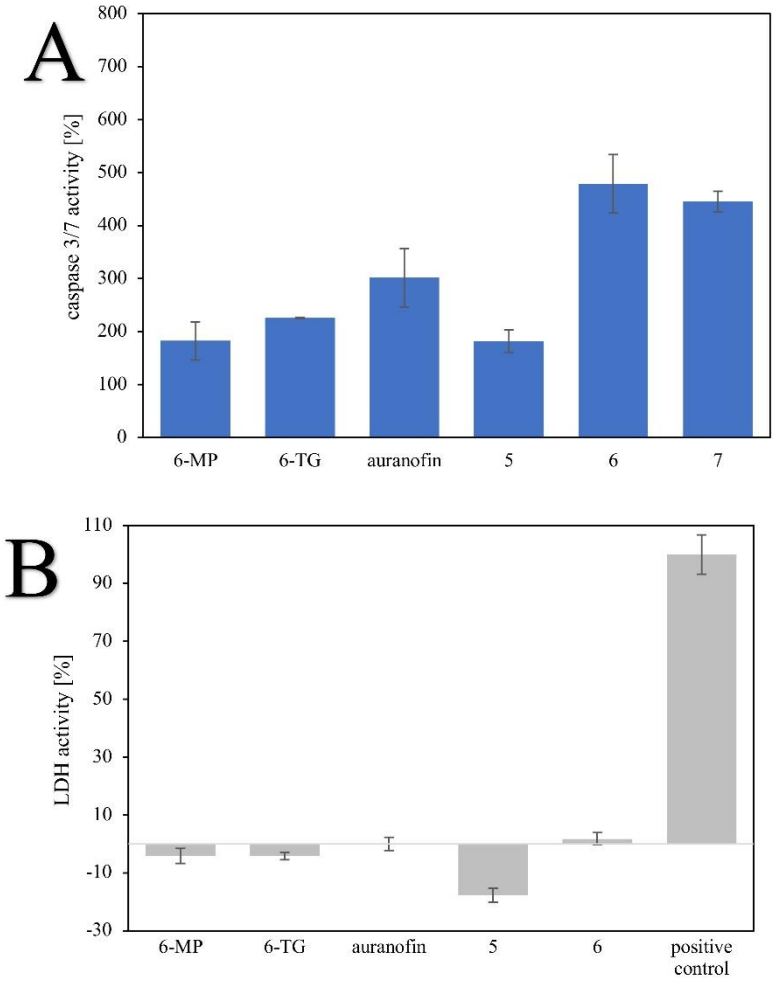

Figure S1. **A** Induction of effector capase-3/-7 activity in 518A2 melanoma cells after treatment with 10 µM mercaptopurine, thioguanine, auranofin and complexes **5**–**7** for 6 h. Vitality of cells was simultaneously tested by MTT assays and was found to be > 85 % for all experiments which were performed in triplicate. Results are quoted as means ± SD. The solvent-treated negative control was set to 100%. **B** Release of intracellular LDH in 518A2 melanoma cells after treatment with 10 µM mercaptopurine, thioguanine, auranofin and complexes **5** and **6** for 24 h. All experiments were performed in at least four independent experiments. Values are means ± SD with positive control, which displayed maximum LDH release, was set to 100%.

Influence on tubulin polymerization

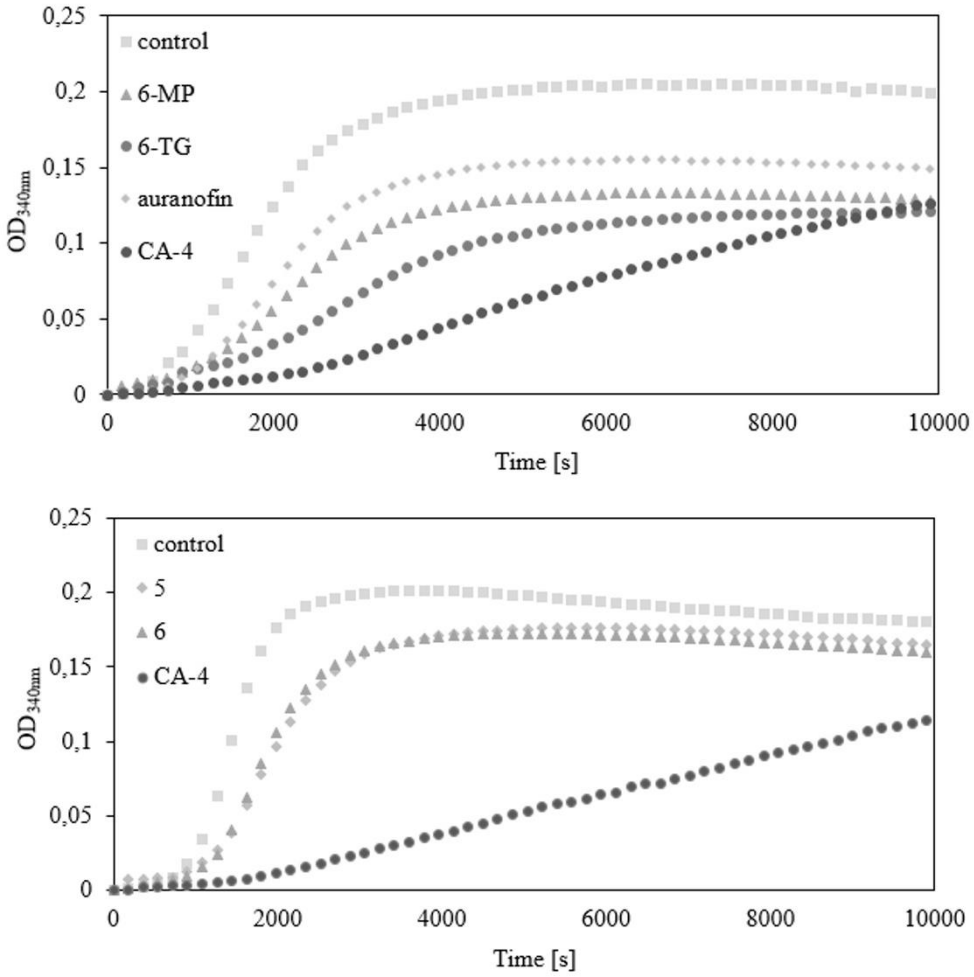

Figure S2. Inhibition of tubulin polymerization by mercaptopurine, thioguanine, auranofin, complexes **5**–**6** and CA-4 as a positive control (10 μM). All experiments were performed as duplicates.

Cellular uptake

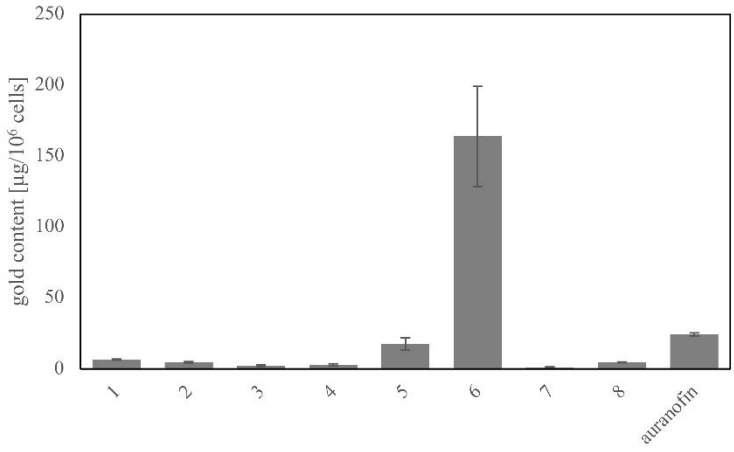

Figure S3. Cellular uptake [µg/10^6 cells] of complexes **1**–**8** and auranofin in 518A2 melanoma cells. Values were derived from substance treated lysed cells after 5 h of incubation measured via ICP-MS. Values are means ± SD from two independent experiments.

Dose-Response Curves of 5

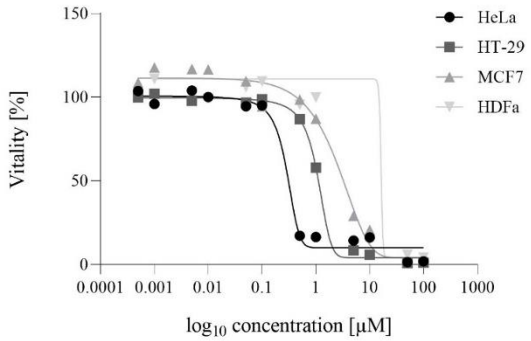

Figure S4. Dose-response curves of complex **5** with various human cancer cell lines as well as HDFa cells.

NMR spectra of complexes **1-10**

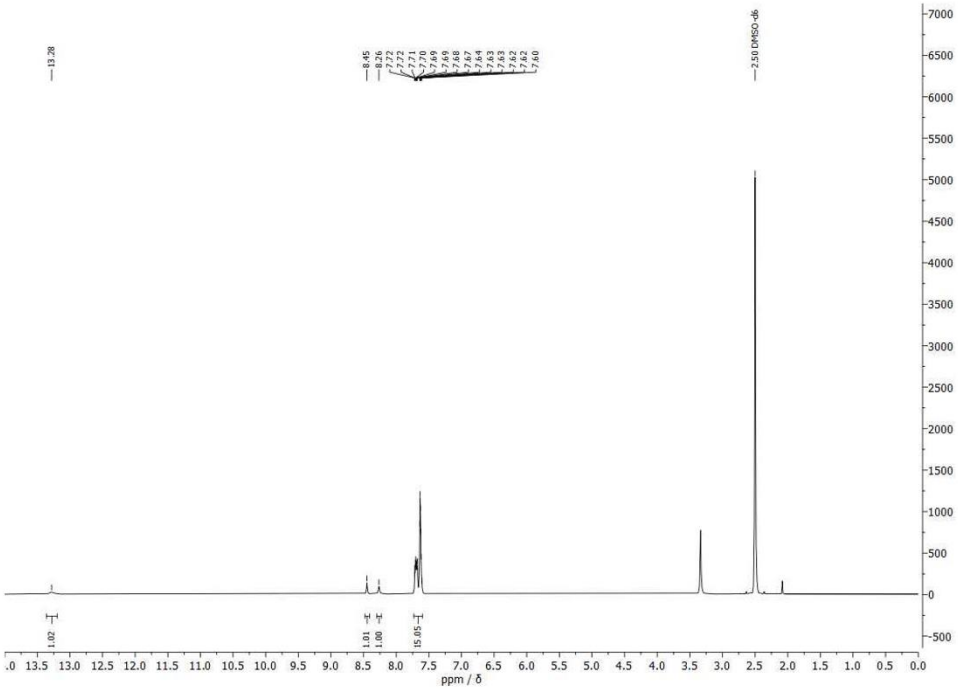

Figure S5. ^{1}H NMR spectrum of **1** in DMSO-d_6

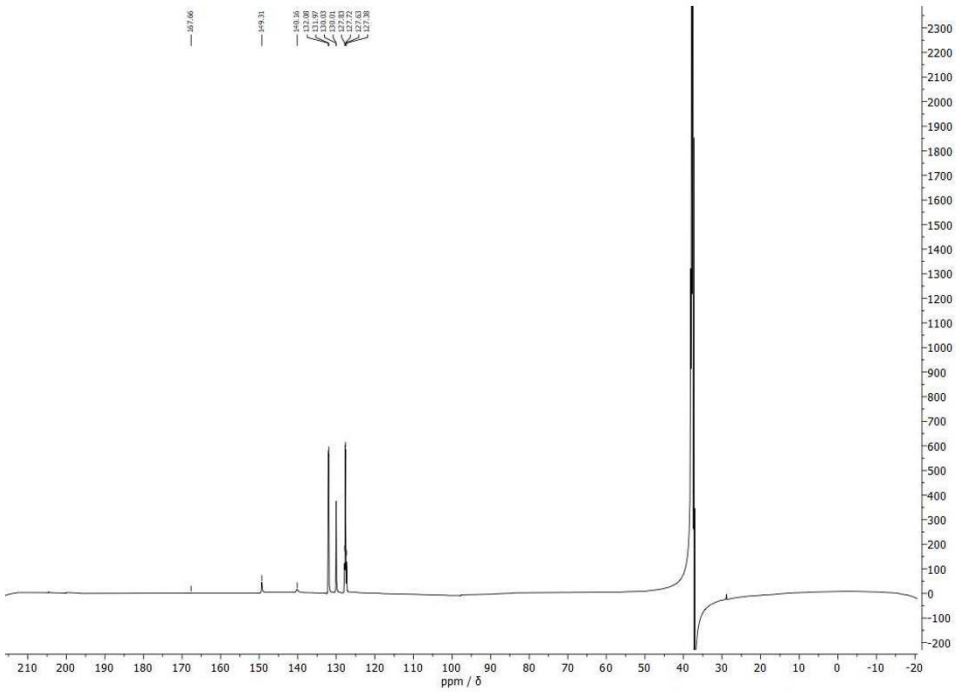

Figure S6. ^{13}C NMR spectrum of **1** in DMSO-d_6.

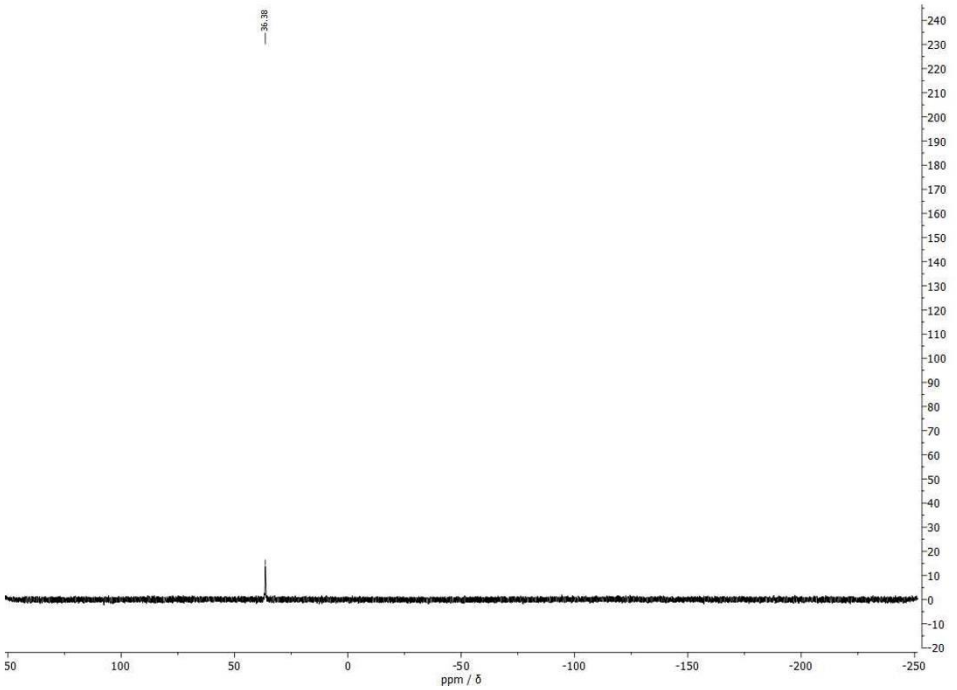

Figure S7. ^{31}P NMR spectrum of **1** in DMSO-d_6.

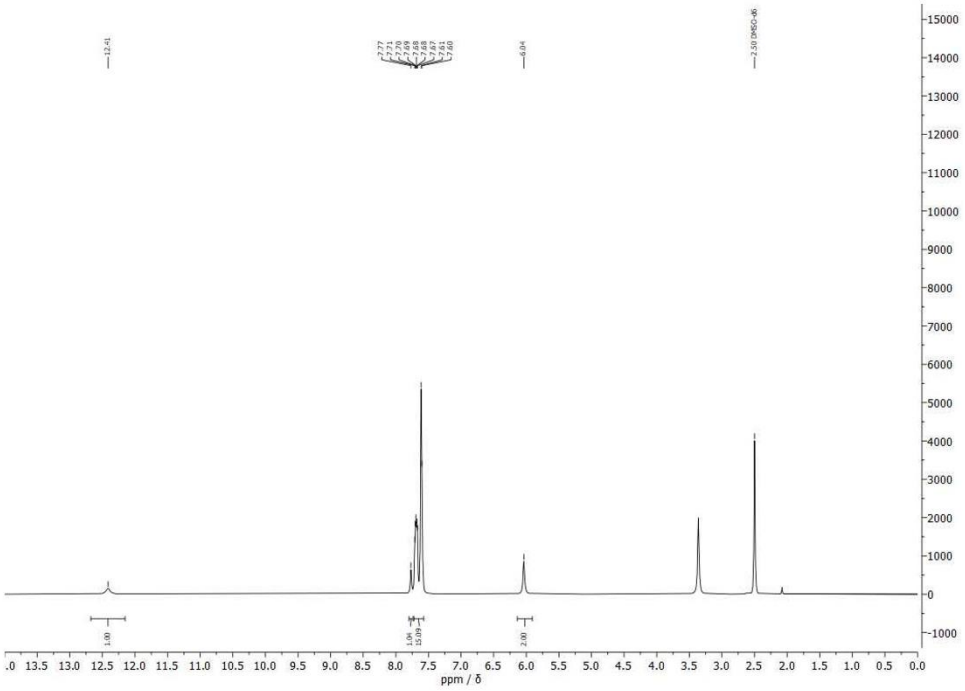

Figure S8. ^{1}H NMR spectrum of **2** in DMSO-d_6.

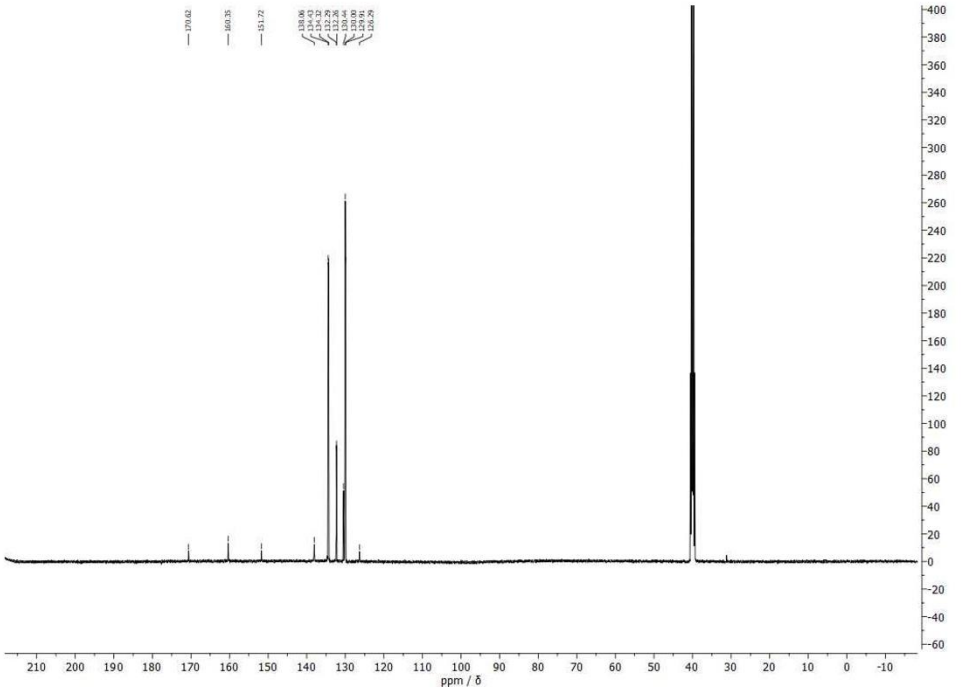

Figure S9. ^{13}C NMR spectrum of **2** in DMSO-d_6.

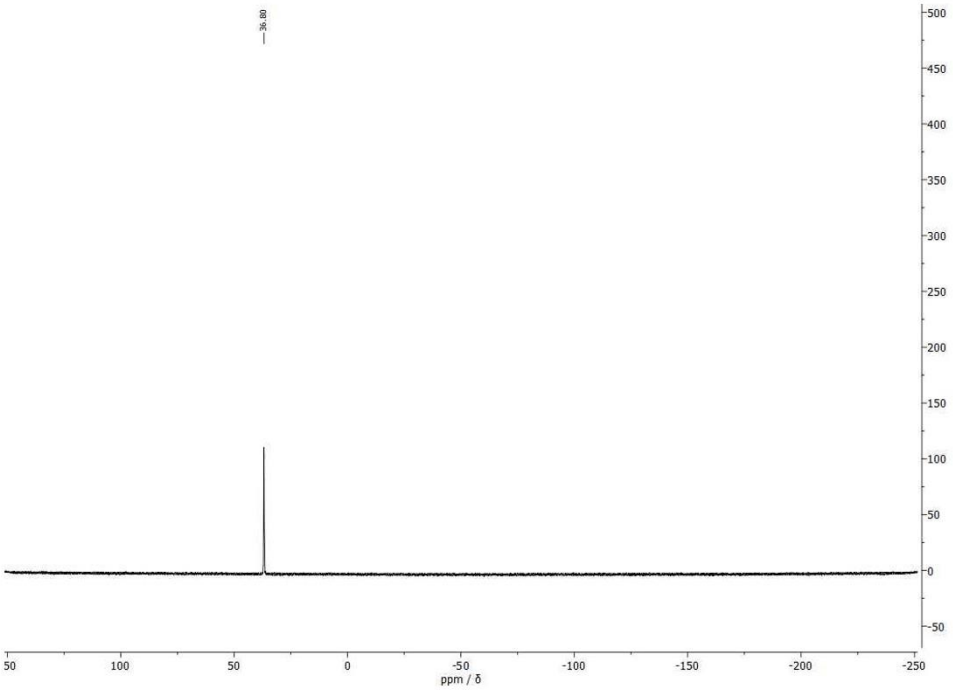

Figure S10. ^{31}P NMR spectrum of **2** in DMSO-d_6.

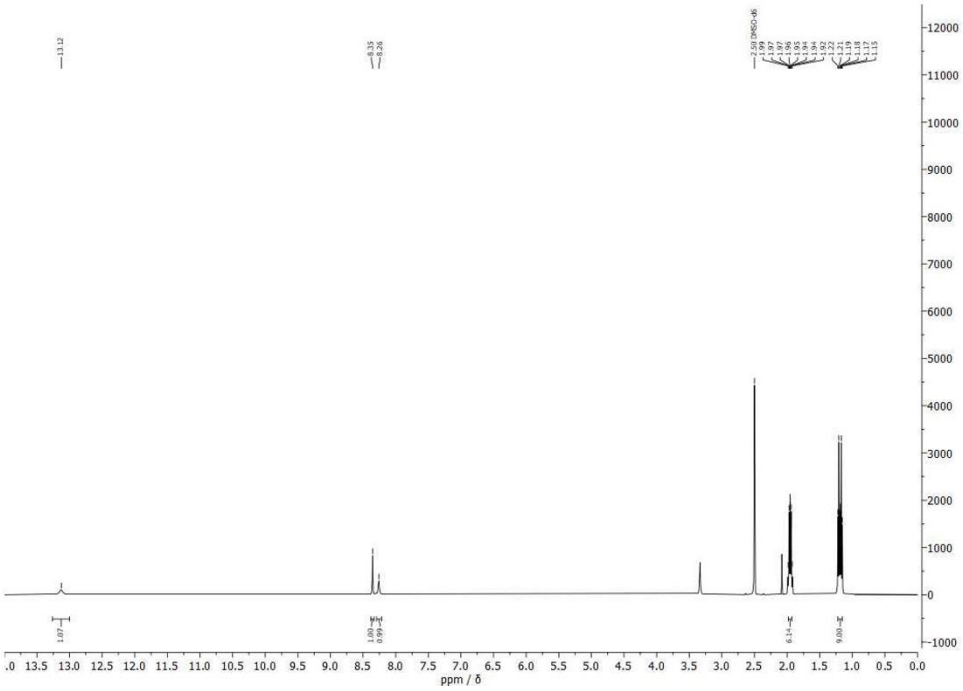

Figure S11. ^{1}H NMR spectrum of **3** in DMSO-d_6.

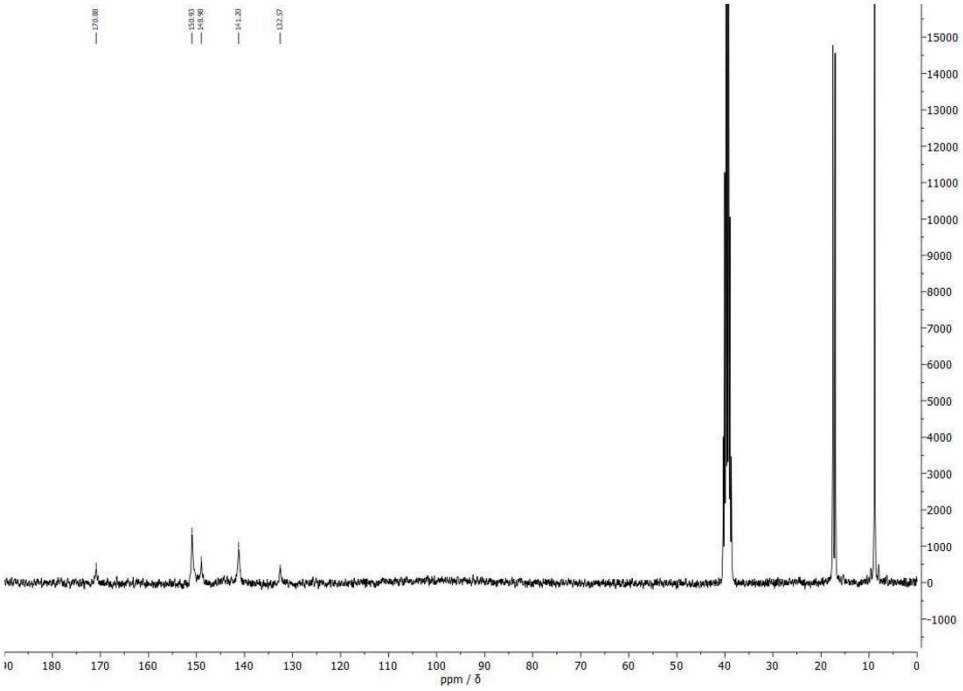

Figure S12. ^{13}C NMR spectrum of **3** in DMSO-d_6.

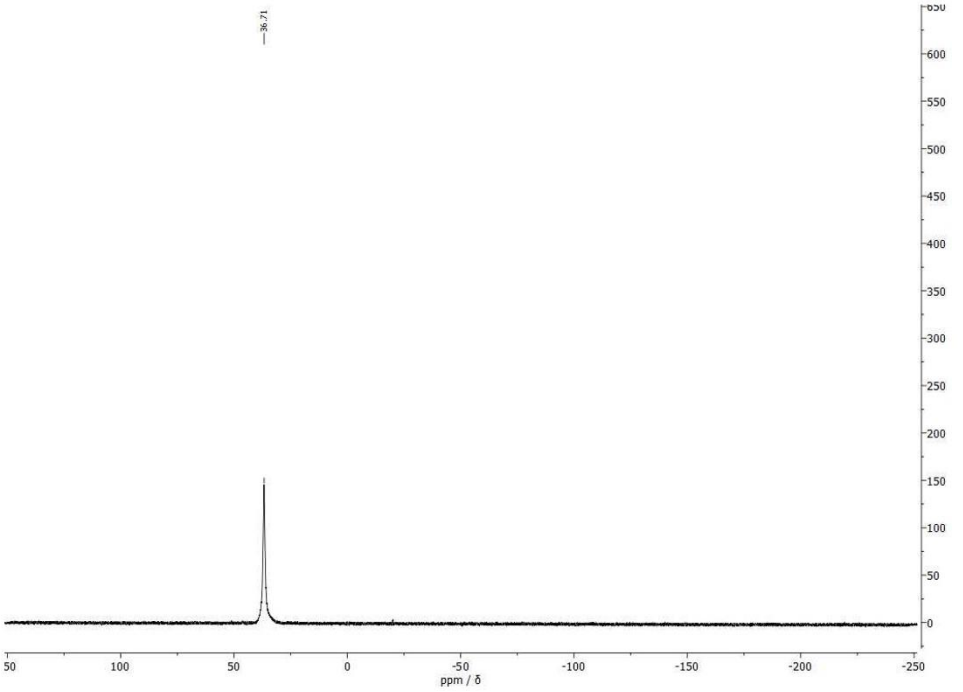

Figure S13. ^{31}P NMR spectrum of **3** in DMSO-d_6.

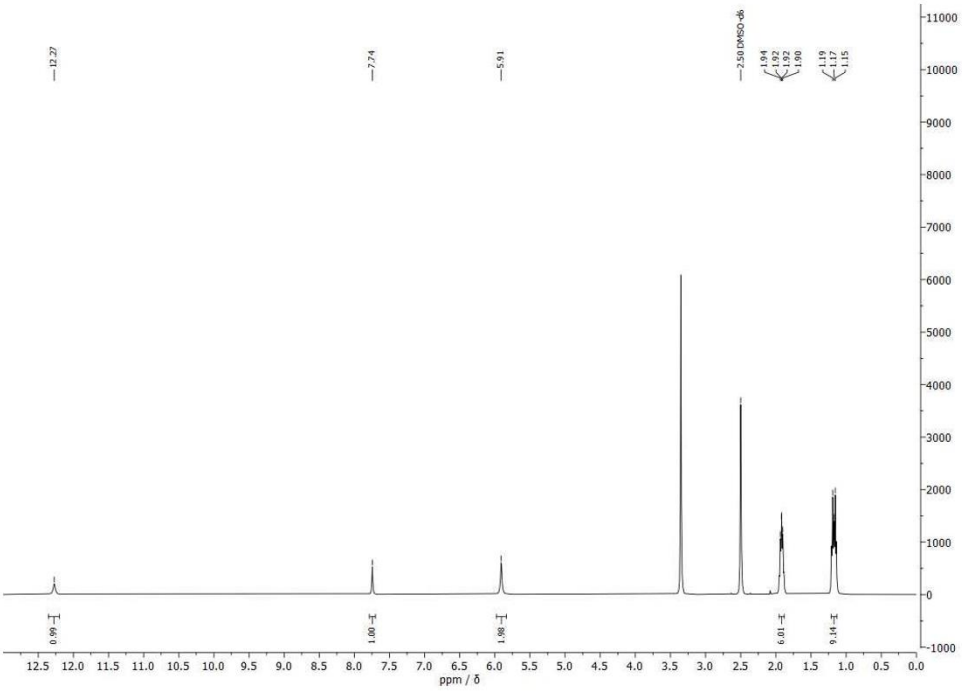

Figure S14. ^{1}H NMR spectrum of **4** in DMSO-d_6.

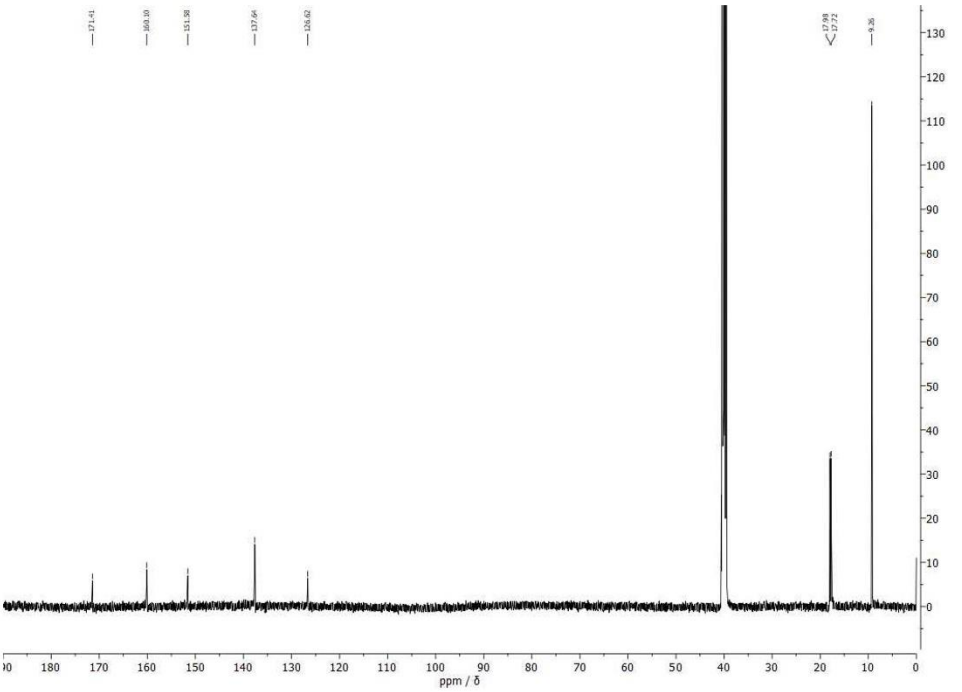

Figure S15. ^{13}C NMR spectrum of **4** in DMSO-d_6.

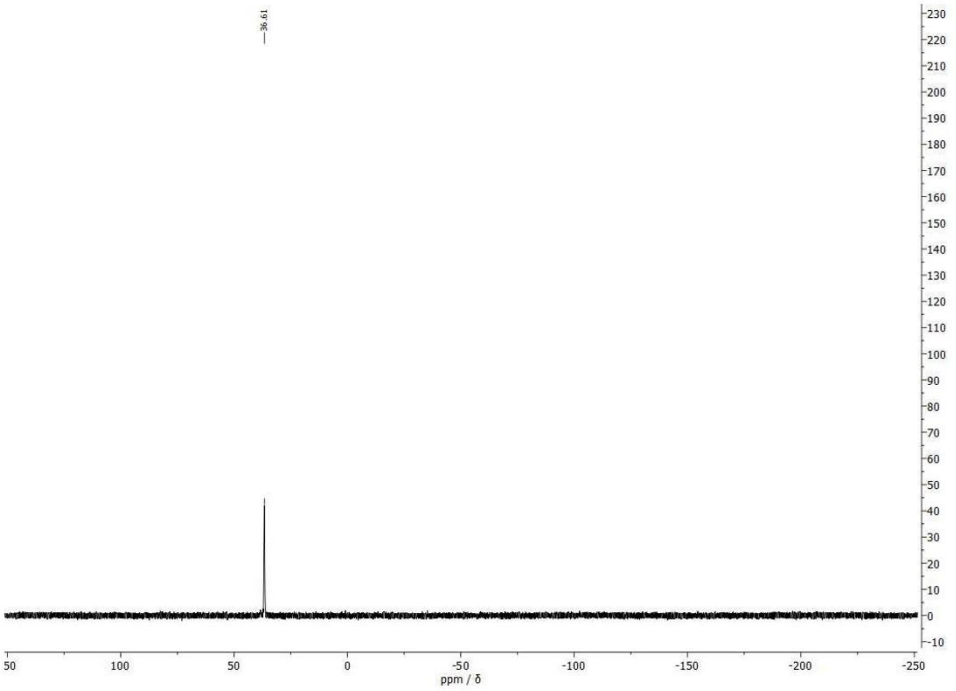

Figure S16. ^{31}P NMR spectrum of **4** in DMSO-d_6.

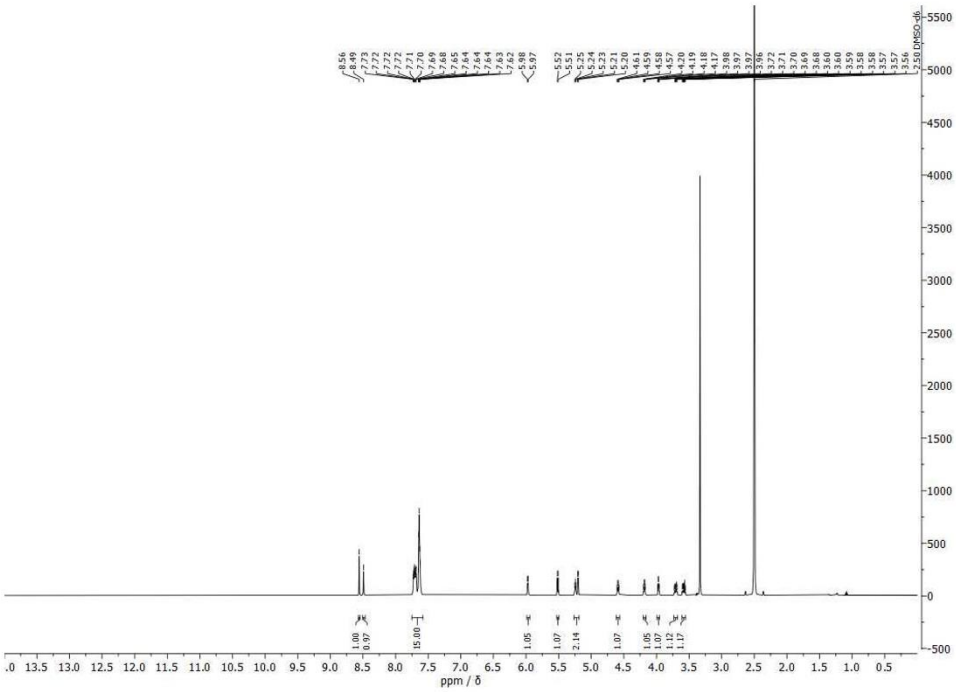

Figure S17. ^{1}H NMR spectrum of **5** in DMSO-d_6.

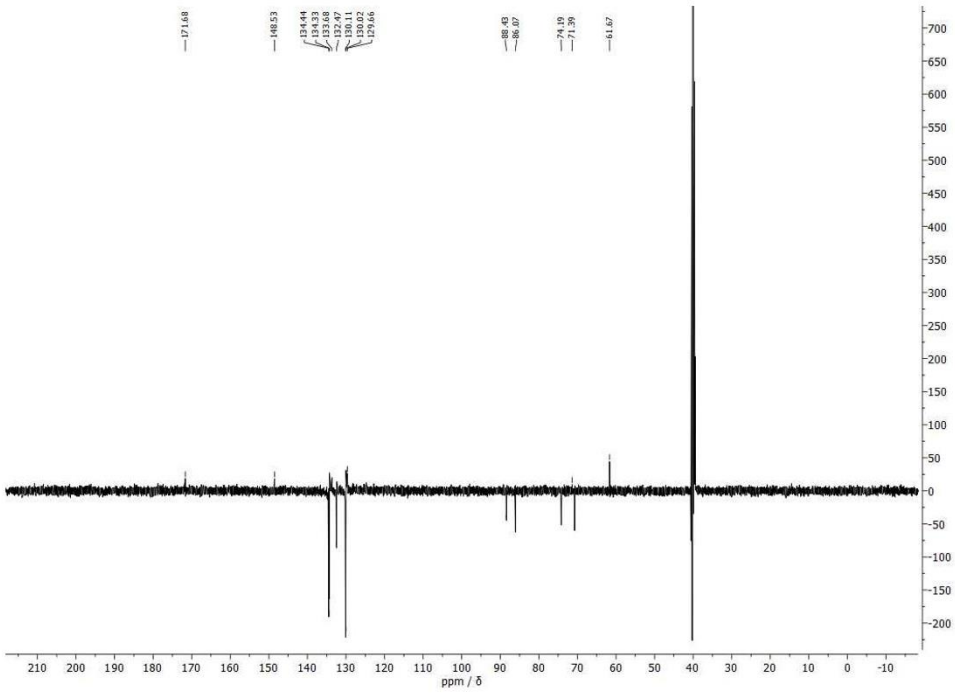

Figure S18. ^{1}H NMR spectrum of **5** in DMSO-d_6.

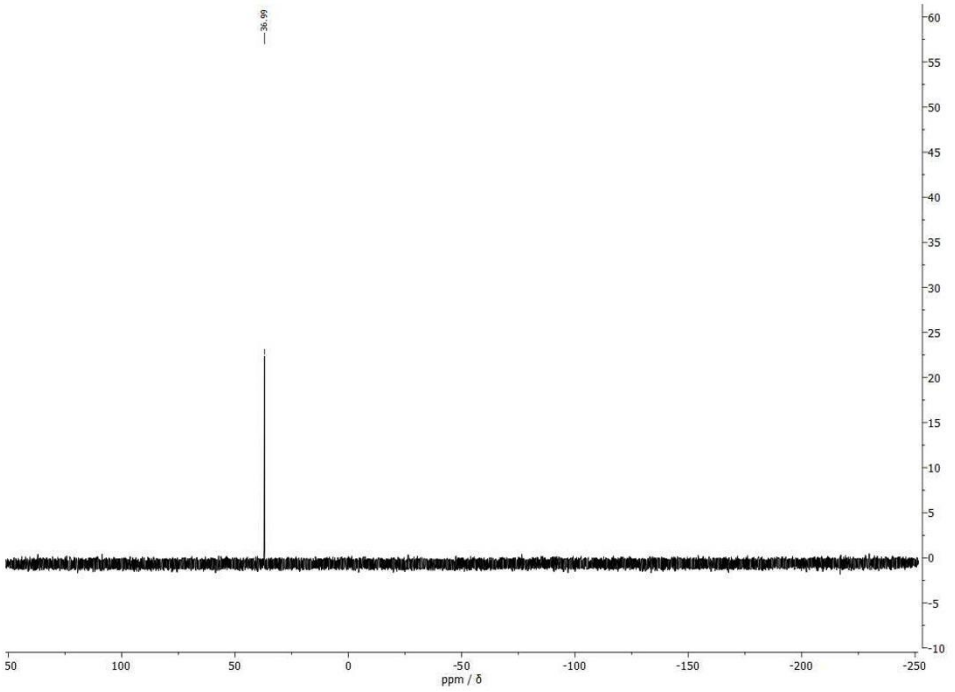

Figure S19. ^{31}P NMR spectrum of **5** in DMSO-d_6.

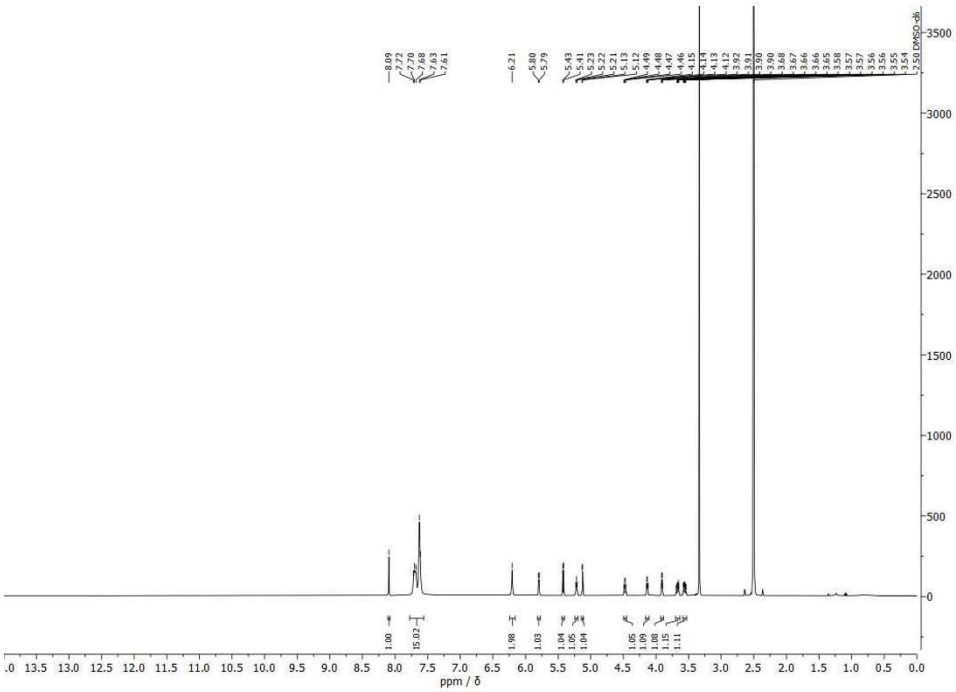

Figure S20. ^{1}H NMR spectrum of **6** in DMSO-d_6.

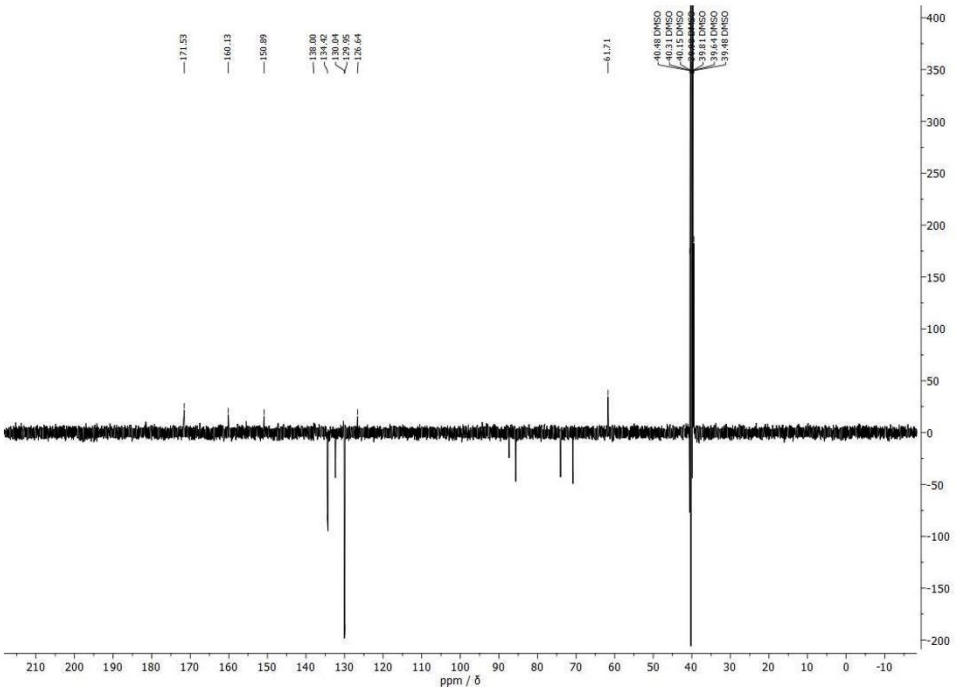

Figure S21. ^{1}H NMR spectrum of **6** in DMSO-d_6.

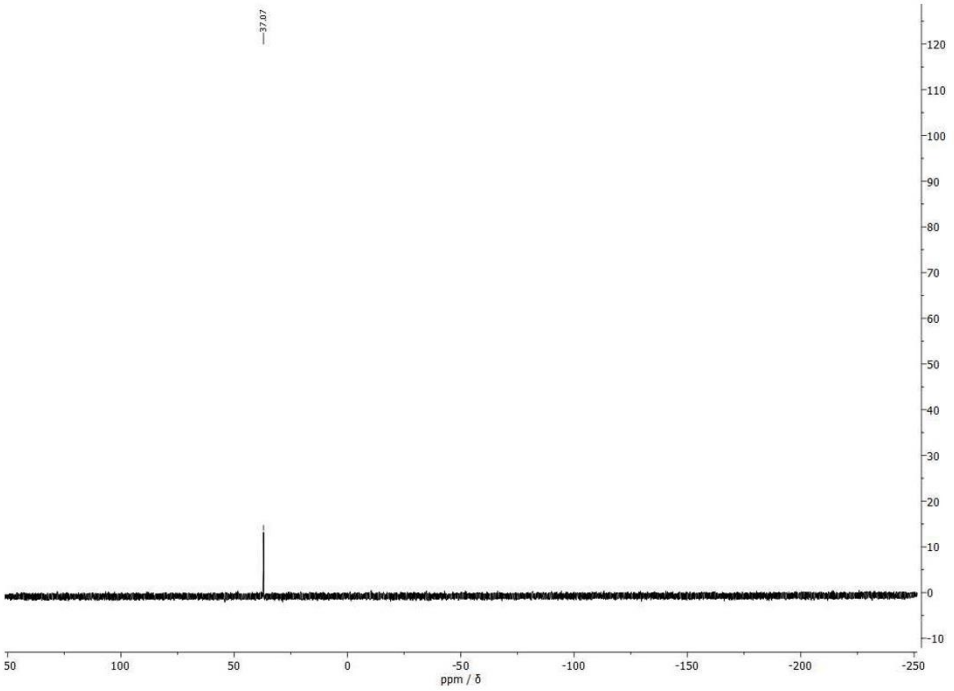

Figure S22. ^{31}P NMR spectrum of **6** in DMSO-d_6.

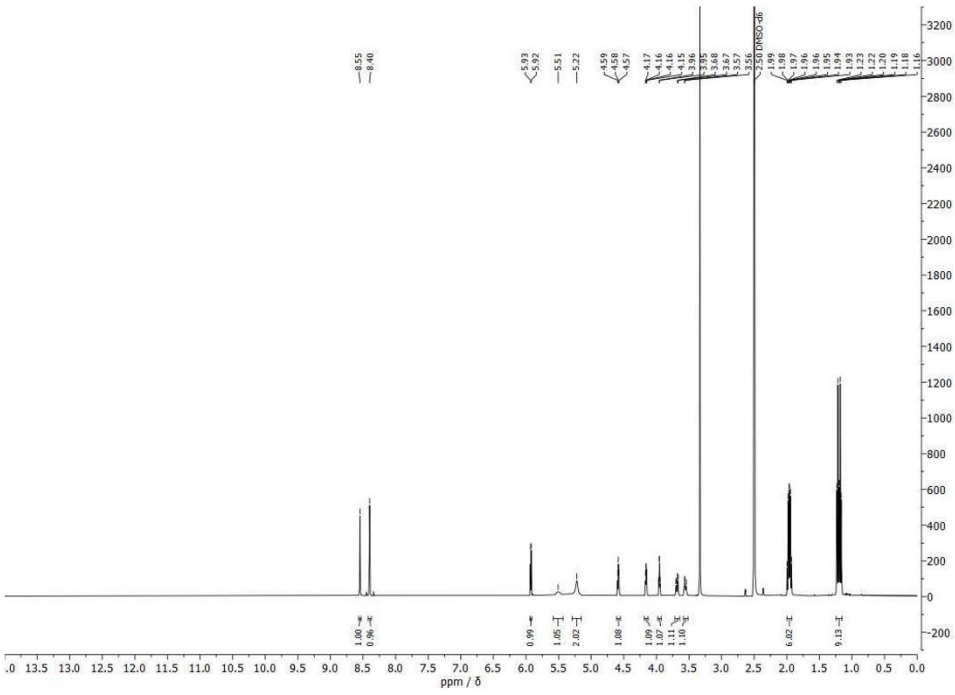

Figure S23. ^{1}H NMR spectrum of **7** in DMSO-d_6.

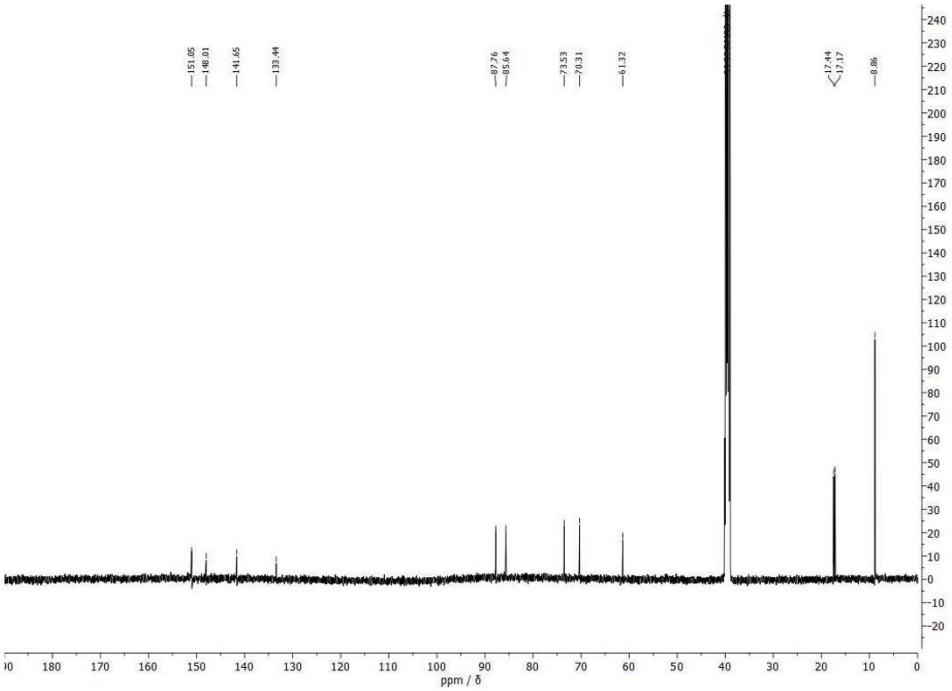

Figure S24. ^{13}C NMR spectrum of **7** in DMSO-d_6.

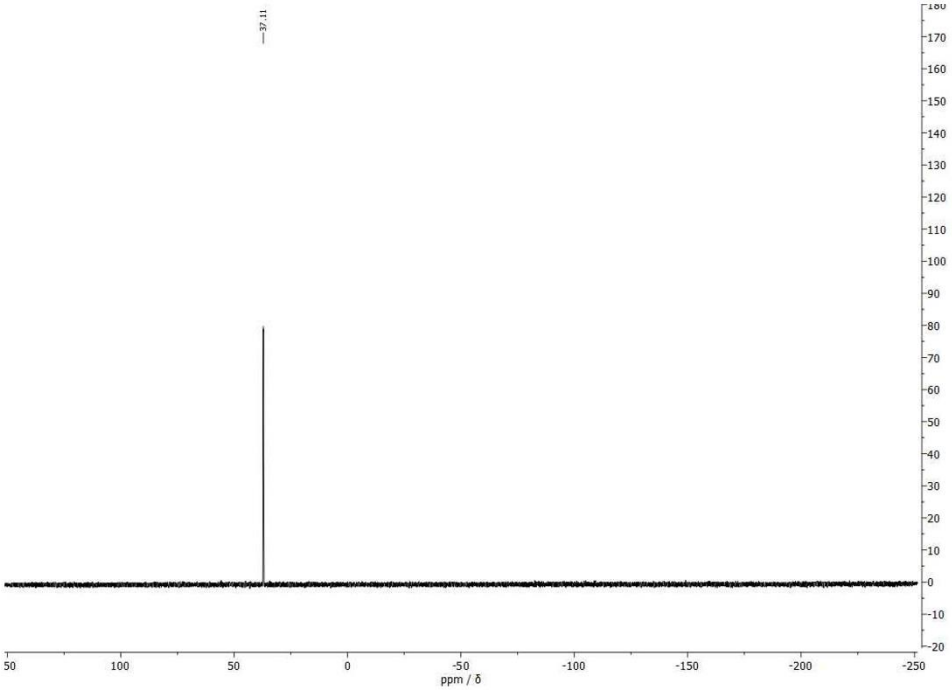

Figure S25. ^{31}H NMR spectrum of **7** in DMSO-d_6.

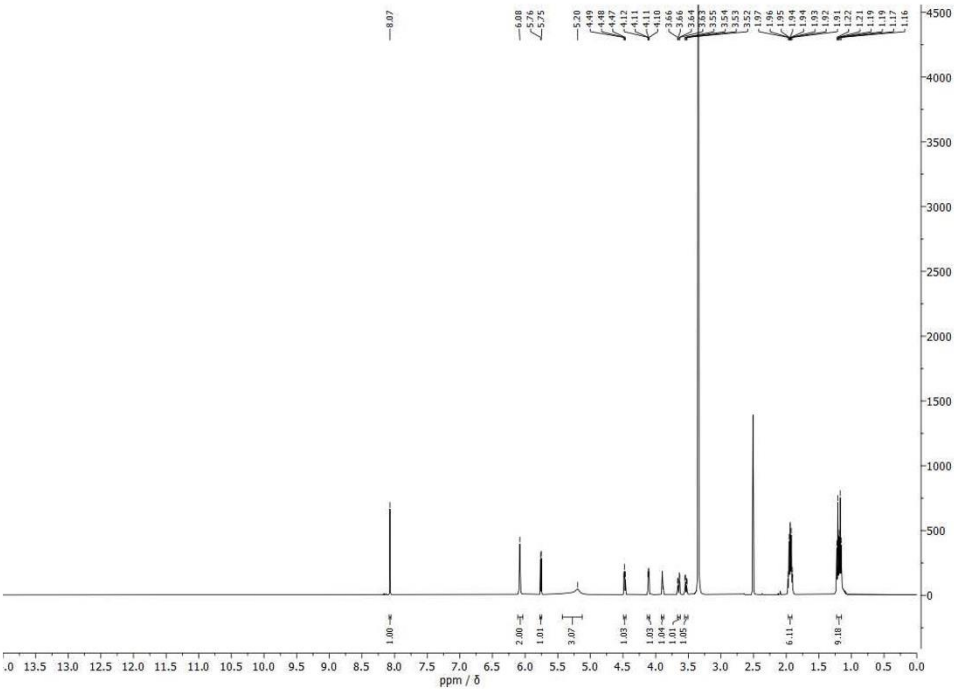

Figure S26. ^{1}H NMR spectrum of **8** in DMSO-d_6.

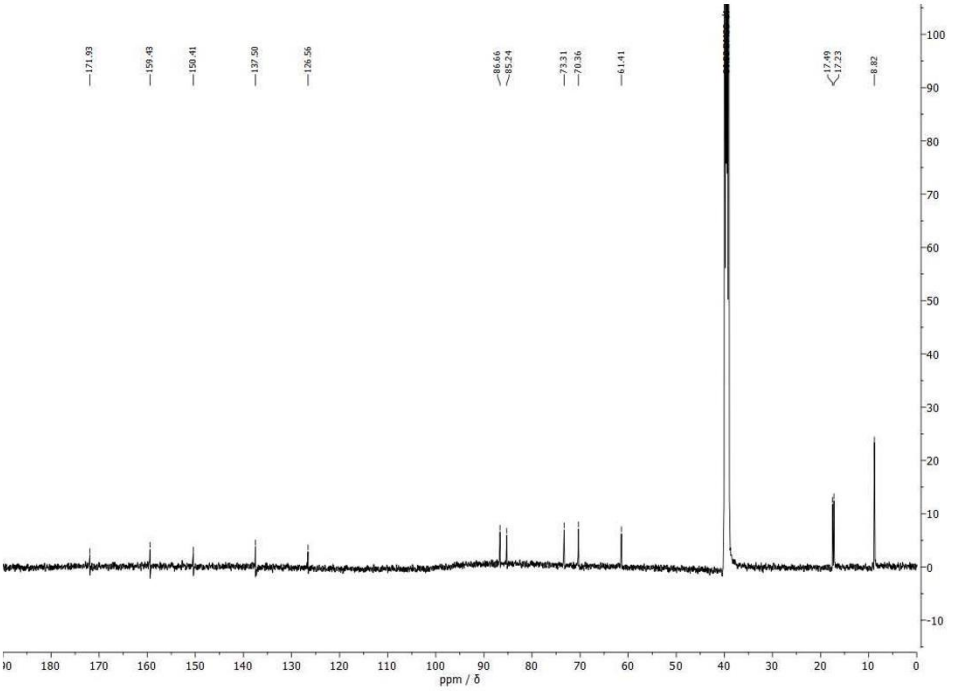

Figure S27. ^{13}C NMR spectrum of **8** in DMSO-d_6.

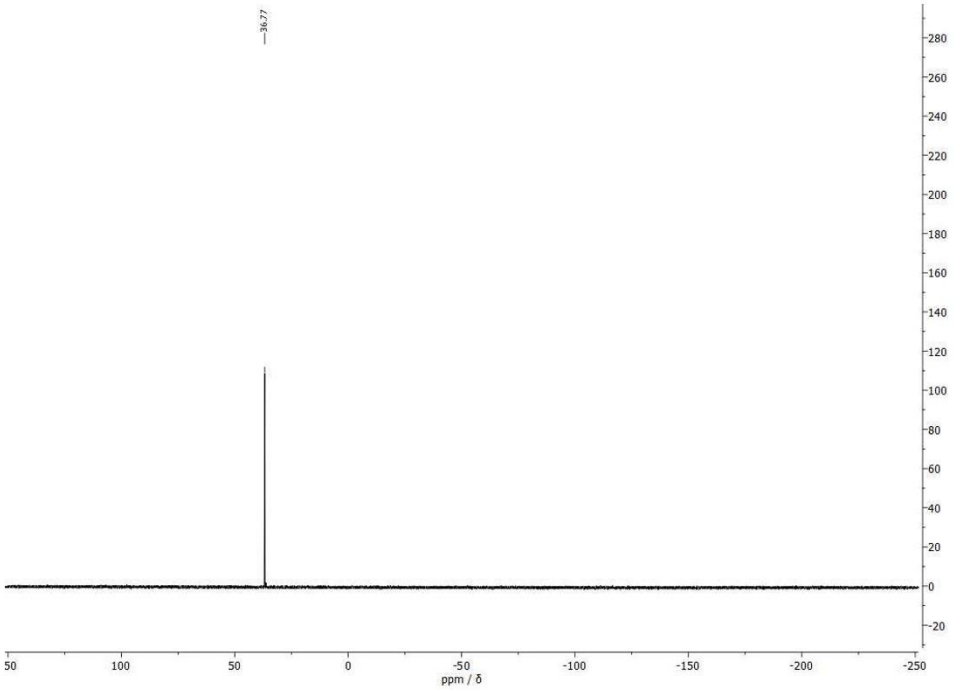

Figure S28. ^{31}P NMR spectrum of **8** in DMSO-d_6.

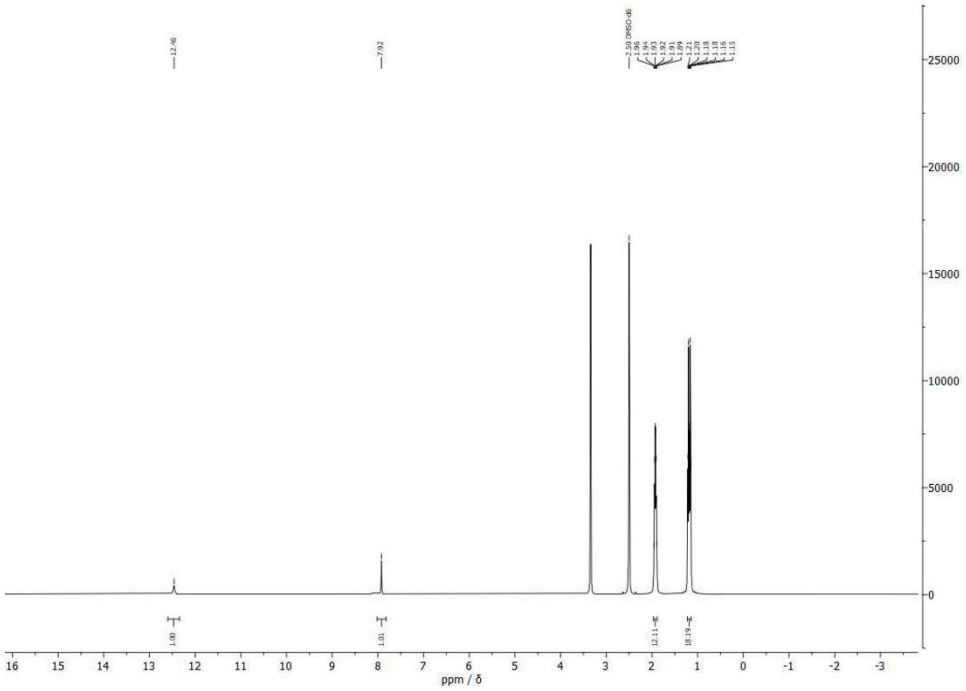

Figure S29. ^{1}H NMR spectrum of **9** in DMSO-d_6.

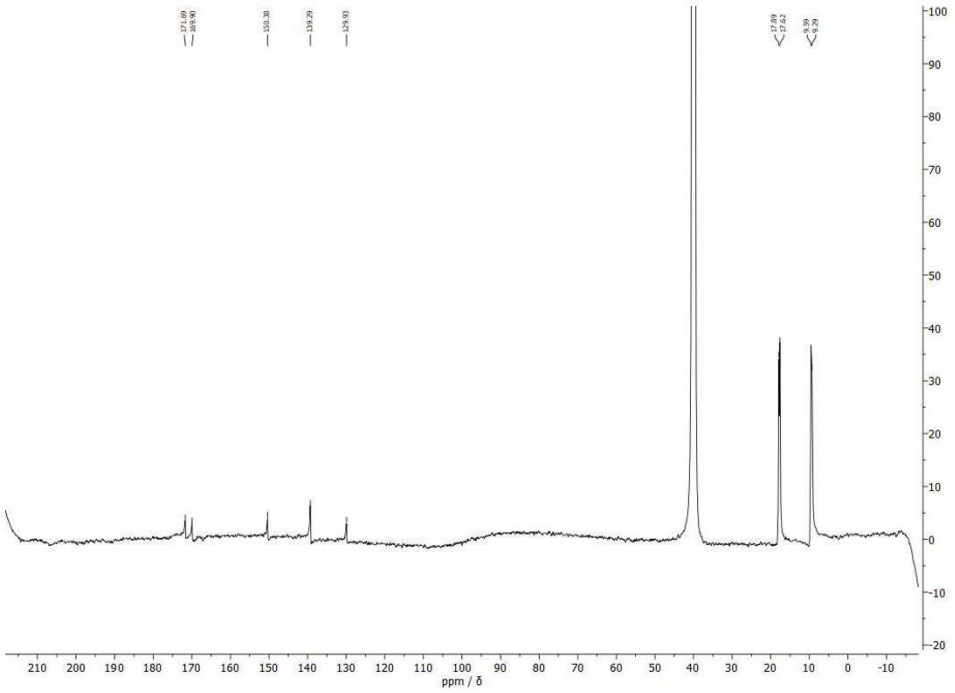

Figure S30. ^{13}C NMR spectrum of **9** in DMSO-d_6.

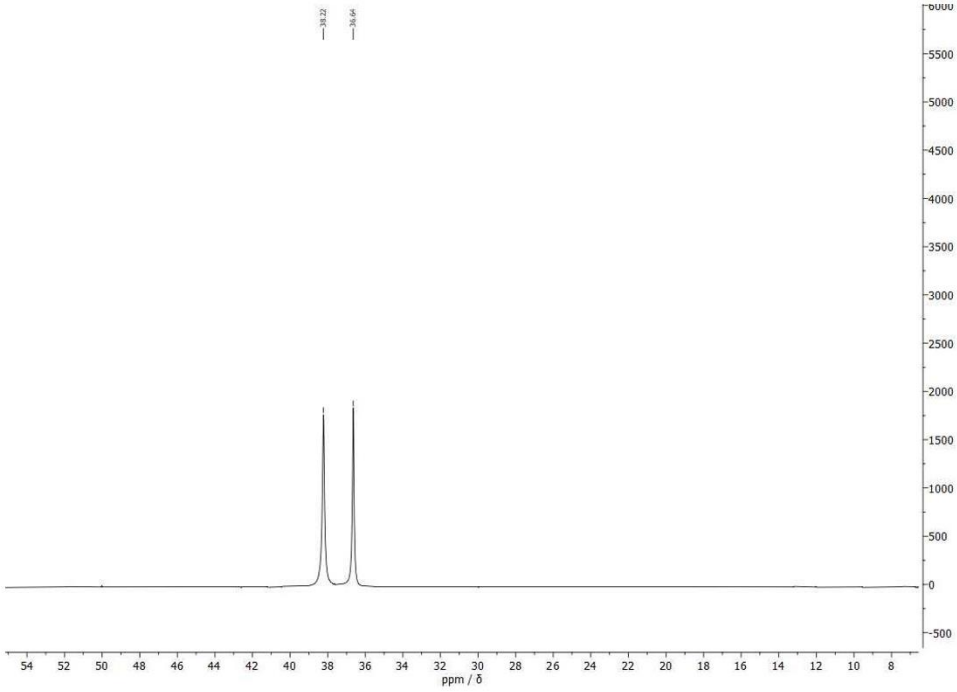

Figure S31. ^{31}P NMR spectrum of **9** in DMSO-d_6.

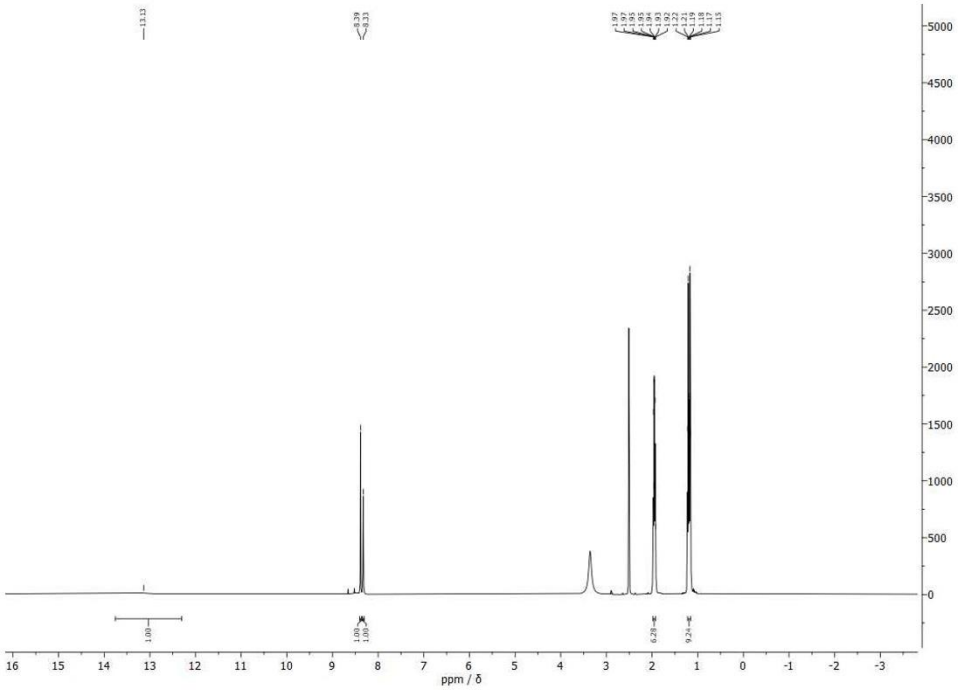

Figure S32. ^{1}H NMR spectrum of **10** in DMSO-d_6.

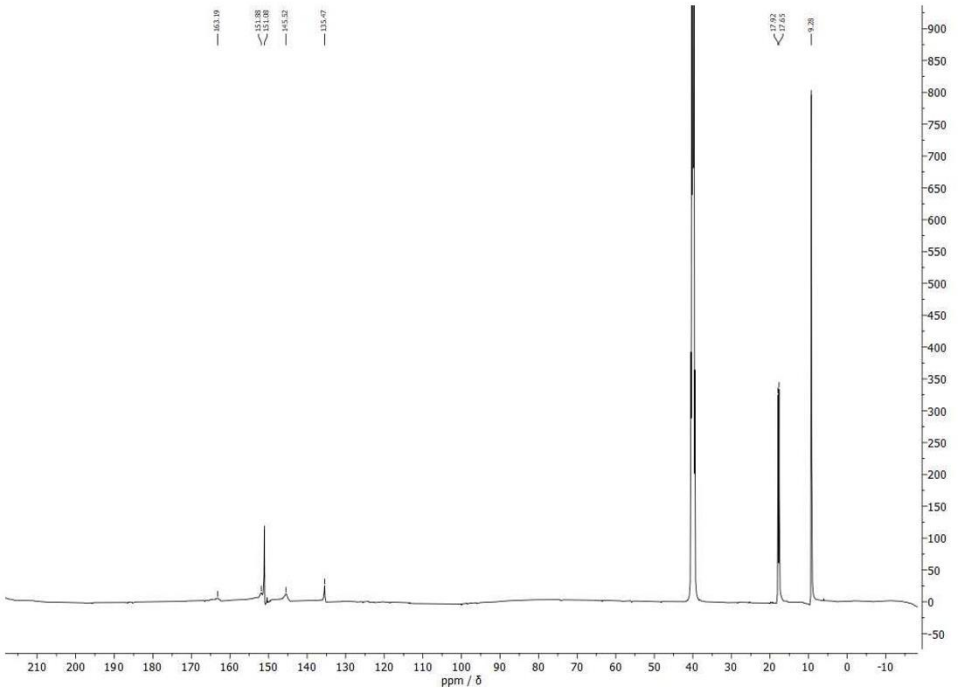

Figure S33. ^{13}C NMR spectrum of **10** in DMSO-d_6.

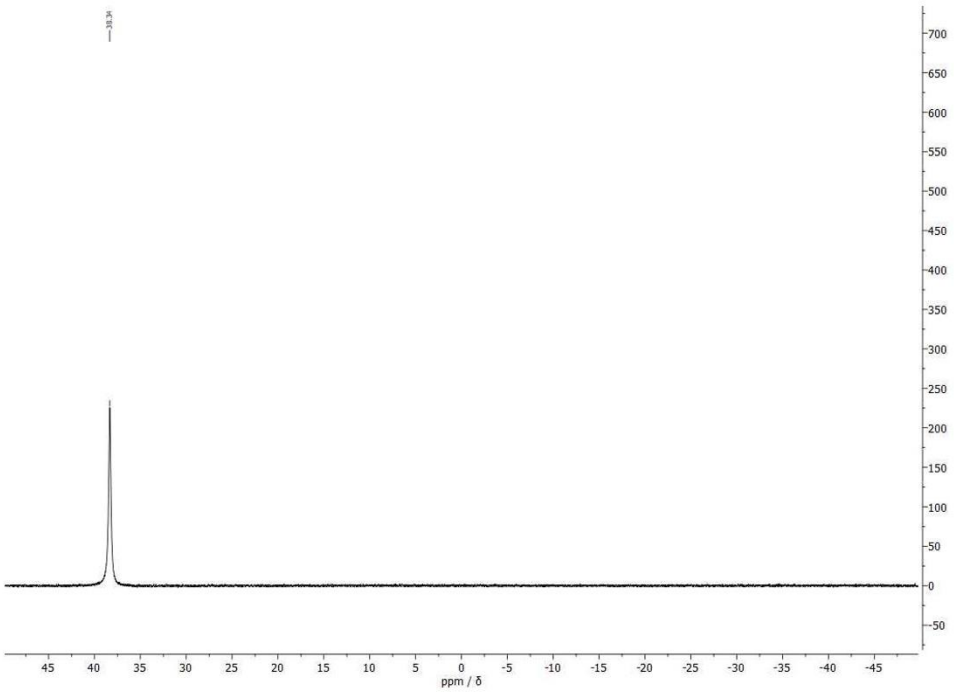

Figure S34. ^{31}P NMR spectrum of **10** in DMSO-d_6.

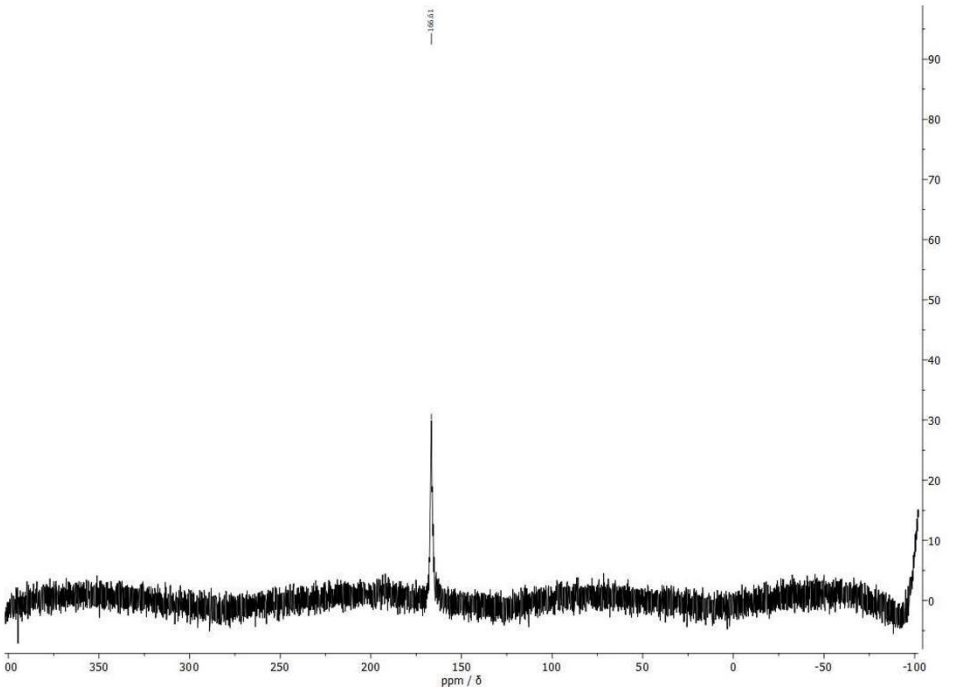

Figure S35. ^{77}Se NMR spectrum of **10** in DMSO-d_6.

Stability testing via ^{1}H, ^{31}P and ^{77}Se-NMR spectroscopy

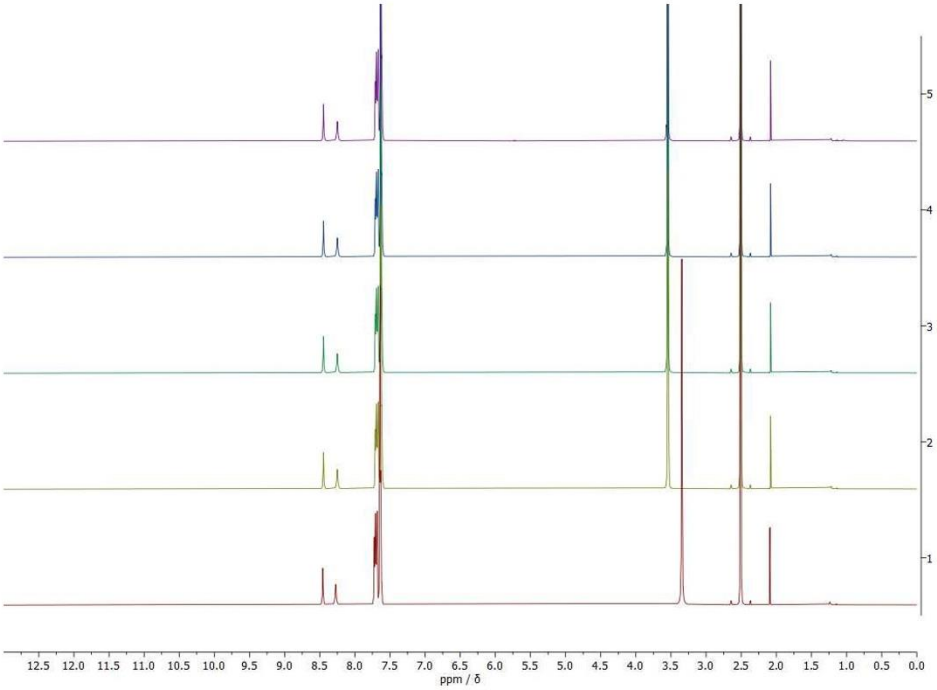

Figure S36. ^{1}H-NMR spectrum of **1** in DMSO-d_6. Addition of 5% D_2O after 0 h (yellow), 24 h (green), 48h (blue) and 72 h (purple).

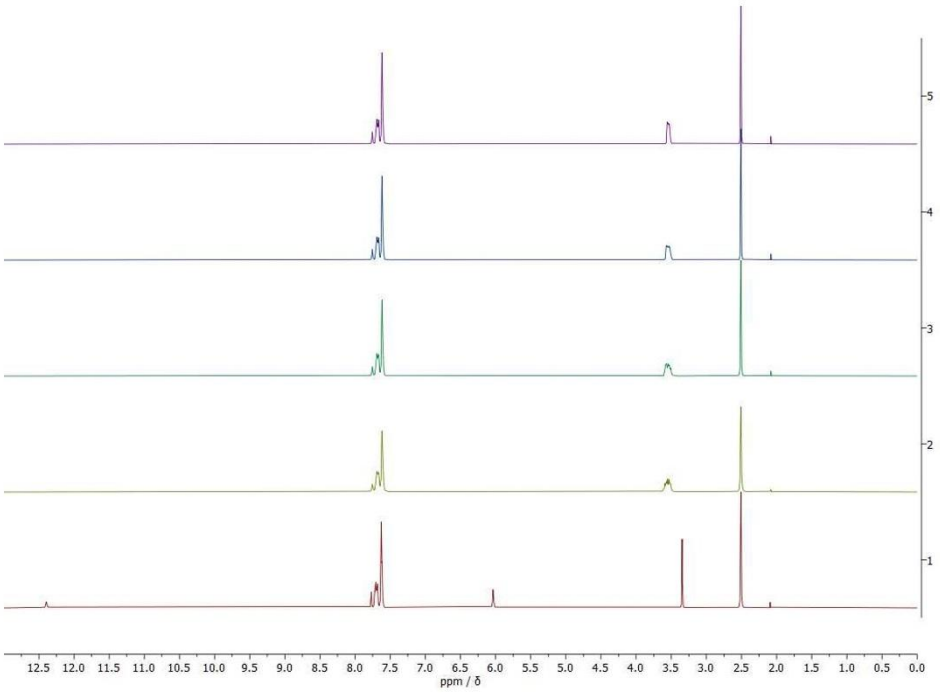

Figure S37. ^{1}H-NMR spectrum of **2** in DMSO-d_6. Addition of 5% D_2O after 0 h (yellow), 24 h (green), 48 h (blue) and 72 h (purple).

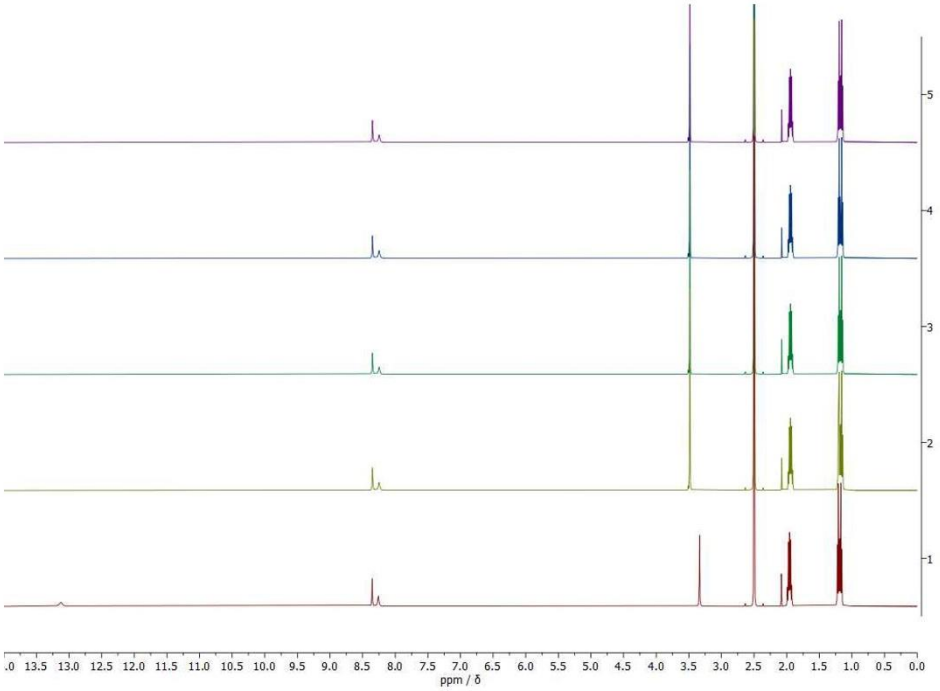

Figure S38. ^{1}H-NMR spectrum of **3** in DMSO-d_6. Addition of 5% D_2O after 0 h (yellow), 24 h (green), 48 h (blue) and 72 h (purple).

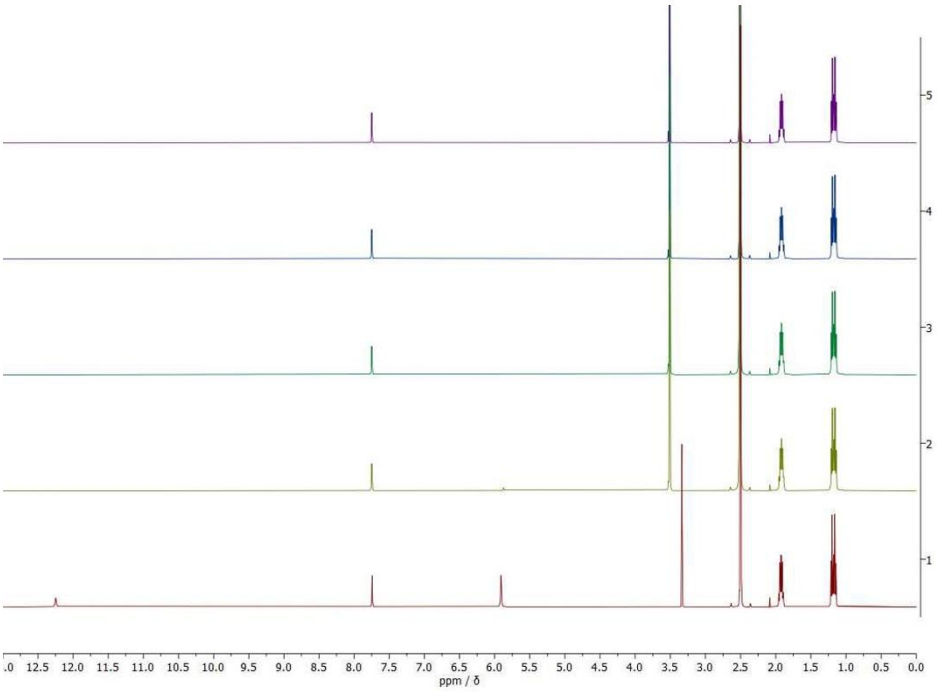

Figure S39. ^{1}H-NMR spectrum of **4** in DMSO-d_6. Addition of 5% D_2O after 0 h (yellow), 24 h (green), 48 h (blue) and 72 h (purple).

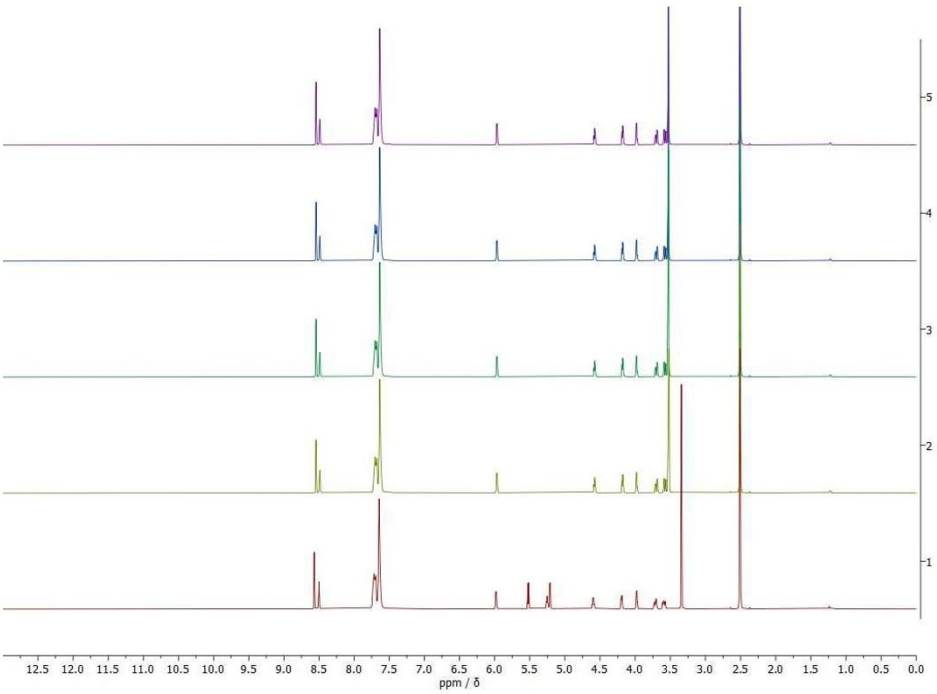

Figure S40. ^{1}H-NMR spectrum of **5** in DMSO-d_6. Addition of 5% D_2O after 0 h (yellow), 24 h (green), 48 h (blue) and 72 h (purple).

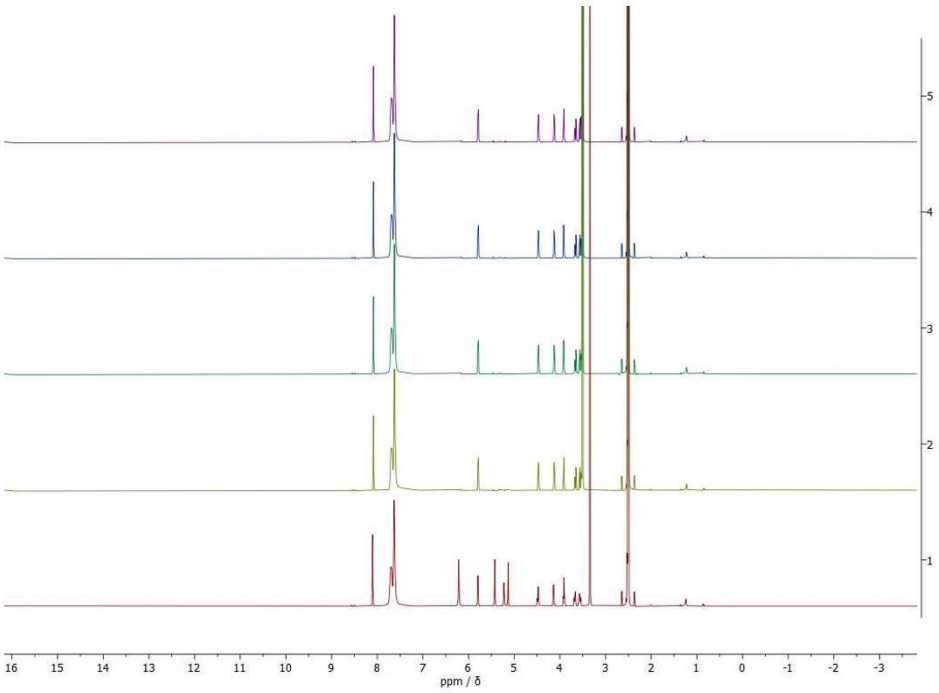

Figure S41. ^{1}H-NMR spectrum of **6** in DMSO-d_6. Addition of 5% D_2O after 0 h (yellow), 24 h (green), 48 h (blue) and 72 h (purple).

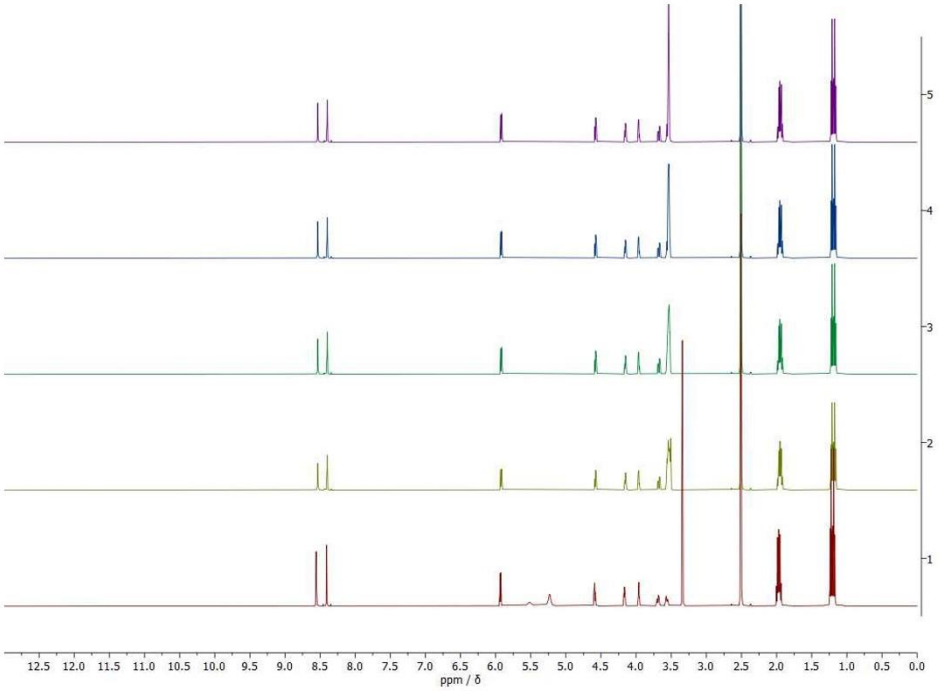

Figure S42. ^{1}H-NMR spectrum of **7** in DMSO-d_6. Addition of 5% D_2O after 0 h (yellow), 24 h (green), 48 h (blue) and 72 h (purple).

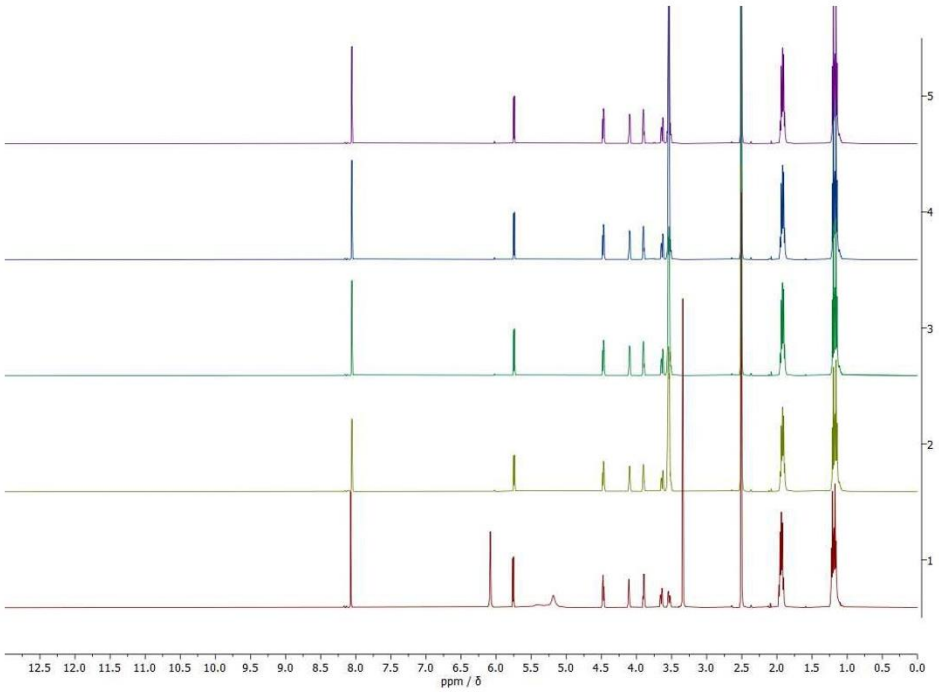

Figure S43. ^{1}H-NMR spectrum of **8** in DMSO-d_6. Addition of 5% D_2O after 0 h (yellow), 24 h (green), 48 h (blue) and 72 h (purple).

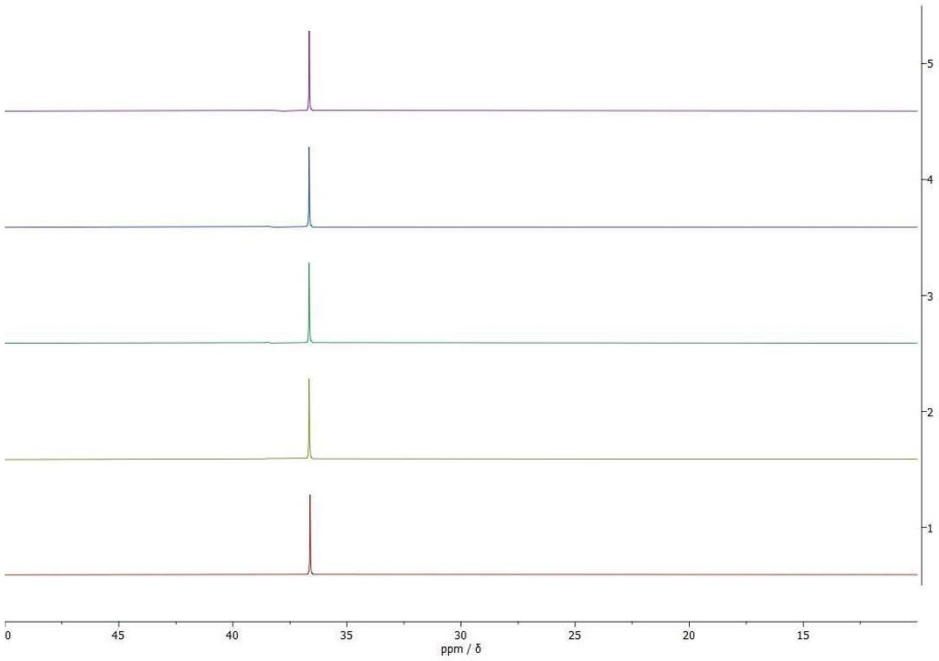

Figure S44. ^{31}P-NMR spectrum of **4** in DMSO-d_6. Addition of 5% D_2O after 0 h (yellow), 24 h (green), 48 h (blue) and 72 h (purple).

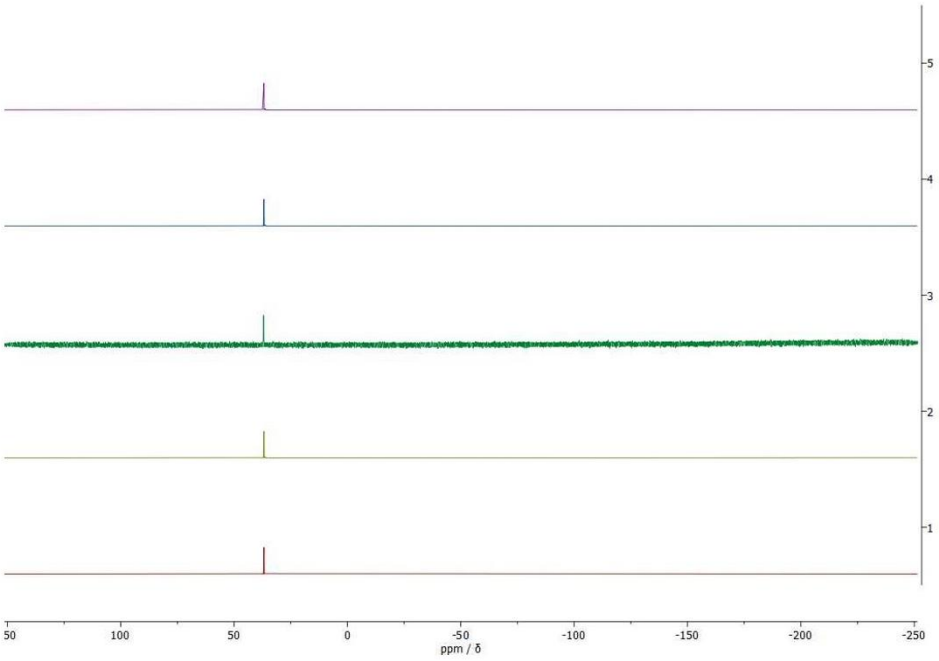

Figure S45. ^{31}P-NMR spectrum of **7** in DMSO-d_6. Addition of 5% D_2O after 0 h (yellow), 24 h (green), 48 h (blue) and 72 h (purple).

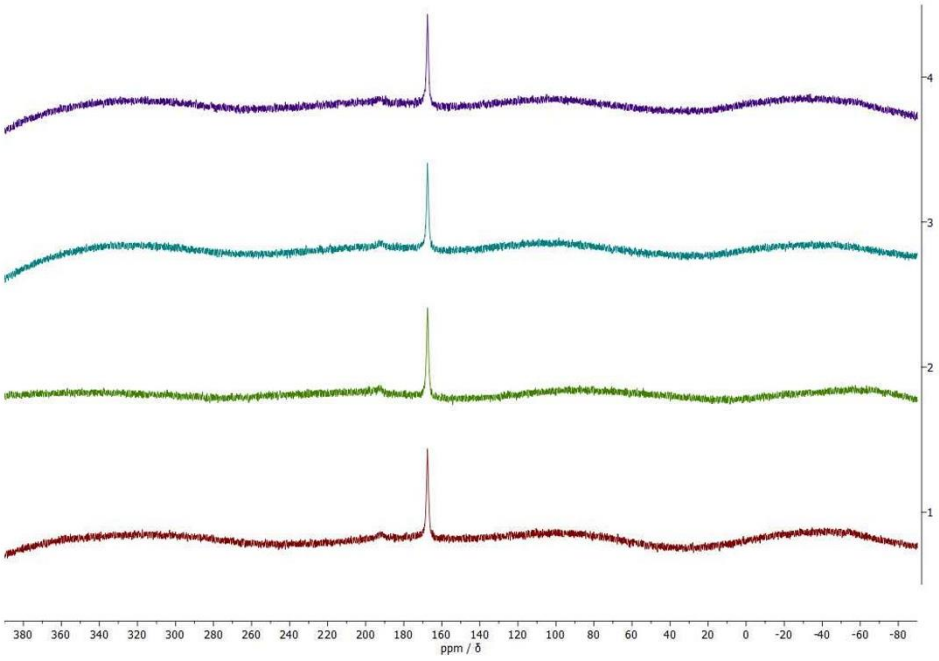

Figure S46. ^{77}Se-NMR spectrum of **10** in DMSO-d_6 + 5% D_2O after 0 h (red), 24 h (green), 48 h (blue) and 72 h (purple).

Stability testing via UV/Vis spectroscopy

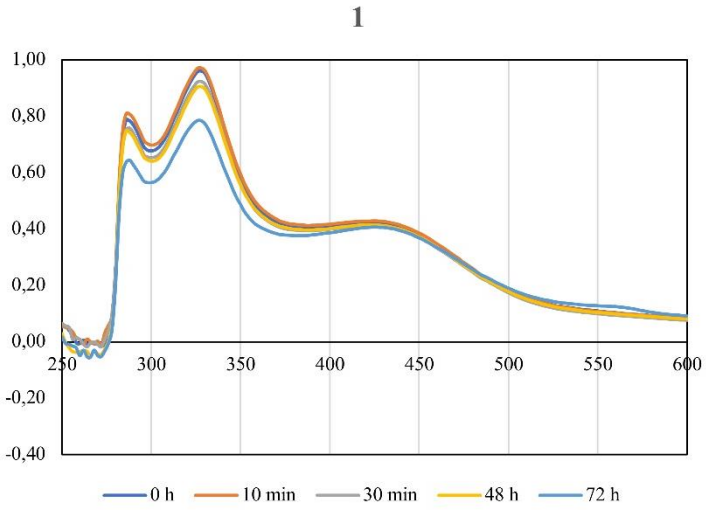

Figure S 47. UV/Vis spectra of complex **1** in EMEM with subtracted background over time.

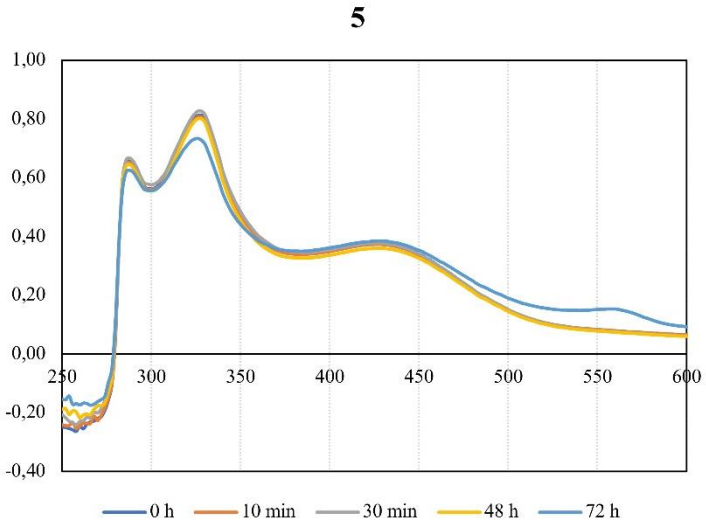

Figure S 48. UV/Vis spectra of complex **5** in EMEM with subtracted background over time.

HPLC Chromatograms

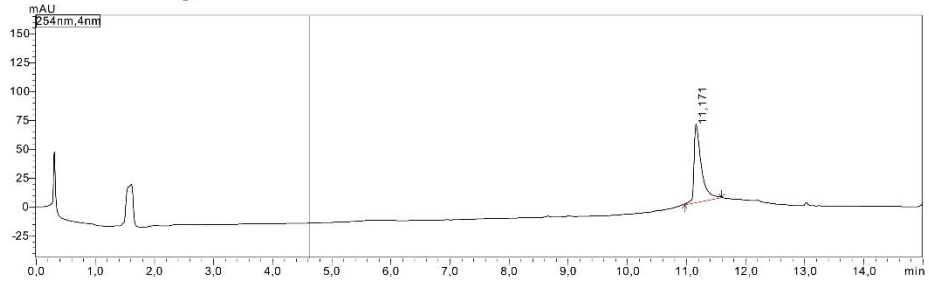

Figure S49. Chromatogram of **1**. Method: 10% → 97% MeCN in H_2O + 0.1% HCOOH, flow: 1.0 ml/min.

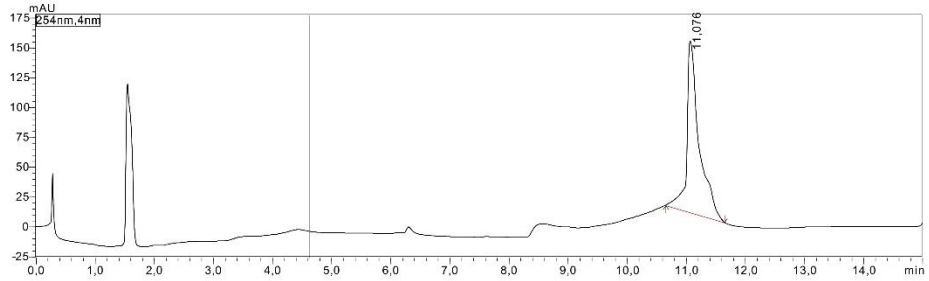

Figure S50. Chromatogram of **2**. Method: 10% → 97% MeCN in H_2O + 0.1% HCOOH, flow: 1.0 ml/min.

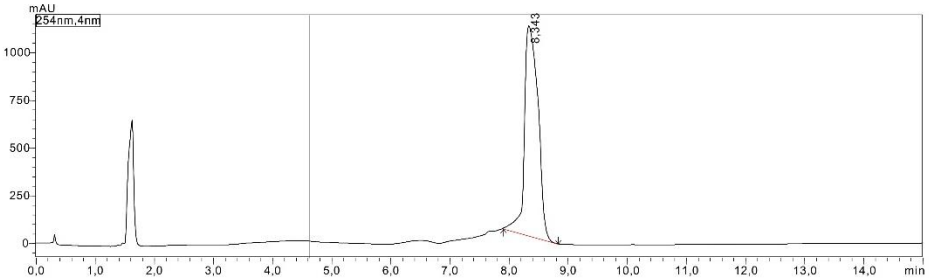

Figure S51. Chromatogram of **3**. Method: 10% → 97% MeCN in H_2O + 0.1% HCOOH, flow: 1.0 ml/min.

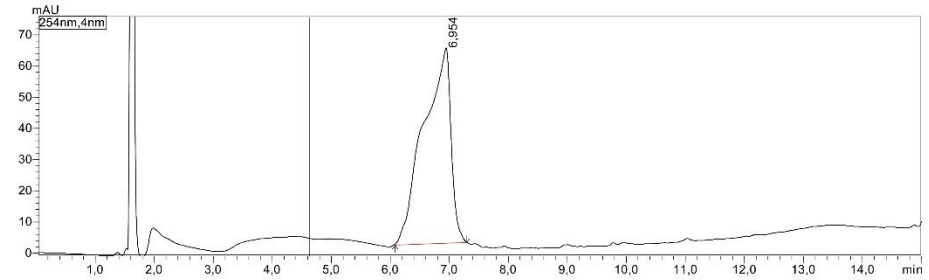

Figure S52. Chromatogram of **4**. Method: 10% → 97% MeCN in H_2O + 0.1% HCOOH, flow: 1.0 ml/min.

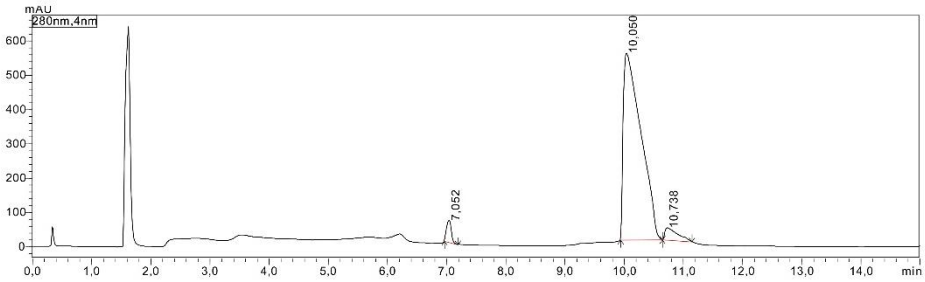

Figure S53. Chromatogram of **5**. Method: 10% → 97% MeCN in H_2O + 0.1% HCOOH, flow: 1.0 ml/min.

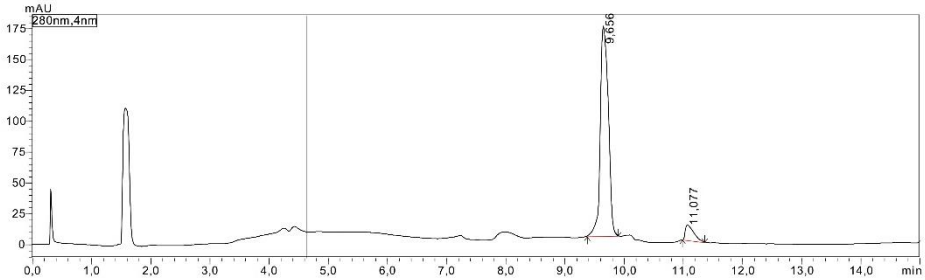

Figure S54. Chromatogram of c **6**. Method: 10% → 97% MeCN in H_2O + 0.1% HCOOH, flow: 1.0 ml/min.

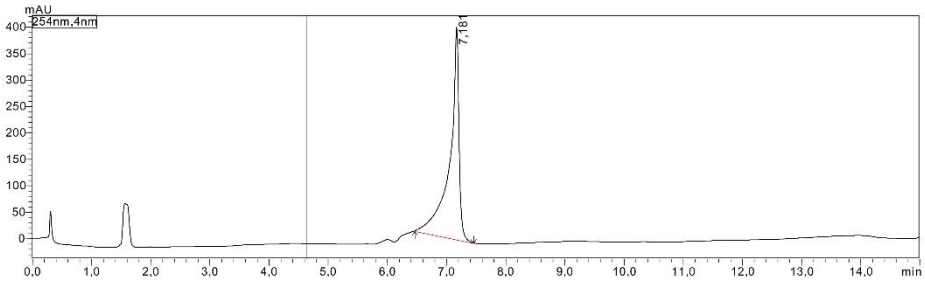

Figure S55. Chromatogram of **7**. Method: 10% → 97% MeCN in H_2O + 0.1% HCOOH, flow: 1.0 ml/min.

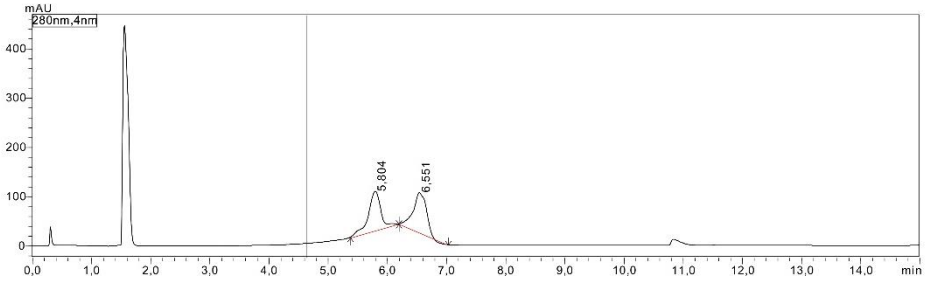

Figure S56. Chromatogram of **8**. Method: 10% → 97% MeCN in H_2O + 0.1% HCOOH, flow: 1.0 ml/min.

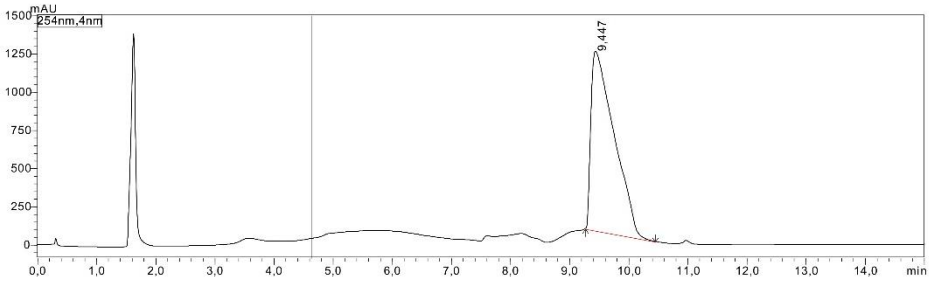

Figure S57. Chromatogram of complex **9**. Method: 10% → 97% MeCN in H_2O + 0.1% HCOOH, flow: 1.0 ml/min.

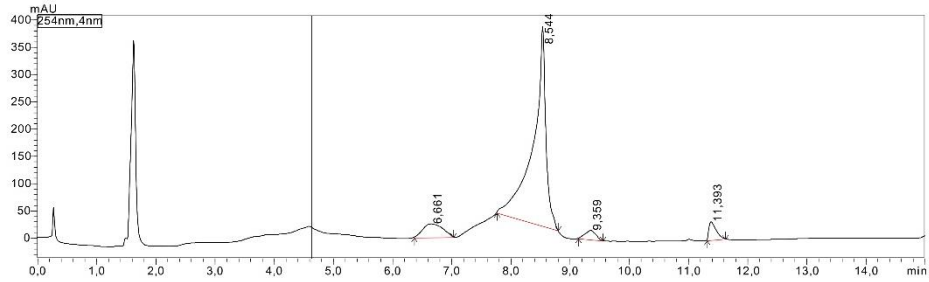

Figure S58. Chromatogram of complex **10**. Method: 10% → 97% MeCN in H_2O + 0.1% HCOOH, flow: 1.0 ml/min.

5.5 Publikation V mit Darstellung des Eigenanteils

Publikation V entstand unter Mitarbeit von Dr. B. Biersack Mitarbeiter des Arbeitskreises Organische Chemie I der Universität Bayreuth unter der Leitung von Prof. Dr. R. Schobert sowie durch Kooperation mit den Mitarbeitern A. Dittmer und B. Nitzsche des Instituts für Physiologie der Charité-Universitätsmedizin Berlin unter der Leitung von Prof. Dr. M. Höpfner. Weiter trugen G. Ter-Avetisyan und M. Fähling vom Institut für vegetative Physiology der Charité-Universitätsmedizin Berlin sowie A. Klefenz und L. Kaps vom Institut für translationale Immunologie der Universitätsmedizin der Johannes-Gutenberg-Universität Mainz zur Entstehung der Publikation bei.

5.5.1 Eigenanteil an Publikation V

Die Publikation wurde im ***International Journal of Oncology*** veröffentlicht, unter dem Titel

„Chimeric HDAC and the cytoskeleton inhibitor broxbam as a novel therapeutic strategy for liver cancer“

von den Autoren

Sofia I. Bär, Alexandra Dittmer, Bianca Nitzsche, Gohar Ter-Avetisyan, Michael Fähling Adrian Klefenz, Leonhard Kaps, Bernhard Biersack, Rainer Schobert und Michael Höpfner

Eigenanteil:	Konzeption, Durchführung, Auswertung und graphischer Darstellung des Zebrafisch Angiogenese Assays. Auswertung, grafische Darstellung und Statistik der iCELLigence Messungen, des LDH Assays, der MMP und Caspase 3 Aktivitäts Messungen sowie der HDAC und HDAC 6 Aktivitäten. Zudem; Verfassen des Manuskripts einschließlich der Diskussion und Interpretation der Ergebnisse und Revision des Manuskripts.
Alexandra Dittmer:	Durchführung des Kristallviolett-Assays, der iCELLigence Messungen, des LDH Assays, Western Blotting, der RT-qPCR, der Apoptose Nachweise, der Immuofluoreszenz Färbung und des *Scratch Wound Healing* Assays.
Gohar Ter-Avetisyan:	Durchführung der siRNA Versuche, Western Blotting und RT-qPCR.
Michael Fähling:	Durchführung, statistische Auswertung und grafische Darstellung der Western Blotting und RT-qPCR Ergebnisse.
Adrian Klefenz und Leonhard Kaps:	Durchführung des Kristallviolett- und des LDH-Assays.
Bernhard Biersack:	Broxbam Synthese und Korrektur des Manuskripts.

Bianca Nitzsche, Michael Höpfner und Rainer Schobert:	Überarbeitung und Korrektur des Manuskripts, Manuskripts einschließlich der Diskussion und Interpretation der Ergebnisse und Revision des Manuskripts

5.5.2 Publikation V

Chimeric HDAC and the cytoskeleton inhibitor broxbam as a novel therapeutic strategy for liver cancer

Sofia I. Bär[a], Alexandra Dittmer[b], Bianca Nitzsche[b,*], Gohar Ter-Avetisyan[c], Michael Fähling[c], Adrian Klefenz[d], Leonhard Kaps[d], Bernhard Biersack[a], Rainer Schobert[a] und Michael Höpfner[b]

[a] Organic Chemistry Laboratory, University of Bayreuth, Universitaetsstrasse 30, 95440 Bayreuth, Germany

[b] Physiology, Charité-Universitätsmedizin Berlin, Corporate member of Freie Universität Berlin, Humboldt-Universität zu Berlin and Berlin, Institute of Health, 10117 Berlin, Germany

[c] Vegetative Physiology, Charité-Universitätsmedizin Berlin, Corporate member of Freie Universität Berlin, Humboldt-Universität zu Berlin and Berlin, Institute of Health, 10117 Berlin, Germany

[d] Institute of Translational Immunology, University Medical Center of the Johannes Gutenberg University, D-55131 Mainz, Germany

*E-mail: bianca.nitzsche@charite.de

Int. J. Oncol., **2022**, 60, 73

https://doi.org/10.3892/ijo.2022.5363

INTERNATIONAL JOURNAL OF ONCOLOGY 60: 73, 2022

Chimeric HDAC and the cytoskeleton inhibitor broxbam as a novel therapeutic strategy for liver cancer

SOFIA ISOLDE BÄR[1], ALEXANDRA DITTMER[2], BIANCA NITZSCHE[2], GOHAR TER-AVETISYAN[3], MICHAEL FÄHLING[3], ADRIAN KLEFENZ[4], LEONARD KAPS[4], BERNHARD BIERSACK[1], RAINER SCHOBERT[1] and MICHAEL HÖPFNER[2]

[1]Organic Chemistry Laboratory, University of Bayreuth, D-95447 Bayreuth;
Institutes of [2]Physiology and [3]Vegetative Physiology, Charité-Universitätsmedizin Berlin,
Corporate member of Freie Universität Berlin, Humboldt-Universität zu Berlin and Berlin
Institute of Health, D-10117 Berlin; [4]Institute of Translational Immunology,
University Medical Center of the Johannes Gutenberg University, D-55131 Mainz, Germany

Received September 7, 2021; Accepted February 11, 2022

DOI: 10.3892/ijo.2022.5363

Abstract. Broxbam, also known as *N*-hydroxy-4-{1-methoxy-4-[4'-(3'-bromo-4',5'-dimethoxyphenyl)-oxazol-5'-yl]-2-phenoxy} butanamide, is a novel chimeric inhibitor that contains two distinct pharmacophores in its molecular structure. It has been previously demonstrated to inhibit the activity of histone deacetylases (HDAC) and tubulin polymerisation, two critical components required for cancer growth and survival. In the present study, the potential suitability of broxbam for the treatment of liver cancer was investigated. The effects of broxbam on cell proliferation and apoptosis, in addition to the underlying molecular mechanism of action, were first investigated in primary liver cancer cell lines Huh7, HepG2, TFK1 and EGI1. Real-time proliferation measurements made using the iCELLigence system and viable cell number counting following crystal violet staining) revealed that broxbam time- and dose-dependently reduced the proliferation of liver cancer cell lines with IC_{50} values <1 μM. In addition, a significant inhibition of the growth of hepatoblastoma microtumours on the chorioallantoic membranes (CAM) of fertilised chicken eggs by broxbam was observed according to results from the CAM assay, suggesting antineoplastic potency *in vivo*. Broxbam also exerted apoptotic effects through p53- and mitochondria-driven caspase-3 activation in Huh7 and HepG2 cells according to data from western blotting (p53 and phosphorylated p53), mitochondrial membrane potential measurements (JC-1 assay) and fluorometric capsase-3 measurements. Notably, no contribution of unspecific cytotoxic effects mediated by broxbam were observed from LDH-release measurements. HDAC1, -2, -4 and -6 expression was measured by western blotting and the HDAC inhibitory potency of broxbam was next evaluated using subtype-specific HDAC enzymatic assays, which revealed a largely pan-HDAC inhibitory activity with the most potent inhibition observed on HDAC6. Silencing HDAC6 expression in Huh7 cells led to a drop in the expression of the proliferation markers Ki-67 and E2F3, suggesting that HDAC6 inhibition by broxbam may serve a predominant role in their antiproliferative effects on liver cancer cells. Immunofluorescence staining of cytoskeletal proteins (α-tubulin & actin) of broxbam-treated HepG2 cells revealed a pronounced inhibition of tubulin polymerisation, which was accompanied by reduced cell migration as determined by wound healing scratch assays. Finally, data from zebrafish angiogenesis assays revealed marked antiangiogenic effects of broxbam *in vivo*, as shown by the suppression of subintestinal vein growth in zebrafish embryos. To conclude, the pleiotropic anticancer activities of this novel chimeric HDAC- and tubulin inhibitor broxbam suggest that this compound is a promising candidate for liver cancer treatment, which warrants further pre-clinical and clinical evaluation.

Correspondence to: Dr Bianca Nitzsche, Institute of Physiology, Charité-Universitätsmedizin Berlin, Corporate member of Freie Universität Berlin, Humboldt-Universität zu Berlin and Berlin Institute of Health, 1 Charitéplatz, D-10117 Berlin, Germany
E-mail: bianca.nitzsche@charite.de

Abbreviations: CA-4, combretastatin A-4; CAM, chorioallantoic membrane; CCC, cholangiocellular carcinoma; GLUT2, glucose transporter 2; HCC, hepatocellular carcinoma; HDAC, histone deacetylase; HDACi, histone deacetylase inhibitor; IC_{50}, mean inhibitory concentration; LDH, lactate dehydrogenase; MMP, mitochondrial membrane potential; SIV, subintestinal veins

Key words: hepatocellular carcinoma, cholangiocellular carcinoma, chimeric histone deacetylase inhibitor, tubulin polymerisation inhibitor

Introduction

The 5-year survival rate of patients with liver cancer (20%) is among the lowest compared with other types of cancer (1). Hepatocellular carcinoma (HCC) and cholangiocellular carcinoma (CCC) are two of the most important types of

primary liver cancers, with HCC being the most common, which accounts for 70-90% of all types of liver cancer (2,3). By contrast, CCC accounts for ~10% of all liver malignancies (2,3). Although CCC is comparatively rare, they are highly aggressive and are typically characterised by poor 5-year survival rates, specifically 5-15% (2,3). The standard systemic therapeutic strategy for HCC is by using the multikinase inhibitor sorafenib, which remains unchanged over the last decade (4-7). However, adverse side effects, coupled with the increasing incidence of resistance, are posing significant therapeutic obstacles that needs to be overcome for the effective treatment of HCC (4-7). In addition, currently available treatment options for CCC are even more limited. At early stages surgical tumour resection is a curative option, but only palliative measures are available for advanced and metastatic CCC (8,9). Therefore, treatment possibilities remain limited, which induce severe side effects and only marginally increase the survival time (8,9). There is an urgent demand for novel treatment options for patients with advanced HCC or CCC.

One potential approach of tackling the therapeutic resistance and metabolic evasiveness of cancer cells is the development of 'chimeric inhibitors', which has been garnering interest over recent years (10,11). Using the advent of molecular hybridisation, two distinct drug pharmacophores can be merged into a single molecule, which can simultaneously attack different cellular and molecular targets (10,11). Due to their extensively researched structure-activity relationships, histone deacetylase inhibitors (HDACi) are at the centre of this chimeric drug approach. In recent years, chimeric agents featuring HDACi pharmacophores linked to either protein kinase inhibitors, modulators of the DNA structure or to moieties that can interfere with the cancer cell cytoskeleton, have been developed (11).

HDACs are amidohydrolases that serve a pivotal role in cellular chromatin remodelling (12). They have been previously implicated in the epigenetic regulation of cell metabolism, proliferation and differentiation of various solid cancers, such as urothelial, cervical, myeloma, ovarian and lung cancer, where they have already been tested in early-stage clinical trials (12,13). In several malignancies, including liver cancer, HDACs were found to be overexpressed, where their activity was also correspondingly enhanced (14). In turn, they stifle the expression of tumour suppressor genes, leading to uncontrolled cell division and insensitivity to cell repair mechanisms and suppression of apoptosis (14). Therefore, HDACi are regarded to be promising novel compounds for the therapy of a number of cancers, including liver cancer (14-16). In particular, vorinostat was the first HDACi to be clinically approved for the treatment of T-cell lymphoma (16-18).

Recently, combined treatment with the new HDACi resminostat and the established liver cancer drug sorafenib was reported to effectively counteract HCC growth and progression (19). Similarly, a synergistic inhibitory effect on the proliferation of HT-29 and HCT116 colon cancer cells has been reported for the combination of HDACi and microtubule disrupting agents (MDAs) (20). MDAs trigger the upregulation of p53 and enhance post-translational modifications on p53, such as phosphorylation and acetylation, in non-small lung cancer cells (21). In this regard, potentiation of apoptosis mediated by the combined treatment of the *o*-phenylenediamine-based HDACi MS-275 (entinostat) with the MDA taxol combretastatin (CA-4) was previously reported in MCF7 (breast cancer) and HCT (colon cancer) cell lines (22). Treatment with this drug combination led to a pronounced inhibition of tubulin polymerisation to impede neovascularisation and disrupt the tumour vasculature (23). These previous findings aforementioned therefore argue for the acceleration in the development of therapeutic agents that can simultaneously address ≥ one target. Drugs that can accomplish this by the means of several covalently-linked pharmacophores are called chimeric drugs (24). Recently, the chimeric inhibitor animacroxam, which induces both HDAC inhibition and cytoskeleton-interfering effects, has been shown to be particularly efficacious against testicular germ cell cancer (15).

Broxbam is a promising chimeric HDACi inhibitor. The pleiotropic effects of broxbam have been previously reported in the 518A2 melanoma cell line, where it was demonstrated to inhibit tubulin polymerisation and HDAC activity, disrupt the cytoskeleton and induce cell cycle arrest (20). Broxbam contains the structural hydroxamate motif of 1st generation HDACi that can also be found on vorinostat in addition to the trimethoxyphenyl motif commonly found on cytostatic MDAs, such as combretastatin A-4 (CA-4) (23,25). In particular, the oxazole bridge of the trimethoxyphenyl motif stabilizes the *cis*-configuration of the alkene (Fig. 1), which is essential for the attachment to the colchicine-binding site of tubulin heterodimers (26). It was recently shown that broxbam can exert antiproliferative effects in melanoma and colorectal cancer cell models (20). However, its potential suitability and efficacy against liver cancer remain poorly understood. Therefore, the present study aims to investigate the effects of broxbam on the physiology of liver cancer cells and the underlying molecular mechanism of action using both *in vivo* and *in vitro* models.

Materials and methods

Compounds. Broxbam was synthesized according to literature (20). In brief, Van Leusen reaction of the 3-bromo-4,5-dimethoxyphenyl toluenesulfonylmethyl isocyanide reagent with ethyl 4-(1-methoxy-4-formyl-2-phenoxy) butyrate led to the ester-functionalised oxazole intermediate, which was reacted with hydroxylamine to form the target compound broxbam. Stock solutions (20 μM) of broxbam and vorinostat (cat. no. V-8477; LC Laboratories), were prepared in DMSO (Thermo Fisher Scientific, Inc.) stored at -20˚C and diluted to the final concentration in fresh media before each experiment. In all experiments, the final DMSO concentration was <0.2%.

Cell culture. HepG2 (hepatoma; DSMZ no. ACC 180), Huh7 (hepatocellular carcinoma; RRID, CVCL_0336), TFK1 [cholangiocellular carcinoma; Deutsche Sammlung von Mikroorganismen und Zellkulturen (DMSZ) no. ACC 344] and EGI1 (cholangiocellular carcinoma; DSMZ no. ACC 385) cells, in addition to the non-transformed hepatocyte cell line non-transformed hepatocyte cell line AML12 (cat. no. CRL-2254) (27) were purchased from ATCC Company and stored for long time in liquid nitrogen in an in-house repository. Only cells in the early passages (<30 passages) were used

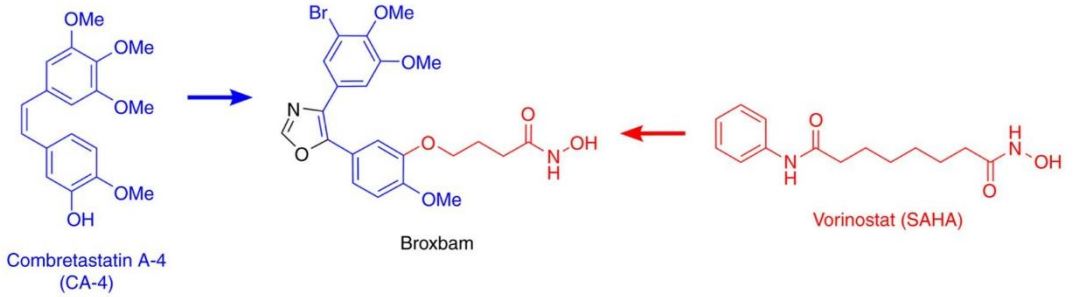

Figure 1. Molecular structures of Broxbam and vorinostat. Structures of the vascular disrupting agents combretastatin A-4 (CA-4), the histone deacetylase-inhibitor vorinostat (red) and the oxazole-bridged hybrid compound broxbam.

for the study. The liver cancer cell lines are representative for the established hepatocellular carcinoma, hepatoblastoma and cholangiocarcinoma cell models for the *in vitro* research of liver cancer (28-32). The murine non-transformed hepatocyte cell line AML-12 (33,34) was used instead of a non-transformed human hepatocyte cell model, which was not available for the present study. However, AML-12 cells represent a widely applied non-transformed hepatocyte cell model (33,34).

The cells were maintained in RPMI 1640 medium containing 10% FBS and 100 U/ml penicillin and streptomycin (all from Gibco, Thermo Fisher Scientific, Inc.) and cultured at 37˚C and 5% CO_2 in a humidified atmosphere unless stated otherwise. Cell lines were serially passaged after trypsinisation, using 0.05% trypsin/0.02% EDTA solution (Bio & SELL GmbH). Only mycoplasma-free cultures were used and potential contamination was routinely monitored. Glucose and lactate levels from the cell culture supernatants were measured using a blood gas analyser (ABL800 Flex; Radiometer GmbH).

Small-interfering (si)RNA transfection. For the siRNA-mediated knockdown of HDAC6, Huh7 cells were seeded into six-well plates and cultured until they reached 40-50% confluency. Cells were then transfected with siRNAs (75 nM; ON-TARGET plus SMART pool human HDAC6, cat. no. L-003499-00-0010 or ON-TARGET plus non-targeting control pool, cat. no. D-001810-10-05; PerkinElmer, Inc.; https://horizondiscovery.com/en/gene-modulation/knockdown/sirna/products/on-target-plus-sirna-reagents?nodeid=entrezgene-10013&catalognumber=L-003499-00-0010) using the transfection reagent DharmaFECT1 (cat. no. T-2005-01) according to the protocol provided by Dharmacon; PerkinElmer, Inc. In the present study, SMART pool siRNAs targeting human HDAC6 and the non-targeting control containing a mixture of four oligonucleotides were used. The target sequences for human HDAC6 are as follows: Sequence (Seq) 1, 5'-GGGAGGUUCUUGUGAGAUC-3'; Seq2, 5'-GGAGGGUCCUUAUCGUAGA-3'; Seq3, 5'-GCAGUUAAAUGAAUUCCAU-3' and Seq4, 5'-GUUCACAGCCUAGAAUAUA-3'. Non-targeting control sequences are as follows: Seq1, 5'-UGGUUUACAUGUCGACUAA-3'; Seq2, 5'-UGGUUUACAUGUUGUGUGA-3'; Seq3, 5'-UGGUUUACAUGUUUUCUGA-3' and Seq4, 5'-UGGUUUACAUGUUUUCCUA-3'. After 48 h of transfection, cells were harvested and analysed by western blotting and reverse-transcription-quantitative PCR (RT-qPCR).

Crystal violet assay. Changes in cell numbers associated with drug treatment were monitored using crystal violet staining as previously described (35). In total, 1,500-3,000 cells/well were first seeded into 96-well plates and allow to detach for 72 h at 37˚C, 5% CO_2 and 95% humidity. The cells were then treated with either broxbam or vorinostat in the following concentrations: 0.1, 0.2, 0.4, 0.8, 1.6, 3.2, 6.4 and 10.0 μM for 24, 48 and 72 h at 37˚C, 5% CO_2 and 95% humidity, fixed with 1% glutaraldehyde for 30 min at room temperature and stained with 0.1% crystal violet (Sigma-Aldrich; Merck KGaA) for 30 min at room temperature. Water rinsing was then performed to remove any unbound dye, before 0.2% Trition-X100 was added to solubilise the bound crystal violet and the absorbance at 570 nm was measured using a microplate reader (Dynex Technologies). The light absorbance was assumed in linear proportion to the number of cells.

Real-time inhibition of cell proliferation. The measurement of cell proliferation in real-time was performed as previously described (15). Briefly, HepG2, Huh7 ($1.0x10^4$ cells/well), TFK1 ($5x10^3$ cells/well) and EGI1 ($3x10^3$ cells/well) cells were seeded into in eight-well E-plates (ACEA Biosciences, Inc.) and maintained under normal cell culture conditions for 24 h. After attachment of the cells, they were treated with concentrations of broxbam (0.1, 0.25, 0.5 and 1.0 μM) for ≤70 h at 37˚C, 5% CO_2 and 95% humidity. An impedance-based iCELLigence system (RTCA Software Vs 2.1.0, ACEA Biosciences) was used to monitor the real-time proliferation of viable cells in the eight-well plates at 37˚C, 5% CO_2 and 95% humidity, every 15 min for 70 h. Cell proliferation was recorded as a unitless parameter called the 'cell index', which was defined as $(R_{tn}-R_{t0})/4.6$ Ohm, with R_{tn} representing the measured resistance at time point n and R_{t0} representing the background resistance measured at time point T_0

Lactate dehydrogenase (LDH) cytotoxicity assay. Cells were seeded into 96-well microtiter plates at a density of $8x10^3$ cells/well and treated with increasing concentrations (0.1, 0.3, 0.6, 1.5, 3.0 and 10.0 μM) of broxbam for 24 h at 37˚C, 5% CO_2 and 95% humidity. Cytoplasmic LDH release into the cell culture medium was measured using a colorimetric

assay kit (cat. no. 11644793001; Sigma-Aldrich; Merck KGaA) according to the manufacturers' protocols (36).

Induction of chorioallantoic membrane (CAM) tumours. In total $2x10^6$ HepG2 cells were resuspended in 10 μl RPMI medium containing 10% FBS and 100 U/ml penicillin and streptomycin (all from Gibco; Thermo Fisher Scientific, Inc.) and 10 μl Matrigel (BD Biosciences), before the cell suspension was applied into a silicone ring 5 mm in diameter onto the CAM of fertilised white Leghorn chicken eggs (*Gallus domesticus*) at day 8 of their embryonic development. Fertilized eggs were obtained from Valo Biomedia GmbH (Cuxhaven, Germany and the embryonic development was induced by incubating the eggs at 37.5˚C and 80% humidity as described earlier (37). The tumour-bearing chicken eggs were incubated for 24 h at 37.5˚C to stimulate tumour formation, followed by the topical application of 20 μl PBS containing three concentrations of broxbam (1.2, 3.0 and 5.0 μM). After an incubation period of 72 h at 37.5˚C and 80% humidity, the tumours were excised and carefully weighed to determine their mass.

Apoptosis detection

Measurement of caspase-3 activity. HepG2 and Huh7 cells were incubated (37˚C, 5% CO_2 and 95% humidity) for 48 h in RPMI growth medium (Gibco; Thermo Fisher Scientific, Inc.) containing the respective concentrations of test compounds (0.1, 0.3, 0.6 and 1.2 μM). The cells were rinsed twice with PBS. All cells were lysed with 500 μl lysis buffer (10 mM Tris-HCl, 10 mM NaH_2PO_4/Na_2HPO_4, 130 mM NaCl, 1% Triton X-100 and 10 mM NaPPi, pH 7.5) per 100 cells. Protein concentration was determined using a BCA protein assay kit (Pierce; Thermo Fisher Scientific, Inc.). The activity of caspase-3 was measured using the fluorogenic substrate AC-DEVD-AMC (cat. no. 14987; Caymen Chemical Company). In brief, the cell lysate was adjusted to a protein concentration of 500 mg/ml before 100 μl of this cell lysate were mixed with 100 μl substrate solution (20 μg/ml caspase-3 substrate AC-DEVD-AMC, 20 mM HEPES, 10% glycerol and 2 mM DTT, pH 7.5; Sigma-Merck; Merck KGaA). The samples were then incubated for 1 h at 37˚C. The fluorescence of the substrate, cleaved by caspase-3, (excitation wavelength=380 nm, emission wavelength=460 nm) was measured using a Varioskan Flash fluorometer (Thermo Fisher Scientific, Inc.).

Detection of changes in the mitochondrial membrane potential (MMP HepG2 and Huh7 cells were seeded at a density of $8x10^3$ cells/well in 96-well plates and maintained for 72 h at 37˚C, 5% CO_2 and 95% humidity until they were treated with 0.6 μM broxbam or 2.0 μM vorinostat for 3, 6 and 18 h at 37˚C, 5% CO_2 and 95% humidity. To measure MMP, cells were stained for 15 min in the dark at 37˚C using the JC-1 dye (1 mg/ml; 5,5',6,6'-tetrachloro-1,1',3,3'-tetraethylbenzimidazolylcarbocyanine iodide; Molecular Probes; Thermo Fisher Scientific, Inc.). The cells were analysed using a Varioscan Flash fluorometer (Thermo Fisher Scientific, Inc.) at excitation wavelengths of 485 nm and emission wavelengths of 535 nm. Signals in the orange region of the fluorescence can be detected when JC-1 aggregates occur because of a negative MMP, which indicates healthy mitochondria. In the event of a positive MMP, which results from mitochondrial damage, JC-1 occurs in its monomeric form giving rise to fluorescence in the green wavelength region (38). Accordingly, measurement of the ratio of orange to green fluorescence signal intensities allows the determination of changes in the MMP.

Western blotting. Whole cell extracts were prepared after harvesting substance-treated cells. HepG2 and Huh7 cells were incubated (37˚C, 5% CO_2 and 95% humidity) for 24 h in RPMI growth medium (Gibco; Thermo Fisher Scientific, Inc.) containing the respective concentrations of test compounds (BB: 0.6 and 1.2 μM; Vs, 4.0 μM). Lysis was performed by using lysis buffer (0.1% SDS, 0.5% sodium deoxycholic acid, 1% Nonidet P-40, 0.1 mM PMSF, 1 mg/ml aprotinin and 1 mg/ml pepstatin A1; all from Sigma Aldrich; Merck KGaA). Protein contents of samples were determined using a BCA protein assay kit and samples containing 30 μg protein subjected to 7.5% or 12% SDS-PAGE. Proteins were then transferred onto PVDF membranes by electroblotting for 1.5 h. Membranes were blocked for 1 h using 5% skimmed milk powder solution followed by incubation at 4˚C overnight with primary antibodies. The following antibodies were used: Glucose transporter (GLUT) 2 (1:1,000; cat. no. 071402 MilliporeSigma), p53 and phosphorylated (p-) p53 (1:1,000; cat. nos. 9282 and 9286, respectively; Cell Signalling Technology, Inc.), HDAC1, HDAC2, HDAC4 and HDAC6 (1:1,000; cat. nos. 5356, 5113, 7628 and 7558, respectively; Cell Signalling Technology, Inc.). Detection of tubulin (anti-Tubb2B, cat. no. TA337744; Origene Technologies, Inc.) served as a loading control. Membranes were washed with 0.1% Tween in PBS and incubated with HRP-coupled anti-IgG antibody (1:10,000; cat. nos. NA934 and NA931, Amersham; Cytiva) for 1 h at room temperature. Protein signals were visualised using enhanced chemiluminescent detection kit (Amersham; Cytiva) and a Fusion SL camera (Vilber Lourmat Deutschland GmbH). For quantification, ImageJ (Vs 1.53j, National Institutes of Health) was used and the density of the protein bands was normalised to tubulin as a loading control.

RT-qPCR. Cellular RNA of untreated HepG2 and Huh7 cells were extracted using GeneMATRIX Universal RNA Purification Kit (Roboklon GmbH) according to the manufacturers' protocols, followed by treatment with 1 U DNAse I (Gibco; Thermo Fisher Scientific, Inc.) per μg RNA for the elimination of possible DNA contaminations. Reverse transcription into cDNA and qPCR were performed using GoTaq® 1-Step RT-qPCR System (Promega Corporation) on a QuantStudio 5 Real-Time PCR System (Thermo Fisher Scientific, Inc.). The mixture for each sample/primer mix had a final volume of 10 μl containing 20 ng RNA and 250 nM of each primer. Melt curve controls were run to ensure primer specificity. The parameters for reverse transcription were as follows: 37˚C for 15 min, 95˚C for 10 min. Primer sequences are listed in Table SI. The obtained cDNA was analysed by using GoTaq® 1-Step RT-qPCR System (Promega Corporation) and qPCR was run on a StepOne-Cycler (Thermo Fisher Scientific, Inc.) for 40 cycles of amplification (initial denaturation for 5 min at 95˚C; followed by denaturation at 95˚C for 15 sec, annealing at 60˚C for 20 sec, elongation at 72˚C for 45 sec for 40 cycles). All samples were run in triplicate. The relative target gene expression was calculated using the $2^{-\Delta\Delta Cq}$ method using GAPDH, β-actin or 18S rRNA as an internal control (39).

Inhibition of HDAC activity. The ability of broxbam to inhibit HDAC1, -2, -4 and was measured using a cell free fluorogenic HDAC Assay (cat. nos. 50061, 50062, 50064, 50076 BPS Bioscience, Inc.). The HDAC activity was measured according to the protocols of the manufacturer. Briefly, purified human recombinant HDAC enzymes contained with the assay kit and fluorogenic HDAC substrates were used to measure HDAC activity. In total, 50 μl assay buffer containing 1 μg/μl BSA, the human recombinant HDAC enzyme, the test compound and the corresponding HDAC substrate was added into a black 96-well assay plate. The reaction in each well was incubated at 37˚C for 30 min, followed by the addition of 50 μl HDAC developer reagent and incubation at room temperature for 15 min. Fluorescence intensity was measured using a Varioskan Flash Fluorometer (Thermo Fisher Scientific, Inc.) using an excitation wavelength of 380 nm and an emission wavelength of 460 nm.

Immunofluorescence staining of the cytoskeleton. HepG2 cells were seeded onto glass coverslips at a density of $1x10^5$ and were allowed to attach and proliferate for 24 h (37˚C, 5% CO_2 and 95% humidity). Cells were treated with broxbam (0.6 μM) and vorinostat (4 μM) whereas a corresponding volume of DMSO was used as a negative control. Treated cells were incubated for additional 24 h (37˚C, 5% CO_2 and 95% humidity) and fixed with 4% formaldehyde in PBS for 20 min at room temperature. The samples were then blocked and permeabilised (1% BSA and 0.1% Triton X-100 in PBS) for 30 min at room temperature. For the immunostaining of the microtubule structures, the cells were incubated for 1 h at 37˚C in the dark with mouse primary anti-human α-tubulin monoclonal antibody (1:500; cat. no. T6199; Sigma Aldrich; Merck KGaA), followed by treatment with a AlexaFluor®-conjugated 546 goat anti-mouse secondary antibody (1:500; cat. no A-21133; Thermo Fisher Scientific, Inc.) for 1 h at room temperature in the dark. Cellular actin filaments were stained for 1 h at 37˚C in the dark using phalloidin (1:1,000, cat. No A12379 AlexaFluor®-conjugated 488; Invitrogen; Thermo Fisher Scientific, Inc.). Coverslips were mounted in DAPI containing Mowiol (Mowiol 4-88; 1 μg/ml DAPI; Carl Roth GmbH) for additional nuclei counterstaining. Fluorescence microscopic imaging (magnification, x60; Spinning Disk Confocal microscope; Nikon Corporation) was performed at the Charité Advanced Medical BioImaging Core Facility (Berlin, Germany).

Scratch wound healing assay. HepG2 cells were allowed to proliferate to confluence in six-well plates. Using a 10 μl pipette tip, the cell monolayer was scratched once horizontally and vertically. Wells were rinsed with PBS and fresh medium was added, containing two concentrations of broxbam (0.6 and 1.2 μM), whereas a corresponding volume of DMSO was used for a control. The cell monolayers were incubated for 24 h (37˚C, 5% CO_2 and 95% humidity), followed by photographic documentation using a digital camera (Kappa Optronics GmbH). Migration of cells was quantified using the TScratch software (version 1.0; CSElab). Migration values were normalised to control, which was set as 100%. The experiments were performed under normal FBS conditions (10%), since HepG2 cells could not tolerate serum deprivation and reacted with immediate and pronounced cell detachment. In addition, serum deprivation is a procedure that is preferable necessary for long-term observations (>24-48 h), where cell proliferation instead of migration becomes the predominant factor for wound healing (40,41).

Zebrafish angiogenesis assay. To examine the angiogenesis *in vivo*, experiments with zebrafish embryos were performed, which represents a viable model for the evaluation of angiogenic effects of small molecules (42). In the developing zebrafish embryo, the sub-intestinal veins (SIVs) represent a characteristic blood vessel system that can be easily visualised (42). Eggs from the transgenic Tg(fli1:EGFP)^{y1} mutant Casper zebrafish stem were obtained 2-5 h after egg deposition connected to spawning process from the animal breeding facility of the University of Bayreuth, which has the permission to keep and breed vertebrates and cephalopods for experimental purposes according to § 11 German animal Welfare Law (permission no. OBK/A 2; Bayreuth, Germany). Zebrafish are kept at 20-26˚C in water pH 6.0-8.0 under standard atmosphere.

After the egg deposition, the spawn fish eggs (1 day post fertilisation) were collected, rinsed, and transferred into a petri dish filled with E3-medium (5 mM NaCl, 0.17 mM KCl, 0.33 mM $CaCl_2$, 0.33 mM $MgSO_4$ and 0.01% methylene blue in ddH_2O; pH 7.2) and incubated for 24 h at 28˚C. Healthy embryos were then dechorionated, which means the removal of the egg shell, and five embryos per well were transferred into six-well plates in 5 ml E3-medium. In total, 100-fold pre-dilutions of test compounds (final concentrations were 1 μM, 750 and 500 nM) in ddH_2O were prepared and added to the E3-medium at 50.5 μl per well, followed by incubation for 48 h at 28˚C. After the addition of 50 μl 0.04% tricaine solution (ethyl-3-aminobenzoate-methanesulfonate; Sigma Aldrich; Merck KGaA) to the E3-medium in the six-well plates, the embryos (3 days post fertilisation) were anaesthetised (5 min at room temperature) to a final tricaine concentration of 0.0004% before the blood vessel system was visualised and documented by fluorescence microscopy with up to two-fold magnification (excitation wavelength, 488 nm; emission wavelength, 510 nm; Leica MZ10F fluorescence microscope; Leica Microsystems GmbH; AxioCam 1 cm; Carl Zeiss AG). The area of SIVs was measured using Image J version 1.52a. At the end of the experiments, 1 ml anaesthetic tricaine (tricaine mesylate; 5 g/l) was added to 5 ml E3-media to kill the zebrafish larvae (3 days post fertilisation) with an overdose of the anaesthetic, at a final concentration of 833 mg/l.

Statistical analysis. Statistical analysis of the data was performed using GraphPad Prism 8 software for Windows (GraphPad Software, Inc.). If not indicated otherwise, data were presented as the mean ± standard error of the mean. Unpaired Student's t-tests were used for two-group comparisons. To test for statistical significance between > two groups, one-way ANOVA coupled with Tukey's post hoc tests was used. $P<0.05$ were considered to indicate a statistically significant difference. All experiments were performed in triplicate unless otherwise stated. The exact number of independent repetitions for each assay is provided in the figure legends.

Table I. Growth inhibitory concentrations (IC_{50}) of compounds applied to liver cancer cell lines HepG2 and Huh7, CCC cell lines TFK-1 and EGI-1 and mouse hepatocytes (AML12)[a].

Origin	Cell line	Broxbam (μM)	Vorinostat (μM)
Liver cancer	HepG2	0.6±0.2	2.1±0.4
	Huh7	0.6±0.1	1.8±0.5
CCC	TFK-1	0.6±0.1	1.4±0.1
	EGI-1	0.6±0.2	3.2±0.1
Non-transformed mouse hepatocytes	AML12	1.9±0.2	1.7±0.2

[a]Values are derived from dose-response curves obtained by measuring the percentage of vital cells relative to untreated controls 48 h after incubation using crystal violet staining. Results are shown as mean ± SD from n ≥3 independent experiments. CCC, human cholangiocellular carcinoma.

Results

Inhibition of cell proliferation and cytotoxicity. It was previously reported that broxbam exerts selective anti-tumour effects at half maximal inhibitory concentrations (IC_{50}) in the low μM to two-digit nM range (20). In the present study, the potential effects of broxbam in liver cancer cell models were evaluated. Table I summarises the IC_{50} values calculated for broxbam and vorinostat in liver cancer cell lines HCC and CCC and non-transformed hepatocytes. Notably, broxbam exhibited higher antiproliferative potency in all liver cancer cell lines compared with non-transformed hepatocytes, which required three-times higher IC_{50} concentrations (Table I). This suggests the selectivity of broxbam towards liver cancer cells. In addition, broxbam exerted higher antiproliferative capabilities compared with the clinically relevant HDACi vorinostat in all liver cancer cell models test. Unlike broxbam, vorinostat did not appear to display cancer specificity, since its IC_{50} values did not differ between the liver cancer cell lines and the non-transformed AML-12 cells (Table I).

Using the iCELLigence real-time cell viability and proliferation analysis system, the kinetic profile and onset of the inhibition of proliferation mediated by broxbam were determined. In case of the HepG2 and Huh7 cell lines, a distinct reduction in cell proliferation was observed at as early as 12 h after the application of broxbam in a dose-dependent manner (Fig. 2A and B). In CCC cell lines, this dose-dependent inhibitory effect was also detected, but instead becoming more pronounced 24 h after treatment (Fig. 2C and D). To exclude the contribution of unspecific cytotoxicity to these antiproliferative effects exerted by broxbam, the release of lactate dehydrogenase (LDH) from the cytosol into the cell culture supernatant of HepG2, Huh7 and AML12 cells was measured (Fig. 3). Increased LDH release would indicate the presence of nonspecific and necrotic cell death due to treatment-induced damage of cell membranes (36). However, treatment of HepG2 or Huh7 cells with rising concentrations of broxbam (0.1-10 μM) did not lead to significant increases in LDH release after 24 h (Fig. 3). The same effects were also observed in non-transformed hepatocytes (AML12) after broxbam treatment (Fig. 3). This suggests that broxbam does not compromise cell membrane integrity and that it exerted no immediate cytotoxic effects even at concentrations as high as 10 μM.

In vivo tumour growth reduction. The potential antineoplastic effects of broxbam in liver cancer tumours was next tested using *in vivo* chick embryo experiments, specifically by applying the modified chorioallantoic membrane (CAM) assay. HepG2-derived microtumours from an initial volume of 20 μl were grown on the CAM of fertilised chicken eggs for 24 h. Subsequently, the microtumours were treated for 72 h with either PBS (control) or rising concentrations of broxbam (1.2-5.0 μM). At the end of the experiment, tumour masses were excised and weighed. Compared to PBS-treated controls, broxbam (3 and 5 μM) induced a significant reduction in liver cancer microtumour growth (Fig. 4).

To further characterise the underlying signalling and metabolic events underlying these antitumor effects of broxbam observed in the present study, its potential effects on glucose metabolism were next assessed. Cancer cells preferentially use glycolysis to consume glucose as the substrate for energy metabolism, in a process known as the Warburg effect (43). Therefore, the impact of broxbam on the expression of GLUT2, which is crucial for hepatic glucose uptake (44), was investigated. In addition, the glycolytic activity of HepG2 and Huh7 cells was also assessed by measuring the consumption of glucose, production of lactate and its release into the supernatant of the cell culture medium. Protein expression levels of GLUT2 were not affected by broxbam, though the HDACi vorinostat markedly reduced the expression of GLUT2 compared to broxbam treated group in both HepG2 and Huh7 cells (Fig. S1). This finding suggests that vorinostat, but not broxbam, can inhibit cellular glucose uptake by downregulating GLUT2 expression. By contrast, the glycolytic activity of broxbam-treated liver cancer cells was found to be decreased significantly. Compared with that in the untreated controls, the remaining glucose in the cell culture supernatant of broxbam-treated HepG2 cells was markedly higher whereas the production and release of lactate was decreased (Fig. S1). This lower glucose consumption and reduced lactate production indicate reduced glycolytic activity in broxbam-treated cells. In addition, no such reduction in glycolytic activity could be observed in HepG2 cells

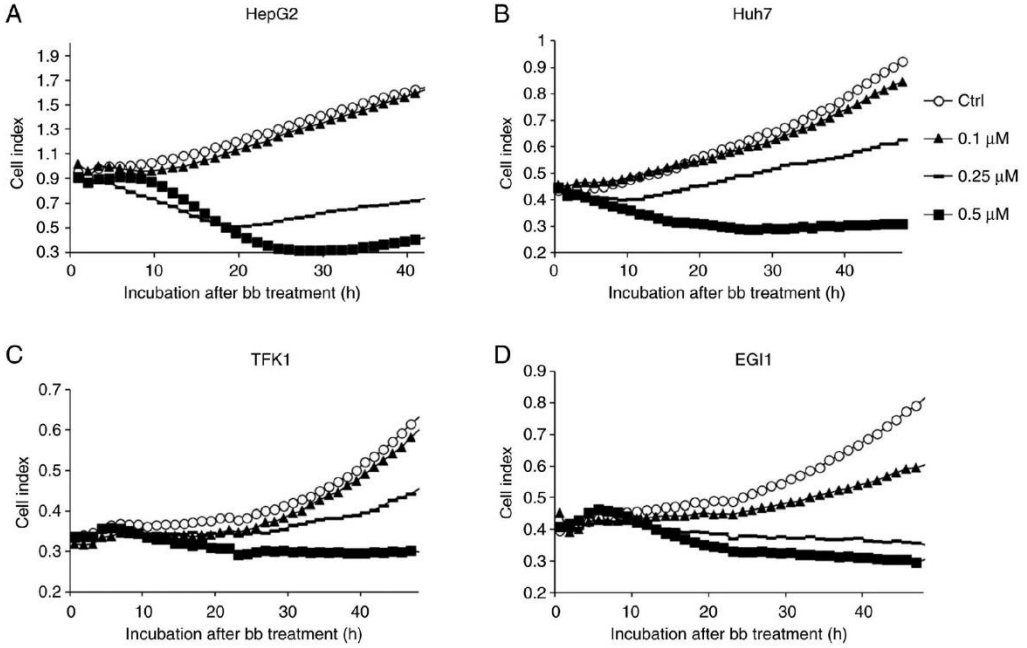

Figure 2. Real-time measurements of liver cancer and cholangiocellular carcinoma cell proliferation. Dose- and time-dependent effects of bb on (A) HepG2, (B) Huh7, (C) TFK1 and (D) EGI1 cell proliferation as assessed by the iCELLigence real-time monitoring system. Data show the cell viability index measured over 48 h after the application of broxbam. Representative graphs out of three independent experiments were shown for each cell line. Bb, broxbam.

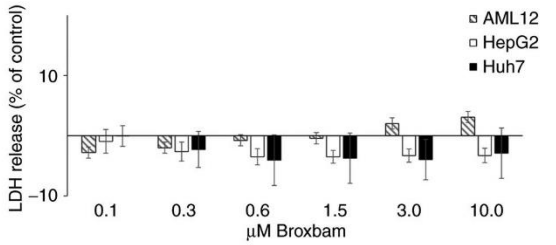

Figure 3. LDH release by liver cancer cell lines HepG2 and Huh7 and the non-transformed hepatocyte cell line AML12 into the media after 24 h treatment with broxbam in different concentrations. Data are presented as the LDH release relative to those in untreated controls, where basal LDH release was set to 0%. Values are presented as the mean ± SEM. n=4. LDH, lactate dehydrogenase; ctrl, control.

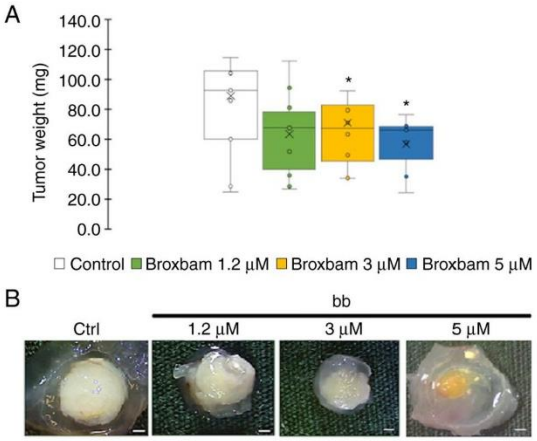

Figure 4. Measurement of tumour size grown on the chorioallantoic membranes of fertilised chicken eggs. (A) Tumour mass of HepG2 tumours after treatment with different concentrations of bb and PBS as control for 72 h. Data are presented as the mean ± SEM from seven independent experiments. *P<0.05. (B) Representative images of control and bb-treated HepG2 tumours after excision. Scale bar 800 μm. bb, broxbam; Ctrl, control.

following vorinostat treatment, suggesting no effects were mediated by vorinostat on glucose uptake or lactate production and release.

Proapoptotic mode of action. To further elucidate the mechanisms by which broxbam exerted antitumour effects on the liver cancer cells the extent of apoptosis induction was next measured. Apoptosis induction considered to be one of the primary objectives of targeted cancer therapy since it results in the specific and inflammation-free elimination of cancer cells. Apoptosis induction occurs through two distinct mechanisms, either by the activation of cellular death receptors or through the mitochondria-driven activation of caspase-3 (45). Broxbam was found to induce mitochondria-driven apoptosis in liver cancer cells, as evidenced by fluorometric changes in the MMP of broxbam treated cells (Fig. 5A). An increase in the green/red ratio indicates a reduction in the MMP and therefore mitochondrial damage, which may have served as a trigger for the activation of the apoptosis-associated tumour suppressor protein p53. A significant increase in the green/red ratio following treatment with the IC_{50} concentration of broxbam at 0.6 μM was observed after 3 and 6 h (Fig. 5A).

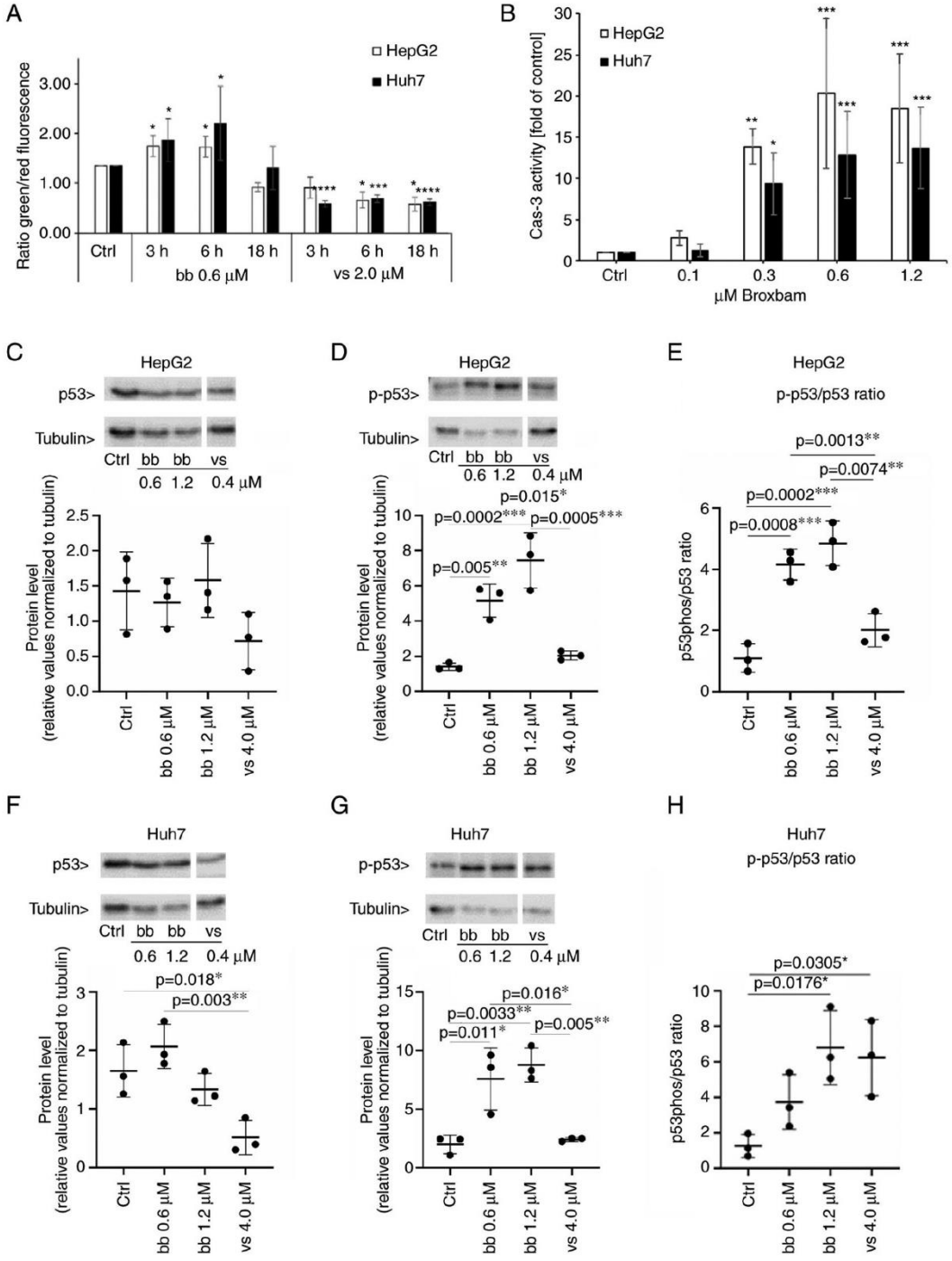

Figure 5. Detection of proapoptotic events in liver cancer cells. (A) Influence of bb and vs on the loss of mitochondrial membrane potential of liver cancer cell lines HepG2 and Huh7. Indicated values were measured by fluorometric measurement of JC-1-stained cells. The effect of IC_{50} concentrations of bb and vs was monitored after 3, 6 and 18 h. Mitochondrial accumulation of JC-1 results in red fluorescence whereas loss of MMP results in monomeric JC-1, which emits green fluorescence. Data are presented as the ratio of green/red fluorescence of cells. Data are presented as the mean ± SEM from three experiments. One-way ANOVA with Tukey's post hoc test was used to test for significance. *P<0.05, ***P<0.001 and ****P<0.0001 vs. Ctrl. (B) Caspase-3 activity in HepG2and Huh7 cells upon treatment with bb for 24 h. Data are presented as the mean ± SEM percentage of untreated controls from four experiments. One-way ANOVA with Tukey's post hoc test was used to test for significance. *P<0.05, **P<0.01 and ***P<0.001 vs. ctrl. (C-H) HepG2 and Huh7 cells were treated either with solvent (Ctrl), bb at IC_{50} (0.6 μM), bb at two-fold IC_{50} (1.2 μM) or vs. at two-fold IC50 (4.0 μM). Western blotting results of (C) p53 expression and (D) phosphorylation levels in HepG2 cells. (E) p-p53/p53 ratio was also quantified in HepG2 cells. Western blotting results of (F) p53 expression and (G) phosphorylation levels in Huh7 cells. (H) p-p53/p53 ratio was also quantified in Huh7 cells. Corresponding representative western blotting images are shown in Fig. S2. n=3 per group. One-way ANOVA with Tukey's post hoc test was used to test for significance. Bb, broxbam; vs, vorinostat; Ctrl, control; Cas 3, caspase 3; p-, phosphorylated.

By contrast, treatment with vorinostat at its IC_{50} concentration of 2 μM, did not lead to an apoptosis-indicating increase in the green/red ratio. Instead, a significant reduction was observed, suggesting that vorinostat was not likely to induce mitochondria-driven apoptosis (Fig. 5A).

In following experiments broxbam treatment was shown to induce a dose-dependent increase in the phosphorylation of p53 of HepG2 and Huh7 cells (Fig. 5C-H), consistent with the aforementioned data on the broxbam-induced changes in MMP for the initiation of mitochondria-driven apoptosis (Fig. 5A). In addition, no increase in p53 phosphorylation in HepG2 (Fig. 5D) or Huh7 (Fig. 5G) cells could be observed after vorinostat treatment, which is in accordance with the failure of vorinostat to decrease the MMP (Fig. 5A).

Mitochondria serve a pivotal role in the regulation of apoptotic caspase activation. The caspase cascade lies downstream of the loss of MMP and activation of p53 (46-48). This cascade eventually leads to the activation of the executioner caspase-3 (49). Therefore, Caspase-3 activity was next assessed using a fluorogenic caspase-3 assay, which functions by the specific recognition of the enzymatic activity of phosphorylated caspase-3 (15). After broxbam treatment, HepG2 and Huh7 cells exhibited a dose-dependent increase in apoptotic caspase-3 activity compared with that in the control group (Fig. 5B). Of note, maximal capsase-3 activity could already be observed at the concentration of 0.6 μM broxbam (Fig. 5B), which corresponded to the IC_{50} values of broxbam in these cells (Table I).

HDAC expression and activity. To clarify if HDAC inhibition forms part of the antitumour mechanism of broxbam, its effects on HDAC expression and activity were investigated. RT-qPCR was used to measure the expression levels of the 11 subtypes of HDACs (HDACs 1-11) in the HepG2 and Huh7 cells. Although the mRNA expression levels of HDAC1 and HDAC2 were considerably lower compared with those of the other HDAC subtypes, all 11 HDACs tested were found to be expressed in both cell lines (Fig. 6).

Subsequently, the potential treatment-induced changes in the protein expression levels of HDAC1, -2, -4 and -6 were assessed by western blotting and densitometric analysis. HDAC1 and HDAC2 belongs to class I HDACs and are localized in the nucleus of the cell (50). HDAC4 and HDAC6 are class II HDACs and both can be found in the cytoplasm as well as in the nucleus of a cell (50). These HDACs were previously found to be overexpressed in human pancreatic adenocarcinoma and hepatocellular carcinoma (50,51). Exposure of HepG2 and Huh7 cells to 0.6 μM and 1.2 μM broxbam, concentrations corresponding to their respective IC_{50} and two-fold IC_{50} values, did not lead to significant changes in any of the HDAC subtypes (Fig. 7). An exception was the significant increase in HDAC4 expression in Huh7 cells treated with 1.2 μM broxbam compared with that in the control group (Fig. 7C). This finding suggests that broxbam functions as an inhibitor of HDAC activity instead of being a regulator of HDAC expression (Fig. 7).

The activities of HDACs -1, -2, -4 and -6 following treatment with IC_{50} and two-fold IC_{50} concentrations of broxbam and vorinostat were assessed using a cell-free enzymatic assay system. HDAC subtype-specific inhibition of the cleavage of

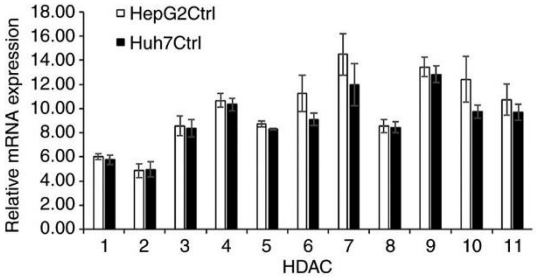

Figure 6. mRNA expression levels of HDACs 1-11 in untreated liver cancer cell lines HepG2 and Huh7. mRNA expression levels of HDACs 1-11 in liver cancer cell lines were measured using reverse transcription-quantitative PCR, which were then normalised to those of GAPDH, the housekeeping gene. Data are presented as the means ± SEM from three independent experiments. HDAC, histone deacetylase; Ctrl, control.

fluorogenic peptide substrates (Fig. 8A) was next detected and compared with the untreated control group, which was set to 100%. Broxbam exerted an attenuating effect on the activity of HDAC1 and -6, but did not affect the activities of HDACs -2 and -4. Vorinostat mediated potent inhibitory effects on the HDACs -1 and -2, which exceeded that of broxbam. Therefore, broxbam and vorinostat inhibited the individual HDAC isoforms with distinct profiles. However, both compounds were concluded inhibit HDAC1, with broxbam showing specificity towards HDAC6 whereas vorinostat showed specificity towards HDAC2. Due to this potent inhibitory effect of broxbam against HDAC6, the present study next examined its potential dose dependency over the concentration range from 0.6 to 10 μM, which revealed 90% inhibition of HDAC6 activity at 10 μM, the highest broxbam concentration tested (Fig. 8B).

To investigate the contribution of HDAC6 inhibition towards the antiproliferative effects of broxbam in liver cancer cells (Fig. 2), HDAC6 knockdown was performed using siRNA. After 48 h of transfection with HDAC6-specific siRNA, the expression of HDAC6 protein in Huh7 cells was significantly decreased compared with that in cells transfected with the si-mock (Fig. 8C and D). Furthermore, the expression of typical markers of cell proliferation Ki-67 and E2F3 (52,53), were also found to be decreased significantly compared with that in cells transfected with the si-mock (Fig. 8E and F) suggesting a distinct contribution of HDAC6 inhibition towards the antiproliferative (Figs. 1 and 2) and antineoplastic (Fig. 4) effects of broxbam in liver cancer.

Dynamics of the cytoskeleton and cellular migration. Since broxbam contains the trimethoxystilbene motif of the vascular disrupting natural product CA-4 within its structure (23,25,26), it was next examined for its possible effects on the tubulin cytoskeleton and associated processes. Its inhibitory effects on the polymerisation of purified tubulin *in vitro* have already been previously reported (20). As HDAC6 has been found to function as a tubulin deacetylase to interfere with microtubule-dependent cell motility (54), the effects of broxbam on the microtubule and F-actin cytoskeleton of HepG2 cells were investigated using immunofluorescence staining. The formation of F-actin stress fibres and focal adhesions was observed

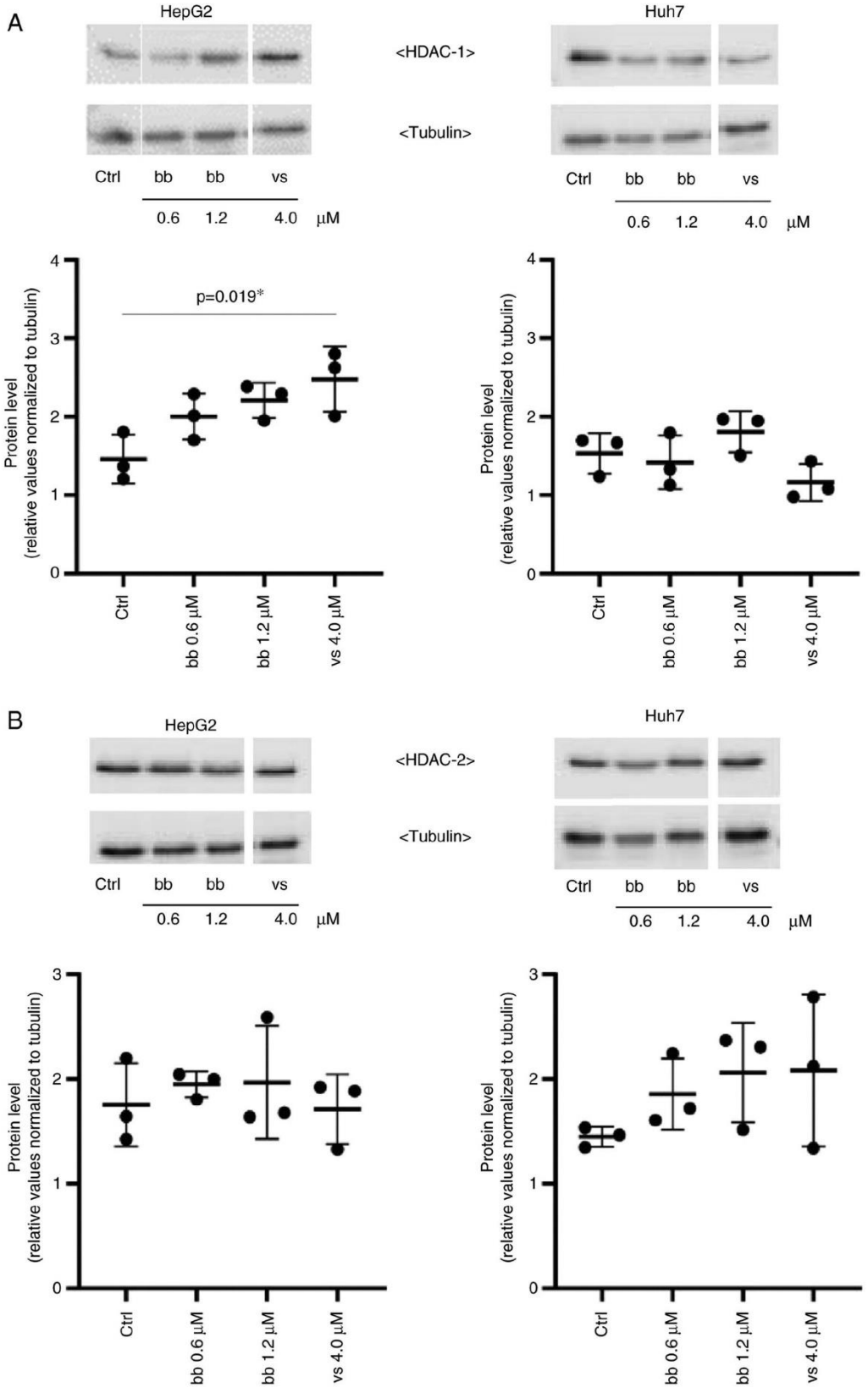

Figure 7. Continued.

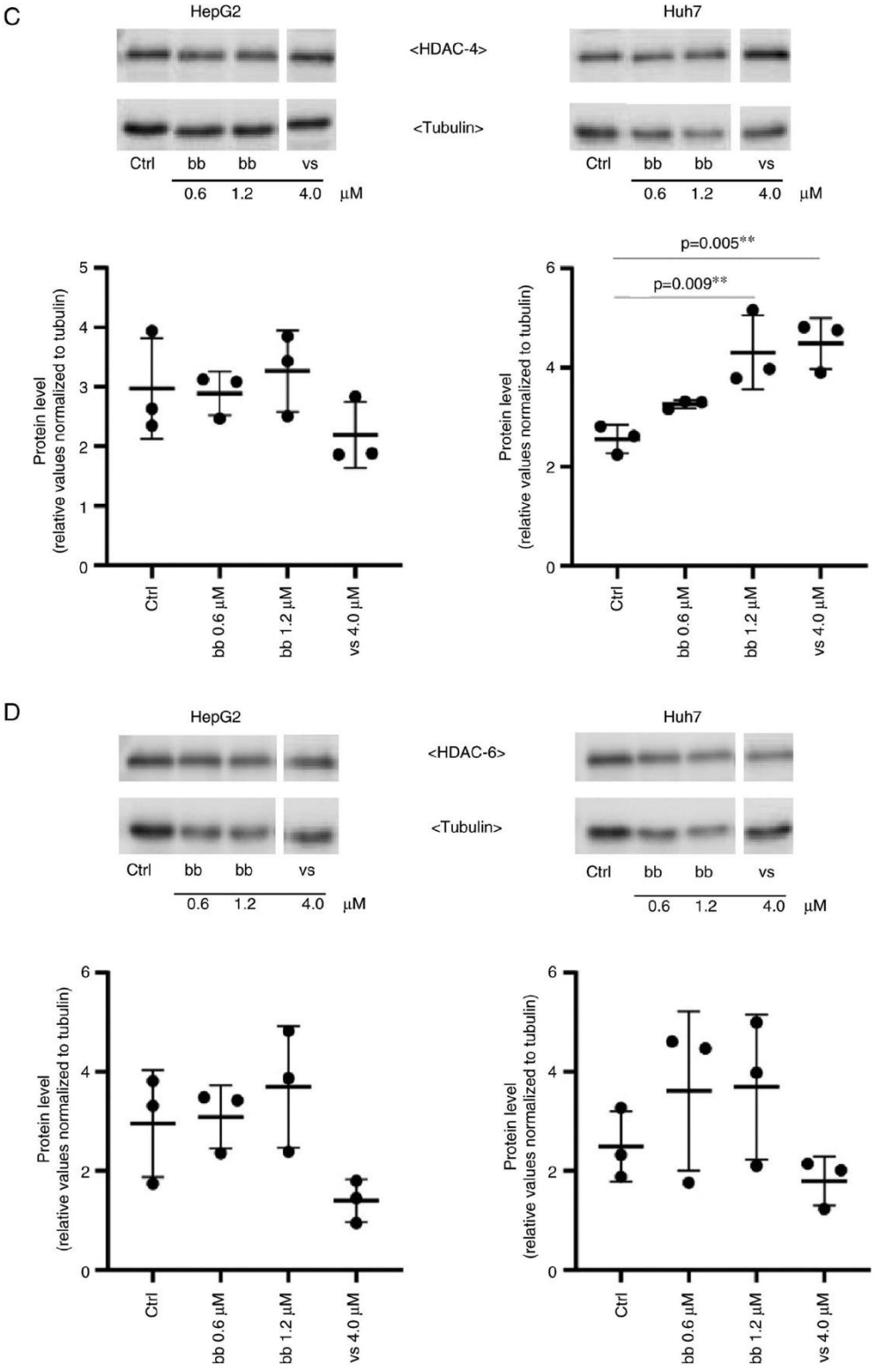

Figure 7. Quantification of the expression of selected HDAC proteins. HepG2 and Huh7 cells were treated for 24 h with either solvent (Ctrl), bb at IC_{50} (0.6 μM), bb at two-fold IC_{50} (1.2 μM) or vs. at two-fold IC_{50} (4.0 μM). Western blotting was used to measure protein expression, using tubulin as loading control. (A) HDAC1 expression in Hep2G and Huh7 cells. (B) HDAC2 expression in Hep2G and Huh7 cells. (C) HDAC4 expression in Hep2G and Huh7 cells. **P<0.01 vs. ctrl. (D) HDAC6 expression in Hep2G and Huh7 cells. Corresponding representative western blotting images are provided in Fig. S2. n=3 per group. One-way ANOVA with Tukey's post hoc test was used to test for significance. HDAC, histone deacetylase; Ctrl,. control; bb, broxbam; vs, vorinostat.

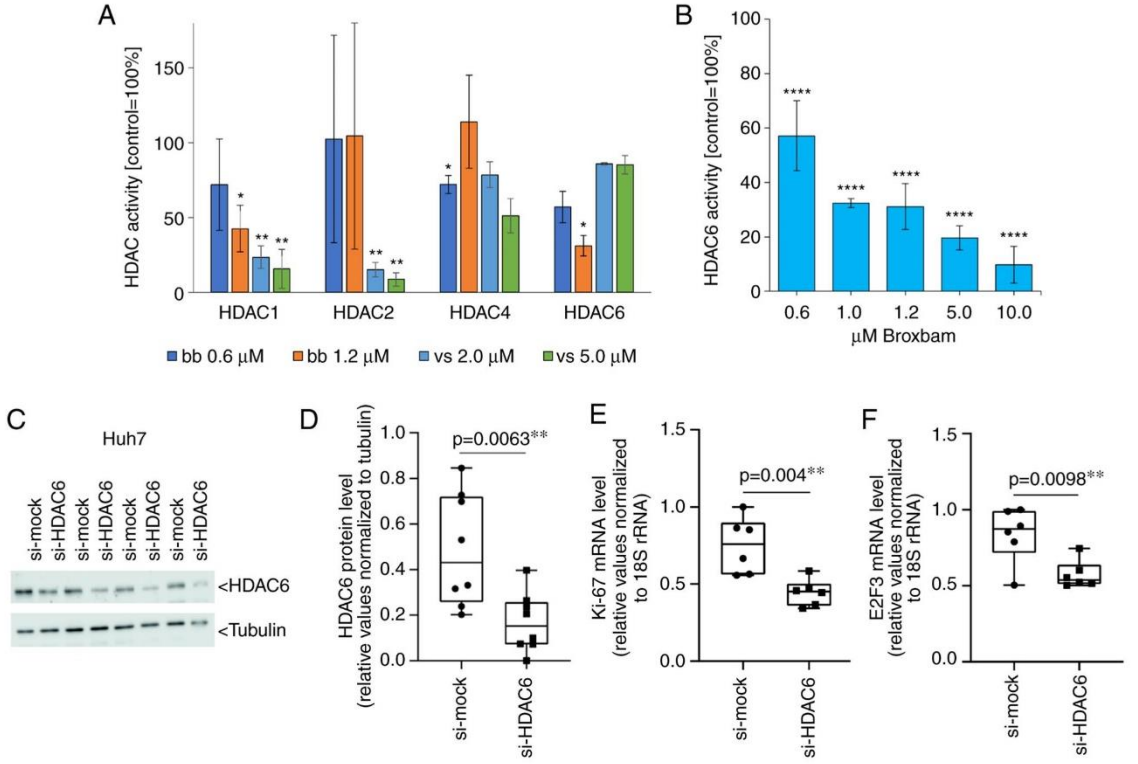

Figure 8. Effects of inhibiting the selective HDACs of broxbam in Huh-7 cells. (A) Activities of HDAC1, -2, -4 and -6 after treatment with bb or vs at concentrations corresponding to their respective IC_{50} and two-fold IC_{50}. Data are presented as the means ± SEM percentage of untreated control, which was set to 100%, from three experiments. *P<0.05, **P<0.01 vs. Ctrl. One-way ANOVA with Tukey's post hoc test was used to test for significance (B) Dose-dependent inhibitory effect of bb on the activity of HDAC6 relative to control, represented as the means ± SEM from three independent experiments. ****P<0.0001 vs. Ctrl. One-way ANOVA with Tukey's post hoc test was used to test for significance. (C) Western blot analysis and (D) quantification of siRNA-mediated knockdown of HDAC6 protein expression in Huh7 cells transfected with control (si-mock) or HDAC6-specific (si-HDAC6) siRNAs for 48 h. Each set of si-mock and si-HDAC6 lanes represents one transfection experiment. Tubulin was used as the loading control. Analysis of (E) Ki-67 and (F) E2F3 mRNA expression by reverse transcription-quantitative PCR. The mRNA expression levels were normalised to that of 18S rRNA. Data was presented as the mean ± SEM from six independent experiments. One-way ANOVA with Tukey's post hoc test was used to test for significance. HDAC, histone deacetylase; bb, broxbam; vs, vorinostat; si, small interfering.

following treatment with broxbam at its IC_{50} concentration (Fig. 9). Furthermore, the microtubule cytoskeleton appeared to be markedly altered compared with that in the control group. In general, broxbam-treated cells were considerably enlarged, especially their nuclei (Fig. 9). These effects were more prominent compared with those mediated by vorinostat, even after treatment with vorinostat at a concentration of two-fold IC_{50} (Fig. 9).

Cytoskeletal components, such as microtubules and actin fibres, are critical for cell migration (55,56). To investigate the effect of broxbam on cell migration, a scratch wound healing assay was performed. An observation period of 24 h was chosen to minimise the possibility of the migratory process being distorted by cell proliferation. The average doubling time of HepG2 cells is ~48 h, suggesting that HepG2 cell proliferation is unlikely to contribute significantly to wound closing (57). Broxbam treatment led to a significant reduction in gap closing by the HepG2 cell monolayer compared with that in the untreated control group (Fig. 10). In addition, broxbam exerted a potent antimigratory effect even when applied at its IC_{50} concentration of 0.6 μM (Fig. 10B).

Antiangiogenic effects in vivo. A previous study validated the properties of the two structural motifs on broxbam, which are HDAC-inhibition mediated by the hydroxamic acid pharmacophore and interference with cytoskeletal dynamics by its trimethoxystilbene motif (20). There is a possibility that inhibition of tubulin polymerisation and HDAC activity by broxbam may also translate into an antiangiogenic effect. Due to the previously known antiangiogenic effects of CA-4 (23) and the well-established association between HDACs as modulators of hypoxia-induced factor-1α and vascular endothelial growth factor (VEGF) expression (58), it was hypothesised that broxbam may also exert antiangiogenic properties. Therefore, *in vivo* zebrafish angiogenesis assays were performed (42). Broxbam mediated a dose-dependent antiangiogenic effect in reducing the area of the sub-intestinal veins (SIV) in developing zebrafish embryos, which became visible at concentrations equating to its IC_{50} value (Figs. 11 and 12). Signs of cardiotoxicity, such as dilation of the pericardial sac, which is a known unwanted side effect of antiangiogenic substances, such as CA-4 (59), could not be observed (Figs. 11 and 12).

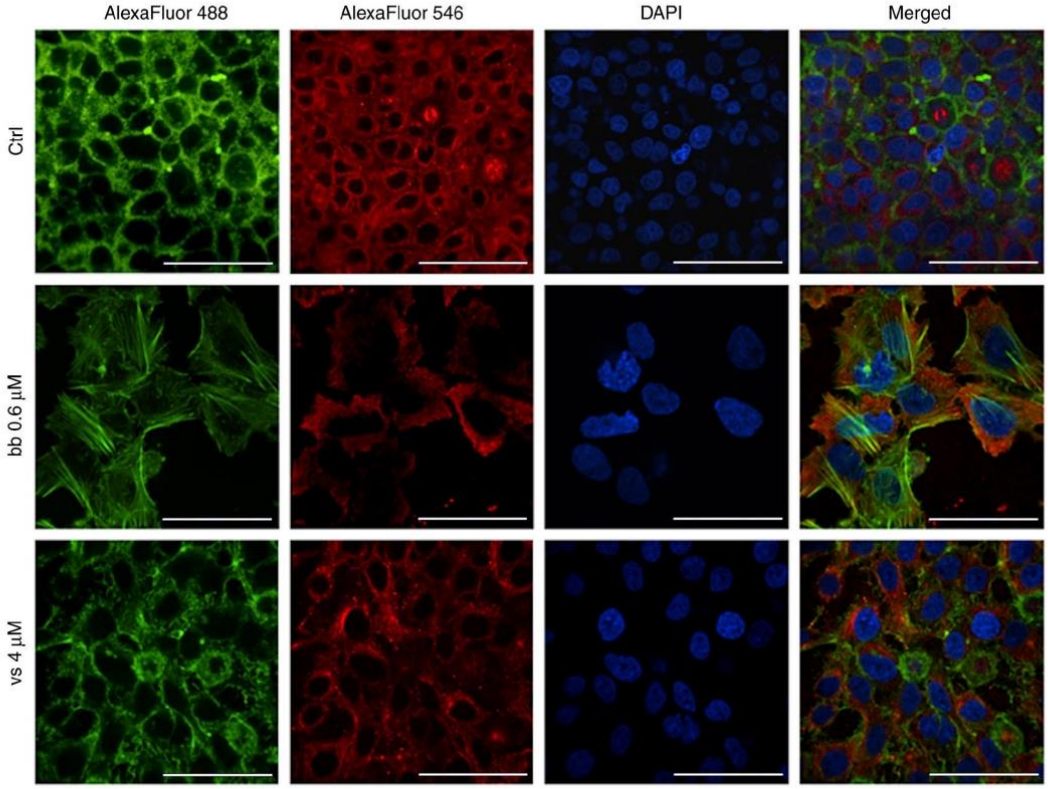

Figure 9. Responses of the cytoskeleton in HepG2 cells to bb treatment. Confocal immunofluorescence images 24 h after incubation with bb (0.6 μM) or vs. (4 μM). α-Tubulin (red), f-actin (green) and DAPI-stained nuclei (blue) staining are shown. Scale bar, 30 μm. Ctrl, control; bb, broxbam; vs, vorinostat. Images are representative of n=3 independent experiments.

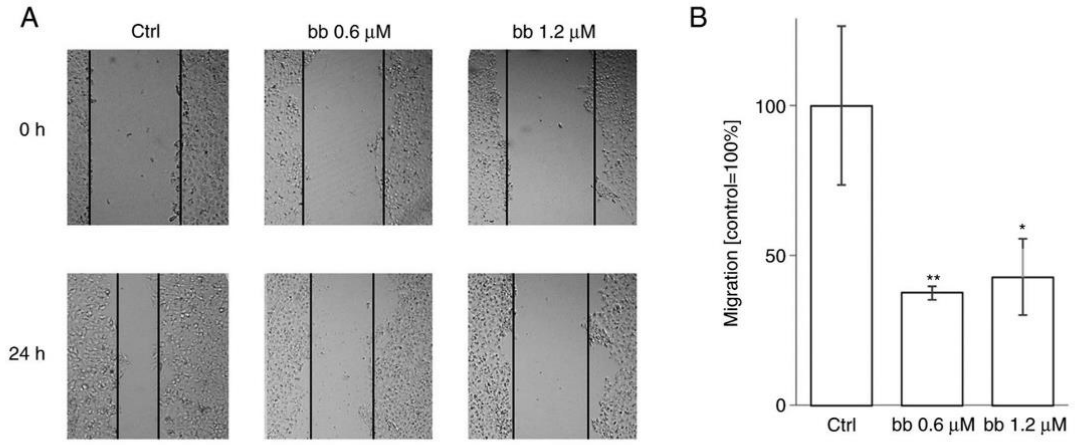

Figure 10. Effects of different concentrations of bb on the migration of HepG2 cells. HepG2 cell migration was measured using wound healing assays 24 h after treatment. (A) Representative images from five independent experiments, where the cells were treated with at IC_{50} two-fold IC_{50} of bb. (B) Cell migration was presented as the mean ± SEM percentage of control from three experiments. One-way ANOVA with Tukey's post hoc test was used to test for significance. *P<0.05 and **P<0.01 vs. ctrl. ctrl, control; bb, broxbam.

Discussion

Broxbam was recently reported to be a potent anticancer agent against various non-liver cancer cell models (20). In the present study, it was shown to exert antiproliferative properties in HCC and CCC liver cancer cell models. This novel chimeric compound, which consists of a HDAC-inhibitory hydroxamic acid pharmacophore and a cytoskeleton-interfering

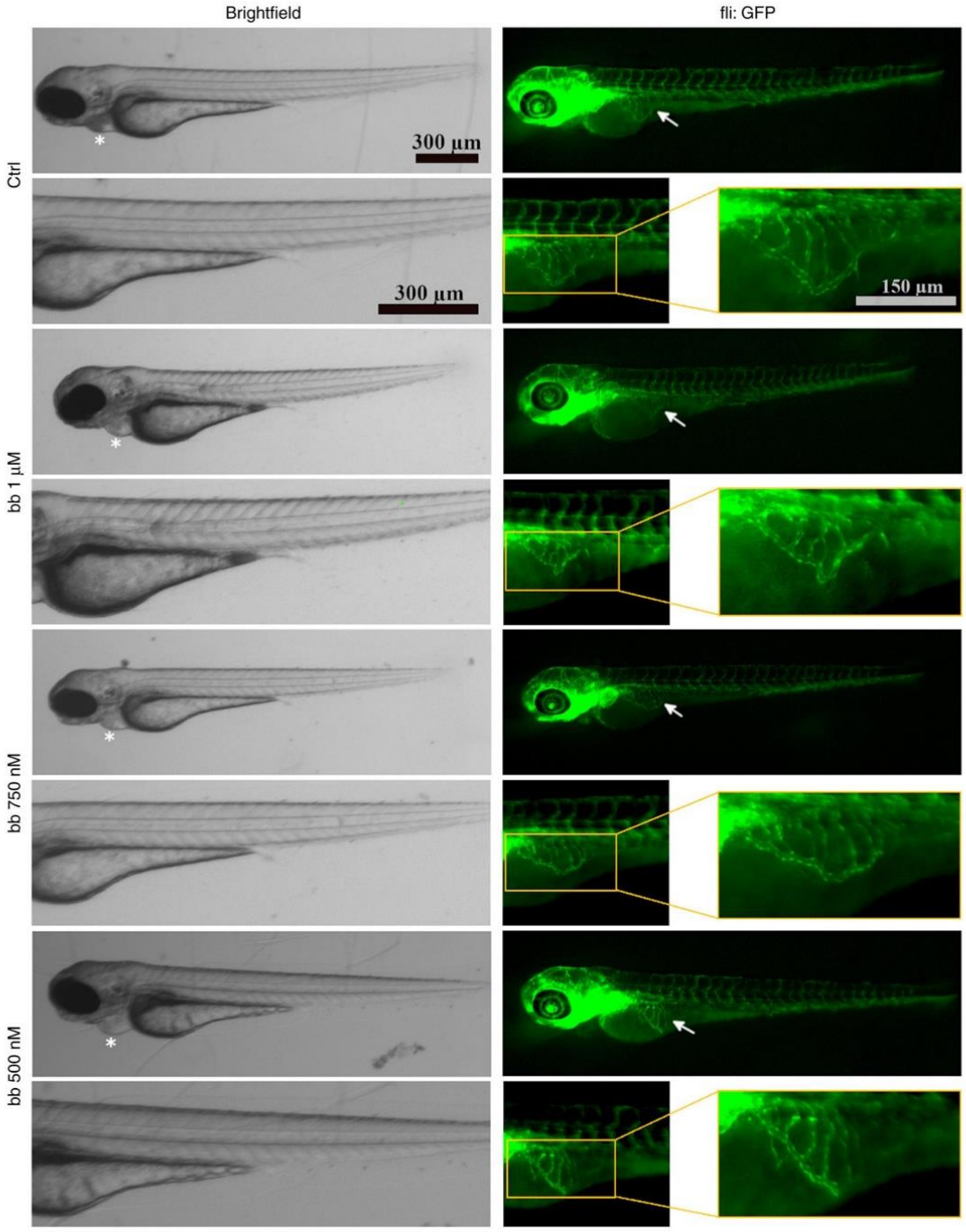

Figure 11. Morphology of the blood vessel system of transgenic Tg(fli1:EGFP)y1 mutant Casper zebrafish embryos 72 h post-fertilisation. Embryos were treated for 48 h with either a corresponding amount of DMSO, with bb concentrations of 1 μM, 750 or 500 nM. Brightfield and green fluorescent images, denoted as fli:GFP, are shown. The pericardial region was marked with asterisks whereas SIVs are marked with arrows. Fluorescent SIV areas are marked with yellow boxes, which were then magnified two-fold magnification. Individuals shown are representative for ≥20 embryos per concentration. bb, broxbam; GFP, green fluorescent protein; SIV, sub-intestinal veins.

trimethoxystilbene motif, inhibited the proliferation of liver cancer cells at near-nanomolar concentrations (IC_{50}, ~0.6 μM). This exceeded the antiproliferative potency of the clinically established HDACi vorinostat (IC_{50}, 1.4-3.2 μM). Unlike vorinostat, broxbam exerted preferential specificity for cancer cells over non-transformed murine hepatocytes. Real-time kinetic investigation of the antiproliferative effects of broxbam revealed an early onset of this effect, at 12-24 h, after drug

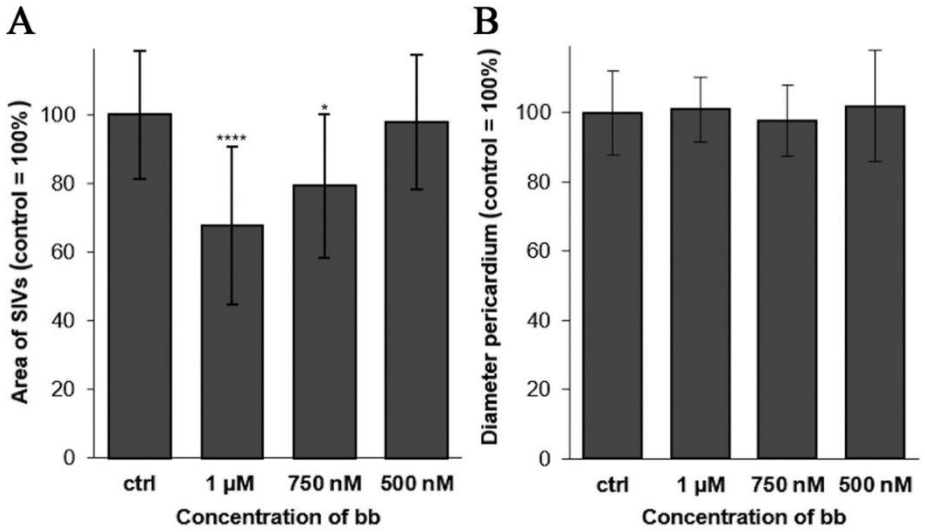

Figure 12. Effects of bb on developing zebrafish embryos at 3 days post fertilisation. (A) Area of SIVs after bb treatment with concentrations of 1 μM, 750 and 500 nM for 48 h. Values were normalised to the negative control, DMSO. (B) Percentage pericardial diameter relative to the negative control, DMSO. Data are presented as the percentage means ± SEM of control from ≥20 experiments. Significance levels were determined using one-way ANOVA and Tukey's post hoc test. *P<0.05 and ****P<0.0001 vs. ctrl. bb, broxbam; SIV, sub-intestinal veins.

application. The prohibitive effects of broxbam on liver cancer cells was found not likely to be due to unspecific cytotoxicity, but instead likely to be due to the targeted and orchestrated modulation of cancer cell-specific signalling pathways. This in turn lead to antiproliferative, anti-angiogenic, anti-migratory and apoptotic effects, in addition to the breakdown of cellular energy metabolism. The decrease in the glycolytic activity of liver cancer cells after broxbam treatment may be of therapeutic importance in terms of the glucose addiction of cancer cells, which is required for the maintenance of metabolism (the Warburg effect) (43).

Broxbam was found to induce the apoptosis of liver cancer cells through the mitochondrial-driven apoptosis pathway. A protein of importance for mitochondrial apoptosis is the p53 tumour suppressor protein, the phosphorylation of which is associated with the disruption of mitochondrial function and subsequent cell death (48). Phosphorylation of p53 induces the expression of p53 regulated apoptosis inducing protein 1, which is localised in the mitochondria and leads to the disruption of MMP en route to triggering apoptosis (60,61). Consistent with this mechanism, the present study found that broxbam induced p53 phosphorylation, reduced MMP and subsequently activated the apoptosis-specific effector caspase-3. The activation of caspase-3 directly contributes to core apoptotic processes, such as the dismantling of cell components and formation of apoptotic bodies therefore, it represents a direct marker for the activation of apoptosis (62). The extent of apoptosis mediated by broxbam was studied in the present study in two liver cancer cell lines with distinct p53 statuses. HepG2 cells represents a p53-wild-type cell line whereas Huh7 cells harbour a mutated codon in the p53 gene leading to the overexpression of the functionally-repressed p53 (63). Caspase-3 activation by broxbam was more pronounced in the p53-native HepG2 cells compared with that in the p53-mutated Huh7 cells. However, broxbam promoted p53 phosphorylation in both cell models without altering the expression of the total p53 protein. By contrast, vorinostat did not alter p53 phosphorylation in either of the cell models, whilst significantly downregulating p53 expression in Huh7 cells. It is tempting to speculate that this may be the result of differences in the HDAC subtype specificity between broxbam and vorinostat, especially in their inhibitory activities towards HDAC6 activity. However, further research is required to clarify this putative association. It is noteworthy that broxbam can induce p53 phosphorylation both in cells with wild-type and mutant p53, whilst vorinostat could not induce p53 phosphorylation.

Evaluation of the effects of broxbam and vorinostat on HDAC revealed that neither of the compounds significantly influenced the protein expression of the HDAC subtypes -1, -2, -4 and -6, instead inhibiting their HDAC enzyme activity. Subtype-specific profiling revealed pronounced differences in the ability of broxbam and vorinostat to inhibit HDAC6. Whilst broxbam potently inhibited HDAC6 activity (>90%) at a concentration of 10 μM, vorinostat could only mediate a comparatively weak inhibition of 20%.

HDAC6 is a unique member of the HDAC family not only for its role in histone acetylation and deacetylation, but also in targeting several non-histone substrates, such as cortactin and heat shock protein 90, thereby regulating cell proliferation, metastasis, invasion, and mitosis in tumours of SKOV3 human ovarian cancer cells (64). Accordingly, it has been previously demonstrated that HDAC6 inhibition can lead to the inhibition of cell proliferation, apoptosis, reduction in migration and motility of fibroblasts, SKOV3 ovarian cancer, SKBR3 breast carcinoma, and MCF7 breast cancer cell lines (65). This is consistent with observations in the present study with regards to the broxbam-mediated HDAC6 inhibition of liver cancer cells. HDAC6-specific siRNA silencing in Huh7 cells,

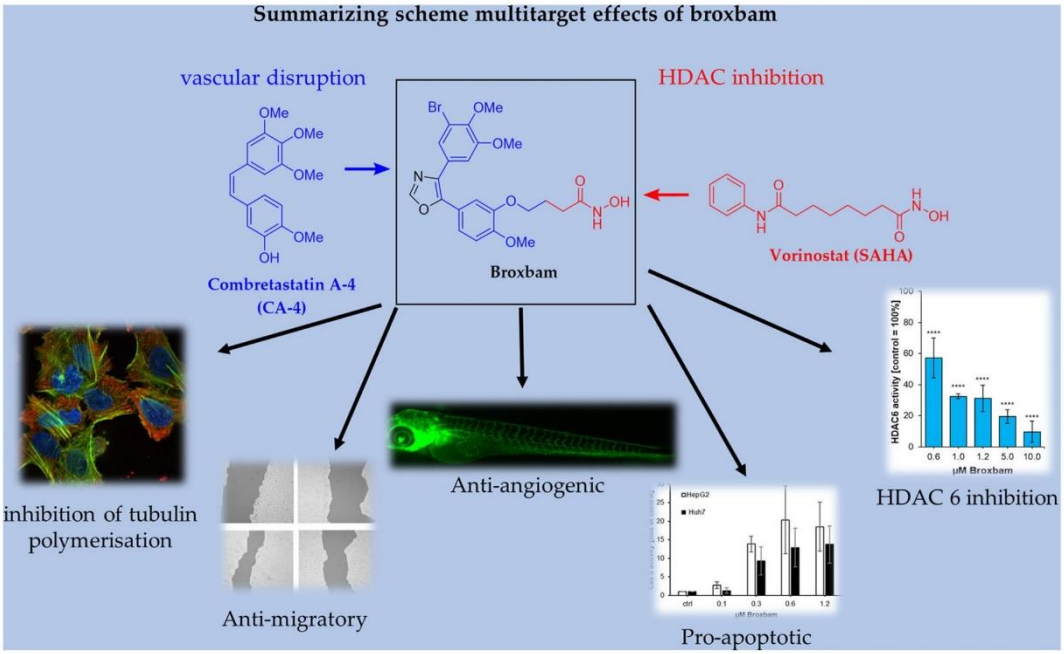

Figure 13. Pleiotropic effects of broxbam. According to the present study, broxbam exerted anti-angiogenic functions, inhibited HDAC activity, disrupted cytoskeletal dynamics and induced apoptosis. HDAC, histone deacetylase.

which mimicked the effects of HDAC6 inhibition exerted by broxbam, led to a significant downregulation of proliferation markers Ki67 and E2F3. α-Tubulin is another non-histone substrate that can be deacetylated by HDAC6 (54,56,66). HDAC6-dependent deacetylation of tubulin has been reported to result in potent effects on cytoskeletal dynamics and cell migration (54,66,67). HDAC6 has also been previously associated with the function of microtubule dynamics and regulation of microtubule-dependent cell migration (54). In the present study, broxbam-treated liver cancer cells displayed profound alterations in their cytoskeleton components F-actin and microtubules. After microtubules become disrupted, f-actin stress fibres and focal adhesions are formed in response (68,69). The cytoskeletal effects of broxbam exceeded those mediated by vorinostat, which corresponded with the weaker inhibitory effects of vorinostat on HDAC6 activity.

Broxbam was also found to exert antiangiogenic effects *in vivo*, as shown by the suppression of SIV growth in the zebrafish embryos. This effect was visible already at nM concentrations, resembling the antiproliferative IC_{50} values of broxbam in liver cancer cells. Notably, the antiangiogenic effects of broxbam were not accompanied by signs of cardiotoxicity or impairments in the development of zebrafish embryos, which are known to be highly sensitive to toxic stress (70). The antiangiogenic effects of broxbam were likely to be due to a combination of mechanisms, with contributions from both pharmacophores contained within the structure of this chimeric compound. In this respect, HDACis are known to inhibit VEGF-induced angiogenesis *in vitro* as well as *in vivo* (71), such that CA-4-driven anti-angiogenesis has also been linked to the inhibition of VEGF (72). However, tumour vasculature disrupting agents, especially those derived from CA4, have been shown to confer a high toxicity risk (59). Therefore, although broxbam contains a CA4-derived pharmacophore, it did not mediate toxic effects. This suggests that the effects of this novel chimeric compound may instead arise from its inhibitory effects on HDACs. The present study revealed that HDAC6-specific knockdown resulted in the downregulation of E2F3 expression in Huh7 cells. E2F3 is regarded to be a key factor for endothelial cell proliferation and angiogenesis (73). Therefore, it is conceivable that the pronounced HDAC6 inhibition of broxbam substantially contributed to its antiangiogenic effects due to the suppression of endothelial E2F3 expression. Further study is warranted to verify this hypothesis. The effects of broxbam on liver cancer cells revealed in the present study are summarized in Fig. 13.

Currently available treatment options for advanced and inoperable liver cancer are restricted to multi-kinase inhibitors, such as sorafenib or regorafenib (74). Although the therapeutic concentration of sorafenib is ~8 μM (75), lower concentrations of broxbam was able to induce pronounced antitumor effects in the *in vivo* experiments with liver cancer xenografts on the CAM of fertilised chicken eggs. In addition to the therapeutic effects mediated by this low dosage of broxbam, which probably does not induce pronounced side effects, it also exhibited pronounced antineoplastic effects. This renders broxbam to be the experimental compound for alternative approaches for clinical liver cancer treatment.

The combination of HDACis and sorafenib has previously been demonstrated to exert enhanced anticancer activity and may therefore be an advantageous approach compared with sorafenib monotherapy (51,76,77). Freese *et al* previously reported that HDACi sensitised HCC cells to sorafenib treatment (78), which may be due to the overexpression of HDACs

in HCCs. In a recent review, Garmpis *et al* (51) highlighted the potential suitability of HDACis as anticancer agents and their application in combinatorial therapies for the enhanced treatment of HCC. Although the preclinical data of HDACi-based combination therapies are promising, these authors also reported results from a critical phase 1 clinical trial in which sorafenib was tested in combination with vorinostat in patients with liver cancer. Although some patients showed good tolerability and stable disease, this treatment also led to adverse toxicities in the majority of patients, which necessitated dose modifications and prevented progression towards phase 2 clinical trial (79). In the present study, results from the preclinical *in vitro* and *in vivo* studies suggest the suitability and tolerability of this chimeric hydroxamate-trimethoxystilbene conjugate for liver cancer treatment. The fact that signs of toxicity were observed in neither zebrafish embryos nor in the CAM, couple with the findings that the chicken embryos developed and survived, suggest that broxbam may exert fewer toxic effects compared with other HDACis, including vorinostat. Future studies involving the effects of combination therapies with broxbam and sorafenib should clarify this important issue. In addition, to address the suitability of broxbam for personalised therapeutic approaches, investigation of patient-derived primary liver cancer cells should be executed.

To conclude, the present study evaluated the recently-introduced chimeric inhibitor broxbam (20) for its potential anticancer activity in liver cancer cells and the underlying molecular mechanism. Additionally, its possible antitumoral and antiangiogenic effects were examined in *in vivo* settings by performing in chick embryo and zebrafish experiments. On the basis of the presented data, broxbam is implicated to be a promising chimeric HDACi that should be evaluated further as a potential compound for liver cancer treatment, either as a monotherapy or in combination with other clinically-relevant HCC therapeutics, such as sorafenib.

Acknowledgements

Not applicable.

Funding

The present study was funded by the Else Kröner-Fresenius-Stiftung Grant No. 2016 A47 (to AD).

Availability of data and materials

The datasets used and/or analysed during the current study are available from the corresponding author on reasonable request.

Authors' contributions

SIB: Investigation, zebrafish angiogenesis assay and data analysis. AD: Investigation, crystal violet assay, real-time inhibition of cell proliferation, lactate dehydrogenase (LDH) cytotoxicity assay, western blotting, reverse transcription-quantitative PCR (RT-qPCR), apoptosis detection, HDAC activity assay, immunofluorescence assay and scratch wound healing assay. GTA: Investigation, small-interfering (si)RNA assay, western blotting and RT-qPCR. MF: Western blotting and RT-qPCR. AK: Investigation, crystal violet staining and LDH-Assay. LK: Investigation, crystal violet staining and LDH-Assay. BB: Conceptualisation, proof reading, validation. RS: Conceptualisation, validation and language proof reading. BN: Conceptualisation and CAM Assay. MH: Conceptualisation and validation and proof reading. All authors have read and agreed to the published version of the manuscript. SIB, BN, MF and AK confirm the authenticity of all the raw data.

Ethics approval and consent to participate

Not applicable.

Patient consent for publication

Not applicable.

Competing interests

The authors declare that they have no competing interests.

References

1. Siegel RL, Miller KD, Fuchs HE and Jemal A: Cancer statistics, 2021. CA Cancer J Clin 71: 7-33, 2021.
2. Mosconi S, Beretta GD, Labianca R, Zampino MG, Gatta G and Heinemann V: Cholangiocarcinoma. Crit Rev Oncol Hematol 69: 259-270, 2009.
3. Bray F, Ferlay J, Soerjomataram I, Siegel RL, Torre LA and Jemal A: Global cancer statistics 2018: GLOBOCAN estimates of incidence and mortality worldwide for 36 cancers in 185 countries. CA Cancer J Clin 68: 394-424, 2018.
4. Vogel A, Cervantes A, Chau I, Daniele B, Llovet JM, Meyer T, Nault JC, Neumann U, Ricke J, Sangro B, *et al*: Hepatocellular carcinoma: ESMO clinical practice guidelines for diagnosis, treatment and follow-up. Ann Oncol 29 (Suppl 4): iv238-iv255, 2018.
5. Lim H, Ramjeesingh R, Liu D, Tam VC, Knox JJ, Card PB and Meyers BM: Optimizing survival and the changing landscape of targeted therapy for intermediate and advanced hepatocellular carcinoma: A systematic review. J Natl Cancer Inst 113: 123-136, 2021.
6. Li Y, Gao ZH and Qu XJ: The adverse effects of sorafenib in patients with advanced cancers. Basic Clin Pharmacol Toxicol 116: 216-221, 2015.
7. Tang W, Chen Z, Zhang W, Cheng Y, Zhang B, Wu F, Wang Q, Wang S, Rong D, Reiter FP, *et al*: The mechanisms of sorafenib resistance in hepatocellular carcinoma: Theoretical basis and therapeutic aspects. Sig Transduct Target Ther 5: 87, 2020.
8. Doherty B, Nambudiri VE and Palmer WC: Update on the diagnosis and treatment of cholangiocarcinoma. Curr Gastroenterol Rep 19: 2, 2017.
9. Morise Z, Sugioka A, Tokoro T, Tanahashi Y, Okabe Y, Kagawa T and Takeura C: Surgery and chemotherapy for intrahepatic cholangiocarcinoma. World J Hepatol 2: 58-64, 2010.
10. Goehringer N, Biersack B, Peng Y, Schobert R, Herling M, Ma A, Nitzsche B and Höpfner M: Anticancer activity and mechanisms of action of new chimeric EGFR/HDAC-inhibitors. Int J Mol Sci 22: 8432, 2021.
11. Biersack B, Polat S and Höpfner M: Anticancer properties of chimeric HDAC and kinase inhibitors. Semin Cancer Biol: Nov 12, 2020 (Epub ahead of print).
12. Park SY and Kim JS: A short guide to histone deacetylases including recent progress on class II enzymes. Exp Mol Med 52: 204-212, 2020.
13. Kaletsch A, Pinkerneil M, Hoffmann MJ, Jaguva Vasudevan AA, Wang C, Hansen FK, Wiek C, Hanenberg H, Gertzen C, Gohlke H, *et al*: Effects of novel HDAC inhibitors on urothelial carcinoma cells. Clin Epigenetics 10: 100, 2018.
14. Gong D, Zeng Z, Yi F and Wu J: Inhibition of histone deacetylase 11 promotes human liver cancer cell apoptosis. Am J Transl Res 11: 983-990, 2019.

15. Steinemann G, Dittmer A, Kuzyniak W, Hoffmann B, Schrader M, Schobert R, Biersack B, Nitzsche B and Höpfner M: Animacroxam, a novel dual-mode compound targeting histone deacetylases and cytoskeletal integrity of testicular germ cell cancer cells. Mol Cancer Ther 16: 2364-2374, 2017.
16. Manal M, Chandrasekar MJN, Gomathi Priya J and Nanjan MJ: Inhibitors of histone deacetylase as antitumor agents: A critical review. Bioorg Chem 67: 18-42, 2016.
17. Juan LJ, Shia WJ, Chen MH, Yang WM, Seto E, Lin YS and Wu CW: Histone deacetylases specifically down-regulate p53-dependent gene activation. J Biol Chem 275: 20436-20443, 2000.
18. Mann BS, Johnson JR, Cohen MH, Justice R and Pazdur R: FDA approval summary: Vorinostat for treatment of advanced primary cutaneous T-cell lymphoma. Oncologist 12: 1247-1252, 2007.
19. Streubel G, Schrepfer S, Kallus H, Parnitzke U, Wulff T, Hermann F, Borgmann M and Hamm S: Histone deacetylase inhibitor resminostat in combination with sorafenib counteracts platelet-mediated pro-tumoral effects in hepatocellular carcinoma. Sci Rep 11: 9587, 2021.
20. Schmitt F, Gosch LC, Dittmer A, Rothemund M, Mueller T, Schobert R, Biersack B, Volkamer A and Höpfner M: Oxazole-bridged combretastatin A-4 derivatives with tethered hydroxamic acids: Structure-activity relations of new inhibitors of HDAC and/or tubulin function. Int J Mol Sci 20: 383, 2019.
21. Méndez-Callejas GM, Leone S, Tanzarella C and Antoccia A: Combretastatin A-4 induces p53 mitochondrial-relocalisation independent-apoptosis in non-small lung cancer cells. Cell Biol Int 38: 296-308, 2014.
22. Kim JH, Yoon EK, Chung HJ, Park SY, Hong KM, Lee CH, Lee YS, Choi K, Yang Y, Kim K and Kim IH: p53 acetylation enhances Taxol-induced apoptosis in human cancer cells. Apoptosis 18: 110-120, 2013.
23. Tron GC, Pirali T, Sorba G, Pagliai F, Busacca S and Genazzani AA: Medicinal chemistry of combretastatin A4: present and future directions. J Med Chem 49: 3033-3044, 2006.
24. Hesham HM, Lasheen DS and Abouzid KAM: Chimeric HDAC inhibitors: Comprehensive review on the HDAC-based strategies developed to combat cancer. Med Res Rev 38: 2058-2109, 2018.
25. Griggs J, Metcalfe JC and Hesketh R: Targeting tumour vasculature: The development of combretastatin A4. Lancet Oncol 2: 82-87, 2001.
26. Gaspari R, Prota AE, Bargsten K, Cavalli A and Steinmetz MO: Structural basis of cis-and trans-combretastatin binding to tubulin. Chem 2: 102-113, 2017.
27. Schaller E, Ma A, Gosch LC, Klefenz A, Schaller D, Goehringer N, Kaps L, Schuppan D, Volkamer A, Schobert R, *et al*: New 3-Aryl-2-(2-thienyl)acrylonitriles with high activity against hepatoma cells. Int J Mol Sci 22: 2243, 2021.
28. Nwosu ZC, Battello N, Rothley M, Piorońska W, Sitek B, Ebert MP, Hofmann U, Sleeman J, Wölfl S, Meyer C, *et al*: Liver cancer cell lines distinctly mimic the metabolic gene expression pattern of the corresponding human tumours. J Exp Clin Cancer Res 37: 211, 2018.
29. Kasai F, Hirayama N, Ozawa M, Satoh M and Kohara A: HuH-7 reference genome profile: Complex karyotype composed of massive loss of heterozygosity. Hum Cell 31: 261-267, 2018.
30. Nakabayashi H, Taketa K, Miyano K, Yamane T and Sato J: Growth of human hepatoma cells lines with differentiated functions in chemically defined medium. Cancer Res 42: 3858-3863, 1982.
31. Monteil M, Migianu-Griffoni E, Sainte-Catherine O, Di Benedetto M and Lecouvey M: Bisphosphonate prodrugs: Synthesis and biological evaluation in HuH7 hepatocarcinoma cells. Eur J Med Chem 77: 56-64, 2014.
32. Xu L, Hausmann M, Dietmaier W, Kellermeier S, Pesch T, Stieber-Gunckel M, Lippert E, Klebl F and Rogler G: Expression of growth factor receptors and targeting of EGFR in cholangiocarcinoma cell lines. BMC Cancer 10: 302, 2010.
33. Jo JR, An S, Ghosh S, Nedumaran B and Kim YD: Growth hormone promotes hepatic gluconeogenesis by enhancing BTG2-YY1 signaling pathway. Sci Rep 11: 18999, 2021.
34. Kuete V, Sandjo LP, Ouete JLN, Fouotsa H, Wiench B and Efferth T: Cytotoxicity and modes of action of three naturally occurring xanthones (8-hydroxycudraxanthone G, morusignin I and cudraxanthone I) against sensitive and multidrug-resistant cancer cell lines. Phytomedicine 21: 315-322, 2014.
35. Gillies RJ, Didier N and Denton M: Determination of cell number in monolayer cultures. Anal Biochem 159: 109-113, 1986.
36. Korzeniewski C and Callewaert DM: An enzyme-release assay for natural cytotoxicity. J Immunol Methods 64: 313-320, 1983.
37. Nitzsche B, Gloesenkamp C, Schrader M, Ocker M, Preissner R, Lein M, Zakrzewicz A, Hoffmann B and Höpfner M: Novel compounds with antiangiogenic and antiproliferative potency for growth control of testicular germ cell tumours. Br J Cancer 103: 18-28, 2010.
38. Sivandzade F, Bhalerao A and Cucullo L: Analysis of the mitochondrial membrane potential using the cationic JC-1 dye as a sensitive fluorescent probe. Bio Protoc 9: e3128, 2019.
39. Livak KJ and Schmittgen TD: Analysis of relative gene expression data using real-time quantitative PCR and the 2(-Delta Delta C(T)) method. Methods 25: 402-408, 2001.
40. Bobadilla AV, Arévalo J, Sarró E, Byrne HM, Maini PK, Carraro T, Balocco S, Meseguer A and Alarcón T: In vitro cell migration quantification method for scratch assays. J R Soc Interface 16: 20180709, 2019.
41. Almeida VM, Bezerra MA Jr, Nascimento JC and Amorim LMF: Anticancer drug screening: Standardization of in vitro wound healing assay. J Bras Patol Med Lab 55: 606-619, 2019.
42. Serbedzija GN, Flynn E and Willett CE: Zebrafish angiogenesis: A new model for drug screening. Angiogenesis 3: 353-359, 1999.
43. Warburg O: On the origin of cancer cells. Science 123: 309-314, 1956.
44. Thorens B: GLUT2, glucose sensing and glucose homeostasis. Diabetologia 58: 221-232, 2015.
45. Kaufmann SH and Earnshaw WC: Induction of apoptosis by cancer chemotherapy. Exp Cell Res 256: 42-49, 2000.
46. Reers M, Smiley ST, Mottola-Hartshorn C, Chen A, Lin M and Chen LB: Mitochondrial membrane potential monitored by JC-1 dye. Methods Enzymol 260: 406-417, 1995.
47. Kim R, Emi M and Tanabe K: Role of mitochondria as the gardens of cell death. Cancer Chemother Pharmacol 57: 545-553, 2006.
48. Fridman JS and Lowe SW: Control of apoptosis by p53. Oncogene 22: 9030-9040, 2003.
49. Kim R, Tanabe K, Uchida Y, Emi M, Inoue H and Toge T: Current status of the molecular mechanisms of anticancer drug-induced apoptosis. The contribution of molecular-level analysis to cancer chemotherapy. Cancer Chemother Pharmacol 50: 343-352, 2002.
50. Giaginis C, Damaskos C, Koutsounas I, Zizi-Serbetzoglou A, Tsoukalas N, Patsouris E, Kouraklis G and Theocharis S: Histone deacetylase (HDAC)-1, -2, -4 and -6 expression in human pancreatic adenocarcinoma: Associations with clinicopathological parameters, tumor proliferative capacity and patients' survival. BMC Gastroenterol 15: 148, 2015.
51. Garmpis N, Damaskos C, Garmpi A, Georgakopoulou VE, Sarantis P, Antoniou EA, Karamouzis MV, Nonni A, Schizas D, Diamantis E, *et al*: Histone deacetylase inhibitors in the treatment of hepatocellular carcinoma: Current evidence and future opportunities. J Pers Med 11: 223, 2021.
52. Scholzen T and Gerdes J: The Ki-67 protein: From the known and the unknown. J Cell Physiol 182: 311-322, 2000.
53. Kim HR, Rahman FU, Kim KS, Kim EK, Cho SM, Lee K, Moon OS, Seo YW, Yoon WK, Won YS, *et al*: Critical roles of E2F3 in growth and musculo-skeletal phenotype in mice. Int J Med Sci 16: 1557-1563, 2019.
54. Hubbert C, Guardiola A, Shao R, Kawaguchi Y, Ito A, Nixon A, Yoshida M, Wang XF and Yao TP: HDAC6 is a microtubule-associated deacetylase. Nature 417: 455-458, 2002.
55. Garcin C and Straube A: Microtubules in cell migration. Essays Biochem 63: 509-520, 2019.
56. Schaks M, Giannone G and Rottner K: Actin dynamics in cell migration. Essays Biochem 63: 483-495, 2019.
57. Norouzzadeh M, Kalikias Y, Mohammadpour Z, Sharifi L and Mahmoudi M: Determining population doubling time and the appropriate number of HepG2 cells for culturing in 6-well plate. IJSBAR 10: 299-303, 2016.
58. Deng B, Luo Q, Halim A, Liu Q, Zhang B and Song G: The antiangiogenesis role of histone deacetylase inhibitors: Their potential application to tumor therapy and tissue repair. DNA Cell Biol 39: 167-176, 2020.
59. Tomaszewska B, Muzolf M, Grabysa R and Bodnar L: Cardiotoxicity of antiangiogenic drugs: Causes and mechanisms. OncoReview 11: 12-18, 2021.
60. Oda K, Arakawa H, Tanaka T, Matsuda K, Tanikawa C, Mori T, Nishimori H, Tamai K, Tokino T, Nakamura Y and Taya Y: p53AIP1, a potential mediator of p53-dependent apoptosis, and its regulation by Ser-46-phosphorylated p53. Cell 102: 849-862, 2000.

61. Matsuda K, Yoshida K, Taya Y, Nakamura K, Nakamura Y and Arakawa H: p53AIP1 regulates the mitochondrial apoptotic pathway. Cancer Res 62: 2883-2889, 2002.
62. Porter AG and Jänicke RU: Emerging roles of caspase-3 in apoptosis. Cell Death Differ 6: 99-104, 1999.
63. Lee YR and Park SY: P53 expression in hepatocellular carcinoma: Influence on the radiotherapeutic response of the hepatocellular carcinoma. Clin Mol Hepatol 21: 230-231, 2015.
64. Li T, Zhang C, Hassan S, Liu X, Song F, Chen K, Zhang W and Yang J: Histone deacetylase 6 in cancer. J Hematol Oncol 11: 111, 2018.
65. Aldana-Masangkay GI and Sakamoto KM: The role of HDAC6 in cancer. J Biomed Biotechnol 2011: 875824, 2011.
66. Gao Y, Hubbert CC, Lu J, Lee YS, Lee JY and Yao TP: Histone deacetylase 6 regulates growth factor-induced actin remodeling and endocytosis. Mol Cell Biol 27: 8637-8647, 2007.
67. Tran AD-A, Marmo TP, Salam AA, Che S, Finkelstein E, Kabarriti R, Xenias HS, Mazitschek R, Hubbert C, Kawaguchi Y, *et al*: HDAC6 deacetylation of tubulin modulates dynamics of cellular adhesions. J Cell Sci 120: 1469-1479, 2007.
68. Enomoto T: Microtubule disruption induces the formation of actin stress fibers and focal adhesions in cultured cells: Possible involvement of the rho signal cascade. Cell Struct Funct 21: 317-326, 1996.
69. Liu BP, Chrzanowska-Wodnicka M and Burridge K: Microtubule depolymerization induces stress fibers, focal adhesions, and DNA synthesis via the GTP-binding protein Rho. Cell Adhes Commun 5: 249-255, 1998.
70. Zhang C, Willett C and Fremgen T: Zebrafish: An animal model for toxicological studies. Curr Protoc Toxicol 17: 1.7.1-1.7, 2003.
71. Deroanne CF, Bonjean K, Servotte S, Devy L, Colige A, Clausse N, Blacher S, Verdin E, Foidart JM, Nusgens BV and Castronovo V: Histone deacetylases inhibitors as anti-angiogenic agents altering vascular endothelial growth factor signaling. Oncogene 21: 427-436, 2002.
72. Su M, Huang J, Liu S, Xiao Y, Qin X, Liu J, Pi C, Luo T, Li J, Chen X and Luo Z: The anti-angiogenic effect and novel mechanisms of action of Combretastatin A-4. Sci Rep 6: 28139, 2016.
73. Zhou J, Cheng M, Wu M, Boriboun C, Jujo K, Xu S, Zhao TC, Tang YL, Kishore R and Qin G: Contrasting roles of E2F2 and E2F3 in endothelial cell growth and ischemic angiogenesis. J Mol Cell Cardiol 60: 68-71, 2013.
74. Heo YA and Syed YY: Regorafenib: A review in hepatocellular carcinoma. Drugs 78: 951-958, 2018.
75. Labeur TA, Hofsink Q, Takkenberg RB, van Delden OM, Mathôt RAA, Schinner R, Malfertheiner P, Amthauer H, Schütte K, Basu B, *et al*: The value of sorafenib trough levels in patients with advanced hepatocellular carcinoma-a substudy of the SORAMIC trial. Acta Oncol 59: 1028-1035, 2020.
76. Yuan H, Li AJ, Ma SL, Cui LJ, Wu B, Yin L and Wu MC: Inhibition of autophagy significantly enhances combination therapy with sorafenib and HDAC inhibitors for human hepatoma cells. World J Gastroenterol 20: 4953-4962, 2014.
77. Bitzer M, Horger M, Giannini EG, Ganten TM, Wörns MA, Siveke JT, Dollinger MM, Gerken G, Scheulen ME, Wege H, *et al*: Resminostat plus sorafenib as second-line therapy of advanced hepatocellular carcinoma-The SHELTER study. J Hepatol 65: 280-288, 2016.
78. Freese K, Seitz T, Dietrich P, Lee SML, Thasler WE, Bosserhoff A and Hellerbrand C: Histone deacetylase expressions in hepatocellular carcinoma and functional effects of histone deacetylase inhibitors on liver cancer cells in vitro. Cancers (Basel) 11: 1587, 2019.
79. Gordon SW, McGuire WP III, Shafer DA, Sterling RK, Lee HM, Matherly SC, Roberts JD, Bose P, Tombes MB, Shrader EE, *et al*: Phase I study of sorafenib and vorinostat in advanced hepatocellular carcinoma. Am J Clin Oncol 42: 649-654, 2019.

Figure S1. Cellular glycolytic activity of Hep2G and Huh7 cells. Hep2G and Huh7 cells were either treated with solvent (Ctrl), bb at IC_{50} (0.6 μM), bb at two-fold IC_{50} (1.2 μM) or vs at two-fold IC_{50} (4.0 μM). Quantification of western blot results for GLUT2 expression in (A) Hep2G and (B) Huh7 cells. Corresponding representative western blotting images are shown in Fig. S2C-F. (C-F) Estimation of glycolytic activity. Estimation of glucose in the cell culture supernatant of (C) HepG2 and (D) Huh7 cells following 24 h of treatment. Estimation of lactate in the cell culture supernatant of (E) HepG2 and (F) Huh7 cells following 24 h of treatment. Values were normalized to cell number. n=3 per group. One-way ANOVA with Tukey's post hoc test was used to test for significance. bb, broxbam; vs, vorinostat; ctrl, control; GLUT, glucose transporter. *P<0.05 and **P<0.01 vs. ctrl.

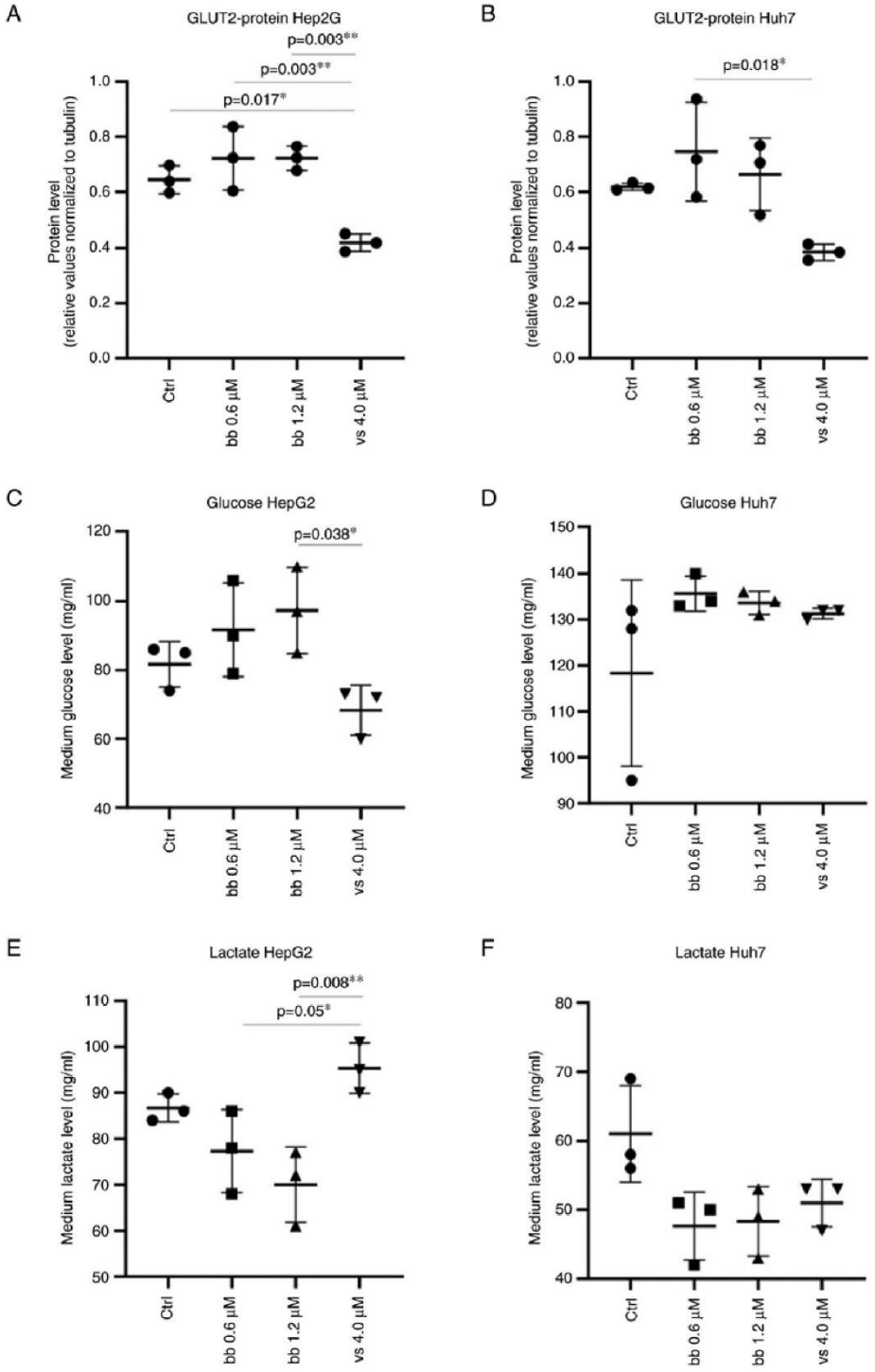

Figure S2. Representative images of the western blots in the present study. (A) Representative p53 and tubulin western blotting images of Hep2G and Huh7 cells for Fig. 5C and D. (B) Representative p-p53 and tubulin western blotting of Hep2G and Huh7 cells Fig. 5E and F. (C) Representative HDAC1 and tubulin western blotting images of Hep2G and Huh7 cells for Fig. 7A and B. (D) Representative HDAC2 and tubulin western blotting images of Hep2G and Huh7 cells for Fig. 7C and D. (E) Representative HDAC4 and tubulin western blotting images of Hep2G and Huh7 cells for Fig. 7E and F. For the detection of HDAC2 (55-60 kDa) and HDAC4 (140 kDa), the membranes were cut horizontally since their molecular weights are highly distinct. Therefore, HDAC2 and HDAC4 shared the same tubulin loading control in (D) and (E). (F) Representative HDAC6 and tubulin western blotting images of Hep2G and Huh7 cells for Fig. 7G and H. For the detection of p53 (53 kDa) and HDAC6 (160 kDa), the membranes were cut horizontally as molecular weights are highly distinct. Therefore, p53 and HDAC6 shared the same tubulin loading control in (A) and (F). (G) Representative HDAC6 and tubulin western blotting images of Huh7 cells after HDAC6 knockdown for Fig. 8D. (H) Representative GLUT2 and tubulin western blotting images of Hep2G and Huh7 cells for Fig. S1. Ctrl, control; bb, broxbam; ac, animacroxam; vs, vorinostat; p-, phosphorylated; HDAC, histone deacetylase; siRNA, small interfering RNA; GLUT, glucose transporter.

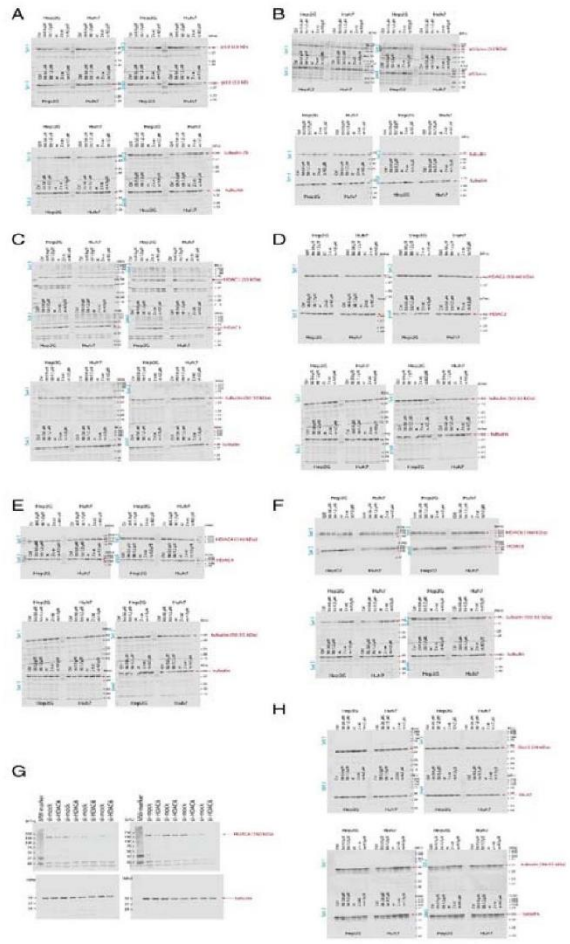

Table SI.Primer sequences used for reverse transcription-quantitative PCR.

Gene	Forward (5‘-3‘)	Reverse (5‘-3‘)
HDAC 1	ACCGGGCAACGTTACGAAT	CTATCAAAGGACACGCCAAGTG
HDAC 2	TCATTGGAAAATTGACAGCATAGT	CATGGTGATGGTGTTGAAGAAG
HDAC 3	TTGAGTTCTGCTCGCGTTACA	CCCAGTTAATGGCAATATCACAGAT
HDAC 4	AATCTGAACCACTGCATTTCCA	GGTGGTTATAGGAGGTCGACACT
HDAC 5	TTGGAGACGTGGAGTACCTTACAG	GACTAGGACCACATCAGGTGAGAAC
HDAC 6	TGGCTATTGCATGTTCAACCA	GTCGAAGGTGAACTGTGTTCCT
HDAC 7	CTGCATTGGAGGAATGAAGCT	CTGGCACAGCGGATGTTTG
HDAC 8	TCCCGAGTATGTCAGTATATATGA	GCTTCAATCAAAGAATGCACCA
HDAC 9	CAGGCGGAAGGATGGAAATG	ATGCGTTGCTGTGAAACCAT
HDAC 10	GGCCTTTGAGTTTGACCCTG	CAGCGTCTGTACTGTCATGC
HDAC 11	TGTCTACAACCGCCACATCT	CGGTGCCTGCATTGTATACC
GAPDH	GCTCATTTCCTGGTATGAC	ACAGGGTACTTTATTGATGGT
Ki-67	CGGATCGTCCCAGTGGAAG	TTGCCTCCTGCTCATGGATT
E2Ftranscriptionfactor	GCTGGAGCTAGGAGAAAGCG	CAAGAGACGTATCATACCGCGT
18SrRNA	GATCAAAACCAACCCGGTCA	CCGTTTCTCAGGCTCCCTCT

HDAC, histonedeacetylase; E2F3,

5.6 Publikation VI mit Darstellung des Eigenanteils

Publikation VI entstand unter Mitarbeit von Dr. B. Biersack Mitarbeiter des Arbeitskreises Organische Chemie I der Universität Bayreuth unter der Leitung von Prof. Dr. R. Schobert sowie unter Mitarbeit von Rohan Pradhan von der Care Group Sight Solution in Vadodara, Indien.

5.6.1 Eigenanteil an Publikation VI

Die Publikation wurde in ***Angewandte Pharmazie*** veröffentlicht, unter dem Titel

„New chimeric HDAC inhibitors for the treatment of colorectal cancer“

von den Autoren

Sofia I. Bär, Bernhard Biersack, Rohan Pradhan und Rainer Schobert

Eigenanteil:	Konzeption, Durchführung, Auswertung, graphische Darstellung und Statistik des MTT Assays, der Zellzyklusmessung, des *Colony Formation* Assays, des *Scratch Migration* Assays, der Immunofluoreszenz-Analyse des Mikrotubuli Zytoskeletts, der HDAC Aktivitätsmessung und der Western Blots. Zudem; Verfassen des Manuskripts einschließlich der Diskussion und Interpretation der Ergebnisse und Revision des Manuskripts.
Rohan Pradhan:	Durchführung der *docking* Studien sowie Verfassen der entsprechenden Manuskriptpassagen.
Bernhard Biersack:	Synthese und Charakterisierung der Testsubstanzen sowie Verfassen der entsprechenden Manuskriptpassagen.
Rainer Schobert:	Überarbeitung und Korrektur des Manuskripts, einschließlich der Diskussion und Interpretation der Ergebnisse und Revision des Manuskripts

5.6.2 Publikation VI

New chimeric HDAC inhibitors for the treatment of colorectal cancer

Sofia I. Bär [a,*], Rohan Pradhan [b], Bernhard Biersack [a] and Rainer Schobert [a]

[a] Organic Chemistry Laboratory, University of Bayreuth, Universitaetsstrasse 30, 95440 Bayreuth, Germany

[b] Care Group Sight Solution Pvd. Ltd., Dabhasa, Vadodara, 391440, India

*E-mail: sofia.baer@uni-bayreuth.de

Arch. Pharm. Inorg., **2023**, 356, 2200422

https://doi.org/10.1002/ardp.202200422

Received: 8 August 2022 | Revised: 12 October 2022 | Accepted: 14 October 2022

DOI: 10.1002/ardp.202200422

FULL PAPER

ARCH PHARM DPhG
Archiv der Pharmazie

New chimeric HDAC inhibitors for the treatment of colorectal cancer

Sofia I. Bär[1] | Rohan Pradhan[2] | Bernhard Biersack[1] | Bianca Nitzsche[3] | Michael Höpfner[3] | Rainer Schobert[1]

[1]Organic Chemistry Laboratory, University of Bayreuth, Bayreuth, Germany

[2]Care Group Sight Solution Pvt. Ltd., Dabhasa, Vadodara, India

[3]Institute of Physiology, Charité-Universitätsmedizin Berlin, Corporate member of Freie Universität Berlin, Humboldt-Universität zu Berlin and Berlin Institute of Health, Berlin, Germany

Correspondence
Sofia I. Bär, Organic Chemistry Laboratory, University of Bayreuth, Universitätsstraße 30, D-95447 Bayreuth, Germany.
Email: sofia.baer@uni-bayreuth.de

Abstract

Colorectal cancer is the third most common cause of cancer-associated deaths due to a high recurrence rate and an increasing occurrence of resistance to established therapies. This highlights the importance of developing new chemotherapeutic agents. The current study focuses on cancer-specific targets such as apoptosis-inhibiting survivin, which distinguishes cancer cells from healthy tissue. A combination of pharmacophores of established anticancer agents to afford chimeric pleiotropic chemotherapeutic agents was tested on this cancer entity. We analysed the effects of the dual mode anticancer agents, animthioxam, brimbam, troxbam, and troxham, as well as their structural congeners suberoylanilide hydroxamic acid and combretastatin A-4 on human cancer cell lines. Their cytotoxicity was determined using the MTT assay, further techniques for detecting apoptotic events, cell cycle analyses, clonogenic and wound healing assays, immunostaining, histone deacetylase (HDAC) activity measurements, and Western blot analysis for the detection of survivin expression in HCT116 colon cancer cells. Molecular docking studies were conducted to assess potential molecular targets of the test compounds. The test compounds were found selectively cytotoxic toward cancer cells by inducing apoptosis. The metastatic potential was effectively reduced by disruption of the microtubular cytoskeleton. The test compounds were also proven to be general HDAC inhibitors and to lead to reduced survivin expression.

KEYWORDS
chimeric compounds, colorectal cancer, histone deacetylase, hydroxamic acid, survivin

Abbreviations: CA-4, combretastatin A-4; HDAC, histone deacetylase; HDACi, HDAC inhibitor; IAP, inhibitor of apoptosis protein; LDH, lactate dehydrogenase; MTT, 3-(4,5-dimethylthiazol-2-yl)-2,5-diphenyltetrazolium bromide; SAHA, suberoylanilide hydroxamic acid.

1 | INTRODUCTION

Colorectal cancer is the third most common cause of new cases and deaths associated with cancer disease.[1] It features a high recurrence rate, not least because of aggressive medical procedures.[2] In addition, the frequency of occurrence of resistance against established drug regimens, for example, such employing 5-fluorouracil, is soaring for this cancer entity.[3] Hence, the quest for new treatment options needs to be intensified. One such new approach might be to identify cancer-only molecular modulators and targets for specially tailored new chemotherapeutic agents. The modulators of malignant tumors are as diverse as the disease itself. However, cancer cells share some common features, dubbed the hallmarks of cancer, that distinguish them from nonmalignant cells.[4–6] So far, these hallmarks comprise 14 central distinctive features, innate and acquired.[4,5] Histone deacetylase (HDAC) inhibitors (HDACis), show significant anticancer activity against leukemia as well as solid tumors, targeting the hallmark of replicative immortality through disruption of the DNA replication machinery.[4,5,7] The anticancer HDACi SAHA (vorinostat) is FDA approved for the treatment of patients with cutaneous T-cell lymphoma. Today, there are also numerous preclinical studies investigating the suitability of SAHA and other HDACi for the treatment of solid tumors, with promising results.[8,9] There are four classes of human HDAC enzymes containing a family of 18 members; class I comprises of HDACs 1–3 and 8, class II contains HDACs 4-7 as well as 9 and 10, class III members are called sirtuins and class IV comprises HDAC 11.[10,11] Each HDAC member displays different functions including deacetylation of histones as well as acting on non-histone substrates such as transcription factor p53 or cytoskeletal protein tubulin.[11] HDAC classes fall into two main groups as to their catalytic mechanisms. Classes I, II and IV are so called classical HDACs whose mechanisms of action are Zn^{2+} dependent, whereas class III sirtuins act NAD^{+} dependently.[11] SAHA inhibits class I and II HDACs at nanomolar concentrations.[11,12] A distinct downstream association of inhibition of HDAC 3 and 6 (members of class I and II HDACs) with a reduced survivin expression was reported.[13] This may be due to the inhibition of acetylation, where HDACs 3 and 6 specifically interact with survivin.[13] In particular, HDAC 6 which is present as a cytosolic protein, is known to control nuclear transport and thus the activity of survivin.[14,15] Survivin plays several roles regarding cell proliferation and survival as it improves the stability of microtubules, it is involved in cell cycle regulation, and as a member of the inhibitor of apoptosis proteins (IAP) it interferes with caspases 3 and 7. Further, it is nearly exclusively expressed in cancer cells and usually not expressed in most adult tissues, therefore it represents an interesting target for cancer therapy.[16–19] Since survivin is overexpressed in most cancer types, including colon, therapies inhibiting survivin expression might be highly cancer-specific, yet entity overarching.[16,20] Substances that target survivin have been of great interest in the last 20 years and there are several studies on survivin-related cancer treatments using small molecule inhibitors. Unfortunately, these studies failed due to various problems, such as too low selectivity, too high toxicity. An approach to circumvent these problems and to increase the effectiveness of the inhibitors is the use of hybrid substituents comprising a dual or synergistic mechanism of action.[21] Structural hybridization has already yielded several promising new anticancer compounds showing enhanced potency when compared to their individual structural constituents.[22] The structural motif "hydroxamic acid" is the central pharmacophore of HDACi SAHA and it is particularly easy to introduce into hybrid drugs.[23] In this work, a series of chimeric structures was synthesized by combining the crucial structural hydroxamic acid of SAHA with the *cis*-stilbene motif of the microtubule-destabilizing combretastatin A-4 (CA-4) (Figure 1). The resulting chimeric compounds were expected to have a pleiotropic mechanism of action and thus to achieve an optimization of action when compared to the lead compound SAHA. As a result of the dual attack with HDACi-mediated action and CA-4 mediated action, an enhanced or even synergistic effect can be expected, as has already been demonstrated for similar compounds.[24,25]

2 | RESULTS AND DISCUSSION

2.1 | Chemistry

The synthesis of the test compounds troxbam and troxham was described before (Scheme 1).[24] The new compound animthioxam was prepared from *t*-butyl 3-(5-formylthien-2-yl)acrylate **1** (obtained by Heck reaction of 5-bromo-2-formylthiophene with *t*-butyl acrylate), which underwent a van Leusen reaction with anisyl-TosMIC and methylamine leading to *t*-butyl cinnamate **2** in *t*-butanol (Scheme 1). Deprotection with TFA followed by reaction with THP-protected hydroxylamine led to compound **3**, which was converted to animthioxam upon treatment with 4 M HCl/dioxane in a methanolic solution. Brimbam was obtained in a similar way from

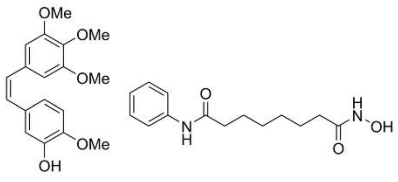

FIGURE 1 Lead structures of the chimeric compound series presented in this work. CA-4 is a microtubule polymerization inhibitor and SAHA an established HDACi. CA-4, combretastatin A-4; SAHA, suberoylanilide hydroxamic acid.

SCHEME 1 Syntheses and structures of hydroxamic acids used in this study. Reagents and conditions: (i) anisyl-TosMIC reagent, 33% $MeNH_2$/EtOH, K_2CO_3, *t*-BuOH, reflux, 2 h, 31%–79%; (ii) TFA, CH_2Cl_2, r.t., 1 h, then EDCI, DMAP, Et_3N, THPO-NH_2, CH_2Cl_2, r.t., 24 h, 57%–94%; (iii) 4 M HCl/dioxane, CH_2Cl_2/MeOH, r.t., 1 h, 81%–91%; (iv) 1 M NaOH, MeOH, r.t., 24 h, 100%; (v) *t*-BuOH, EDCI, DMAP, CH_2Cl_2, r.t., 24 h, 48%.

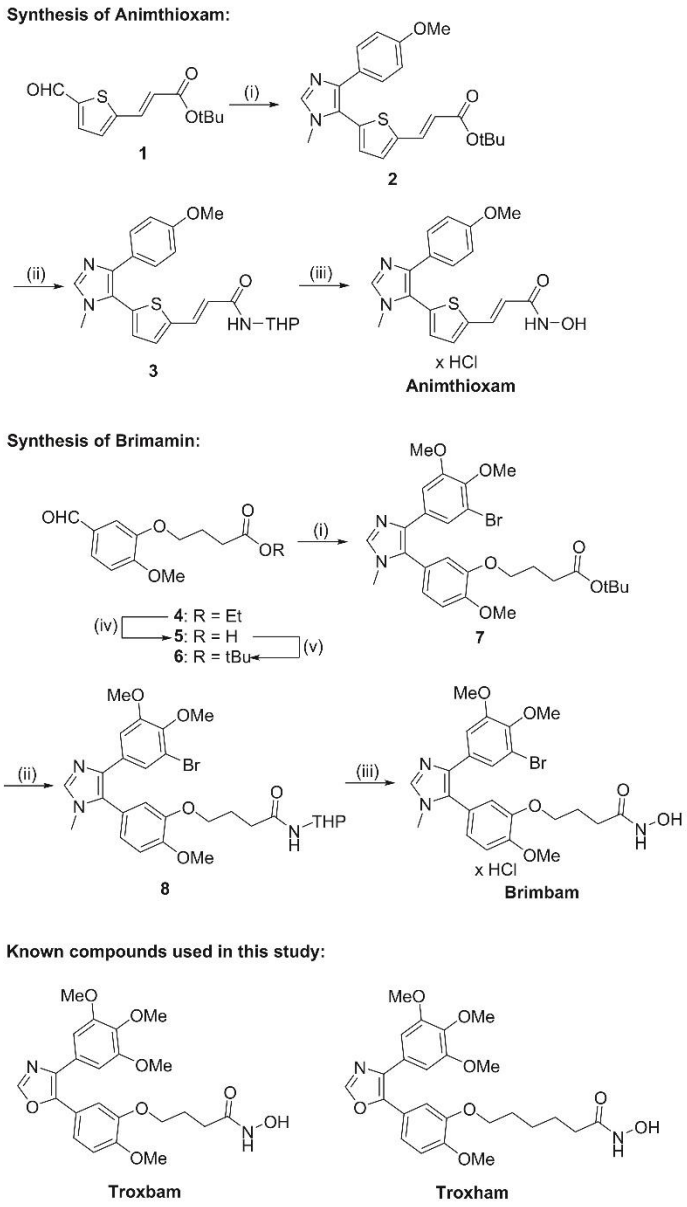

t-butyl ester **6**, which was obtained from ethyl-ester **4** followed by hydrolysis and esterification with *t*-butanol (Scheme 1).[24] Compound **6** was converted to imidazole **7** by reaction with 3-bromo-4,5-dimethoxyphenyl-TosMIC and methylamine. Removal of the *t*-butyl group by TFA afforded a carboxylic acid which was reacted with THP-protected hydroxylamine to give amide **8** which was deprotected with 4 M HCl/dioxane to furnish the target compound brimbam.

2.2 | Biological and biochemical evaluation

2.2.1 | Cytotoxicity toward cancer cells via the apoptotic pathway

Previously, some chimeric HDACi were reported to show distinct antiproliferative activity against cancer cells with IC_{50} values ranging from low µM to nM.[24,25] Troxbam and troxham already showed potent anticancer activity in earlier preliminary studies, which were not followed up on.[24] To ascertain the antiproliferative activity of the new chimeric HDACi candidates animthioxam and brimbam their IC_{50} values against several human cancer cell lines were assessed using MTT viability assays. Also, the IC_{50} values of the known analogues were completed to enable a meaningful comparison of their activities. Healthy cells (HDFa) were included in the cell line panel, and a selectivity index (SI) was calculated for each test compound. Table 1 summarizes the IC_{50} and SI values of the test compounds as well as of their structural congeners CA-4 and SAHA. All tested compounds exhibited IC_{50} values in the low µM to nM range whereas their cytotoxicity against the nonmalignant HDFa cells was low (≥50 µM). Troxbam stands out as the most active substance with the highest selectivity for cancer cells with an SI of >68.1. Regarding structure–activity relations, a longer linker (as in troxham vs. troxbam), or insertion of heteroatoms and changes of the trimethoxy motif (animthioxam and brimbam), appear to have a slightly negative effect on the antiproliferative activity.

In this study, the potential suitability of hybrid HDACi for the treatment of solid tumor entities was to be investigated. Since, on average, all test compounds were most active in colorectal cancer and comprise IC_{50} values in a similar concentration range, these cells were used for further experiments. Because many cancers lack a regulated induction of apoptosis, new potential anticancer drugs should be capable of inducing apoptotic cancer cell death.[26] The activities of effector caspases 3 and 7 are directly linked to activation of apoptosis pathways since they are key mediators of the mitochondrial apoptotic pathway.[27] To exclude necrosis playing a role in cancer cell death initiated by the new compounds, the lactate dehydrogenase (LDH) release by cancer cells upon compound treatment was measured.[28] As shown by fluorescent caspase 3/7 activity assays, all test compounds led to a significant induction of apoptosis when applied to colon cancer cells (Figure 2a), whereas no appreciable rise in LDH was detectable (Figure 2b). The induction of apoptosis in cancer cells is crucial for potential anticancer drugs since the suppression of apoptosis is one of those hallmarks of cancer, modulated by IAPs through direct inhibition of caspase 3/7.[29,30] The main cancer-specific IAP is called survivin, involved in several cancer-specific survival mechanisms and therefore comprising an interesting target for anticancer drugs.[17]

2.2.2 | Effects on the cell cycle progression of HCT116 colon carcinoma cells

To further elucidate the mechanism of action of our compounds, we analysed their effects on the progression of the cell cycle of $HCT116^{wt}$ colon carcinoma cells. Whereas all tested compounds led to a slight enhancement of the apoptotic cell fraction, only troxbam induced a distinct cell cycle arrest in the G2-M phase. This G2-M arrest is considerably more pronounced than that initiated by treatment with SAHA which is known to induce a G2-M arrest (Figure 3). A G2-M arrest is often associated with HDAC inhibition and induction of apoptosis by downregulation of the IAP survivin.[31,32]

2.2.3 | Metastatic potential and cellular dynamics

Virtually limitless cellular reproductive potential is one of the hallmarks of cancer. Therefore, we assessed the influence of our test compounds on this characteristic using the

TABLE 1 IC_{50} values (µM) of test compounds animthioxam, brimbam, troxbam, troxham as well as positive controls CA-4 and SAHA against the human cancer cell lines $HCT116^{wt}$ and its knockout mutant $HCT116^{p53}$ colon cancer, 518A2 melanoma, Huh7 and HepG2 liver cancer, as well as healthy human dermal fibroblasts (HDFa)

Compound	$HCT116^{wt}$	$HCT116^{p53-/-}$	518A2	Huh7	HepG2	HDFa	SI
Animthioxam	2.09 ± 0.45	1.42 ± 0.22	2.49 ± 0.28	3.53 ± 0.39	2.3 ± 0.2	>50	≥21.1
Brimbam	3.19 ± 0.21	1.9 ± 0.2	8.08 ± 0.92	9.27 ± 0.47	3.44 ± 0.80	>50	≥9.7
Troxbam	0.92 ± 0.12[a]	0.98 ± 0.03	0.64 ± 0.07[a]	0.95 ± 0.06[a]	0.18 ± 0.02[a]	>50	≥68.1
Troxham	0.61 ± 0.07[a]	0.8 ± 0.08	3.3 ± 0.3[a]	1.05 ± 0.04	3.4 ± 1	>50	≥27.3
CA-4	0.0026 ± 0.0002[a]	0.095 ± 0.03	0.018 ± 0.007[a]	0.045 ± 0.0041	0.0044 ± 0.00067	0.098 ± 0.0058	19.5
SAHA	0.9 ± 0.1[a]	1.10 ± 0.16	1.8 ± 0.1[a]	1.8 ± 0.5[b]	2.1 ± 0.4[b]	>50	≥32.5

Note: The selectivity index (SI) indicates the selectivity of the substances for cancer cells. Shown are the means ± standard deviation (SD) determined of four independent experiments. IC_{50} values were obtained by MTT assays from dose-response curves after 72 h incubation.

[a]Values obtained from Schmitt et al.[24]

[b]Values obtained from Bär et al.[25]

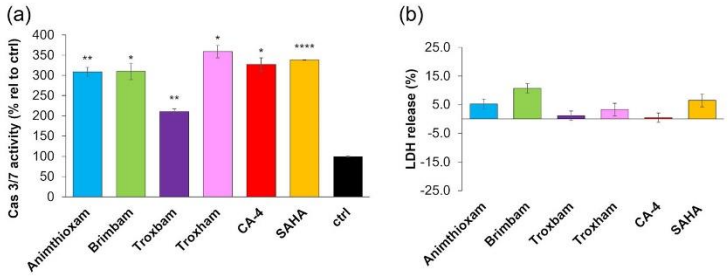

FIGURE 2 Results of the investigation of the type of cell death induced by treatment of the cells with the compounds. (a) Activation levels of effector caspases 3 and 7 in HCT116^{wt} cells after treatment with fourfold IC_{50} concentrations of compounds for 24 h. Corresponding concentration of DMSO was used as control (ctrl), set to 100%. Data shown represents means ± SD of four independent experiments, $^{****}p \le 0.001$; $^{**}p \le 0.01$; $^{*}p \le 0.05$, no sign means not significant. (b) LDH release of HCT116^{wt} cells after treatment with fourfold IC_{50} concentrations of compounds for 24 h. Corresponding concentration of DMSO was used as control (ctrl) which was set as 0% and maximum LDH release obtained by cell lysis was set as 100%. Data shown represents means ± SD of four independent experiments. CA-4, combretastatin A-4; DMSO, dimethyl sulfoxide; LDH, lactate dehydrogenase; SAHA, suberoylanilide hydroxamic acid.

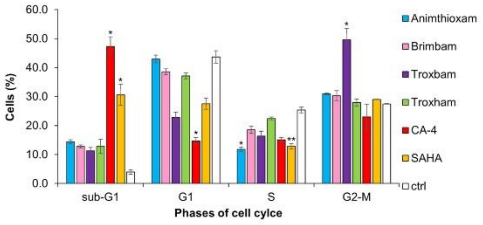

FIGURE 3 Distribution of HCT116^{wt} cells in different phases of the cell cycle measured by flow cytometry of PI stained cells. Cells were treated with IC_{50} of compounds for 24 h. Corresponding amounts of DMSO served as control (ctrl). Data represents the percentage of cells in each phase of the cell cycle as well as dead cells (sub-G1). Values represent means ± SD of three independent experiments. $^{**}p \le 0.01$; $^{*}p \le 0.05$, no sign means not significant. CA-4, combretastatin A-4; DMSO, dimethyl sulfoxide; SAHA, suberoylanilide hydroxamic acid.

clonogenic assay.[33,34] The clonogenic assay is used to assess the clonogenic potential of cells under the influence of test compounds or to assess the influence of other factors on the ability of single cells to form colonies. The clonogenic assay allows to measure and compare the percentage of cells that have the characteristic of being colony-forming.[34] As shown in Figure 4, the treatment of HCT116^{wt} colon carcinoma cells with IC_{50} concentrations of brimbam and troxbam resulted in a significant reduction of the clonogenic potential, whereas animthioxam and troxham did not significantly reduce the clonogenic potential. Both control substances CA-4 and SAHA induced a significant reduction of the clonogenic potential whereas the effect of CA-4 was clearly stronger and SAHA had only a weak effect. The effect induced by the test compounds brimbam and troxbam exceeded that of SAHA.

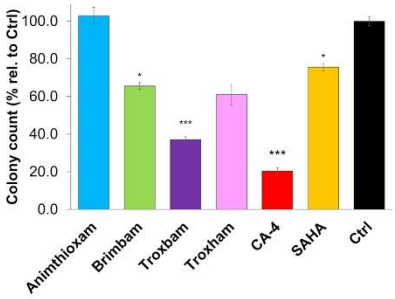

FIGURE 4 Colony count of HCT116^{wt} colon carcinoma cells obtained by colony formation assays after treatment of cells with IC_{50} of compounds for 24 h, respective concentration of DMSO served as control (Ctrl). The number of colonies is calculated as a percentage relative to the control which was set as 100%. Data shown represents means ± SD of three independent experiments, $^{***}p \le 0.005$; $^{*}p \le 0.05$, no sign is equivalent to not significant. CA-4, combretastatin A-4; DMSO, dimethyl sulfoxide; SAHA, suberoylanilide hydroxamic acid.

Taking into account the reduced clonogenic potential as well as the induction of potential HDACi-associated cell cycle arrests of colon carcinoma cells, we determined the influence of the test compounds on cellular migration using in vitro wound healing assays, monitoring the migration of the cells on a 2D surface. Brimbam and troxbam led to significant reductions in cellular migration when applied at IC_{50} concentration. Animthioxam and troxham did not attenuate the cellular motility much (Figure 5). While the effects of brimbam and troxbam were comparable to that of SAHA, CA-4 led to distinctly stronger retardation of cell migration.

To understand more precisely what the antimigratory effect is based on, we further observed the effect of test compounds on the

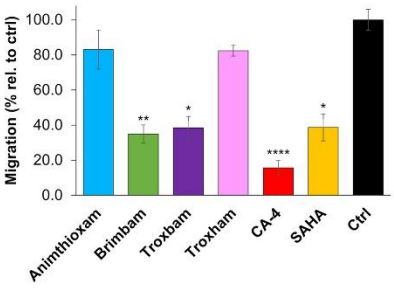

FIGURE 5 Cell migration of HCT116^{wt} colon carcinoma cells obtained by scratch migration assays under treatment of cells with IC_{50} of compounds for 24 h, respective concentration of DMSO served as control (Ctrl). Migration is calculated as a percentage relative to control which was set as 100%. Data shown represents means ± SD of three independent experiments, ****$p \leq 0.001$; ***$p \leq 0.005$; **$p \leq 0.01$; *$p \leq 0.05$, no sign is equivalent to not significant. CA-4, combretastatin A-4; DMSO, dimethyl sulfoxide; SAHA, suberoylanilide hydroxamic acid.

polymerization of purified tubulin monomers (Supporting Information: Figure 1). No inhibitory effect on tubulin polymerization could be observed for any of our test compounds, indicating a mode of action different to that of CA-4. HDACs mainly regulate the acetylation level of histones but also regulate the acetylation levels of nonhistone substrates such as tubulin.[35] HDACi like SAHA are known to act antimigratorily by inhibiting HDAC 6, which is a known key regulator of cytoskeleton dynamics, cell migration and cell–cell interactions.[35,36] As an effect of inhibiting these HDACs, the deacetylation of ac-α-tubulin is inhibited, which is resulting in altered cell dynamics as it disrupts the microtubule polymerization-depolymerization balance.[35] We immunostained the microtubule cytoskeleton of substance-treated cells to assess whether there are structural abnormalities associated with over-acetylation as a result of inhibited HDACs. The immunofluorescence images in Figure 6 reveal distinct structural changes of the microtubule skeleton upon treatment with active compounds. Brimbam and troxbam, in particular, led to clumpy-looking microtubules in colon cancer cells. The effect of CA-4 on the microtubules differs conspicuously, leading to a complete dissolution of the tubulin cytoskeleton.

2.2.4 | HDAC-associated mode of action

Results obtained so far clearly indicate an HDAC-associated mode of action for our test compounds. Based on this, their general HDAC inhibitory potential in HCT116 colon cancer cells was assessed using a commercial HDAC activity assay. The test compounds led to a reduction of general HDAC activity, with troxbam displaying the strongest effect, not much weaker than that of the clinically established HDACi SAHA (Figure 7a). Based on the demonstrated changes in tubulin dynamics, an association with inhibition of HDAC 6 is possible. Therefore, the most potent compound troxbam was investigated for its inhibitory effect on human HDAC 6. As shown in Figure 7b, concentration-dependent inhibition of HDAC 6 was obtained after troxbam treatment. The activity of HDAC 6 is almost halved by the addition of 1 µM troxbam, which corresponds to the IC_{50}. Therefore, it can be concluded that HDAC 6 inhibition is the key mechanism of action of this compound.

2.2.5 | Ac-α-tubulin levels and survivin expression levels

Taking into account the HDACi activity of our compounds, associated with apoptosis, and the cell cycle arresting effect of troxbam and alterations in microtubule cytoskeleton, we assumed HDAC 6 and downstream survivin to be very likely primary targets of them. As already mentioned by inhibition of HDAC 6, deacetylation of ac-α-tubulin is inhibited which results in reduced cellular dynamics.[35] Therefore, the expression levels of ac-α-tubulin and survivin in compound-treated colon cancer cells were assessed by means of western blot analysis. Troxbam and troxham led to significantly enhanced levels of ac-α-tubulin, while animthioxam and brimbam had no comparable effect. This is a further indication of HDAC 6 inhibition by the compounds troxbam and troxham, both comprising a stronger effect than SAHA. Troxbam and troxham also led to significantly reduced survivin expression levels, comparable to SAHA (Figure 8b). Survivin is a member of the IAP family and is involved in the regulation of the mitotic spindle dynamics, the cell cycle, angiogenesis, and chemoresistance.[17] It is a desirable target of anticancer compounds since it is strongly expressed only in cancer cells where it acts as part of the survival machinery preventing induction of apoptosis.[17] Thus, the distinct downregulation of survivin by troxbam and troxham is a milestone of their preclinical evaluation as anticancer drug candidates.

2.3 | Molecular docking

HDAC6 is associated with the cell cycle and the cellular dynamics, as well as survivin, and therefore might be a central target of test compounds. Docking studies of test compounds bound to the catalytic center of human HDAC 6 (PDB ID 5EDU) were performed to determine their binding modes. The molecular docking was carried out with the Dockthor software in the presence of the catalytic Zn^{2+} ion at the binding site (Figure 9).

Except CA-4 all the compounds are forming bonds with the Zn. The Binding energies of all the molecules are more or less in the same region (−7 to −6 kcal) with animthioxam displaying the highest binding energy at −7.1 kcal (Table 2). Troxbam and troxham are forming hydrogen bonds with high number of amino acid residues and this maybe the reason for their relatively better biological activity. CA-4 is predominantly a tubulin inhibitor and does not seem to form a bond with Zn. But it is forming bonds with three amino acid

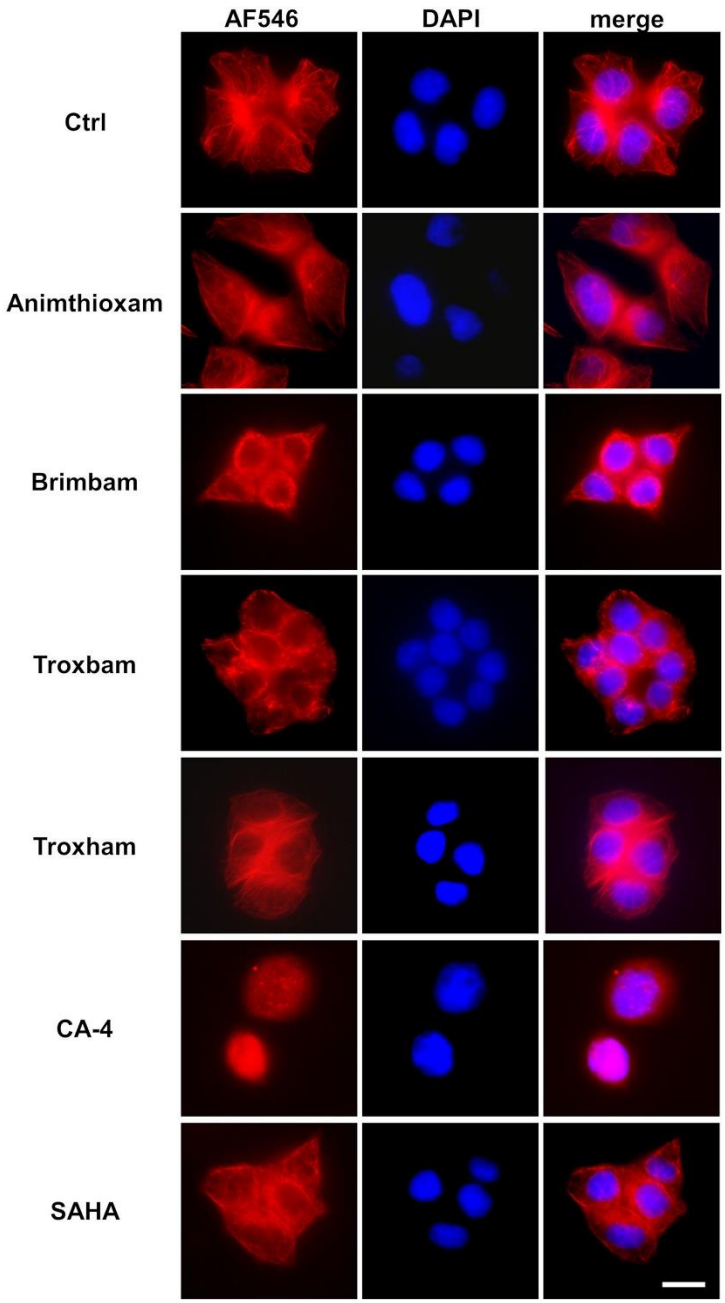

FIGURE 6 Immunofluorescence images of HCT116^{wt} cells, stained with anti-α-tubulin (AF546) and DAPI after treatment with IC_{50} concentrations of test compounds. Corresponding concentration of DMSO was used for treatment of control (Ctrl). Shown images are representative of at least three independent experiments. CA-4, combretastatin A-4; SAHA, suberoylanilide hydroxamic acid.

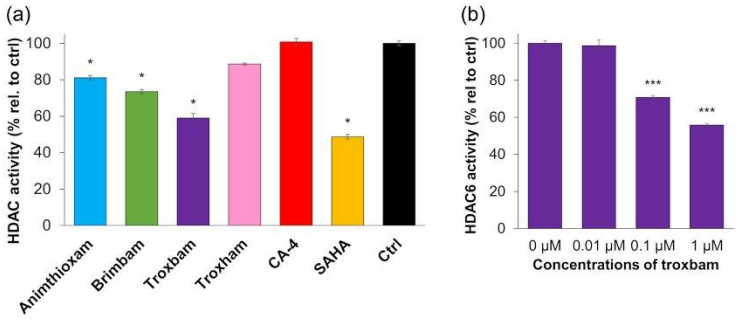

FIGURE 7 HDAC inhibitory activity of test compounds. (a) General HDAC activity of HCT116^{wt} cell lysate after treatment with IC_{50} concentrations of test compounds (animthioxam 2 µM, brimbam 3.2 µM, troxbam 0.9 µM, troxham 0.6 µM, and SAHA 0.9 µM). (b) Activity of human HDAC 6 after treatment with different concentrations of troxbam. Activities were normalized to Ctrl, respectively 0 µM, which was set to 100%. Data shown represent means ± SD of three independent experiments, $^{*}p \leq 0.05$; $^{***}p \leq 0.005$, no sign is equivalent to not significant. CA-4, combretastatin A-4; SAHA, suberoylanilide hydroxamic acid.

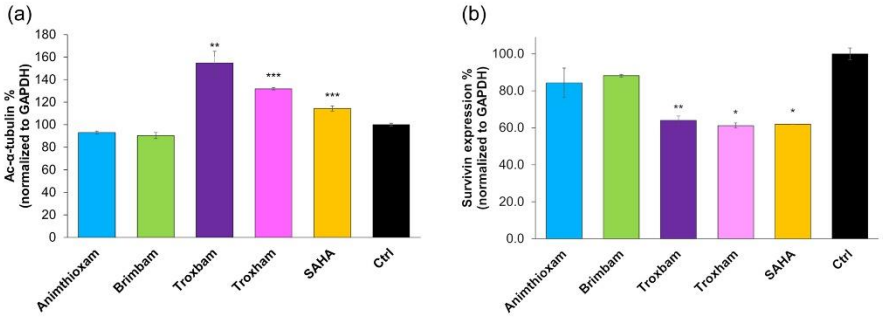

FIGURE 8 Levels of ac-α-tubulin and survivin in compound treated colon carcinoma cells. (a) Levels of ac-α-tubulin in HCT116 colon carcinoma cells, treated with corresponding IC_{50} concentrations of test compounds. (b) Survivin expression levels in HCT116 cells treated with IC_{50} concentrations of test compounds. Expression levels were normalized to GAPDH and relative to Ctrl which was set as 100%. Data shown represents means ± SD of three independent experiments, $^{*}p \leq 0.05$; $^{**}p \leq 0.01$; $^{***}p \leq 0.005$, no sign is equivalent to not significant.

residues (PHE565, THR563, and SER453) in the pocket. However, the amino acids with which it is forming bonds are quite different from the ones formed by our ligands. This difference maybe one of the reasons for the vastly different biological activities displayed by CA-4 and the compounds designed by us.

3 | CONCLUSION

Two new chimeric Z-stilbene–hydroxamate conjugates, animthioxam and brimbam, were modeled on the monomodal drugs CA-4 and SAHA. Unlike the latter, they showed multimodal, pleiotropic effects in a series of assays for anticancer activities. They were tested alongside their known structural congeners troxbam and troxham, as well as CA-4 and SAHA. Except for brimbam, all chimeric conjugates tested showed a higher selectivity for cancer cells than CA-4. Troxbam was particularly impressive with a cancer selectivity exceeding that of the established HDACi SAHA. Moreover, the cell cycle inhibitory effect of troxbam on colon carcinoma cells in G2-M phase was exceptional and significantly stronger than the effect elicited by SAHA. Troxbam also outperformed SAHA when it comes to the antimigratory effect and HDAC inhibition. Generally, HDAC 6 inhibition appears to be the main mechanism of action of the chimeric test compounds, an assumption also supported by molecular docking studies. In particular, HDAC 6 is associated with cell dynamics, and expression levels of the apoptosis inhibiting and cell cycle regulating protein survivin. In addition

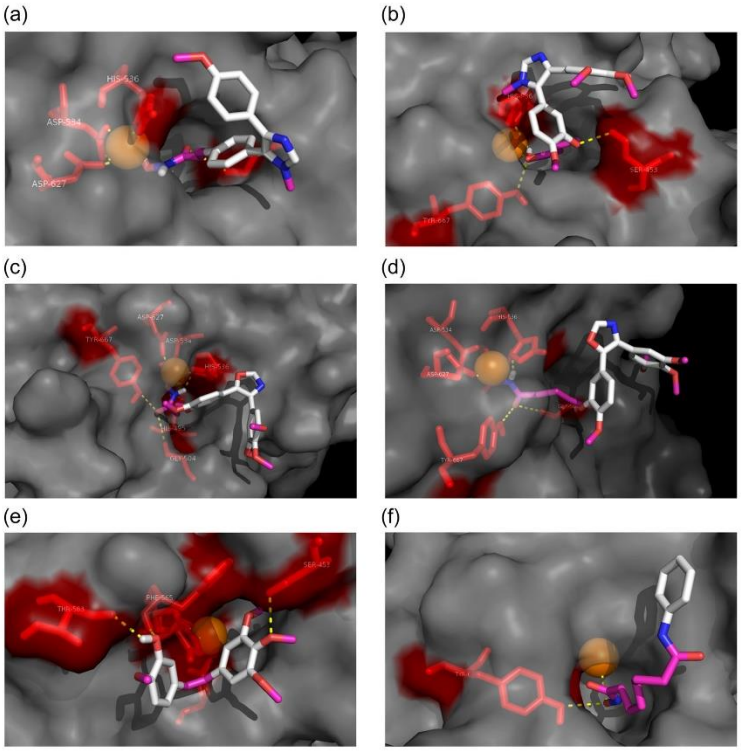

FIGURE 9 Molecular docking poses on class II HDAC6 using Docthor software. Docking images of (a) animthioxam, (b) brimbam, (c) troxbam, (d) troxham, (e) combretastatin A-4, and (f) suberoylanilide hydroxamic acid.

TABLE 2 Calculated binding energies (BE) with 5EDU of test compounds animthioxam, brimbam, troxbam, troxham, SAHA, and CA-4 using AutoDock-Vina 1.1.2 software

Compound	BE (kcal/mol)	Residues	Bond with Zn
Animthioxam	−7.1	GLY504, ASP627, HIS536, ASP534,	Yes
Brimbam	−6.5	SER453, HIS536, TYR667	Yes
Troxbam	−6.4	ASP534, HIS536, ASP627, HIS495, TYR667, GLY504	Yes
Troxham	−6.6	ASP534, GLY504, HIS495, ASP627, HIS536, TYR667	Yes
CA-4	−5.9	PHE565, THR563, SER453	No
SAHA[a]	−6.2	TYR667	Yes

to the HDAC 6 inhibitory effect, associated hyperacetylation of alpha-tubulin and decreased expression of survivin were detected upon compounds treatment of colon carcinoma cells. The observed downregulation of the cancer-specific protein survivin by troxbam and troxham adds to the multimodal and cancer-specific character of this new structural motif, recommending them for a further assessment of their suitability as chemotherapeutic agents. The results obtained in this study contribute to consider the suitability of hybrid HDACi for the treatment of solid tumors. As HDACi have so far only been approved for the treatment of leukemic disease, this raises the prospect of a new field of application for structurally related hybrid compounds.

4 | EXPERIMENTAL

4.1 | Chemistry

4.1.1 | General remarks

All starting compounds and reagents were purchased from the usual retailers and used without further purification. Column chromatography: silica gel 60 (230-400 mesh). Melting points (uncorrected), Electrothermal 9100; NMR spectra (see the Supporting Information), Bruker Avance 300 spectrometer; chemical shifts are given in parts per million (δ) downfield from tetramethylsilane as internal standard; Mass spectra, Thermo Finnigan MAT 8500 (EI), UPLC/Orbitrap (ESI-HRMS). Elemental analysis were carried out with an Elementar UNICUBE (Elementar Analysensysteme GmbH).

4.1.2 | Synthesis of animthioxam

1-Methyl-4-(4-methoxyphenyl)-5-(4′-tert.-butoxycarbonylethenyl-thienyl)imidazole (2)

A mixture of 4-formyl-tert.-butyl-2-thienylacrylate **1** (100 mg, 0.42 mmol) and 33% $MeNH_2$/ethanol (260 µl, 2.10 mmol) in *t*-butanol (15 ml) was refluxed for 2 h. After cooling to room temperature, anisyl-tosylmethylisocyanide (126 mg, 0.42 mmol) and K_2CO_3 (500 mg, 3.62 mmol) were added and the reaction mixture was refluxed for 4 h. The solvent was evaporated, the residue diluted with ethyl-acetate, washed with water and brine, dried over Na_2SO_4, filtered, and concentrated in vacuum. The residue was purified by column chromatography (silica gel 60, ethyl-acetate/methanol 9:1). Yield: 50 mg (0.13 mmol, 31%); R_f = 0.72 (ethyl-acetate/methanol, 9:1); yellow oil; ν_{max} (ATR)/cm^{-1} 2968, 2936, 2901, 2837, 1699, 1623, 1526, 1504, 1454, 1389, 1368, 1292, 1207, 1144, 1104, 1029, 968, 921, 833, 798, 743, 706, and 640; ^{1}H-NMR (300 MHz, $CDCl_3$) δ 1.49 (9H, s), 3.54 (3H, s), 3.76 (3H, s), 6.13 (1H, d, *J* = 15.6 Hz), 6.79 (2H, d, *J* = 9.0 Hz), 6.95 (1H, d, *J* = 3.7 Hz), 7.19 (1H, d, *J* = 3.7 Hz), 7.46 (2H, d, *J* = 9.0 Hz), 7.60 (1H, s), 7.63 (1H, d, *J* = 15.6 Hz); ^{13}C-NMR (75.5 MHz, $CDCl_3$) δ 28.2, 32.3, 55.1, 80.7, 113.7, 119.8, 126.6, 127.8, 128.0, 128.1, 129.9, 130.5, 130.8, 133.3, 135.5, 138.4, 141.2, 142.0, 158.7, and 165.8; *m/z* (%) 396 (37) [M^+], 340 (100), 57 (20).

1-Methyl-4-(4-methoxyphenyl)-5-(4′-tetrahydropyranyloxyaminocarbonylethenyl-thienyl)imidazole (3)

Compound **2** (79 mg, 0.20 mmol) was dissolved in CH_2Cl_2 (3 ml), treated with TFA (2 ml) and stirred at room temperature for 1 h. The solvent was evaporated, the residue was dried in vacuum and used for the next step without further purification. It was dissolved in dry CH_2Cl_2 and EDCI (101 mg, 0.52 mmol), DMAP (19 mg, 0.15 mmol), triethyl-amine (120 µl, 0.57 mmol), and tetrahydropyranyl-hydroxylamine (73 mg, 0.63 mmol) were added. After stirring at room temperature for 24 h, the solvent was evaporated and the residue was purified by column chromatography (silica gel 60, ethyl-acetate/methanol, 9:1). Yield: 50 mg (0.11 mmol, 57%), R_f = 0.56 (ethyl-acetate/methanol, 9:1); ν_{max} (ATR)/cm^{-1} 3167, 2949, 2872, 1659, 1615, 1526, 1504, 1454, 1389, 1347, 1292, 1246, 1204, 1175, 1133, 1113, 1031, 966, 947, 924, 895, 873, 834, 812, and 728; ^{1}H-NMR (300 MHz, $CDCl_3$) δ 1.58–1.96 (6H, m), 3.46 (3H, s), 3.62–3.74 (1H, m), 3.73 (3H, s), 4.05–4.10 (1H, m), 5.00–5.07 (1H, m), 5.98–6.12 (1H, m), 6.75 (2H, d, *J* = 9.0 Hz), 6.89 (1H, d, *J* = 3.7 Hz), 7.12–7.14 (1H, m), 7.47 (2H, d, *J* = 9.0 Hz), 7.58 (1H, s), 7.70–7.77 (1H, m); ^{13}C-NMR (75.5 MHz, $CDCl_3$) δ 14.1, 18.5, 21.0, 24.8, 25.0, 25.6, 28.0, 32.2, 55.1, 60.3, 62.3, 67.9, 102.5, 113.7, 117.4, 119.8, 126.2, 128.0, 130.6, 130.8, 131.0, 132.3, 138.3, 140.8, 142.8, 158.8, and 171.1; *m/z* (%) 439 (26) [M^+], 355 (100), 339 (88), 296 (37), 243 (34), 165 (21), 85 (56), and 41 (34).

1-Methyl-4-(4-methoxyphenyl)-5-(4′-hydroxyaminocarbonylethenylthienyl)-imidazole × HCl (animthioxam)

Compound **3** (50 mg, 0.11 mmol) was dissolved in CH_2Cl_2/MeOH (5 ml, 4:1) and 4 M HCl/dioxane (3 ml) was added. The reaction mixture was stirred at room temperature for 1 h. The solvent was evaporated and the residue was crystallized from ethanol/*n*-hexane. Yield: 35 mg (0.089 mmol, 81%); yellow solid of mp 178–180°C; ν_{max} (ATR)/cm^{-1} 3122, 3007, 2969, 2840, 2539, 1647, 1599, 1575, 1558, 1536, 1511, 1462, 1422, 1399, 1357, 1335, 1296, 1250, 1224, 1210, 1182, 1107, 1050, 1023, 1003, 962, 920, 852, 815, 798, 720, 709, and 689; ^{1}H-NMR (300 MHz, DMSO-d_6) δ 3.72 (3H, s), 3.77 (3H, s), 6.26 (1H, d, *J* = 15.6 Hz), 7.02 (2H, d, *J* = 8.8 Hz), 7.41–7.45 (3H, m), 7.52 (1H, d, *J* = 3.8 Hz), 7.63 (2H, d, *J* = 8.8 Hz), 9.23 (1H, s), 10.70–10.92 (1H, br s); ^{13}C-NMR (75.5 MHz, DMSO-d_6) δ 33.9, 55.3, 114.5, 119.3, 119.8, 121.3, 126.2, 129.0, 130.5, 131.0, 132.1, 133.3, 136.6, 143.7, 160.0, and 161.9; *m/z* (%) 355 (18) [M^+], 340 (100), 311 (88), 44 (77); Elemental analysis, Anal. calcd. for $C_{18}H_{18}ClN_3O_3S$: C, 55.17; H, 4.63; N, 10.72. Found: C, 55.30; H, 4.68; N, 10.64.

4.1.3 | Synthesis of brimbam

5-Formyl-2-methoxyphenyloxybutyric acid (5)

Ethyl-5-formyl-2-methoxyphenyloxybutyrate **4** (120 mg, 0.42 mmol) was dissolved in MeOH (10 ml), aqueous NaOH (1 M, 10 ml) was added and the reaction mixture was stirred at room temperature for 24 h. The solution was acidified with aqueous HCl (1 M, to pH < 2) and extracted with ethyl-acetate. The organic phase was dried over Na_2SO_4 and concentrated in vacuum. Yield: 99 mg (0.42 mmol, 100%); colorless solid of mp 127–128°C; ν_{max} (ATR)/cm^{-1} 3025, 2974, 2922, 2708, 2625, 1708, 1682, 1581, 1509, 1472, 1439, 1410, 1397, 1361, 1341, 1295, 1263, 1243, 1213, 1184, 1161, 1137, 1088, 1061, 1029, 1015, 931, 883, 858, 818, 796, 769, 750, 680, and 641; ^{1}H-NMR (300 MHz, $CDCl_3$) δ 2.15–2.19 (2H, m), 2.59 (2H, t, *J* = 7.2 Hz), 3.91 (3H, s), 4.11 (2H, t, *J* = 6.2 Hz), 6.95 (1H, d, *J* = 8.2 Hz), 7.38 (1H, s), 7.44 (1H, d, 8.2 Hz), 9.91 (1H, s); ^{13}C-NMR (75.5 MHz, $CDCl_3$) δ 24.1, 30.4, 56.1, 67.7, 110.7, 126.9, 130.0, 148.8, 154.9, 178.7, and 191.0; *m/z* (%) 238 (57) [M^+], 221 (4), 151

(100), 137 (14), 123 (22), 109 (16), 95 (13), 87 (38), 77 (13), and 43 (25).

tert.-Butyl 5-formyl-2-methoxyphenyloxybutyrate (6)

Compound **5** (99 mg, 0.42 mmol), DMAP (25 mg, 0.21 mmol) and tert.-butanol (45 µl, 0.48 mmol) were dissolved in CH_2Cl_2 (5 ml) and EDCI (88 mg, 0.46 mmol) was added. The reaction mixture was stirred at 0°C for 2 h and then at room temperature for 24 h. The reaction solution was purified by column chromatography. Yield: 60 mg (0.20 mmol, 48%); R_f = 0.76 (ethyl-acetate/*n*-hexane, 1:1); ν_{max} (ATR)/cm^{-1} 2977, 2935, 2843, 1724, 1684, 1595, 1585, 1509, 1436, 1392, 1367, 1339, 1322, 1263, 1239, 1151, 1133, 1020, 960, 922, 865, 846, 808, 778, 747, 734, and 640; ^{1}H-NMR (300 MHz, $CDCl_3$) δ 1.43 (9H, s), 2.18–2.26 (2H, m), 2.43 (2H, t, J = 7.4 Hz), 3.93 (3H, s), 4.09 (2H, t, J = 6.4 Hz), 6.95 (1H, d, J = 8.2 Hz), 7.39 (1H, s), 7.43–7.47 (1H, m), 9.82 (1H, s); ^{13}C-NMR (75.5 MHz, $CDCl_3$) δ 24.6, 28.1, 32.0, 56.1, 68.1, 80.4, 110.7, 110.9, 126.6, 130.1, 149.0, 154.9, 172.3, and 190.9; *m/z* (%) 294 (15) [M$^+$], 221 (86), 152 (100), 143 (23), 87 (96), 69 (34), 57 (45), and 41 (19).

1-Methyl-4-(3-bromo-4,5-dimethoxyphenyl)-5-(4′-methoxy-3′-tert.-butoxycarbonylpropylphenyl)-imidazole (7)

Compound **6** (141 mg, 0.48 mmol) was dissolved in tert.-butanol (10 ml) and 33% $MeNH_2$/EtOH (297 µl, 2.4 mmol) was added. The reaction mixture was stirred under reflux for 1 h. (3-Bromo-4,5-dimethoxyphenyl)-tosylmethylisocyanide (175 mg, 0.48 mmol) and K_2CO_3 (500 mg, 3.62 mmol) were added and the reaction mixture was stirred under reflux for 2 h. The solvent was evaporated, the residue was taken up in ethyl-ester and washed with water. The organic phase was dried over Na_2SO_4, filtered and the filtrate was concentrated in vacuum. The residue was purified by column chromatography (silica gel 60). Yield: 213 mg (0.38 mmol, 79%); R_f = 0.63 (ethyl-acetate); ν_{max} (ATR)/cm^{-1} 2978, 2936, 2836, 1726, 1599, 1584, 1547, 1510, 1484, 1464, 1416, 1392, 1368, 1320, 1247, 1151, 1137, 111, 1042, 1026, 1000, 947, 890, 865, 808, 759, 737, 680, 659, 638, and 619; ^{1}H-NMR (300 MHz, DMSO-d_6) δ 1.37 (9H, s), 1.88–1.93 (2H, m), 2.31–2.35 (2H, m), 3.44 (3H, s), 3.56 (3H, s), 3.67 (3H, s), 3.82 (3H, s), 3.91–3.96 (2H, m), 6.90–6.97 (2H, m), 7.05–7.16 (2H, m), 7.22 (1H, s), 7.75 (1H, s); ^{13}C-NMR (75.5 MHz, DMSO-d_6) δ 24.3, 27.7, 31.2, 31.7, 55.4, 55.6, 60.0, 67.6, 79.6, 109.5, 112.5, 115.6, 116.4, 120.9, 122.1, 123.5, 128.9, 132.5, 134.7, 137.7, 143.6, 148.1, 149.6, 152.8, and 171.7; *m/z* (%) 562 (100) [M$^+$], 560 (98) [M$^+$], 506 (23), 504 (22), 491 (25), 489 (43), 487 (22), 420 (41), 418 (45), 405 (15), 403 (16), 87 (23), 57 (17).

1-Methyl-4-(3-bromo-4,5-dimethoxyphenyl)-5-(4′-methoxy-3′-tetrahydropyranyloxyaminocarbonyl-propylphenyl)-imidazole (8)

Compound **7** (202 mg, 0.36 mmol) was dissolved in CH_2Cl_2 (3 ml), treated with TFA (2 ml) and stirred at room temperature for 1 h. The solvent was evaporated, the residue was dried in vacuum and used for the next step without further purification. It was dissolved in dry CH_2Cl_2 and EDCI (108 mg, 0.56 mmol), DMAP (21 mg, 0.15 mmol), triethyl-amine (130 µl, 0.61 mmol) and tetrahydropyranyl-hydroxylamine (78 mg, 0.67 mmol) were added. After stirring at room temperature for 24 h, the solvent was evaporated and the residue was purified by column chromatography (silica gel 60, ethyl-acetate/methanol, 9:1). Yield: 205 mg (0.34 mmol, 94%), R_f = 0.44 (ethyl-acetate/methanol, 9:1); ν_{max} (ATR)/cm^{-1} 2946, 2877, 2841, 1674, 1600, 1548, 1512, 1487, 1465, 1417, 1320, 1249, 1205, 1172, 1135, 1113, 1040, 1022, 1001, 947, 897, 868, 801, 760, 725, 680, 659, 645, 618, and 604; ^{1}H-NMR (300 MHz, $CDCl_3$) δ 1.52–1.61 (3H, m), 1.76–1.84 (3H, m), 2.08–2.13 (2H, m), 2.29–2.38 (2H, m), 3.44 (3H, s), 3.50–3.58 (1H, m), 3.64 (3H, s), 3.88–3.90 (4H, m), 3.98 (2H, *t*, J = 6.1 Hz), 4.90–4.94 (1H, m), 6.81 (1H, s), 6.81–6.96 (2H, m), 7.06 (1H, s), 7.22 (1H, s), 7.50 (1H, s), 8.95–9.02 (1H, br s); ^{13}C-NMR (75.5 MHz, $CDCl_3$) δ 18.7, 24.7, 25.0, 28.0, 29.8, 32.1, 55.7, 56.0, 60.5, 62.5, 68.2, 102.4, 109.8, 112.1, 116.0, 17.3, 122.3, 122.5, 122.8, 123.9, 128.9, 131.9, 136.3, 137.1, 144.7, 148.5, 150.1, 153.2, and 170.1; *m/z* (%) 605 (2) [M$^+$], 603 (2) [M$^+$], 561 (3), 559 (4), 521 (3), 519 (3), 505 (6), 503 (7), 477 (100), 475 (97), 420 (59), 418 (62), 405 (38), 403 (39), 380 (63), 85 (27), and 44 (49).

1-Methyl-4-(3-bromo-4,5-dimethoxyphenyl)-5-(4′-methoxy-3′-hydroxyaminocarbonylpropylphenyl)-imidazole × HCl (brimbam)

Compound **8** (205 mg, 0.34 mmol) was dissolved in CH_2Cl_2/MeOH (5 ml, 4:1) and 4 M HCl/dioxane (3 ml) was added. The reaction mixture was stirred at room temperature for 1 h. The solvent was evaporated and the residue was crystallized from ethanol/*n*-hexane. Yield: 175 mg (0.31 mmol, 91%); colorless solid of mp 157–158°C; ν_{max}(ATR)/cm^{-1} 3350, 3060, 3014, 2947, 2876, 2837, 1732, 1638, 1547, 1524, 1494, 1459, 1418, 1398, 1342, 1311, 1260, 1247, 1215, 1182, 1139, 1114, 1042, 1019, 994, 947, 888, 853, 809, 758, 739, 724, 676, 639, 620; ^{1}H NMR (300 MHz, DMSO-d_6) δ 1.85–1.98 (2H, m), 2.09–2.17 (2H, m), 3.58 (3H, s), 3.63 (3H, s), 3.72 (3H, s), 3.84 (3H, s), 3.93–3.97 (2H, m), 7.05–7.07 (1H, m), 7.15–7.26 (4H, m), 9.33 (1H, s), 10.50–10.57 (1H, br s); ^{13}C-NMR (75.5 MHz, DMSO-d_6) δ 24.6, 28.6, 33.8, 55.7, 56.1, 60.2, 68.0, 111.3, 112.6, 115.4, 116.8, 117.6, 122.3, 124.0, 127.6, 130.1, 135.5, 145.9, 148.4, 150.7, 153.2, 168.5; *m/z* (%) 520 (94) [M$^+$], 518 (93) [M$^+$], 505 (25), 503 (25), 477 (14), 475 (14), 420 (16), 418 (15), 405 (11), 403 (12), 101 (100), 59 (24), 36 (54); HRMS for $C_{23}H_{27}O_6N_3{}^{79}Br$ [M$^+$+H] calcd. 520.10777, found 520.10688, for $C_{23}H_{27}O_6N_3{}^{81}Br$ [M$^+$+H] calcd. 522.10573, found 522.10464.

4.1.4 | Synthesis of troxbam and troxham

Troxbam and troxham were obtained according to the literature.[24]

4.2 | Biological assays

4.2.1 | Stock solutions

Compounds were dissolved in DMSO to obtain a concentration of 10 mM and stored at −23°C. Before biological experiments, they

were diluted to the desired concentration with sterile Millipore water. CA-4 and SAHA were purchased from TCI chemicals.

4.2.2 | Cell lines and cell culture conditions

518A2 human melanoma cells (Department of Radiotherapy & Radiobiology, University Hospital Vienna, Austria), HCT116^{wt} (DSMZ ACC-581) and its HCT116$^{p53-/-}$ knockout mutant colon carcinoma cells, Huh7 (CVCL_0336) and HepG2 (DSMZ ACC-180) liver carcinoma as well as HDFa human dermal fibroblasts (ATCC PCS-201-012) as healthy control cell line were cultivated in Dulbeccos Modified Eagle medium (DMEM, PAN biotech), supplemented with 10% (v/v) fetal bovine serum (Sigma Aldrich) and 1% (v/v) ZellShield (Minerva Biolabs) at 37°C under 95% humidity and 5% CO_2. If not noted otherwise, all bioassay steps including cells were conducted under these standard cell culture conditions.

4.2.3 | MTT cell viability assay

The antiproliferative effect of test compounds on cancer cell lines as well as on human dermal fibroblasts was examined using the 3-(4,5-dimethylthiazol-2-yl)-2,5-diphenyltetrazolium bromide (MTT) based cell viability assay. The MTT cell viability assay was conducted as described before.[37] Briefly, cells were seeded in 96-well microtiter plates (Sarstedt) with a cell density of 0.05×10^6 cells per ml with 100 µl per well and incubated for 24 h under standard cell culture conditions. Afterwards, a dilution series of test compounds was added, followed by a further incubation step for 72 h. A 0.05% in MTT in PBS solution was added (12.5 µl/well), followed by another incubation period of 2 h. Following a centrifugation step, the medium was discarded and 25 µl per well of SDS solution in DMSO (10% SDS, 0.6% AcOH in DMSO) were added, and plates were further incubated for 1 h. Absorbance was measured at 570 nm and 630 nm using a Tecan Plate reader. Background absorbance (630 nm) was subtracted from formazan signal (570 nm). Resulting absorbance is directly proportional to viable cells, control was normalized to 100% viable cells and accordingly the viability of cells treated with test compounds was calculated. IC_{50} was calculated based on a sigmoidal fit model using GraphPad Prism. Means and SD were calculated from at least four independent experiments.

4.2.4 | Caspase 3/7 assay

Activation of caspases 3 and 7 is strongly associated with induction of apoptotic type of cell death. Levels of active caspase 3/7 in HCT116^{wt} cells were measured using a commercial caspase 3/7 activity apoptosis assay kit (green fluorescence, CellMeter™, AAT Bioquest, catalog number 22796). The protocol was in accordance with the procedure specified by the manufacturer. Briefly, the cells were seeded into a black 96-well plate as well as into a clear 96-well plate for the corresponding MTT assay. After treatment with test compounds for 24 h, the caspase 3/7 working solution was added, followed by further incubation in the dark at room temperature for 1 h. Fluorescence intensity was monitored at ex/em = 485/535 nm using a Tecan plate reader.

4.2.5 | LDH release assay[28]

HCT116^{wt} colon carcinoma cells were seeded in 96 well flat bottom microtiter plates (Sarstedt) with 100 µl per well and a cell density of 0.05×10^6 cells per ml, wells containing medium alone were additionally set for background measurement. Cells were allowed to grow overnight under standard cell culture conditions followed by substance treatment with 11.1 µl of 10-fold concentrated test compound dilutions for 24 h. For maximum LDH release 10 µl per well of lysis solution (9% Triton-X100 in Millipore H_2O) were added and incubated for 45 min, same amount was added to maximum release background correction wells containing only medium. After centrifugation (4°C, 150*g*, 5 min) 50 µl of the supernatant of each well were transferred on a fresh microtiter plate followed by addition of 50 µl LDH assay buffer (223 mg 2-*p*-iodophenyl-3-*p*-nitrophenyl-5-phenyl-tetrazolium-chloride, 57 mg *N*-methylphenazonium-methyl-sulfate, 575 mg *N*-adenine-dinucleotide, 3.2 g lactic acid in 480 ml 200 mM Tris-Cl, pH 8.0) per well. Plate was incubated in the dark for 10–30 min at room temperature. Then 50 µl stop solution (1 M acetic acid) were added per well and absorbance was measured at 490 nm. Mean value of background wells was subtracted from negative control and test wells as well as maximum LDH release wells. Afterwards percentage of LDH release was calculated, setting maximum LDH release as 100%. Means and SD were calculated from at least three independent experiments.

4.2.6 | Cell cycle distribution

The distribution of HCT116 colon carcinoma cells in the different phases of the cell cycle under influence of test compounds was analyzed using flow cytometry as recently described.[38] Briefly, cells were seeded in 6-well microtiter plates (Sarstedt) and allowed to grow for 24 h, followed by treatment with test compounds to obtain final concentrations corresponding the IC_{50} and further incubation period of 24 h. Afterward, medium and cells of each well were transferred into precooled centrifugation tubes (on ice) and centrifuged (300 g, 5 min, 4°C). The pellet was resuspended with 1 ml ice-cold EtOH (70%) and cells were fixed for at least 1 h at 4°C. Cellular DNA was stained with 200 µl propidium iodide solution (50 µg/ml PI, 0.1% sodium citrate, 50 µg/ml RNase A, freshly added in PBS) for 40 min at 37°C and 500 µl PBS were added per sample. Cell cycle distribution of cells was obtained using flow cytometry and analyzed by CXP analysis software (Beckman Coulter). Means ± SD of $n = 3$.

4.2.7 | Clonogenic assay[33]

The clonogenic assay also known as colony formation assay monitors the ability of single cancer cells to grow into a colony. To monitor influence of test compounds on this ability, HCT116 colon carcinoma cells were treated with compounds before the assay. After 24 h of treatment, cells were rinsed with PBS and harvested using trypsination. Afterwards, 500 cells per well were seeded into 6-well plates (Sarstedt), containing 3 ml DMEM and incubated for 7 days under regular medium change. After the growth period, medium was discarded, and wells were carefully rinsed with PBS followed by fixation of colonies by adding 1 ml EtOH absolute (VWR) per well for 3 min. Colonies were stained for 5 min using 1 ml per well of a 0.5% crystal violet solution, then wells were rinsed with water. Resulting stained colonies were counted using imageJ (Vs 1.53j, National Institutes of Health). Colony count was normalized to control which was set as 100%.

4.2.8 | Scratch migration assay[39]

The scratch migration assay also known as wound healing assay is an easy and cheap method for investigating cell migration in vitro. For the assay, HCT116wt colon cancer cells were seeded in wells of a 24-well microtiter plate (Sarstedt) in 500 µl DMEM containing 10% (v/v) FBS (Sigma Aldrich) and 1% (v/v) ZellShield (Minerva Biolabs) with a density of 0.5×10^6 cells per ml. When cells reached a confluent level, medium was changed to DMEM containing 0.1% FBS followed by further incubation overnight. The following day, a 10 µl pipette tip was used to scratch a wound into the cell monolayer. Afterward, each well was rinsed with PBS to remove detached cells and 1 ml per well of fresh DMEM containing 0.1% FBS was added. Substance treatment ensued by adding 10.1 µl per well of 100-fold test compound dilutions. Images of scratch areas were acquired using inverted brightfield microscopy. Cells were further incubated, and images of the same areas were acquired after 6 and 24 h. The course of migration of the cells into the area of the artificially created wound was evaluated using ImageJ (vs. 1.53j, National Institutes of Health). Cellular migration capability was calculated relative to control which was set as 100%.

4.2.9 | Tubulin polymerization assay

To monitor the effect of test compounds on the polymerization of tubulin monomers a tubulin polymerization assay was conducted. Before the assay 10-fold predilutions of test compounds were prepared in Brinkley's Buffer (BRB80; 80 mM PIPES KOH, 1 mM $MgCl_2$, 1 mM EGTA). A volume of 11.1 µl of substance predilution were added per well containing 50 µl 2× polymerization buffer (20% glycerin, 3 mM GTP in BRB80, sterile) into a flat black 96-well plate (Brand). Then, 50 µl of purified pork brain tubulin (10 mg/ml) were added in each well, obtaining a final concentration of 10 µM of test compounds. The corresponding dilution of DMSO served as control (ctrl). Tubulin polymerization at 37°C was measured via OD340 nm using a TECAN plate reader.

4.2.10 | Immunofluorescence staining

To visualize the effects of test compounds on the morphology of the α-tubulin cytoskeleton of HCT116 colon cancer cells, immunofluorescence staining was conducted as described before.[38] Briefly $HCT116^{wt}$ colon cancer cells were seeded onto cover slips (borosilicate glass, Carl Roth) inside the wells of 24-well microtiter plates and allowed to grow for 24 h. Followed by compound treatment with concentrations corresponding the IC_{50} of test compounds for 24 h, whereas corresponding amount of DMSO served as control (ctrl). Before immunofluorescence staining cells were fixed using a 3.7% formaldehyde solution in PBS. Immunofluorescence staining of α-tubulin, as well as DAPI counterstaining, were conducted. The condition of the α-tubulin cytoskeleton was documented by fluorescence microscopy.

4.2.11 | HDAC activity assays

For measuring the HDAC activity of $HCT116^{wt}$ colon cancer cells under the influence of test compounds, a commercial fluorometric HDAC activity kit was used (Amplite™, Fluorimetric HDAC Activity Assay Kit, green fluorescence, AAT Bioquest, Catalog number: 13601). Before the assay, a cell lysate was prepared from $HCT116^{wt}$ colon cancer cells. The assay was conducted as described by the provider. Briefly, a fivefold dilution of $HCT16^{wt}$ cell lysate in assay buffer was treated for 15 min at 37°C with different concentrations of prediluted test compounds (final concentrations corresponding the IC_{50}; animthioxam 2 µM, brimbam 3.2 µM, troxbam 0.9 µM, troxham 0.6 µM and SAHA 0.9 µM). After adding HDAC Green™ Substrate working solution, an incubation step followed (room temperature, 30–60 min, in the dark). Fluorescence was measured at ex/em = 490/525 nm using a TECAN plate reader.

For measuring HDAC 6 activity of human HDAC 6, a commercial fluorometric HDAC 6 activity kit (BioVision, HDAC 6 Activity Assay Kit [Fluorometric], Catalog Number K466). The assay was conducted as described by the provider. Briefly, a dilution of 2 µl of human HDAC 6 in 0.5 ml of HDAC 6 assay buffer was used. Samples were treated for 15 min at 37°C with different concentrations of prediluted troxbam (final concentrations 0.01, 0.1, and 1 µM). After adding HDAC 6 Substrate working solution, an incubation step followed (37°C, 30 min, in the dark). Developers were added and samples were further incubated for 10 min at 37°C, afterwards, fluorescence was measured at ex/em = 380/490 nm in an end point mode at 37°C.

4.2.12 | Western blot

Western blots were conducted following a standard protocol.[40] Briefly, cells were seeded into six-well plates (0.15×10^6 cells per well) and allowed to grow overnight. The following day cells were treated with desired concentrations of test compounds. After further incubation for 24–72 h, cells were lysed to obtain whole cell lysate and amount of protein was determined using Pierce™ BCA Protein Assay Kit (Catalog Number 23225). Protein samples were mixed with 4× Lämmli buffer (Biorad, Catalog Number 1610747) and denatured for 5 min at 95°C. A total amount of 30 µg protein per sample was applied to a precast 12% polyacryl amide Mini-PROTEAN gel (Biorad) and electrophoresis was conducted. Afterward, proteins were electroblotted onto a 0.2 µm PVDF membrane (ROTI®PVDF, CarlRoth). After blocking for 1 h in 5% skimmed milk solution, primary antibody incubation (anti-GAPDH, 1:1000, CellSignaling, Catalog Number 5174; anti-survivin, 1:1000, CellSignaling, Catalog Number 2808, anti-ac-α-tubulin 1:1000, Merck Catalog-Number T7451) followed over night at 4°C. Following day membranes were washed in 0.1% Tween in TBS and incubated with secondary HRP-conjugated antibody (anti-rabbit 1:2000, CellSignaling, Catalog Number 7074, anti-mouse 1:2000, CellSignaling, Catalog Number 7076) for 1 h at room temperature. Protein signals were obtained using Clarity Max Western ECL Substrate (Biorad, Catalog Number 1705062) and captured using ChemiDoc system (Biorad). For quantification, ImageJ (vs. 1.53j, National Institutes of Health) was used and the density of the protein bands was normalized to GAPDH as a loading control.

4.3 | Statistics

Statistical data analysis was performed using DATAtab Team (2022) Online Statistics Calculator.DATAtab e.U. Graz, Austria. URL https://datatab.net. If not indicated otherwise, the presented data is the mean ± SD. To test statistical significance one-way analysis of variance coupled with Tukey's post hoc tests was used. Several replicates of each experiment were carried out, the exact number is given in the respective figure or table description.

4.4 | Molecular docking

Docking studies of test compounds on the active site of human HDAC6 (PDB ID 5EDU) were carried out using AutoDock Vina in the presence of the catalytic Zn^{2+} ion at the binding site. The cocrystallized ligands and the Zn^{2+} ion were used as reference to define the binding pockets within a radius of 30 Å. The protein preparation and ligand preparation procedures were done using the open-source web server Dockthor (www.dockthor.lncc.br, accessed on October 19, 2021) and Merck molecular force field was applied. The protein preparation was done at physiological pH 7.4. All dockings and calculations were performed using AutoDock-Vina 1.1.2 software.[41] All other settings for ligand and receptor definitions were used as defaults. The docking strategy, scoring, and chemical parameters were kept as default. For each compound, nine poses were generated, and all were evaluated with the built-in scoring function. PyMOL software is utilized to visualize, compare and analyze binding pose predictions, and to create images.[42] For visualization, the protein was used in the cartoon mode and the surface mode, wherein the metal chelation of Zn^{2+} was visualized in the sphere mode and nb sphere mode. The binding energies do have some variability of 1–2 kcal. The development of computational methods for protein flexibility is still in its infancy and thereby remains one of the major future directions in protein-ligand docking which will increase its accuracy.

ACKNOWLEDGMENT

Open Access funding enabled and organized by Projekt DEAL.

CONFLICTS OF INTEREST

The authors declare no conflicts of interest.

ORCID

Sofia I. Bär http://orcid.org/0000-0002-8612-3516
Bernhard Biersack http://orcid.org/0000-0001-7305-346X
Rainer Schobert http://orcid.org/0000-0002-8413-4342

REFERENCES

[1] R. L. Siegel, K. D. Miller, H. E. Fuchs, A. Jemal, *CA Cancer J. Clin.* **2022**, *72*, 7. https://doi.org/10.3322/caac.21708
[2] Z. Liu, T. Lu, J. Li, L. Wang, K. Xu, Q. Dang, C. Guo, L. Liu, D. Jiao, Z. Sun, X. Han, *Cancer Cell. Int.* **2021**, *21*, 359. https://doi.org/10.1186/s12935-021-02070-z
[3] W. A. Hammond, A. Swaika, K. Mody, *Ther. Adv. Med. Oncol.* **2016**, *8*, 57. https://doi.org/10.1177/1758834015614530
[4] D. Hanahan, R. A. Weinberg, *Cell* **2011**, *144*, 646. https://doi.org/10.1016/j.cell.2011.02.013
[5] D. Hanahan, *Cancer Discov.* **2022**, *12*, 31. https://doi.org/10.1158/2159-8290.CD-21-1059
[6] D. Hanahan, R. A. Weinberg, *Cell* **2000**, *100*, 57. https://doi.org/10.1016/S0092-8674(00)81683-9
[7] P. A. Marks, R. Breslow, *Nat. Biotechnol.* **2007**, *25*, 84. https://doi.org/10.1038/nbt1272
[8] A. C. West, R. W. Johnstone, *J. Clin. Invest.* **2014**, *124*, 30. https://doi.org/10.1172/JCI69738
[9] B. Biersack, B. Nitzsche, M. Höpfner, *Cancer Drug Resist.* **2022**, *4*, 64. https://doi.org/10.20517/cdr.2021.105
[10] M. I. Y. Elmallah, O. Micheau, *Cancers* **2019**, *11*, 850. https://doi.org/10.3390/cancers11060850
[11] I. Gregoretti, Y.-M. Lee, H. V. Goodson, *J. Mol. Biol.* **2004**, *338*, 17. https://doi.org/10.1016/j.jmb.2004.02.006
[12] W. K. Kelly, P. A. Marks, *Nat. Clin. Pract. Oncol.* **2005**, *2*, 150. https://doi.org/10.1038/ncponc0106
[13] J. Y.-C. Lee, C.-W. Kuo, S.-L. Tsai, S. M. Cheng, S.-H. Chen, H.-H. Chan, C.-H. Lin, K.-Y. Lin, C.-F. Li, J. R. Kanwar, E. Y. Leung, C. C. H. Cheung, W.-J. Huang, Y.-C. Wang, C. H. A. Cheung, *Front. Pharmacol.* **2016**, *7*, 81. https://doi.org/10.3389/fphar.2016.00081
[14] S. Kaur, P. Rajoria, M. Chopra, *Cell. Oncol.* **2022**, *45*, 779. https://doi.org/10.1007/s13402-022-00704-6
[15] M. T. Riolo, Z. A. Cooper, M. P. Holloway, Y. Cheng, C. Bianchi, E. Yakirevich, L. Ma, Y. E. Chin, R. A. Altura, *J. Biol. Chem.* **2012**, *287*, 10885. https://doi.org/10.1074/jbc.m111.308791

[16] K. Roy, N. Singh, R. K. Kanwar, J. R. Kanwar, *Recent Pat. Anticancer Drug Discov.* **2016**, *11*, 152. https://doi.org/10.2174/1574892811666160229121815

[17] A. C. Mita, M. M. Mita, S. T. Nawrocki, F. J. Giles, *Clin. Cancer Res.* **2008**, *14*, 5000. https://doi.org/10.1158/1078-0432.CCR-08-0746

[18] D. C. Altieri, *Cancer Lett.* **2013**, *332*, 225. https://doi.org/10.1016/j.canlet.2012.03.005

[19] D. C. Altieri, *Nat. Rev. Cancer* **2003**, *3*, 46. https://doi.org/10.1038/nrc968

[20] P. J. Kim, J. Plescia, H. Clevers, E. R. Fearon, D. C. Altieri, *Lancet* **2003**, *362*, 205. https://doi.org/10.1016/s0140-6736(03)13910-4

[21] Y. Li, W. Lu, J. Yang, M. Edwards, S. Jiang, *Expert Opin. Biol. Ther.* **2021**, *21*, 1429. https://doi.org/10.1080/14712598.2021.1918672

[22] A. Shalini, V. Kumar, *Expert Opin. Drug Discov.* **2021**, *16*, 335. https://doi.org/10.1080/17460441.2021.1850686

[23] B. Biersack, S. Polat, M. Höpfner, *Semin. Cancer Biol.* **2022**, *83*, 472. https://doi.org/10.1016/j.semcancer.2020.11.005

[24] F. Schmitt, L. Gosch, A. Dittmer, M. Rothemund, T. Mueller, R. Schobert, B. Biersack, A. Volkamer, M. Höpfner, *Int. J. Mol. Sci.* **2019**, *20*, 383. https://doi.org/10.3390/ijms20020383

[25] S. Bär, A. Dittmer, B. Nitzsche, G. Ter-Avetisyan, M. Fähling, A. Klefenz, L. Kaps, B. Biersack, R. Schobert, M. Höpfner, *Int. J. Oncol.* **2022**, *60*, 73. https://doi.org/10.3892/ijo.2022.5363

[26] S. W. Fesik, *Nat. Rev. Cancer* **2005**, *5*, 876. https://doi.org/10.1038/nrc1736

[27] S. A. Lakhani, A. Masud, K. Kuida, G. A. Porter, C. J. Booth, W. Z. Mehal, I. Inayat, R. A. Flavell, *Science* **2006**, *311*, 847. https://doi.org/10.1126/science.1115035

[28] F. K.-M. Chan, K. Moriwaki, M. J. de Rosa, *Methods Mol. Biol.* **2013**, *979*, 65. https://doi.org/10.1007/978-1-62703-290-2_7

[29] E. C. LaCasse, S. Baird, R. G. Korneluk, A. E. MacKenzie, *Oncogene* **1998**, *17*, 3247. https://doi.org/10.1038/sj.onc.1202569

[30] A. M. Hunter, E. C. LaCasse, R. G. Korneluk, *Apoptosis* **2007**, *12*, 1543. https://doi.org/10.1007/s10495-007-0087-3

[31] S. Zhu, Y. Li, L. Zhao, P. Hou, C. Shangguan, R. Yao, W. Zhang, Y. Zhang, J. Tan, B. Huang, J. Lu, *J. Cell. Biochem.* **2012**, *113*, 2375. https://doi.org/10.1002/jcb.24109

[32] W. Feng, D. Cai, B. Zhang, G. Lou, X. Zou, *Biomed. Pharmacother.* **2015**, *74*, 257. https://doi.org/10.1016/j.biopha.2015.08.017

[33] N. A. P. Franken, H. M. Rodermond, J. Stap, J. Haveman, C. van Bree, *Nat. Protoc.* **2006**, *1*, 2315. https://doi.org/10.1038/nprot.2006.339

[34] M. Kurt Yüksel, P. Topçuoğlu, M. Kurdal, O. Ilhan, *Cytotherapy* **2010**, *12*, 38. https://doi.org/10.3109/14653240903313958

[35] J. Schemies, W. Sippl, M. Jung, *Cancer Lett.* **2009**, *280*, 222. https://doi.org/10.1016/j.canlet.2009.01.040

[36] A. Valenzuela-Fernández, J. R. Cabrero, J. M. Serrador, F. Sánchez-Madrid, *Trends Cell Biol.* **2008**, *18*, 291. https://doi.org/10.1016/j.tcb.2008.04.003

[37] S. I. Bär, M. Gold, S. W. Schleser, T. Rehm, A. Bär, L. Köhler, L. R. Carnell, B. Biersack, R. Schobert, *Chemistry—A European Journal* **2021**, *27*, 5003. https://doi.org/10.1002/chem.202005451

[38] M. Rothemund, S. I. Bär, T. Rehm, H. Kostrhunova, V. Brabec, R. Schobert, *Dalton Trans.* **2020**, *49*, 8901. https://doi.org/10.1039/d0dt01664k

[39] C.-C. Liang, A. Y. Park, J.-L. Guan, *Nat. Protoc.* **2007**, *2*, 329. https://doi.org/10.1038/nprot.2007.30

[40] T. Mahmood, P.-C. Yang, *N. Am. J. Med. Sci.* **2012**, *4*, 429. https://doi.org/10.4103/1947-2714.100998

[41] O. Trott, A. J. Olson, *J. Comput. Chem.* **2009**, *31*, NA. https://doi.org/10.1002/jcc.21334

[42] W. DeLano, *CCP4 Newsl. Protein Crystallogr.* **2002**, *44*, 1.

SUPPORTING INFORMATION

Additional supporting information can be found online in the Supporting Information section at the end of this article.

How to cite this article: S. I. Bär, R. Pradhan, B. Biersack, B. Nitzsche, M. Höpfner, R. Schobert, *Arch. Pharm.* **2023**;356:e2200422. https://doi.org/10.1002/ardp.202200422

ARCH PHARM
Archiv der Pharmazie

Supplemental Material: Novel Compounds and Biological Screening Results

New chimeric hydroxamic acids reducing survivin expression levels in HCT116 colon carcinoma cells by a dual HDACi- / microtubule-associated mode of action

Sofia I. Bär[1,*], Rohan Pradhan[2], Bernhard Biersack[1] and Rainer Schobert[1]

1 Organic chemistry laboratory, University of Bayreuth, Universitätsstraße 30, D-95447 Bayreuth, Germany
Bernhard Biersack, ORCID 0000-0001-7305-346X
Rainer Schobert, ORCID 0000-0002-8413-4342
2 Care Group Sight Solution Pvt. Ltd., Dabhasa, Vadodara 391440, India

*Correspondence: Sofia I. Bär, ORCID 0000-0002-8612-3516, Organic chemistry laboratory, University of Bayreuth, Universitätsstraße 30, D-95447 Bayreuth, Germany
Email: sofia.baer@uni-bayreuth.de

Compound	InChI	Biological Activity (IC_{50})[a]
Animthioxam	InChI=SRSLPEFGRNQQMA-CSKARUKUSA-N	2.1 µM
Brimamin	InChI=RROYVIRXZVIZQG-UHFFFAOYSA-N	3.2 µM
Troxbam	InChI=RSOQQZTUTMPIOG-UHFFFAOYSA-N	0.9 µM
Troxham	InChI=XFQXYONXLZHUAD-UHFFFAOYSA-N	0.6 µM

[a] IC_{50} in $HCT116^{wt}$ colon carcinoma cells was assessed using MTT based cytotoxicity assay, according to J Immunol Methods, 65 (1983) 55-63

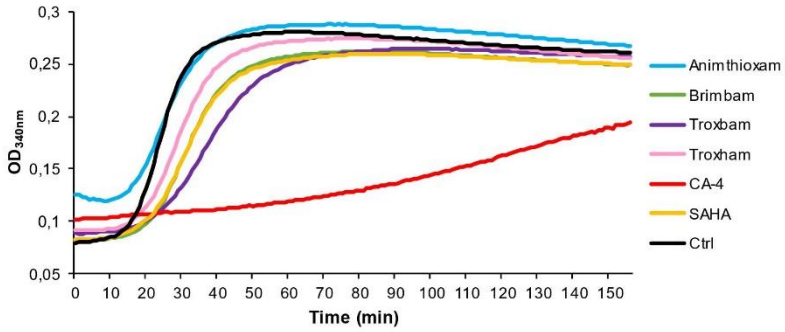

FIGURE SI 1 Tubulinpolymerisation assay of purified pork brain tubulin monomers under influence of compound treatment. 10 µM of test compounds were applied and polymerisation was observed at 37°C over 160 min, corresponding volume of DMSO served as control (Ctrl). Data shown is mean of tow independent experiments.

ARCH PHARM
Archiv der Pharmazie

^{1}H NMR spectrum of **2**

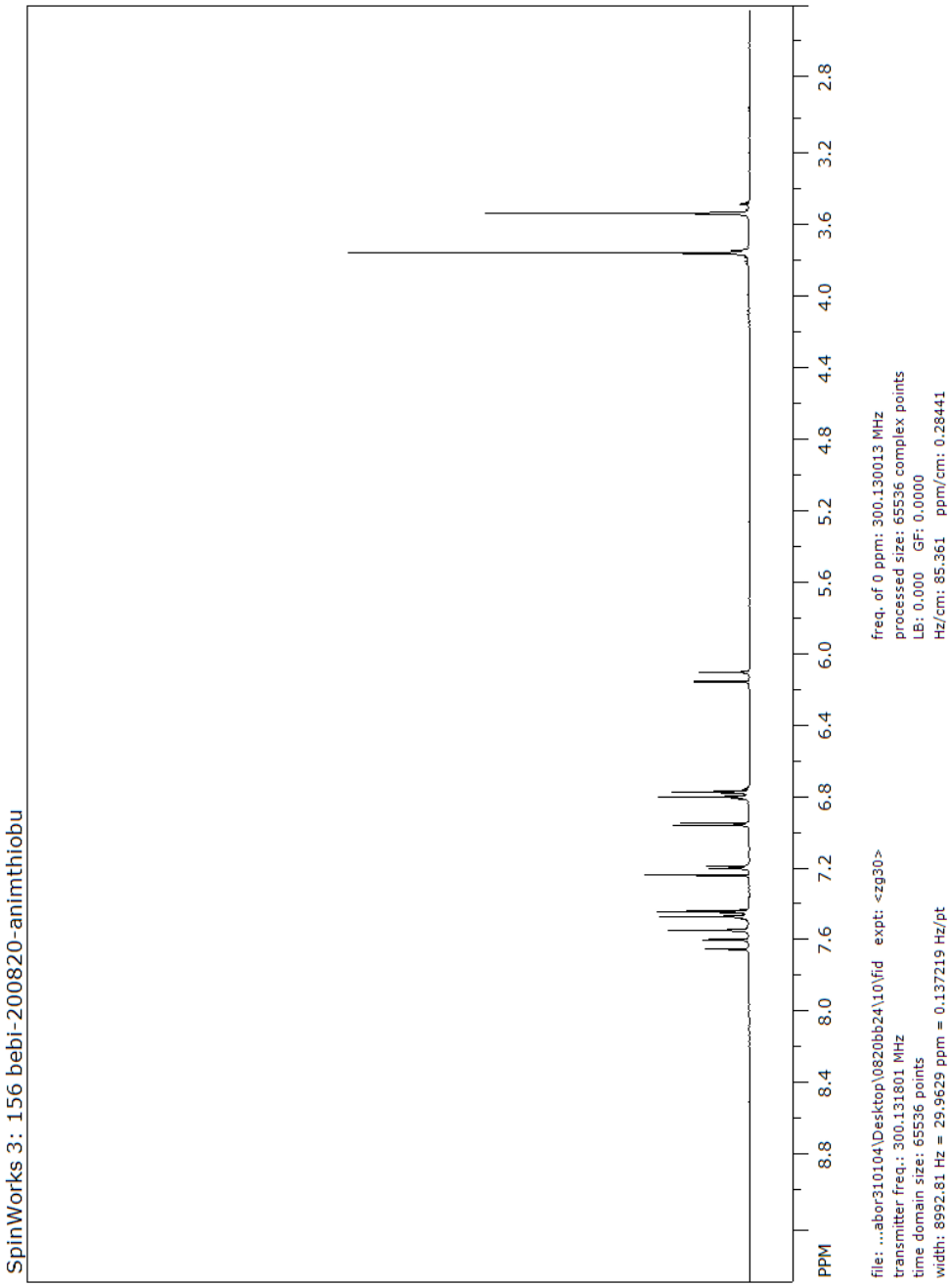

ARCH PHARM
Archiv der Pharmazie

^{13}C NMR spectrum of **2**

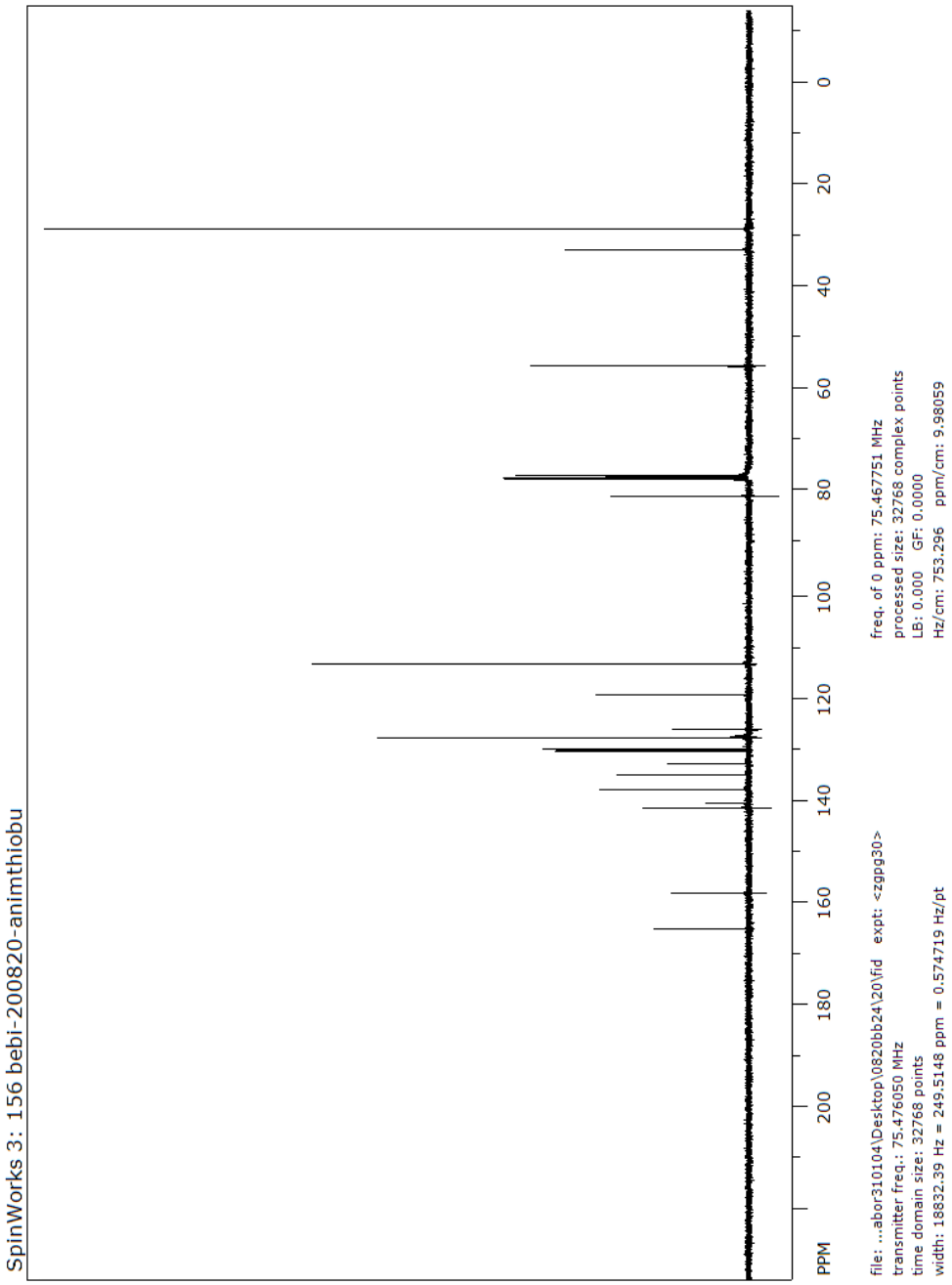

ARCH PHARM
Archiv der Pharmazie

^{1}H NMR spectrum of **3**

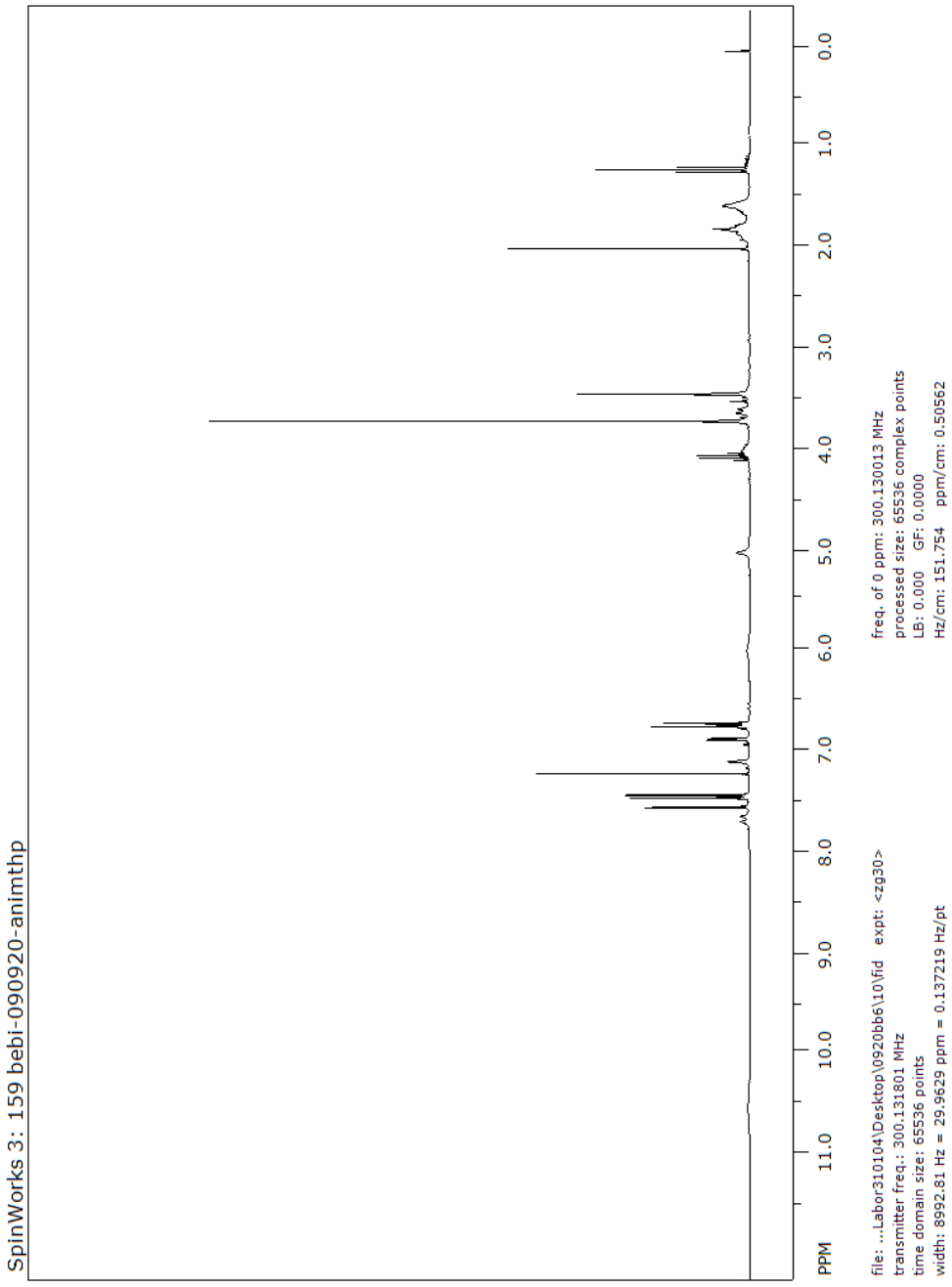

ARCH PHARM
Archiv der Pharmazie

^{13}C NMR spectrum of **3**

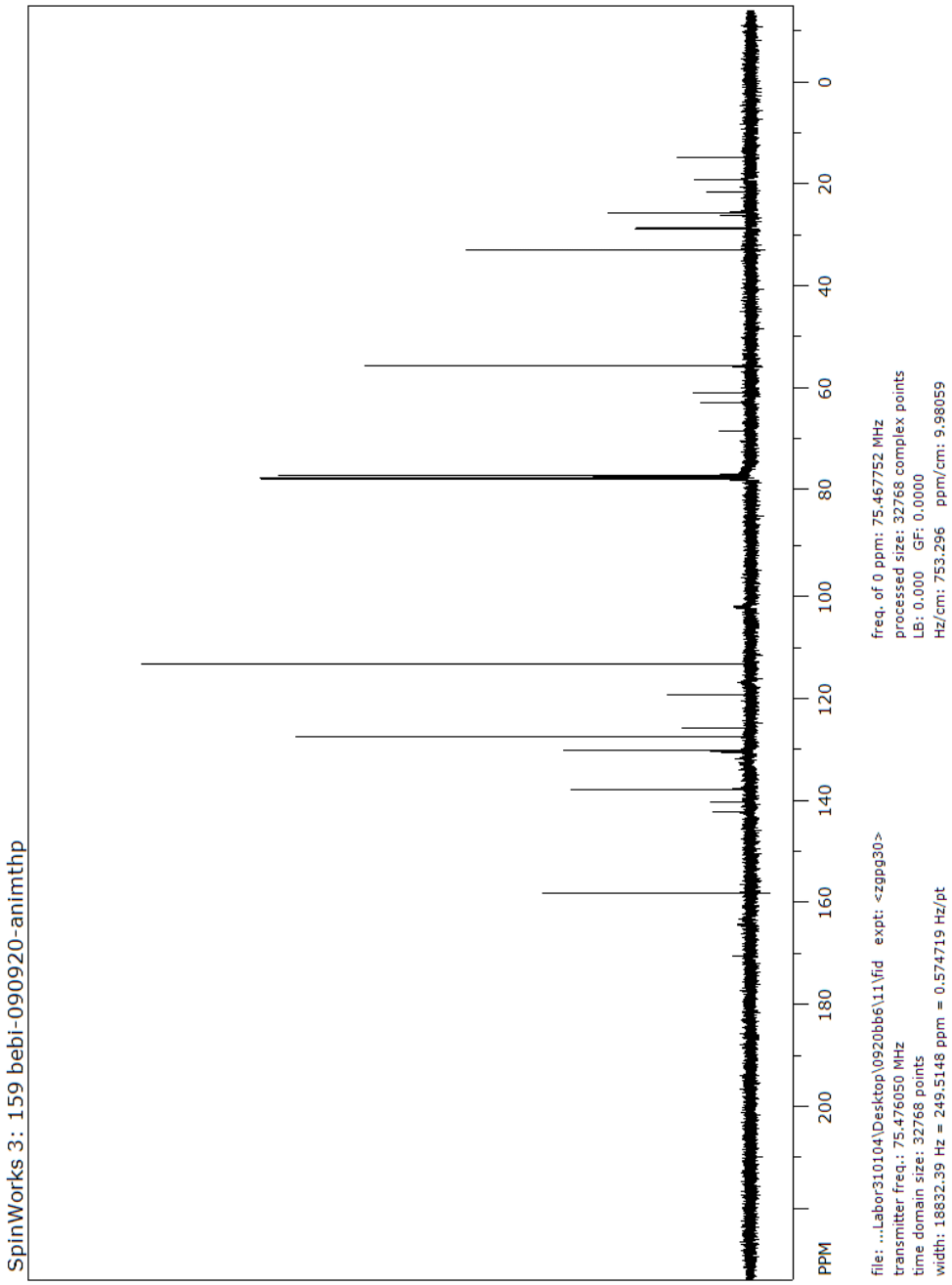

ARCH PHARM
Archiv der Pharmazie

^{1}H NMR spectrum of **Animthioxam**

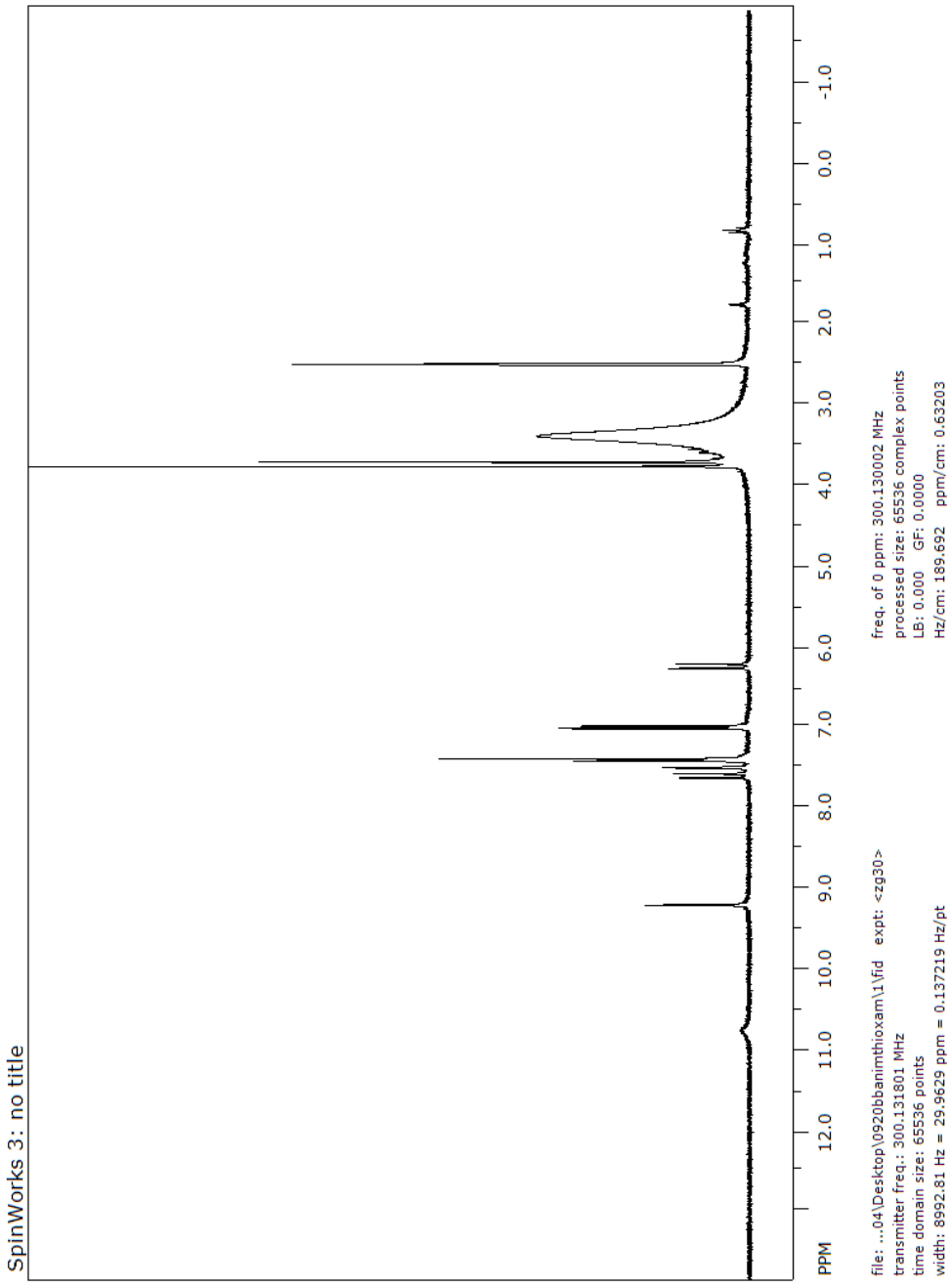

ARCH PHARM
Archiv der Pharmazie

^{13}C NMR spectrum of **Animthioxam**

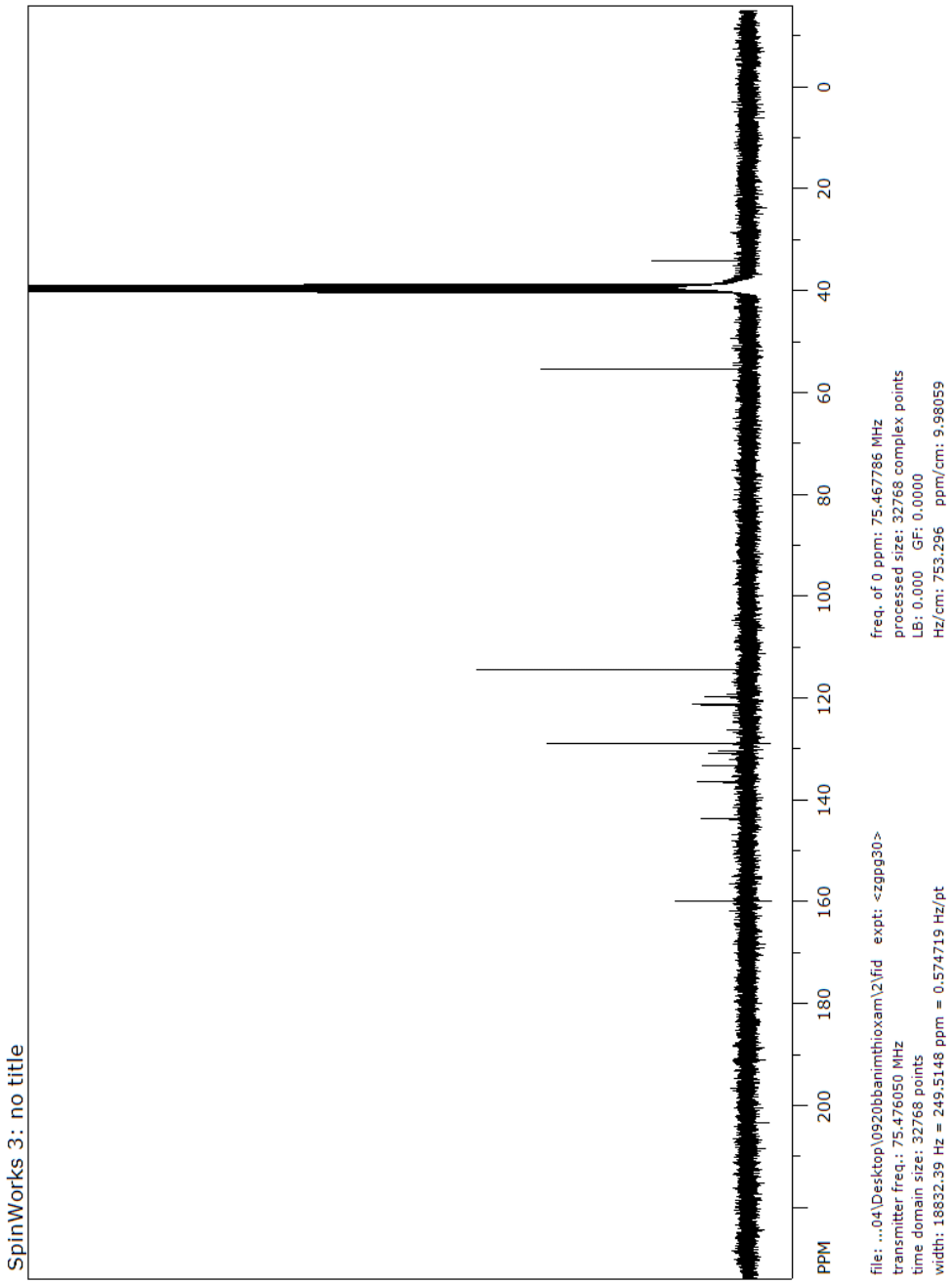

ARCH PHARM
Archiv der Pharmazie

^{1}H NMR spectrum of **5**

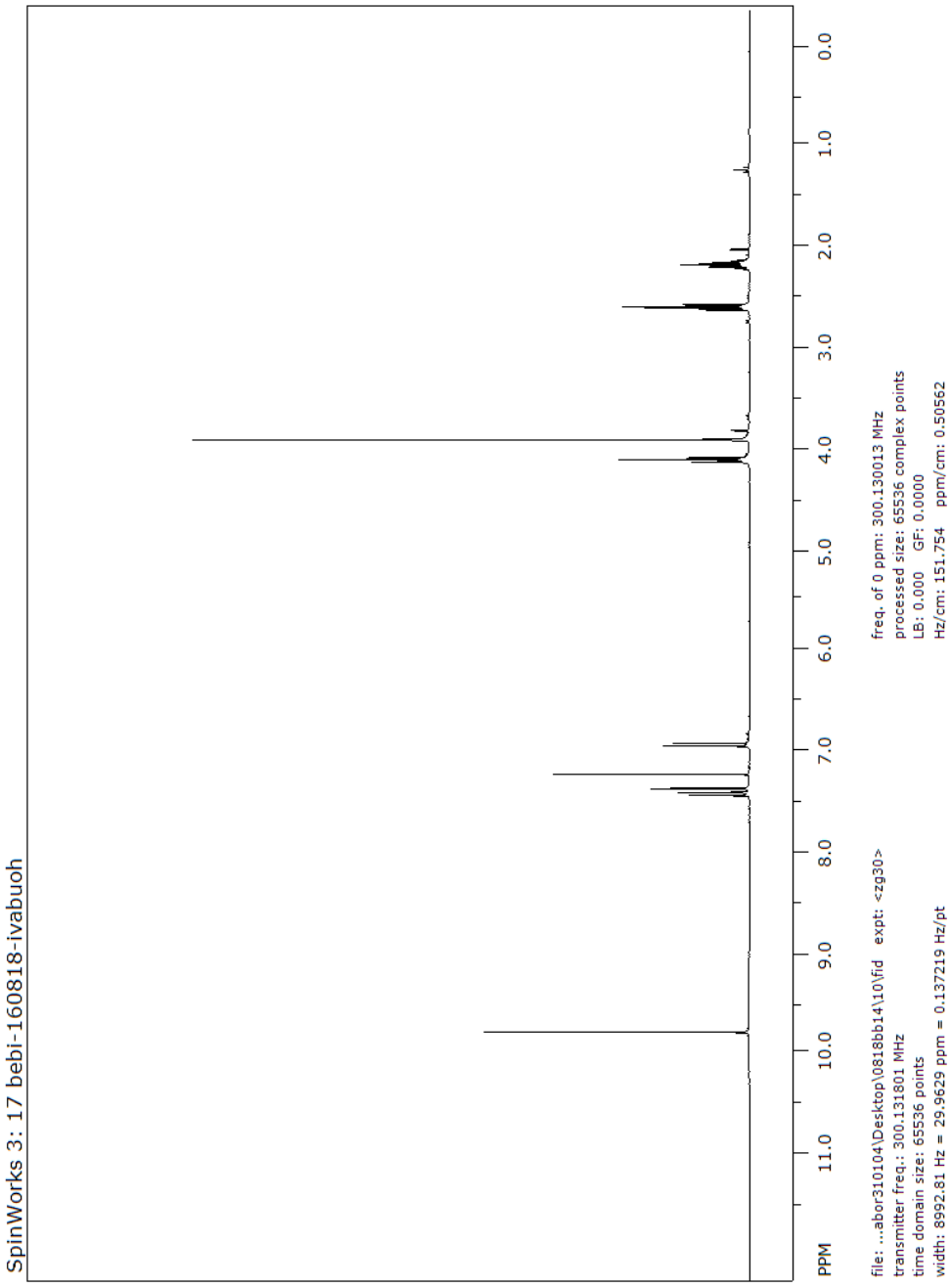

ARCH PHARM
Archiv der Pharmazie

^{13}C NMR spectrum of **5**

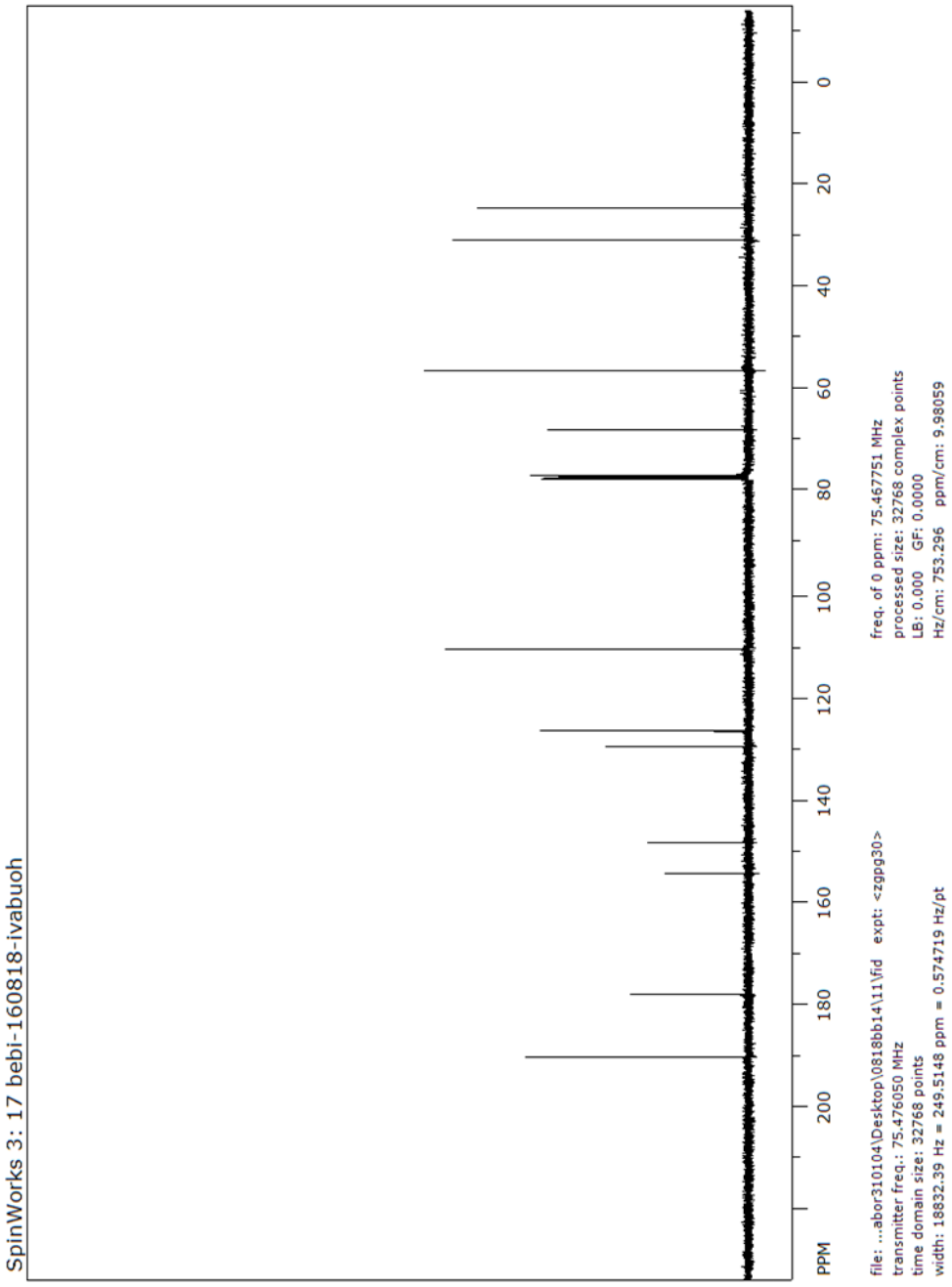

ARCH PHARM
Archiv der Pharmazie

^{1}H NMR spectrum of **6**

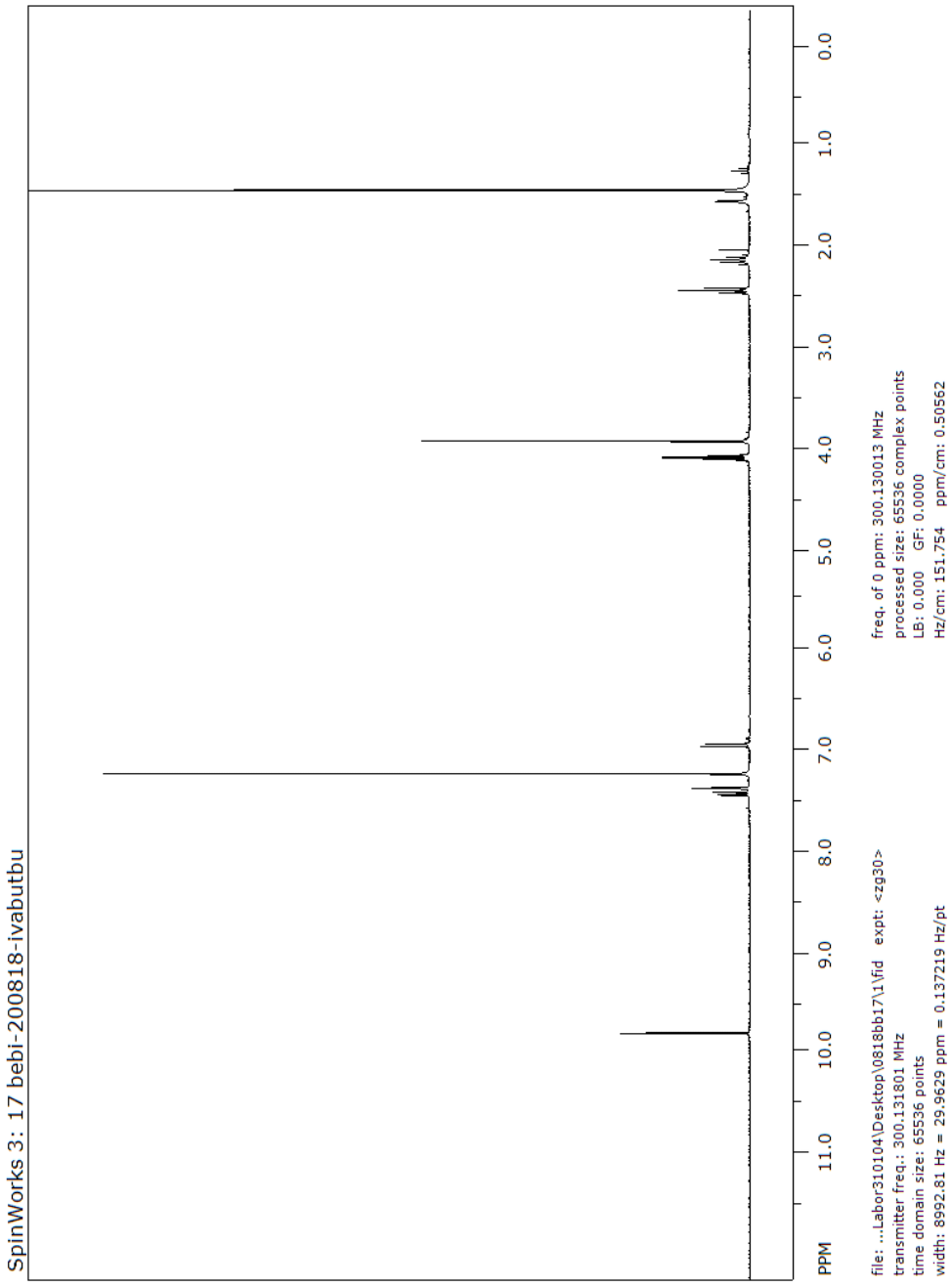

ARCH PHARM
Archiv der Pharmazie

^{13}C NMR spectrum of **6**

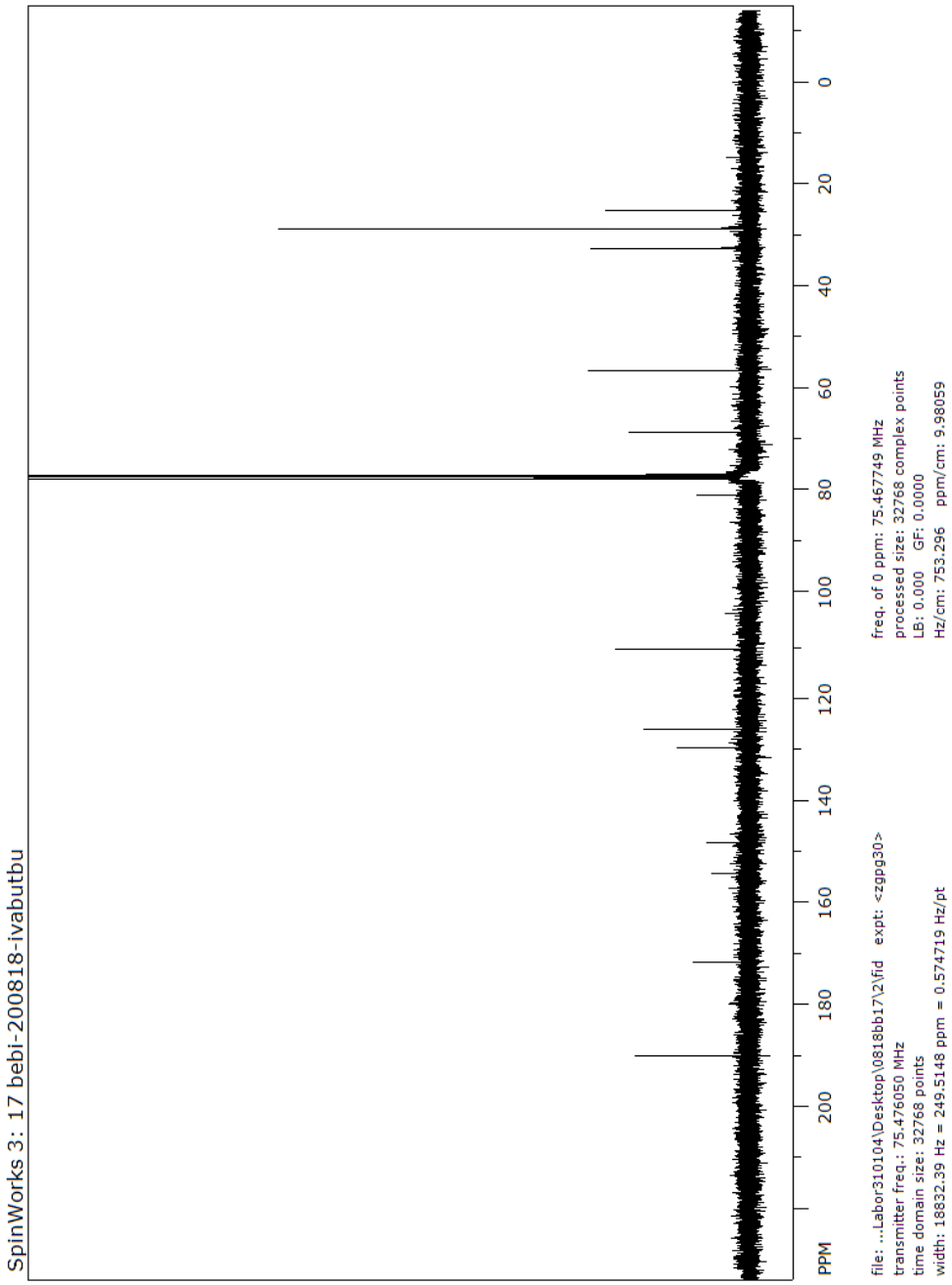

ARCH PHARM
Archiv der Pharmazie

^{1}H NMR spectrum of **7**

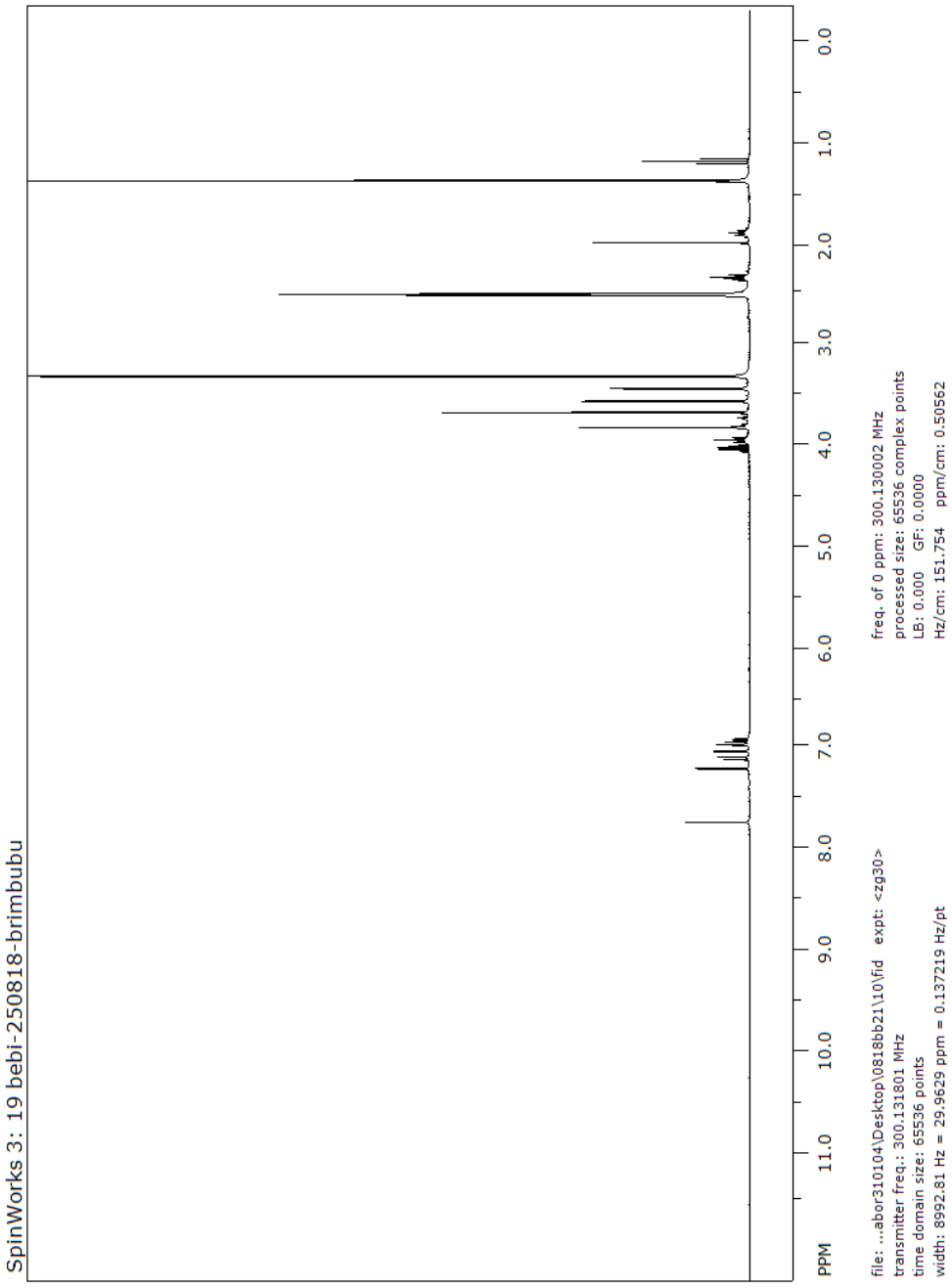

ARCH PHARM
Archiv der Pharmazie

^{13}C NMR spectrum of **7**

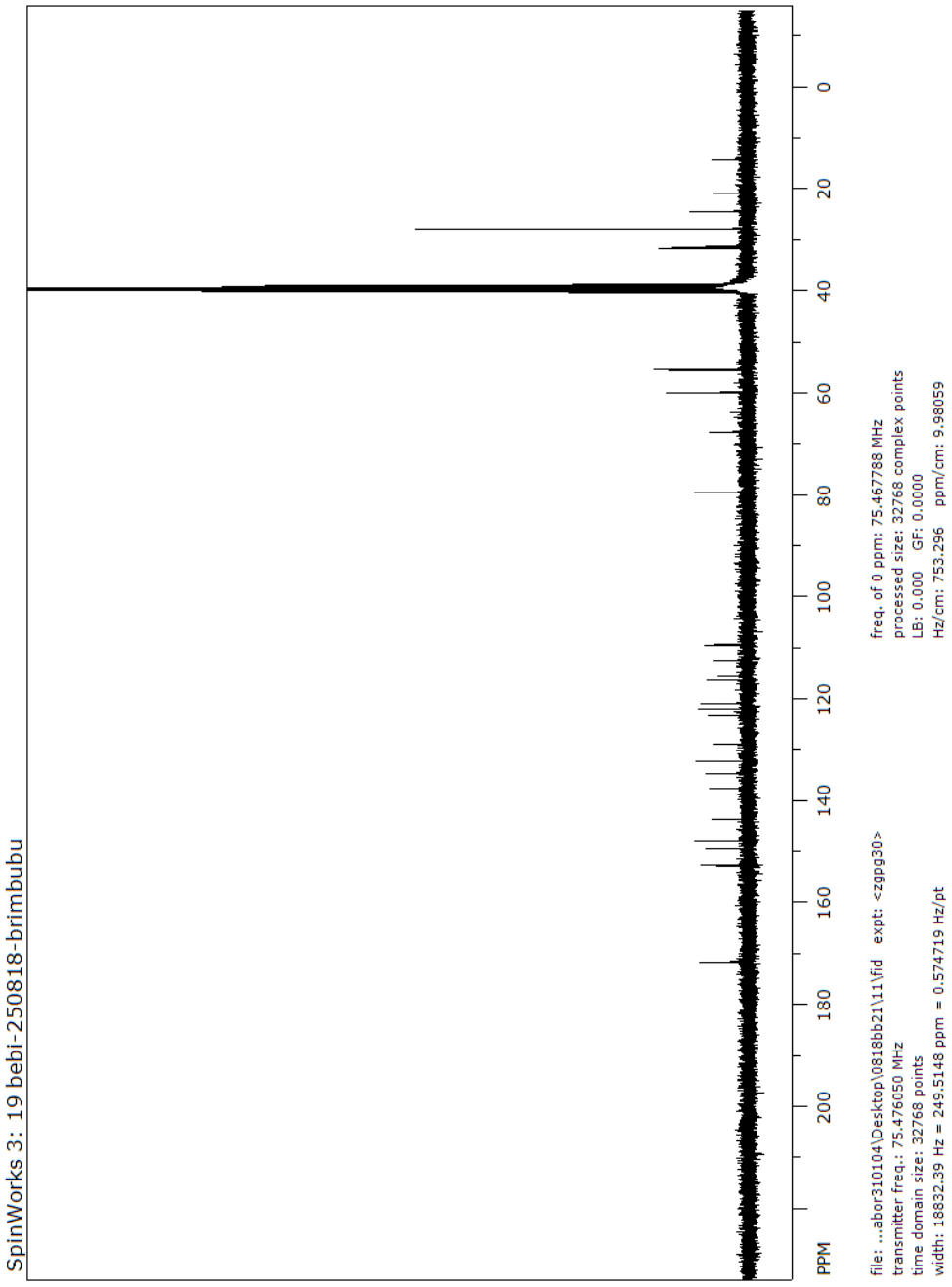

ARCH PHARM
Archiv der Pharmazie

^{1}H NMR spectrum of **8**

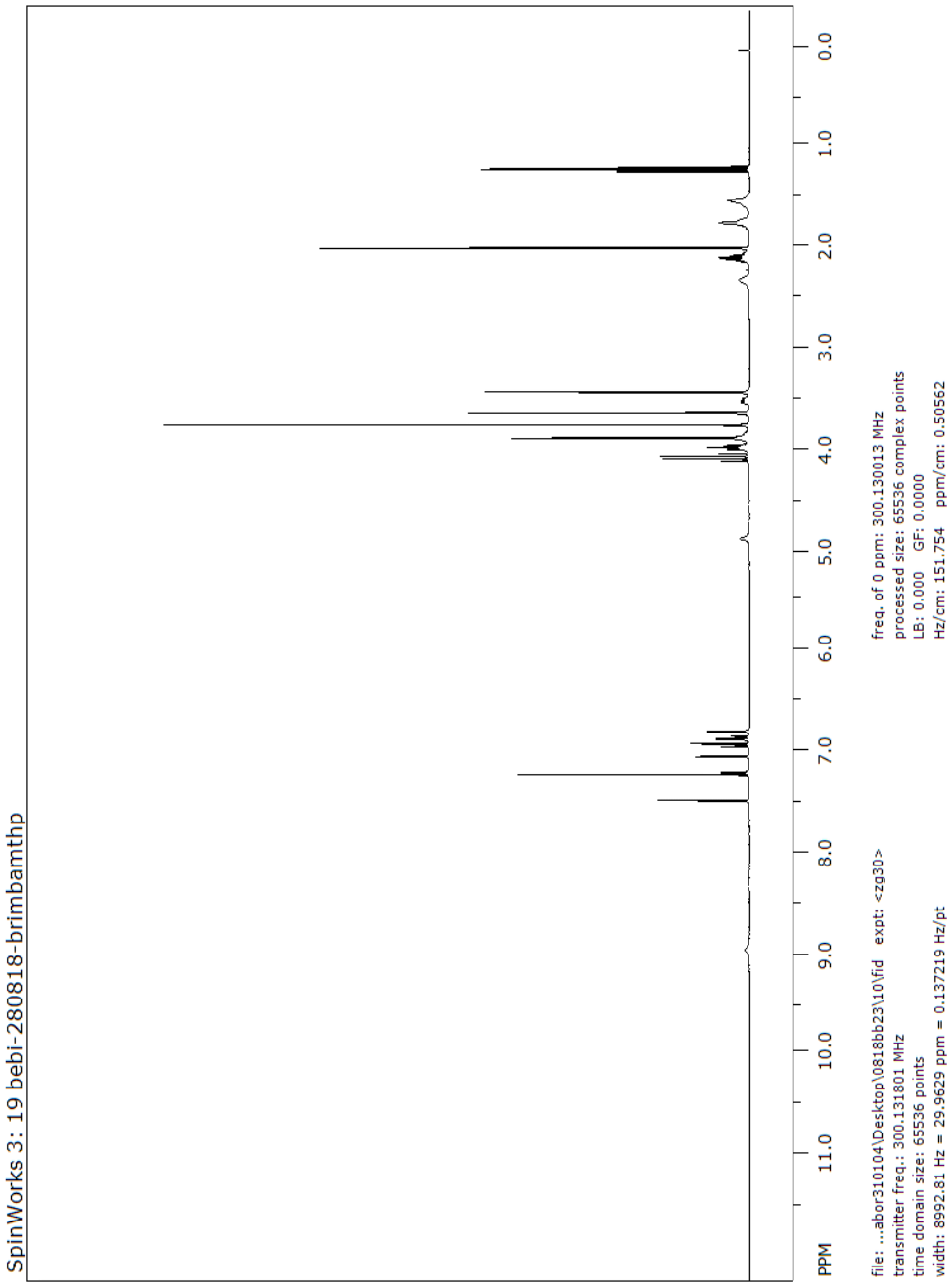

ARCH PHARM
Archiv der Pharmazie

^{13}C NMR spectrum of **8**

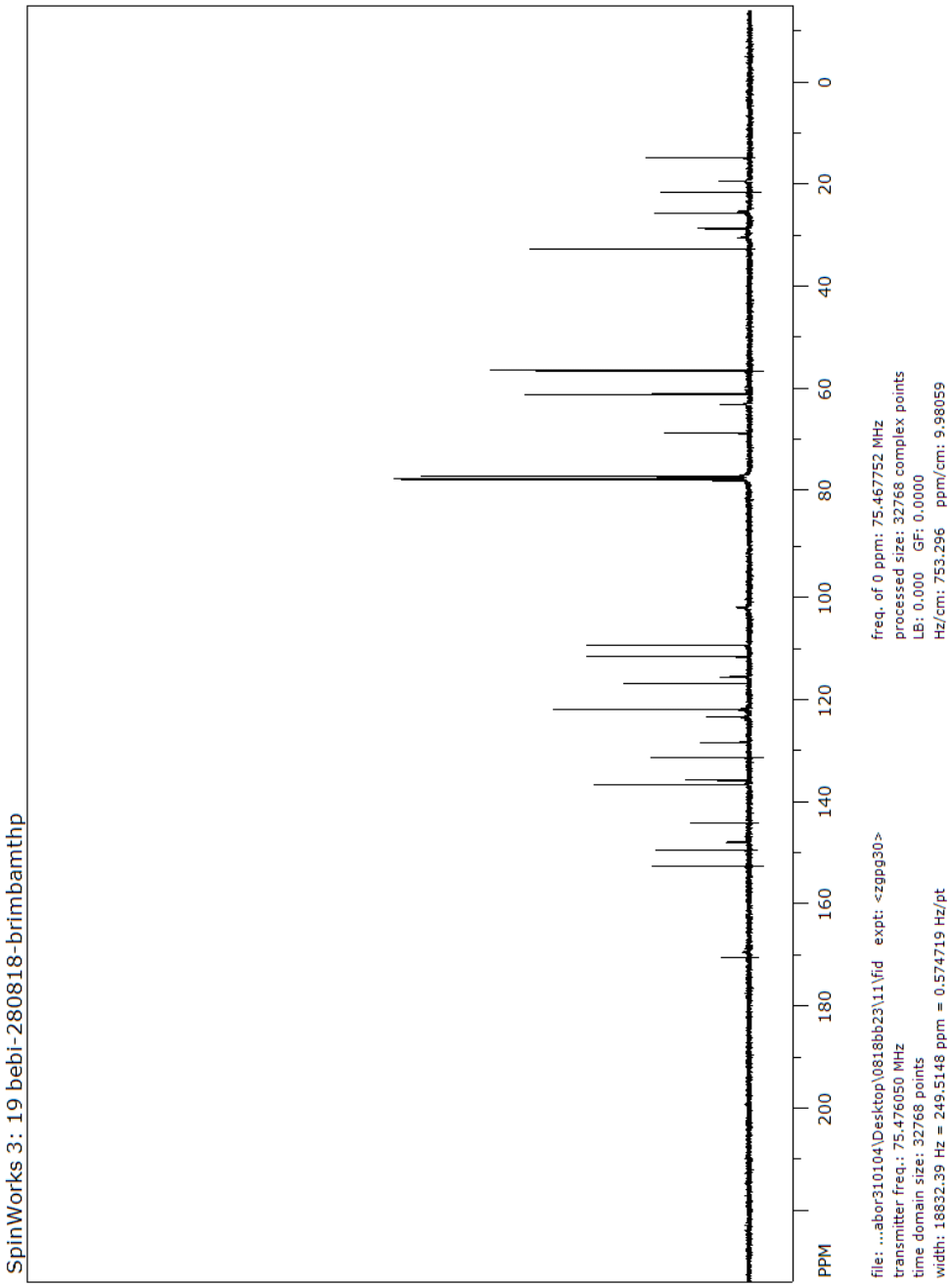

ARCH PHARM
Archiv der Pharmazie

^{1}H NMR spectrum of **Brimbam**

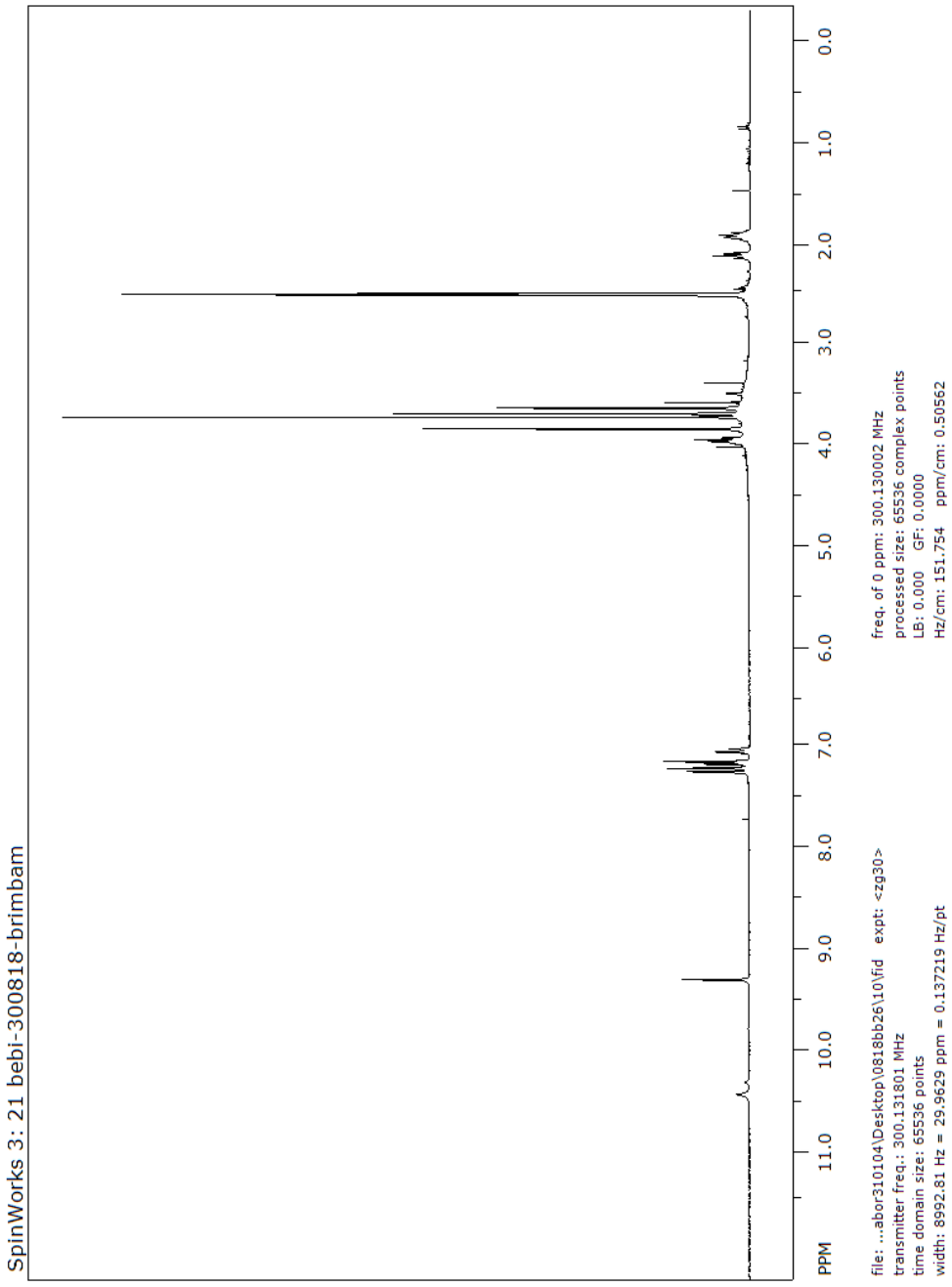

ARCH PHARM
Archiv der Pharmazie

^{13}C NMR spectrum of **Brimbam**

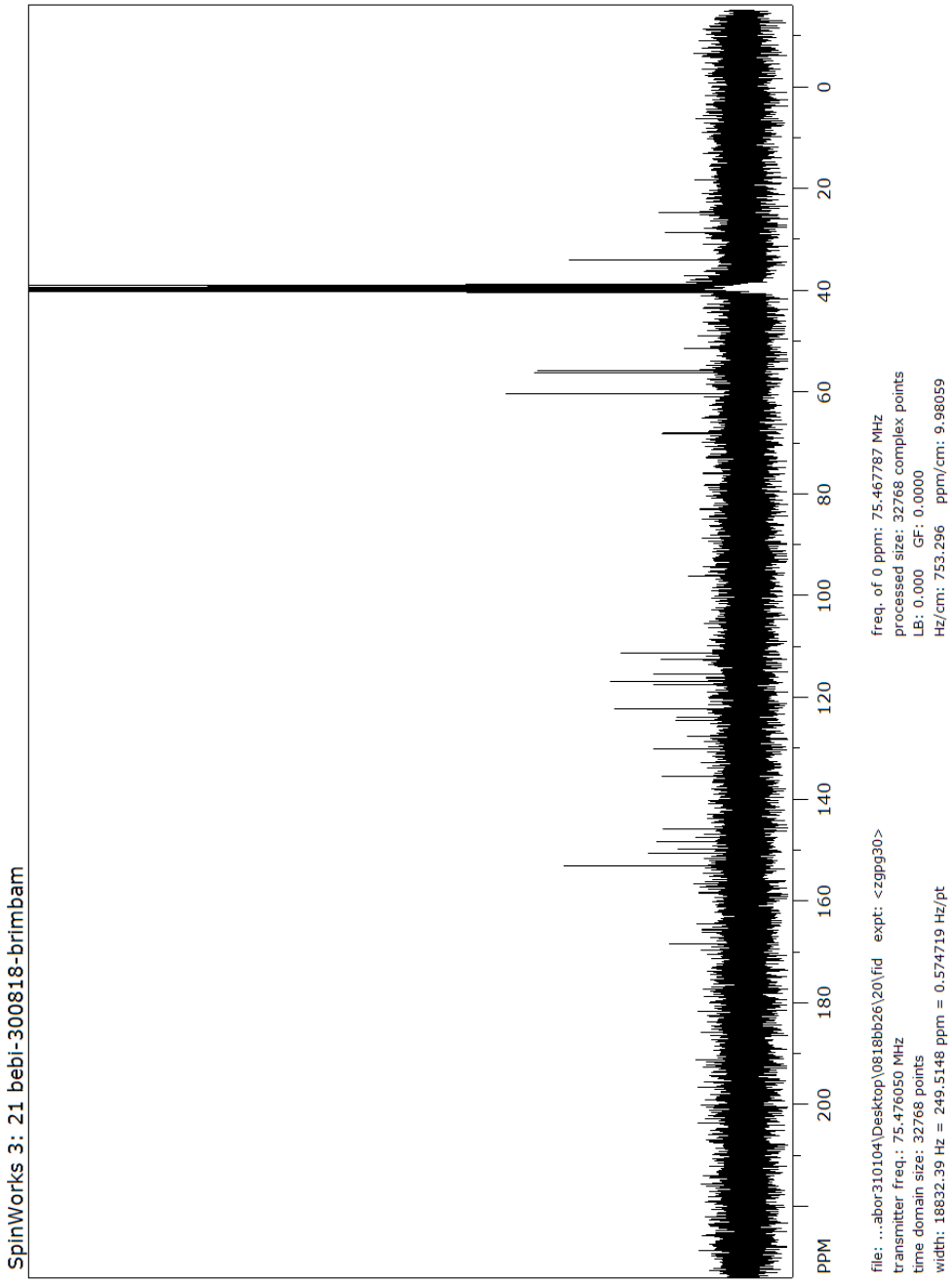

5.7 Publikation VII mit Darstellung des Eigenanteils

Publikation VII entstand unter Mitarbeit von Dr. B. Biersack Mitarbeiter des Arbeitskreises Organische Chemie I der Universität Bayreuth unter der Leitung von Prof. Dr. R. Schobert.

5.7.1 Eigenanteil an Publikation VII

Die Publikation wurde in ***Investigational New Drugs*** veröffentlicht, unter dem Titel

„3D cell cultures, as a surrogate for animal models, enhance the diagnostic value of preclinical in vitro investigations by adding information on the tumour microenvironment: a comparative study of new dual-mode HDAC inhibitors“

von den Autoren

Sofia I. Bär, Bernhard Biersack und Rainer Schobert

Eigenanteil:	Konzeption, Durchführung, Auswertung, graphische Darstellung und Statistik der biochemischen Assays; MCTS Generation und Wachstumsquantifizierung, PI Färbung, Caspase 9 Immunofluoreszenz, LDH Assay, ROS Assay und Generation von *in vitro* Mikrotumoren. Zudem; Verfassen des Manuskripts einschließlich der Diskussion und Interpretation der Ergebnisse und Revision des Manuskripts.
Bernhard Biersack:	Synthese und Charakterisierung der Testsubstanzen sowie Verfassen der entsprechenden Manuskriptpassagen.
Rainer Schobert:	Überarbeitung und Korrektur des Manuskripts.

5.7.2 Publikation VII

3D cell cultures, as a surrogate for animal models, enhance the diagnostic value of preclinical in vitro investigations by adding information on the tumour microenvironment: a comparative study of new dual-mode HDAC inhibitors

Sofia I. Bär*, Bernhard Biersack and Rainer Schobert[a]

[a] Organic Chemistry Laboratory, University of Bayreuth, Universitaetsstrasse 30, 95440 Bayreuth, Germany

*E-mail: sofia.baer@uni-bayreuth.de

Invest. New Drugs, **2022**, 40, 953

https://doi.org/10.1007/s10637-022-01280-0

Investigational New Drugs
https://doi.org/10.1007/s10637-022-01280-0

RESEARCH

3D cell cultures, as a surrogate for animal models, enhance the diagnostic value of preclinical in vitro investigations by adding information on the tumour microenvironment: a comparative study of new dual-mode HDAC inhibitors

Sofia I. Bär[1] · Bernhard Biersack[1] · Rainer Schobert[1]

Received: 14 June 2022 / Accepted: 1 July 2022

Abstract
Anchorage-independent 3D-cultures of multicellular tumour spheroids (MCTS) and in vitro microtumours of cancer cells can provide upfront information on the effects of anticancer drug candidates, tantamount to that obtained from animal xenograft studies. Unlike 2D cancer cell cultures, 3D-models take into account the influence of the tumour microenvironment and the location dependence of drug effects and accumulation. We exemplified this by comparison of the effects of two new dual-mode anticancer agents, Troxbam and Troxham, and their monomodal congeners SAHA (suberoylanilide hydroxamic acid) and CA-4 (combretastatin A-4). We assessed the growth of MCTS of HCT116^{wt} human colon carcinoma cells exposed to these compounds, as well as the spatial distribution of dead HCT116^{wt} cells in these MCTS. Also, fluorescence imaging of live and fixed MCTS was used to assess the type of cellular death induced by test compounds. Furthermore, an innovative perfusion bioreactor system was used to grow microtumours in the presence or absence of test compounds. Both new investigational compounds led to significant reductions of the size of such MCTS and also of corresponding in vitro microtumours by inducing caspase-9 dependent apoptosis and elevated levels of reactive oxygen species. 3D multicellular tumour spheroids are easy to grow and employ for compound tests in the familiar well-plate set-up. Together with 3D microtumours grown at scaffolds in continuously perfused bioreactors they allow to study, early on in the course of drug evaluations, the communication of tumour cells with their microenvironment to an extent hitherto available only in animal experiments.

Keywords Cancer research · Colon cancer · 3D cell culture · Tumour spheroids · Microtumours · HDACi

Abbreviations

CA-4	Combretastatin A-4
DCFH-DA	2´,7´-Dichlorodihydrofluorescin diactetate acetyl ester
DMEM	Dulbeccos modified eagle medium
ECM	Extracellular matrix
HCT	Human colorectal tumour
HDAC	Histone deacetylase
HDACi	HDAC inhibitor
IC_{50}	Half maximum inhibitory concentration
LDH	Lactate dehydrogenase
MCTS	Multicellular tumour spheroids
NID	New investigational drugs
PI	Propidium iodide
ROS	Reactive oxygen species
SAHA	Suberoylanilide hydroxamic acid
SD	Standard deviation

✉ Sofia I. Bär
sofia.baer@uni-bayreuth.de

[1] Organic Chemistry Laboratory, University of Bayreuth, Universitätsstraße 30, 95447 Bayreuth, Germany

Introduction

Assays employing 2D monolayer cultures of adherent cancer cells are customarily used at early stages of drug development due to their little cost and high throughput screenability, in spite of their drawbacks [1]. A key disadvantage is that 2D tumour cell models disregard most of the many physiological ramifications of in vivo tumours, such as alterations in their signal transduction, gene expression, supply of nutrients and oxygen, and in their accumulation of drugs when compared with non-malignant cells and tissues [1–3]. However, the main causative factor for these

Published online: 07 July 2022

shortcomings, the anchorage dependence of 2D cell cultures, can be circumvented by anchorage-independent 3D cell growth models. While cells cultured in adherent 2D systems typically react by anoikis (apoptosis induced by cell-detachment) when detached, 3D cell models behave more like real in vivo tumours [4]. They are also devoid of other intrinsic limitations of 2D monolayer cell models and thus should be given preference for preclinical screening of new investigational drugs (NID) [5]. 3D cell models are even more appropriate than 2D cell models for an early tentative dose finding, since a reduced efficacy of test compounds in 3D cell models was frequently reported, mirroring the physiological barriers of drug distribution in vivo. HCT116 colon cancer cells, for instance, were found more resistant to certain anticancer drugs when cultured in 3D *vs.* 2D cell models [6]. Therefore, 3D cell culture models are clearly preferable over the conventional 2D models, given a reasonable pricing, ease of application, and the possibility of high throughput methods.

The development of 3D cell culture applications gathered momentum in recent years [7]. Publications and patents on this topic have increased exponentially since the beginning of the twenty-first century. In the year 2021 alone, 2340 articles on "3D cell culture" were listed by the PubMed database whereas one decade before the number of articles was a mere 838. Despite their many advantages over established 2D assays, 3D models are still rarely used at early stages of drug discovery, probably due to high effort and high cost. A comparatively simple and affordable method for investigating the effects of potentially active compounds on a 3D cell culture model is presented here. In addition to analysing the growth of MCTS under the influence of test compounds, other markers commonly used in basic research on new drugs are also transferred from the 2D to the 3D cell culture model in this work.

3D cell models are a potential alternative to animal models, the indispensability of which is rather contentious. The societal pressure to do away with animal studies is building up fast, and alternatives are sought-after [8]. A current topic in cancer cell research is the development of more accurate and innovative in vitro 3D cell models. The combination of perfusion bioreactor systems with established porous chitosan-hyaluronic acid scaffolds is such an innovative approach. It allows the growth of 3D MCTS as it mimics the extracellular matrix (ECM) of a typical tumour microenvironment [9].

3D cell culture models have been described several times in recent years yet have hardly been used for the actual investigation of NID. In this study we used an anchorage independent 3D cell culture model for an assessment of the effects of two multimodal NID, Troxbam and Troxham, in comparison to the related known monomodal anticancer drugs CA-4 and SAHA (SI Fig. 1).

Materials and methods

Test compounds and stock solutions

Test compounds were dissolved in DMSO with a concentration of 10 mM and stored at -23 °C. Combretastatin A-4 and SAHA were purchased from TCI chemicals, Troxbam and Troxham were prepared according to literature [10].

Cell culture

HCT116^{wt} colon carcinoma cells (DSMZ ACC 581) were cultured in DMEM (Dulbeccos Modified Eagle Medium, ThermoFisher), supplemented with 10% fetal bovine serum (Biochrom) and 1% ZellShield® (MinervaBiolabs). Unless noted otherwise, cells were maintained at 37 °C, 95% humidity and 5% CO_2. Cells were serially passaged and only mycoplasma free cultures were used.

MCTS

The MCTS were generated using an adapted hanging drop method [11] which was further improved for generating homogeneous MCTS. Briefly, drops containing 500 cells per 20 µL were placed on the inside of the lid of a petri dish filled with phosphate buffered saline (PBS). After an incubation period of 48 h the suspension was transferred into 1.5% agarose coated wells of a 24-well plate, transferring one drop per well in 1 mL DMEM. The spheroids thus prepared were allowed to grow for a further 5 days. This is a simple, efficient and reliable method for generating homogeneous MCTS of HCT116 colon cancer cells with a high success rate. For compound treatment 10.1 µL of 100-fold predilutions of compounds per well containing 1 mL DMEM were added 72 h before completion of the 7 d growth period. For a meaningful comparison of the 2D cell culture results and the results of the new 3D models, the MCTS were each treated with the IC_{50} (72 h) determined in 2D assays [10].

MCTS growth quantification

The growth of MCTS was documented using an inverted transmission light microscope. The size of the MCTS was determined by measuring two orthogonal diameters (d_1 and d_2) per MCTS and calculating the volume using the following formula $V = \frac{4}{3}\pi \cdot r3$ with $r = \frac{(0.5*(d_1+d_2))}{2}$ [11].

Analysis of compound induced cytotoxicity

For visualising dead cells within MCTS, spheroids were stained for 30 min under cell culture conditions with 6 µg/mL propidium iodide (PI) which stains dead cells

only because of their permeabilised cell membranes [12]. MCTS were then rinsed with PBS to remove excess PI. Immediately thereafter, brightfield and fluorescence images were acquired by inverted fluorescence microscopy using a Zeiss Axiovert 135 fluorescence microscope and AxioVision software. ImageJ was used for further image processing.

Analysis of compound induced caspase 9 expression

For visualisation of caspase 9 expression in MCTS, spheroids were rinsed with PBS after 7 d of growth including a 72 h treatment with IC_{50} of test compounds [10]. They were fixed in 3.7% formaldehyde in PBS for 2 h at room temperature, followed by permeabilisation with 0.3% Triton X-100 in 1% bovine serum albumin (BSA) in PBS for a further 2 h. After rinsing with PBS, MCTS were incubated with primary antibody (Caspase 9 mouse anti-human mAb, CellSignaling, 1:300 in 1% BSA in PBS) for 16 h at 4 °C or for 2 h at 37 °C. Spheroids were rinsed once with PBS before incubation with secondary antibody (AlexaFluor 555 goat anti-mouse, ThermoFisher, 1:250 in 1% BSA in PBS) for 2 h at room temperature in the dark. After rinsing with PBS, the nuclei were stained with 1 µg/mL DAPI in PBS for 10 min at room temperature in the dark and rinsed once again, before mounting in VECTASHIELD® PLUS Antifade Mounting Medium (VektorLaboratories). Confocal fluorescence microscopy images were acquired at ex/em 555/565 nm as well as ex/em 350–380/450-460 nm and further processed using ImageJ, as well as for obtaining surface plots.

LDH assay [13]

To measure the tendency of substances to induce necrosis, the LDH content of the media was determined which is directly linked to necrosis. After an incubation period of 7 d, 50 µL of medium supernatant of the spheroid containing wells were transferred to a 96-well plate. As a positive control, 100 µL per well of lysis solution (9% Triton-X100 in Millipore H_2O) were added to untreated spheroids and incubated for 45 min to maintain maximum LDH release. Then 50 µL of each positive control well were also transferred into the 96-well plate. 50 µL of LDH assay buffer (223 mg of 2-*p*-iodophenyl-3-*p*-nitrophenyl-5-phenyl tetrazolium chloride, 57 mg of *N*-methylphenazonium methyl sulfate, 575 mg of *N*-adenine dinucleotide, 3.2 g of lactic acid in 480 mL 200 mM Tris–Cl, pH 8.0) were added per well. The 96-well plate was incubated in the dark for 10–30 min at room temperature. Then 50 µL of stop solution (1 M acetic acid) were added per well and the absorbance was measured at 490 nm. The mean value of background wells was subtracted from negative controls and test wells. Finally, the percentage of LDH release was calculated, setting the maximum LDH release at 100% and the negative control at 0% release. Means and SD were calculated from at least four independent experiments.

Analysis of the compound induced ROS generation

To monitor formation of reactive oxygen species (ROS) inside the MCTS, the 2',7'-dichlorodihydrofluorescin diactetate acetyl ester (DCFH-DA), which is membrane-pervasive and per se non fluorescent, was used. After deactetylation of DCFH-DA by cellular esterases to DCFH it is oxidised by intracellular ROS to DCF which is strongly fluorescent [14]. After treatment of MCTS with IC_{50} concentrations of test compounds, DCFA-DA was added into the medium to obtain a final concentration of 20 mM, followed by an incubation for 1 h at 37 °C. The spheroids were rinsed with PBS to remove excess dye and images were immediately acquired using an inverted Zeiss Axiovert 135 fluorescence microscope with AxioVision software. For further image processing ImageJ software was used.

Generation of in vitro microtumours

Using an innovative perfusion bioreactor system (SI Fig. 2) 3D microtumours were generated in vitro. The system enabled the growth of colon cancer microtumours whereby an exchange of oxygen and nutrients over a longer period of time was provided without having to intervene in the system. Replacing the in vivo tumour microenvironment with 3D porous scaffolds allows for the generation of reliable in vitro 3D tumour models for preclinical studies of NID [9].

In vitro microtumours were generated by means of a perfusion bioreactor system (BioMedCenter Innovations). Using Chitosan-Hyaluronic acid-based scaffolds, as established in the field of scaffold-supported 3D cell culture [9, 15, 16], the growth of colon cancer microtumours under influence of test compounds was monitored over a period of 28 d. Scaffolds were prepared according to literature [9, 15, 16]. Freeze-dried and gamma-sterilised scaffolds were placed in 24-well plates, covered with 1.5 mL DMEM (ThermoFisher), supplemented with 10% fetal bovine serum (Biochrom) and 1% ZellShield® (MinervaBiolabs), and incubated under standard cell culture conditions. The medium was replaced every 60 min, five times. Two days before seeding the scaffolds, cell pellets containing 2 10^6 cells were generated and cultivated under cell culture conditions with regular medium change. The medium-saturated scaffolds were each seeded with a pre-incubated cell pellet and incubated overnight to ensure cell attachment. The perfusion bioreactor system was filled with 150 mL DMEM (ThermoFisher), supplemented with 10% fetal bovine serum (Biochrom) and 1% ZellShield®

(MinervaBiolabs) and the seeded scaffolds were placed inside the flow chamber, followed by a perfusion period of 28 d under standard cell culture conditions. The engineered flow ensured the right nutrient supply for the growing microtumours, while the system was operated with a peristaltic pump (Masterflex L/S Digital 7551–30, Cole Parmer, flowrate 1 mL/min) providing a continuous flow, a schematic graphic representation is shown in the supporting information (SI Fig. 2). The test compounds were added via the medium at day 21 of the incubation period. After a total incubation period of 28 days the scaffolds were eventually removed and grown microtumours were measured and weighed.

Statistics

Statistical data analysis was done using GraphPad Prism software (GraphPad Software, Inc.). Data is presented as mean ± standard error of the mean if not indicated otherwise. For determination of statistical significance one-way ANOVA coupled with Tukey's post hoc tests was used, whereas $P < 0.05$ were considered to indicate a statistically significant difference. Numbers of repetitions per experiment as indicated in the respective captions.

Graphics

For creation of the artwork the following programs were used; Adobe Illustrator, ChemDraw Professional 15.0, GIMP 2.10.12, Microsoft Excel 16.0 and Power Point 16.0.

Results and discussion

Generation of homogeneous MCTS of HCT116 colon cancer cells

An optimal cell number for the generation of HCT116 MCTS was determined to be 500 cells. These were incubated using the hanging drop method for 2 d before being transferred to an agarose-coated 24-well plate. The agar coating of the standard 24-well plates served to avoid the need for costly low attachment plates. The growth of the MCTS was documented over a period of seven days (SI Fig. 3). During this period, a linear growth process was observed. The resulting spheroids had a diameter of > 500 µm which is considered as a critical size to closely mimic various properties of solid human tumours [17]. This model is capable to mimic tumour associated ECM interactions as well as gradients of gases, nutrients, pH and especially the delivery of potential drugs under compound treatment [1, 18].

Influence of compounds on MCTS growth

First, the growth of MCTS under the influence of the test substances was observed. For treatment, the published IC_{50} values of the drug candidates Troxbam (0.9 µM) and Troxham (0.6 µM) as well as of their lead compounds SAHA (0.9 µM) and CA-4 (0.0026 µM) were used [10]. Right here, the first difference to the established 2D system became apparent. As shown in Fig. 1, unlike the other substances investigated in the 3D system, the established vascular-disrupting agent CA-4 did not lead to a significant reduction in cell growth when applied at its IC_{50} for 72 h. Despite the

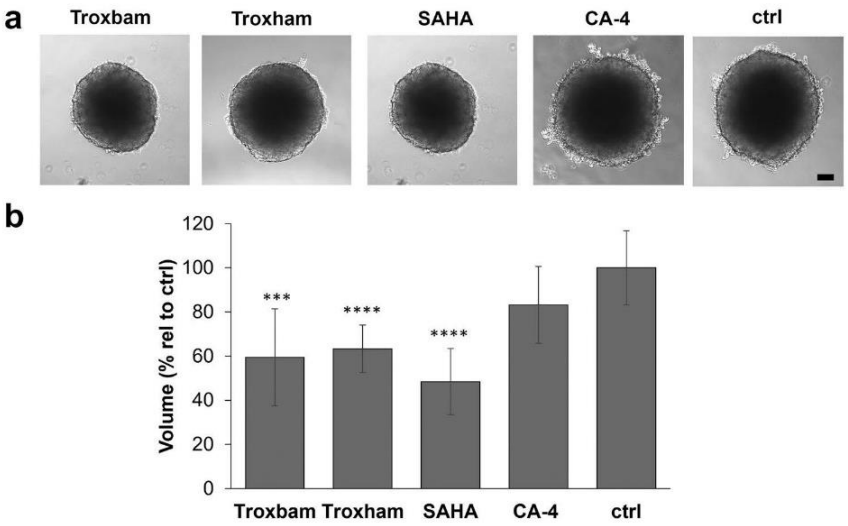

Fig. 1 Size and volume of HCT116.^{wt} colon carcinoma MCTS after 7 d of growth with exposure to test compounds at their IC_{50} or the negative control DMSO over the last 72 h. **a** Representative images of treated MCTS, brightfield images acquired using inverted microscopy, 100-fold magnification; scale bar represents 100 µm. **b** MCTS volumes after 3 d treatment with IC_{50} of test compounds, SAHA or CA-4, related to corresponding DMSO treated controls (ctrl). Data represents the means ± SD percentage related to untreated control set to 100%. SD of n = 18, P*** < 0.001, **** P < 0.0001

known higher resistance of 3D cell models to antitumoural compounds, Troxbam and Troxham reduced the growth of MCTS in the same order of magnitude as the established HDACi SAHA which indicates them as potential antitumoural drug candidates.

Substance induced cytotoxicity in MCTS

The cytotoxic effects of the test compounds were assessed by selectively staining the dead cells within treated MCTS with propidium iodiode (PI). As shown in Fig. 2, treatment of HCT116 MCTS with the new investigational compound Troxbam led to a distinct accumulation of red, PI-positive and thus dead cancer cells. Troxham, when applied at the same concentration range, gave a less pronounced effect, while IC_{50} of SAHA gave rise to a larger core of dead cancer cells within the respective MCTS when compared with the effect of Troxbam. In contrast, the vascular-disrupting agent CA-4 had a merely marginal cytotoxic effect on HCT116 MCTS which is in keeping with its weak growth-retarding effect as shown in Fig. 2. Besides their MCTS growth-inhibiting effect, the compounds led to a significant increase in the proportion of PI-positive and thus dead cells in the remaining spheroids, predominantly in the centre of the MCTS. This is proof that the compounds also permeate the inner regions of the spheroids. The obviously higher susceptibility of the more centreward cells is likely the result of an accumulation of metabolic products, a drop in the pH value, and a depletion of nutrients and oxygen in the core of the MCTS. A lower pH in the centre of cancer spheroids was previously reported [18].

For an assessment of a possible necrosis induction by the test compounds, the medium of the MCTS was examined for LDH after substance treatment. As shown in Fig. 3a, none of the tested compounds led to a significant enhancement of LDH levels secreted into the media. Elevated LDH release is typically associated with unselective cytotoxicity and necrosis [13]. Considering the significant growth

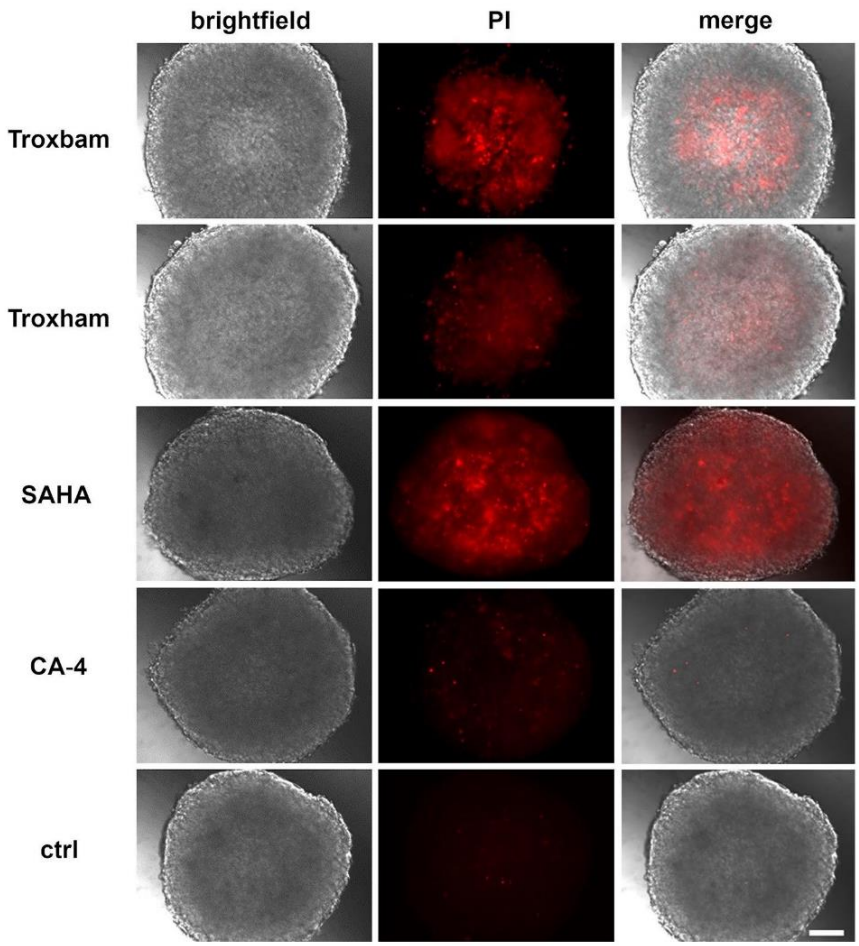

Fig. 2 Images of PI stained MCTS, after treatment for 72 h with IC_{50} of Troxbam and Troxham, respectively SAHA and CA-4 as positive controls, and corresponding amounts of DMSO as negative control. Brightfield and fluorescence images were acquired using inverted fluorescence microscopy. The scale bar corresponds to 100 µm. The images shown are representative of three independent experiments

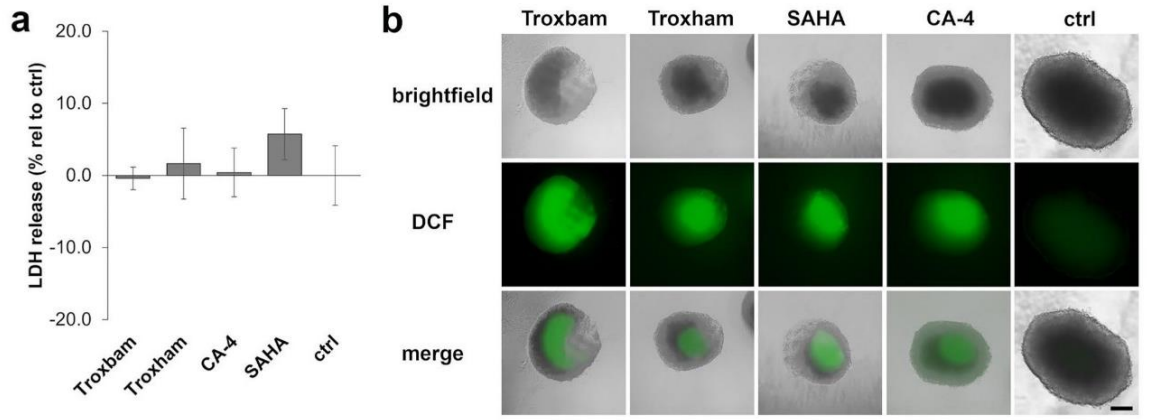

Fig. 3 **a** LDH release by HCT116 colon cancer MCTS after treatment with IC_{50} concentrations of test compounds for 3 d. Data are presented as the LDH release relative to controls, with their basal LDH levels set to 0% and the maximum LDH release, achieved by treatment with lysis solution for 1 h, set to 100%. Data represents the mean ± SD of n = 4. **b** ROS levels in MCTS treated for 3 d with IC_{50} concentrations of test compounds, observed as DCFH fluorescence by inverted fluorescence microscopy. Images shown are representative of four independent experiments. 100-fold magnification, scale bar corresponds to 100 µm

reduction of treated MCTS and the high percentage of their PI-positive fraction, an apoptotic mechanism of cell death can arguably be assumed. A rise in reactive oxygen species is frequently observed when treating cancer cells with chemotherapeutic agents. The formation of ROS within MCTS treated with the test compounds was investigated using the membrane-pervasive pre-fluorescent DCFH-DA. All tested compounds led to a distinct enhancement of ROS levels in MCTS, with the DCFH fluorescence intensity being strongest in the middle of the spheroids (Fig. 3b). Treatment with Troxbam resulted in the highest ROS levels, yet only with a slight edge on Troxham, SAHA and CA-4. Increasing cellular ROS levels in cancer cells is considered an interesting approach to circumvent resistance and thus achieve more effective killing of cancer cells [19]. The increase in ROS levels in the MCTS is associated with the induction of apoptosis. The strong increase in ROS levels upon treatment with Troxbam, concomitant with a comparatively low caspase 9 expression, suggests caspase 8 associated apoptosis [20]. Caspase 8 associated apoptosis in conjunction with increased ROS levels in HCT116 colon cancer cells has been described previously [20].

Substance induced expression of apoptosis associated caspase 9 in MCTS

The expression of caspase 9 upon treatment with the test compounds was investigated by immunofluorescence staining using a primary antibody for caspase 9 (mouse anti-human mAb) followed by a secondary antibody (AlexaFluor 555 goat anti-mouse). As shown in Fig. 4, an overexpression of caspase 9 was particularly pronounced in the outer rim of the treated MCTS. It also shows the average fluorescence distribution across the entire MCTS diameter for the individual test compounds. The overall strongest induction of caspase 9 expression was observed after treatment with Troxham, closely followed by SAHA. CA-4 caused only about half of this effect, while Troxbam led to a comparatively small increase in caspase 9 expression, which was, however, still twice as high as in untreated control MCTS controls. A certain basic level of caspase 9 expression is typical even of the untreated controls [21]. An overexpression of caspase 9 is a benchmark of apoptosis. When observed upon treatment with chemical compounds, elevated levels of caspase 9 expression are an indication for them being inducers of apoptosis [22]. The comparatively weak expression of caspase 9 upon treatment with Troxbam suggests the activation of a further apoptosis-inducing mechanism, considering the distinct increase in the PI-positive percentage of cells within the MCTS (*cf.* Fig. 2) and the fact that there was no increase of LDH levels (*cf.* Fig. 3a).

Substance induced mass reduction of in vitro 3D HCT116 microtumours

The effects of Troxbam and Troxham on the growth and persistence of 3D HCT116 microtumours were examined by means of an innovative in vitro bioreactor perfusion system. The constant perfusion of the scaffold with cell culture medium and oxygen allowed for the cells to be kept and supplied in a closed system, mimicking the conditions of in vivo studies with xenografted animals more closely than tests on MCTS in agarose-coated wells. Both new dual-mode HDAC inhibitors Troxbam and Troxham led to significant reductions of size and weight of preformed microtumours (Fig. 5).

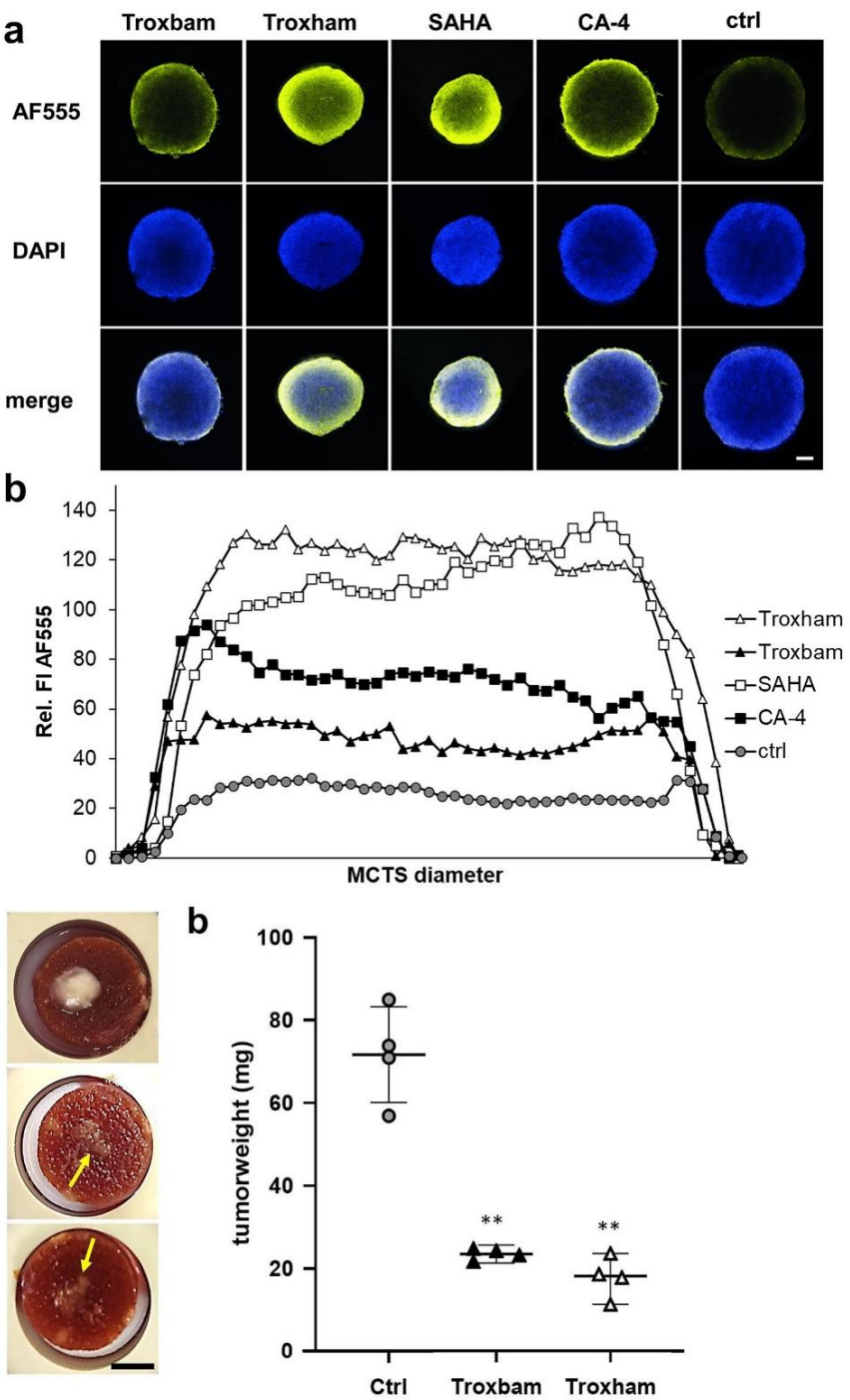

Fig. 4 Monitoring caspase 9 expression in MCTS after substance treatment for 3 d. **a** Visualisation of caspase 9 expression in MCTS by immunofluorescence staining (AF555) and of nuclei by DAPI fluorescence staining. Images are representative of at least three independent experiments, acquired by confocal fluorescence microscopy, 100-fold magnification. Scale bar represents 100 µm. **b** Relative fluorescence intensity (FI) of AF555, representative of caspase 9 expression, plotted across the diameter of MCTS

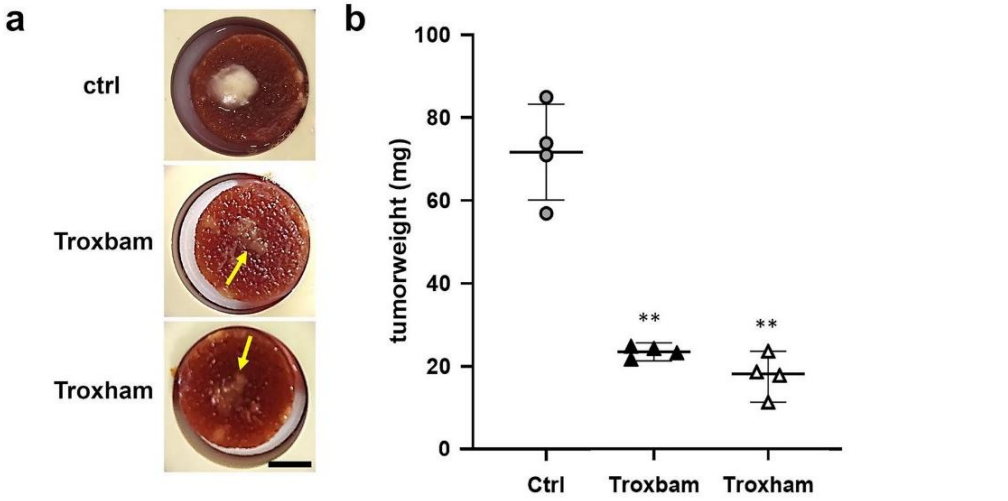

Fig. 5 Size and weight of HCT116 colon cancer microtumours after a growth period of 28 days in a bioreactor perfusion system; substance treatment (2 IC_{50}) was conducted on day 21. **a** Representative images of microtumours, grown on chitosan-hyaluronic acid scaffold. Scale bar corresponds 0.5 cm. Microtumours after substance treatment are marked with arrows. **b** Final tumour masses after total growth period of 28 days. Controls represent tumours treated with corresponding amounts of DMSO at day 21. Mean standard deviations are shown, data represent four measurements with the means ± SD. SD of n = 4, **P < 0.001

Conclusion

The consideration of the tumour microenvironment has been identified as an important aspect in the in vitro evaluation of new investigational anticancer drugs. While 3D multicellular tumour spheroids are easy to grow and apply for compound tests in the familiar well-plate set-up, 3D microtumours grown at scaffolds in continuously perfused bioreactors come even closer to the quality of information hitherto obtained only from in vivo experiments. In the long run, they might even replace a good deal of them, concerning the elucidation of drug induced communication of tumour cells among themselves and with the tissues they are imbedded in. 3D-based cell assays are likely the future in cancer drug screening, offering far more possibilities than the established 2D assays.

The dual-mode HDAC inhibitors Troxbam and Troxham, which we used to put the new 3D cellular assays through their paces, are interesting in their own right, even as a possible alternative to the clinically established SAHA. They led to a comparable reduction in MCTS as well as microtumour mass by inducing apoptosis in cancer cells, associated with overexpression of caspase 9 and enhanced ROS levels.

Supplementary Information The online version contains supplementary material available at https://doi.org/10.1007/s10637-022-01280-0.

Acknowledgements We thank the BioMed Center Innovation gGmbH for the good cooperation and the exchange of experiences with the bioreactor perfusion system, with a special gratitude to Florian Gaudig.

Authors' contributions All authors contributed to the study conception and design. Conceptualisation: Sofia I. Bär; Methodology: Sofia I. Bär; Chemical synthesis of test compounds: Bernhard Biersack; Formal analysis and investigation: Sofia I. Bär; Writing—original draft preparation: Sofia I. Bär; Writing—review and editing: Sofia I. Bär, Rainer Schobert; Supervision and validation: Rainer Schobert.

Funding Open Access funding enabled and organized by Projekt DEAL. The authors declare that no funds, grants, or other support were received during the preparation of this manuscript.

Data availability The datasets generated during and/or analysed during the current study are available from the corresponding author on reasonable request.

Declarations

Competing interests The authors declare no competing interests.

Ethical approval and consent to participate Not applicable.

Consent to publish All authors agree to the publication of the present work.

Competing interest The authors have no relevant financial or non-financial interests to disclose.

References

1. Chaicharoenaudomrung N, Kunhorm P, Noisa P (2019) Three-dimensional cell culture systems as an in vitro platform for cancer and stem cell modeling. World J Stem Cells 11:1065–1083. https://doi.org/10.4252/wjsc.v11.i12.1065
2. Lovitt CJ, Shelper TB, Avery VM (2014) Advanced cell culture techniques for cancer drug discovery. Biology 3:345–367. https://doi.org/10.3390/biology3020345
3. Rodrigues J, Heinrich MA, Teixeira LM, Prakash J (2021) 3D In Vitro Model Revolution: Unveiling Tumor-Stroma Interactions. Trends Cancer 7:249–264. https://doi.org/10.1016/j.trecan.2020.10.009
4. Guadamillas MC, Cerezo A, Del Pozo MA (2011) Overcoming anoikis—pathways to anchorage-independent growth in cancer. J Cell Sci 124:3189–3197. https://doi.org/10.1242/jcs.072165
5. Thoma CR, Zimmermann M, Agarkova I, Kelm JM, Krek W (2014) 3D cell culture systems modeling tumor growth determinants in cancer target discovery. Adv Drug Deliv Rev 69:29–41. https://doi.org/10.1016/j.addr.2014.03.001
6. Karlsson H, Fryknäs M, Larsson R, Nygren P (2012) Loss of cancer drug activity in colon cancer HCT-116 cells during spheroid formation in a new 3-D spheroid cell culture system. Exp Cell Res 318:1577–1585. https://doi.org/10.1016/j.yexcr.2012.03.026
7. Ravi M, Paramesh V, Kaviya SR, Anuradha E, Solomon FDP (2015) 3D cell culture systems: advantages and applications. J Cell Physiol 230:16–26. https://doi.org/10.1002/jcp.24683
8. Bédard P, Gauvin S, Ferland K, Caneparo C, Pellerin È, Chabaud S, Bolduc S (2020) Innovative human three-dimensional tissue-engineered models as an alternative to animal testing. Bioengineering 7. https://doi.org/10.3390/bioengineering7030115
9. Florczyk SJ, Wang K, Jana S, Wood DL, Sytsma SK, Sham J, Kievit FM, Zhang M (2013) Porous chitosan-hyaluronic acid scaffolds as a mimic of glioblastoma microenvironment ECM. Biomaterials 34:10143–10150. https://doi.org/10.1016/j.biomaterials.2013.09.034
10. Schmitt F, Gosch LC, Dittmer A, Rothemund M, Mueller T, Schobert R, Biersack B, Volkamer A, Höpfner M (2019) Oxazole-bridged combretastatin A-4 derivatives with tethered hydroxamic acids: structure activity relations of new inhibitors of HDAC and/or tubulin function. Int J Mol Sci 20. https://doi.org/10.3390/ijms20020383
11. Lobjois V, Frongia C, Jozan S, Truchet I, Valette A (2009) Cell cycle and apoptotic effects of SAHA are regulated by the cellular microenvironment in HCT116 multicellular tumour spheroids. Eur J Cancer 45:2402–2411. https://doi.org/10.1016/j.ejca.2009.05.026
12. Zhang L, Mizumoto K, Sato N, Ogawa T, Kusumoto M, Niiyama H, Tanaka M (1999) Quantitative determination of apoptotic death in cultured human pancreatic cancer cells by propidium iodide

and digitonin. Cancer Lett 142:129–137. https://doi.org/10.1016/S0304-3835(99)00107-X
13. Chan FK, Moriwaki K. De rosa MJ (2013) Detection of necrosis by release of lactate dehydrogenase activity. Methods Mol Biol 979:65–70. https://doi.org/10.1007/978-1-62703-290-2_7
14. Rastogi RP, Singh SP, Häder D-P, Sinha RP (2010) Detection of reactive oxygen species (ROS) by the oxidant-sensing probe 2',7'-dichlorodihydrofluorescein diacetate in the cyanobacterium Anabaena variabilis PCC 7937. Biochem Biophys Res Commun 397:603–607. https://doi.org/10.1016/j.bbrc.2010.06.006
15. Huang Y, Seitz D, König F, Müller PE, Jansson V, Klar RM (2019) Induction of articular chondrogenesis by chitosan/hyaluronic-acid-based biomimetic matrices using human adipose-derived stem cells. Int J Mol Sci 20. https://doi.org/10.3390/ijms20184487
16. Huang Y, Seitz D, Chevalier Y, Müller PE, Jansson V, Klar RM (2020) Synergistic interaction of hTGF-β3 with hBMP-6 promotes articular cartilage formation in chitosan scaffolds with hADSCs: implications for regenerative medicine. BMC Biotechnol 20:48. https://doi.org/10.1186/s12896-020-00641-y
17. Nunes AS, Barros AS, Costa EC, Moreira AF, Correia IJ (2019) 3D tumor spheroids as in vitro models to mimic in vivo human solid tumors resistance to therapeutic drugs. Biotechnol Bioeng 116:206–226. https://doi.org/10.1002/bit.26845
18. Zagaynova EV, Druzhkova IN, Mishina NM, Ignatova NI, Dudenkova VV, Shirmanova MV (2017) Imaging of Intracellular pH in Tumor Spheroids Using Genetically Encoded Sensor SypHer2. Adv Exp Med Biol 1035:105–119. https://doi.org/10.1007/978-3-319-67358-5_7
19. Cui Q, Wang J-Q, Assaraf YG, Ren L, Gupta P, Wei L, Ashby CR, Yang D-H, Chen Z-S (2018) Modulating ROS to overcome multidrug resistance in cancer. Drug Resist Updat 41:1–25. https://doi.org/10.1016/j.drup.2018.11.001
20. Nishi K, Iwaihara Y, Tsunoda T, Doi K, Sakata T, Shirasawa S, Ishikura S (2017) ROS-induced cleavage of NHLRC2 by caspase-8 leads to apoptotic cell death in the HCT116 human colon cancer cell line. Cell Death Dis 8:3218. https://doi.org/10.1038/s41419-017-0006-7
21. Gomyo Y, Sasaki J, Branch C, Roth JA, Mukhopadhyay T (2004) 5-aza-2'-deoxycytidine upregulates caspase-9 expression cooperating with p53-induced apoptosis in human lung cancer cells. Oncogene 23:6779–6787. https://doi.org/10.1038/sj.onc.1207381
22. Drušković M, Šuput D, Milisav I (2006) Overexpression of Caspase-9 Triggers Its Activation and Apoptosis in Vitro. Croat Med J 47:832–840

SUPPORTING INFORMATION

3D cell cultures, as a surrogate for animal models, enhance the diagnostic value of preclinical *in vitro* investigations by adding information on the tumour microenvironment: a comparative study of new dual-mode HDAC inhibitors

Sofia I. Bär[1,*], Bernhard Biersack[1], and Rainer Schobert[1]

[1] Organic chemistry laboratory, University of Bayreuth, Universitätsstraße 30, D-95447 Bayreuth, Germany

* corresponding author; Sofia I. Bär, sofia.baer@uni-bayreuth.de, ORCID 0000-0002-8612-3516

Bernhard Biersack, ORCID 0000-0001-7305-346X

Rainer Schobert, ORCID 0000-0002-8413-4342

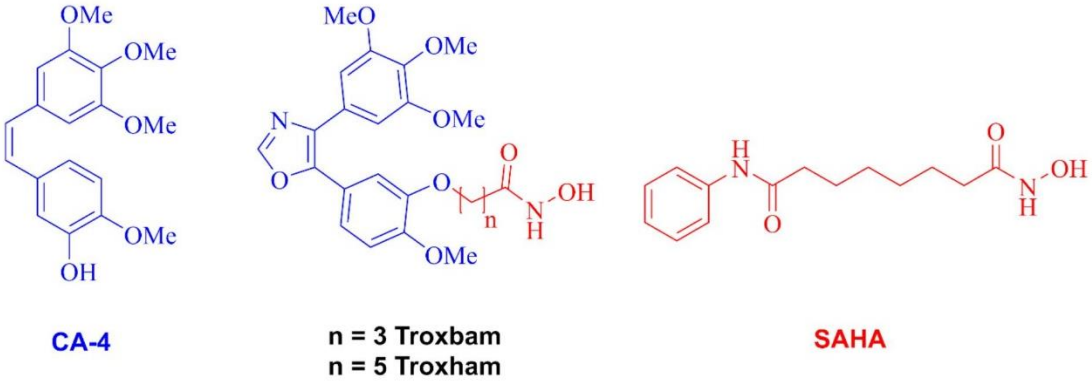

SI Fig. 1 Structures of the dual-mode HDAC inhibitors Troxbam and Troxham and their known constituent congeners CA-4 and SAHA

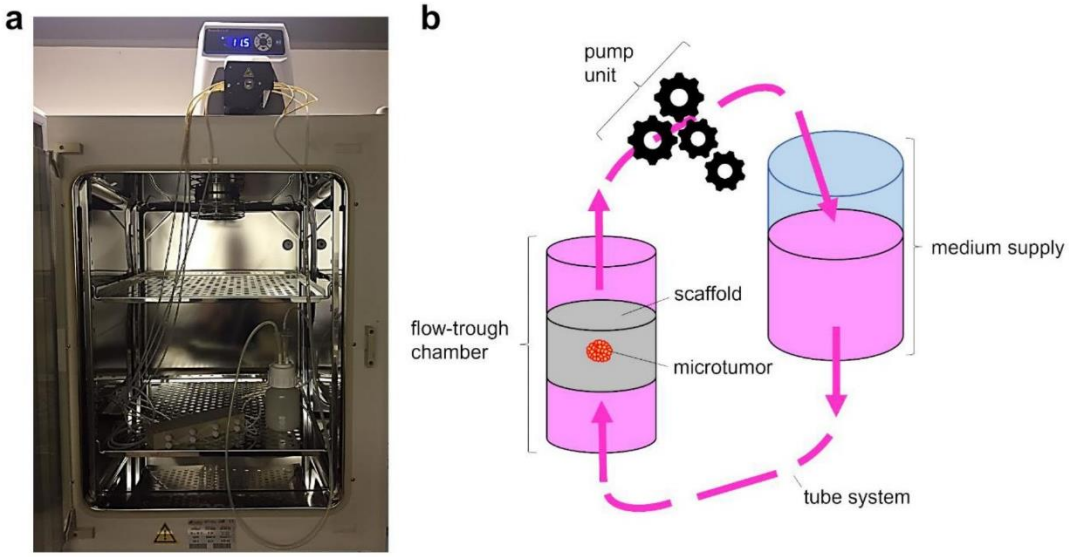

SI Fig. 2 Illustration of the bioreactor perfusion system used. a) Image of the bioreactor system, operated in a CO_2 incubator under sterile conditions. b) Schematic illustration of the perfusion bioreactor system

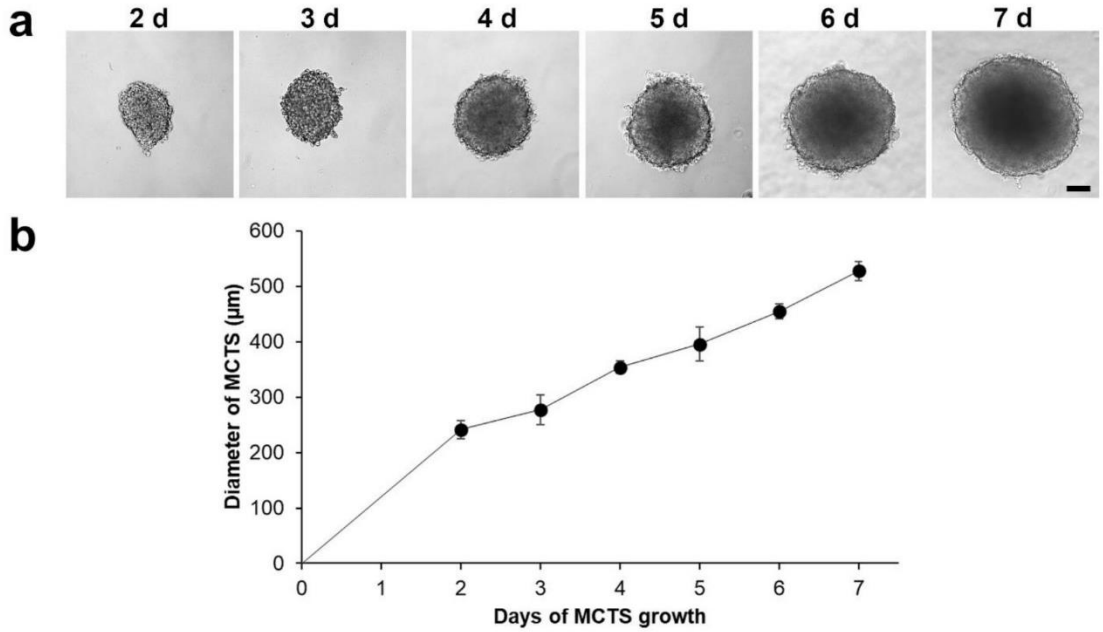

SI Fig. 3 Growth of HCT116 colon carcinoma MCTS over 7 days, measured by means of the spheroid diameter. a) Representative images of MCTS at each point of the measurement. Brightfield images were acquired using inverted microscopy. Scale bar corresponds to 100 µm. b) Graphical summary of the growth process of MCTS over a period of 7 days. Data represents mean ± SD of n = 8.

6 Danksagung

Mein besonderer Dank gilt meinem Doktorvater Prof. Dr. Rainer Schobert sowohl für die Ermöglichung dieser Arbeit als auch die jederzeit offene Tür für wissenschaftliche und persönliche Anliegen. Vielen Dank für das entgegengebrachte Vertrauen, den großen Forschungsfreiraum und die wissenschaftliche Entfaltungsmöglichkeit die Sie mir damit geboten haben.

Zudem möchte ich mich bei allen Personen bedanken, welche die im Rahmen dieser Arbeit untersuchten Substanzen synthetisiert und meine Arbeit damit erst ermöglicht haben. Besonders zahlreich vertreten waren hierbei die Substanzen von Dr. Bernhard Biersack, vielen Dank dafür! Auch bei allen weiteren Mitarbeitern des Lehrstuhls möchte ich mich für ihre Unterstützung während meiner Zeit, die ich dort verbringen durfte, bedanken. Namentlich erwähnen möchte ich hierbei Dr. Madeleine Gold, Dr. Matthias Rothemund, Laura Treiber, Manuel Schiefer und Franziska Gillsch, welche mir jederzeit für fachliche und organisatorische Fragen zur Verfügung standen. Mein Dank gilt auch all meinen Praktikanten und Praktikantinnen für ihr Interesse und Mitarbeit an meinem Thema, besonders erwähnt seien hierbei Natalie Oberhuber, Luisa Kober und Madlen Schatz.
Des Weiteren gilt mein Dank allen externen Kooperationspartnern für die gute Zusammenarbeit an zahlreichen Projekten. Hier möchte ich mich bei Prof. Dr. Olaf Stemmann bedanken, für die Möglichkeit der Benutzung verschiedener Geräte und Räumlichkeiten, besonders erwähnt sei hierbei Markus Herrmann - vielen Dank für die zahlreichen fachlichen und zwischenmenschlichen Gespräche und Ratschläge. Bei Prof. Dr. Gerrit Begemann und seinen Mitarbeitern bedanke ich mich für die Möglichkeit der Durchführung des *in vivo* Zebrafisch-Angiogenese Assays und der damit verbundenen Mitbenutzung der Geräte und Anlagen. Ebenso gilt mein Dank den Mitarbeitern der BioMed Center Innovation GmbH, Daniel Seitz und Florian Gaudig, für die gute Zusammenarbeit. Bei Prof Dr. Victor Brabec, Dr. Michael Fähling, Dr. Leonard Kaps, Rohan Pradhan und ihren Mitarbeitern bedanke ich mich für die gute Zusammenarbeit im Rahmen verschiedener Projekte. Besonders bedanken möchte ich mich bei Prof. Dr. Michael Höpfner und Dr. Bianca Nitzsche sowie ihren Mitarbeitern für die gute Zusammenarbeit und die Ermöglichung sowie die angenehme Atmosphäre meines Forschungsaufenthalts an der Charité.
Auch gilt mein Dank all jenen, welche mir mit Rat und Tat bei der Entstehung dieser Arbeit zur Seite standen und hier nicht namentlich erwähnt wurden.

Ein großes Dankeschön auch an alle meine Freunde welche mich während meines Studiums begleitet und unterstützt haben. Meinem Partner Moritz Röder gilt großer Dank für die Unterstützung und das stets offene Ohr für die vielen Diskussionen während meiner Promotion.

Zu guter Letzt, gilt mein besonderer Dank meiner Familie, auf welche ich mich immer verlassen kann und welche mich immer unterstützt – ohne euch wäre das nicht möglich gewesen.

7 Eidesstattliche Versicherungen und Erklärungen

(§ 8 Satz 2 Nr. 3 PromO Fakultät)

Hiermit versichere ich eidesstattlich, dass ich die Arbeit selbstständig verfasst und keine anderen als die von mir angegebenen Quellen und Hilfsmittel benutzt habe (vgl. Art. 64 Abs. 1 Satz 6 BayHSchG).

(§ 8 Satz 2 Nr. 3 PromO Fakultät)

Hiermit erkläre ich, dass ich die Dissertation nicht bereits zur Erlangung eines akademischen Grades eingereicht habe und dass ich nicht bereits diese oder eine gleichartige Doktorprüfung endgültig nicht bestanden habe.

(§ 8 Satz 2 Nr. 4 PromO Fakultät)

Hiermit erkläre ich, dass ich die Hilfe von gewerblichen Promotionsberatern bzw. – vermittlern oder ähnlichen Dienstleistern weder bisher in Anspruch genommen habe noch künftig in Anspruch nehmen werde.

(§ 8 Satz 2 Nr. 7 PromO Fakultät)

Hiermit erkläre ich mein Einverständnis, dass die elektronische Fassung der Dissertation unter Wahrung meiner Urheberrechte und des Datenschutzes einer gesonderten Überprüfung unterzogen werden kann.

(§ 8 Satz 2 Nr. 8 PromO Fakultät)

Hiermit erkläre ich mein Einverständnis, dass bei Verdacht wissenschaftlichen Fehlverhaltens Ermittlungen durch universitätsinterne Organe der wissenschaftlichen Selbstkontrolle stattfinden.

……

Ort, Datum Unterschrift (Sofia I. Bär)